



The  
University  
Of  
Sheffield.

NATIONAL NUCLEAR  
LABORATORY



# **The Effects of Lithium Nitrate on Highly Active Liquor in the Calcination Process**

**Robert Shaw**

**A Thesis Submitted to the Department of Materials  
Science and Engineering at the University of Sheffield  
for the Degree of Doctor of Engineering (EngD)**

**September 2014**

# Executive Summary

A major concern of the Health and Safety Executive (HSE) is the hazard surrounding the storage of high level liquid waste (HLLW). Targets have been put in place to encapsulate all of this waste in a borosilicate glass matrix as soon as possible through Sellafield's Waste Vitrification Plants (WVPs). The efficiency of a WVP is reduced by blockages which form in the off-gas system, causing the plant to be shut-down for significant periods of time. This thesis is focussed on understanding the chemistry and mechanisms by which dust is carried from the calciner to the off-gas system.

Lithium nitrate is currently used as a process aid to reduce the amount of dust carried over to the dust scrubber on WVP, however, the mechanisms by which it achieves this were not fully understood. The first series of experiments, therefore, were set up to determine the effects of lithium nitrate on the reactions of metal nitrates found in HLLW, at temperatures thought to be experienced in the calcination process (Chapter 5). The products formed from the reaction of the component nitrates found in the HLLW were also found to be significantly affected by both time and temperature. On timescales relevant to the calcination process, the reaction between Mg and Al nitrates, two of the most abundant HAL components, formed MgO and  $\gamma$ -Al<sub>2</sub>O<sub>3</sub> at 550 °C, *via* an unidentified Al containing intermediate. At longer reaction times, however, Mg<sub>a</sub>Al(OH)<sub>3+2a-c</sub>(NO<sub>3</sub>)<sub>c</sub>.xH<sub>2</sub>O was formed. On addition of LiNO<sub>3</sub>, MgAl<sub>2</sub>O<sub>4</sub> was the major reaction product, suggesting LiNO<sub>3</sub> acted as a molten salt.

The reaction between phosphomolybdic acid (H<sub>3</sub>PMoO<sub>12</sub>O<sub>40</sub>.xH<sub>2</sub>O, PMA) and zirconyl nitrate yielded Zr(MoO<sub>4</sub>)<sub>2</sub> (a primary component of the POG blockage material) above 350 °C, with no reaction occurring below this temperature. On addition of LiNO<sub>3</sub>, Li<sub>2</sub>Zr(MoO<sub>4</sub>)<sub>3</sub> was formed via an intermediate (Li<sub>2</sub>MoO<sub>4</sub>), which was isolated from the reaction at 350 °C. Reaction time had no significant effect on these reactions.

Experiments to determine the effects of LiNO<sub>3</sub> on the chemistry and dust generation properties of full Highly Active Liquor (HAL) simulants were carried out (Chapter 6). On freeze drying, Caesium phosphomolybdate (Cs<sub>3</sub>PMoO<sub>12</sub>O<sub>40</sub>, CPM), Mg<sub>3</sub>RE<sub>2</sub>(NO<sub>3</sub>)<sub>12</sub>.24H<sub>2</sub>O and Al(NO<sub>3</sub>)<sub>3</sub>.9H<sub>2</sub>O were identified as the crystalline products found in Blend HAL simulant, with Mg(NO<sub>3</sub>)<sub>2</sub>.6H<sub>2</sub>O also present in Magnox. After calcination for 10 minutes at 350 °C, Mg<sub>3</sub>RE<sub>2</sub>(NO<sub>3</sub>)<sub>12</sub>.24H<sub>2</sub>O, and Mg(NO<sub>3</sub>)<sub>2</sub>.6H<sub>2</sub>O in Magnox HAL simulant, were the only crystalline products remaining, with decomposition occurring between 380-400 °C. Poorly crystalline CeO<sub>2</sub> was formed above 450 °C. Addition of LiNO<sub>3</sub> to Blend HAL simulant resulted in formation of BaCeO<sub>3</sub> at 550 °C, again implying LiNO<sub>3</sub> acted as a molten salt.

Using the small scale calciner, dust and calcine samples of varying particle sizes were collected under a range of calcination conditions. During these experiments, it was found that low temperatures, the addition of  $\text{LiNO}_3$  and high feed rates resulted in a reduction in the normalised amount of dust generated. The mechanism by which this dust was formed appeared to occur first by the abrasive breakdown of larger calcine particles, which created the majority of the dust, followed by carry-over of the smallest calcine particles, making up a minor fraction of the dust.

Using a short simulant, the temperatures experienced by the calcine in the small scale calciner were determined (Chapter 7). These were found to be highly dependent on the particle size of the calcine, as only the outer surface of a calcine particle would have come into contact with the heated calciner tube.

To allow the collection of dust particles generated on the small scale calciner, which was not possible in historic studies, a dirt trap was designed and installed. Chapter 8 details the design specification along with installation and experimental issues encountered during this project. The commercial benefits of maintaining the capacity to produce calcine at lab scale and the impact this project has had on the calciner rig are also outlined.

The major outcomes of this project were the identification of a range of species present in the HAL simulant, both before and after calcination, the temperatures experienced in the calcination process and the mechanism by which the dust is created and carried to the off-gas system. These can be used to help model the processes which occur in the calcination process on WVPs and allow optimisation of set-points to minimise dust carry-over to the off-gas system, therefore reducing downtime. By carrying out further experiments on the VTR, the temperatures experienced on the full-scale process can be better determined.

# Acknowledgements

Firstly, I would like to express my thanks to the National Nuclear Laboratory (NNL) and University of Sheffield for allowing the use of their facilities during this project. My sincere gratitude also goes to Sellafield Ltd and the Engineering and Physical Science Research Council (EPSRC) for their financial support and provision of materials used throughout this project.

Without the support of my two supervisors, Professor Neil Hyatt and Dr Rick Short, the completion of this project would not have been possible. My sincere thanks, therefore, go to them for their patience, guidance and support. The input of Dr Paul Bingham, Carl Steel, Fiona Wright and Andrew Riley during project meetings was also highly appreciated. I would also like to express my gratitude to Cath Stephen for her assistance and guidance throughout the project.

My sincere gratitude goes to the NNL design, facilities, engineering and vitrification teams for their various supporting roles throughout the project. In particular I would like to thank Geoff Brown and Julian Roe for training me and helping me solve the issues encountered on the small scale calciner rig, from which most of the major issues during this project arose. I would also like to thank Dr Nik Reeves-McLaren and Ben Palmer for training me to use the helium pycnometer and X-ray diffractometers at the University of Sheffield. The efforts of David Apperley and Fraser Markwell from the University of Durham NMR service are also acknowledged.

My love and gratitude go to my parents and brother for their unwavering support during the course of this project. Without their patience and understanding, this project would not have been a success. Finally, I would like to dedicate this thesis to my fiancée, Louise O'Neill, and our daughter, Darcie Kate Shaw. They have inspired and pushed me through the difficult times experienced during this project.

# Table of Contents

	Page
<b>1. INTRODUCTION.....</b>	<b>1</b>
1.1. Issues with New Nuclear Build.....	1
1.2. The Arising of High Level Liquid Waste.....	1
1.3. Immobilisation of High Level Liquid Waste.....	2
1.4. Issues with the Sellafield Vitrification Process.....	3
<b>2. LITERATURE REVIEW.....</b>	<b>4</b>
2.1. Introduction .....	4
2.1.1. The Nuclear Reaction.....	4
2.1.2. Reactor Design.....	6
2.1.3. Spent Fuel Reprocessing.....	9
2.2. Nuclear Waste.....	9
2.2.1. Classification.....	9
2.2.1. Storage and Disposal.....	10
2.3. Vitrification.....	12
2.3.1. History of Vitrification.....	13
2.3.2. Processing.....	14
2.3.2.1. The Calciner.....	15
2.3.2.2. The Melter.....	16
2.3.2.3. Primary Off-Gas System.....	18
2.3.2.4. Decontamination and Storage.....	22
2.4. Current Problems and Blockages.....	23
2.5. Calciner Chemistry.....	26
2.5.1. Caesium Phosphomolybdate and Zirconium Molybdate Formation.....	26
2.5.2. Reactivity of Lithium.....	29

2.5.3. Nitrate Decomposition.....	32
2.5.4. Molten Salts.....	34
2.5.5. Ruthenium chemistry.....	36
2.5.6. Dust scrubber solids composition.....	40
2.5.7. VTR campaigns 4 and 5.....	41
2.5.8. The effects of temperature, waste oxide concentration and acidity.....	43
2.6. Chapter Summary.....	45
<b>3. EXPERIMENTAL METHODS.....</b>	<b>46</b>
3.1. Introduction.....	46
3.2. Materials.....	47
3.3. Sample Preparation.....	47
3.3.1. Calcination.....	50
3.3.2. Freeze Drying.....	51
3.3.3. Calcination of Freeze Dried Samples.....	52
3.4. Sample Nomenclature.....	53
3.5. Scanning Electron Microscopy.....	54
3.6. X-ray Diffraction.....	56
3.7. Thermogravimetric Analysis.....	58
3.8. <sup>7</sup> Li Magic Angle Spinning Nuclear Magnetic Resonance Spectroscopy .....	58
3.9. Helium Pycnometry.....	61
<b>4. INTRODUCTION TO THE SMALL SCALE CALCINER RIG..</b>	<b>63</b>
4.1. Introduction.....	63
4.2. Experimental.....	66
4.3. Small Scale Calciner Rig Design and Rebuild.....	68
4.3.1. Dirt Trap Design.....	68
4.3.2. Working on a Nuclear Licensed Site.....	71
4.3.3. Small Scale Calciner Re-build.....	77

4.3.3.1. Dirt trap Installation.....	77
4.3.3.2. Other Issues.....	78
4.3.4. Commissioning and Testing.....	80
4.3.5. Experimental Issues.....	81
4.3.5.1. Off-gas Fan and Rig Depression Issues.....	81
4.3.5.2. NO <sub>x</sub> Release Event.....	82
4.3.6. Original and Revised Timelines.....	83
<b>5. THE EFFECTS OF LITHIUM NITRATE ON SHORT SIMULANTS.....</b>	<b>85</b>
5.1. Introduction.....	85
5.2. Experimental.....	85
5.2.1. Calculating theoretical TGA results.....	86
5.3. Results and Discussion.....	88
5.3.1. Reactions between Aluminium Nitrate and Magnesium Nitrate.....	88
5.3.1.1. Lab scale experiments.....	88
5.3.1.1.1. AMN1 and AMN2.....	88
5.3.1.1.2. LMN1.....	93
5.3.1.1.3. LAN1.....	96
5.3.1.1.4. LAMN1.....	99
5.3.1.1.5. MIN1 and MIN2.....	103
5.3.1.1.6. AIN1 and AIN2.....	106
5.3.1.1.7. LAIN1.....	106
5.3.1.2. Freeze dryer experiments.....	114
5.3.1.2.1. AMN1.....	114
5.3.1.2.2. LMN1.....	119
5.3.1.2.3. LAMN1.....	122
5.3.1.3. Small scale calciner experiments.....	128
5.3.1.3.1. LMN1.....	128

5.3.1.3.2. LAMN1.....	130
5.3.1.4. Discussion.....	131
5.3.2. Reactions between Phosphomolybdic Acid and Zirconyl Nitrate.....	136
5.3.2.1. Lab scale experiments.....	136
5.3.2.1.1. PZN2 .....	136
5.3.2.1.2. LPN1 .....	139
5.3.2.1.3. LPZN1.....	142
5.3.2.2. Freeze dryer experiments.....	144
5.3.2.2.1. PZN2 .....	144
5.3.2.2.1. LPN1 .....	148
5.3.2.2.1. LPZN1.....	150
5.3.2.3. Small scale calciner experiments.....	156
5.3.2.3.1. PZN2 .....	156
5.3.2.3.2. LPN1 .....	158
5.3.2.4 Discussion.....	160
5.4. Conclusions.....	162
5.4.1. Reactions between Aluminium Nitrate and Magnesium Nitrate .....	162
5.4.2. Reactions between Phosphomolybdic Acid and Zirconyl Nitrate .....	163
5.4.3. Small Scale Calciner Experiments.....	163
5.5. Future Work.....	164
<b>6. THE EFFECTS OF LITHIUM NITRATE ON FULL HAL SIMULANTS.....</b>	<b>165</b>
6.1. Introduction.....	165
6.2. Experimental.....	166
6.2.1. Freeze dryer experiments.....	166
6.2.2. Small scale calciner experiments.....	166
6.2.2.1 Calculating the expected yield from the small scale calciner experiments.....	169



6.3. Results and Discussion.....	170
6.3.1. Freeze dryer experiments.....	170
6.3.1.1. WRW16-RLF.....	170
6.3.1.2. WRW16-RF.....	174
6.3.1.3. WRW17-RLF.....	178
6.3.1.4. WRW17-RF.....	183
6.3.2. Small scale calciner experiments.....	187
6.3.2.1. WRW17-RLF.....	187
6.3.2.1.1. Calcine Analysis.....	189
6.3.2.1.1.1. Effects of Temperature.....	189
6.3.2.1.1.2. Effects of Feed Rate .....	193
6.3.2.1.2. Dust Analysis.....	197
6.3.2.1.2.1. Effects of Temperature.....	197
6.3.2.1.2.2. Effects of Feed Rate .....	202
6.3.2.2. WRW17-RF.....	205
6.3.2.2.1. Calcine Analysis.....	206
6.3.2.2.1.1. Effects of Temperature.....	206
6.3.2.2.1.2. Effects of Feed Rate .....	212
6.3.2.2.2. Dust Analysis.....	215
6.3.2.2.2.1. Effects of Temperature.....	215
6.3.2.2.2.2. Effects of Feed Rate.....	224
6.3.2.3. WRW16-RLF.....	227
6.3.2.3.1. Calcine Analysis.....	228
6.3.2.3.1.1. Effects of Temperature.....	228
6.3.2.3.2. Dust Analysis.....	232
6.3.2.3.2.1. Effects of Temperature.....	232
6.3.3. Discussion.....	235
6.3.3.1. Freeze Dryer Experiments.....	235

6.3.3.2. Small Scale Calciner Experiments.....	238
6.3.3.2.1. The Effects of Lithium Nitrate.....	239
6.3.3.2.2. The Effects of Temperature.....	241
6.3.3.2.3. The Effects of Feed Rate.....	242
6.3.3.3. The mechanism of dust creation and breakdown of calcine.....	244
6.4. Conclusions.....	246
6.4.1. Freeze Dryer Experiments.....	246
6.4.1.1. Blended HAL Simulant (WRW16).....	246
6.4.1.2. Magnox HAL Simulant (WRW17).....	246
6.4.2. Small Scale Calcine Experiments.....	247
6.4.2.1. Calcine analysis.....	247
6.4.2.1.1 Effects of temperature.....	247
6.4.2.1.2 Effects of feed rate.....	247
6.4.2.1.3 Effects of LiNO <sub>3</sub> addition.....	247
6.3.2.1.4 Effects of simulant composition.....	247
6.4.2.2 Dust analysis.....	248
6.4.2.2.1 Effects of temperature.....	248
6.4.2.2.2 Effects of feed rate.....	248
6.4.2.2.3 Effects of LiNO <sub>3</sub> addition.....	248
6.3.2.2.4 Effects of simulant composition.....	248
6.4.2.3 Mechanism of dust carry-over.....	248
6.5. Future Work.....	249
<b>7. DETERMINATION OF TEMPERATURES EXPERIENCED IN THE CALCINATION PROCESS.....</b>	<b>251</b>
7.1. Introduction.....	251
7.2. Experimental.....	251
7.2.1. Freeze dryer experiments.....	252
7.2.2. Small scale calciner experiments.....	252

7.3. Results and Discussion.....	252
7.3.1. Freeze dryer experiments.....	252
7.3.2. Small scale calciner experiments.....	255
7.3.2.1. Calcine Analysis.....	256
7.3.2.2. Dust Analysis.....	260
7.3.3. Discussion.....	264
7.4. Conclusions.....	265
7.4.1 Temperature experienced in the calcination process.....	265
7.4.2 Dust generation in the small scale calciner.....	266
7.5. Future Work.....	266
7.5.1 Further freeze dryer experiments.....	266
7.5.2 Further small scale calciner experiments.....	266
7.5.3 VTR experimental proposal.....	266
<b>8. PROJECT IMPACT.....</b>	<b>269</b>
8.1. Introduction.....	269
8.2. Project Summary and Benefit to WVP.....	269
8.2.1. Simulant composition.....	269
8.2.2. The Effect of Lithium Nitrate Addition.....	270
8.2.3. Temperatures Experienced in the Calciner.....	270
8.2.4. Conceptual Model of Dust Generation.....	271
8.3. Benefits of the Small Scale Calciner Rig Rebuild to Sellafield Ltd.....	273
8.3.1. Future Plans for the Small Scale Calciner Rig.....	274
<b>9. REFERENCES.....</b>	<b>276</b>
<b>10. APPENDIX.....</b>	<b>288</b>

# List of Acronyms

AGR	Advanced Gas-Cooled Reactor
AVM	Atelier de Vitrification de Marcoule
BNFL	British Nuclear Fuels Ltd
BWR	Boiling Water Reactor
COSHH	Control of Substances Hazardous to Health
CPM	Caesium Phosphomolybdate
DEFRA	Department of Environmental, Farming and Rural Affairs
DSL	Dust Scrubber Liquor
DSRV	Dust Scrubber Recycle Vessel
DTA	Differential Thermal Analysis
EDS	Energy Dispersive Spectroscopy
EIM&T	Electrical Isolation, Maintenance and Testing
FINGAL	Fixation of Glass in Active Liquor
FREA	Facilities Register of Environmental Aspects
FWR	Facilities Work Request
HAL	Highly Active Liquor
HALES	Highly Active Liquor Evaporation and Storage
HARVEST	Highly Active Residue Vitrification Experimental Studies
HAST	Highly Active Storage Tank
HLLW	High Level Liquid Waste
HLW	High Level Waste
HSE	Health and Safety Executive
ICDD	International Centre for Diffraction Data
ICP-OES	Inductively Coupled Plasma Optical Emission Spectrometry
ILW	Intermediate Level Waste
ITC	Isolation Test Certificate
Li-Al-LDH	Lithium-Aluminium-Layered Double Hydroxide
LLW	Low Level Waste
LMR	Liquid Metal Cooled Reactor
LWR	Light Water Reactor
MAS	Magic Angle Spinning
Mg-Al-LDH	Magnesium-Aluminium-Layered Double Hydroxide
MSM	Master Slave Manipulator
NII	Nuclear Installations Inspectorate

NNL	National Nuclear Laboratory
NMR	Nuclear Magnetic Resonance
OCM	Operations Control Management
OI	Operating Instruction
OSHANS	On-line Safety and Health at NNL sites
PMA	Phosphomolybdic Acid
PMP	Plant Modification Proposal
PNNL	Pacific National Nuclear Laboratory
POCO	Post Operational Clean Out
POG	Primary Off-Gas
POW	Person of Work
PUREX	Plutonium Uranium Extraction
PWR	Pressurised Water Reactor
RA	Risk Assessment
RCVF	Recycle Constant Volume Feeder
RNN	Ruthenium Nitrosyl Nitrate
RPE	Respiratory Protective Equipment
SEM	Scanning Electron Microscopy
SQEP	Suitably Qualified and Experienced Personnel
SSOW	Safe System of Work
TGA	Thermogravimetric Analysis
VLLW	Very Low Level Waste
VTR	Vitrification Test Rig
WCA	Work Control Authorisation
WVP	Waste Vitrification Plant
XRD	X-ray Diffraction
ZMH	Zirconium Molybdate Hydrate

# 1. Introduction

## 1.1 Issues with New Nuclear Build

With the price of fossil fuels rising and the increasing concerns over CO<sub>2</sub> emissions contributing to global warming, the nuclear option is becoming more viable as a source for the production of electricity. The nuclear industry supplies approximately 15 % of the world electricity, and around 13.5 % of that in the UK as of 2008<sup>1</sup>. This number is falling in the UK, as most of the reactors were built 40-50 years ago, and are in the process of being decommissioned. The future for nuclear energy, however, looks bright, as proposals are being drawn up for new possible reactor sites in the UK, and the government are behind the advancement of nuclear technologies (BERR, 2008).

The major issue with the advancement of nuclear power is the production of nuclear waste. The waste is hazardous and must be contained in a suitable manner. It must be proved that both future and legacy waste can be treated, stored and disposed of in a suitable manner, in order to build public confidence in nuclear power. This will allow new build, and final disposal solutions, to progress with the backing of the public to fulfil future energy needs.

When HLW waste is in liquid form it is highly mobile, and therefore if released can be transported to the surrounding environment. As the waste is highly active, it also produces heat, causing the liquor to boil if not cooled. If a fault with the cooling system was to occur for an extended period of time, this could cause boiling of the liquor releasing radioactive gases to the atmosphere. These storage tanks are one of the greatest concerns of the Health and Safety Executive (HSE), hence the UK government, through the Nuclear Installations Inspectorate (NII), have put targets in place to reduce high level liquid waste (HLLW) stocks to set levels by 2015 (Bradshaw et al., 2007).

## 1.2 The Arising of High Level Liquid Waste

Nuclear fuel rods are comprised of UO<sub>2</sub>, of which approximately 5 % is <sup>235</sup>U and the remainder <sup>238</sup>U. When a uranium-235 atom fissions, it splits into two daughter products. Some of these daughter products poison the fuel, which causes fewer fission reactions to occur. These poisons reduce the efficiency of the reactor. Once the efficiency drops to an unviable level, after approximately three years, the fuel is removed from the core and replaced with new enriched fuel (IAEA, 2006).

---

<sup>1</sup> Taken from <http://www.world-nuclear.org>, 27<sup>th</sup> September 2009.

The spent fuel, which has been removed from the reactor, will have a composition of approximately 1 %  $^{235}\text{U}$ , 95 %  $^{238}\text{U}$ , 3 % fission products and 1 %  $^{239}\text{Pu}$ . After a period of cooling, this fuel is dissolved in nitric acid and reprocessed to recover the uranium and plutonium from the fuel using the PUREX process (World Nuclear Association, 2008). The remaining solution containing the fission products is classed as high level liquid waste and is concentrated and stored in underground tanks, which are internally cooled. At Sellafield, when the waste has been cooled for a sufficient period of time, it is transported to the waste vitrification plant (WVP) to be immobilised in glass.

### **1.3 Immobilisation of High Level Liquid Waste**

The HLLW is solidified by passing through a rotating kiln known as a calciner. This solid is mixed with borosilicate glass frit in a ratio of approximately 1:3 in a melter where they react to produce the immobilised glass product. The glass is poured into a canister which is welded shut, then decontaminated and sent to storage (this is discussed in more detail in section 2.3.2).

In the calciner, small particles of HLW are created and drawn into the off-gas system. The process of gases containing the particles being drawn into the off-gas system is driven by the negative pressure under which the vitrification system runs, which ensures all leakage in the system are in-leakages, so there is no risk of releasing radioactive particles to the environment. This air intake pushes about 20 litres of air per minute through the calciner picking up these small particles transporting them to the dust scrubber (Hollebecque, 2008). Here the particles are re-dissolved in boiling nitric acid and recycled to the calciner (this is discussed in more detail in section 2.3.2.3).

It is in the dust scrubber that a major cause of plant downtime occurs. Blockages of pressure tapings and the recycle feed back to the calciner are major problems in the process, and can cause the plant to be shut down. As the plant deals with highly radioactive materials, the process is highly automated and shielded behind thick concrete and lead glass. To remove blockages in the dust scrubber master slave manipulators (MSMs) must be used to clear them. This project was designed to reduce blockage formation in the dust scrubber, by understanding the chemical processes from which they originate.

## 1.4 Issues with the Sellafield Vitrification Process

Lithium nitrate is added to the HLLW as an aid in the calcination process. It is well documented that lithium nitrate acts as a binding agent in the dried calcine, increasing the particle size and therefore reducing carry-over to the off-gas system (Magrabi, 1981). What is not understood, however, are the processes which take place in the calciner that cause this binding effect to happen. Lithium is also responsible for better homogeneity of the final glass product when added to the calciner, as the amount of refractory oxides, containing primarily iron and aluminium, are significantly reduced (Brace, 2005b). By understanding the interactions of lithium nitrate with other compounds present in the HLLW, it will help provide a way of increasing the productivity of the WVP.

Analysis of the problem compounds which cause the blockages in the dust scrubber has been carried out, and it has been found that zirconium molybdate and ruthenium dioxide are the main causes. Both of these compounds have low solubility in nitric acid, and therefore precipitate in the dust scrubber liquor. The effects of ruthenium on the WVP process are well researched, but not fully understood, as it has been known as a major problem for many years, because of its high volatility (Morris and Haig, 2010; Sarsfield et al., 2008; Moss and Haile, 2004).

It is not fully understood where in the process zirconium molybdate formation takes place. It does precipitate in the HLLW, in the highly active storage tanks (HASTs) and in the dust scrubber. The formation of zirconium molybdate is due to the transformation of caesium phosphomolybdate in the presence of zirconium in solution. It is not clear whether this transformation takes place in the solid state in the calciner. This reaction was investigated to see if it can be inhibited or slowed to reduce the levels present in the dust scrubber.

As the major issues have been identified, a series of experiments were devised to test the effects of lithium nitrate in the calciner, in order to better understand the processes which take place. The main objective of this project was to reduce the amount of blockages which occur in the WVP dust scrubber. This will help improve the efficiency of the process and thus mitigate the risks of HLLW over a shorter time frame.



## **2. Literature Review**

### **2.1 INTRODUCTION**

Nuclear fission can be defined as the splitting of a large nucleus, usually uranium or plutonium, into smaller nuclei with the simultaneous release of energy. It was discovered and named by physicists Lise Meitner and Otto Frisch in 1939 after initial experiments carried out by Otto Hahn and Fritz Strassmann. The experiments carried out were designed to try and extend the periodic table beyond uranium (the heaviest element known at the time). This was carried out by bombarding the element with neutrons, causing a neutron to bind and create a new element. This worked for most elements up to uranium. Uranium was found to break down into smaller elements, discovered by tracing an increase in barium concentration (Bowersox, 2012). These results were sent to Meitner who postulated the process of nuclear fission occurring. This phenomenon is now the basis for the production of nuclear energy throughout the world.

Enrico Fermi, was amongst the first people to realise the significance of the discovery of nuclear fission. It was under his supervision that the first artificial nuclear reactor (Chicago-Pile 1) was constructed in 1942 (Greenwood and Earnshaw, 2002). This used graphite blocks as a moderator, with both pure uranium metal and uranium dioxide pellets as fuel. The reactor was controlled by inserting cadmium rods to act as a neutron absorber. The cadmium rods were slowly removed, allowing the reactor to go critical, and a self-sustaining reaction to occur. This ran successfully for 30 minutes, running at a power of 0.5 Watts, before it was shut down by re-inserting the rods. This experiment proved it was possible to create and sustain energy production by harnessing the power of the atom.

#### **2.1.1 The nuclear reaction**

Nuclear fission is the splitting of nuclei of heavy atoms by the absorption of a neutron causing it to become unstable. Upon splitting, a large amount of energy is released, which is used to create steam to drive a turbine and generate electricity. The reaction is self-sustaining, as several fast moving nuclei are created during the fission reaction (Figure 2.1), each of which can be absorbed by another atom, causing the fission reaction to continue.

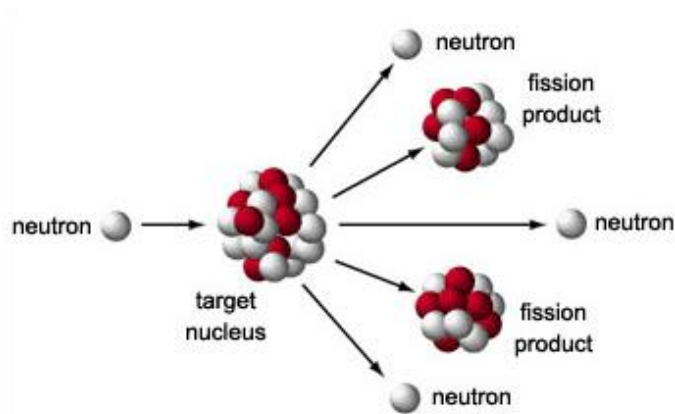


**Figure 2.1<sup>2</sup> – Schematic diagram of the nuclear fission process**

Fission of uranium typically yields two daughter nuclides, termed fission products (Figure 2.1). These daughter nuclei form due to the high probability of asymmetric fission occurring. The fission products formed in nuclear waste reprocessing cover about a third of the periodic table, with atomic mass ranging from approximately 70 through to 165 (Figure 2.2). These peak at around 90 and 140, meaning the fission reaction producing  $^{141}\text{Ba}$  and  $^{92}\text{Kr}$  is amongst the most common in the nuclear process (Bowersox, 2012).

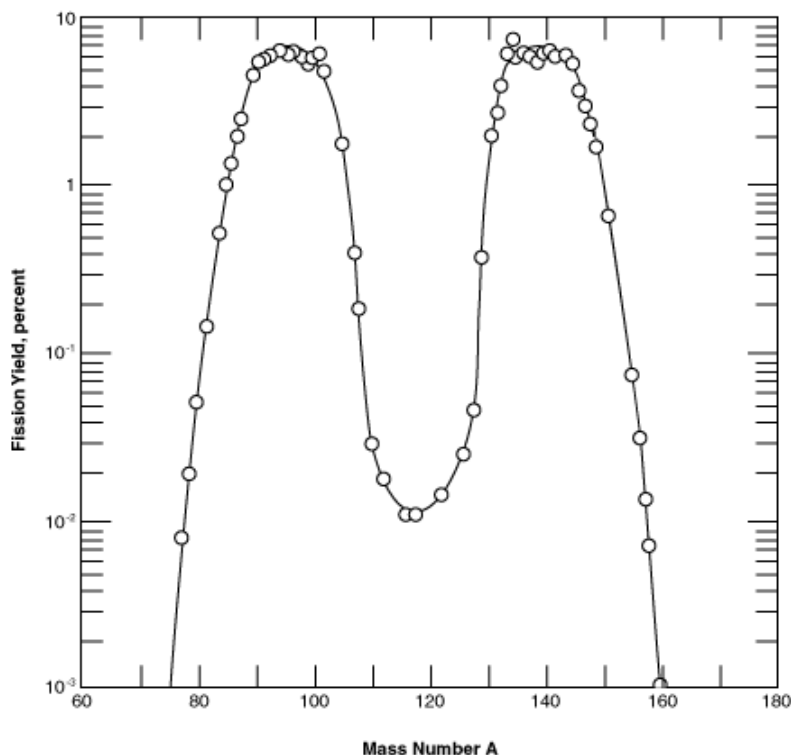


**Figure 2.2<sup>3</sup> – Graph showing the atomic weight distribution of the fission products of  $^{235}\text{U}$**

<sup>2</sup> Taken from <http://www.atomicarchive.com/Fission/Fission1.shtml>, 10<sup>th</sup> March 2010

<sup>3</sup> Taken from <http://www.science.uwaterloo.ca/~cchieh/cact/nucfig/fissionyield.gif>, 10<sup>th</sup> March 2010.

During the fission reactions, different amounts of energy will be released. The energy released follows according to the theory of relativity ( $E=mc^2$ ). The energy released arises because the mass of the fission products and neutrons created in the fission process is minutely lower than the original atom. The mass difference is not the same for each reaction, as different fission products are formed. This loss of mass is responsible for nuclear fission producing energy, with many uranium atoms undergoing this process simultaneously. It was calculated, and later proved experimentally, by Frisch that the energy released from this fission is 200 MeV (World Nuclear Association, 2010).

$^{235}\text{U}$  is the element of choice for most nuclear reactors ( $^{239}\text{Pu}$  is also used), as its nucleus is highly unstable, making it susceptible to fission. In naturally occurring uranium deposits,  $^{235}\text{U}$  only exists in 0.7 % abundance (Freundlich and Hedley, 1988). It must therefore undergo an enrichment process to be a viable fuel source in most reactors, to about 3-5 %  $^{235}\text{U}$  (Freundlich and Hedley, 1988). This allows a self-sustaining reaction to be maintained within the reactor. The isotope ratio of the uranium used will depend on the design of the reactor.

### **2.1.2 Reactor design**

The majority of the reactors which exist in the world today are light water reactors (LWR). This fact is largely due to the pioneering work done by the US navy in the development of this technology for submarine propulsion systems. The first nuclear submarine (Nautilus) sailed for half a million miles over a 25 year lifespan with no problems occurring in the reactor (Oldham, 2004). Due to this impeccable safety record, the first American commercial power-stations were based on this technology.

LWRs use water, as both a moderator (slows down neutrons) and a coolant in the reactor's core. There are two types of LWR, the boiling water reactor (BWR) and pressurised water reactor (PWR). In the BWR, steam is generated directly from the water in the core, and the radioactive steam goes straight to the turbines to produce electricity. This is condensed and transported back to the core keeping the cycle going. To minimise the release of radiation, the entire structure must be shielded, to the generator.

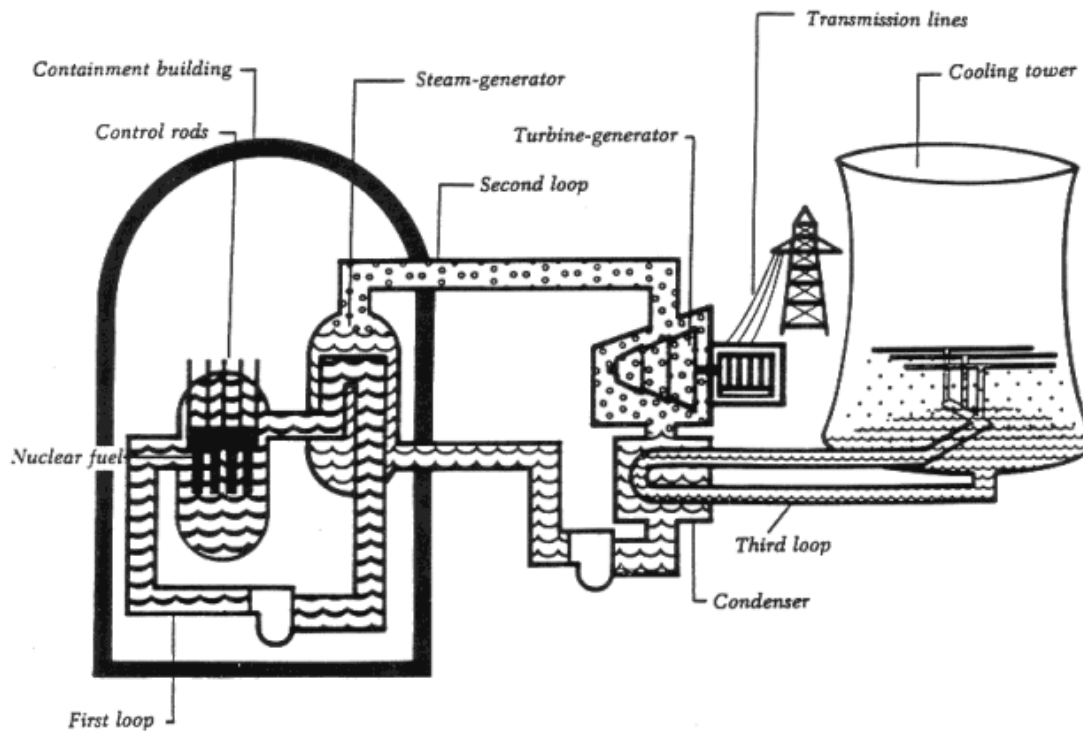


**Figure 2.3 – Schematic diagram showing how a pressurised water reactor (PWR) is used to generate electricity (United States Nuclear Regulatory Commission, 2009)**

The PWR (Figure 2.3) runs on a two loop system. The first loop involves the water in the reactor core being pressurised to stop the formation of steam. This heated water is then passed through a heat exchanger, where the heat is transported to a secondary water system. This system is not pressurised, and the water transforms to steam and drives the turbine. The condenser then cools the water and returns it to the cycle. PWRs are advantageous as only the core and heat exchanger need to be shielded. Any complication with the generators can therefore be fixed manually, and this is generally regarded as the easier option.

Other reactor designs include the advanced gas-cooled reactor (AGR) and liquid metal cooled reactors (LMR). These are based on the same principles as the PWR, but generally use graphite as a moderator, and either carbon dioxide (AGR) or a liquid metal (eg. sodium, lead) as the coolant within the core. These will again pass through a heat exchanger where steam is produced in a secondary loop to produce electricity. The first commercial power-station, Calder Hall (opened in 1956), was an example of a gas-cooled reactor, and paved the way for the next generation AGR.

Due to the famous international disasters at Three Mile Island in 1979, and Chernobyl in 1986, the safety of nuclear reactors is a major concern. Along with the need for higher thermodynamic efficiencies and proliferation concerns, this has driven governments and nuclear bodies the world over to propose new generations of nuclear power-station (summarised in Figure 2.4).

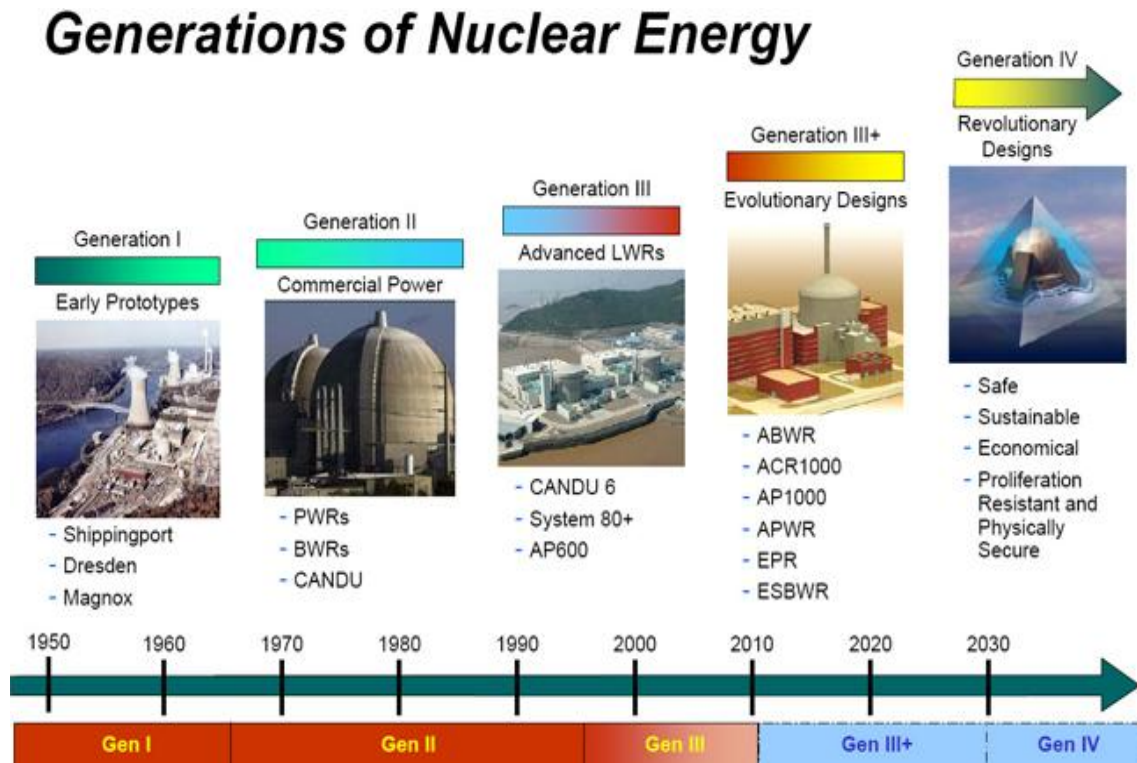


**Figure 2.4 – The evolution of nuclear power stations  
(The Generation IV International Forum, 2008)**

The proposed Generation IV designs will have inherent safety features, which do not rely on the operators to trigger them. These features rely on the material properties and stored energy in order to shutdown the reactor, rather than human intervention, if an emergency situation should arise. For example, in a fast breeder reactor the coolant is a liquid metal. When the core overheats, the cladding and fuel will thermally expand allowing more neutrons to escape from the core, so a reaction is no longer sustainable. The liquid metal then acts as a heat sink, so even if the coolant system fails the core will be cooled (World Nuclear Association, 2008a). Generation IV Power-stations are expected to be in operation by 2030, improving the safety and efficiency of the nuclear industry.

### 2.1.3 Spent fuel reprocessing

The uranium used in nuclear reactors is first processed and transformed into fuel rods. These are encased in a cladding material which protects the fuel from corrosion, and keeps the fission products contained. The fuel elements will generally have lifetime of between three and seven years due to the build up of neutron absorbing elements (poisons), which reduces the efficiency of the reactor (IAEA, 2006). The fuel rods are placed in cooling ponds to allow the short-lived highly active species to decay. There will still be an abundance of fissionable material left in the fuel rods once taken out of service, so fuel rods are reprocessed, in some countries, to recover these materials.

The plutonium-uranium extraction (PUREX) system is the most recognised way to recover useful elements from used reactor fuel rods. Firstly the cladding is mechanically removed, followed by dissolution in nitric acid. The uranium and plutonium can then be removed by solvent extraction in a tributyl phosphate/kerosene mixture (Devolpi et al., 2005), following filtration to remove fine insoluble particles. The remaining nitric acid contains the rest of the fission products, and is stored in stainless steel tanks until ready for vitrification and disposal.

Other methods of spent fuel reprocessing involve the dissolution of the whole fuel rod, with the cladding. This avoids mechanical processing, and therefore cuts out a step where nuclear waste would be produced.

## 2.2 Nuclear Waste

Commercial nuclear reactors are the main source of nuclear waste, although hospitals, universities and weapons decommissioning also contribute. For this project, the main focus was on the processing of high level liquid waste (HLLW), formed from the reprocessing of the spent fuel.

### 2.2.1 Classification

There are 4 main classifications for radioactive waste in the UK (DEFRA, 2001; Wilson, 1996), which are:

- **Very Low Level Waste (VLLW)** – Wastes which can be safely disposed of with ordinary refuse, each 0.1 m<sup>3</sup> of material containing less than 400 kBq of beta/gamma activity or single items containing less than 40 kBq (DEFRA, 2001). Wastes of this type would include contaminated disposable gloves, hospital wastes etc.

- **Low Level Waste (LLW)** – Containing radioactive materials other than those suitable for disposal with ordinary refuse, but not exceeding 4 GBq per tonne of alpha or 12 GBq per tonne of beta/gamma activity (DEFRA, 2001). Wastes can be accepted for authorised disposal by controlled burial. University research equipment, building rubble and metals housing reactors are usually classified as LLW.
- **Intermediate Level Waste (ILW)** – Waste with radioactivity exceeding the upper boundaries for LLW, but which do not need heating to be taken into account in the design of storage or disposal facilities (DEFRA, 2001). The cladding for fuel cells and reactor core materials will have high levels of radioactivity, but are designed not to heat after the reactor is decommissioned, so will be classified as ILW.
- **High Level Waste (HLW)** – Wastes in which the temperature may raise significantly as a result of their radioactivity, so this factor has to be taken into account in designing storage or disposal facilities (DEFRA, 2001). These are all associated with spent fuel rods and their reprocessing. HLW is about 2 % volume of the total nuclear waste formed, but contains over 90 % of the radioactive materials formed in the nuclear industry (Wilson, 1996).

### 2.2.2 Storage and disposal

VLLW, due to its low activity, can be incinerated and placed in landfill sites. No special disposal methods are required. LLW is, however, monitored at specially designated landfill sites. These forms of waste are not considered a threat to the surrounding environment due to the low levels of radiation that they emit.

ILW and HLW are usually stored at the nuclear plant site, and are encapsulated in an inert medium (immobilised). This media can be a range of different glasses, ceramics and cements depending on the properties required (Table 2.1). This is a major area of research and development within the nuclear industry.

**Table 2.1 – Properties of various waste forms and their uses in the immobilisation of nuclear waste (Donald et al., 1997)**

Wasteform	Process Temp <sup>1</sup>	Waste Loading <sup>2</sup>	Economics <sup>3</sup>	Current/Studied Applications
<b>Alkali Borosilicate Glasses</b>	High	Int	Int	<ul style="list-style-type: none"> <li>• Vitrification</li> <li>• High U and Pu wastes</li> </ul>
<b>Alkali Phosphate glasses</b>	Int	Int	High	<ul style="list-style-type: none"> <li>• High actinide wastes</li> <li>• Pu wastes</li> </ul>
<b>Clay-based Inorganics</b>	Low	Int	Low	<ul style="list-style-type: none"> <li>• Studied for high U, Pu and Zr wastes</li> </ul>
<b>Cement</b>	Low	Int	Low	<ul style="list-style-type: none"> <li>• LILW encapsulation</li> </ul>
<b>SYNROC</b>	High	Int	Int-High	<ul style="list-style-type: none"> <li>• Defence wastes</li> </ul>
<b>Phosphate Ceramics</b>	Int	Int	Int-High	<ul style="list-style-type: none"> <li>• High lanthanide and actinide wastes</li> </ul>
<b>Barium Aluminosilicate</b>	High	Int	Int-High	<ul style="list-style-type: none"> <li>• Limited HLW use</li> </ul>
<b>Calcium Titanium Silicate</b>	V. High	Int	Int-High	<ul style="list-style-type: none"> <li>• CANDU waste</li> <li>• 50% UO<sub>2</sub> waste loadings</li> </ul>

Int = Intermediate, V. High = Very High

<sup>1</sup> Process Temp: Low, <200 °C; Int, 200-1000 °C; High, 1000-1250 °C; V. High, >1250 °C

<sup>2</sup> Waste Loading: Low, <10 %; Int, 10-25 %; High, >25 %

<sup>3</sup> Economics: Low, <Borosilicate glass; Int, Comparable to borosilicate glass; High, >Borosilicate glass

At the Sellafield site, HLLW is stored in double walled stainless steel storage tanks shielded by concrete, known as highly active storage tanks (HAST's). These tanks are internally cooled to stop the waste from boiling, which could lead to leakages. Due to the liquid nature of the waste, it is highly hazardous as it is corrosive and could lead to a breach from containment if not actively managed. The tanks are closely monitored to ensure agitation and cooling mechanisms are in place to minimise the hazard, but the tanks are not suitable for long term storage. To minimise this hazard, the waste is immobilised by the vitrification process. The HLLW is pumped to the waste vitrification plant (WVP), where it is solidified, and incorporated into a glass matrix (see section 2.3). The glass is poured into a container which is welded shut, and decontaminated before being placed in a shielded, convection cooled store (Bradshaw et al., 2007).



There is currently no permanent nuclear waste disposal facility in the UK, for several reasons. These include the positioning of this site, production of a safety case, and research to prove a safe method of disposal. The current preferred option for disposal in the UK is the use of a deep geological disposal facility. This would involve creating a series of tunnels between 500-1000 metres below the surface, and placing waste canisters in a specially designed repository. This would also be surrounded with further engineered barriers to stop radioactive elements being released to the surrounding environment (Figure 2.5).

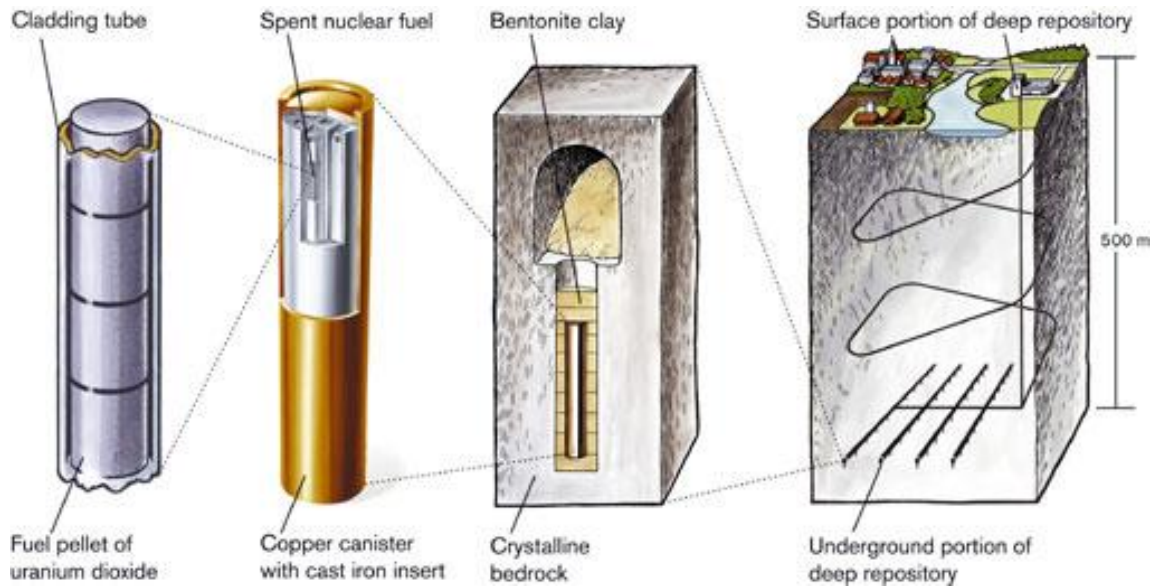


**Figure 2.5 – A schematic of the proposed deep geological disposal route made by SKB in Sweden (Svensk Karnbranslehantering AB, 2006)**

One of the major problems is the leaching of radioactive elements into mobile ground water. Elements such as technetium have a long half life (215 000 years), and will form highly soluble anions (eg  $\text{TcO}_4^-$ ). These should be contained so no bodies of water become contaminated. This is the reason that engineered and natural barriers are important considerations when designing a nuclear waste repository. The idea of the deep geological disposal facility came about due to this phenomenon, as at 500 metres down the ground water moves very slowly in certain environments, such as granitic rock (Rempe, 2008).

### **2.3 Vitrification**

Glass making has been carried out for thousands of years, but only in the past 60 years has it been considered for the immobilisation of nuclear waste. The major reasons for the choice of glass as a host material include (Marples, 1988):

- Most fission products are soluble in glass, so a homogeneous matrix is formed.
- Flexible amorphous structure allows incorporation of a wide variety of oxidation states, atom sizes, bonding requirements.
- High loadings (up to 50 %) of waste can be incorporated into the structure.
- Glasses are inert materials so can withstand chemical attack and natural erosion which are important requirements for final disposal.
- The processing and materials for manufacture are reasonably economical compared to other possible hosts.
- The structure is unchanged by radiation effects.

Alkali borosilicate glasses are used worldwide, as they have been the source of extensive study, so properties are well documented (Donald, Metcalfe and Taylor, 1997). They have a reasonable processing temperature (1000-1100 °C), and can be easily modified to improve chemical resistance, mechanical strength, etc where required. Other glasses such as phosphate and rare earth oxide glasses have been tested, but none can provide the low cost and high flexibility of the current systems (Donald, Metcalfe and Taylor, 1997).

### **2.3.1 History of vitrification**

The first attempts to vitrify nuclear wastes into a glass product were carried out in the early 1950's in Canada using nepheline syenite as the starting material (Donald, Metcalfe and Taylor, 1997). By 1958 a pilot plant had been constructed producing radioactive glass, to prove that the concept of vitrification was possible.

Over the same period of time in the UK, natural soils were being investigated as base material for HLW glass production. These however needed processing temperatures of over 1500 °C to produce a homogeneous product, so alternative glasses were investigated. The investigation led to the development of the FINGAL (Fixation In Glass of Active Liquor) process. The FINGAL process involved the calcining of the HLLW, melting and homogenising with the glass frit all taking place in a stainless steel crucible. The crucible also served as the storage vessel for the glass, so no pouring mechanism was needed (Lutze and Ewing, 1988).

The crucibles in the FINGAL process could only hold about 50 kg of product, so subsequently this project had to be scaled up. In 1975 the HARVEST (Highly Active Residue Vitrification Experimental Studies) process, which could produce batches of approximately 1000 kg, was begun. It was through these two processes that the identification of borosilicate glass as a good immobilisation host was identified. The problems of caesium and ruthenium volatility, forming compounds which cause blockages in the off-gas system were also discovered at this time (Marples 1988). These are problems which still exist today.

By the early 1980's, the French has developed a continuous vitrification route, named the atelier de vitrification de Marcoule (AVM) process. British Nuclear Fuels Ltd (BNFL), now Sellafield Ltd, adopted this process for its commercial waste vitrification plant (WVP). This process still exists today as the method of immobilisation for HLLW formed during the reprocessing of spent nuclear fuels.

### 2.3.2 Processing

In the AVM process (Figure 2.6), the calcination is carried out separately from the melting by passing the waste through a rotating kiln (calciner). Any volatile elements, compounds and small radioactive particles are recycled by the primary off-gas system, to minimise the radiation released. The secondary off-gas system is used to reduce the amount of NO<sub>x</sub> released to the atmosphere. The dried and de-nitrated waste is then fed into the melter with the borosilicate glass frit, where homogenisation takes place. The glass is then poured into a canister, a lid is welded on and the canister is decontaminated, before being taken to a temporary store on site. A breakdown of the processes involved in each stage, is given below.

### Continuous Vitrification Process

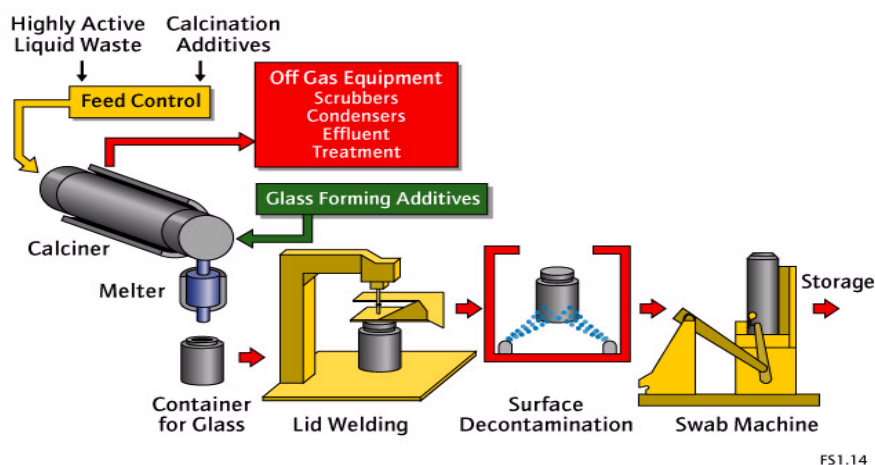


**Figure 2.6 – Schematic of the continuous AVM process used for vitrification of high level liquid waste (Courtesy of the National Nuclear Laboratory)**

### 2.3.2.1 The Calciner

The calciner is a rotating kiln which has a diameter of 0.3 metres and a length of ~4 metres. It is elevated at a 3 % angle from horizontal (Marples, 1988) and is supported by roller bearings at each end. It also has special gas tight seals which allow for tube expansion, made from graphite. The tube is split into 4 zones, and is heated by 8 half-shell electric resistance furnaces (one top and one bottom in each zone). A rabble bar is placed inside the calciner, which is free to move around as the calciner rotates.

The calciner is fed from a feed tank, where the HAL is mixed with glass forming additives, such as lithium nitrate to reduce the amount of calcine passing to the off-gas system and to reduce the viscosity of the glass, and process aids such as sugar to reduce the volatility of the ruthenium (Marples, 1988). The HAL is fed into the calciner usually between 40-70 litres an hour depending on feed concentration and the source of the waste (Magneox, oxide or blend). The calciner rotates at around 25 rpm, with the rabble bar tumbling to prevent solids build up on the walls. The temperature set points are generally about 800 °C in zones 1 and 2, dropping to 650-700 °C by zone 4 (Veyer, 1995), although these temperatures are never reached (Figure 2.7) due to the energy consuming processes and heat transfer occurring inside the calciner.

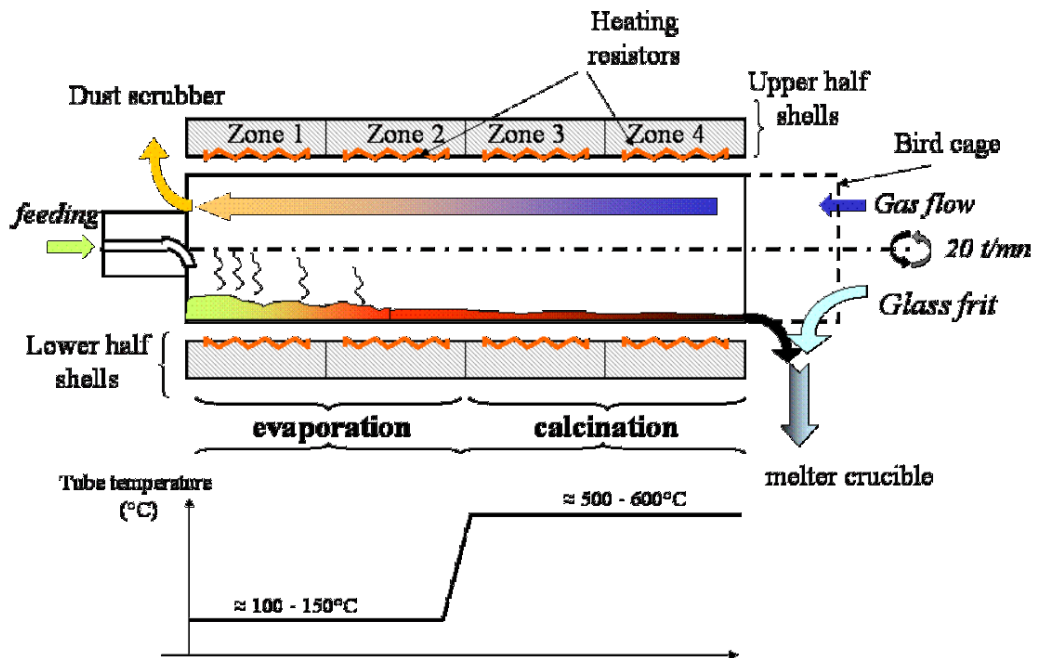


Figure 2.7 – Schematic diagram of the calciner with the temperature profile in the different zones (Courtesy of the National Nuclear Laboratory)

The calciner is designed to fulfil two major purposes, which are the evaporation of the liquids from the HAL, and the de-nitration of the waste forms into oxides so they can be incorporated into the glass matrix. Evaporation is the first process to take place, and this happens in the first two zones of the calciner. The process conditions are such that the evaporative front is maintained at the interface between Zones 2 and 3 (Bradley, 2010). This may be monitored by the power input to each zone, as evaporation consumes more energy than the de-nitration phase. This is also apparent from the measurement of the external tube temperature in these zones, as although set to 800 °C it will only reach between 100 °C and 150 °C (Veyer, 1995). After Zone 2, all the liquid should be evaporated, and a solid blend of metal nitrates will be present.

In Zones 3 and 4 of the calciner, there is a significant rise in the tube temperature to between 500-600 °C (Veyer, 1995). This allows most of the metal nitrates to decompose into their oxide forms. Some nitrates are more stable however (eg.  $\text{LiNO}_3$ ,  $\text{NaNO}_3$  and some rare earth nitrates) and will not decompose at these temperatures (Chun, 1977). Approximately 25 % of the nitrates will remain once the waste has passed through the calciner. The retention of some nitrates is helpful for the melting stage of the process, as they increase the reactivity of the calcine with the glass frit (Owens, Leung and Magrabi, 1985), producing a more homogeneous glass product.

### **2.3.2.2 *The Melter***

The melter is an elliptical shaped vessel made from Inconel 601 (Marples, 1988), which is an alloy of iron, nickel and chromium. This material is chosen because it is ferromagnetic, so has a high dielectric constant and low specific resistance. This allows an alternating current to be used to induce localised electrical currents, causing eddy currents to be formed (Bonnetier, 2007). The eddy currents act as charge carriers, and will overcome the specific resistance, and cause the melter to heat up. This allows the high temperatures needed for melting glass to be reached.

The melter is split into several zones (Figure 2.8), each of which is independently controlled. Wall temperatures of up to 1150 °C are induced to ensure the target of a glass internal temperature of 1050 °C, which will allow a homogeneous glass to be formed in the timescale allowed. 1050 °C is approaching the melting point of the inconel melter (1300 °C), meaning it has to be monitored closely. Coupled with the fact that the glass will react with the Inconel, removing chromium, these factors severely reduce the life expectancy of the melter (BNFL, 2007). The melter typically lasts for around 300-400 pours before fatigue and creep mechanisms cause it to be taken out of service.

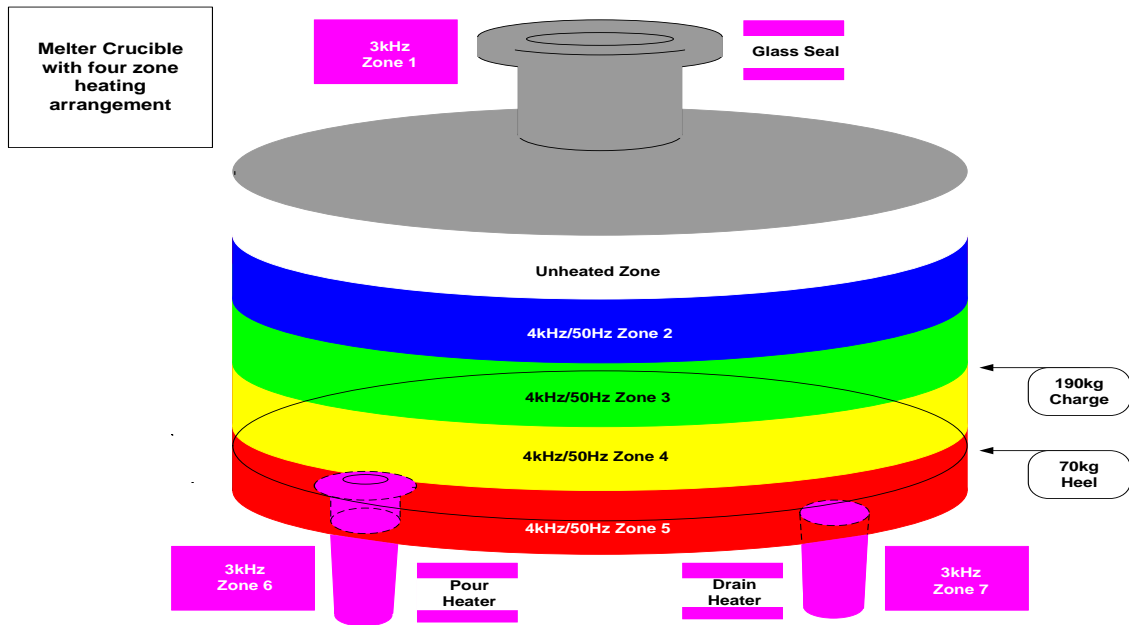


**Figure 2.8 – Schematic diagram of the melter in the vitrification process**  
**(Courtesy of the National Nuclear Laboratory)**

The capacity of the melter is approximately 200 litres (520 kg) of glass, although it is only half filled before each pour. A batch is typically fed at 25 kg an hour, comprising of approximately 7 kg of calcine and 18 kg glass frit (Dawson, 2010). The glass is mixed by having an air sparge in the melt. This reduces the settling of insoluble compounds such as RuO<sub>2</sub> and iron-chromium spinel phases into the heel. The heel is the bottom section of glass (approximately 70 kg) which lies below the pour nozzle, and is only removed when the melter is fully drained. Once every 8 hours (190 kg charge) the glass is poured from the melter and collected in canisters (BNFL, 2007), where they have a lid welded on, and are sent for decontamination and temporary storage (see 2.3.2.4). It takes two pours to fill one canister on the WVPs at Sellafield.

At the temperatures in the melter, the remaining nitrates decompose to oxides allowing them to be incorporated in to the glass structure. While this process is on-going, there are releases of NO<sub>x</sub> gases which need to be controlled from both the melter and the calciner. In this gas stream there are small particles (dust) which need to be captured and returned to the process. This gas is pulled out of the upper end of the calciner by the vacuum in the primary off-gas system.

### 2.3.2.3 Primary Off-Gas System

There are many different gases released from reactions taking place within the melter and calciner, some of which (especially  $\text{NO}_x$ ) need to be controlled, along with small radioactive particles which get carried in the gas stream. The first stage of this process is to re-dissolve the solid particles in nitric acid, which is done in the dust scrubber.

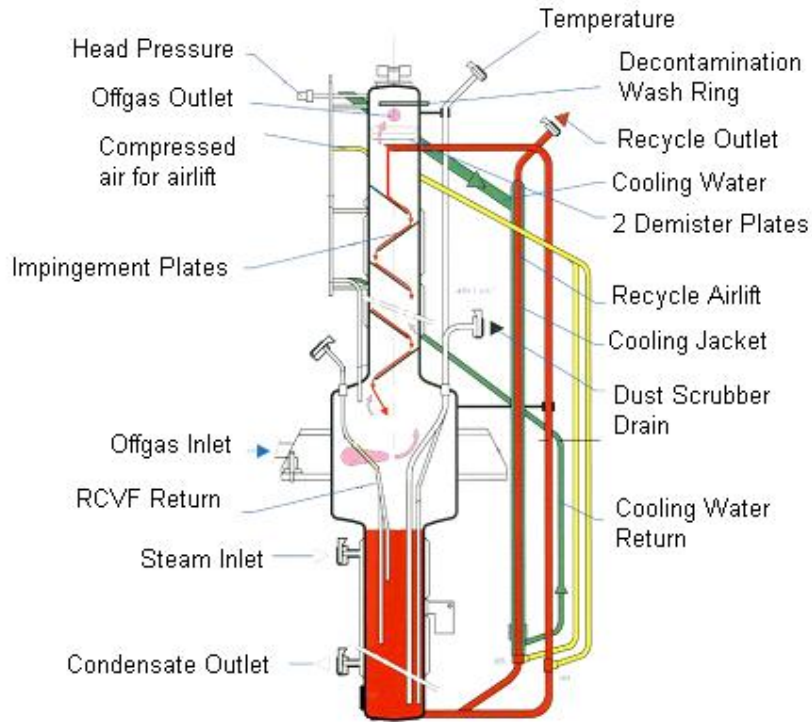


**Figure 2.9 – Schematic diagram of the dust scrubber  
(Courtesy of the National Nuclear Laboratory)**

The waste gas stream passes from the calciner to the dust scrubber, driven by the negative pressure differential between the two systems (Roe, 2003). By running at negative pressure, it also forces any leakages in the system to be in-leakages, so no radioactive material can escape from the system. The gas flows in tangentially, creating a cyclone effect. This allows the larger particles to be separated from the gas by centrifugal force. Smaller particles can be caught on the impingement plates, as the dense particles cannot change direction as quickly as the gas molecules. There are six of these plates in the dust scrubber to maximise capture of the radioactive solids (Roe, 2003). Any solids not caught on the plates will collide with the nitric acid liquid droplets flowing from the top of the dust scrubber. This ensures that the minimum amounts of solid particles are able to pass through the dust scrubber and onto the next stage of the POG.

There are several factors which affect the efficiency of particle dissolution in the dust scrubber. The most important of these include (Hollebecque, 2008; Roe, 2003):

- **Number of impingement plates** – the higher the number, the more probable the particles will become trapped removing them from the gas stream.
- **Acidity of liquid** – the higher the acidity, the greater the solubility of the particles improving efficiency of particle removal.
- **Particle Size** – the finer the particles, the more likely they are to remain in the gas stream, and therefore reduce the chances of capture.
- **Gas flow rate** – if the gas flows faster, particles will not be able to change direction as quickly allowing the impingement plates to gather more of the finer particles, improving efficiency.
- **Liquid flow rate** – particles have a higher chance of colliding with the droplets, dissolving them and removing them from the gas stream.
- **Temperature** – dust scrubber liquor kept at boiling point to increase dissolution and prevent condensation.

All of these factors are taken into account in the design of the dust scrubber. The gas enters at the widest point where the cyclone is formed. There is a narrowing above this in order to accelerate the gas up the dust scrubber to increase the velocity allowing smaller particles to be picked up by the impingement plates (Roe, 2003). These plates have a large cross section to maximise particle capture. An air lift takes the nitric acid from the reservoir to the top of the dust scrubber, and causes a liquid curtain to be formed, running down the plates. The dust scrubber liquor is recycled around the loop at around 195 litres per hour (Hollebecque, 2008), which will dissolve any small particles which collide with it. The acidity is monitored to ensure maximum dissolution efficiency.

The dust scrubber liquor is fed back into the calciner at a rate of 15 litres per hour (Hollebecque, 2008). The liquor is air-lifted into a recycling constant volume feeder (RCVF), which ensures this rate is kept constant.



After the solid particles have been removed by the dust scrubber, the gases pass to the condenser (Figure 2.10). Approximately 75 % of the gas released from the calciner is water vapour (Hollebecque, 2008), which is cooled, condensed and recirculated back around the condenser to cool the new gas influx. Some of the free  $\text{NO}_x$  in the system will undergo a recombination reaction with water to form nitric acid. The flow rate of the gases drops from  $120 \text{ m}^3/\text{h}$  entering the condenser from the dust scrubber to  $36 \text{ m}^3/\text{h}$  leaving the top of the condenser (Hollebecque, 2008) due to the condensation and recycling of the water vapour which makes up most of the gas flow.

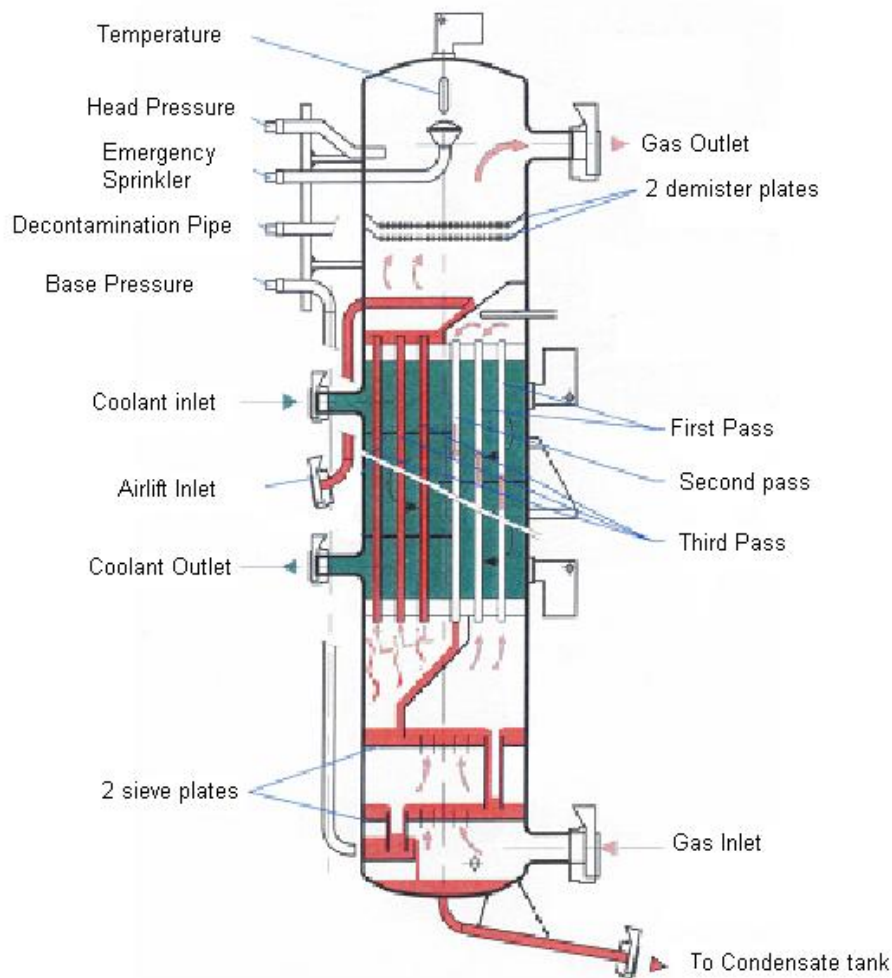


**Figure 2.10 – Schematic diagram of the condenser**  
**(Courtesy of the National Nuclear Laboratory)**

The gases enter the condenser at the bottom, and are passed through two sieving plates. These act as scrubbing units, as any small particles not removed by the dust scrubber will be removed here (Sellafield Ltd, 2008). The gases also pass through the condensate liquor, helping remove solid particles and allowing some of the  $\text{NO}_x$  to be removed by reacting with the water. This also helps with the initial cooling of the gases in the condenser.

The condenser works on a three pass system. These systems are isolated by a hydraulic guard (top sieve plate). The first pass is designed to cool the gas stream to the point where the water vapour will begin to condense. This system consists of a tube bundle up which the gas will rise, while being surrounded by cooling water (Hollebecque, 2008). The second pass system is similar to the first, except the gas is pushed down the column. In this pass, most of the condensate is formed, and the liquid flows to the bottom of the condenser and out to the condensate tank.

The third pass is designed to maximise the efficiency of the NO<sub>x</sub> recombination reaction with water to form nitric acid. In this pass, the condensate is present inside the tube bundles, and can therefore interact with the gas stream. The large amounts of water present will increase the probability of the reaction occurring (Sellafield Ltd, 2008). The remaining gases will then pass through two demister plates to remove any moisture droplets, before moving on to the NO<sub>x</sub> absorber.

The NO<sub>x</sub> absorber (Figure 2.11) is a series of plates through which the off-gas passes. Each of these trays has a layer of liquid, which is designed to react with the NO<sub>x</sub> and remove it from the gas stream. The gases pass up through bubble caps, which have narrow openings to increase the velocity of the gas going into the liquid at each stage. By increasing the velocity and forming bubbles, it is more probable that a recombination reaction will occur. The liquid temperature is kept between 10-20 °C, as low temperatures increase the rate of reaction (Hollebecque, 2008).

There are 16 trays present in the NO<sub>x</sub> absorber, each one designed to remove NO<sub>x</sub> from the system. However, as the gas rises up through the plates, the harder it becomes to remove the NO<sub>x</sub> from the stream. For this reason, the overflow liquor is airlifted back to the thirteenth tray. Fresh water is pumped in at the top (sixteenth tray) at a rate of 20 litres per hour (Hollebecque, 2008), as the water dilutes the acid in the reservoir to below 1 M acidity, which improves the efficiency of the NO<sub>x</sub> absorption.

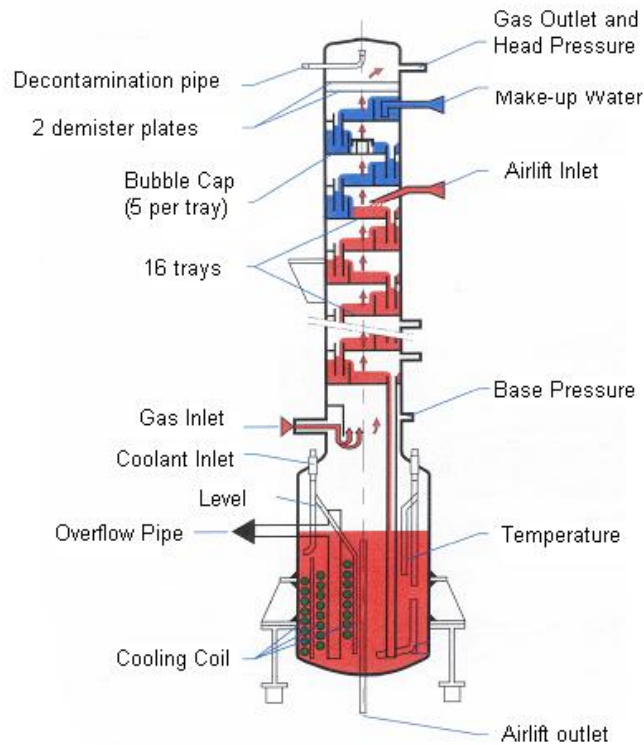


**Figure 2.11 – Schematic diagram of the NO<sub>x</sub> absorber  
(Courtesy of the National Nuclear Laboratory)**

The primary off-gas (POG) system needs to be kept at a negative pressure to prevent the leakage of radioactive materials. The negative pressure is caused by a motive force used to eject the off-gas. As the pressure of the off-gas coming from the calciner is variable, an in-bleed valve is positioned before the ejector, in order to keep it constant. The pressure at the ejector is approximately -100 mbar, rising to -90 mbar in the NO<sub>x</sub> absorber, -30 mbar in the condenser, and -15 mbar in the dust scrubber (Hollebecque, 2008). This pressure cascade ensures the off-gas is driven from the calciner and through the POG system to the ejector. The remaining gases pass through filters to ensure any remaining solids are removed, before being released into the atmosphere from the stack.

#### **2.3.2.4 Decontamination and storage**

After the glass has been poured into the stainless steel canisters, the surface is decontaminated. Decontamination is done using high pressure water jets to remove any residual material from the outer surface. The surface is remotely swabbed, and tested for any contaminants which may have been missed. If this test is passed, the canisters are taken to the interim storage facility on the Sellafield site (Figure 2.12).



**Figure 2.12 – The interim storage facility for vitrified HLW at Sellafield  
(World Nuclear Association, 2008b)**

The storage facility is comprised of large slabs of concrete, with many vertical holes cast in the top. The canisters are loaded using a remote automated system into large flasks (Figure 2.12) which lower the canisters into the holes (Benbow, 1997). The loading structures are very heavy and are moved around by an overhead crane allowing remote operation.

The interim storage facility at Sellafield can accommodate up to 8,000 canisters. As the canisters contain high level waste, they are heat generating and have to be cooled. The canisters are air cooled using natural convection throughout the concrete structure. The store has been designed to store waste for up to 100 years, to allow time for a final disposal solution to become available.

## **2.4 Current Problems and Blockages**

There are two main causes of downtime on the waste vitrification plant (WVP) which are; the changing of the melter due to failure, and blockages in the HAL feed and off-gas systems. Downtime due to melter change is unavoidable due to the corrosive nature of the glass product on the melter walls, and is a lengthy process due to the hot-cell environment it resides in. In this project, the focus was to support a programme to reduce the downtime of the WVP caused by blockages in the system to improve the efficiency of the plant and help meet targets for converting HLLW into a solid waste-form.

During normal operations of WVP, pressure tappings and feed lines can become blocked by solids (Turner, 2007). This has required WVP to stop operations in order to remove the blockage. Any blockages which take place in the pipe-work will cause a plant shutdown to occur if they cannot be removed to avoid any unnecessary complications arising. The main areas where these blockages occur are in horizontal pipes with a low flow-rate of material passing through them. The parts which have been blocked and have caused a plant shutdown to occur include (Talford, 2003):

- Recycle Constant Volume Feeder (RCVF) Airlift from the Dust Scrubber.
- Dust Scrubber Feed line from the Calciner.
- Dust Scrubber Pressure Tappings.

Analysis on the materials which cause the blockages on the VTR showed it to contain the species zirconium molybdate hydrate  $[\text{ZrMo}_2\text{O}_7(\text{OH})_2(\text{H}_2\text{O})_2]$  and ruthenium dioxide. These compounds are insoluble in nitric acid, and are therefore precipitated in the dust scrubber liquor. These solids can then accumulate, causing blockages and causing downtime on the plant.

There are systems in place on the WVP to try to reduce the build up of materials. The auto debouchage (a pressurised water jet) is used to clear debris from the dust scrubber feed line to avoid build up of material. For blockages which cannot be removed, there are three options:

1. Use a master slave manipulator (MSM) to physically remove the blockage by rodding.
2. Remove and replace the pipe which contains the blockage.
3. Chemically remove the blockage using ammonium carbamate which dissolves the zirconium molybdate.

The chemical solvent route is only used in areas of the plant which cannot be easily removed.

During VTR Campaign 9, there was a significant amount of dust carryover to the off-gas system (Short, 2010). The extra dust carryover resulted in the build up of solids in the RCVF and dust scrubber inlet (Figure 2.13). The HAL simulant used was not dosed with lithium nitrate. This extent of solids build up is not observed on the VTR when lithium nitrate is added to the HAL simulant.



**Figure 2.13 – Photograph of the dust scrubber inlet during VTR campaign 9 (Short, 2010)**

Blockages in the RCVF were also a concern during campaign 9. These were attributable to a combination of flaked material, which had dried out and fallen off the walls of the dust scrubber during non-operational periods and excessive dust carryover during operational periods (Short, 2010). XRD analysis on this material showed the main component of the blockage material was zirconium molybdate, with chemical analysis also showing an elevated concentration of iron.

A summary of VTR Campaign 9 blockages was recorded (Table 2.2). These blockages occurred in the RCVF and dust scrubber inlet (from the calciner), which are the main pipes blocked on the WVP's.

In order for the off-gas system to pull the gas from the calciner to the dust scrubber, there must be a pressure differential. Formation of blockages in the dust scrubber inlet and pressure tappings seriously affects the pressure control system of the POG, leading to shut down of the process (Roe, 2003). This can be detected on the plant as it manifests as a drop in pressure differential in the off-gas coupling. Once this reaches a critical level, an alarm will sound. If the pressure differential cannot be raised then the plant must be shut down to allow the blockage to be removed.

The other major blockage issue is in the RCVF. The RCVF is responsible for the recycle of the DSL back to the calciner. Blockages therefore slow down or stop this process, which results in more liquid being present in the dust scrubber. This first manifests on plant as a reduction in level and temperature in the RCVF tundish, due to the lack of feed caused by the blockage. This is a clear sign of a blockage and the plant must be shut down to allow the blockage to be removed.

**Table 2.2 - POG blockages and debris build-up during Campaign 9 (Short, 2010)**

Date	Cumulative hours in feed (hrs)					
	Campaign 9 part 1		Campaign 9 part 2			
	Blend cal.	Blend vit.	Dilute Blend cal.	Mag cal.	Mag vit.	
Pre 18 <sup>th</sup> May	0	0	0	0	0	DSRV washed out after Campaign 8a & PPD006. Left dry prior to start of Campaign 9
2 <sup>nd</sup> Jun	20	0	62	24	27	RCVF breakpot-inner bowl line blocked, ~40ml solids retrieved by rodding. DSRV NOT washed/emptied
10 <sup>th</sup> Jun	20	0	62	24	163	~0.5cm thick layer on inner surface of POG coupling, & some loose material in DSRV inlet. Coupling replaced as found.
25 <sup>th</sup> Jun	20	0	62	24	360	Some calcine build-up around melter neck and still only ~0.5cm in off-gas coupling. Significant build-up in DSRV inlet
<b>End of Campaign 9 part 1. DSRV washed with water and left empty over summer. Off-gas coupling and DSRV inlet cleaned</b>						
21 <sup>st</sup> Sep	20 0	0 0	62 0	24 0	360 0	RCVF breakpot-RCVF inner bowl line blocked. Required rodding and washing to clear
24 <sup>th</sup> Sep	20 9	0 0	62 0	24 0	360 0	RCVF breakpot-RCVF inner bowl line blocked. Required rodding and washing to clear. Large lump of solids retrieved from DSRV
29 <sup>th</sup> Sep	20 61	0 0	62 9	24 0	360 0	Knife gate seal on Calcine collection kit required cleaning due to (baked) calcine build-up
<b>End of Campaign 9 part 2</b>						
22 <sup>nd</sup> Oct	20 72	0 76	62 9	24 8	360 41	Very little solid material found in DSRV, but RCVF breakpot-RCVF line, and RCVF inner bowl were clogged with ~80ml of fine solids

## 2.5 Calciner Chemistry

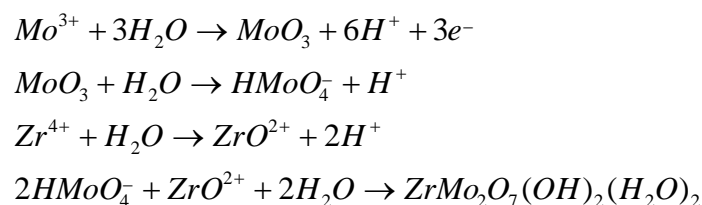
### 2.5.1 Caesium phosphomolybdate and zirconium molybdate formation

Caesium phosphomolybdate,  $\text{Cs}_3\text{PMo}_{12}\text{O}_{40}\cdot x\text{H}_2\text{O}$  (CPM), is precipitated, as a yellow solid, from highly active liquor (HAL) when the molybdenum concentration exceeds approximately 0.015 M (Richardson, 2000). This occurs during the evaporation process after reprocessing, before HAL is transferred to the HAST's. Studies of this precipitation (Magnaldo et al., 2007; Richardson, 2000; Doucet et al., 2002) have shown that when subjected to various conditions, conversion of CPM to ZMH is observed.

The rate of conversion of CPM to ZMH has been found to increase at higher temperatures and lower acidities (Bradley et al., 2004; Doucet et al., 2002). Increased tellurium concentration (at higher levels than in HAL) also increases the rate of precipitation of ZMH (Kubota and Fukase, 1980). Testing done between 50 °C and 80 °C, to simulate temperatures experienced in HASTs, showed that complete conversion of CPM to ZMH at 80 °C occurred within one week. At 50 °C very little conversion had occurred after a week (Richardson, 2000). ZMH is insoluble in nitric acid, and is one of the main causes of blockages on the waste vitrification plant (WVP).

Studies carried out by Doucet et al. (2002) showed the precipitation of ZMH from CPM proceeds from surface reactions, rather than from the solution, and the rate of formation follows an ‘S-shaped’ curve. The ZMH formed a highly ordered cubic crystal structure, after being grown from an amorphous film. A subsequent study by Magnaldo, Masson and Champion (2007) suggested surface nucleation in combination with crystal growth was responsible for the build up of ZMH within nuclear waste reprocessing. Neither of these studies resulted in a mechanism being discovered for the conversion of CPM to ZMH.

Formation of precipitates from high-level liquid waste simulant was investigated by Izumida and Kawamura (1990). Precipitation of zirconium molybdate hydrate,  $ZrMo_2O_7(OH)_2(H_2O)_2$  (ZMH) was confirmed through XRD analysis, from a sample with low acidity aged at high temperature. The following reactions were used to explain this:



This suggests that the formation of ZMH takes place in solution, increasing the likelihood that these reactions take place in the dust scrubber rather than in the calciner. The precipitation of ZMH is known to occur in the highly active storage tanks (HASTs) under aqueous conditions.

The build-up of ZMH in the HAST’s causes problems as it settles to the bottom of the HASTs and is very difficult to remove. The post operation clean out (POCO) waste residues left in the tanks, after pumping all the liquid to WVP, would ideally be encapsulated using the vitrification process, although recovering this waste could prove a challenge. ZMH is a stable product, however, with a low thermal expansion and high radiation stability (Tadros and Metwally, 2006) so it will not change structure once encapsulated.



In the dust scrubber, the formation of ZMH is not desirable. In its cubic form, ZMH is difficult to keep in suspension in the dust scrubber liquor (DSL), and so settles and causes blockages. Therefore, preventing the formation of ZMH, or changing the morphology, would be beneficial to reducing blockages in the dust scrubber. A current investigation is dedicated to understanding the crystal growth, morphology and properties of ZMH.

The investigation (Masheded, 2009) has shown the morphology of ZMH can be changed from cubic to a ‘wheatsheaf’ structure by the addition of tellurium (Te). The morphology is altered as a function of Te concentration. ZMH in the ‘wheatsheaf’ morphology was found to be removed more easily from the surfaces from which they were grown, and would therefore be more easily kept in suspension in the DSL. Additives such as citric acid have been shown to decrease the average crystallite size of zirconium molybdate (Edmondson, 2009). This could also be beneficial in reducing blockages caused by ZMH formation in the dust scrubber.

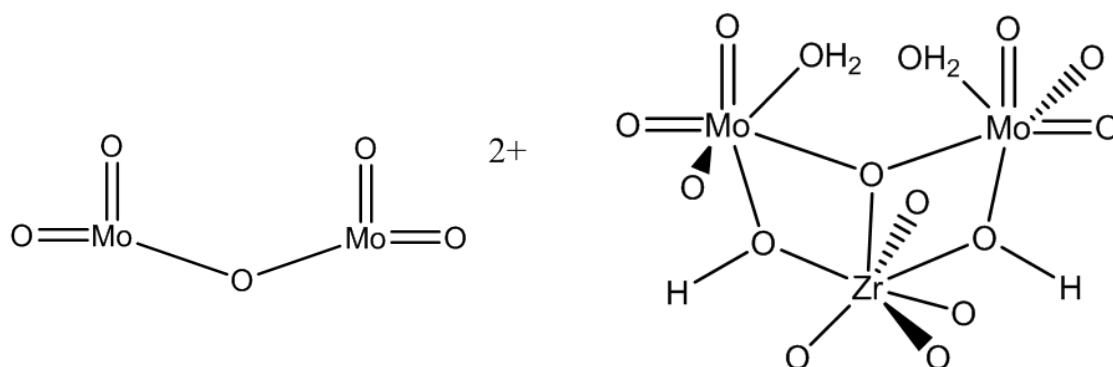


**Figure 2.14 – Structures of  $\text{Mo}_2\text{O}_5^{2+}$  and ZMH (Edmondson, 2010)**

It is theorised that the reason for the reduction in crystal size of ZMH on the addition of citric acid is the formation of a complex between the citric acid and the di-molybdate species,  $\text{Mo}_2\text{O}_5^{2+}$  (Figure 2.15), thought to be part of the CPM to ZMH conversion reaction. At 10 mol % addition of citric acid, twinning of the crystals can be seen, causing elongation of the crystals. At higher addition levels, fractured growth is seen, resulting in the formation of ‘wheat-sheaf’ shaped crystals (Edmondson, 2010).

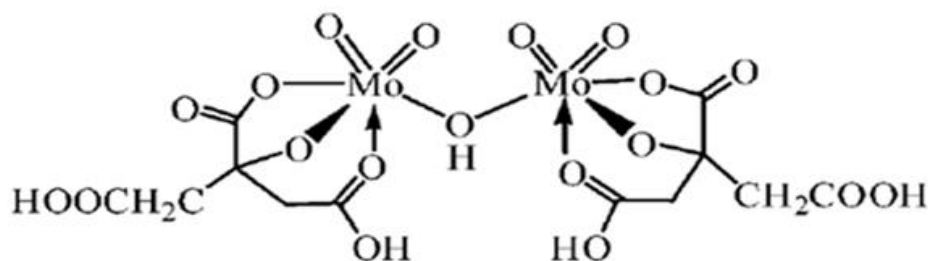
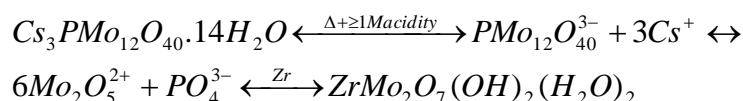


**Figure 2.15 – Di-molybdate : Citric Acid Complex (Edmondson, 2010)**

An ongoing morphological study of zirconium molybdate (Edmondson, 2010) has postulated that the formation of ZMH from the conversion of CPM begins with the formation of the phosphomolybdate keggion ion  $[PMo_{12}O_{40}]^{3-}$ . This is then broken down to form  $H_3PO_4$  and free molybdates. Raman spectroscopy has shown that  $PMo_{12}O_{40}^{3-}$  and  $Mo_2O_5^{2+}$  species exist in equilibrium in a nitric acid solution (Sarsfield, 2004).  $Mo_2O_5^{2+}$  is of interest, as its structure transposes directly into the structure of ZMH (Figure 2.14). It is thought that zirconium ions react with this species, resulting in the formation of ZMH through the following reaction scheme (Edmondson, 2010):



It is currently unknown whether the conversion of CPM to ZMH occurs within the calcination process.

### 2.5.2 Reactivity of lithium

Lithium plays an important role in the vitrification process. Originally, lithium was only used as a component in the glass frit, but investigations have shown that it also has a profound effect in the calcination process. From full-scale inactive trials carried out by BNFL, it is hypothesised that the roles of lithium in the vitrification of high level waste include (Magrabi, 1981):

- Formation of complex oxides with aluminium and iron, allowing higher reactivity in the melter improving the homogeneity of the glass product.
- Acting as a binding agent, reducing dust carry-over to the off-gas system and therefore reducing blockages in the dust scrubber.
- Reducing the viscosity of the glass, allowing a higher portion of waste oxides to be incorporated, and improving the pour characteristics of the melt.

The amount of lithium present in the system must be carefully controlled, as too little can result in high dust carry-over and high glass viscosity. This would result in high probability of blockages in the off-gas system, poor homogeneity of the glass product and difficulty in controlling the pour rates (Magrabi, 1981). A high lithium content can also be detrimental to the process causing the calcine to become too sticky, causing blockages in the calciner. It could also lead to higher leach rates from the glass product, causing problems with final disposal (Marples, 1988; Larkin 1986; Harrison et al., 2010).

The target amount of lithium oxide present in the final glass product is about 4 wt%<sup>4</sup>. Half of this is present in the glass frit as lithium oxide (Li<sub>2</sub>O) and the other half is added to the HAL as lithium nitrate (LiNO<sub>3</sub>·3H<sub>2</sub>O (aq)) before calcination. This combination provides a good balance of properties in both the calciner and the melter.

Oxides of aluminium and iron are stable and take a long time to react in the melter. The addition of lithium promotes the formation of complex oxides which are more reactive than the pure oxide. This is important for Magnox waste-forms, where the levels of aluminium and iron are relatively high (Wills, 2002). Oxide and Blended waste-forms have much lower concentrations of aluminium and iron, and therefore the need to add lithium to the simulant is reduced. This would need to be taken into account by adding the lithium to the glass frit, so the level of lithium in the final glass product remained at the desired level.

There are, however, a number of benefits which could be achieved by eliminating lithium addition to the HAL, (Brace, 2005b):

- As lithium is added as a dilute solution it takes up a large volume of HAST's 18 and 19. Removing this would allow more flexibility within HALEs and provide benefits to upstream reprocessing operations.
- Lithium analysis of HAL could be eliminated.
- Full-lithium base glass may give greater fluidity allowing better mixing and faster waste incorporation within the melter.
- Formation of alkali molybdates in the calciner causes yellow phase formation. Yellow phase is not easily incorporated into the glass and is corrosive to the melter crucible, reducing the lifetime of the melter.

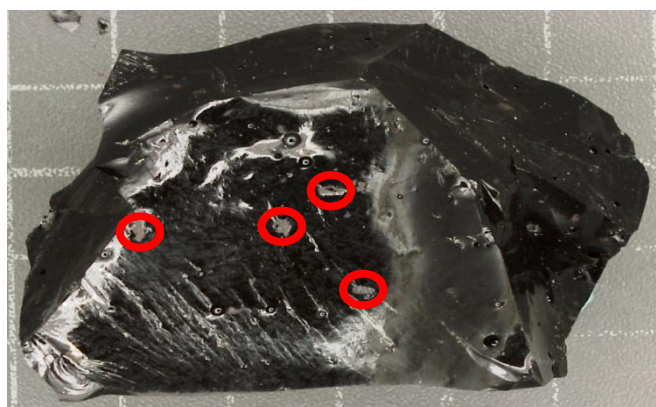


**Figure 2.16 - Full scale full Li MW Magnox glass (Short, 2006b)  
(Grid markings are 1cm<sup>2</sup>, refractory phase particles are circled)**

<sup>4</sup> This figure of 4wt% is based on a 25% waste oxide incorporation, which results in a 1:1 ratio of lithium to sodium. At different waste oxide incorporations, this value is changed to maintain the lithium to sodium ratio in the final glass product.

Although the benefits of adding lithium to the calciner are well documented and researched (Magrabi, 1981; Larkin, 1986; Marples 1988), there seems to be little understanding of the reactions which take place in the calciner. When lithium is not added, spinel phases containing iron and aluminium can be seen in the glass as grey oxide particles (Figure 2.16), which can be separated from the glass. This allows analysis to be carried out, and the oxides present can be detected. Upon the addition of lithium to the calciner, these phases are present in a much smaller scale and quantity and therefore become difficult to separate. Analysis of the new lithium containing phase is therefore limited to SEM, as this can be done in the glass product (Figure 2.17).

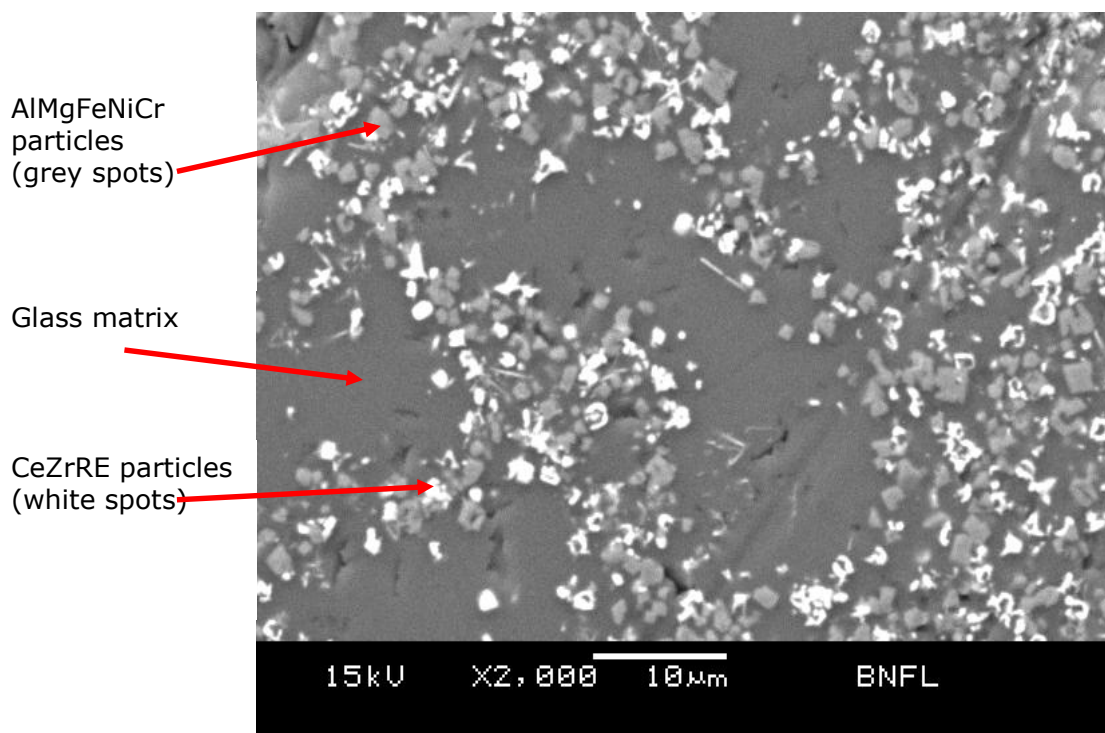


**Figure 2.17 – High magnification backscattered electron image of a refractory rich particle in WRW17 4 % Li<sub>2</sub>O (Short, 2006b)**

SEM and EDS analysis (Figure 2.17) revealed that one phase was composed of the refractory metals Al, Mg, Cr, Ni and Fe in various relative abundances (Short, 2006b), and probably present in the form of oxides with a spinel type crystal structure (although X-ray diffraction analysis would be required to confirm this). The other phase often had particles containing cerium, zirconium and rare-earth metals entrained in it too.

**Table 2.3 – The possible reactions of lithium nitrate with metal nitrates in the calcination process**

Product	Reaction Scheme	Melting Point (°C)
LiNO <sub>3</sub>	NO REACTION	255
Li <sub>2</sub> O	$4LiNO_3 \xrightarrow{Heat} 2Li_2O + 4NO_2 + O_2$	1432
LiAlO <sub>2</sub>	$LiNO_3 + Al(NO_3)_3 \rightarrow LiAlO_2 + 4NO_2 + O_2$	1625
Li <sub>2</sub> ZrO <sub>3</sub>	$2LiNO_3 + ZrO(NO_3)_2 \rightarrow Li_2ZrO_3 + 3NO_2 + 2O_2$	1695
Li <sub>2</sub> MoO <sub>4</sub>	$2LiNO_3 + MoO_3 \rightarrow Li_2MoO_4 + NO_2 + \frac{3}{2}O_2$	705
CsLiMoO <sub>4</sub>	$LiNO_3 + Cs^+ + MoO_3 \rightarrow LiCsMoO_4 + NO_2$	770-800

Lithium nitrate has a noticeably low melting point, meaning if un-reacted it would be present as a liquid in the calcination process. This may be one of the reasons that lithium acts as a binder, reducing the dust carry-over to the dust scrubber (Magrabi, 1981). It is highly likely that some of the lithium nitrate will remain un-reacted, due to the high concentration of lithium compared to possible reactants, such as aluminium, and the relatively short residence time in the calciner.

### 2.5.3 Nitrate decomposition

One of the main processes which take place in the calcination process is the de-nitration of metal nitrates. The objective of the calcination process is to produce a material with good reactivity and low volatility when in the melter (Jervis, 1985). Some residual nitrates will remain in the calcine from compounds with high decomposition temperatures (Table 2.4). The amount of residual nitrates after calcination will depend on the process aids and temperatures used. These nitrates will increase the reactivity in the melter (Owens, Leung and Magrabi, 1985), giving a more homogeneous glass product. As the melter is operated at around 1050 °C, these residual nitrates will decompose to their oxide form in the melter, allowing a uniform glass, containing waste oxides, to be formed.

**Table 2.4 – De-nitration temperatures for metal nitrates found in simulated HAL (Chun, 1977)**

Nitrate	Oxide Form	Decomposition Starting Temp (°C)	Decomposition Terminal Temp (°C)	Denitration at 400 °C (%)
Al(NO <sub>3</sub> ) <sub>3</sub> .9H <sub>2</sub> O	Al <sub>2</sub> O <sub>3</sub>	53	460	99
Ba(NO <sub>3</sub> ) <sub>2</sub>	BaO	296	805	0.5
CsNO <sub>3</sub>	Cs <sub>2</sub> O	522	Volatile	0
Cr(NO <sub>3</sub> ) <sub>3</sub> .9H <sub>2</sub> O	Cr <sub>2</sub> O <sub>3</sub>	33	466	97
Fe(NO <sub>3</sub> ) <sub>3</sub> .9H <sub>2</sub> O	Fe <sub>2</sub> O <sub>3</sub>	46	367	100
Mg(NO <sub>3</sub> ) <sub>2</sub> .6H <sub>2</sub> O	MgO	43	502	60
Ni(NO <sub>3</sub> ) <sub>2</sub> .6H <sub>2</sub> O	NiO	55	665	99
Rare Earth	M <sub>2</sub> O <sub>3</sub>	50	836	65
Ruthenium Sol	RuO <sub>2</sub>	37	557	95
Sr(NO <sub>3</sub> ) <sub>2</sub>	SrO	339	738	0.1
Zn(NO <sub>3</sub> ) <sub>2</sub> .6H <sub>2</sub> O	ZnO	74	372	100
Zirconium Sol	ZrO <sub>2</sub>	24	656	98
LiNO <sub>3</sub> .3H <sub>2</sub> O	Li <sub>2</sub> O	600*	Volatile	0
NaNO <sub>3</sub>	Na <sub>2</sub> O	588	Volatile	0

\* loss of 3H<sub>2</sub>O between 56-254 °C.

The decomposition temperature of metal nitrates has been found to be inversely proportional to the charge density of the metal cation (Yuvaraj et al., 2003). The charge density of the metal cation determines the bond type between the metal and the nitrate. Metals with a low charge density (Na<sup>+</sup>, K<sup>+</sup>, Ba<sup>+</sup>) form an ionic bond which is strong, and therefore the decomposition temperature is relatively high. A high charge density cation (Al<sup>3+</sup>, Ga<sup>3+</sup>, Fe<sup>3+</sup>) results in the formation of covalent bonds between the metal and the nitrate anion. This reduces the bond order, weakening the nitrate bond, resulting in a low decomposition temperature (Yuvaraj et al., 2003).

#### 2.5.4 Molten salts

Lithium nitrate is currently added to the calciner in order to reduce the dust carry-over from the calciner to the dust scrubber. As lithium has a low melting point it will be present as a liquid in the calciner. This gives rise to the possibility of molten salt reactions occurring.

Molten salts can provide an alternative media, which can change the reactivity and solubility of reactants (Afanasiev and Geantet, 1998). This provides a different environment in which chemical reactions can occur, which would not usually take place in an aqueous medium. An example of this was performed by Xu et al. (2009) creating metal oxides with polar surfaces exposed, by using lithium nitrate as a molten salt. This is due to the strong interaction between the polar surfaces and the molten salt lowering the surface energy, allowing these compounds to be formed. These polar surfaces have a high surface energy, and may give novel properties to the products. These types of reactions could occur in zones 3 and 4 of the calciner where the lithium nitrate will exist in a molten state.

There are two main mechanisms by which reactions proceed in a molten salt host, which are the 'template-growth' and 'dissolution-precipitation' mechanisms (Zhang, 2007). 'Template-growth' reactions occur when one of the reactants is much more soluble in the molten salt than the other. The soluble reactant diffuses on to the surface of the other reactant causing a reaction to occur. The product of this reaction retains the morphology of the insoluble reactant.

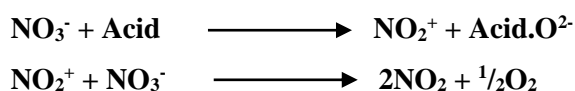
The 'dissolution-precipitation' mechanism occurs when both reactants are soluble in the molten salt (Zhang, 2007). These reactions are faster than those using the 'template-growth' mechanism and can occur at much lower temperatures. This is due to the increased interaction between the reactants and faster diffusion. The products from this reaction have no fixed morphology and can be very different from the reactants.

Alkali metal nitrates are low cost and have relatively low melting points, such as lithium nitrate (255 °C), and are therefore often used in investigations for molten salt synthesis. When two or more of these alkali metal nitrates are mixed the melting points can be made even lower, forming a deep-eutectic molten salt. The melting points of some alkali metal nitrates and their deep-eutectic mixtures are shown in Table 2.5.

**Table 2.5 – Melting points of alkali metal nitrates and their deep eutectic mixtures (Afanasiev and Geantet, 1998)**

Molten Salt	Composition (%)	Melting Point (°C)
Lithium Nitrate	0 – 100	255
Sodium Nitrate	0 – 100	310
Potassium Nitrate	0 – 100	337
LiNO <sub>3</sub> – KNO <sub>3</sub> eutectic	43 - 57	132
LiNO <sub>3</sub> – NaNO <sub>3</sub> – KNO <sub>3</sub> eutectic	30 – 17 - 53	120

Lithium nitrate and other alkali metal nitrates, act as Lux-Flood bases. They are, therefore, good O<sup>2-</sup> donors and can lower the temperatures needed for an oxidation reaction to occur. The following equations describe the Lux-Flood interactions between molten nitrates and oxoacids (Afanasiev and Geantet, 1998):



This type of reaction is used in the formation of metal oxides. The cation (Li<sup>+</sup>, Na<sup>+</sup>, K<sup>+</sup> etc) of the molten nitrate has a strong impact on the reactivity of the melt. This will control the basicity of the molten salt and therefore the concentration of O<sup>2-</sup> available for reaction. Lithium nitrate is the most basic of the alkali metal nitrates, making it the best O<sup>2-</sup> donor, giving it the highest reactivity (Afanasiev, 2007). Combined with the fact that lithium nitrate has the lowest melting point of the pure alkali metal nitrates, it is a good molten salt to use in the molten salt synthesis of metal oxides.

In the calcination process, it is possible that the addition of lithium nitrate facilitates reactions which would not occur in the aqueous phase. Experiments will be designed to determine whether lithium nitrate undergoes or facilitates reactions in the calciner, causing a lower dust carry-over to the dust scrubber, or simply binds the calcine together while in its molten salt state.



### 2.5.5 Ruthenium chemistry

Ruthenium is formed as a fission product and is present in HAL resulting from the reprocessing of spent fuel. The HAL is evaporated and stored in HAST's, where it encounters temperatures in which volatilisation can occur. Volatile species are removed through the off-gas system to avoid them being released to the environment through the plant stack. An incident occurred in 1997 where there was a release of radioactive ruthenium from the WVP stack (Watson, 1997). The release was small in terms of a radiological event, but highlighted the need to carry out further research into ruthenium behaviour under the range of conditions experienced during the vitrification process.

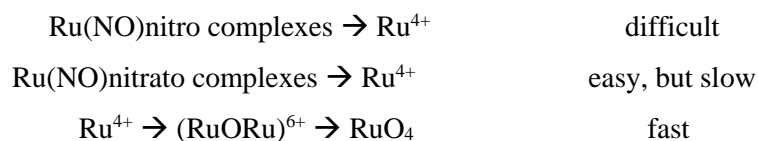
Ruthenium is also present in the dust scrubber as a significant portion of the insoluble solids, in the form  $\text{RuO}_2$ . This contributes to blockages forming in the off-gas system on WVP, reducing the throughput of the plant. Several investigations have been carried out (Morris and Haig, 2010; Sarsfield et al., 2008; Moss and Haile, 2004) to help understand the behaviour of ruthenium species within the operating conditions on the WVP's.

Early work on speciation of ruthenium in nitric acid solutions carried out by Brown et al. (1961) identified 4 classes of ruthenium complexes in plant processes (Table 2.6). The majority of these contain the stable nitrosyl ruthenium  $\text{RuNO}$  (III) cation (Newby and Rhodes, 1978) and exist in a six co-ordination species made up with aquo ligands with the formula  $[\text{RuNO}(\text{NO}_3)_x(\text{H}_2\text{O})_{5-x}]^{3-x+}$ . The value of x increases as the strength of the nitric acid increases.

**Table 2.6 – Summary of ruthenium species present in nitric acid solutions**

Species (and colour)	Behaviour in $\text{HNO}_3$ at room temperature	Oxidation to $\text{RuO}_4$ in $\text{HNO}_3$ solution
(1) $\text{RuNO}$ nitrate complexes (Red/Brown)	Moderately stable, conversion to (4) possible	Easy (slow)
(2) $\text{RuNO}$ nitro complexes (yellow)	Stable	Difficult
(3) $\text{RuNO}$ uncomplexed	Converted to (1) and (2) under appropriate conditions	Easy (slow)
(4) $\text{RuORu}$ nitrate (brown)	Stable in the absence of $\text{HNO}_2$	Very easy

The following reaction schemes show the relative rates of oxidation to the Ru (IV) cation ( $\text{Ru}^{4+}$ ) or  $\text{RuO}_4$  (Waring, 1999):



In the evaporators, ruthenium volatility is relatively low (Cains, 1980). However, under calcination conditions the ruthenium volatility is greatly increased. Work carried out by Weisenburger and Weiss (1980) showed the volatility of ruthenium depends on the waste composition and processing conditions.

An extensive study of ruthenium volatility was carried out at Harwell in the 1980's with the main author being P. W. Cains. This study showed (Berg and Monteith, 1998):

- Volatile forms of ruthenium are transients eg.  $\text{RuO}_4$ .
- When ruthenium is volatilised to  $\text{RuO}_4$  it rapidly decomposes to form very fine particles of  $\text{RuO}_2$  under conditions used on the WVP plant.
- Lab results do not simulate what happens under plant conditions due to there being more places for deposition on the plant.

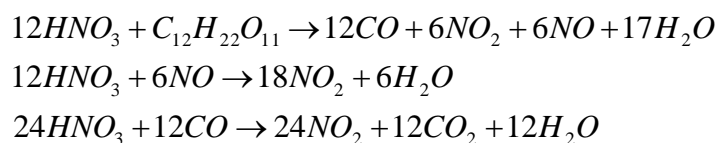
Klein et al. (1985) asserted the existence of volatile ruthenium nitrosyl species formed either through the reaction between  $\text{RuO}_4$  with  $\text{NO}_x$  or the calcination of RNN solutions in nitric acid. Ruthenium nitrosyl species are more stable than  $\text{RuO}_4$  and can therefore be condensed from the gas phase more easily. This postulation could explain the existence of both soluble (RNN) and insoluble ( $\text{RuO}_2$ ) species of ruthenium being present in the off-gas system.

Evaporation studies on dust scrubber liquors (Moss and Haile, 2004; Wright and Brown, 2003; Wright and Brace, 2004) have all shown that no loss of ruthenium is detectable. However, when dissolved calcine is used there are significant amounts of ruthenium volatilised from the samples (Sarsfield et al., 2008). It is possible that operations in the dust scrubber during the running of the VTR either cause all the ruthenium to form stable species in the DSL, or that the volatile forms of ruthenium are driven off.

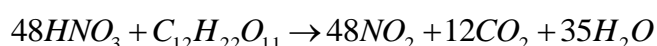
Morris (2010) identified that nitric acid, cerium and chromium are the most likely species in the HAL to cause the oxidation of ruthenium to form RuO<sub>4</sub>. They are all present in the dust scrubber and have high enough oxidation potentials to oxidise ruthenium under dust scrubber conditions. Motojima (1989) reported that cerium nitrate can completely oxidise Ru (III) to RuO<sub>4</sub> when the ratio of cerium to ruthenium is above 1.5. The ratio of cerium to ruthenium is lower in the dust scrubber than in the calcine, which could account for the differences in ruthenium volatility behaviour (Morris, 2010).

Ruthenium is added to HAL simulant as ruthenium nitrosyl nitrate (RNN), which thermally decomposes to form RuO<sub>2</sub>. Under calcination conditions, oxidising species are formed due to the decomposition of nitrates, which can oxidise the ruthenium to form RuO<sub>4</sub>. This is a volatile species, and is therefore preferentially carried over to the off-gas system. By adding sugar to the HAL simulant, the number of oxidising species is reduced in the calciner, decreasing the amount of RuO<sub>4</sub> formed. This reduces the carryover of ruthenium to the dust scrubber.

MacDougal et al. (1982) studied the reactions of sugar with nitric acid, quoting the reaction as:



Resulting in the overall reaction:



These reactions will also take place with the metal nitrates present in the HAL as well as with nitric acid. Due to the nature of these reactions the following observations were noted upon increasing the concentration of sugar added (Undre, 1985):

1. The acidity of the dust scrubber decreases.
2. The acidity of the condensate and NO<sub>x</sub> absorber liquors increase.
3. The residual nitrate within the calcine decreases.
4. The calciner tube expansion increases.
5. The mean particle size of the calcine decreases.
6. The ruthenium carryover to the off-gas system decreased to a minimum before increasing (Figure 2.18).

The first 3 points can be explained by the destruction of nitrate ions originating from the nitric acid and waste metals in the HAL (Brace, 2005c). This reduces the amount of residual nitrate, reducing the acidity of the dust scrubber liquor and increasing the amount of NO<sub>x</sub> gas liberated and collected in the NO<sub>x</sub> absorber and condenser.

The reaction between sugar and nitrates is an exothermic one, releasing extra energy as heat. This manifests as an increase in calciner tube expansion. The extra gases released from these reactions also help to break up the calcine, increasing the proportion of small particles created in the calciner (Brace, 2005c). This increases the dust carryover to the dust scrubber, increasing the chance of blockages occurring.

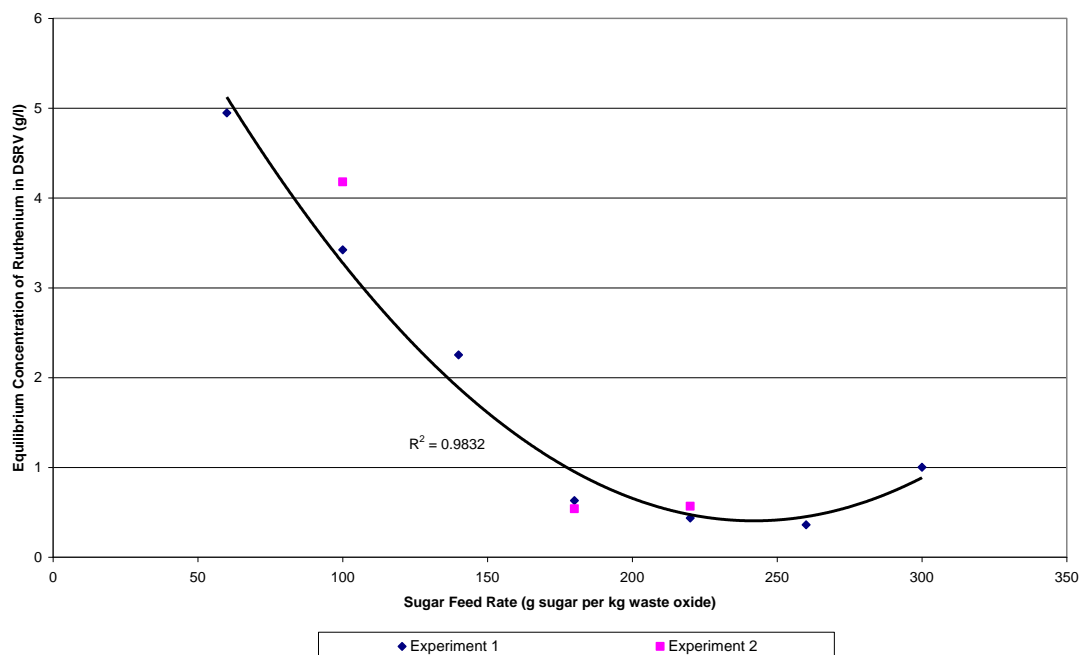


**Figure 2.18 – Graph showing the effects of sugar concentration on the carryover of ruthenium to the off-gas system (Brace, 2006d)**

The reduction in ruthenium present in the DSRV is due to the reduction in ruthenium volatility as more sugar is added (Figure 2.18). This, however, reaches a minimum at 240 g sugar per kg waste oxide (Brace, 2006d). Above this sugar addition, the amount of ruthenium in the DSRV begins to increase. This can be attributed to the increase in dust carryover caused by the exothermic reaction between sugar and nitric acid. This results in a larger proportion of fines being produced in the calciner, which is more easily carried over to the dust scrubber.

### 2.5.6 Dust scrubber solids composition

Filtration of dust scrubber liquor (DSL) samples, and subsequent EDX analysis of the solids, showed that there are 4 distinct sample morphologies present within DSL solids (Morris and Haig, 2010). One of these comprised mainly of silicon, which can be attributed to carryover of small glass particles from the melter to the dust scrubber. The second region was comprised mainly of zirconium and molybdenum, probably in the form of zirconium molybdate. This is known as a major cause of blockages within the dust scrubber. The third region analysed contained high levels of barium and ruthenium, and the final morphology was comprised mainly of ruthenium.

Blend and Magnox calcine samples were also re-dissolved during the same study and filtered to collect the insoluble material (Morris and Haig, 2010). In both cases, the major component of the sample was zirconium, with much lower levels of molybdenum and ruthenium than seen in the DSL samples. This suggests that zirconium exists mainly as  $ZrO_2$  or zirconium phosphate in the calcine. The formation of zirconium molybdate therefore most likely takes place in solution in the dust scrubber, although it is possible it is formed in the calciner, gets preferentially broken down into small particles and transferred to the dust scrubber through the off-gas.

Calcination work carried out by Short (2005) at PNNL showed there are several fluorite-type phases present within the calcine, belonging to the Fm-3m space group. These same phases have been seen in calcine dissolution work, where XRD analysis was carried out on milled and un-dissolved calcine samples (Short, 2006). This showed that one of the fluorite type phases in the calcine was insoluble in nitric acid. EDS analysis on this material showed it to have a high level of zirconium present in the sample. Possible structures of this type include  $Sm_{0.5}Zr_{0.5}O_{1.75}$  and  $Zr_2Gd_2O_7$  (Short, 2005).

On the addition of lithium nitrate to the HAL, there are 2 additional phases which can be seen using XRD analysis that are not present when the sample is lithium free (Short, 2005) and a different phase related to the fluorite structure. The related phase had the same fluorite-type structure, but the  $2\theta$  values were shifted to lower scattering angles. This type of structure can accommodate a large variety of elements, and is therefore likely to form as a complex oxide.

The first additional phase which arises is also a fluorite related structure, but belongs to the Pm-3m space group. The other additional phase is that of  $CsLiMoO_4$ . This has been identified in previous studies (Morgan et al., 2004) as being present as part of yellow-phase formation in the vitrified product.

Previous studies on HAL simulant aging (Sarsfield et al., 2004) have shown that there is no significant change in composition of the simulant when aged at 50 °C both with and without agitation. The only major change in composition is the conversion of CPM to ZMH. The rate of this conversion increases at low acidity, low fission product concentration and increased agitation. Increase agitation also causes CPM to de-agglomerate, reducing the particle size. This allows better suspension of the CPM in the HAL, although on formation of ZMH the particles fall out of suspension and are much more difficult to re-suspend.

### **2.5.7 VTR campaigns 4 and 5**

During VTR campaign 4A, the effects of feed rate, waste oxide concentration, acidity, temperature and sugar concentration on the response of the calciner, off-gas system and calcine properties were monitored. The following observations were made (Brace, 2006a; Brace, 2006b):

- Increasing the acidity of the HAL increases the volatility of ruthenium in the calciner to the off-gas system.
- Increasing the waste oxide concentration and feed rate of HAL to the calciner had no significant effect on calcine properties and calciner or off-gas performance (other than the higher set points required to keep the evaporative front at the zone 2/3 interface).
- Increasing the zone 3 and 4 temperatures by 60 °C reduced the residual nitrate present in the calcine by approximately 7 %.
- The effect of sugar on the reduction of the volatility of ruthenium was dependant on the nitrate concentration in the HAL. The optimum concentration was found to be between 4 and 5.5 g of sugar per mole of nitrate.

The condition of the rabble bar was also found to be influential in the amount of dust carried over to the dust scrubber. When the rabble bar was deformed, a significant increase in fine calcine particles was produced, increasing the amount of dust carryover. It was therefore found to be important to monitor the condition of the rabble bar more closely in future trials to reduce the probability of blockages forming in the off-gas system.

As part of VTR campaign 5, the effects of the addition of lithium nitrate to the HAL were monitored. This was done using both magnox and blended simulants. Lithium nitrate was dosed into the HAL based on having 0 %, 1 % and 2 % of the lithia present in the final glass product contained within the simulant. In all 3 cases, the amount of dust carryover was reduced as the amount of lithium nitrate added was increased (Vickers, 2006b). This is because lithium nitrate will be present as a molten salt in the calciner and has a high decomposition temperature, so helps to bind the calcine together.

In VTR campaign 5, substituting blended simulants for magnox simulants reduced the amount of dust carryover and ruthenium carryover to the off-gas system. This was despite only small changes in residual nitrate and the particle size distributions of the resultant calcines (Vickers, 2006c).

It was noted that when comparing results from VTR campaign 4B and campaign 5, there was a decrease in ruthenium carryover despite the amount of dust carryover increasing. The only major difference between the trials was the difference in zone 3 and 4 temperatures. It was postulated that an increase in temperature had reduced the amount of nitrate present in the HAL, reducing the number of oxidising species present in the calciner (Vickers, 2006c). This would reduce the amount of the volatile RuO<sub>4</sub> species being produced and therefore lower the carryover to the off-gas system. Zone 1 and 2 temperature set points seemed to have little effect on the ruthenium carryover (Vickers, 2006a). This is probably due to the boiling of water keeping the temperature constant, just moving the evaporative front toward the top end of the calciner.

Experiments have been run on the VTR using both magnox and blended simulants, with and without the addition of lithium. The dust carryover from an individual experiment can be calculated (Equation 1) so a comparison can be drawn. This allows factors which affect the dust carryover to be identified. Table 2.7 gives a brief overview of the effects of calciner temperature, HAL feed type, feed rate, waste oxide concentration, sugar : nitrate ratio and lithium addition on the dust carryover from experiments carried out on the VTR.

$$c = \frac{M_D}{R} + \left( c_0 - \frac{M_D}{R} \right) e^{-Rt/V}$$

Equation 1: Dust Scrubber Solids Build Up (Brace, 2006c)

Where:

- $c$  is the concentration of solids in the dust scrubber liquor at time  $t$ , g / l
- $M_D$  is the rate at which solids are abated in the dust scrubber, g / h (note: if the DS is 100 % efficient then this is equal to the dust carryover, if 90 % efficient  $0.9 \times$  dust carryover etc.)
- $R$  is the dust scrubber recycle rate, l / h
- $c_0$  is the concentration of solids in the dust scrubber liquor at time 0 h, g / l
- $V$  is the volume of dust scrubber liquor, l
- $t$  is the elapsed time, h

Equation 1 does not take into account the efficiency of the dust scrubber (some particles may not be removed in the dust scrubber and make it to the condenser, therefore not contributing to the total solids) or if there are any blockages in the dust scrubber inlet preventing the dust getting to the dust scrubber. The  $M_D$  values are a useful tool for assessing dust carryover, but are not absolute values. Any anomalies in these values can be investigated, however, by visual inspections for blockages and analysis of the condenser liquor.

### **2.5.8 The effects of temperature, waste oxide concentration and acidity**

Experimental work carried out by Brace (2005a) compared the solubility of Magnox calcines with a 75 % / 25 % oxide/Magnox blend under dust scrubber conditions. The results of this work showed that blend and Magnox calcines have different solubility characteristics. Magnox calcines display a maximum solubility in nitric acid in the range 5-7 M, where as Blend calcine solubility increases with increasing acidity up to 10 M. Blend calcines are also significantly less soluble due to the higher concentration of zirconium and molybdenum present in the simulant. A reduction of temperature, carried out in these experiments (Brace, 2005a), did not result in any significant reduction in solubility of both calcines.

Other factors which affect the solubility of the calcines in nitric acid are the waste oxide concentration and the dissolution time (Brace, 2005a). The higher the waste oxide concentration, the greater the amount of insoluble material is present, reducing the solubility of the calcine. Other species, which are soluble at lower incorporation rates, may also have reached their solubility limits contributing to the increase in insoluble fraction. Dissolution time also affects the solubility of the calcine. The greater the dissolution time, the more insoluble material precipitates from the solution. This can be explained by the formation of insoluble species through reactions in the solution. As the dust scrubber has a reservoir of dissolved calcine, the fraction of insoluble material will build and eventually lead to blockages within the off-gas system.



**Table 2.7 – Factors which affect dust carryover to the off-gas system on the VTR (Short, 2005b; Vickers, 2006a; Vickers, 2006c)**

Campaign/ Experiment Number	Feed Type	Feed Rate (l / h)	Calciner Temperature (°C)				Sugar:Ni trate	Lithium Addition (g / l)	Waste Oxide Conc (g / l)	M <sub>D</sub>
			Zone 1	Zone 2	Zone 3	Zone 4				
C5 E2/1	Magnox	42.46	<b>770</b>	<b>770</b>	680	680	4.9	0	184.65	157.5
C5 E2/2	Magnox	42.46	<b>830</b>	<b>830</b>	680	680	4.9	0	184.65	154.1
C5 E3	Magnox	42.46	<b>800</b>	<b>800</b>	680	680	4.9	0	184.65	221.9
C5 E4/1	Magnox	42.46	800	800	680	680	<b>3.5</b>	0	184.65	305.9
C5 E4/2	Magnox	42.46	800	800	680	680	<b>6.5</b>	0	184.65	307.1
C5 E5	Magnox	<b>45.80</b>	800	800	680	680	4.9	<b>6.1</b>	<b>171.2</b>	130.8
C5 E6	Magnox	<b>49.15</b>	800	800	680	680	4.9	<b>11.4</b>	<b>159.5</b>	47.1
C5 E19	<b>Blend</b>	<b>39.67</b>	800	800	703	703	4.9	0	<b>197.6</b>	162.0
C5 E20	Blend	<b>43.01</b>	800	800	703	703	4.9	<b>6.5</b>	<b>182.3</b>	69.0
C4B E	Blend	<b>49.85</b>	800	800	735	735	4.9	<b>11.2</b>	<b>169.7</b>	88.1
C6 E1	<b>Dil. Blend</b>	<b>60.3</b>	<b>870</b>	<b>870</b>	685	685	4.9	0	<b>130</b>	188.6
C6 E2	Dil. Blend	<b>63.6</b>	<b>880</b>	<b>880</b>	685	685	4.9	0	<b>110</b>	160.6
C6 E3	Dil. Blend	<b>69.0</b>	<b>910</b>	<b>910</b>	685	685	4.9	0	<b>90</b>	151.4

Owens et al. (1985) carried out a series of experiments in which a series of HAL simulants were calcined in a muffle furnace at temperatures of 300 °C, 400 °C and 500 °C. The purposes of these experiments were to monitor the residual nitrate and ruthenium retention as a function of temperature, lithium addition and sucrose addition. During these experiments it was found that residual nitrate decreases with increasing temperature and sucrose addition and increases with the addition of lithium nitrate. By comparing the residual nitrate in samples with lithium addition to those without, it was shown that some of the lithium nitrate had reacted at 300 °C.

During this work (Owens et al., 1985) some of the calcined HAL samples were subjected to DTA analysis. It was reported that when no lithium was present in the sample, a single peak was observed at 400 °C due to the evolution of NO<sub>2</sub>. Upon the addition of lithium nitrate, 2 further peaks were reported at temperatures of 300 °C and 500 °C, which were considered to be characteristic of the presence of lithium.

## **2.6 Chapter Summary**

Over the past 50 years, there have been numerous methods devised to encapsulate high level liquid waste (HLLW) from reprocessing. The AVM method was found to be the most suitable, and was adopted at the Sellafield site with the building of three waste vitrification plants (WVP's). This method involves passing the liquid waste through a rotary kiln (calciner) and encapsulating the waste in a borosilicate glass, in a continuous process. This gives the best combination of properties such as durability, high waste loading and radiation stability at a relatively low cost.

Although the AVM process is the best method for waste vitrification, there are some problems which arise, which force the shut-down of the WVP plants. The most common of these are blockages which arise in the dust scrubber and recycle constant volume feeder (RCVF). These blockages arise due to the formation of insoluble precipitates, such as zirconium molybdate and ruthenium dioxide. By understanding the chemistry behind the formation of these precipitates, and of the highly active liquor (HAL) and dust scrubber liquor (DSL), it may be possible to reduce or control the amount of blockages which occur on the WVP lines.

Lithium nitrate has a significant effect on the properties of the calcine, and reduces the amount of carry-over to the dust scrubber. This has helped to reduce the number of blockages which occur on the WVP plant, but the reasons for this are not fully understood. As lithium nitrate will exist as a molten salt in the calciner, it could be simply binding the calcine together, reducing the amount of dust released to the dust scrubber. An investigation in the reactivity of lithium nitrate could allow an understanding of how the chemistry in the calciner can be manipulated to reduce the number of blockages which occur, increasing the efficiency of the WVP plants.

## 3. Experimental Methods

### 3.1 Introduction

If lithium nitrate is added to the simulated highly active liquor (HAL) processed on the VTR, a reduction in the amount of refractory oxides, high in aluminium and iron, is observed in the resulting product glass. A series of lab-scale experiments were therefore designed to determine the reactivity of lithium nitrate with other metal nitrates present in the HAL. These were carried out under conditions designed to simulate those experienced in the calciner, and the reaction mixtures (Table 3.2) based on the stoichiometry of Magnox HAL simulant used on the vitrification test rig (VTR).

As identification of the lithium containing phases is very difficult in a large scale multi-component system, the reactions of lithium with other species were also investigated. The possible reactions of lithium nitrate with aluminium nitrate, iron nitrate, zirconyl nitrate and caesium phosphomolybdate (CPM) were investigated. A systematic approach was taken when designing these reactions, to ensure the effects of lithium on the reactions could be monitored.

The experimental approach consisted of first reacting lithium nitrate with the other compounds individually to determine if any reactions were observed. Reactions between the other HAL simulant components were then carried out without the presence of lithium nitrate, with lithium nitrate and with an equivalent amount of nitrate added through addition of excess nitric acid. This was to determine whether the additional nitrate was responsible for any of the reactions which took place, rather than the lithium cation. By carrying out reactions with and without the presence of lithium nitrate, the role of lithium in the calciner could be better understood. This research on simplified HAL simulants has allowed identification of some reaction products which may form in the calcination process.

### 3.2 Materials

The materials shown in Table 3.1 were used in this project. All materials were used as received without any further purification.

**Table 3.1 – Materials used in sample preparation**

Chemical	Purity (%)	Supplier
LiNO <sub>3</sub>	>98	Fisher Scientific
Al(NO <sub>3</sub> ) <sub>3</sub> .9H <sub>2</sub> O	98	Alfa Aesar
Mg(NO <sub>3</sub> ) <sub>2</sub> .6H <sub>2</sub> O	>99	Acros Organics
Fe(NO <sub>3</sub> ) <sub>3</sub> .9H <sub>2</sub> O	98 - 101	Alfa Aesar
ZrO(NO <sub>3</sub> ) <sub>2</sub> (161 g/l)	N/A	Alfa Aesar
H <sub>3</sub> PMo <sub>12</sub> O <sub>40</sub>	N/A	Alfa Aesar
Cr(NO <sub>3</sub> ) <sub>3</sub> .9H <sub>2</sub> O	98.5	Alfa Aesar
Nitric Acid (16M)	N/A	Fisher Scientific
Sucrose	N/A	

### 3.3 Sample preparation

All of the simplified HAL simulants were made using the same method, using the chemicals and quantities listed in Table 3.2. Quantities of reagents shown in Table 3.2 were placed in a 100 ml container. Water and nitric acid were added and the mixture was shaken thoroughly until a homogeneous solution was formed. Samples were left overnight to allow any reactions to occur. Sugar solution was added and the mixture shaken thoroughly for 30 s to ensure homogeneity. The samples were stored at room temperature for further treatment.

**Table 3.2: Sample Preparation Table\***

Sample Name	Anhydrous Lithium Nitrate	Aluminium Nitrate Nonahydrate	Magnesium Nitrate Hexahydrate	Iron Nitrate Nonahydrate	Chromium Nitrate Nonahydrate	Phospho-molybdic Acid	Zirconyl Nitrate (161 g / l)	Nitric Acid (16 M)	Sugar Solution (200 g / l)	Water
LAN1	1.739 g	7.481 g	-	-	-	-	-	4.588 g	3.349 g	36.192 g
LMN1	1.885 g	-	7.335 g	-	-	-	-	4.588 g	3.339 g	36.192 g
LIN1	3.171 g	-	-	6.049 g	-	-	-	4.588 g	3.494 g	36.192 g
LPN1	2.711 g	-	-	-	-	6.509 g	-	4.588 g	2.230 g	36.192 g
LZN1	6.824 g	-	-	-	-	-	14.875 g	4.588 g	4.199 g	23.713 g
AMN1	-	4.841 g	4.379 g	-	-	-	-	4.588 g	3.053 g	36.192 g
AIN1	-	6.387 g	-	2.833 g	-	-	-	4.588 g	3.033 g	36.192 g
MIN1	-	-	6.187 g	3.033 g	-	-	-	4.588 g	3.001 g	36.192 g
PZN1	-	-	-	-	-	8.044 g	7.307 g	4.588 g	1.517 g	30.061 g
LAMN1	1.003 g	4.315 g	3.903 g	-	-	-	-	4.588 g	3.214 g	36.192 g
LAIN1	1.279 g	5.502 g	-	2.440 g	-	-	-	4.588 g	3.244 g	36.192 g
LMIN1	1.356 g	-	5.726 g	2.587 g	-	-	-	4.588 g	3.312 g	36.192 g
LPZN1	2.457 g	-	-	-	-	5.899 g	5.357 g	4.588 g	2.323 g	31.697 g
AMN2	-	4.315 g	3.903 g	-	-	-	-	5.936 g	3.214 g	36.192 g
AIN2	-	5.502 g	-	2.440 g	-	-	-	6.307 g	3.244 g	36.192 g
MIN2	-	-	5.726 g	2.587 g	-	-	-	6.411 g	3.312 g	36.192 g
PZN2	-	-	-	-	-	5.899 g	5.357 g	7.891 g	2.323 g	31.697 g
LAMCN1	0.959 g	4.126 g	3.731 g	-	0.401 g	-	-	4.588 g	3.202 g	36.192 g
AMCN2	-	4.126 g	3.731 g	-	0.401 g	-	-	5.877 g	3.202 g	36.192 g
AMCN1	-	4.607 g	4.167 g	-	0.448 g	-	-	4.588 g	3.048 g	36.192 g

\* Chemical Stoichiometries represent those found in Magnox HAL simulant, with sugar added at 4.9 g / [NO<sub>3</sub><sup>-</sup>].

All values weighed within an error of ±0.001 g

**Table 3.3: Molar ratios of elements**

Sample Name	Molar Ratios of Elements Present in the Sample								
	Li	Al	Mg	Fe	Cr	P	Mo	Zr	C
LAN1	1.3	1.0	-	-	-	-	-	-	0.5
LMN1	1.0	-	1.0	-	-	-	-	-	0.4
LIN1	3.1	-	-	1.0	-	-	-	-	0.7
LPN1	1.0	-	-	-	-	0.1	1.1	-	0.2
LZN1	1.5	-	-	-	-	-	-	1.0	0.2
AMN1	-	1.0	1.3	-	-	-	-	-	0.7
AIN1	-	2.4	-	1.0	-	-	-	-	1.3
MIN1	-	-	3.2	1.0	-	-	-	-	1.2
PZN1	-	-	-	-	-	0.1	1.7	1.0	0.1
LAMN1	1.3	1.0	1.3	-	-	-	-	-	0.8
LAIN1	1.3	1.0	-	0.4	-	-	-	-	0.6
LMIN1	3.1	-	3.2	1.0	-	-	-	-	1.5
LPZN1	1.5	-	-	-	-	0.1	1.7	1.0	0.3
AMN2	-	1.0	1.3	-	-	-	-	-	0.8
AIN2	-	2.4	-	1.0	-	-	-	-	1.6
MIN2	-	-	3.2	1.0	-	-	-	-	1.5
PZN2	-	-	-	-	-	0.1	1.7	1.0	0.3
LAMCN1	1.3	1.0	1.3	-	0.1	-	-	-	0.9
AMCN2	-	1.0	1.3	-	0.1	-	-	-	0.9
AMCN1	-	1.0	1.3	-	0.1	-	-	-	0.7

### 3.3.1 Calcination

30 ml of each simplified HAL simulant was transferred to a porcelain crucible using a pipette. The crucibles were placed in a furnace at room temperature and subjected to the following heat cycle (Figure 3.1) to replicate the conditions which would be experienced in the calciner:

1. Increase the temp at 5 °C / min to 110 °C and dwell for 20 minutes to simulate the evaporation conditions (Zones 1 and 2) in the calciner.
2. Increase temp to 250 °C at 5 °C / min and dwell for 20 minutes to prevent loaming of the nitrates.
3. Increase temp to 350 °C at 5 °C / min and dwell for 20 minutes to simulate temperatures experienced by the calcine in the denitration process (Zones 3 and 4) in the calciner.
4. Decrease temp to 110 °C and dwell to preclude any deliquescence until sample was collected.

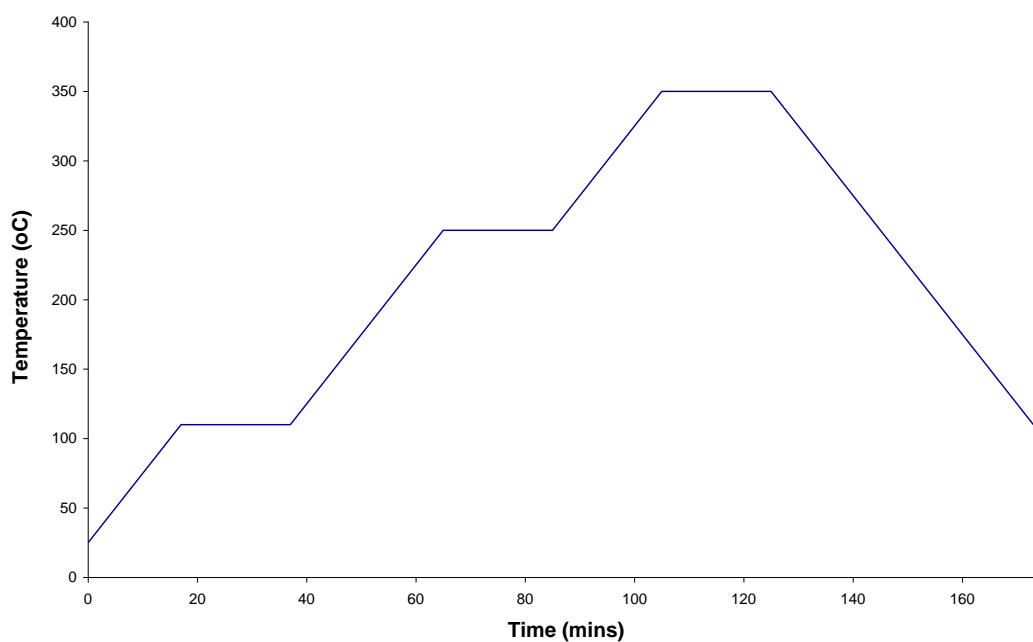


**Fig 3.1 – Temperature profile of calcination at 350 °C**

The crucibles were removed from the furnace and allowed to cool to room temperature. The resultant solid was transferred to a sample jar and placed in a dessicator ready for further analysis. The process was repeated twice more, with fresh combined solution samples, taking the furnace up to 450 °C and 550 °C respectively in heat cycle part 3, leaving everything else unchanged.

### 3.3.2 Freeze Drying

Freeze drying, or lyophilisation, is the process of removing water from a frozen material by sublimation. This is achieved by reducing the pressure under vacuum allowing the solid ice phase to be converted directly to vapour (shown in Figure 3.2). This leaves behind a solid product with the same characteristics as the original product if water was added without any decomposition taking place.

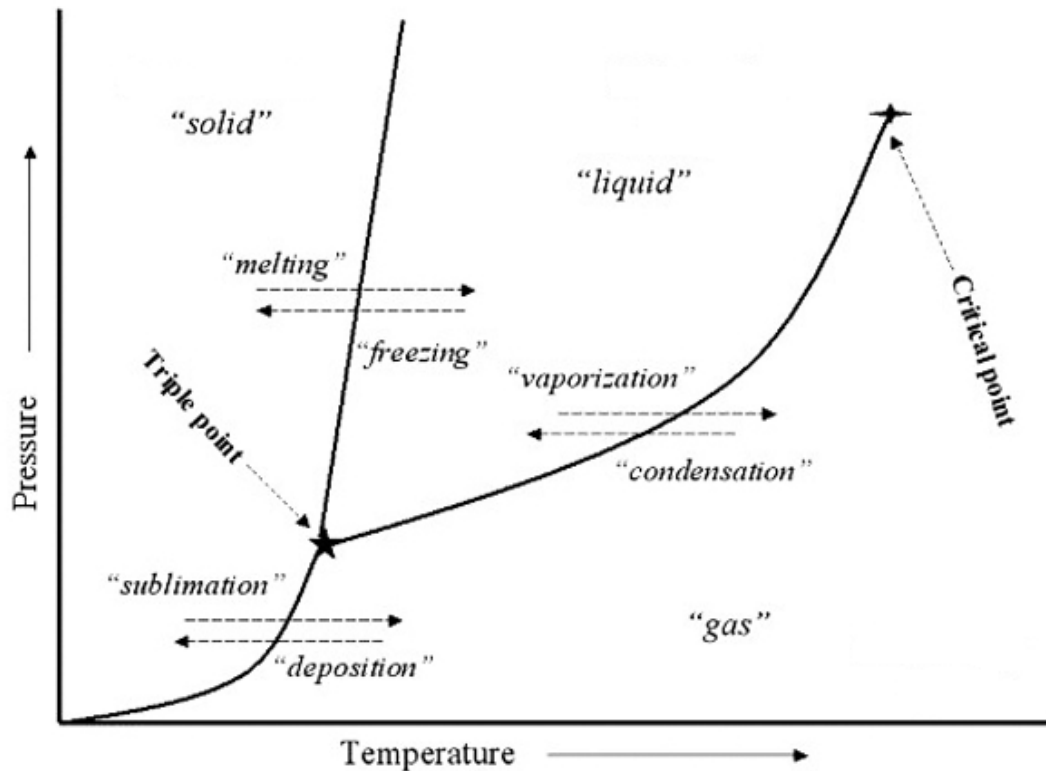


Figure 3.2 – Phase diagram of Water<sup>5</sup>

The purpose of freeze drying is to produce a solid product without thermally decomposing the species present within the samples. This allows solid state analysis to be carried out on the samples and gives a starting point to determine which reactions take place in solution and which take place under calcination conditions.

There are two main stages to freeze drying; the first is freezing of the sample. This was done by adding the chosen solution (as prepared in section 3.2) dropwise into liquid nitrogen using a Pasteur pipette. The resultant frozen pellets were placed in suitable 75 ml wide neck flasks using a spoon headed spatula. The flasks were attached to a Christ Alpha 1-2LD plus freeze dryer using the rubber attachments around the acrylic chamber (shown in Figure 3.3). The freeze dryer was then turned on and the main drying stage started.

<sup>5</sup> Adapted from <http://www.laetusinpraesens.org>.





**Figure 3.3 – Photo of Christ Alpha 1-2LD plus freeze dryer**

The freeze dryer was set to main drying mode and the ice condenser temperature and pressure were monitored on the display. Typical pressures of 0.05 mbar were reached equating to an ice condenser temperature of approx  $-48\text{ }^{\circ}\text{C}$ . The samples were left for 24 hours to dry completing the main drying stage. Once the samples were dried the vacuum was released from the freeze dryer and the flasks removed from the rubber attachments. The solids were collected in a suitable container and were stored for either further heat treatment (see section 3.3.3) or analysis.

### **3.3.3 Calcination of freeze dried samples**

Further calcination was carried out on a selection of the freeze dried samples to replicate the residence time experienced in the calciner on the VTR, as this could not be achieved using the calcination method outlined in section 3.2.1 due to the ramp up period required to ensure the liquid didn't boil over. This was done by preheating a furnace to the desired calcination temperature. Approx 5 g of the freeze dried sample was then placed in a porcelain crucible and placed in the preheated furnace for a set period of time (between 2 and 15 minutes). The sample was then removed and allowed to cool to room temperature before being placed in a suitable container and stored awaiting analysis.

### 3.4 Sample nomenclature

As there were many samples, an identification system was introduced in order for them to be distinguishable when comparing results. Each chemical added was given a symbol to represent its presence in the sample. These symbols are shown in Table 3.4.

**Table 3.4 – Sample Naming System**

Symbol	Meaning
L	Contains Lithium Nitrate
A	Contains Aluminium Nitrate
M	Contains Magnesium Nitrate
I	Contains Iron Nitrate
C	Contains Chromium Nitrate
P	Contains Phosphomolybdic Acid
Z	Contains Zirconyl Nitrate
N1	Contains Standard Nitrate
N2	Contains Added Nitrate
-XXX	Calcination Temperature in °C

For example, a sample containing lithium nitrate, magnesium nitrate and iron nitrate with a standard amount of nitric acid added and a calcination temperature of 500 °C would be called LMIN1-500. The samples are named accordingly in Table 3.2. The sample LMIN1-500 which has been heated for 24 hours in the furnace would be called LMIN1-500-24h. If heat treated for 30 minutes the sample would be LMIN1-500-30m.

### 3.5 Scanning electron microscopy

Scanning electron microscopy (SEM) operates on the same principles as optical microscopy, using lenses to magnify the image of a object. However in SEM magnetic fields are used as lenses to focus a beam of electrons on to the surface of the sample rather than using curved glass lenses to focus light. These electrons are scattered from the object and focussed to form an image through digital conversion. Electrons have a much shorter wavelength than light, and so higher resolutions can be achieved (as resolution is a function of the wavelength). Improvements in resolution of SEM over optical microscopy can be up to  $10^4$  times. Egerton (2005) provides an in depth overview of the principles of SEM.

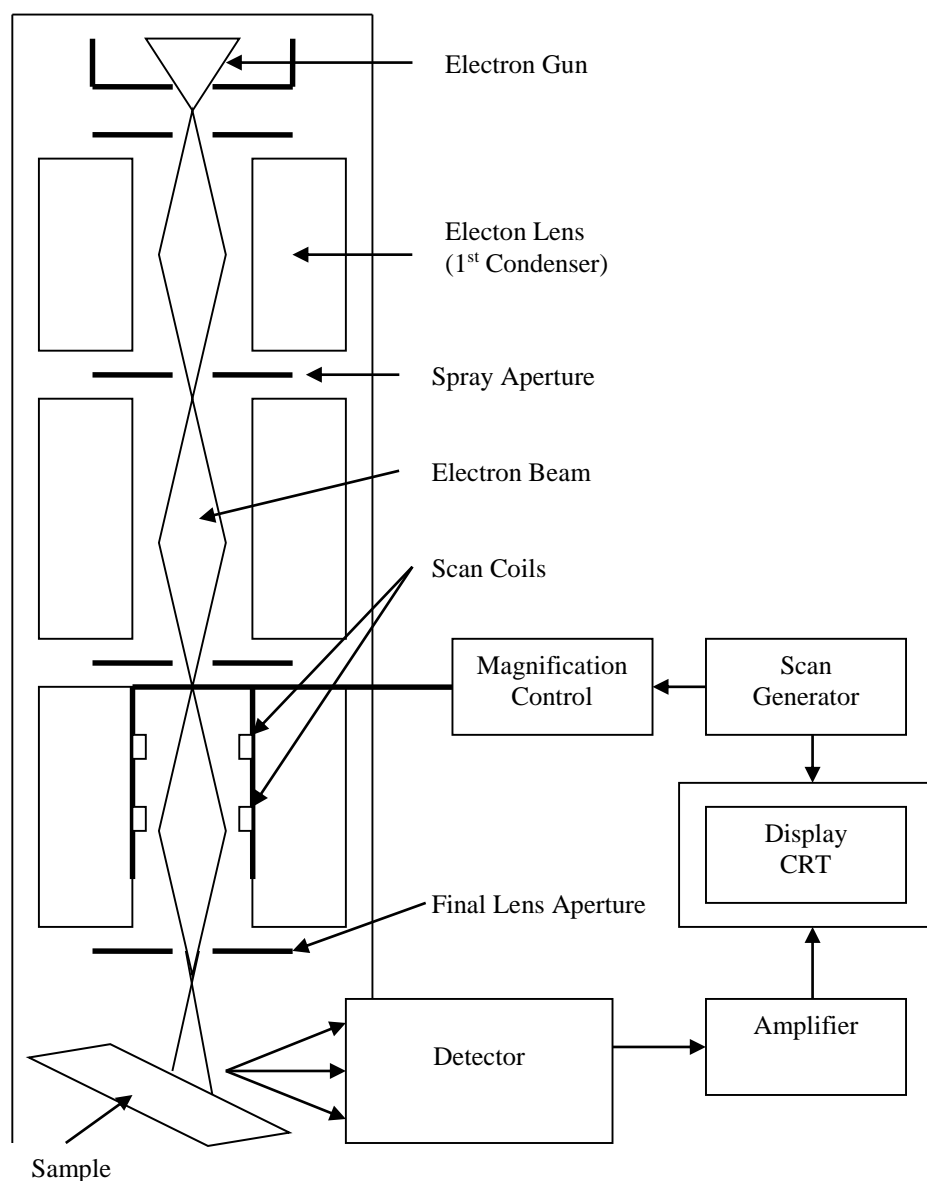


**Figure 3.4 – Schematic Diagram of an SEM**

A scanning electron microscope (SEM) with energy-dispersive X-ray spectroscopy (EDS) capability was used to determine the chemical composition of the samples. EDS operates on the principle of a primary electron from the SEM beam knocking an electron from the inner shell of an atom, within the sample, out of its orbit. This leaves the atom in an excited state, and causes an electron from an outer shell to move to fill the core hole and reduce the overall energy of the system. This transition produces an X-ray photon with an energy proportional to the energy gap between the two shells (Figure 3.5) which is distinctive to that element. The X-rays produced are captured and processed by a detector and can therefore be used to identify the elements present in the sample.

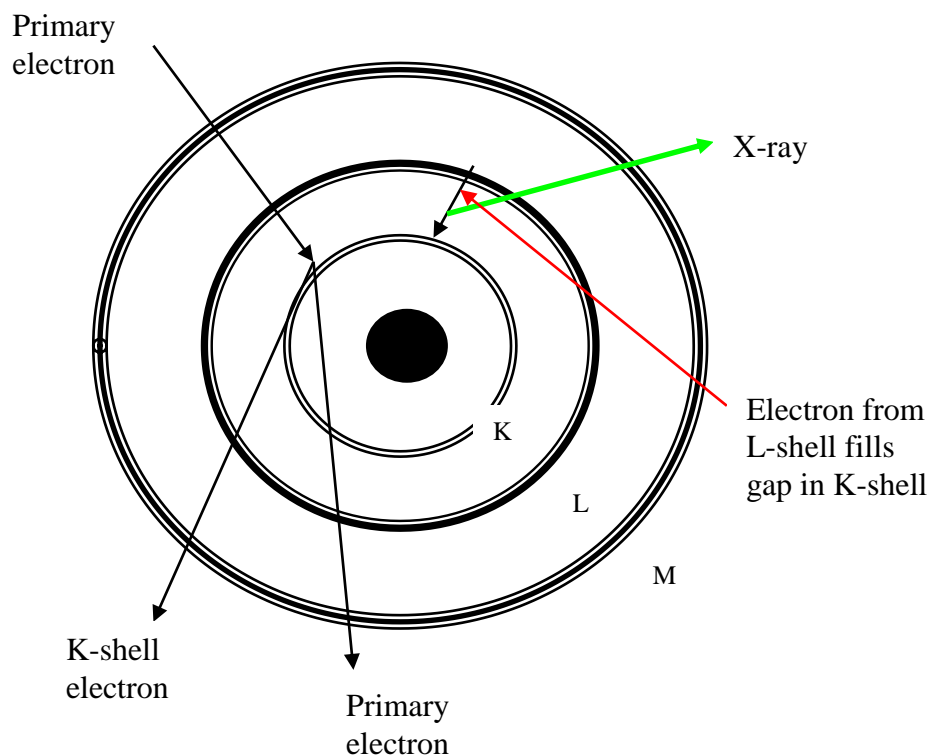


**Figure 3.5 – Schematic diagram of electron movement during EDS spectroscopy**

Samples for EDS analysis were prepared by grinding to a fine powder using a porcelain mortar and pestle, and sprinkling a small amount on a sticky carbon tab. The tab was then placed on a carbon stub to reduce sample charging, and placed under high vacuum in the microscope chamber. An electron accelerating voltage of 10 kV was used on all the samples, with a working distance set to 35 mm and a spot size of 25  $\mu\text{m}$ .

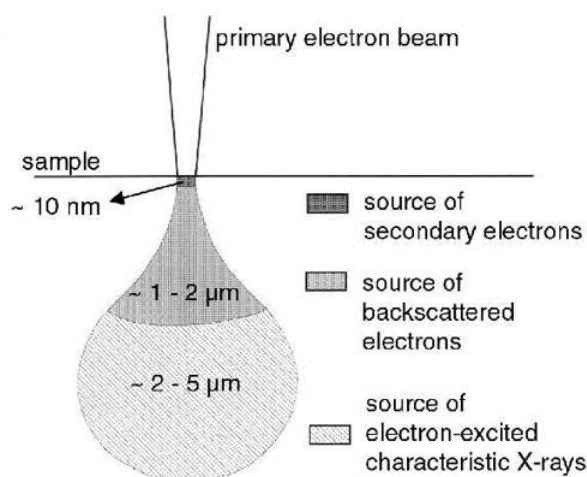


**Figure 3.6 – Diagram showing the interaction volume of the SEM Electron beam with the sample (Goodhew et al, 2001)**

Due to the interaction volume of the electrons with the sample when using EDS, more than one phase may contribute to the detected signal. The measurement of more than one phase could give rise to multiple peaks, suggesting a reaction has occurred, contradicting the XRD data. When using EDS data to identify reaction products, the interaction volume was taken into account. A comparison to the XRD data was made where possible.

The use of SEM (EDS analysis) had limitations, as elements with  $Z < 10$  were not represented accurately. This is due to the beryllium windows in the EDS spectrophotometer, which absorb the characteristic X-rays from elements with  $Z < 10$ , not allowing them to reach the detector. Thus, peaks showing lithium, oxygen and nitrogen contained in the samples were not taken into account. The absence of any distinct peaks in this analysis may suggest lithium nitrate is present in the sample, as all the elements have  $Z < 10$  so would not be detected in the analysis.

### 3.6 X-ray diffraction

X-ray Diffraction (XRD) is used to identify crystalline compounds by measuring the counts of X-rays diffracted at an angle of  $2\theta$  in accordance with Bragg's Law

$$n \lambda = 2 d \sin \theta$$

where  $n$  is an integer,  $\lambda$  is wavelength,  $d$  is the lattice spacing and  $\theta$  is the angle of the incident beam. This is shown schematically in Figure 3.7. An x-ray source of known wavelength is used, so the diffraction angle ( $\theta$ ) is dependant on the lattice spacing ( $d$ ).

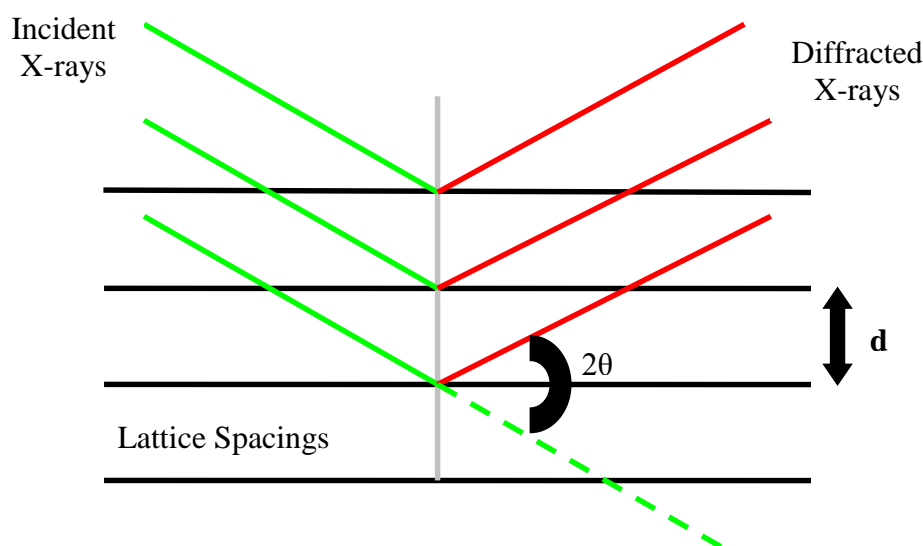


**Figure 3.7 – Schematic of X-ray Diffraction**

In most powder X-ray diffractometers, the sample is rotated about a point at  $\theta^\circ / \text{min}$ , perpendicular to the direction of the X-ray beam, while the X-ray source remains fixed. The detector moves at twice the speed of the sample ( $2\theta^\circ / \text{min}$ ), in order to keep the angle of incidence and diffraction the same, and measures the counts caused by diffraction of the X-ray beam. This allows a range of  $2\theta$  values to be measured to build up a diffraction pattern. The detector and the source are equidistant from the sample to keep the beam in focus. This ensures minimum peak broadening occurs. Cullity and Stock (2001) provide a more in depth overview of the principles of XRD.

The sample was powdered to ensure the orientation of the lattice planes was random. When the diffraction conditions are satisfied, a peak of a distinctive intensity is recorded by the detector. This peak can be matched to reference diffraction patterns for standardised materials recorded in the International Centre for Diffraction Data (ICDD) database.

For samples containing iron a Siemens D5000 diffractometer with a cobalt source was used to avoid fluorescence. The samples were prepared by grinding down to a fine powder using an agate mortar and pestle, and loading the powder into an aluminium sample tray. The sample was smoothed over using a microscope slide to ensure the top layer was flat and positioned at the correct sample height. The sample was loaded into the diffractometer and scanned using Co  $K\alpha$  radiation using a step size of  $0.05^\circ$ , and a scanning speed of  $0.5^\circ / \text{min}$  over the range of  $10^\circ$  to  $80^\circ 2\theta$ . The resulting patterns were peak matched to the corresponding ICDD files using the Stoe x-ray diffraction analysis software WinXPOW.

A Stoe diffractometer was used for all samples not containing iron. These samples were prepared by grinding to a fine powder using an agate mortar and pestle, and placing a thin layer on sticky tape mounted in a sample holder. This was then placed in a sample changer, which loaded the samples into the machine. The samples were scanned using Cu K $\alpha$  radiation using a step size of 0.03  $^{\circ}$ , and a scanning speed of 0.5  $^{\circ}$ /min over the range of 0  $^{\circ}$  to 130  $^{\circ}$  2 $\theta$ . The resulting patterns were again peak matched to the corresponding ICDD files using WinXPOW.

### **3.7 Thermogravimetric analysis**

Thermogravimetry allows a sample to be simultaneously weighed while being heated or cooled in a controlled manner (Gabbott, 2007). The sample was placed on a thermobalance, which was suspended within a furnace, and subjected to an inert nitrogen atmosphere. The sample was heated at a constant rate, and the weight of the sample recorded every second. A weight vs temperature graph is plotted, which shows the range of temperatures at which gases were evolved from the sample. From this graph, it was possible to determine decomposition temperatures of materials and identify the temperature range over which reactions occur which involve the evolution of gases. Gabbott (2007) provides an overview of the principles and applications of thermal analysis.

Thermogravimetric analysis (TGA) was performed on all of the samples using a Mettler Toledo TGA/SDTA851 $^{\circ}$  Module, calibrated using zinc (melting point 419.6  $^{\circ}$ C) and aluminium (melting point 660.3  $^{\circ}$ C) standards and the analysis software STAR $^{\circ}$  System version 8.1x. The samples were ground to a fine powder using a porcelain mortar and pestle, and approximately 30 mg was placed in an alumina crucible and the weight of the sample recorded to  $\pm$  0.00005 g. The samples were heated at 5  $^{\circ}$ C / min over the temperature range 30  $^{\circ}$ C to 1000  $^{\circ}$ C. The weight was recorded once every second. All measurements took place under a nitrogen atmosphere, with a nitrogen flow through the furnace of 50 ml / min.

### **3.8 $^7$ Li Magic Angle Spinning Nuclear Magnetic Resonance Spectroscopy**

Nuclear magnetic resonance (NMR) spectroscopy measures the energy levels of nuclear spins, using  $E = h\nu$  (where  $h$  is Planck's constant and  $\nu$  is the frequency), in the presence of a strong magnetic field. The nuclear spins experience a series of magnetic interactions, which are dependent on the orientation of the molecules to the magnetic field. Using NMR, these interactions can be characterised to obtain information about the electronic environment of the observed nuclei (Wong, 2001), in this case  $^7$ Li.

There are three major interactions which occur in solid-state NMR experiments on the nuclei of alkali metals, denoted by the following Hamiltonian (Wong, 2001):

$$H = H_Z - H_{CS} - H_Q$$

The main interaction is between the nuclear magnetic moment ( $\mu$ ) and the external magnetic field ( $B_0$ ), known as the Zeeman interaction ( $H_Z$ ), shown by the following Hamiltonian:

$$H_Z = -\mu \cdot B_0$$

The electron cloud surrounding the nucleus generates a secondary magnetic field, changing the external field at the nucleus, known as chemical shielding ( $H_{CS}$ ). This can be expressed as the Hamiltonian:

$$H_{CS} = \mu \cdot \sigma \cdot B_0$$

where  $\sigma$  is the chemical shield tensor, providing three-dimensional information of the shielding of the nucleus. As the magnetic field may not be symmetrical, this leads to the possibility of differing chemical shifts arising depending on the directionality of these fields. This leads to line broadening and asymmetry in the solid-state NMR spectra, known as chemical shift anisotropy (CSA), shown in Figure 3.8.

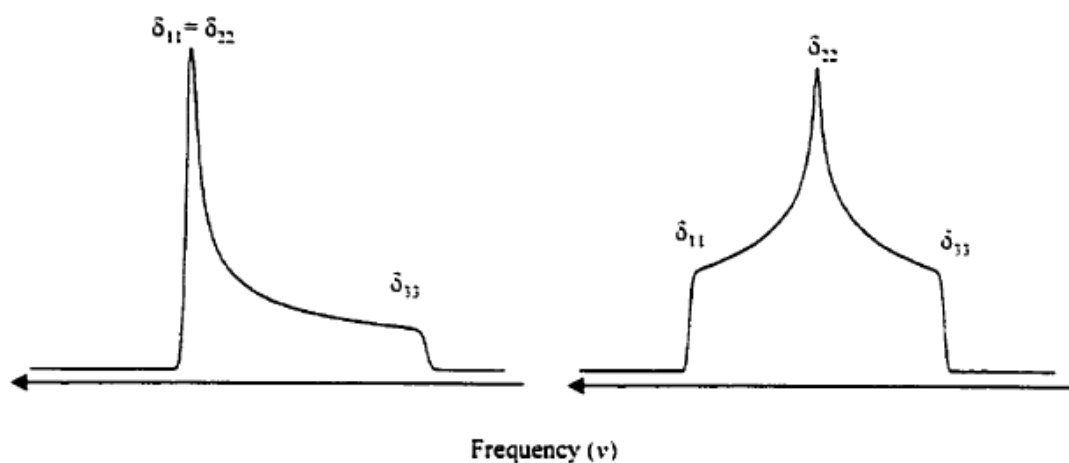


**Figure 3.8 – The possible effects of CSA on solid-state NMR spectra (Wong, 2001)**

The quadrupolar interaction ( $H_Q$ ) arises due to the asymmetrical charge distribution associated with nuclei with a nuclear spin  $> \frac{1}{2}$ . It is a measure of the interaction between the electric field gradient and the nuclear quadrupole moment ( $eQ$ ) and can be expressed as:

$$H_Q = \frac{eQV.J}{6J(2J-1)}$$



where  $J$  is the nuclear spin angular momentum and  $V$  is the electric field gradient tensor. All of these interactions contribute to the effective interaction felt at the nucleus. Available literature (Duer, 2008) provides further information on these interactions and their effects on the NMR spectra produced.

The chemical shift of an NMR signal depends on the molecular orientation to the direction of the magnetic field ( $B_0$ ). Since molecules can change position, conformation, etc. over time, the NMR signal is dependent on how fast those changes occur relative to the NMR timescale (Spano, 2011). Small molecules in solution exhibit rotational correlation times in the order of nanoseconds, which motionally average out the anisotropic interactions. The resulting spectra, therefore contain peaks at the isotropic frequency positions for the different sites in the molecule (Spano, 2011). In contrast, solid-state NMR experiments focus on sample systems with restricted molecular motion, such that on the NMR timescale, a large number of orientations are simultaneously present. This results in spectra exhibiting broad features which consist of a superposition of signals from different orientations. While these spectra can provide a wealth of information, they lack the site-specific resolution necessary for operations like structural characterization (Spano, 2011). To obtain high resolution spectra in solid-state NMR, a coherent averaging of the anisotropic frequencies via mechanical rotation, magic-angle-spinning (MAS), is employed (Figure 3.9).

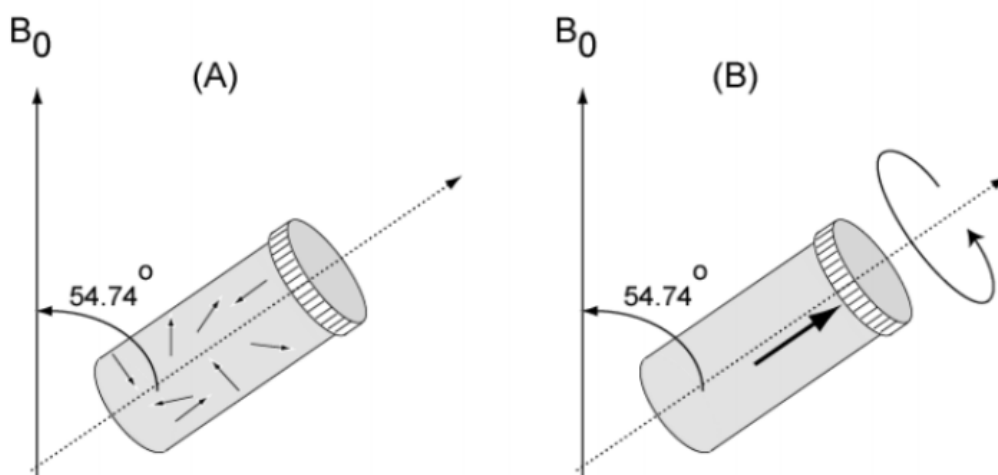


**Figure 3.9 – Depiction of the MAS process where (A) shows the z-components of spin angular momenta aligned in random directions without MAS and (B) shows the average orientation of the spins (shown by the single arrow) using the MAS technique (Spano, 2011)**

MAS is used to cancel out the contributions of the anisotropic interactions to the spectra. This works by aligning the sample at  $54.74^\circ$  from the direction of the magnetic field, which reduces the  $P_2(\cos\theta) = 0.5(3\cos^2\beta - 1)$  value to zero, and rotating the sample at high frequency. This removes the orientation dependence of the nuclear spins, thus cancelling the anisotropic contribution (Spano, 2011), effectively aligning the spins along the magic angle axis (Figure 3.9). This reduces the spectra down to peaks at the isotropic frequency positions for the different sites in the molecule. Duer (2004) provides a comprehensive guide to solid-state NMR techniques.

$^7\text{Li}$  MAS NMR spectroscopy was performed using a Varian VNMRS spectrometer operating at Larmor frequency of 155.4 MHz. All chemical shifts were referenced to 1 M LiCl (aq) by setting the signal of LiCl to  $\delta = 0$  ppm. The solid samples were ground to a fine powder and packed into a 4 mm MAS rotor spinning at 14 kHz. The simplified HAL simulant samples had a full spectral width of 40.32 kHz, with an acquisition time of 100 ms and a relaxation delay of 5 seconds was inserted between scans. For the full HAL simulant samples, a spectral width of 208.3 kHz with an acquisition time of 30 ms and a relaxation delay of 1 second between scans was utilised. Single pulse excitation with a pulse width of  $0.1 \mu\text{s}$  was used for all experiments.

### 3.9 Helium Pycnometry

Helium pycnometry works by detecting the pressure change caused by gas displacement due to the presence of a solid sample. Helium is used as the gas as it is inert and small in size, therefore able to penetrate into sample pores. Figure 3.10 shows a schematic of the helium pycnometer.

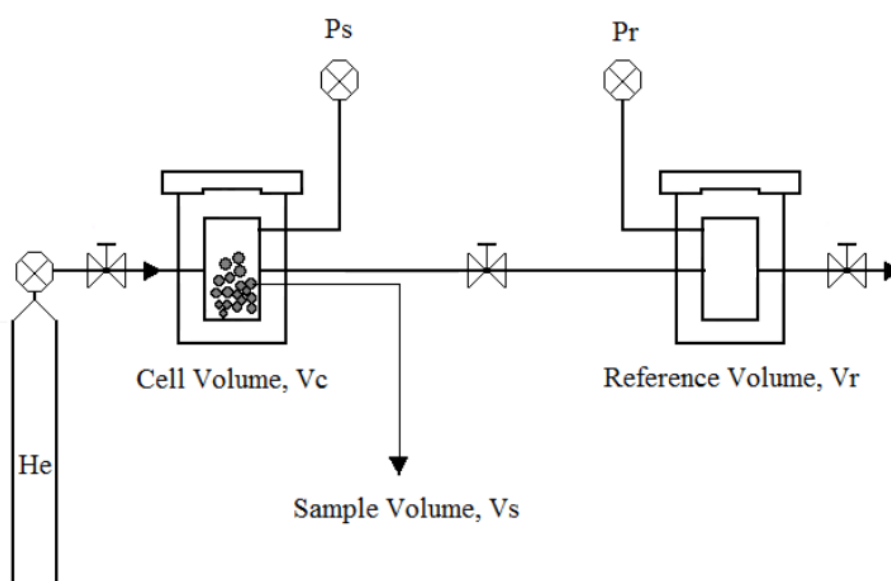


Figure 3.10 – Schematic diagram of the helium pycnometer (Kolodziejczyk, 2013)

An unknown volume of a solid sample ( $V_s$ ) is placed inside a cell of known volume ( $V_c$ ) and the cell is pressurised to a known value ( $P_c$ ). An isolated reference cell, of known volume ( $V_r$ ), is also charged to a known pressure ( $P_r$ ). Once pressurised, a valve between the two cells is opened and the system pressure ( $P_{sys}$ ) goes to equilibrium. Using the ideal gas law,  $PV = nRT$ , the volume of the solid sample can be calculated using the following sequence of equations (Kolodziejczyk, 2013; Aligizaki, 2006):

Under the initial conditions, where the sample cell is isolated from the reference cell, the gas law can be expressed as:

$$P_c(V_c - V_s) + P_r V_r = nRT$$

where  $P$  is the pressure of the gas,  $V$  is the volume of the gas,  $n$  is number of moles,  $T$  is temperature of the gas and  $R$  is the molar gas constant. On opening the valve between the sample and reference cells, the conditions become:

$$P_{sys}(V_c + V_r - V_s) = nRT$$

Which can be expressed as:

$$P_{sys}(V_c + V_r - V_s) = P_c(V_c - V_s) + P_r V_r$$

The unknown value of  $V_s$  can be obtained through rearrangement to:

$$V_s = \frac{(P_{sys} V_c + P_{sys} V_r - P_c V_c - P_r V_r)}{(P_{sys} - P_c)}$$

As the sample weight is known, the density of the sample can therefore be calculated using the sample volume.

Helium pycnometry was performed using a Micrometrics AccuPyc II 1340 pycnometer. The samples were used as produced on the small scale calciner rig with no further treatment. The samples were weighed using an external mass balance ( $\pm 0.0001$  g) and placed in the sample cell, filling it to approximately half of its capacity. The sample volume was pressurised to 7.00 psig at 0.005 psig / min before the cell valve was opened to the reference chamber. The measured density in this work was averaged after 10 purges (used to clean the sample cell and remove any volatile contaminants) followed by 10 sample runs.

# 4. Introduction to the Small Scale Calciner Rig

## 4.1 INTRODUCTION

The small scale calciner rig is a piece of research equipment which was designed to bridge the gap between lab scale and full scale calcination experiments. It consists of two main sections, a rotary tube furnace and an off-gas system. HAL simulant and sugar solution are simultaneously fed into the calciner, where evaporation and denitration processes occur, and the resultant calcine product is collected in a glass pot sealed to the lower end fitting. The system is kept under depression by a fan which pulls the mix of air, H<sub>2</sub>O, HNO<sub>3</sub>, NO<sub>x</sub> and dust created in the calciner through the off-gas system, where the vapours are condensed and the dust dissolved / suspended in the scrubber. This was designed to mimic the processes which occur in the full scale process. It is not, however, a scale model of the VTR and WVP plants. It was bought and designed to achieve the following objectives (Brace, 2003):

- To develop a greater understanding of the calcination process and investigate the chemistry surrounding fundamental plant issues such as the formation of zirconium molybdate.
- To provide sufficient technical understanding at lab and small scale to reduce, where possible, the duration and therefore cost of the VTR campaigns.
- To enable R&T to make recommendations to plant earlier than currently envisaged from the VTR without a calcination programme.

The key differences between the small scale calciner and the VTR include:

- The rotary furnace on the small scale calciner has 3 heated zones as opposed to the 4 on the VTR.
- The calciner tube is approximately a third of the size of the full scale tube.
- The waste oxide throughput on the small scale calciner is usually between 368.8 g / h (at a feed rate of 2 l / h) and 737.6 g / h (at a feed rate of 4 l / h) compared to the VTR waste oxide throughput, which is typically range of 6-10 kg / h, depending on feed concentration and rate.
- The off-gas system on the small scale calciner uses a vortex scrubber, which acts as the dust scrubber and condenser as opposed to the impingement baffle plate column used on the VTR.

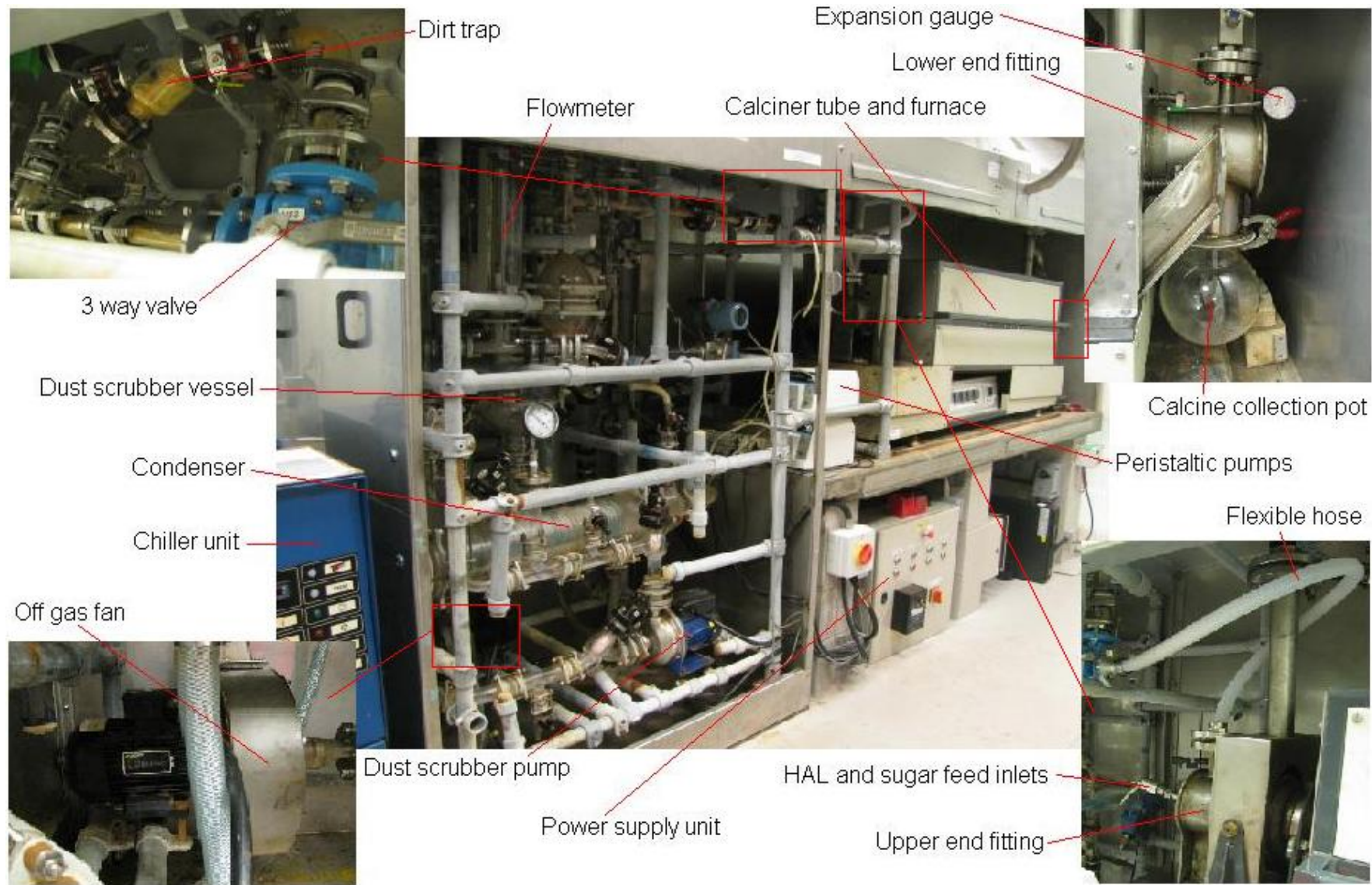


**Figure 4.1 – Photos showing the layout of the Small Scale Calciner Rig**

The small scale calciner is therefore not thought to be suitable to directly determine new operational set points for the VTR, but is suitable to identify trends which arise from changing the experimental parameters. The fundamental chemistry is thought to be sufficiently independent of scale to allow investigation into the objectives outlined above. To attain these objectives, there is a degree of in-built versatility, allowing the following variables to be controlled:

- HAL simulant composition
- HAL feed rate
- Sugar addition
- Calciner temperatures
- Rotational speed of the tube
- Angle of inclination of the tube
- Air in-bleed flow

The angle of the tube, speed of rotation and feed rate all influence the residence time in the calciner, which is known to have an impact on the properties of the resultant calcine product (Short, 2012; Brace, 2004). The effects of temperature, sugar addition and simulant composition on calcine properties and amount of dust carry-over have also been well documented (Brace, 2006b). However, analysis of the density, particle size and chemical composition of the dust had not been possible in previous studies, as there were no sample collection points before the dust scrubber, where the majority of the dust is dissolved, on either the small scale calciner or the VTR.

The small scale calciner rig had not been used for approximately 2 years before this project began. This led to a number of issues being encountered with the existing equipment. Also, the original configuration of the rig did not allow for the capture of dust particles entrained in the off-gas from the calciner, which passes to the off-gas system. As the existing rig needed to be partially rebuilt, the opportunity was taken to design and install a dirt trap.<sup>6</sup> This allowed collection of dust for further analysis, which was not possible in historic studies.

---

<sup>6</sup> The details of the design and installation of the dirt trap and the issues encountered during this process, and with the rig rebuild are fully discussed in Chapter 8.

## 4.2 EXPERIMENTAL

Before the small scale calciner was operated, a series of checks were carried out to ensure the rig ran efficiently and that safety protocols were followed. The off-gas system contains 30 litres of ~2 M nitric acid, so must be set to this level before the run begins. The flexible hose and pipework that connects the calciner to the off-gas system were cleaned to minimise the chances that a blockage would form, which would lead to the possibility of a NO<sub>x</sub> release. Cleaning the flexible hose also ensured all the dust collected was produced from the new experiment. The off-gas flow was set to run through the flow meter to allow this to be measured and all the valves in the off-gas system checked to ensure they are in the correct positions when setting up the calciner rig. Finally, the calcine collection pot was sealed to the lower end fitting. Once these checks had been completed, the calciner was ready for operation.

A minimum of 5 litres of the appropriate HAL simulant and 2 litres of sugar solution (200 g / l) were prepared and decanted into the designated containers where they were kept under constant agitation. The feed pipes were immersed in these solutions and run through a pair of calibrated peristaltic pumps connected to the calciner inlet nozzles. The dust scrubber pump and chiller unit were switched on to circulate the cooled liquor round the off-gas system and the off-gas fan was set to create a depression of -13 mbar throughout the system. The calciner rotation speed was set to 30 rpm and the calciner temperatures set to the appropriate values in the three heated zones. The rig was left for ~60 mins to allow the calciner tube to reach temperature to ensure the correct calcination conditions were created. Once the off-gas flow had been recorded, it was set to by-pass the flowmeter to improve rig depression and reduce the risk of blockages occurring through dust being carried through the flowmeter. The calciner was considered ready to start feed once the calciner tube expansion remained constant for a minimum of 10 mins and the rig depression had stabilised at -13 mbar, through adjustment of the off-gas fan speed.

The HAL feed was started by turning on the peristaltic pumps which had been pre-set to the desired feed rate. The pumps were left running for a period of one hour, after which they were stopped. During this period, the off-gas flow was diverted through the dirt trap by altering the position of the 3 way valve, allowing dust to be collected for the full duration of the experiment. Checks were also carried out on the rig every 10 mins during this period to ensure it was running correctly. Once the feed had been stopped, the rig was left running for 30 mins to allow all the calcine and dust produced to make its way to the collection pot and dirt trap respectively. After this, the temperature set-points were adjusted to room temperature and the calciner allowed to cool for a minimum of 2 hours before the calciner rotation, dust scrubber pump, chiller and off-gas fan were stopped. The rig was further cooled overnight before the calcine and dust samples were taken.

The pre-weighed calcine collection pot was weighed with the calcine made during the experiment to determine the mass produced. The calcine was then passed through sieves with pore sizes of 2 mm and 0.5 mm to split the calcine into three size fractions (<0.5 mm, 0.5-2 mm and >2 mm). Each size fraction was weighed to determine the particle size distribution of the calcine and analysed using XRD, TGA and EDS to show if any differences in chemical composition arose as a function of particle size. Conventional particle size analysis was not possible due to the solubility of the calcine in aqueous media.

The dust sample was collected from the dirt trap and flexible hose (shown in Figure 4.2). To remove the dust from the dirt trap, the base plate was removed allowing the filter cartridge to slide out and be emptied into a pre-weighed container. The dust collected in the flexible hose was loosened using a pipe cleaning brush and collected in the pre-weighed container. The combined sample was then weighed with this value being taken as the amount of the dust collected during the experiment<sup>7</sup>. This was thought to give a representative value to allow trends to be observed, though is not the total value of dust produced due to the hold up of dust in the apparatus which could not be collected. The value for the mass of dust collected was normalised against the mass of calcine produced for each experiment to allow comparisons to be made in dust carry-over as a function of calcination conditions. The combined dust sample was analysed and compared to the calcine fractions of different particle size.

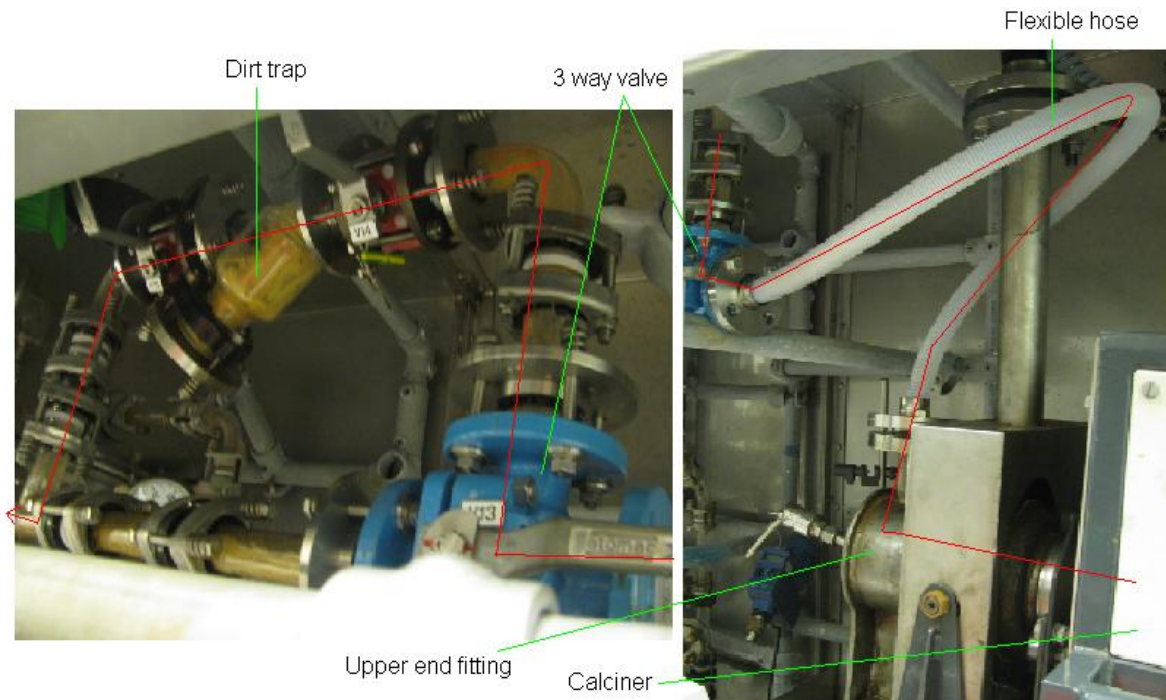


**Figure 4.2 – Photos showing the off-gas flow path (red line) from the calciner through the flexible hose and dirt trap where the dust samples were collected**

<sup>7</sup> There would have been dust collected in the upper end fitting, 3 way valve and a portion passing through the dirt trap filter during the small scale calciner experiments which could not be collected.



## 4.3 SMALL SCALE CALCINER RIG DESIGN AND REBUILD

Blockages have been known to form in the pipework connecting the calciner and the off-gas system causing downtime on WVP. As a consequence there is an interest in discovering the composition, particle size and density of calcine particles which are carried from the calciner to the dust scrubber during VTR and WVP operations. The first sampling point on the VTR in the off-gas system is that of the dust scrubber liquor. As the majority of the particles are soluble in nitric acid, it is difficult to measure the size and densities of these calcine particles. This section focuses on the design and rebuild of the small scale calciner rig to allow collection of dust samples from the calciner, so the size, density and composition of these calcine particles could be measured.

The small scale calciner rig had not been used for approximately 2 years before this project began. This led to a number of issues being encountered with the existing equipment. Also, the original configuration of the rig did not allow for the capture of dust particles entrained in the off-gas from the calciner, which passes to the off-gas system. As the existing rig needed to be partially rebuilt, the opportunity was taken to design and install a dirt trap. This allowed collection of dust for further analysis, which was not possible in historic studies.

### 4.3.1 Dirt trap design

In order to allow the capture of dust particles in their solid form, a filter had to be added to the existing off-gas pipe work between the calciner and the off-gas system. Originally, the off-gas system and calciner upper end fitting were connected by a flexible hose approximately 1.2 metres in length, with the majority of the dust being trapped in either this hose or in a designated trap, where it would be dissolved in the condensate. As the dust was partially trapped in the flexible hose, it was decided that the filter would benefit from being as close to the calciner upper end fitting as possible. These ideas were taken to the NNL design team with the following design specifications:

- The off-gas flow must be allowed to by-pass the dirt trap to prevent a NO<sub>x</sub> release occurring in the event of filter blinding.
- The dirt trap must be isolated during filter change operations to allow dust collection during routine operations without the possibility of a NO<sub>x</sub> release.
- The filter must be removable to allow dust samples to be taking during an experiment.
- The dirt trap loop must fit in the designated fumehood, and not block access to the HAL simulant feed buckets or peristaltic pumps.
- The dirt trap loop should be made of glassware, in keeping with the current off-gas system, thus allowing visual inspection.

- Where possible, the dirt trap should avoid build-up of condensation, allowing the dust samples to remain in their solid state for further analysis.

After a period of consultation with the NNL design team, a design was proposed which used components from the same manufacturer as the off-gas system, ensuring compatibility. Figure 4.3 shows the design and components list of the agreed dirt trap loop. The major components of this dirt trap loop were:

- The 3-way-valve (multi-port ball valve) – Allowed the off-gas flow to either by-pass the dirt trap or flow through to allow the collection of dust.
- The dirt trap – Houses a PTFE cartridge covered with a 100 µm mesh filter to collect any dust whilst allowing the off-gas flow to pass through. It has a removable base plate to allow changing of the cartridge and filter during routine operation of the calciner rig.
- Two compact ball valves to allow isolation of the dirt trap, ensuring no NO<sub>x</sub> releases or off-gas flow will be present while changing the filter. These were designed to be used as an additional safety feature.
- A new, smooth bore steel braided flexible hose designed to trap the minimum amount of dust, allowing it to travel to the off-gas system to be caught in the dirt trap.

The remaining components (Figure 4.3) were identical to those already used to construct the off-gas system on the small scale calciner rig.

As the new dirt trap loop would add extra weight to the existing glass pipe work, new scaffolding was also required. However, it was decided that this would be built at the discretion of the NNL engineering team during installation of the dirt trap loop. An assortment of scaffolding components were listed to order, but no further design work was carried out. Once the design work had been completed and the components sourced, the implications on the safety of the small scale calciner rig had to be assessed before any work could begin.

PARTS LIST		
PART NO.	CATALOGUE DESCRIPTION	CATALOGUE NO.
1	MULTI PORT BALL VALVE AMP3	NISPO1
2	NOT USED	-
3	BEND 90 DEG	F880/25
4	NOT USED	-
5	NOT USED	-
6	FLAT BLUE GYCON GASKET	TF25
7	O RING PIPE GASKET	TR25
8	FLEXIBLE PIPE GASKET	K5025
9	COUPLING SS FLANGES	C5025
10	FLANGE ADAPTOR SS ANSI 150	CRS5A25
11	PLASTIC INSERT DN25	CP25
12	REDUCING WASHER	RWS515/9
13	NOT USED	-
14	HEX NUT DN8.34-M8-A2-70	D634-8-A2
15	WASHER DN125-B8.4-A2	D125-B.4-A2
16	SPRING	DFSSR.5
17	HEX SETSCREW DN63.3-MBK110-A2-70	D633-BK110-A2
18	COMPACT BALL VALVE	KHK25
19	EQUAL TEE DN25	PT25
20	NOT USED	-
21	PIPE SECTION DN25	PS25/100
22	NOT USED	-
23	FLANGE ADAPTOR SS PN10	CRS5E25
24	NOT USED	-
25	SPACER DN25	SS25/10
26	PIPE SECTION DN25	PS25/150
27	PIPE SECTION DN25	PS25/175
28	PIPE SECTION DN25	PS25/75
29	DIRT TRAP 100 MICRON	PSF25/100

**NOTES**

1. ALL GLASSWARE IS SOURCED FROM QVF. PURCHASE ORDER NO. 7012853. PART NUMBERS GIVEN ABOVE CORRESPOND TO PURCHASE ORDER.
2. FLEXIBLE HOSE IS SOURCED FROM AFLEX. PURCHASE ORDER NO.7012817.
3. THESE PARTS MAY BE OMITTED AT FINAL INSTALLATION AND THE FLEXIBLE HOSE CONNECTED DIRECTLY TO THE MULTI PORT BALL VALVE.

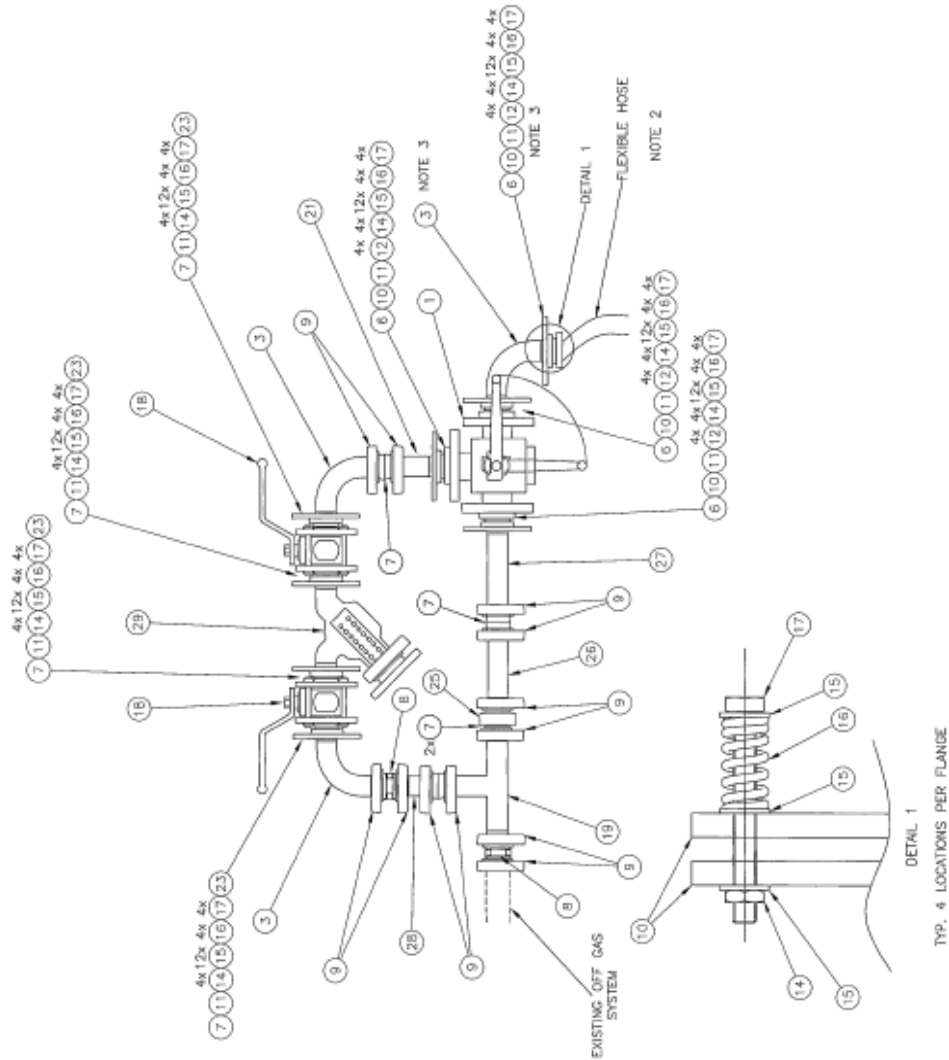


**Figure 4.3 – Drawing of the proposed dirt trap loop with parts list  
(Courtesy of the National Nuclear Laboratory)**

### 4.3.2 Working on a nuclear licensed site

In order to carry out work on a nuclear licensed site, there were procedures which had to be followed. Within the NNL central laboratory, before work could begin, a facilities work request (FWR) was raised, completed and approved by the facilities team, as well as other stakeholders, including the engineering, design, lab leader and operations control management teams. The purpose of the FWR form was to ensure the operators were aware of the nature of the work which was to be carried out, the hazards associated with the work and that all the stakeholders had an input to determine whether the work was inherently safe. The information captured on this form included (Webb, 2014):

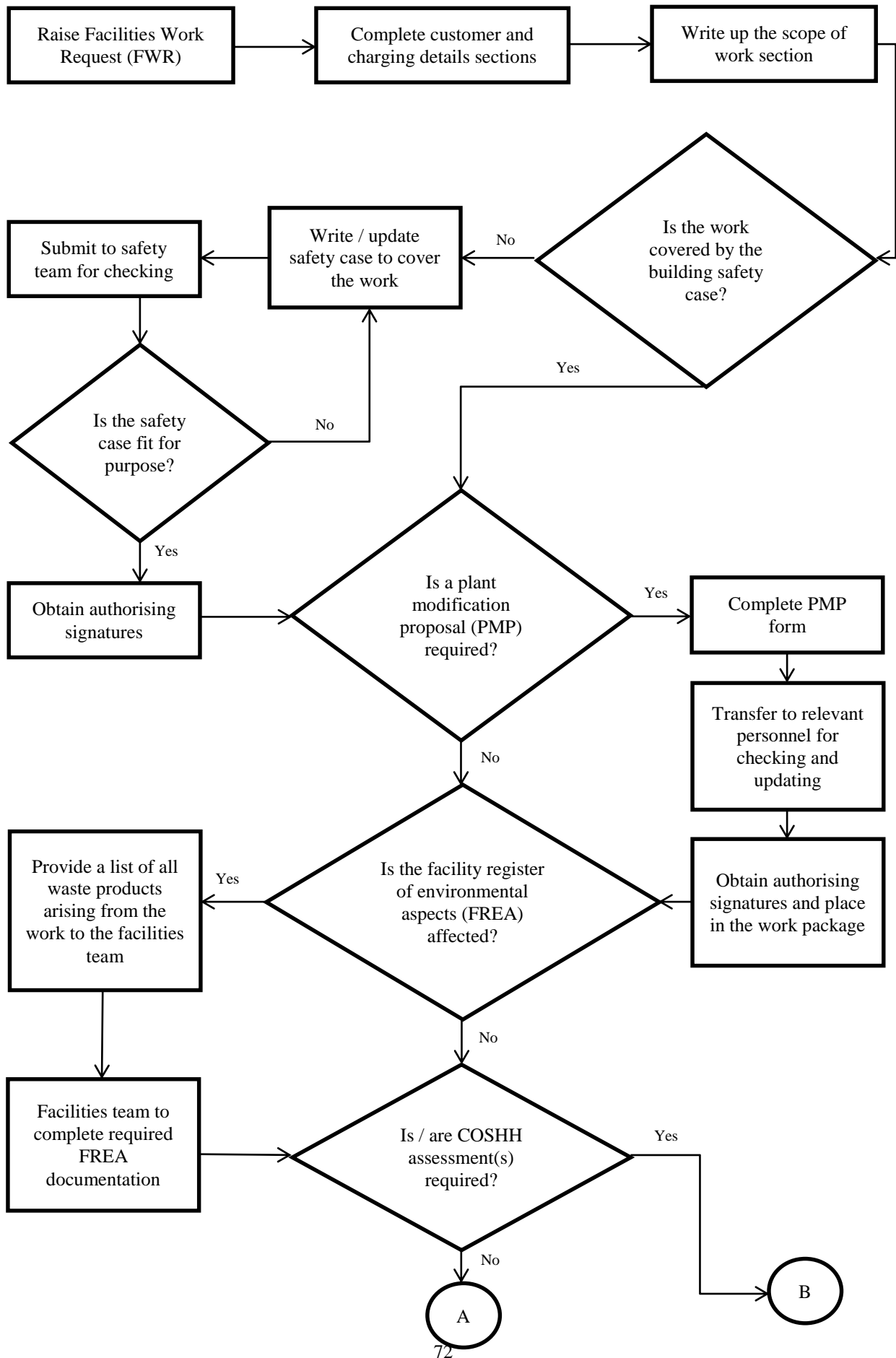
- A description of the work to be done.
- References to the associated safety documentation and instructions.
- Required resources and technical input for the work.
- A section for authorising signatures.
- A section for operator signatures.

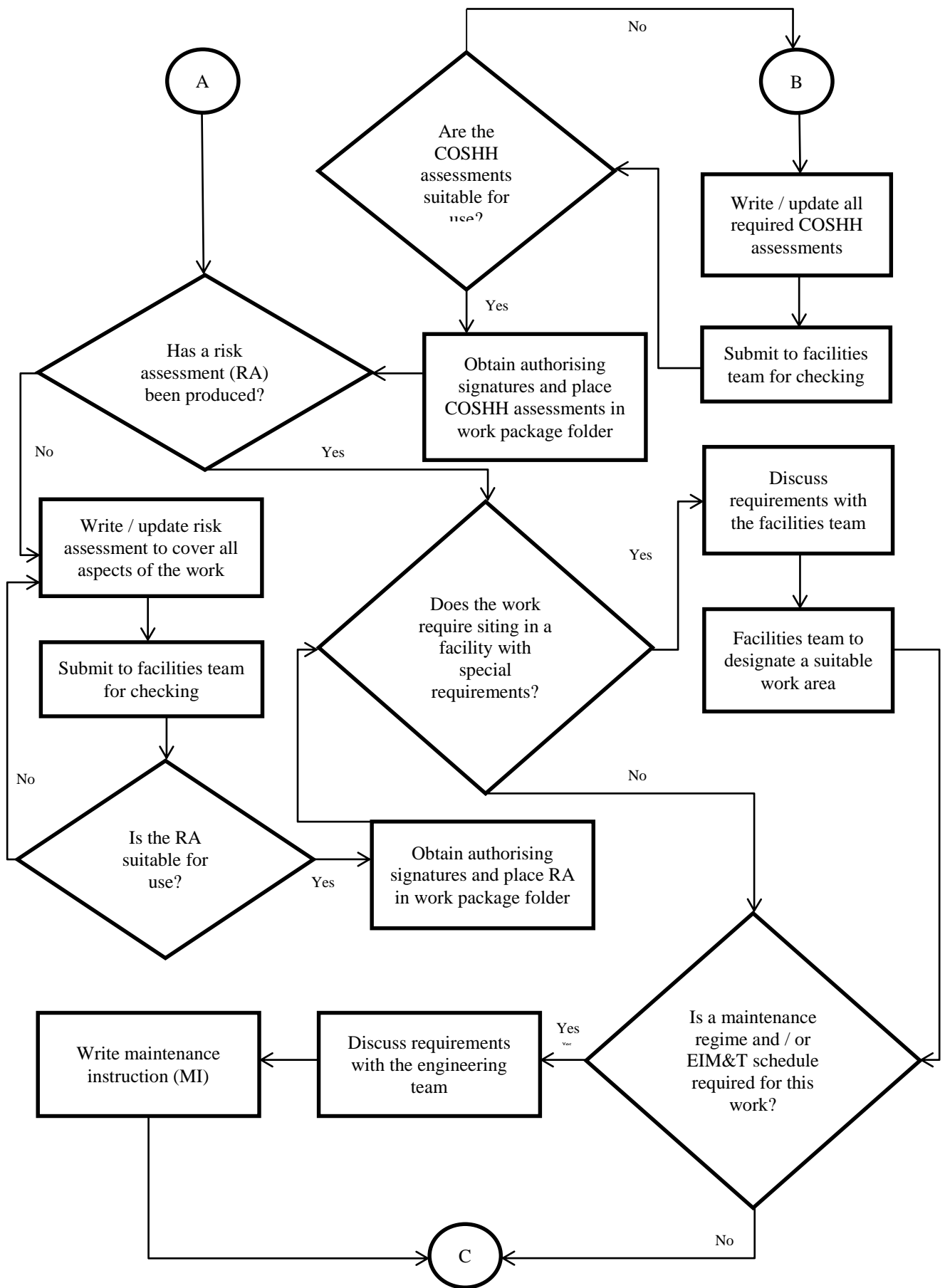
By capturing this information in one place, it ensured that all of the associated documentation had been reviewed and authorised as well as acting as a reference to all resources required to carry out the work should a new operator need trained. Figure 4.4 shows a flow chart which was followed to allow completion of the FWR form and the associated paperwork, thus allowing the design work to be implemented and the experiments carried out.

The first task was the completion of the customer details and charging details. The customer details were a requirement, as they would have been needed in the case of an emergency. The charging details were to ensure the facilities required for the work could be paid for once the work commences. Once these sections were cleared by the project manager, the scope of the work section was completed. The scope of work section included (Webb, 2014):

- Clear description of work to be carried out from ‘cradle to grave.’
- Short description of why the work is required.
- A photo of the equipment or rig being used.
- Details of the services required.
- Details of the parameters covering normal working operations.
- Requirements for overnight or lone working.

This ensured both the operators and the lab leaders were aware of the work which was to be carried out, where the work was to be carried out and which facilities were required to complete the work.





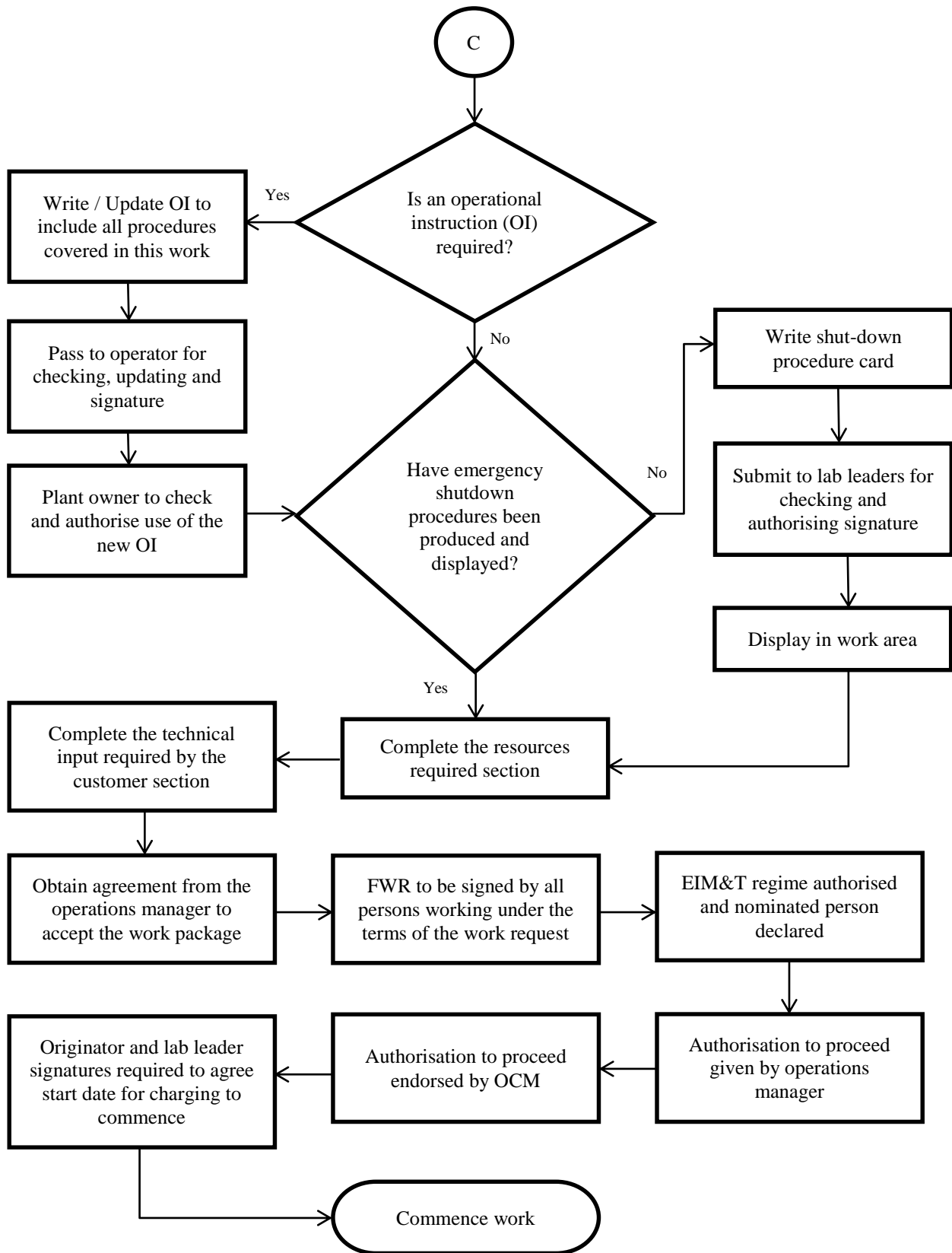


**Figure 4.4 – Flow chart showing the procedure for preparation of documentation before commencing work within the NNL central laboratory**

As this work was covered by the building safety case, the next task was to complete a plant modification proposal (PMP) form. A PMP is required for any changes in design or the installation of new equipment on an engineering plant. The application of the PMP process ensured that:

- The full extent of what is or what could be affected by the modification, both during and following its implementation, is identified and adequately considered.
- All new and increased risks to safety and the environment are identified, assessed and adequately controlled.
- Safety and environmental classifications are assigned to the modification which reflect its safety and environmental significance and ensure that it is the subject of adequate scrutiny.
- The correct standards and procedures are applied to any engineering or operational changes.
- The correct standards and procedures are applied to any design changes.
- All requirements to update any records associated with the modification are identified.
- All training and communication requirements associated with the modification are identified.

As an engineering plant has effects on operational safety and environmental impact, the PMP had to be reviewed and authorised by the operations, engineering and building managers as well as environmental and radiological impact personnel for the Sellafield site.

The facility register of environmental aspects (FREA) would not be affected by this work as the quantity of NO<sub>x</sub> produced by the experiments was taken into account. The building emissions were already reported as if the off-gas system was not operational and all of the NO<sub>x</sub> produced was released through the building stack via the fume-hood. The next step, therefore, was the preparation of COSHH and risk assessments to cover the proposed experimental programme. COSHH assessments were required for handling HAL simulant, nitric acid, off-gas system liquors, chiller coolant and calcine, which all occur through routine operation of the calciner rig. Due to the fact these hazardous chemicals needed to be handled and machinery would be in operation, the major hazards were identified as:

- Chemotoxic hazards associated with the handling of strong acids.
- High temperature hazard if in contact with the off-gas pipework and calciner tube.
- Trapping hazards associated with rotating machinery and use of hand tools.
- Working at height while opening and closing fire damper valves and emptying dirt trap.

These hazards were captured in the risk assessment with an assessment of what remedial action should be taken to reduce the probability of these occurring. This was also captured in the next stage of the process, updating of the operating instruction (OI).



Operations which require multi-step processes necessitate the use of an OI. An OI contains a step by step guide for the operator to use and should capture any set-up, calibration, sampling, operational, shut-down and clean-up processes. Within each step, any hazards should be identified and the appropriate PPE, beyond what is already worn in the lab, identified. As this work required the addition of extra equipment to the rig, the small scale calciner OI had to be updated to include the use of the dirt trap loop during routine operation. This work did not affect the emergency shut-down procedures for the rig from previous experiments.

Within the resources required section of the FWR, the following must be considered:

- Who will carry out the work and what training do they require?
- What facility resources are required?
- What raw materials are required?
- Timescales and possible impact on other related projects.

The technical input section required information on the emissions and waste generated from the operation of the small scale calciner rig. NO<sub>x</sub> emissions were calculated for each experiment as the worst case scenario, as if all the nitrate anions (NO<sub>3</sub><sup>-</sup>) from the metal nitrates and nitric acid were given off as NO<sub>2</sub>. These values were reported in the FWR giving a value for the total NO<sub>x</sub> produced throughout the whole experimental programme, thus allowing a check against the building emissions limits. The waste HAL simulants and off-gas liquors were stored in 10 litre containers in a designated banded area in the lab. These were then taken for final disposal via the same route as VTR wastes. Once these sections were completed, the work originator and operations manager's signatures were required to signify that the work package had been accepted. The operators, due to work under the conditions of the FWR, then had to sign to show they have read and understand the FWR and associated paperwork. The final step, before submitting the paperwork to the facilities team, was to authorise the EIM&T regime by obtaining the signature of the engineering manager, and nominate a qualified person to supervise the engineering work.

The process for the authorisation to proceed then involved passing the FWR and associated paperwork to the appropriate lab leaders. This was then checked by the facilities team before being passed on to the OCM for final approval at their weekly meetings. Once all parties were satisfied with the work laid out in the FWR, work could then proceed. If there were any issues, these would be pointed out and discussed, with the paperwork being re-submitted for the following weeks meeting (Webb, 2102).

### **4.3.3 Small scale calciner re-build**

#### **4.3.3.1 Dirt trap installation**

Once the FWR had been approved, signifying the completion of amendments to all of the associated paperwork, all of the components were ordered for the building of the dirt trap loop. Whilst waiting for the components to arrive, a job order number was raised and the safety documentation prepared to allow the NNL engineering team to install the components. The work pack required before starting the work included:

- Job card – A form where the unique job number is recorded and signature is gathered from the plant owner to ensure they approve of the work which will be carried out.
- Risk Assessment – List of hazards, their consequences and measures taken to reduce the probability of these occurring.
- COSHH assessments – Identification of hazards and remedial action required to reduce the risks associated with any chemical considered hazardous to a workers health.
- Isolation Test Certificate (ITC) – This ensures that an electrical isolation has been carried out on the plant to prevent any moving parts being activated during the job, eliminating the hazards associated with moving machinery.
- Pre-job brief form – This highlights the major hazards associated with the work and is required to be signed by the job supervisor and the personnel carrying out the work to ensure they have read and understand these hazards.
- Work Control Assessment (WCA) form – A brief description of the job and a list of the associated documentation required for the job. Must be signed by a qualified person of work (POW) and the Safe Systems of Work (SSOW) controller before work can commence.

The preparation of this work pack was required before every job which was carried out by the NNL engineering team. Once completed, it is passed to the SSOW controller for final approval and recorded in the work log for the building. The work pack was then passed to the engineering team and the pre-job brief was conducted by the job supervisor to ensure the personnel conducting the work were aware of the hazards associated with the job. Once the components had arrived, the job was ready to begin.

Before installing the components on to the small scale calciner rig, the dirt trap loop was constructed to ensure all the parts fit together (Figure 4.5). During this process, the internal components of the 3-way-valve were found to be faulty and had to be sent back to the manufacturer, taking a total of 10 weeks to be returned in the correct configuration. During this time, a scaffold was built to support the weight of the dirt trap loop.

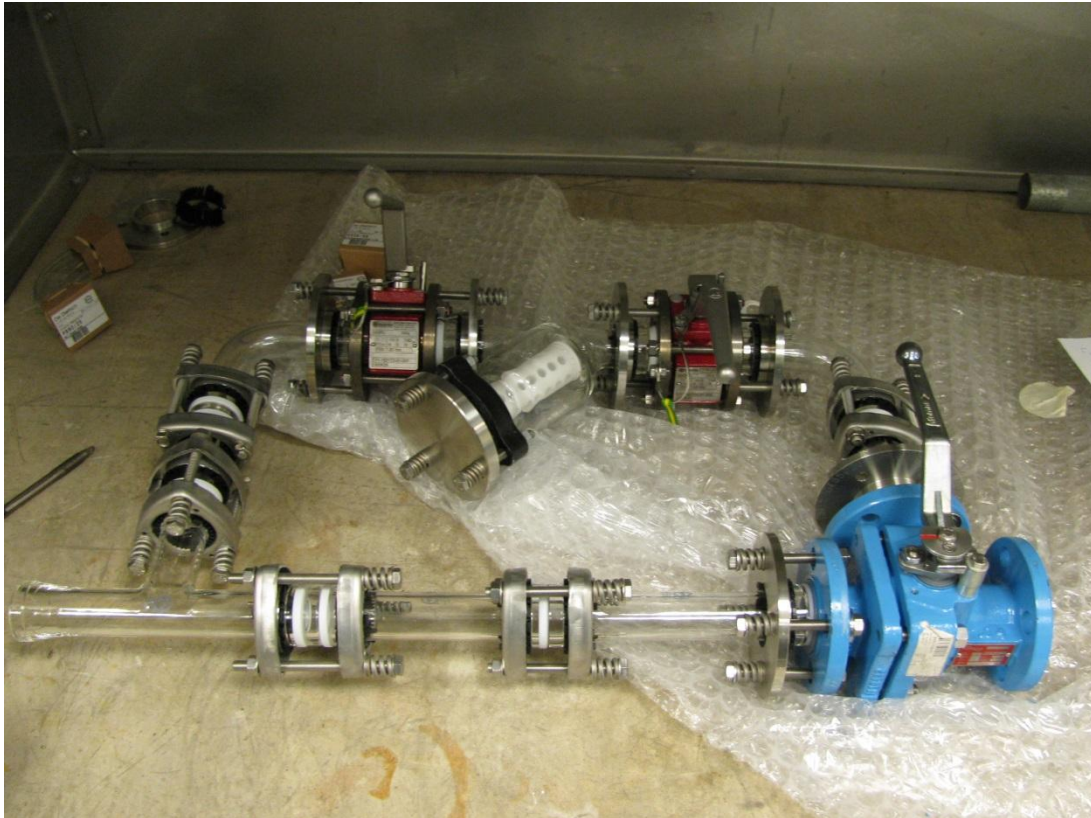


**Figure 4.5 – Photo of the assembled dirt trap loop before installation**

Once the 3-way-valve had been returned, the dirt trap loop was installed successfully on to the existing off-gas pipework. However, the steel braided hose, which was designed to connect the calciner upper end fitting to the 3-way-valve, was too short to bridge this gap due to the misalignment of the respective flanges. Therefore, one of the existing flexible hoses was used to connect the calciner to the off-gas system in order to carry out a test of the small scale calciner to determine if the rig was in working order. During this test, there were several issues identified which required further attention to get the rig in working order (see section 4.3.3.2).

#### **4.2.3.2 Other issues**

After installation of the dirt trap loop, the other components of the rig were inspected and tested to determine the condition of the rig. During this investigation, the following issues were identified:

- The off-gas fan had seized due to corrosion inside the fan casing.
- Dust scrubber pump failure.
- Degradation of the valve V12, which allows the off-gas to be diverted through the flowmeter.
- The calciner rotation and heating had no power.

To resolve these issues, a new dust scrubber pump and valve were resourced and the spare off-gas fan was utilised. A work pack was put together (as outlined in section 4.3.3.1) and approved by the SSOW controllers to install these new components and determine the cause of the lack of power to the calciner. Once these issues had been resolved, the rig depression was tested and found to be insufficient. The cause of this was identified to be a fracture of the glass tubing in the off-gas system (Figure 4.6), thought to be caused by a combination of vibrations from the off-gas fan and the additional weight added from the installation of the dirt trap loop. The opportunity was taken to order spare glass tubing to avoid significant downtime occurring in the future due to this issue. The glass T-piece was replaced and extra support was added to the dirt trap loop to remove any excess stresses caused by the increased load on the glassware.



**Figure 4.6 – Photo showing fracture of the glassware during testing of the small scale calciner**

After these modifications had been made, further testing revealed insufficient rig depression was still an issue. The cause of this was isolated to the calciner tube, which suggested the seals in either the upper or lower end fittings were loose. These seals were replaced by the NNL engineering team, which resolved the issues. The rig, now in working order, was ready to be tested and commissioned in feed.

#### 4.3.4 Commissioning and testing

Before experimentation on the small scale calciner could begin, the rig had to be commissioned, first using water feed followed by HAL simulant feed in accordance with the PMP. A commissioning checklist was therefore agreed, raising the following questions:

1. Is the off-gas diverted down the original off-gas pipe when the 3 way valve is in position 1?
2. Is the off-gas diverted through the dirt trap loop when the 3 way valve is in position 2?
3. Is the temperature of the dirt trap blanking plate below 60 °C?
4. Is the pressure differential at PI 001 between -11 mbar and -15 mbar when the off-gas is diverted through the dirt trap loop?

The first two questions were answered by observing the direction of the condensate flow through the 3-way-valve and were put in place to ensure the valve seating was in the correct configuration. The dirt trap blanking plate temperature was measured using a contact thermocouple. This temperature was important as the blanking plate must be removed during routine operation to obtain the dust sample. Finally the pressure differential had to be in the range -11 to -15 mbar, as this is the operating window in which the rig operates to run in line with the -13 mbar at which the VTR is run. In order to proceed to the HAL feed commissioning trial, the answers to the above questions all had to be affirmative in two, separate water feed trials. Once this had been completed and approved by the plant owner, the HAL feed trials were conducted. Before the rig could be considered for experimental use, the following question was posed:

- Is the pressure differential at PI 001 between -11 mbar and -15 mbar when the off-gas is diverted through the dirt trap loop?

This was an important issue in HAL feed, as the consequence of collecting dust in the dirt trap on the pressure differential in the system was unknown. If the filter had blinded, restricting or blocking the off-gas flow, there was a possibility of a NO<sub>x</sub> release from the upper and lower end seals of the calciner tube. Signs of this occurring would have manifested as a rise in the negative pressure differential throughout the system. However, there were no issues encountered throughout the two HAL feed trials which were conducted.

The four commissioning trials (two water feed and two HAL feed) were also used as training runs for the operators to become suitably qualified, experienced personnel (SQEP'd), which shows the operator is fully trained to operate the rig. This was the final part of the PMP requirements, which allowed the authorisation of the rig to be used for further experimentation.

### **4.3.5 Experimental issues**

#### **4.3.5.1 Off-gas fan and rig depression issues**

During small scale calciner operations, there were several issues which resulted in lengthy delays to the project. The main issue with the small scale calciner was the unreliability of the off-gas fan, which is used to maintain depression throughout the rig. This was replaced during the initial testing of the calciner with a spare which had been sourced during the original commissioning of the rig. However, due to a valve failure on the off-gas fan casing, which was used to drain the entrained condensate, there was an increased rate of corrosion which led to the fan having a shortened life span than was expected.

During the lifespan of the off-gas fan, it had seized several times, either due to corrosion causing the motor shaft to stick or due to excessive build-up of condensate within the fan casing. To deal with this issue, the NNL engineering team were alerted to any issues and an instruction was issued, alongside the associated work package (outlined in section 4.3.3.1) to allow drainage and/or freeing up of the off-gas fan. Due to the regularity which this occurred, a maintenance regime could not be put in place due to the high work load of the NNL engineering team. Each occurrence, therefore, led to anywhere between a week and two months downtime depending on availability. Ultimately, the off-gas fan reached a point of failure and a replacement had to be resourced. This was an issue, as the company which produced the original off-gas fan was no longer trading.

In the original small scale calciner construction and commissioning records, an engineering drawing of the off-gas fan was present. This allowed a new fan to be fabricated, though as it was custom built, it had a lead time of three months, further delaying the project.

Another issue which arose throughout this project was the loss of depression in the off-gas system of the small scale calciner, causing the alarm to sound, triggering a shut-down of the rig. There were several causes of this, the major cause being in-leakage past the seals in the upper and lower end fittings of the calciner tube. The procedure for overcoming this issue was again to provide the NNL engineering team with a work package (section 4.3.3.1) to allow them to replace the seals. There were again issues with resource availability, leading to further delays. This was a constant issue throughout the experimental programme, leading to it being shortened due to time and resource restraints.

#### 4.3.5.2 NO<sub>x</sub> release event

During one of the small scale calciner experiments conducted during this project, the NO<sub>x</sub> alarm sounded, indicating a level above 5 ppm was released from the calciner into the fumehood, prompting an evacuation of the lab. An investigation into the cause of this showed that a blockage was formed in the 3-way-valve from the build-up of dust passing from the calciner to the off-gas system. As the NO<sub>x</sub> containing off-gas stream was unable to pass to the off-gas system, it would have been released through the upper and lower end fittings of the calciner tube into the surrounding fumehood. Due to the hazards associated with a NO<sub>x</sub> release, an event was raised through the on-line safety and health at NNL sites (OSHANS) system.

As part of the OSHANS procedure, an inspection of the small scale calciner rig was carried out by the operations control management (OCM) team as well as a review of all the associated safety documentation and operational instructions. The major outcomes from this review were (Mattinson, 2014):

- Work place air monitoring and air flow checks to be carried out to determine whether there is a NO<sub>x</sub> hazard in the vicinity of the dirt trap and safety screens.
- Currently a dust mask is used for certain operations to negate dust hazard. This should be revisited to determine whether a NO<sub>x</sub> hazard is also present, resulting in the need to wear a respirator fitted with the appropriate filter. Training should be undertaken by the operators for the associated respiratory protective equipment (RPE).
- The risk assessments, COSHH assessments, operating instruction and facilities work request should be updated to cover RPE use, consideration of other lab users and lone working issues.
- Associated documentation should also be updated to cover additional checks to the 3-way-valve to ensure the probability of the same issue arising in future trials.
- Additional signs on the doors to the furnace room (which houses the small scale calciner) should be produced highlighting a personal NO<sub>x</sub> monitor is to be worn while the calciner is in operation.

Once these issues had been addressed, another review of the small scale calciner rig and the associated documentation was undertaken by the OCM. This was to ensure the safety of the operators had been fully considered and all previous issues had been addressed. Only once this had been completed could small scale calciner operations re-commence.

#### 4.3.6 Original and revised timelines

All of the issues covered in this chapter resulted in a delay in the final delivery of the project. Table 4.1 outlines the original project plan and the result of each delay. The extra, unscheduled work that was carried out as a result is also outlined.

**Table 4.1 – Overview of original project timeline and the effects of the issues encountered**

<b>Task</b>	<b>Original Date for Completion</b>	<b>Actual Date Completed</b>	<b>Major Additional Work Carried out to Allow Completion of the Task</b>
Design of the dirt-trap loop	January 2011	January 2011	<ul style="list-style-type: none"> <li>• No additional work required.</li> </ul>
Complete FWR and associated paperwork	April 2011	September 2011	<ul style="list-style-type: none"> <li>• PMP paperwork reviewed several times, delaying authorising signatures.</li> <li>• Addendum required to PMP due to additional drawings being required.</li> <li>• Complete review of OI.</li> <li>• Paperwork required re-writing due to new document templates being released.</li> </ul>
Order parts for installation	July 2011	December 2011	<ul style="list-style-type: none"> <li>• No additional work required.</li> </ul>
Installation of dirt-trap loop	September 2011	May 2012	<ul style="list-style-type: none"> <li>• 3-way-valve sent back to manufacturer for re-configuration.</li> <li>• New flexible hose ordered.</li> </ul>



Calciner test runs	October 2011	August 2012	<ul style="list-style-type: none"> <li>• New DS pump, glassware and V12 ordered.</li> <li>• Spare off-gas fan utilised.</li> <li>• Extra support added to dirt-trap loop.</li> <li>• Upper and lower end fitting calciner seals replaced.</li> <li>• SSOW package put together (See section 8.2.3.1) to allow installation of new components.</li> </ul>
Commissioning and training runs	December 2011	October 2012	<ul style="list-style-type: none"> <li>• No additional work required.</li> </ul>
Carry out experiments	April 2012	September 2013	<ul style="list-style-type: none"> <li>• Maintenance instruction written for draining and freeing of off-gas fan.</li> <li>• New off-gas fan sourced and manufactured.</li> <li>• Upper and lower end fitting calciner seals replaced.</li> <li>• NO<sub>x</sub> release event triggered OSHANS investigation.</li> <li>• FWR and all associated paperwork reviewed and updated.</li> <li>• RPE training undertaken.</li> </ul>

This shows that these issues delayed the project by a total of 17 months. Some of these issues would have been expected to occur throughout the project and time was allowed in the original project plan as a contingency. However, the severity of some of these issues could not have been anticipated, and hence project delivery was delayed.

# 5. Effects of Lithium Nitrate on Short Simulants in the Calcination Process

## 5.1 INTRODUCTION

Lithium nitrate is added to highly active liquor (HAL) before calcination and vitrification. The main benefit of this addition is to reduce dust carry-over and hence blockages in the off-gas system. It is also reported to improve the reactivity of the calcine in the melter (Magrabi, 1981). Although these benefits are well documented, the underlying mechanisms by which these benefits are realised remain unclear. One of the focuses of this work, therefore, was to understand the reactivity of lithium nitrate in the calciner to determine why lithium nitrate acts as a binding agent, reducing dust carry-over.

Previous work (Vickers, 2006) had been carried out using full HAL simulants, which are difficult to analyse due to the large number of components they contain. Another focus of this section of work was therefore to use simplified 'short simulants' to determine the reactivity of the major components of the HAL with lithium nitrate and the other species present in a series of systematic experiments.

## 5.2 EXPERIMENTAL

It was reported that the addition of lithium nitrate to the HAL simulant processed on the vitrification test rig (VTR) reduced the amount of refractory oxides, high in aluminium and iron, observed in the resulting product glass (Short, 2006b). To investigate this observation further, a series of lab-scale experiments were designed to determine the reactivity of lithium nitrate with other metal nitrates present in the HAL. These experiments were carried out under conditions designed to simulate those experienced in the calciner. The reaction mixtures were based on the stoichiometry of Magnox HAL simulant used on the VTR.

The reactions between lithium nitrate and selected HAL components were investigated in a systematic series of simplified experiments, because the complex chemical composition of HAL has, hitherto, prevented elucidation of the underlying mechanisms of reaction. The possible reactions of lithium nitrate with the nitrates of aluminium, magnesium, iron and zirconium (as zirconyl nitrate) and phosphomolybdic acid (PMA) were investigated. These compounds were chosen as they are the major components present in the HAL after the reprocessing of Magnox and  $\text{UO}_2$  fuels. A systematic approach was taken when designing these reactions, to assist in identifying reaction products and intermediates.

The experimental approach consisted of first reacting lithium nitrate with HAL component compounds to identify reactions and characterise the products. Reactions between the HAL simulant components were subsequently carried out without the presence of lithium nitrate, with lithium nitrate and with an equivalent amount of nitrate added through addition of excess nitric acid. These experiments were used to determine whether lithium or the additional nitrate were responsible for any of the reactions. By carrying out reactions with and without the presence of lithium nitrate, the role of lithium in the calciner could be better understood.

Six samples were chosen to determine whether the residence time in the furnace affected the extent of reactions in the calciner. These samples were AMN1, LMN1, LAMN1, PZN2, LPN1 and LPZN1. These samples were freeze dried and calcined at temperatures of 350 °C, 450 °C and 550 °C. XRD, TGA and EDS analysis were carried out on the calcined products. These results were compared to those obtained in the initial investigation.

Achieving short residence times in a muffle furnace, to simulate calcination conditions, was not possible using liquid samples because introducing the samples at the reaction temperature led to flash boiling and loss of the crucible contents. Clearly, preheating with an extended residence time would not be appropriate. The samples were therefore first freeze-dried, to remove water and the resultant solid was placed in the furnace at the desired temperature. This approach was thought to give a representative sample, since the freeze-drying simulated calciner Zones 1 and 2 (without heating), and the furnace simulated the conditions in Zones 3 and 4.

### 5.2.1 Calculating theoretical TGA results

TGA analysis was carried out on each of the starting materials used in these experiments (e.g. lithium nitrate, magnesium nitrate etc.). The data, comprising sample weight at each temperature step, were converted to percentage weight values to give the weight loss curve for each of the starting materials.

From these weight loss curves, theoretical weight loss curves were produced for each reaction. These were constructed by taking into account the ratio of the reactants in each sample, and combining the weight loss curves accordingly (Equation 5.1).

$$TW_x = \frac{(MW_{AX} \times A) + (MW_{BX} \times B)}{A + B} \quad (\text{Equation 5.1})$$

$TW_X$  is theoretical weight at temperature X (%)

$MW_{AX}$  is measured weight of component A at temperature X (%)

$MW_{BX}$  is measured weight of component B at temperature X (%)

A is mass of component A in the sample (g)

B is mass of component B in the sample (g)

This calculation was carried out for each of the measured temperatures and the results combined to form the theoretical traces. It was not possible to conduct TGA investigation of the calcined products immediately following the reaction. Consequently, it was important to acknowledge hydration of dehydrated nitrates or product phases in the calcined material, by absorption of atmospheric water, as a contributing factor in the TGA investigation of the calcine products.

The theoretical weight loss after calcination at set temperatures was also calculated. The first step was to calculate the theoretical mass of each component in the sample after calcination at a set temperature (Equation 5.2).

$$TM_{AX} = A \times (1 - ML_{AX}) \quad (\text{Equation 5.2})$$

$TM_{AX}$  is theoretical mass of component A at temperature X (g)

$ML_{AX}$  is measured weight loss of component A at temperature X (fraction)

A is mass of component A in the sample (g)

These values could then be used to work out the theoretical weight loss of the sample at a set temperature using Equation 5.3. Finally this value was subtracted from the maximum theoretical weight loss (Equation 5.4), which gave the theoretical weight loss which should be observed after calcination at a set temperature.

$$TL_x = 100 - \left( \frac{TM_{AX} + TM_{BX} + \dots}{A + B + \dots} \times 100 \right) \quad (\text{Equation 5.3})$$

$$TL_{obs} = TL_{Max} - TL_x \quad (\text{Equation 5.4})$$

$TL_x$  is theoretical weight loss at temperature X (%)

$TL_{Max}$  is maximum possible theoretical weight loss (%)

$TL_{obs}$  is theoretical weight loss observed after calcination at temperature X (%)

Using this, the actual weight losses observed in the samples after TGA analysis could be compared to the theoretical weight losses calculated from measurements carried out on the starting materials.

## 5.3 RESULTS AND DISCUSSION

### 5.3.1 Reactions between aluminium nitrate and magnesium nitrate

#### 5.3.1.1 Lab scale experiments

##### 5.3.1.1.1 AMN1 and AMN2

The XRD patterns of the reaction products showed strong reflections attributable to  $\text{Mg}(\text{NO}_3)_2 \cdot 6\text{H}_2\text{O}$  [14-101] for samples AMN1-350-3h, AMN2-350-3h, AMCN1-350-3h and AMCN2-350-3h; see Figure 5.1. Reflections associated with  $\text{Mg}(\text{NO}_3)_2 \cdot 6\text{H}_2\text{O}$  essentially account for all reflections in the XRD patterns of the products, and no reflections corresponding to any Al bearing phase were observed. TGA analysis of products AMN1-350-3h and AMN2-350-3h (Figure 5.2) showed total weight losses of 68 wt% and 77 wt% respectively at 1000 °C, compared to the total expected weight loss of 85 wt% corresponding to complete denitration and dehydration of the reagents to form the corresponding metal oxides. Complete denitration and dehydration of  $\text{Al}(\text{NO}_3)_3 \cdot 9\text{H}_2\text{O}$  would result in an expected weight loss of 45 wt% at 1000 °C. Assuming reversible dehydration of  $\text{Mg}(\text{NO}_3)_2 \cdot 6\text{H}_2\text{O}$  below 400 °C, consistent with XRD (Figure 5.1) and literature data (Paulik et al., 1988), this implies partial decomposition of  $\text{Al}(\text{NO}_3)_3 \cdot 9\text{H}_2\text{O}$ , to form an amorphous nitrate bearing product which is likely also hydrated, with a higher retention of the hydrate and nitrate inventory with the addition of extra  $\text{HNO}_3$ . This is consistent with XRD data and the thermal decomposition of  $\text{Al}(\text{NO}_3)_3 \cdot 9\text{H}_2\text{O}$  reported previously (Pacewska and Keshr, 2002). Overall, the presence of strong reflections associated with  $\text{Mg}(\text{NO}_3)_2 \cdot 6\text{H}_2\text{O}$ , and absence of additional reflections corresponding to a reaction product indicated that no observable reaction had occurred to form a crystalline product. This is consistent with thermal analysis of the reagents (Appendix), which showed  $\text{Mg}(\text{NO}_3)_2 \cdot 6\text{H}_2\text{O}$  to undergo (reversible) dehydration between 270-400 °C and denitration above 400 °C, and  $\text{Al}(\text{NO}_3)_3 \cdot 9\text{H}_2\text{O}$  to undergo partial dehydration and denitration below 350 °C to form an amorphous product which would not be observed by XRD, in agreement with previous work by Paulik et al. (1988) and Pacewska and Keshr (2002).

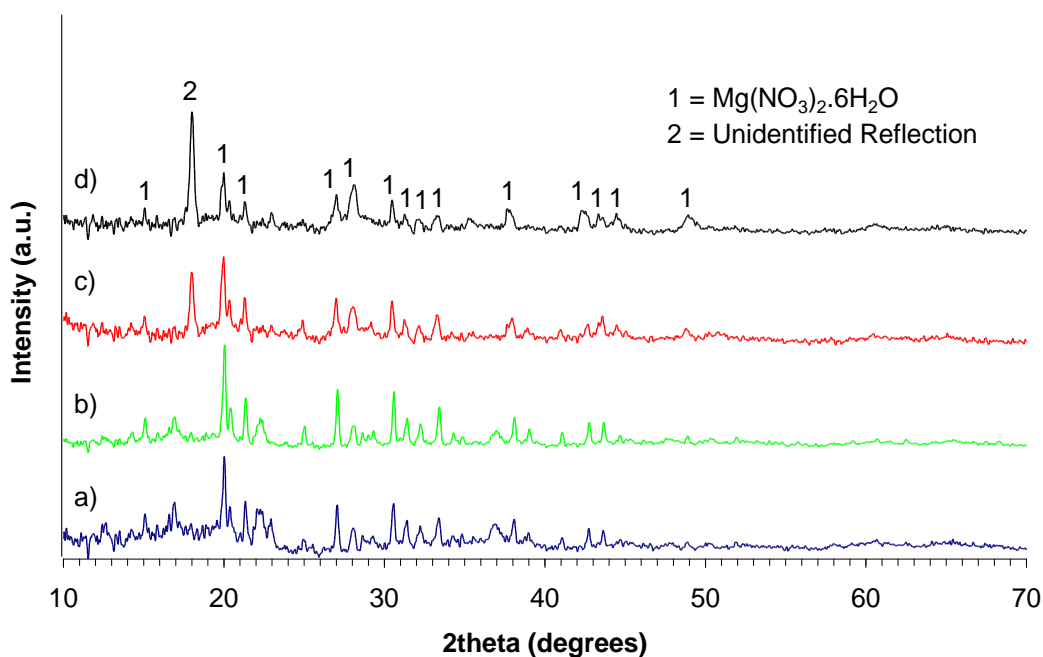


Figure 5.1 – XRD analysis of the samples a) AMN1-350-3h, b) AMN2-350-3h, c) AMCN1-350-3h and d) AMCN2-350-3h using Co K $\alpha$ <sup>8</sup> radiation ( $\lambda = 1.789 \text{ \AA}$ )

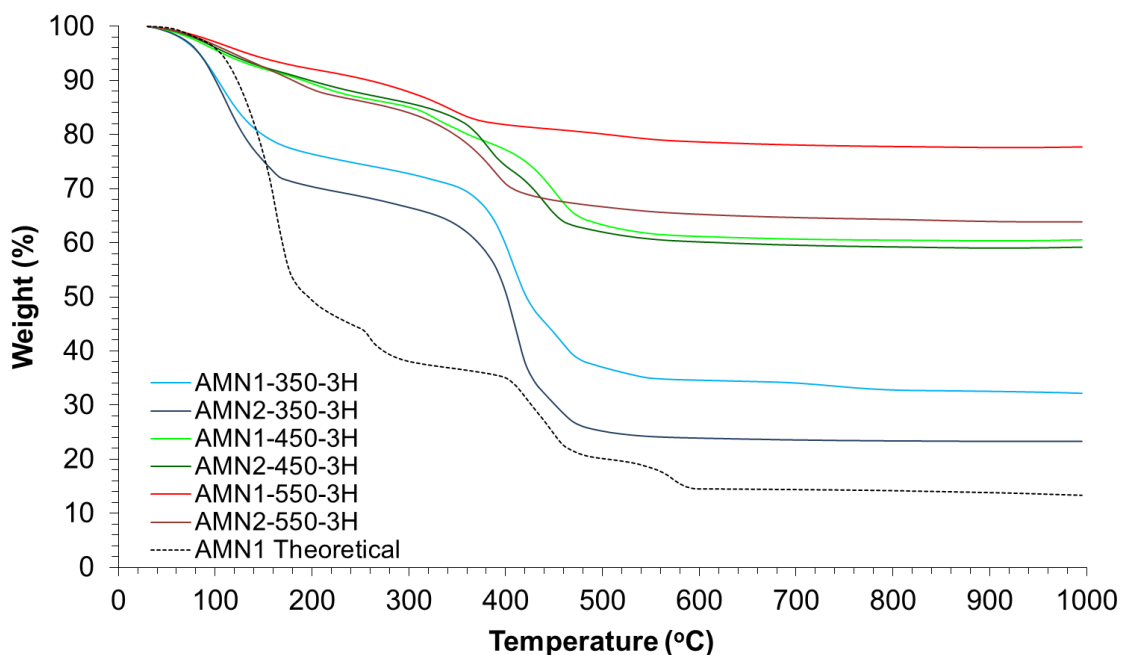
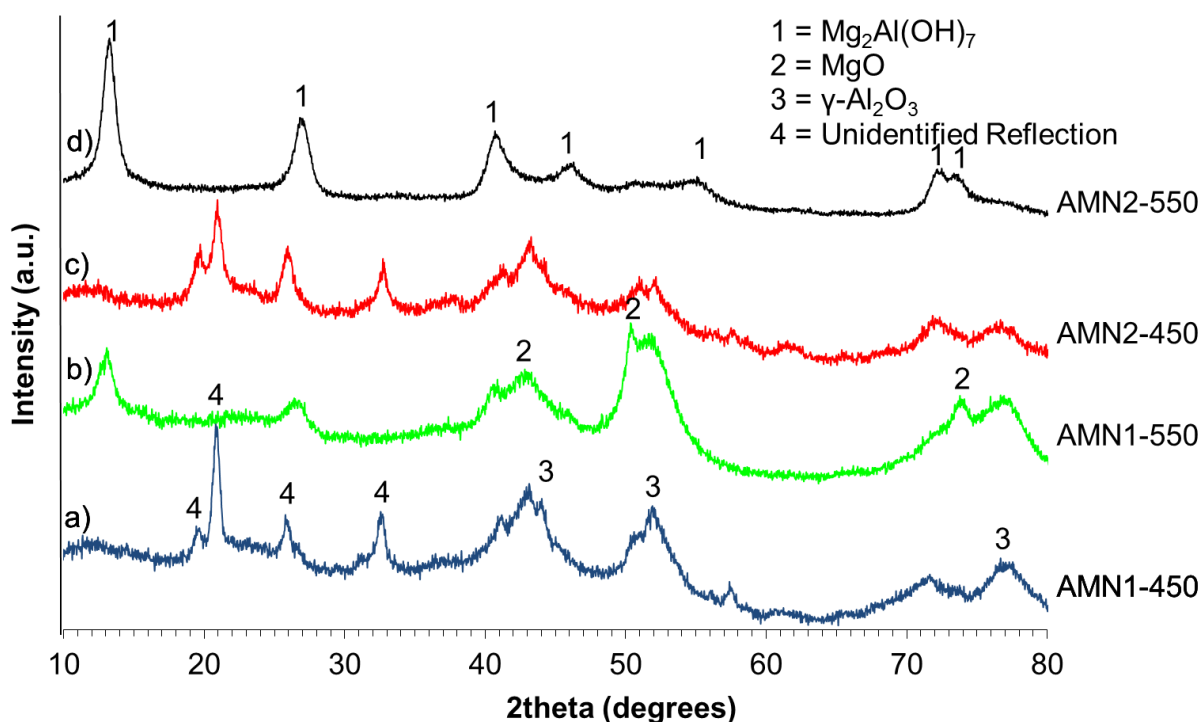


Figure 5.2 – TGA analysis of samples AMN1-350-3h, AMN2-350-3h, AMN1-450-3h, AMN2-450-3h, AMN1-550-3h and AMN2-550-3h

<sup>8</sup> Due to the unavailability of the INEL diffractometer at NNL, which uses Co K $\alpha$  radiation ( $\lambda = 1.789 \text{ \AA}$ ), throughout periods of this project, XRD analysis was carried out at the University of Sheffield using a Siemens D5000 diffractometer, which uses Cu K $\alpha$  radiation ( $\lambda = 1.546 \text{ \AA}$ ). The type of radiation used is therefore signified for each diffraction pattern shown throughout this chapter.

The XRD patterns for the reaction products of samples AMN1-450-3h and AMN2-450-3h (Figure 5.3) showed a set of reflections attributed to MgO [45-946] and  $\gamma$ -Al<sub>2</sub>O<sub>3</sub> [56-457]. An unknown, poorly crystalline phase was also present, which did not correspond to any known compound in the relevant phase diagrams, by reference to the ICDD database. Some diffuse scattering was also apparent, suggesting the presence of non-crystalline component(s). There was a notable absence of reflections attributable to Mg(NO<sub>3</sub>)<sub>2</sub>·6H<sub>2</sub>O from the diffraction pattern. TGA data from the products of AMN1-450-3h and AMN1-450-3h (Figure 5.2) showed total weight losses of 39 wt% and 41 wt% respectively at 1000 °C, consistent with the similarities in the diffraction patterns and indicating substantial retention of the nitrate and hydrate inventory. The weight loss profiles demonstrated two events: a broad weight loss up to 200 °C, attributed to dehydration; and a sharp weight loss at 400 °C, consistent with denitration of Mg(NO<sub>3</sub>)<sub>2</sub>·6H<sub>2</sub>O, by reference to thermal stability data for this compound (Appendix; Paulik et al., 1988). Taken together, these data imply formation of an unidentified intermediate phase through reaction of the amorphous Al nitrate hydrate, with Mg(NO<sub>3</sub>)<sub>2</sub>·6H<sub>2</sub>O, or its decomposition products, together with MgO. The available evidence suggests that this unidentified phase is likely to be a complex Mg and Al nitrate hydrate.



**Figure 5.3 – XRD analysis of samples a) AMN1-450-3h, b) AMN1-550-3h, c) AMN2-450-3h and d) AMN2-550-3h using Co K $\alpha$ 1 radiation ( $\lambda = 1.789 \text{ \AA}$ )**

The XRD pattern for the reaction products of samples AMN1-550-3h and AMN2-550-3h (Figure 5.3) showed a close match to reflections attributable to  $\text{Mg}_2\text{Al}(\text{OH})_7$  [48-601]. However, consideration of the TGA data and available literature (Zhang et al., 2013) suggest the formation of an Al/Mg layered double hydroxide (Mg-Al-LDH) continuous solid solution of the form  $\text{Mg}_a\text{Al}(\text{OH})_{3+2a-c}(\text{NO}_3)_c \cdot x\text{H}_2\text{O}$ . Additional reflections in the XRD pattern of sample AMN1-550-3h showed the presence of MgO [45-946] and  $\gamma\text{-Al}_2\text{O}_3$  [56-457]. On addition of nitric acid (sample AMN2-550-3h), however, the reflections attributed to MgO and  $\gamma\text{-Al}_2\text{O}_3$  were not present. TGA analysis of products AMN1-550-3h and AMN2-550-3h (Figure 5.2) showed total weight losses of 22 wt% and 36 wt% respectively. The presence of residual weight loss, after calcination at 550 °C, implies retention of a proportion of the nitrate and hydrate inventory. This observation is in agreement with the formation of a (possibly hydrated) Mg-Al-LDH phase by XRD (Figure 5.3) and is consistent with previous work carried out by Zhang et al. (2013) and Zhang and Li (2013), reporting that Mg-Al-LDH's, of the form  $\text{Mg}_a\text{Al}(\text{OH})_{3+2a-c}(\text{NO}_3)_c \cdot x\text{H}_2\text{O}$ , were produced under various calcination conditions from  $\text{Mg}(\text{NO}_3)_2 \cdot 6\text{H}_2\text{O}$  and either  $\text{Al}(\text{NO}_3)_3 \cdot 9\text{H}_2\text{O}$  or  $\text{Al}(\text{OH})_3$  starting materials. The presence of MgO in the preparation of an Mg-Al-LDH was noted by Zhang et al. (2013), with the XRD reflections attributed to MgO reducing in intensity at increased reaction time and temperatures, suggesting that the reaction proceeds *via* a reaction involving MgO, in which additional  $\text{HNO}_3$  lowers the reaction temperature. Previous work by Mascolo and Marino (1980), Pausch et al. (1986) and Roy et al. (1953) all showed the formation of an Mg-Al-LDH through reaction of alumina with MgO under various hydrothermal conditions. The backscattered electron image (Figure 5.4) and X-ray maps (Figure 5.5) showed that the distribution of Al and Mg throughout the sample was relatively homogeneous, supporting the identification of a Mg-Al-LDH phase. Overall, these data imply the formation of a Mg-Al-LDH, which must include a significant nitrate and hydrate component, in the form  $\text{Mg}_a\text{Al}(\text{OH})_{3+2a-c}(\text{NO}_3)_c \cdot x\text{H}_2\text{O}$ . Formation must proceed by decomposition of the unidentified intermediate formed at lower temperature (*via* denitration and / or dehydration) and reaction between MgO and  $\gamma\text{-Al}_2\text{O}_3$ , also formed at lower temperature. Higher nitrate content, through addition of  $\text{HNO}_3$ , removed the presence of MgO and  $\gamma\text{-Al}_2\text{O}_3$  from the reaction products.



XRD analysis showed that addition of Cr nitrate had very little effect on the product phases formed from the reaction between Mg and Al nitrates when calcined at 350 °C; see Figure 5.1. Reflections associated with  $\text{Mg}(\text{NO}_3)_2 \cdot 6\text{H}_2\text{O}$  again account for essentially all reflections in the XRD patterns of the products, however, a single additional intense reflection, at  $2\theta = 18.05^\circ$  (Figure 5.1), was observed in the diffraction patterns of products from reactions involving Cr nitrate. This reflection could not be attributed to any known phase in the relevant phase diagram, by reference to the ICDD database. The backscattered electron image (Figure 5.4) and X-ray maps (Figure 5.5) showed that Cr was localised to one area in the sample. This is consistent with the XRD pattern of sample AMCN1-350-3h (Figure 5.1) which showed an additional reflection attributed to the presence of Cr in the sample, suggesting Cr formed an isolated phase, not interacting with other components in the sample.

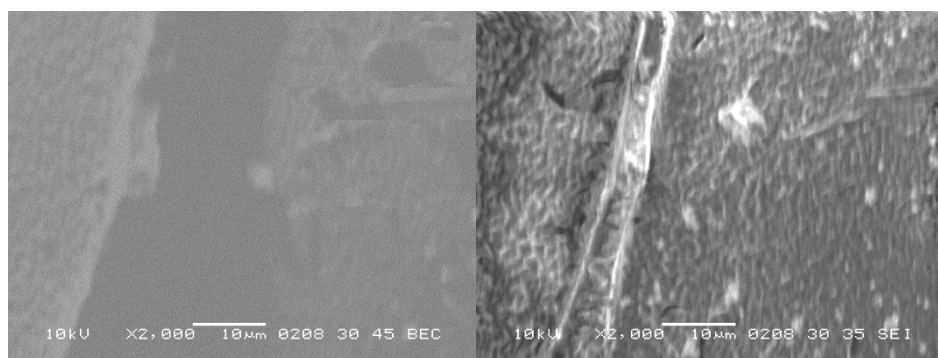


**Figure 5.4 – Backscattered (left) and secondary (right) electron images of sample AMCN1-550-3h.**

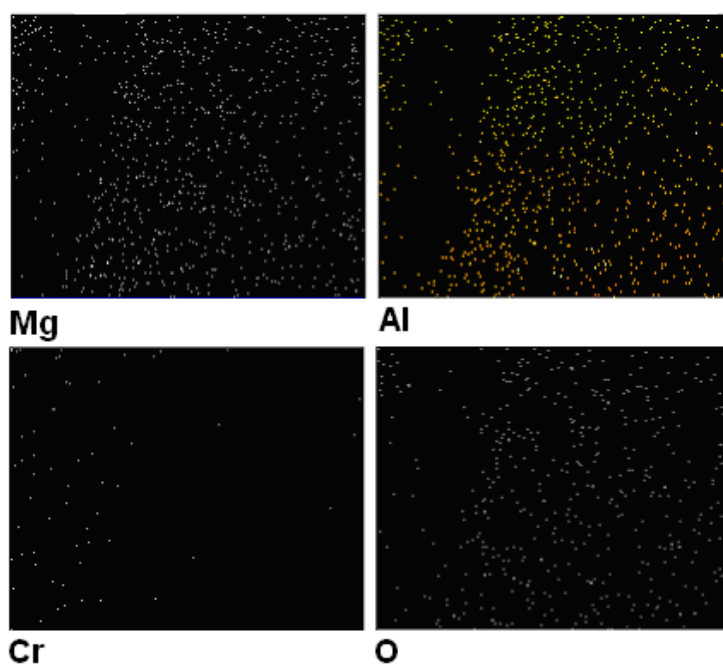


**Figure 5.5 – Digital maps showing the elemental composition of sample AMCN1-550.**

From these experiments, it is possible to infer and conclude the following sequence of reactions:

- Below 350 °C:  $\text{Mg}(\text{NO}_3)_2 \cdot 6\text{H}_2\text{O}$  undergoes reversible dehydration, whereas  $\text{Al}(\text{NO}_3)_3 \cdot 9\text{H}_2\text{O}$  undergoes partial denitration and dehydration to form an amorphous product. These findings are consistent with analysis of the reagents (Appendix) and literature data (Paulik et al., 1988; Pacewska and Keshr, 2002). The possibility of reaction between the reagents below 350 °C cannot be excluded, but the strong XRD reflections associate with  $\text{Mg}(\text{NO}_3)_2 \cdot 6\text{H}_2\text{O}$ , and absence of additional reflections corresponding to a crystalline reaction product, imply that the product must be minor and amorphous in nature.
- Between 350-450 °C: an unidentified intermediate phase is formed together with MgO and  $\gamma\text{-Al}_2\text{O}_3$ ; this suggests (partial) reaction of the amorphous Al nitrate hydrate, with  $\text{Mg}(\text{NO}_3)_2 \cdot 6\text{H}_2\text{O}$  and / or MgO. The available evidence suggests that this unidentified phase is likely to be a complex Mg and Al nitrate hydrate.
- Between 450-550 °C: a layered double hydroxide nitrate of the type  $\text{Mg}_a\text{Al}(\text{OH})_{3+2a-c}(\text{NO}_3)_c \cdot x\text{H}_2\text{O}$ , is formed, together with MgO and  $\gamma\text{-Al}_2\text{O}_3$ . Formation of the Mg-Al-LDH must proceed by decomposition of the unidentified intermediate formed at lower temperature (*via* denitration and / or dehydration) and reaction between MgO and  $\gamma\text{-Al}_2\text{O}_3$  also formed at lower temperature. Higher nitrate content, through addition of  $\text{HNO}_3$ , removed the presence of MgO and  $\gamma\text{-Al}_2\text{O}_3$  from the reaction products.
- Addition of Cr nitrate had no affect on the reactions between Mg and Al nitrates.

#### 5.3.1.1.2 LMN1

The XRD pattern of product LMN1-350-3h (Figure 5.6) showed a set of reflections which could be attributed to  $\text{LiNO}_3$  [8-466] and  $\text{Mg}(\text{NO}_3)_2 \cdot 6\text{H}_2\text{O}$  [14-101]. These components essentially accounted all of the reflections present in the XRD pattern which suggested no reaction had occurred. This was verified by TGA analysis (Figure 5.7), which showed the total weight loss of the product to be 84 wt% at 1000 °C, close to the 86 wt% expected total weight loss arising from complete denitration and dehydration of the metal nitrate hydrates to form the corresponding oxides. Overall, the identification of  $\text{LiNO}_3$  and  $\text{Mg}(\text{NO}_3)_2 \cdot 6\text{H}_2\text{O}$  after calcination at 350 °C is consistent with thermal analysis of the reagents, which showed  $\text{LiNO}_3$  to be stable up to 600 °C, and  $\text{Mg}(\text{NO}_3)_2 \cdot 6\text{H}_2\text{O}$  to undergo dehydration between 270-400 °C and denitration above 400 °C (Appendix, in agreement with Chun, 1977; Paulik et al., 1988).

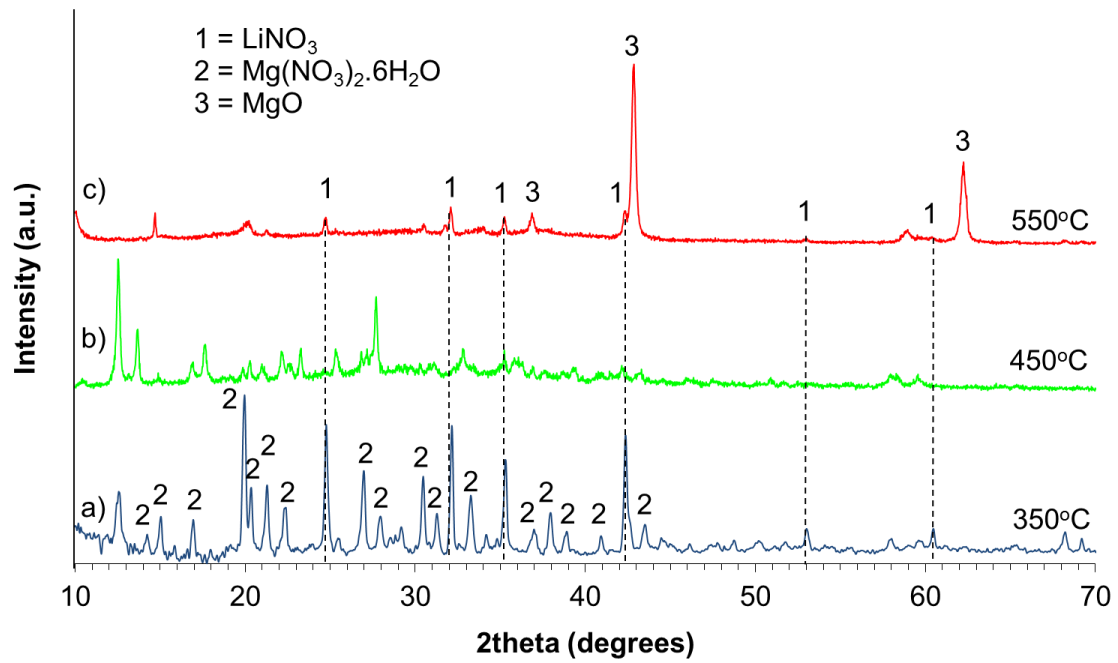


Figure 5.6 – XRD analysis of samples a) LMN1-350-3h, b) LMN1-450-3h and c) LMN1-550-3h using Cu K $\alpha$ 1 radiation ( $\lambda = 1.546 \text{ \AA}$ )

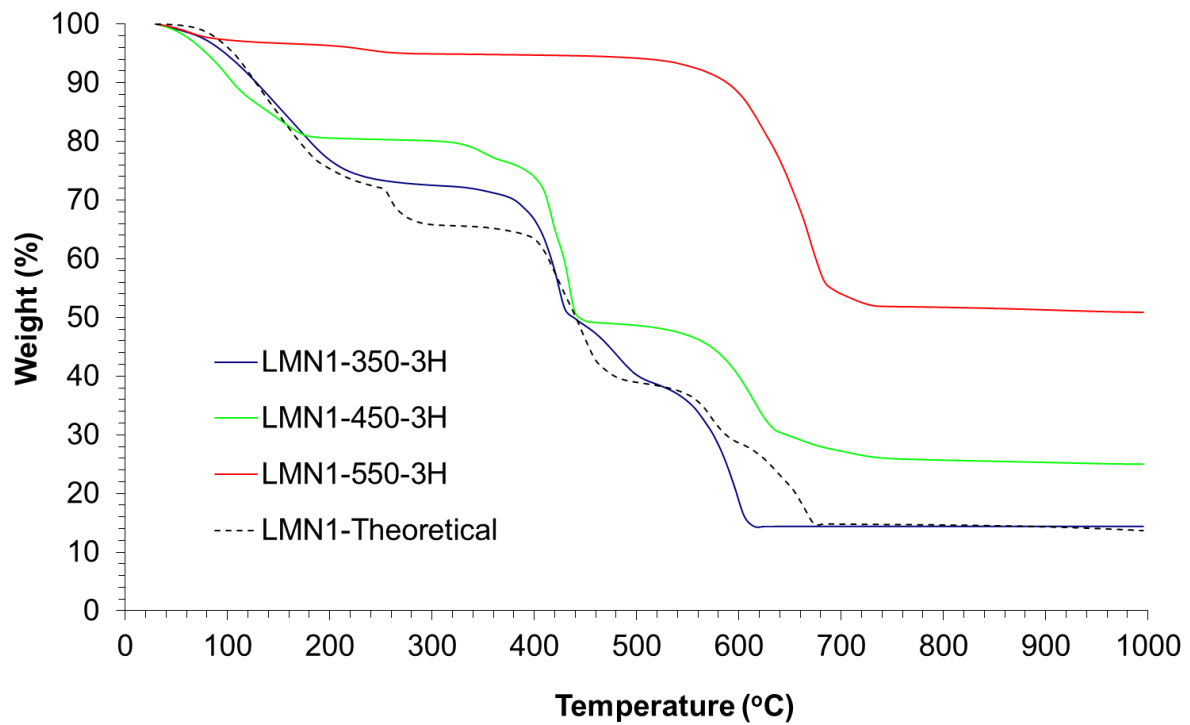


Figure 5.7 – TGA analysis of samples LMN1-350-3h, LMN1-450-3h and LMN1-550-3h

The XRD pattern of product LMN1-450-3h (Figure 5.6) showed a set of reflections which did not correspond to any known compound in the relevant phase diagrams, by reference to the ICDD database; additionally, some diffuse scattering is apparent, suggesting the presence of amorphous component(s). However, reflections associated with  $\text{LiNO}_3$  and  $\text{Mg}(\text{NO}_3)_2 \cdot 6\text{H}_2\text{O}$  were found to be absent from the diffraction pattern. TGA analysis showed the total weight loss of the product to be 75 wt% at 1000 °C, indicating quantitative retention of the nitrate and hydrate inventory. The weight loss profile demonstrated three events: a broad weight loss up to 200 °C, attributed to dehydration; and two well defined weight loss events at 400 °C and 600 °C, consistent with denitration of  $\text{Mg}(\text{NO}_3)_2 \cdot 6\text{H}_2\text{O}$  and  $\text{LiNO}_3$ , respectively, by reference to thermal stability data for these compounds (Appendix; Chun, 1977; Paulik et al., 1988). Taken together, these data imply reaction of  $\text{LiNO}_3$  and  $\text{Mg}(\text{NO}_3)_2 \cdot 6\text{H}_2\text{O}$  between 350-450 °C, to form a metastable crystalline product, of unknown structure, comprising a mixed Li and Mg nitrate hydrate.

The XRD pattern of product LMN1-550-3h (Figure 5.6) demonstrated the formation of  $\text{MgO}$ , together with a set of low intensity reflections, attributed to  $\text{LiNO}_3$ , showing a portion of the starting material had re-formed. At least one other phase was present, which could not be conclusively identified by reference to the ICDD database; some weak diffuse scattering was also apparent, suggesting the presence of amorphous component(s). TGA analysis of the product (Figure 5.7) demonstrated a single weight loss event at 600 °C, with a total weight loss at 1000 °C of 49 wt%; notably, no significant low temperature dehydration event was observed. This is consistent with the thermal data for  $\text{LiNO}_3$  (Appendix; Chun, 1977) which shows a single weight loss event above 600 °C corresponding to decomposition to the component oxide. Complete conversion of  $\text{Mg}(\text{NO}_3)_2 \cdot 6\text{H}_2\text{O}$  to  $\text{MgO}$  would result in an expected weight loss of 67 wt%, which implies that the additional phase must comprise a metastable Li rich nitrate hydrate, possibly incorporating Mg.

From these experiments, it is possible to infer and conclude:

- Below 350 °C:  $\text{LiNO}_3$  and  $\text{Mg}(\text{NO}_3)_2 \cdot 6\text{H}_2\text{O}$  do not undergo any significant reaction.
- Between 350-450 °C: the primary reaction is between  $\text{LiNO}_3$  and  $\text{Mg}(\text{NO}_3)_2 \cdot 6\text{H}_2\text{O}$  to form a metastable crystalline intermediate compound, likely a mixed nitrate hydrate of Mg and Li; an amorphous counterpart was also formed.
- Between 450-550 °C: the metastable intermediate compound decomposes to form  $\text{MgO}$  and a portion of the  $\text{LiNO}_3$  starting material. An amorphous phase was also present, which must be a Li rich nitrate phase possibly incorporating a small amount of Mg.

### 5.3.1.1.3 LAN1

The XRD pattern of product LAN1-350-3h (Figure 5.8) showed a set of reflections attributable to  $\text{LiNO}_3$  [8-466]. No reflections corresponding to  $\text{Al}(\text{NO}_3)_3 \cdot 9\text{H}_2\text{O}$  or any Al bearing phase were observed. TGA analysis of the calcined product (Figure 5.9) demonstrated a total weight loss of 55 wt% at 1000 °C, compared to the expected total weight loss of 85 wt% arising from complete denitration and dehydration of the metal nitrate hydrates to form the corresponding oxides. Complete denitration and dehydration of  $\text{Al}(\text{NO}_3)_3 \cdot 9\text{H}_2\text{O}$  below 350 °C would result in a product yielding an expected weight loss of 70 wt% at 1000 °C. This implies partial decomposition of  $\text{Al}(\text{NO}_3)_3 \cdot 9\text{H}_2\text{O}$  (by loss of 78 % of the nitrate and hydrate inventory), to form an amorphous nitrate bearing product which is likely also hydrated, consistent with XRD data and the thermal decomposition of  $\text{Al}(\text{NO}_3)_3 \cdot 9\text{H}_2\text{O}$  reported previously (Pacewska and Keshr, 2002).

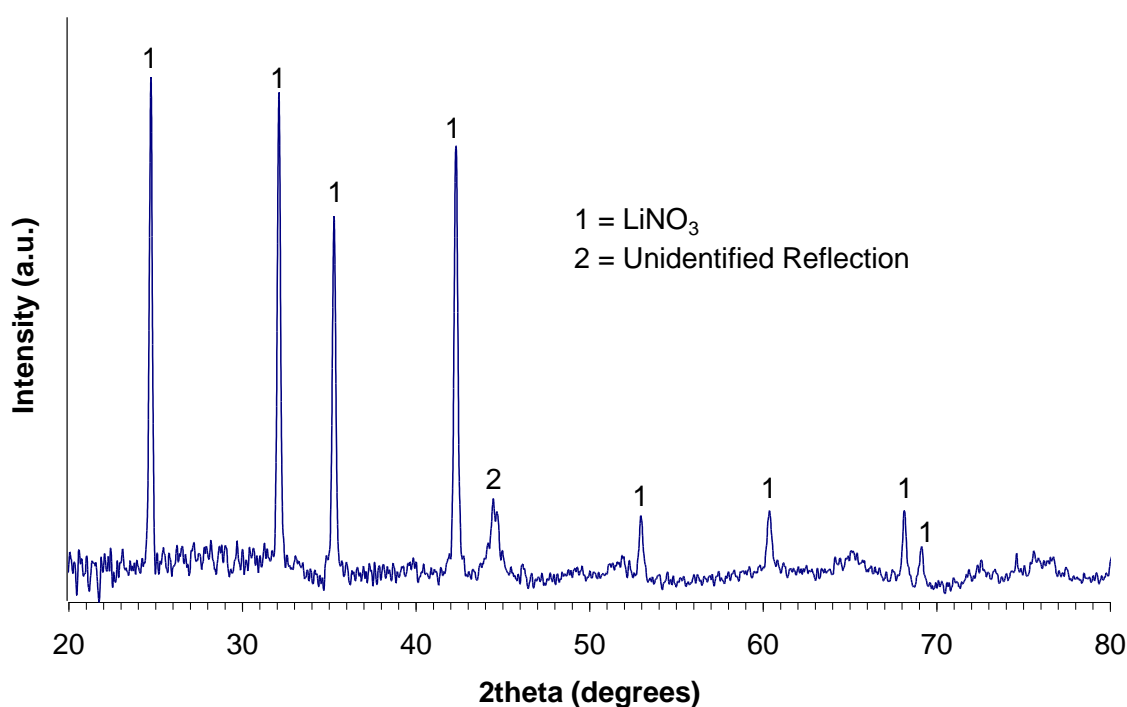
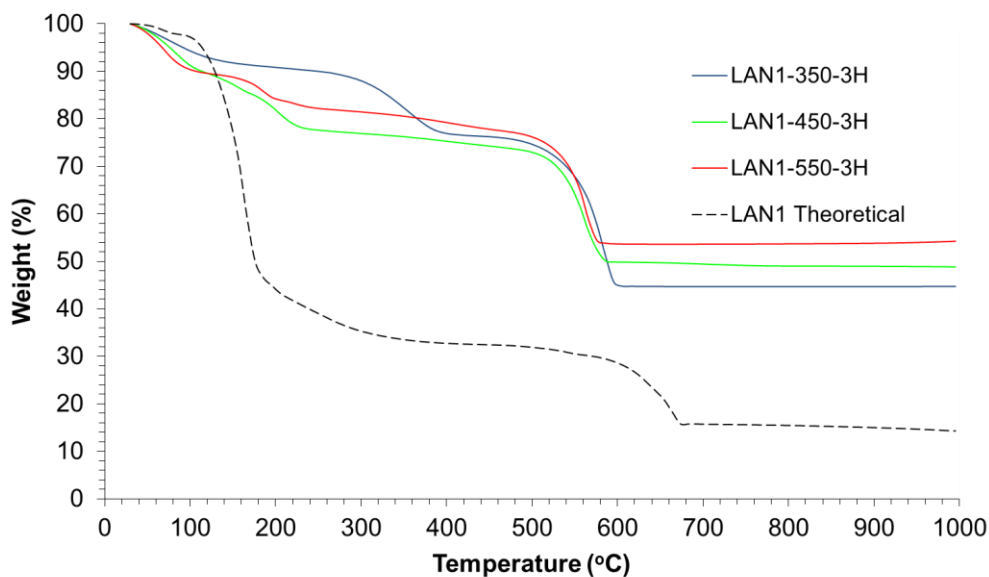


Figure 5.8 – XRD analysis of sample LAN1-350-3h using Cu  $K\alpha 1$  radiation ( $\lambda = 1.546 \text{ \AA}$ )



**Figure 5.9 – TGA analysis of samples LAN1-350-3h, LAN1-450-3h and LAN1-550-3h**

The XRD patterns of products LAN1-450-3h and LAN1-550-3h (Figure 5.10) showed a set of identical broad reflections attributed to  $\text{LiAl}_2(\text{OH})_6(\text{NO}_3) \cdot x\text{H}_2\text{O}$  [51-359] and poorly crystalline  $\gamma\text{-Al}_2\text{O}_3$  [56-457] plus an additional crystalline phase which could not be identified, by reference to the relevant phase diagrams, using the ICDD database. A different set of reflections were present after calcination at 450 °C, identified as  $\text{LiNO}_3 \cdot 3\text{H}_2\text{O}$  [24-645]. Strong diffuse scattering was also apparent, suggesting the presence of amorphous component(s). No reflections corresponding to anhydrous  $\text{LiNO}_3$  or  $\text{Al}(\text{NO}_3)_3 \cdot 9\text{H}_2\text{O}$  were apparent in the diffraction patterns. TGA analysis of LAN1-450-3h and LAN1-550-3h (Figure 5.9) afforded total weight losses of 51 wt% and 45 wt% respectively at 1000 °C, indicating that a similar and substantive fraction of the volatile inventory was retained after reaction at 450-550 °C. The weight loss curve shows two distinct weight loss events: a broad weight loss below 200 °C, typical of dehydration; and a sharp weight loss above 500 °C. The latter event is consistent with the decomposition of a hydrated Li/Al layered double hydroxide (Li-Al-LDH) phase (identified by XRD; Figure 5.10), as reported by Nayak et al. (1997). Bessergeunev et al (1997) showed the reaction of  $\text{LiNO}_3$  with  $\gamma\text{-Al}(\text{OH})_3$  yielded the product  $\text{LiAl}_2(\text{OH})_6(\text{NO}_3) \cdot x\text{H}_2\text{O}$  under hydrothermal conditions. The thermal transformation of  $\text{Al}(\text{NO}_3)_3 \cdot 9\text{H}_2\text{O}$  under acidic conditions is known to form aluminium meta-hydroxide ( $\text{AlOOH}$ ), which decomposes to form  $\gamma\text{-Al}_2\text{O}_3$  at 400-500 °C (Pacowska and Keshr, 2004). Taken together, these data imply the formation of a Li-Al-LDH, which must include a nitrate and hydrate component, in the form  $\text{LiAl}_2(\text{OH})_6(\text{NO}_3) \cdot x\text{H}_2\text{O}$ . An additional, unidentified crystalline phase was also formed between 350-450 °C. This phase is thought to be lithium rich, as the ratio of Al/Li in the starting materials was 1:1.3, whereas there is a 2:1 ratio is evident in the Li-Al-LDH. However, no match could be found using the ICDD database, suggesting the unidentified phase is a complex Li rich nitrate hydrate,

possibly incorporating Al. Formation of  $\text{LiAl}_2(\text{OH})_6(\text{NO}_3)_x \cdot x\text{H}_2\text{O}$  must proceed by reaction of  $\text{LiNO}_3 \cdot 3\text{H}_2\text{O}$  with the non-crystalline products of  $\text{Al}(\text{NO}_3)_3 \cdot 9\text{H}_2\text{O}$  decomposition. The presence of  $\text{LiNO}_3 \cdot 3\text{H}_2\text{O}$  after calcination at 450 °C for 3 h showed the reaction had not gone to completion, however, no  $\text{LiNO}_3 \cdot 3\text{H}_2\text{O}$  was observed in product LAN1-550-3h. This showed further reaction occurred between 450-550 °C to yield Li-Al-LDH, implied by the increase in intensity of the reflections attributed to this phase as identified by XRD. The unidentified crystalline phase was observed after calcination at 550 °C, suggesting it is stable up to at least 560 °C, as shown by TGA analysis.

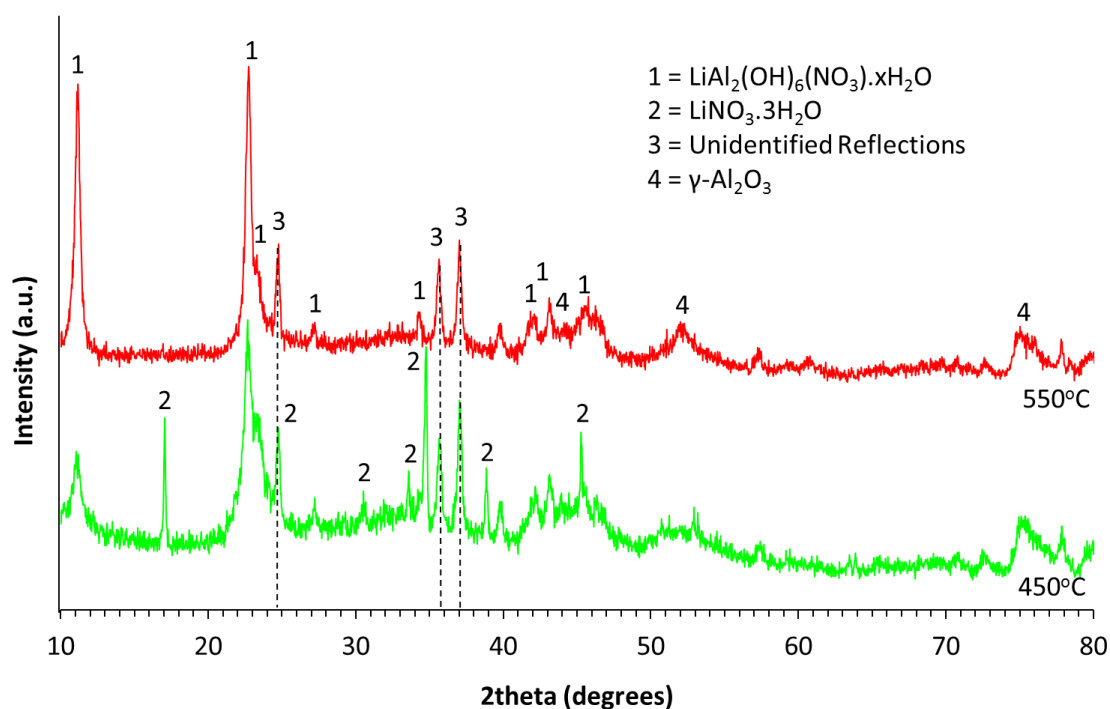


**Figure 5.10 – XRD analysis of samples a) LAN1-450-3h and b) LAN1-550-3h using Co K $\alpha$ 1 radiation ( $\lambda = 1.789 \text{ \AA}$ )**

From these experiments, it is possible to infer and conclude:

- Below 350 °C:  $\text{LiNO}_3$  and  $\text{Al}(\text{NO}_3)_3 \cdot 9\text{H}_2\text{O}$  do not undergo any significant reaction, but the latter undergoes partial decomposition to form a non-crystalline product.
- Between 350-450 °C:  $\text{LiNO}_3$  reacts with the non-crystalline product of  $\text{Al}(\text{NO}_3)_3 \cdot 9\text{H}_2\text{O}$  denitration and dehydration to yield a poorly crystalline Li-Al-LDH, in the form  $\text{LiAl}_2(\text{OH})_{7-a}(\text{NO}_3)_a \cdot x\text{H}_2\text{O}$  and an unidentified crystalline phase, thought to be a Li rich nitrate hydrate (possibly incorporating Al), with  $\text{LiNO}_3 \cdot 3\text{H}_2\text{O}$  present in the product, showing the reaction had not reached completion.
- Between 450-550 °C: The remaining  $\text{LiNO}_3 \cdot 3\text{H}_2\text{O}$  undergoes further reaction with the non-crystalline product of  $\text{Al}(\text{NO}_3)_3 \cdot 9\text{H}_2\text{O}$  decomposition to form Li-Al-LDH. The unidentified crystalline phase is still observed.

#### 5.3.1.1.4 LAMN1

The XRD pattern of product LAMN1-350-3h (Figure 5.11) comprised sharp reflections which did not correspond to any known compound(s) in the relevant phase diagrams, by reference to the ICDD database. No reflections could be attributed to  $\text{LiNO}_3$ ,  $\text{Mg}(\text{NO}_3)_2 \cdot 6\text{H}_2\text{O}$  or  $\text{Al}(\text{NO}_3)_3 \cdot 9\text{H}_2\text{O}$ . These observations are in contrast to reactions involving  $\text{LiNO}_3$  with  $\text{Mg}(\text{NO}_3)_2 \cdot 6\text{H}_2\text{O}$  or  $\text{Al}(\text{NO}_3)_3 \cdot 9\text{H}_2\text{O}$ , in which no significant reaction was observed at 350 °C and  $\text{LiNO}_3$  was retained. TGA analysis (Figure 5.12) showed the total weight loss of the product to be 60 wt% at 1000 °C, compared to the expected total weight loss of 84 wt% arising from complete denitration and dehydration of the metal nitrate hydrates to form the corresponding oxides. The weight loss curve shows three distinct weight loss events: a broad weight loss below 200 °C, typical of dehydration; and two sharp weight loss events at 380 °C and 560 °C. Both these events occurred at lower temperatures than expected for the denitration of  $\text{Mg}(\text{NO}_3)_2 \cdot 6\text{H}_2\text{O}$  and  $\text{LiNO}_3$  (Shown to be 400 °C and 600 °C respectively; Appendix; Paulik et al., 1988; Chun 1977). Overall, these data imply that the crystalline product(s) of LAMN1-350-3h must comprise one or more nitrate hydrate phases incorporating Li, Al and Mg; because,  $\text{LiNO}_3$  does not react with either  $\text{Mg}(\text{NO}_3)_2 \cdot 6\text{H}_2\text{O}$  or  $\text{Al}(\text{NO}_3)_3 \cdot 9\text{H}_2\text{O}$  at 350 °C or below (sections 5.3.1.1.2 and 5.3.1.1.3).

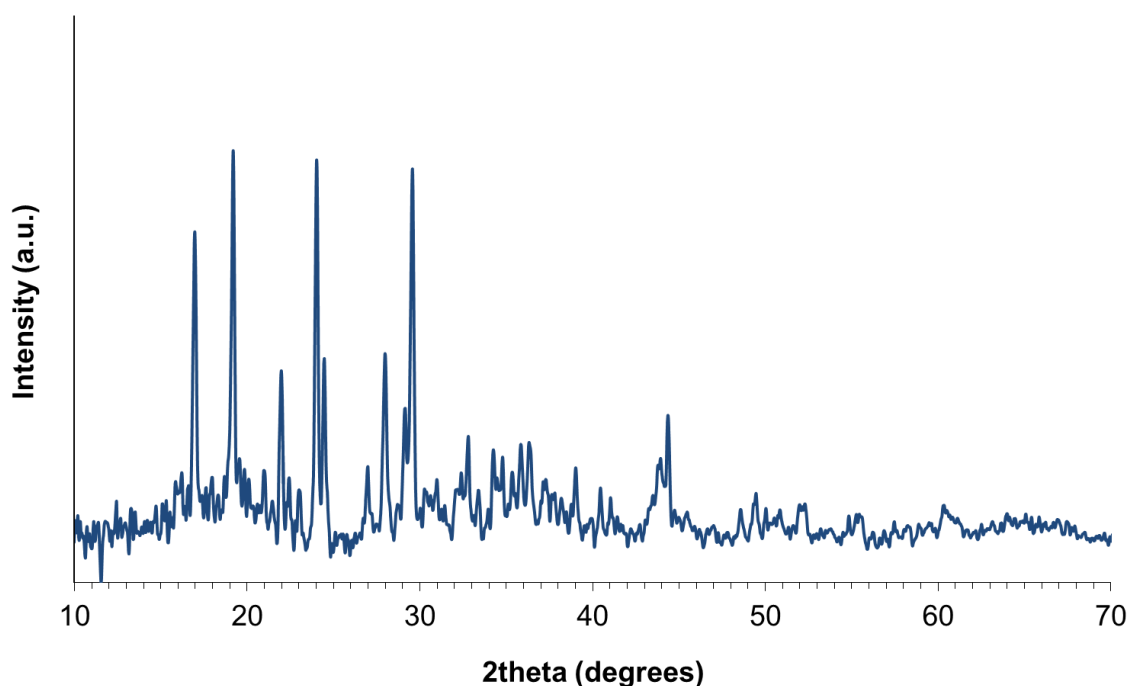


**Figure 5.11 – XRD analysis of sample LAMN1-350-3h  
using Co K $\alpha$ 1 radiation ( $\lambda = 1.789 \text{ \AA}$ )**



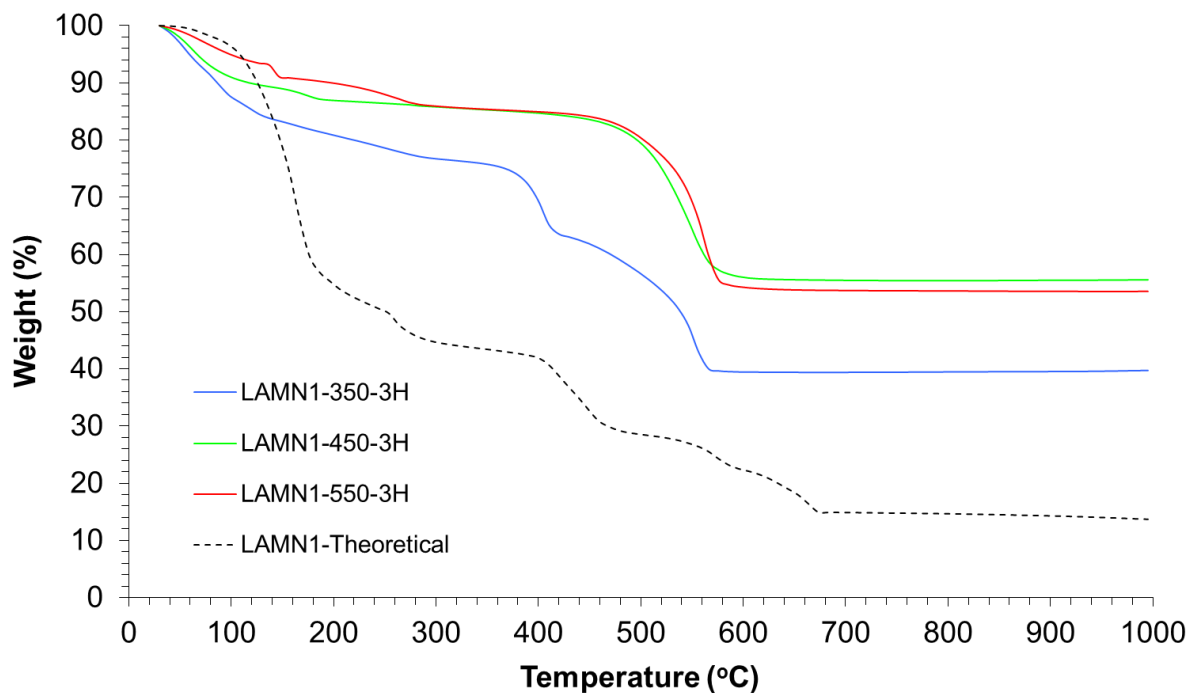


**Figure 5.12 – TGA analysis of samples LAMN1-350-3h, LAMN1-450-3h and LAMN1-550-3h**

The XRD patterns of product LAMN1-450-3h and LAMN1-550-3h (Figure 5.13) exhibited sharp reflections which matched the diffraction pattern of  $\gamma$ -Al<sub>2</sub>O<sub>3</sub> [56-457], no additional reflections were observed, though significant diffuse scattering was apparent, suggesting the presence of a non-crystalline phase. The observation of crystalline  $\gamma$ -Al<sub>2</sub>O<sub>3</sub> is in contrast to sample AMN1 (section 5.3.1.1.1), which shows formation of poorly crystalline  $\gamma$ -Al<sub>2</sub>O<sub>3</sub> and MgO under the same calcination conditions. TGA analysis of these products (Figure 5.12) showed the total weight loss to be 46-49 wt% at 1000 °C, demonstrating the retention of a significant volatile nitrate and hydrate inventory. The weight loss curve shows two distinct weight loss events: a broad weight loss below 200 °C, typical of dehydration; and a sharp weight loss at 560 °C. There was a notable absence of the weight loss event at 380 °C, observed in sample LAMN1-350-3h, which implied this event must be due to the decomposition of the unknown intermediate(s) to form the  $\gamma$ -Al<sub>2</sub>O<sub>3</sub> type structure, with a non-crystalline nitrate hydrate phase, presumably containing Li and Mg, stable up to 560 °C. LiNO<sub>3</sub> is known to act as a molten salt above its melting temperature of 255 °C. Molten salts can provide an alternative media, which can change the reactivity and solubility of reactants (Afanasiev and Geantet, 1998). There are two main mechanisms by which reactions proceed in a molten salt host, which are the ‘template-growth’ and ‘dissolution-precipitation’ mechanisms (Zhang, 2007). ‘Template-growth’ reactions occur when one of the reactants is much more soluble in the molten salt than the other. The soluble reactant diffuses on to the surface of the other reactant causing a reaction to occur. The product of this reaction retains the morphology of the insoluble reactant. Previous studies by Safaei-Naeini et al. (2011) and Fazli et al. (2013) showed the reaction of MgO and  $\gamma$ -Al<sub>2</sub>O<sub>3</sub> in a molten salt

medium results in the formation of  $\text{MgAl}_2\text{O}_4$  *via* a template-growth mechanism, where the structure of  $\gamma\text{-Al}_2\text{O}_3$  is retained, consistent with the XRD pattern shown for products LAMN1-450-3h and LAMN1-550-3h (Figure 5.13). The work by Fazli et al. (2013) showed the formation of  $\text{MgAl}_2\text{O}_4$  began at 650 °C in a LiCl molten salt. However,  $\text{LiNO}_3$  acts as Lux-Flood base, meaning it is a good  $\text{O}^{2-}$  donor, and can lower the temperatures needed for an oxidation reaction to occur (Afanasiev and Geantet, 1998; Afanasiev, 2007). This is consistent with the fact that MgO and  $\gamma\text{-Al}_2\text{O}_3$  are formed in products AMN1-450-3h and AMN1-550-3h, without the presence of  $\text{LiNO}_3$ . Therefore, the observation of the  $\gamma\text{-Al}_2\text{O}_3$  type structure in the diffraction pattern, as well as consideration of the available literature, suggest that  $\text{MgAl}_2\text{O}_4$  is formed *via* a template-growth mechanism using  $\text{LiNO}_3$  as a molten salt, therefore retaining the  $\gamma\text{-Al}_2\text{O}_3$  structure. A non-crystalline phase, which must contain Li and Mg was also shown to be present through the significant diffuse scattering observed by XRD analysis, which appears to decompose above 560 °C, as shown by the TGA trace (Figure 5.12).

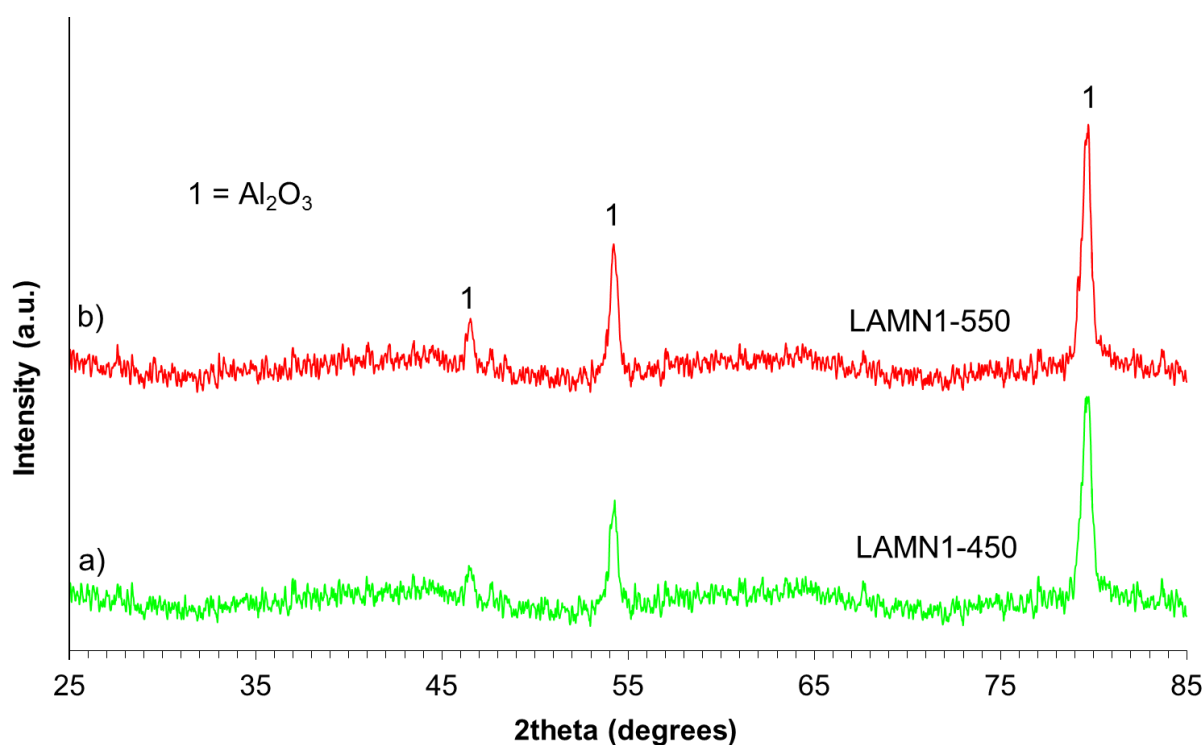


**Figure 5.13 – XRD analysis of a) LAMN1-450-3h and b) LAMN1-550-3h using Co K $\alpha$ 1 radiation ( $\lambda = 1.789 \text{ \AA}$ )**

Confirmation of the retention of Li was made by  $^7\text{Li}$  MAS NMR spectroscopy. Figure 5.14 shows a comparison of the  $^7\text{Li}$  MAS NMR spectra of  $\text{LiNO}_3$  and the product LAMN1-550-3h; the former is dominated by an intense symmetric and sharp resonance at  $-0.09$  ppm, whereas the latter comprises an asymmetric intense resonance at a higher chemical shift of  $-0.06$  ppm (measured relative to  $\text{LiCl}$ ). These data confirm that Li is retained in the calcination reactions but does not exist in the original chemical environment of  $\text{LiNO}_3$  (the estimate accuracy of the derived chemical shifts is  $\pm 0.02$  ppm), consistent with XRD analysis. The signal is slightly broader than that of  $\text{LiNO}_3$ , indicative of a less crystalline environment, signifying the Li is present in a non-crystalline environment, however, the asymmetric nature could suggest the some of the Li is present in a crystalline phase. Since product LAMN1-550-3h was found to comprise a highly crystalline phase with a  $\gamma\text{-Al}_2\text{O}_3$  type structure and a non-crystalline component (thought to contain Li and Mg) by XRD analysis, the NMR data may suggest incorporation of Li in this phase (and its metastable precursors) by a solid solution mechanism. Taken together, these data imply that the intermediate of unknown crystal structure formed at  $350^\circ\text{C}$ , undergoes decomposition in the range  $350\text{-}450^\circ\text{C}$ , to yield a  $\gamma\text{-Al}_2\text{O}_3$  structure, thought to be  $\text{MgAl}_2\text{O}_4$  formed through a molten salt route, which could incorporate Li. Therefore, formation of a solid solution of the type  $\text{Al}_{2-x-y}\text{Mg}_x\text{Li}_y\text{O}_{3-x/2-y}$ , cannot be excluded in these reactions and there is no precedent for formation of such a phase in the available literature. Irrespective, the TGA and NMR data point to the presence of a co-existing non-crystalline nitrate hydrate phase incorporating Li.

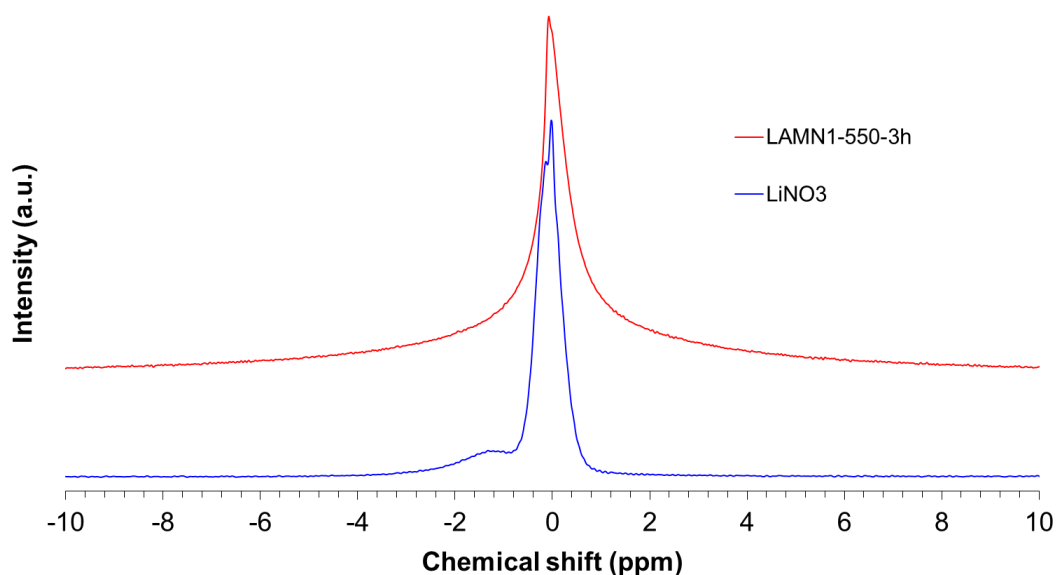


Figure 5.14 –  $^7\text{Li}$  MAS NMR spectra of  $\text{LiNO}_3$  and LAMN1-550-3h

From these experiments it is possible to infer and conclude the following:

- Below 350 °C:  $\text{LiNO}_3$ ,  $\text{Mg}(\text{NO}_3)_2 \cdot 6\text{H}_2\text{O}$ , and  $\text{Al}(\text{NO}_3)_3 \cdot 9\text{H}_2\text{O}$  react to form a complex nitrate hydrate incorporating Li, Mg and Al; this phase or phases are of unknown crystal structure.
- Between 350-450 °C: the complex nitrate hydrate decomposes to form  $\text{MgAl}_2\text{O}_4$  through a molten salt template-growth synthesis, with the structure of  $\gamma\text{-Al}_2\text{O}_3$  being retained, alongside a co-existing non-crystalline nitrate hydrate phase, incorporating Li and Mg.  $^7\text{Li}$  NMR data could show that some Li is incorporated in the crystalline  $\text{MgAl}_2\text{O}_4$  structure, though the broad resonance suggests Li is present in a non-crystalline form, consistent with the XRD data.
- Between 450-550 °C: the non-crystalline nitrate hydrate, incorporating Li and Mg remains thermally stable up to 560 °C, above which denitration occurs.

#### 5.3.1.1.5 MIN1 and MIN2

The XRD patterns for samples MIN1-350-3h and MIN2-350-3h (Figure 5.15) showed strong matching reflections. These were attributed to  $\text{Mg}(\text{NO}_3)_2 \cdot 6\text{H}_2\text{O}$  [14-101] and  $\text{Fe}_2\text{O}_3$  [02-915]. The decomposition of  $\text{Fe}(\text{NO}_3)_3 \cdot 9\text{H}_2\text{O}$  to  $\text{Fe}_2\text{O}_3$  below 350 °C is consistent with thermal analysis of the reagents (Appendix) and in agreement with available literature (Melnikov et al., 2014). Furthermore, TGA analysis (Figure 5.16) showed the total weight loss of the products of MIN1-350-3h to be 61 wt% at 1000 °C, compared to the expected total weight loss of 84 wt% arising from complete denitration and dehydration of the metal nitrate hydrates to form the corresponding oxides. Complete denitration and dehydration of  $\text{Fe}(\text{NO}_3)_3 \cdot 9\text{H}_2\text{O}$  to  $\text{Fe}_2\text{O}_3$  below 350 °C would result in a product yielding an expected weight loss of 58 wt% at 1000 °C, which is in close agreement with the 61 wt% weight loss observed. Overall, the identification of  $\text{Mg}(\text{NO}_3)_2 \cdot 6\text{H}_2\text{O}$  and  $\text{Fe}_2\text{O}_3$  after calcination at 350 °C is consistent with thermal analysis of the reagents, which showed  $\text{Fe}(\text{NO}_3)_3 \cdot 9\text{H}_2\text{O}$  undergoes almost complete thermal decomposition at 350 °C and  $\text{Mg}(\text{NO}_3)_2 \cdot 6\text{H}_2\text{O}$  undergoes (reversible) dehydration between 270-400 °C and denitration above 400 °C (Appendix, in agreement with Melnikov et al., 2014; Paulik et al., 1988).

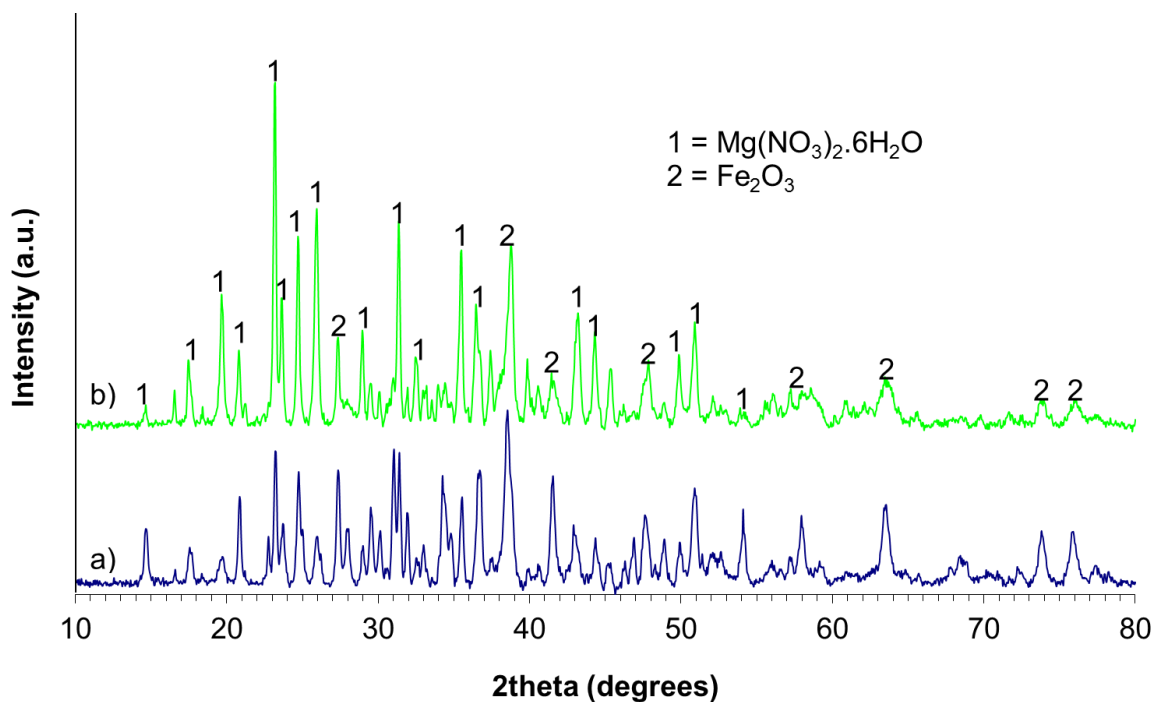


**Figure 5.15 – XRD analysis of samples a) MIN1-350-3h and b) MIN2-350-3h using Co  $K\alpha_1$  radiation ( $\lambda = 1.789 \text{ \AA}$ )**

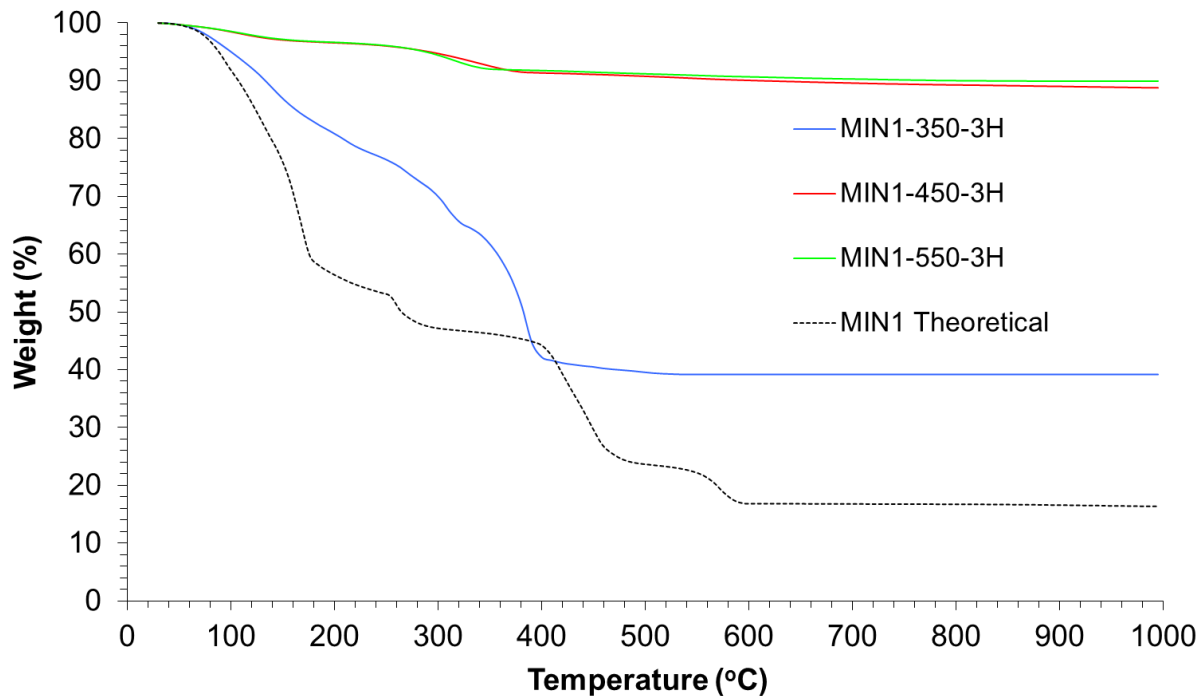


**Figure 5.16 – TGA analysis of samples MIN1-350-3h, MIN1-450-3h and MIN1-550-3h**

The diffraction patterns of samples MIN1-450-3h, MIN1-550-3h, MIN2-450-3h and MIN2-550-3h (Figure 5.17) showed an identical set of reflections, attributed to MgO [45-946] and Fe<sub>2</sub>O<sub>3</sub> [02-915]. In the samples calcined at 450 °C for 3 h, there were some broad, weak reflections which did not appear when the samples were calcined at 550 °C. This indicated that there may have been some poorly crystalline residual nitrates present at 450 °C, which decomposed fully between 450 °C and 550 °C. No reflections corresponding to Mg(NO<sub>3</sub>)<sub>2</sub>·6H<sub>2</sub>O or Fe(NO<sub>3</sub>)<sub>3</sub>·9H<sub>2</sub>O were apparent in the diffraction patterns. TGA analysis (Figure 5.16) showed the total weight losses of samples MIN1-450-3h and MIN1-550-3h were 11 wt% and 10 wt% respectively at 1000 °C, indicating that a similar and substantive fraction of the nitrate and hydrate inventory was retained after reaction at 450-550 °C. The weight loss profiles showed two weight loss events: a broad weight loss below 200 °C, attributed to dehydration; and a second between 300-400 °C consistent with denitration of Fe(NO<sub>3</sub>)<sub>3</sub>·9H<sub>2</sub>O, by reference to thermal data for this compound (Appendix; Melnikov et al., 2014). These data imply that in the temperature range 350-550 °C, no reaction occurred between Fe(NO<sub>3</sub>)<sub>3</sub>·9H<sub>2</sub>O and Mg(NO<sub>3</sub>)<sub>2</sub>·6H<sub>2</sub>O, though the latter undergoes dehydration and dehydration to form MgO, consistent with the thermal behaviour of this reagent (Appendix; Paulik et al., 1988).

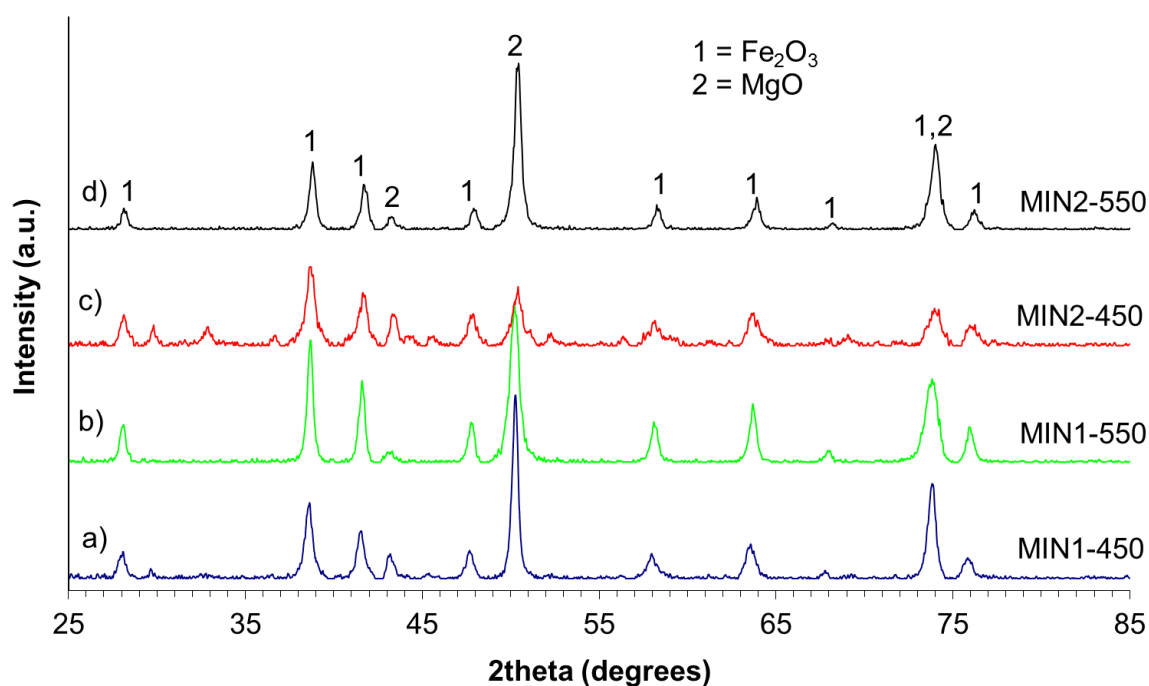


**Figure 5.17 – XRD analysis of a) MIN1-450-3h, b) MIN1-550-3h, c) MIN2-450-3h and d) MIN2-550-3h using Co K $\alpha$ 1 radiation ( $\lambda = 1.789 \text{ \AA}$ )**

From these experiments, it is possible to infer and conclude:

- Below 350 °C:  $\text{Mg}(\text{NO}_3)_2 \cdot 6\text{H}_2\text{O}$  and  $\text{Fe}(\text{NO}_3)_3 \cdot 9\text{H}_2\text{O}$  do not undergo any significant reaction, but the latter undergoes denitration and dehydration to form  $\text{Fe}_2\text{O}_3$ .
- Between 350-550 °C:  $\text{Mg}(\text{NO}_3)_2 \cdot 6\text{H}_2\text{O}$  undergoes denitration and dehydration to yield  $\text{MgO}$  while  $\text{Fe}_2\text{O}_3$  was retained in the reaction product. A portion of the hydrate and nitrate inventory remained.
- The addition of extra nitrate, in the form  $\text{HNO}_3$ , has no significant effect on the reaction.

#### 5.3.1.1.6 AIN1 and AIN2

The XRD pattern for sample AIN1-350-3h (Figure 5.18) showed reflections attributed to  $\text{Fe}_2\text{O}_3$  [02-915] and  $\text{Al}(\text{NO}_3)_3 \cdot 9\text{H}_2\text{O}$  [12-472]. This was unusual, as thermal analysis showed  $\text{Al}(\text{NO}_3)_3 \cdot 9\text{H}_2\text{O}$  is expected to decompose to form an amorphous product after calcination at 350 °C (Appendix; Pacewska and Keshr, 2002). TGA analysis (Figure 5.19) showed the total weight loss of the products to be 30 wt% at 1000 °C compared to the 83 wt% weight loss which would arise from complete dehydration and denitration of the metal hydrate nitrates to form the corresponding oxides. Complete denitration and dehydration of  $\text{Fe}(\text{NO}_3)_3 \cdot 9\text{H}_2\text{O}$  below 350 °C would result in a product yielding an expected weight loss of 60 wt% at 1000 °C. This implies partial decomposition of  $\text{Al}(\text{NO}_3)_3 \cdot 9\text{H}_2\text{O}$  (by loss of up to 50 % of the nitrate and hydrate inventory), had occurred to form an amorphous nitrate bearing product which is likely also hydrated, reported previously by Pacewska and Keshr (2002), with a portion of the starting material remaining in the sample. The weight loss profile showed three distinct weight loss events; a broad weight loss below 200 °C, attributed to dehydration; a sharp weight loss at 300 °C; and a broad weight loss between 350-500 °C consistent with the thermal behaviours of both  $\text{Al}(\text{NO}_3)_3 \cdot 9\text{H}_2\text{O}$  and  $\text{Fe}(\text{NO}_3)_3 \cdot 9\text{H}_2\text{O}$  (Appendix, in agreement with Pacewska and Keshr, 2002 and Melnikov et al., 2014). Overall, these data imply that both  $\text{Al}(\text{NO}_3)_3 \cdot 9\text{H}_2\text{O}$  and  $\text{Fe}(\text{NO}_3)_3 \cdot 9\text{H}_2\text{O}$  undergo (partial) dehydration and denitration to form a non-crystalline product (with a portion of the starting material remaining) and  $\text{Fe}_2\text{O}_3$  respectively.

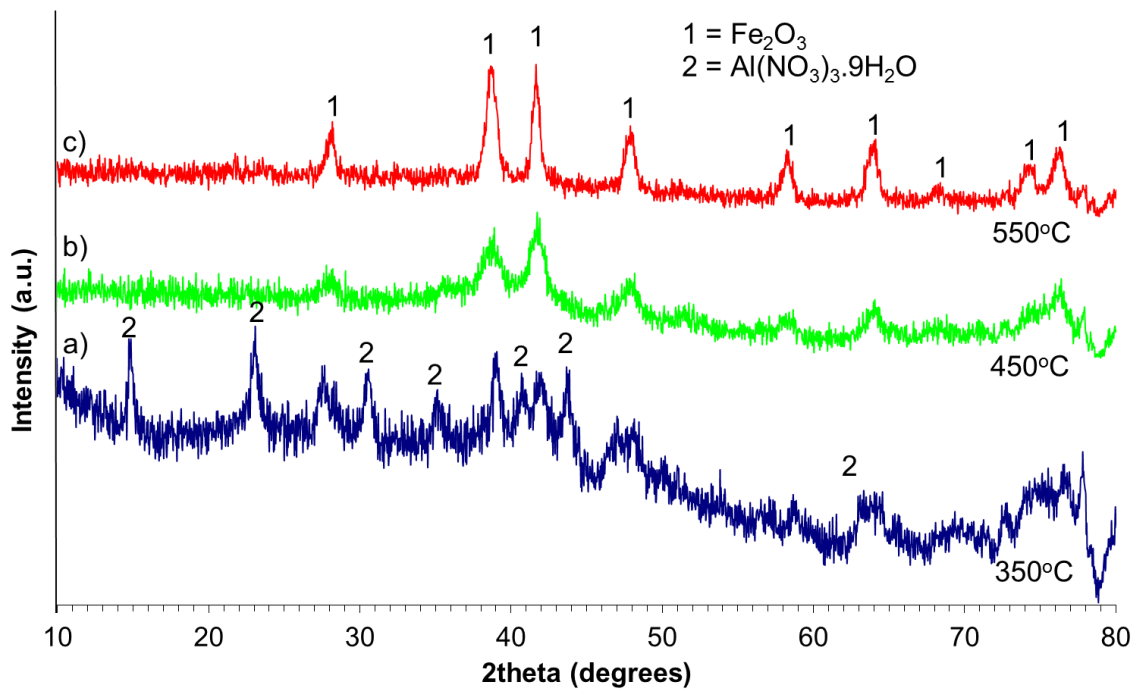


Figure 5.18 – XRD analysis of samples a) AIN1-350-3h, b) AIN1-450-3h and c) AIN1-550-3h using Co  $K\alpha_1$  radiation ( $\lambda = 1.789 \text{ \AA}$ )

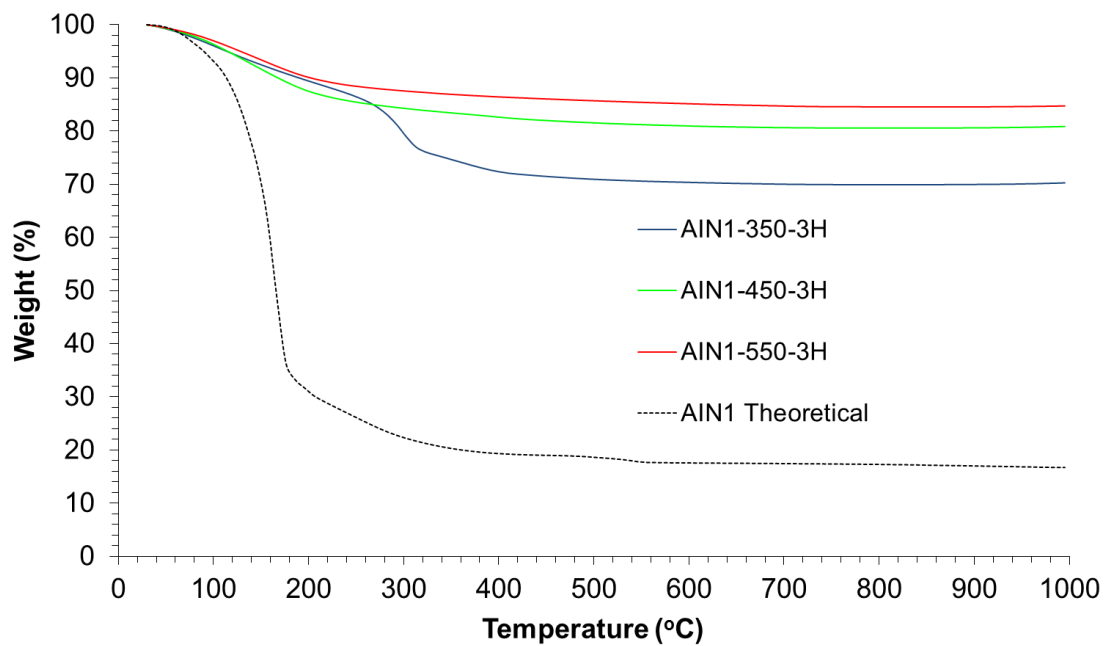


Figure 5.19 – TGA analysis of samples a) AIN1-350-3h, b) AIN1-450-3h and c) AIN1-550-3h



A matching set of reflections were shown in the XRD patterns of samples AIN1-450-3h and AIN1-550-3h (Figure 5.18), attributed to the formation of  $\text{Fe}_2\text{O}_3$  [02-915]. No reflections attributable to  $\text{Al}(\text{NO}_3)_3 \cdot 9\text{H}_2\text{O}$  were present. TGA analysis (Figure 5.19) showed total weight losses of the products of samples AMN1-450-3h and AMN1-550-3h to be 19 wt% and 15 wt% respectively at 1000 °C. The weight loss curves showed a broad weight loss below 200 °C, attributable to dehydration, with only a further 4-5 % weight loss occurring between 200-500 °C. This is congruent with the thermal behaviours of  $\text{Al}(\text{NO}_3)_3 \cdot 9\text{H}_2\text{O}$  and  $\text{Fe}(\text{NO}_3)_3 \cdot 9\text{H}_2\text{O}$  after calcination above 450 °C (Appendix, in agreement with Pacewska and Keshr, 2002 and Melnikov et al., 2014). The evidence implied that no reaction had occurred between  $\text{Al}(\text{NO}_3)_3 \cdot 9\text{H}_2\text{O}$  and  $\text{Fe}(\text{NO}_3)_3 \cdot 9\text{H}_2\text{O}$ , or their decomposition products; although available literature (Tsuchida and Sugimoto, 1990) suggests the formation of a non-crystalline  $\text{Fe}_2\text{O}_3$ - $\text{Al}_2\text{O}_3$  solid solution at these calcination temperatures cannot be discounted.

On addition of extra nitrate, in the form  $\text{HNO}_3$  (samples AMN2-350-3h, AMN2-450-3h and AMN2-550-3h), XRD analysis (Figure 5.20) showed a matching, poorly crystalline pattern for all products. The weak reflections were attributed to formation of  $\gamma$ - $\text{Al}_2\text{O}_3$  [56-457]. There was a notable absence of reflections attributable to  $\text{Al}(\text{NO}_3)_3 \cdot 9\text{H}_2\text{O}$  and  $\text{Fe}_2\text{O}_3$ . TGA analysis (Figure 5.21) showed the products calcined at 350, 450 and 550 °C all showed weight losses of between 20-22 wt% at 1000 °C. The weight loss curves all showed a broad weight loss below 200 °C, attributable to dehydration, with only a further 4-5 % weight loss occurring between 200-500 °C. This is consistent with the thermal behaviours of  $\text{Al}(\text{NO}_3)_3 \cdot 9\text{H}_2\text{O}$  and  $\text{Fe}(\text{NO}_3)_3 \cdot 9\text{H}_2\text{O}$  at these temperatures (Appendix, in agreement with Pacewska and Keshr, 2002 and Melnikov et al., 2014). Available literature (Li et al., 2007) showed that when calcined between 300-550 °C, the decomposition products of  $\text{Al}(\text{NO}_3)_3 \cdot 9\text{H}_2\text{O}$  and  $\text{Fe}(\text{NO}_3)_3 \cdot 9\text{H}_2\text{O}$ , in the molar ratio used in these experiments, formed an amorphous product. It was also reported that a mixture of Fe and Al, preheated at 400 °C, formed a poorly crystalline product, with the broad peaks in the samples attributed to  $\gamma$ - $\text{Al}_2\text{O}_3$  (Shaheen and Hong, 2002), which is consistent with XRD and TGA findings. Thermal transformation of  $\text{Al}(\text{NO}_3)_3 \cdot 9\text{H}_2\text{O}$  under acidic conditions is known to form  $\text{AlOOH}$ , which decomposes to form  $\gamma$ - $\text{Al}_2\text{O}_3$  at 400-500 °C (Pacewska and Keshr, 2004). However, Balek et al. (2003) reported that addition of  $\text{Fe}_2\text{O}_3$  to  $\gamma$ - $\text{Al}_2\text{O}_3$  led to formation of  $\alpha$ - $\text{Al}_2\text{O}_3$  at 100 °C. The retention of  $\gamma$ - $\text{Al}_2\text{O}_3$  in products AIN2-350-3h, AIN2-450-3h and AIN2-550-3h imply that the addition of extra  $\text{HNO}_3$  stabilises its formation, increasing the dispersion of the  $\text{Fe}_2\text{O}_3$  constituents, therefore reducing the grain growth of the  $\alpha$ - $\text{Fe}_2\text{O}_3$  (Shaheen and Hong, 2002) so it is not seen in these products. These findings suggest that the addition of extra nitrate, in the form  $\text{HNO}_3$ , stabilises the  $\gamma$ - $\text{Al}_2\text{O}_3$  phase and therefore hinders the formation of  $\text{Fe}_2\text{O}_3$  between 350-550 °C, accounting for the differences in products containing different levels of nitrate.

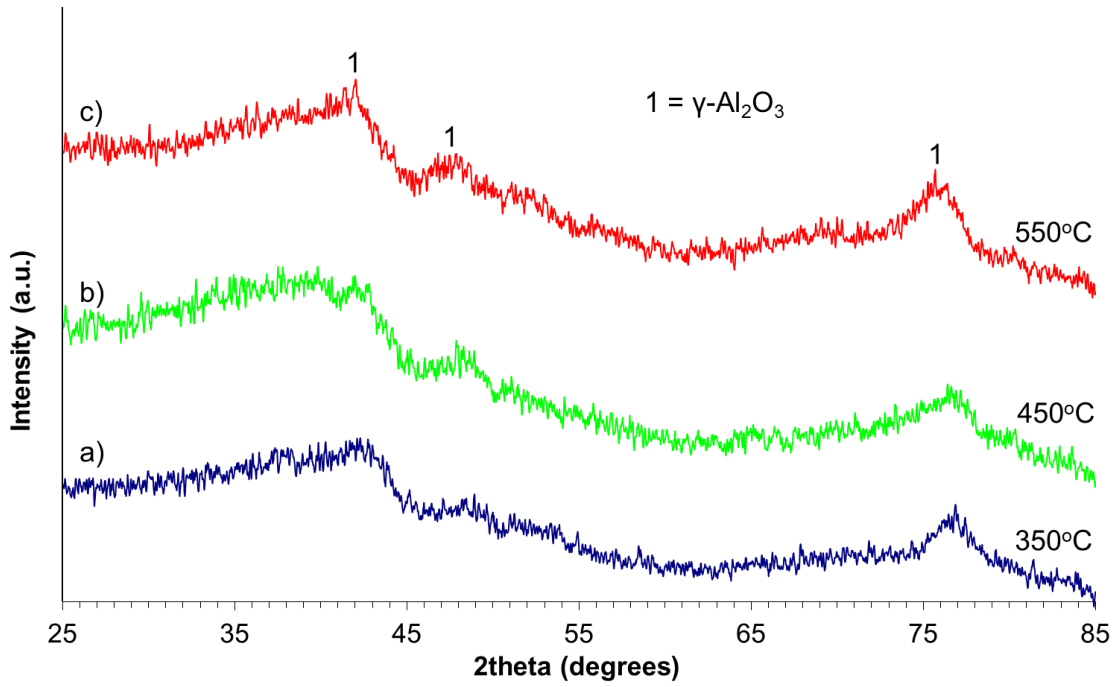


Figure 5.20 – XRD analysis of samples a) AIN2-350-3h, b) AIN2-450-3h and c) AIN2-550-3h using Co K $\alpha$ 1 radiation ( $\lambda = 1.789 \text{ \AA}$ )

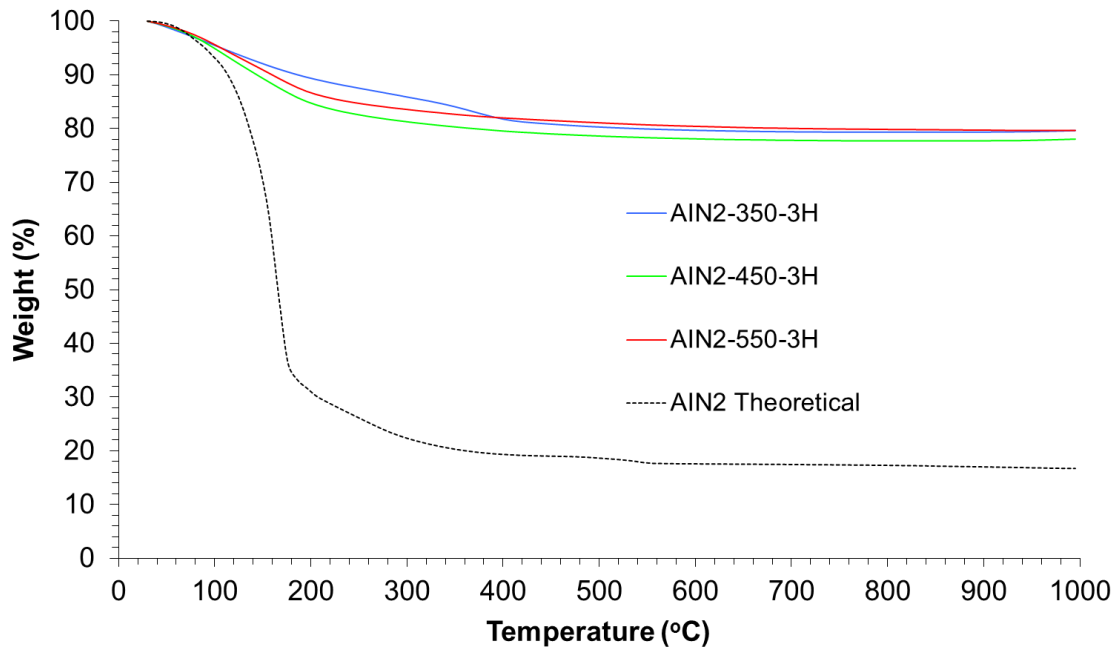


Figure 5.21 - TGA analysis of samples a) AIN2-350-3h, b) AIN2-450-3h and c) AIN2-550-3h

From these experiments, it is possible to infer and conclude:

- Below 350 °C: No reaction is evident between  $\text{Al}(\text{NO}_3)_3 \cdot 9\text{H}_2\text{O}$  and  $\text{Fe}(\text{NO}_3)_3 \cdot 9\text{H}_2\text{O}$ , or their decomposition products; although they do undergo (partial) decomposition to form a non-crystalline phase and poorly crystalline  $\text{Fe}_2\text{O}_3$ . A portion of the  $\text{Al}(\text{NO}_3)_3 \cdot 9\text{H}_2\text{O}$  starting material remained in the product.
- Between 350-550 °C: The remaining  $\text{Al}(\text{NO}_3)_3 \cdot 9\text{H}_2\text{O}$  undergoes dehydration and denitration to form a non-crystalline product with  $\text{Fe}_2\text{O}_3$  remaining in the product. No evidence of a reaction is apparent, although the formation of a non-crystalline  $\text{Fe}_2\text{O}_3$ - $\text{Al}_2\text{O}_3$  solid solution cannot be discounted.
- The addition of excess nitric acid appeared to stabilise a poorly crystalline  $\gamma$ - $\text{Al}_2\text{O}_3$  phase, therefore hindering the formation of  $\text{Fe}_2\text{O}_3$  between 350-550 °C.

#### 5.3.1.1.7 LAIN1

The XRD pattern for sample LAIN1-350-3h (Figure 5.22) showed a strong set of reflections attributed to  $\text{LiNO}_3$  [8-466] with poorly crystalline peaks matched to  $\gamma$ - $\text{Al}_2\text{O}_3$  [56-457]. There were no peaks present matching  $\text{Al}(\text{NO}_3)_3 \cdot 9\text{H}_2\text{O}$ ,  $\text{Fe}(\text{NO}_3)_3 \cdot 9\text{H}_2\text{O}$  or  $\text{Fe}_2\text{O}_3$ . Significant diffuse scattering was also apparent, suggesting the presence of non-crystalline component(s). TGA analysis showed a total weight loss for sample LAIN1-350-3h to be 70 wt% at 1000 °C. Weight loss due to the complete dehydration and denitration of the reagents would result in a weight loss of 83 wt% at 1000 °C, of which 52 wt% would be due to decomposition of  $\text{Al}(\text{NO}_3)_3 \cdot 9\text{H}_2\text{O}$ , 21 wt% due to  $\text{Fe}(\text{NO}_3)_3 \cdot 9\text{H}_2\text{O}$  and 10 wt%  $\text{LiNO}_3$ . This suggested a significant proportion of the hydrate and nitrate inventory was still present. The weight loss profile showed three distinct events: a broad weight loss below 200 °C, attributed to dehydration; and two sharp weight loss events at 400 °C and 560 °C, neither of which are consistent with the thermal behaviour of  $\text{Al}(\text{NO}_3)_3 \cdot 9\text{H}_2\text{O}$ ,  $\text{Fe}(\text{NO}_3)_3 \cdot 9\text{H}_2\text{O}$  or  $\text{LiNO}_3$  (Appendix; Pacewska and Keshr, 2002; Melnikov et al., 2014; Chun, 1977). The event at 560 °C is typical of denitration, however, the event occurred at lower temperature than denitration of  $\text{LiNO}_3$ , suggesting the denitration of a distinct intermediate phase. The absence of Al and Fe containing crystalline phases can be attributed to the formation of a poorly crystalline  $\gamma$ - $\text{Al}_2\text{O}_3$  phase which impedes the grain growth of  $\text{Fe}_2\text{O}_3$  (discussed further in section 5.3.1.1.6). These data imply that no reaction had taken place involving  $\text{LiNO}_3$  due to identification in the XRD analysis (Figure 5.22).  $\text{Al}(\text{NO}_3)_3 \cdot 9\text{H}_2\text{O}$  and  $\text{Fe}(\text{NO}_3)_3 \cdot 9\text{H}_2\text{O}$  undergo partial dehydration and denitration to form amorphous products. The formation of a solid solution of  $\text{Al}(\text{NO}_3)_3 \cdot 9\text{H}_2\text{O}$  and  $\text{Fe}(\text{NO}_3)_3 \cdot 9\text{H}_2\text{O}$  (or their decomposition products) cannot be ruled out.

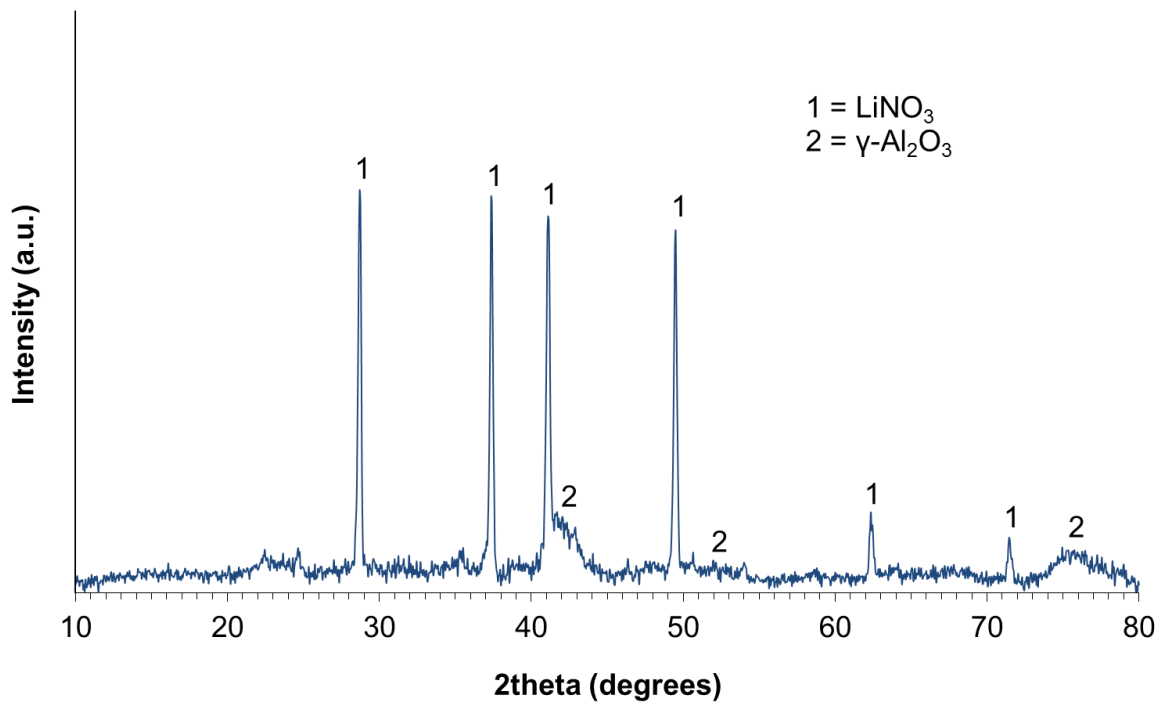


Figure 5.22 – XRD analysis of sample LAIN1-350-3h using Co  $K\alpha_1$  radiation ( $\lambda = 1.789 \text{ \AA}$ )

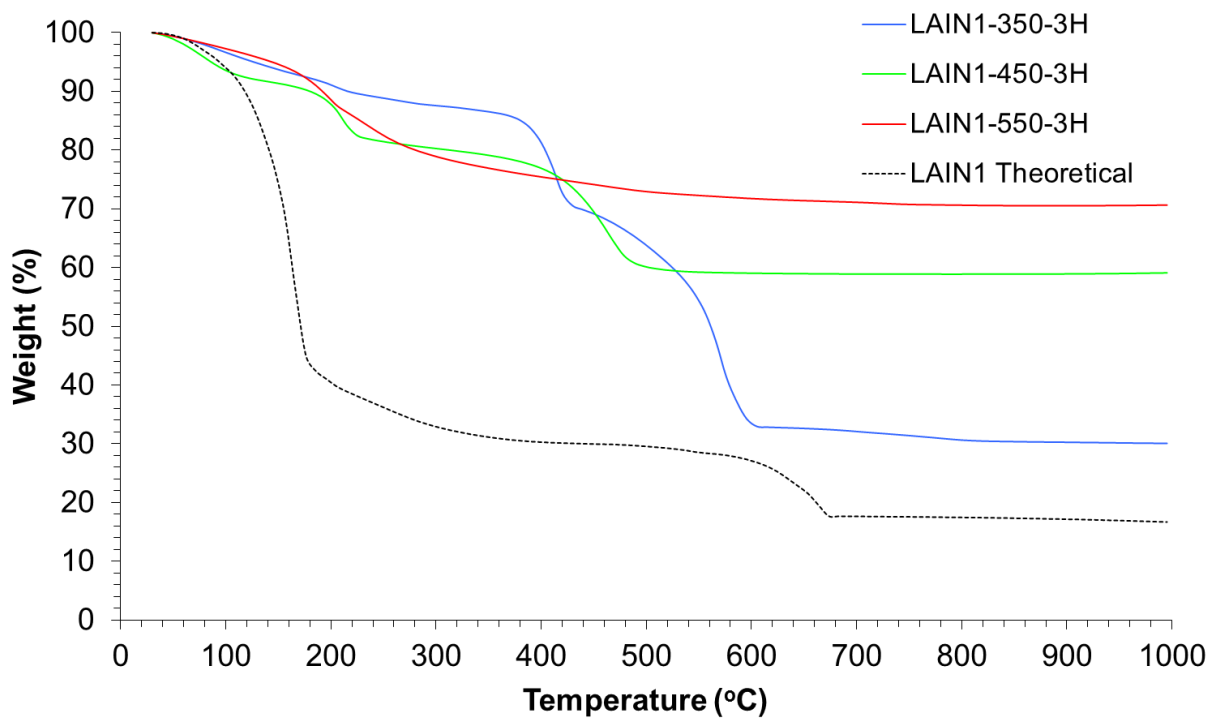
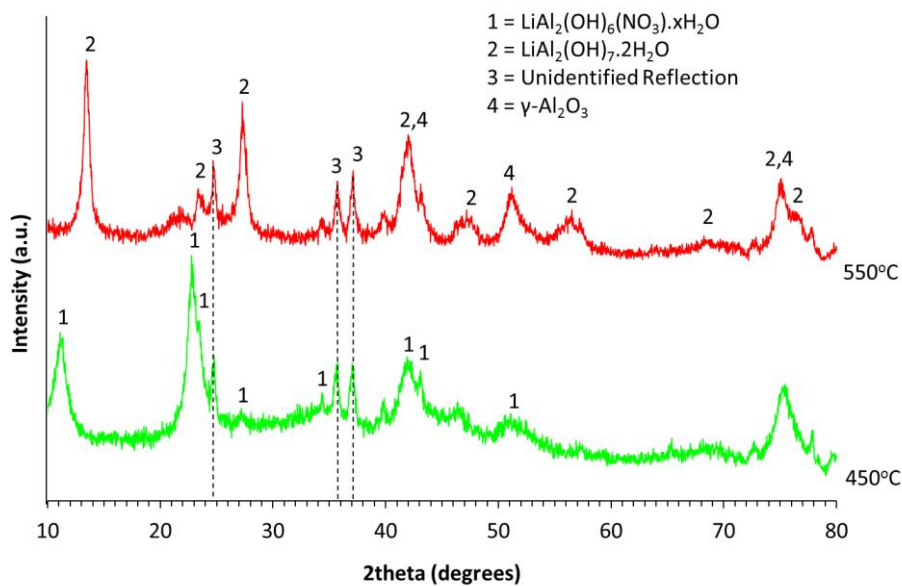


Figure 5.23 – TGA analysis of samples LAIN1-350-3h, LAIN1-450-3h and LAIN1-550-3h

The XRD pattern of sample LAIN1-450-3h (Figure 5.24) showed reflections attributable to poorly crystalline  $\text{LiAl}_2(\text{OH})_6(\text{NO}_3)\cdot x\text{H}_2\text{O}$  [51-359] and  $\gamma\text{-Al}_2\text{O}_3$  [56-457], with the same set of unidentified crystalline reflections observed as in sample LAN1-450 and LAN1-550. Strong diffuse scattering was also apparent, suggesting the presence of amorphous component(s). No reflections corresponding to  $\text{LiNO}_3$ ,  $\text{Al}(\text{NO}_3)_3\cdot 9\text{H}_2\text{O}$ ,  $\text{Fe}(\text{NO}_3)_3\cdot 9\text{H}_2\text{O}$  or  $\text{Fe}_2\text{O}_3$  were apparent in the diffraction patterns. TGA analysis of LAIN1-450-3h (Figure 5.23) showed a total weight loss of 41 wt% at 1000 °C, indicating that a portion of the hydrate and nitrate inventory was retained. The weight loss curve shows two distinct weight loss events at 200 °C and 460 °C. The former could be attributed to dehydration and the latter denitration. However, this does not fit with thermal behaviours of  $\text{LiNO}_3$ ,  $\text{Al}(\text{NO}_3)_3\cdot 9\text{H}_2\text{O}$  or  $\text{Fe}(\text{NO}_3)_3\cdot 9\text{H}_2\text{O}$  (Appendix; Pacewska and Keshr, 2002; Melnikov et al., 2014; Chun, 1977), implying denitration of  $\text{LiAl}_2(\text{OH})_6(\text{NO}_3)\cdot x\text{H}_2\text{O}$  as identified by XRD (Figure 5.24). This Li-Al-LDH phase was also present in the reaction product LAN1-450-3h (discussed further in section 5.3.1.1.3). Previous work by Kustrowski et al. (2005) showed that the  $\text{Fe}^{3+}$  cation can replace Al in the Li-Al-LDH structure. However, the formation of  $\text{LiFe}_2(\text{OH})_6(\text{NO}_3)\cdot x\text{H}_2\text{O}$  is known not to occur (Kustrowski et al., 2005). Any remaining Fe in the product, therefore, must be present in a non-crystalline form, or in solid solution with  $\gamma\text{-Al}_2\text{O}_3$ , in agreement with sample AIN2 (section 5.3.1.1.6). Overall, these data imply that  $\text{LiNO}_3$  reacts with  $\text{Al}(\text{NO}_3)_3\cdot 9\text{H}_2\text{O}$  to form a LDH of the type  $\text{LiAl}_2(\text{OH})_6(\text{NO}_3)\cdot x\text{H}_2\text{O}$  plus an unidentified crystalline phase.  $\text{Fe}(\text{NO}_3)_3\cdot 9\text{H}_2\text{O}$  does not appear to react with either  $\text{LiNO}_3$  or  $\text{Al}(\text{NO}_3)_3\cdot 9\text{H}_2\text{O}$ , shown by the similarity in products formed without the presence of Fe (product LAN1), though available literature shows substitution of Fe into the Li-Al-LDH structure is a possibility (Kustrowski et al., 2005) and formation of a poorly crystalline solid solution between the decomposition products of  $\text{Al}(\text{NO}_3)_3\cdot 9\text{H}_2\text{O}$  and  $\text{Fe}(\text{NO}_3)_3\cdot 9\text{H}_2\text{O}$  (Nayak et al., 1997) cannot be ruled out. These findings are consistent with the previous reaction (LAN1) between Li and Al nitrates forming  $\text{LiAl}_2(\text{OH})_6(\text{NO}_3)\cdot x\text{H}_2\text{O}$  and an unidentified crystalline phase, thought to be Li rich; see section 5.3.1.1.3. It also supported the conclusions for section 5.3.1.1.6 (products AIN1 and AIN2) which suggested  $\text{Al}(\text{NO}_3)_3\cdot 9\text{H}_2\text{O}$  and  $\text{Fe}(\text{NO}_3)_3\cdot 9\text{H}_2\text{O}$  do not react together, but can form solid solutions in their oxide forms, in agreement with Nayak et al. (1997) and Tsuchida and Sugimoto (1990).



**Figure 5.24 – XRD analysis of samples a) LAIN1-450-3h and b) LAIN1-550-3h using Co K $\alpha$ 1 radiation ( $\lambda = 1.789 \text{ \AA}$ )**

XRD analysis of product LAIN1-550-3h (Figure 5.24) showed reflections attributed to  $\text{LiAl}_2(\text{OH})_7 \cdot 2\text{H}_2\text{O}$  [40-710] and  $\gamma\text{-Al}_2\text{O}_3$  [56-457], plus the same unidentified crystalline intermediate as formed at 450 °C and in sample LAN1-550 (section 5.3.1.1.3). Diffuse scattering was also observed, indicating the presence of non-crystalline component(s). Reflections corresponding to  $\text{LiNO}_3$ ,  $\text{Al}(\text{NO}_3)_3 \cdot 9\text{H}_2\text{O}$ ,  $\text{Fe}(\text{NO}_3)_3 \cdot 9\text{H}_2\text{O}$  or  $\text{Fe}_2\text{O}_3$  were noticeably absent from the diffraction patterns. TGA analysis of LAIN1-550-3h (Figure 5.23) showed a total weight loss of 29 wt% at 1000 °C, showing partial retention of the volatile inventory. The weight loss curve showed a broad weight loss event below 200 °C, typical of dehydration, with a gradual weight loss occurring above 200 °C showing no distinct events. This is in agreement with the thermal decompositions of  $\text{Al}(\text{NO}_3)_3 \cdot 9\text{H}_2\text{O}$  and  $\text{Fe}(\text{NO}_3)_3 \cdot 9\text{H}_2\text{O}$ , which both show almost complete dehydration and dehydration above 550 °C (Appendix; Pacewska and Keshr, 2002; Melnikov et al., 2014). However, this does not fit with thermal behaviour of  $\text{LiNO}_3$  which shows a sharp denitration event occurs above 600 °C (Appendix; Chun, 1977). The identification of  $\text{LiAl}_2(\text{OH})_7 \cdot 2\text{H}_2\text{O}$  by XRD (Figure 5.24) implies the denitration of  $\text{LiAl}_2(\text{OH})_6(\text{NO}_3) \cdot x\text{H}_2\text{O}$  occurred between 450-550 °C, consistent with the weight loss event observed in TGA analysis of product LAIN1-450-3h. The formation of  $\text{LiAl}_2(\text{OH})_7 \cdot 2\text{H}_2\text{O}$  was not seen in sample LAN1 (section 5.3.1.1.3), suggesting the presence of Fe has an effect on the denitration temperature of the Li-Al-LDH phase. Overall, these data imply that the formation of  $\text{LiAl}_2(\text{OH})_7 \cdot 2\text{H}_2\text{O}$  takes place between 450-550 °C, *via* dehydration and denitration of  $\text{LiAl}_2(\text{OH})_6(\text{NO}_3) \cdot x\text{H}_2\text{O}$ , formed at 450 °C. The unidentified crystalline phase, formed between 350-450 °C, remained stable in the product after calcination at 550 °C. This is in agreement with sections 5.3.1.1.3 and 5.3.1.1.6.

From these experiments, it is possible to infer and conclude:

- Below 350 °C: no reaction had taken place involving  $\text{LiNO}_3$  with either  $\text{Al}(\text{NO}_3)_3 \cdot 9\text{H}_2\text{O}$  or  $\text{Fe}(\text{NO}_3)_3 \cdot 9\text{H}_2\text{O}$ , although Fe and Al nitrates do undergo partial dehydration and denitration to form amorphous products. The formation of a solid solution of  $\text{Al}(\text{NO}_3)_3 \cdot 9\text{H}_2\text{O}$  and  $\text{Fe}(\text{NO}_3)_3 \cdot 9\text{H}_2\text{O}$  (or their decomposition products) cannot be ruled out.
- Between 350-450 °C:  $\text{LiNO}_3$  reacts with  $\text{Al}(\text{NO}_3)_3 \cdot 9\text{H}_2\text{O}$  to form  $\text{LiAl}_2(\text{OH})_6(\text{NO}_3)_x \cdot \text{H}_2\text{O}$  plus an unidentified crystalline phase and co-existing non-crystalline phase. This is consistent with the previous reactions (LAN1) between Li and Al nitrates forming  $\text{LiAl}_2(\text{OH})_6(\text{NO}_3)_x \cdot \text{H}_2\text{O}$ ; see section 5.3.1.1.3. It also supported the conclusions for section 5.3.1.1.6 (products AIN1 and AIN2) which suggested  $\text{Al}(\text{NO}_3)_3 \cdot 9\text{H}_2\text{O}$  and  $\text{Fe}(\text{NO}_3)_3 \cdot 9\text{H}_2\text{O}$  do not react together, but can form solid solutions in their oxide forms.
- Between 450-550 °C: formation of  $\text{LiAl}_2(\text{OH})_7 \cdot 2\text{H}_2\text{O}$  occurs *via* decomposition of  $\text{LiAl}_2(\text{OH})_6(\text{NO}_3)_x \cdot \text{H}_2\text{O}$ . The unidentified crystalline phase remained present in the product along with a co-existing non-crystalline phase.

### 5.3.1.2 Freeze dryer experiments

#### 5.3.1.2.1 AMN1

Freeze drying was used to identify the products present in the short simulant solutions by drying the product without heating it. This provided a solid sample allowing analysis to be carried out to identify the species present. It also yielded a product which could be further calcined at short residence times, without the concerns of flash boiling, as would be experienced in the calcination process on the VTR.

The XRD pattern for sample AMN1-FD (Figure 5.25) showed reflections attributed to  $\text{Mg}(\text{NO}_3)_2 \cdot 6\text{H}_2\text{O}$  [14-101] and  $\text{Al}(\text{NO}_3)_3 \cdot 9\text{H}_2\text{O}$  [12-472]. TGA data from AMN1-FD (Figure 5.28) produced a weight loss curve with a very similar profile to that produced from summation of the weighted summed data of  $\text{Mg}(\text{NO}_3)_2 \cdot 6\text{H}_2\text{O}$  and  $\text{Al}(\text{NO}_3)_3 \cdot 9\text{H}_2\text{O}$ . The weight loss achieved at 1000 °C was 84 wt%, identical to that expected from the weighted contribution of the individual components at this temperature (Figure 5.26). These data show that no observable reaction had taken place between the component nitrates during the freeze drying process.

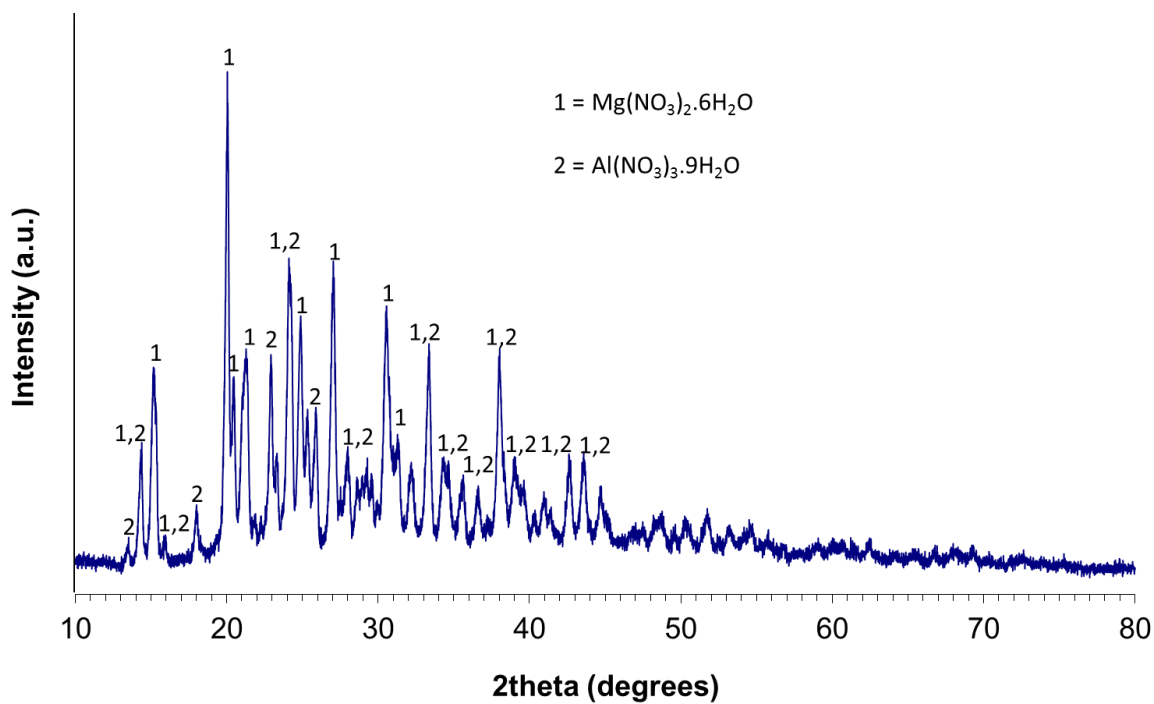


Figure 5.25 – XRD analysis of sample AMN1-FD using Co  $K\alpha_1$  radiation ( $\lambda = 1.789 \text{ \AA}$ )

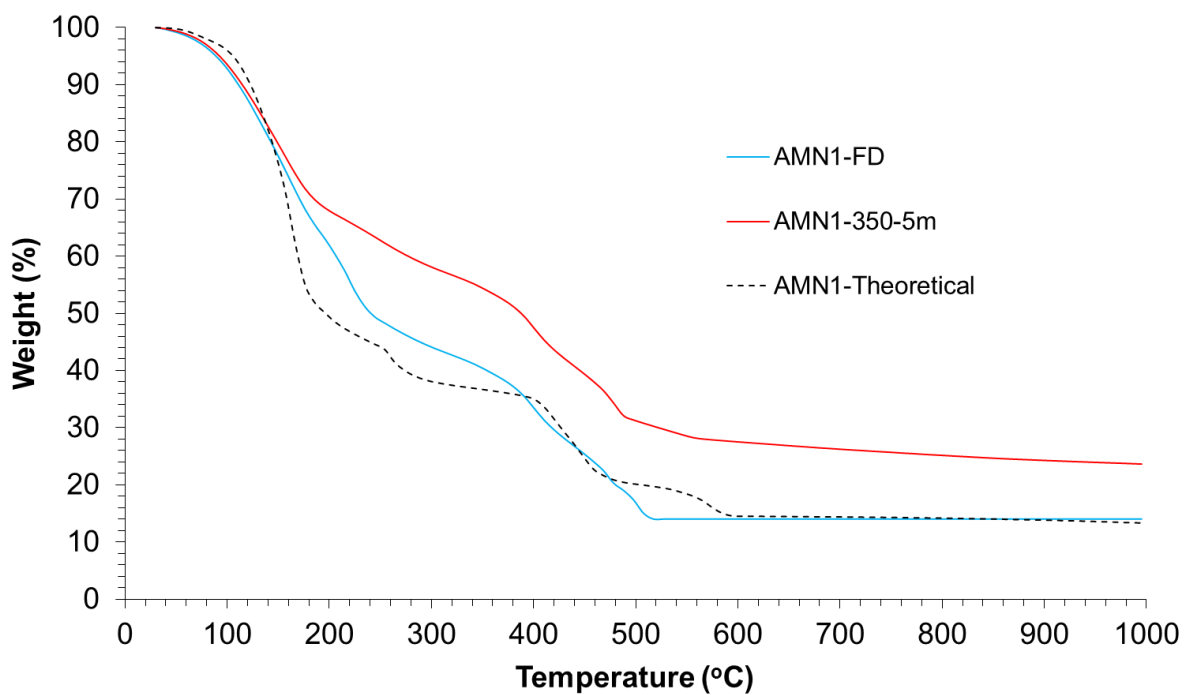
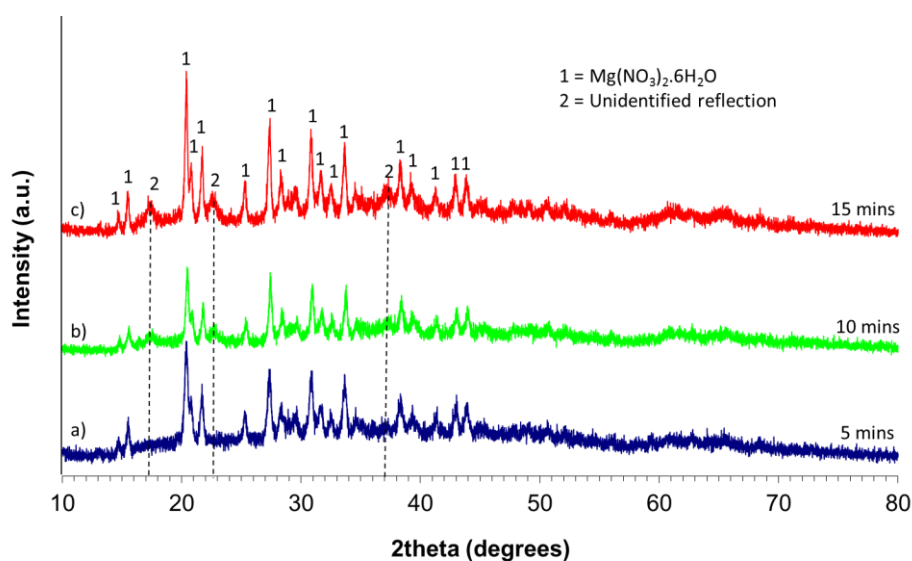


Figure 5.26 – TGA analysis of samples AMN1-FD and AMN1-350-5m,



The XRD patterns of the products from calcination of AMN1-FD at 350 °C and 450 °C, for 5-15 mins, are shown in Figures 5.27 and 5.28, respectively. These data show the presence of  $\text{Mg}(\text{NO}_3)_2 \cdot 6\text{H}_2\text{O}$  in all products, but the absence of  $\text{Al}(\text{NO}_3)_3 \cdot 9\text{H}_2\text{O}$ , no reflections could be conclusively assigned to any reasonable Al bearing phase. All diffraction patterns exhibit significant diffuse scattering, implying the presence of an additional non-crystalline phase. XRD data of the products of calcination at 350 °C and 450 °C, show additional reflections associated with an unidentified phase, which increase in relative intensity with reaction time. Since reflections associated with  $\text{Mg}(\text{NO}_3)_2 \cdot 6\text{H}_2\text{O}$  do not show a reciprocal decrease in relative intensity (except after reaction at 450 °C for 15 min), it is thought probable that the unidentified phase may crystallise from the amorphous component, incorporating Al. The reflections associated with this unidentified phase were not observed in the XRD data of AMN1-350-3h or AMN1-450-3h, which implies that this phase is a metastable intermediate. TGA data of the products of calcination at 350 °C were essentially identical, irrespective of reaction time, therefore only data from product AMN1-350-5m are shown in Figure 5.26. The presence of  $\text{Mg}(\text{NO}_3)_2 \cdot 6\text{H}_2\text{O}$  in all products is in agreement with TGA data from these products, Figures 5.26 and 5.29. These data showed weight loss events in the temperature range 270-400 °C associated with the (reversible) dehydration of this material (Appendix), with denitration occurring above 400 °C, as discussed in Section 5.3.1.1.1 and in agreement with previous work by Paulik et al. (1988). XRD data for the products of calcination at 450 °C, show that the relative intensity of reflections associated with  $\text{Mg}(\text{NO}_3)_2 \cdot 6\text{H}_2\text{O}$  decrease with increasing reaction time, are consistent with denitration of this material above 400 °C. The absence of  $\text{Al}(\text{NO}_3)_3 \cdot 9\text{H}_2\text{O}$  in all products is also in agreement with TGA data of this material, with dehydration and denitration occurring below 400 °C (Appendix), to produce a non-crystalline product (Pacewska and Keshr, 2002).



**Figure 5.27 – XRD analysis of samples a) AMN1-350-5m, b) AMN1-350-10m and c) AMN1-350-15m using Cu  $K\alpha$ 1 radiation ( $\lambda = 1.546 \text{ \AA}$ )**

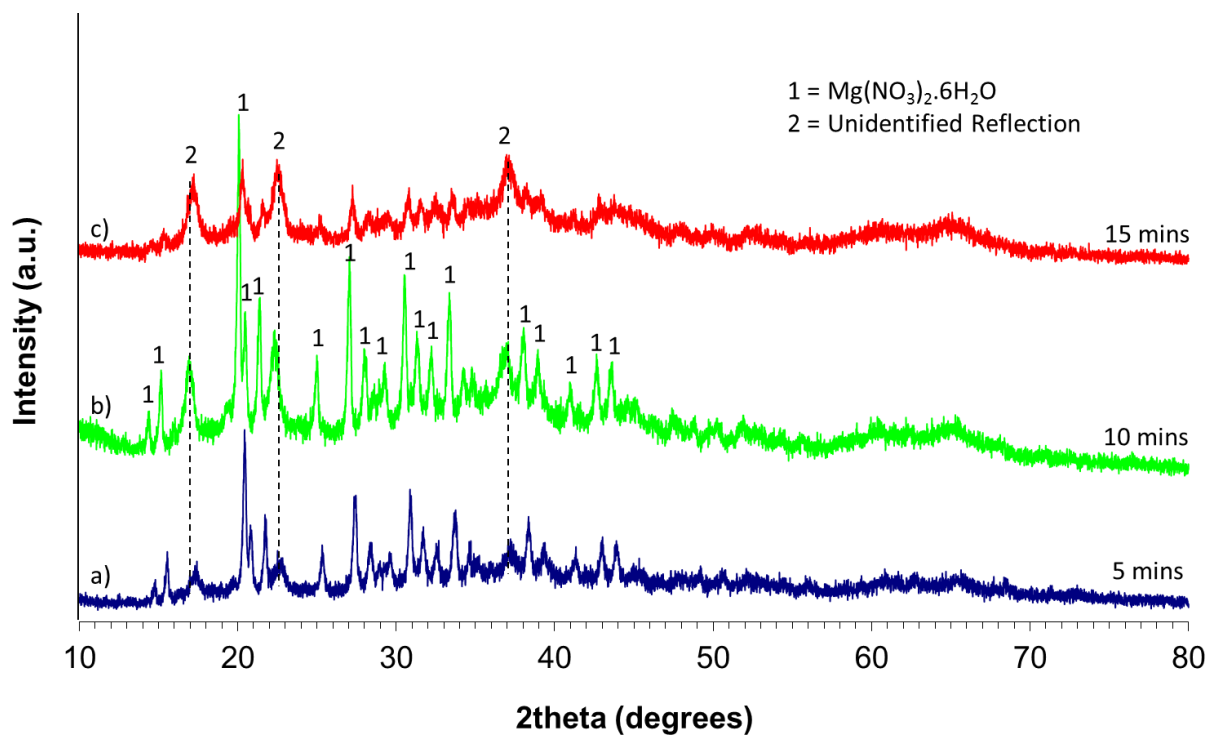


Figure 5.28 – XRD analysis of samples a) AMN1-450-5m, b) AMN1-450-10m and c) AMN1-450-15m using Cu  $K\alpha 1$  radiation ( $\lambda = 1.546 \text{ \AA}$ )

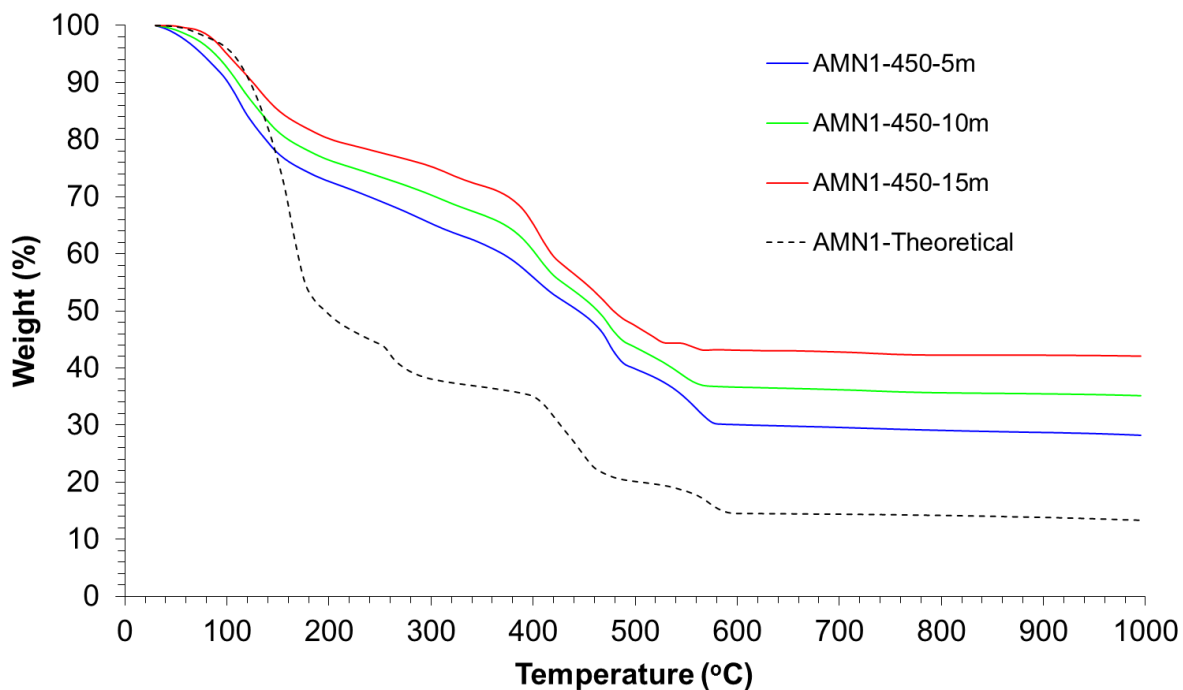
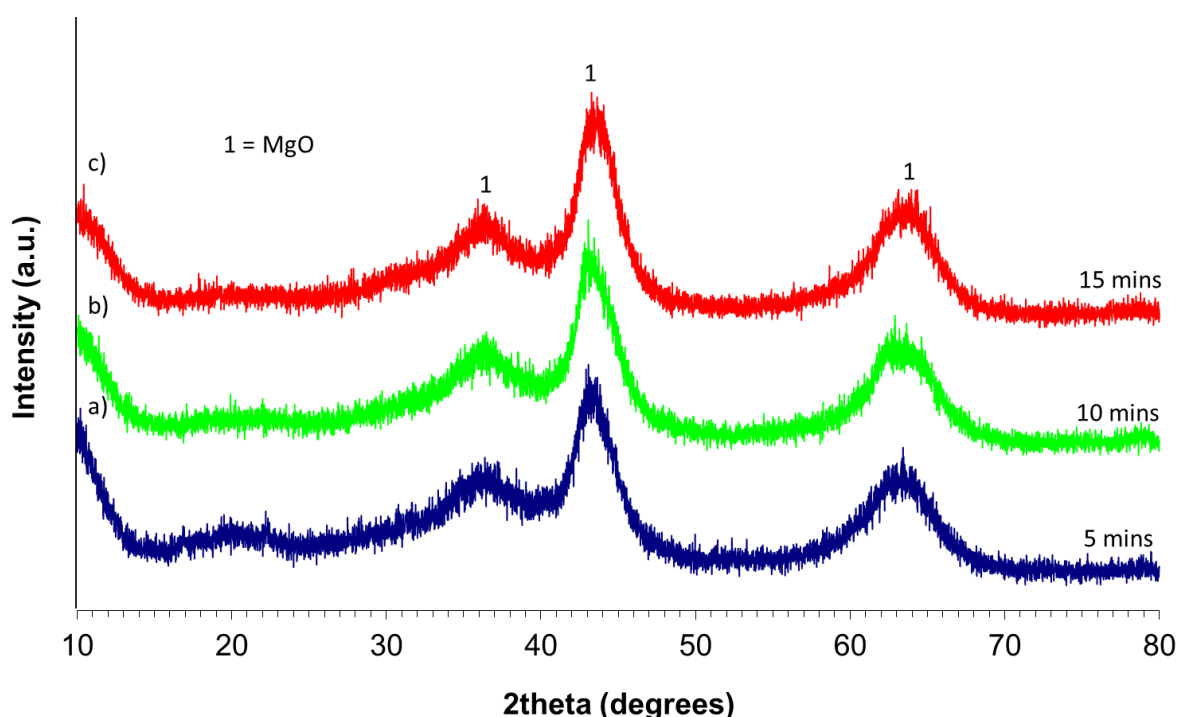
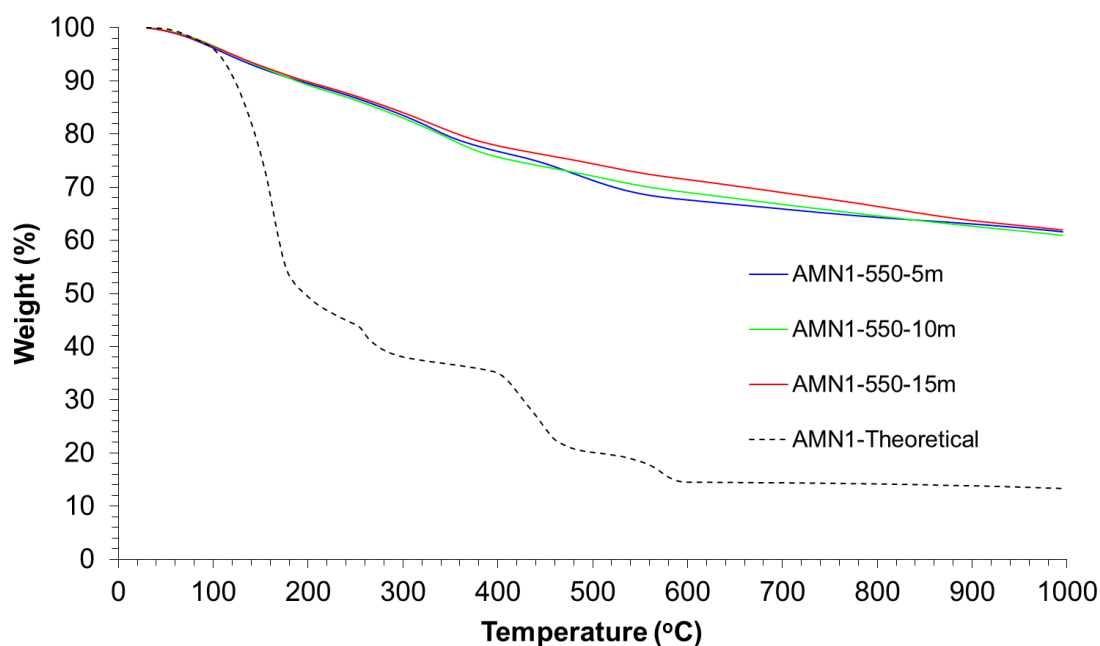


Figure 5.29 – TGA analysis of samples AMN1-450-5m, AMN1-450-10m and AMN1-450-15m

Figure 5.30 shows XRD data of the products of calcination of AMN1-FD at 550 °C, for 5-15 mins; these data clearly show the formation of MgO. All diffraction patterns exhibit significant diffuse scattering, implying the presence of an additional non-crystalline phase. Consistent with these observations, TGA data (Figure 5.31) did not show clearly defined weight loss events in the temperature range 270-500 °C associated with the (reversible) dehydration and denitration of  $\text{Mg}(\text{NO}_3)_2 \cdot 6\text{H}_2\text{O}$ . The absence of  $\text{Al}(\text{NO}_3)_3 \cdot 9\text{H}_2\text{O}$  in all products is in agreement with TGA data of this material, with dehydration and denitration occurring below 400 °C (Appendix); this is consistent with available literature in which decomposition of  $\text{Al}(\text{NO}_3)_3 \cdot 9\text{H}_2\text{O}$  at 350 °C is reported to produce non-crystalline product (Pacowska and Keshr, 2002). The products of calcination of AMN1-FD at 550 °C produced a total weight loss of 38 wt% at 1000 °C, irrespective of reaction time, which implies retention of substantial fraction of the nitrate inventory within the amorphous component. Product AMN1-350-5m produced a total weight loss of 74 wt% at 1000 °C, compared to the total expected weight loss of 85 wt% corresponding to complete denitration and dehydration of the reagents to form the corresponding metal oxides. This implies partial (up to 60 %) decomposition of  $\text{Al}(\text{NO}_3)_3 \cdot 9\text{H}_2\text{O}$  at 350 °C for 15 min, to form an amorphous nitrate bearing product which is likely also hydrated (assuming reversible dehydration of  $\text{Mg}(\text{NO}_3)_2 \cdot 6\text{H}_2\text{O}$ ). The total weight loss of products AMN1-450 increased with increasing reaction time, from 72 wt% for 5 min reaction to 58 wt% for 15 min reaction, due to denitration of  $\text{Mg}(\text{NO}_3)_2 \cdot 6\text{H}_2\text{O}$ .



**Figure 5.30 – XRD analysis of samples a) AMN1-550-5m, b) AMN1-550-10m and c) AMN1-550-15m using Cu K $\alpha$ 1 radiation ( $\lambda = 1.546 \text{ \AA}$ )**



**Figure 5.31 – TGA analysis of samples AMN1-550-5m, AMN1-550-10m and AMN1-550-15m**

Overall, these data are consistent with experiments carried out for 3 h duration over the same temperature range, as discussed in Section 5.3.1.1.1, but provide some additional insight and clarity on the reaction kinetics and mechanism. The key additional findings are that the unidentified intermediate phase formed at 450 °C for 3 h and layered double hydroxide phase ( $\text{Mg}_a\text{Al}(\text{OH})_{3+2-c}(\text{NO}_3)_c \cdot x\text{H}_2\text{O}$ ) formed at 550 °C for 3 h, result from the extended reaction time and are therefore unlikely to occur in the HAL calciner. Experiments conducted using the freeze dried material at 550 °C for up to 15 min show that the kinetic product of calcination is MgO, which must then react with the non-crystalline Al nitrate hydrate phase to yield the double layered hydroxide phase observed in the AMN1-550-3h experiment.

### 5.3.1.2.2 LMN1

Figure 5.32 shows the XRD pattern for sample LMN1-FD, in which all reflections could be attributed to  $\text{LiNO}_3$  or  $\text{Mg}(\text{NO}_3)_2 \cdot 6\text{H}_2\text{O}$  (ICDD cards [8-466] and [14-101], respectively). TGA data from LMN1-FD (Figure 5.33) produced a weight loss curve with a very similar profile to that produced from summation of the weighted summed data of  $\text{LiNO}_3$  and  $\text{Mg}(\text{NO}_3)_2 \cdot 6\text{H}_2\text{O}$ . The weight loss achieved at 1000 °C was 98 wt%, somewhat greater than the 86 wt% expected from the weighted contribution of the individual components at this temperature (Figure 5.33). This discrepancy is likely due to incomplete removal of water during the freeze drying process. These data show that no observable reaction had taken place between the component nitrates during the freeze drying process.

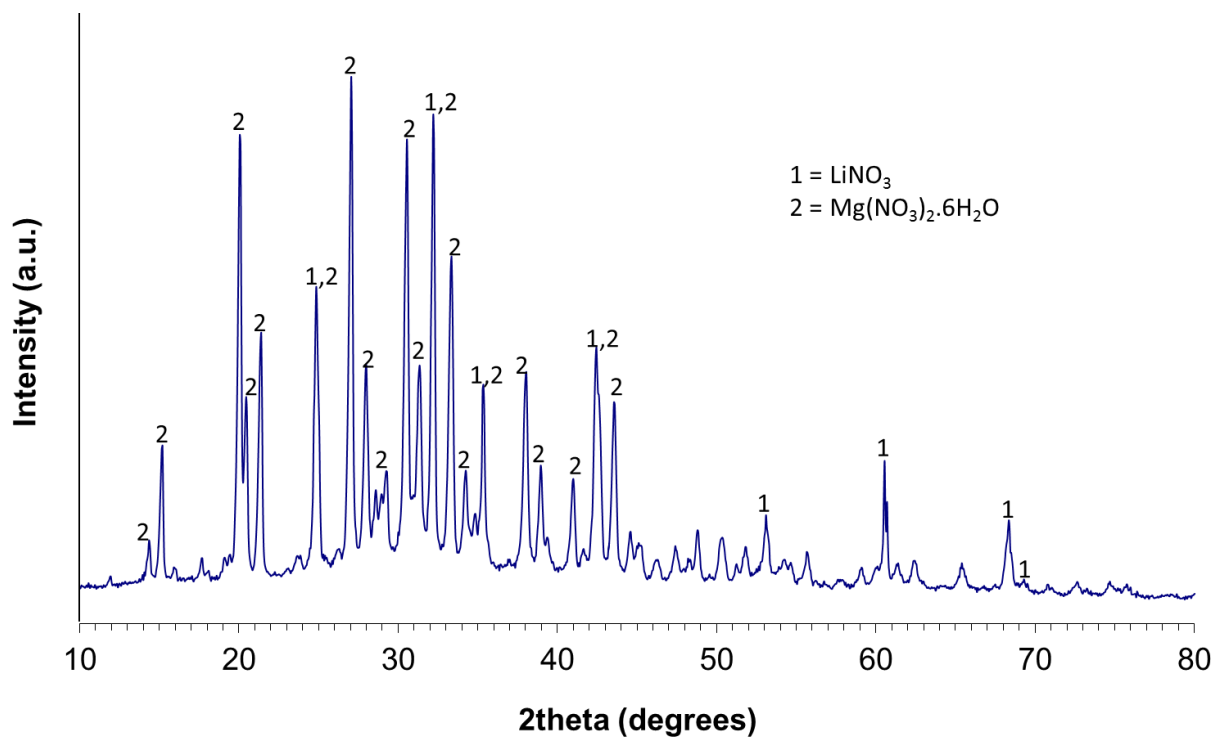


Figure 5.32 – XRD analysis of sample LMN1-FD using Cu K $\alpha$ 1 radiation ( $\lambda = 1.546 \text{ \AA}$ )

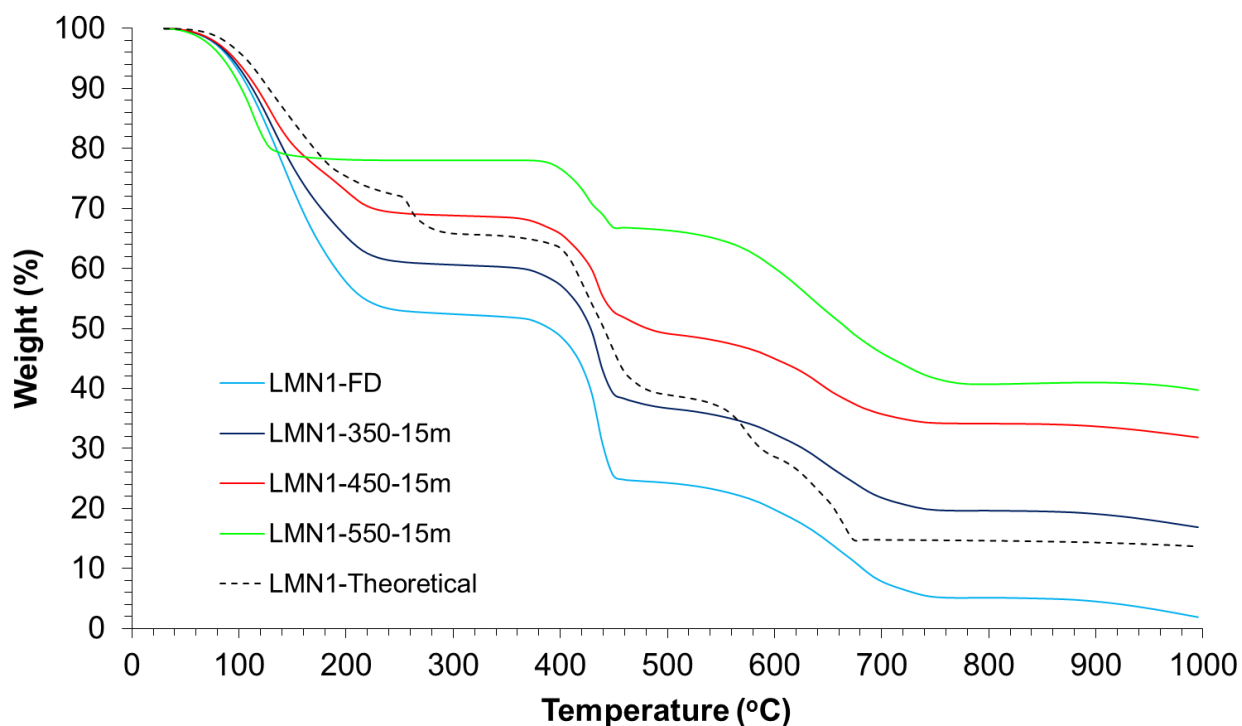
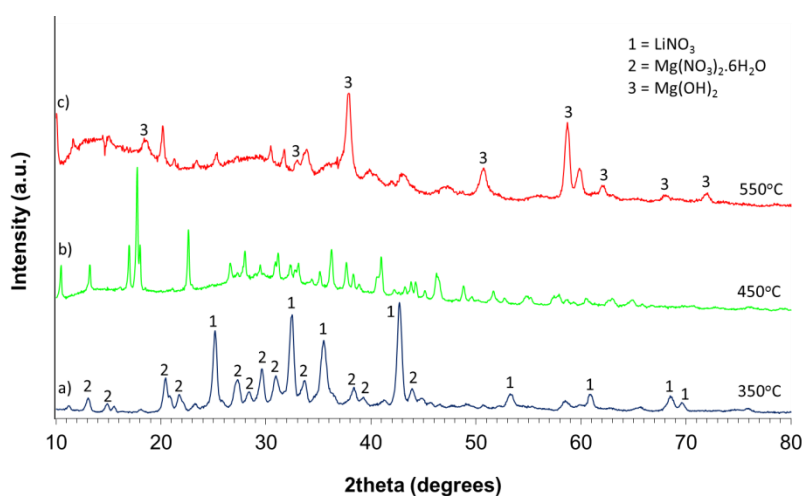


Figure 5.33 – TGA analysis of samples LMN1-FD, LMN1-350-15m, LMN1-450-15m and LMN1-550-15m

XRD analysis of product LMN1-350-15m (Figure 5.34) showed the retention of  $\text{LiNO}_3$  and  $\text{Mg}(\text{NO}_3)_2 \cdot 6\text{H}_2\text{O}$ . TGA data of this product (Figure 5.33) afforded a weight loss profile very similar to that produced from summation of the weighted summed data of  $\text{LiNO}_3$  and  $\text{Mg}(\text{NO}_3)_2 \cdot 6\text{H}_2\text{O}$ , consistent with the retention of these crystalline compounds. The weight loss achieved at  $1000\text{ }^\circ\text{C}$  was 83 wt% compared to the 86 wt% expected from the weighted contribution of the individual components at this temperature (Figure 5.33). This supported the XRD data (Figure 5.34) which showed no reaction between  $\text{LiNO}_3$  and  $\text{Mg}(\text{NO}_3)_2 \cdot 6\text{H}_2\text{O}$  had occurred. XRD and TGA data from the product calcined for 15 min at  $350\text{ }^\circ\text{C}$  were identical to those obtained from products calcined for shorter time periods, hence the latter are omitted for brevity.



**Figure 5.34 – XRD analysis of samples a) LMN1-350-15m, b) LMN1-450-15m and c) LMN1-550-15m using  $\text{Cu K}\alpha_1$  radiation ( $\lambda = 1.546\text{ \AA}$ )**

XRD analysis of product LMN1-450-15m (Figure 5.34) afforded a complex diffraction pattern that could not be matched (in part) to any reference pattern in the ICDD database, relevant to the phase diagram; the presence of significant diffuse scattering implies the co-existence of a non-crystalline phase. Reflections corresponding to crystalline  $\text{LiNO}_3$  and  $\text{Mg}(\text{NO}_3)_2 \cdot 6\text{H}_2\text{O}$  could not be identified in the diffraction pattern. The unidentified phase(s) were different to that observed after reaction at 3 h, as described in Section 5.3.1.1.2 (Figure 5.6). TGA data of this product (Figure 5.33) afforded a weight loss profile in which the denitration weight loss events characteristic of  $\text{LiNO}_3$  (at  $600\text{ }^\circ\text{C}$ ) and  $\text{Mg}(\text{NO}_3)_2 \cdot 6\text{H}_2\text{O}$  (at  $400\text{ }^\circ\text{C}$ ) were much less distinctive, particularly the latter. The weight loss achieved at  $1000\text{ }^\circ\text{C}$  was 68 wt%, consistent with incomplete dehydration and denitration. XRD and TGA data from the product calcined for 15 min at  $450\text{ }^\circ\text{C}$  were identical to those obtained from products calcined for shorter time periods, hence the latter are omitted for brevity. These data imply reaction between  $\text{LiNO}_3$  and  $\text{Mg}(\text{NO}_3)_2 \cdot 6\text{H}_2\text{O}$ , involving partial denitration, to afford an unidentified crystalline intermediate(s), which are metastable, since calcination for 3 h produces a different unidentified product.

XRD analysis of product LMN1-550-15m (Figure 5.34) revealed the presence of  $\text{Mg}(\text{OH})_2$  co-existing with at least one other unidentified phase. No reflections could be assigned to the unknown phase(s) formed by reaction at 450 °C, implying that these phase(s) have limited thermal stability. TGA data of this product (Figure 5.33) afforded a weight loss profile in which the denitration weight loss characteristic of  $\text{Mg}(\text{NO}_3)_2 \cdot 6\text{H}_2\text{O}$  (at 400 °C) was a minor contribution whereas that of  $\text{LiNO}_3$  (at 600 °C) was absent. The weight loss achieved at 1000 °C was 60 wt%, suggesting retention of a significant hydrate and nitrate inventory. XRD and TGA data from the product calcined for 15 min at 450 °C were identical to those obtained from products calcined for shorter time periods, hence the latter are omitted for brevity. These data imply the unidentified crystalline intermediate(s) formed at 450 °C decompose at higher temperature, yielding primarily  $\text{Mg}(\text{OH})_2$  as a kinetic product. An extended reaction time results in dehydroxylation of  $\text{Mg}(\text{OH})_2$  forming  $\text{MgO}$ , as discussed in Section 5.3.1.1.2.

Overall, these data are consistent with experiments carried out for 3 h duration over the same temperature range, as discussed in Section 5.3.1.1.2, but show that different products are formed under kinetic control. In summary, it is possible to infer the following sequence of reactions, relevant to the timescale of calciner operation:

- Below 350 °C:  $\text{LiNO}_3$  and  $\text{Mg}(\text{NO}_3)_2 \cdot 6\text{H}_2\text{O}$  do not undergo any significant reaction.
- Between 350-450 °C: the primary reaction is between  $\text{LiNO}_3$  and  $\text{Mg}(\text{NO}_3)_2 \cdot 6\text{H}_2\text{O}$  to form a metastable crystalline intermediate compound, likely a mixed nitrate hydrate of Mg and Li; a non-crystalline phase is also formed.
- Between 450-550 °C: the metastable intermediate compound decomposes to form  $\text{Mg}(\text{OH})_2$  and a crystalline and amorphous phase, which must be a Li rich nitrate phase possibly incorporating a small amount of Mg.

### 5.3.1.2.3 LAMN1

Figure 5.35 shows the XRD pattern for sample LAMN1-FD, in which all reflections could be attributed to  $\text{LiNO}_3$ ,  $\text{Mg}(\text{NO}_3)_2 \cdot 6\text{H}_2\text{O}$  or  $\text{Al}(\text{NO}_3)_3 \cdot 9\text{H}_2\text{O}$  (ICDD cards [8-466], [14-101], [12-472], respectively). TGA data from LAMN1-FD (Figure 5.38) produced a weight loss curve with a very similar profile to that produced from summation of the weighted summed data of  $\text{LiNO}_3$  and  $\text{Mg}(\text{NO}_3)_2 \cdot 6\text{H}_2\text{O}$ . The weight loss achieved at 1000 °C was 8 wt%, identical to that expected from the weighted contribution of the individual components at this temperature (Figure 5.36). These data confirm that no observable reaction had taken place between the component nitrates during the freeze drying process.

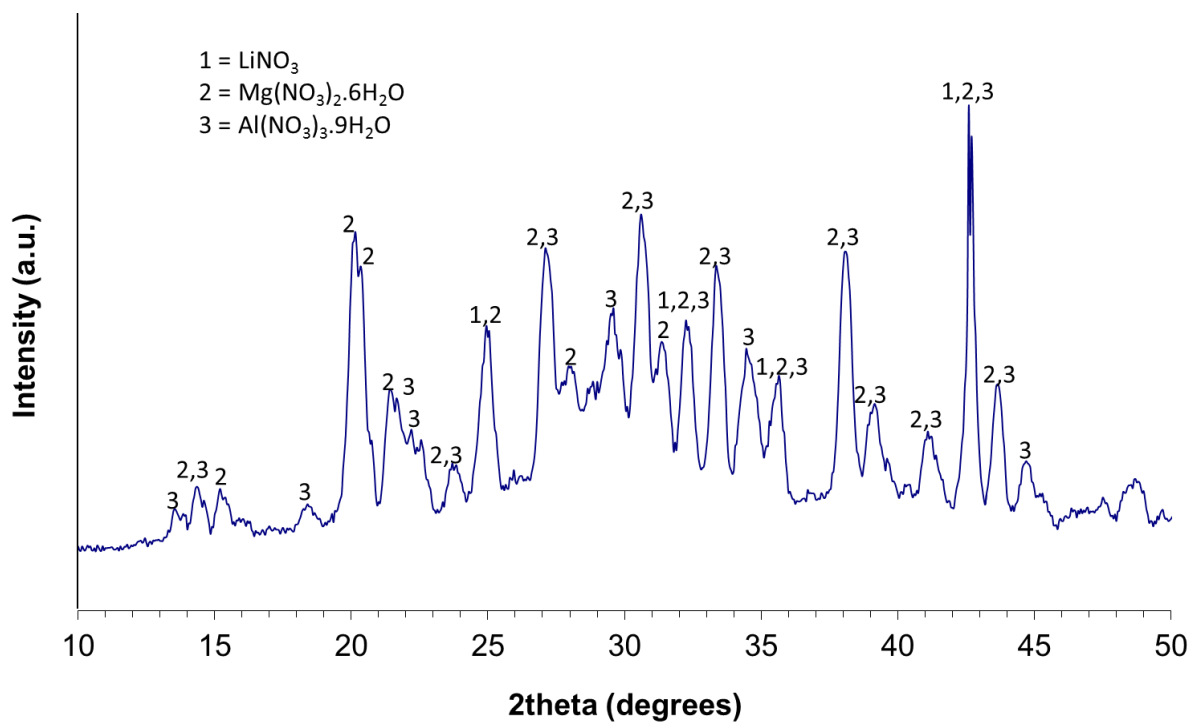


Figure 5.35 – XRD analysis of sample LAMN1-FD using Cu  $K\alpha_1$  radiation ( $\lambda = 1.546 \text{ \AA}$ )

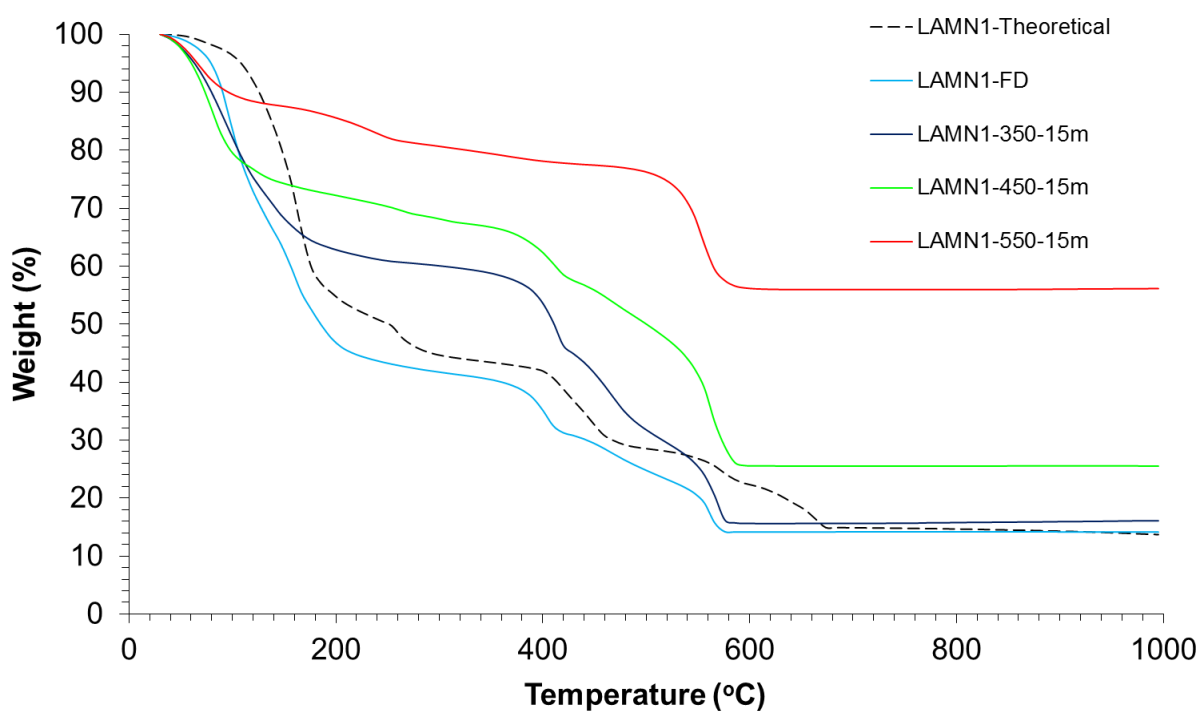
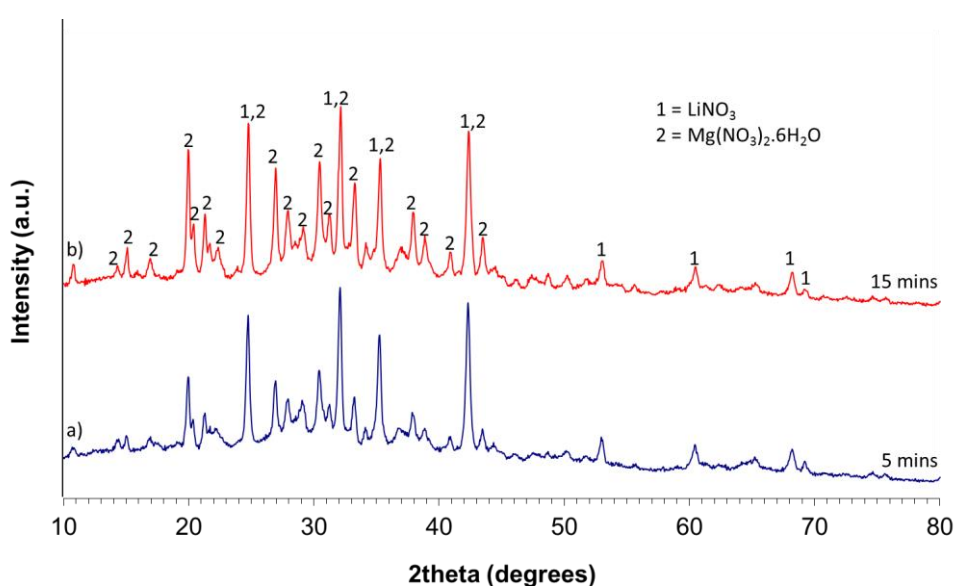


Figure 5.36 – TGA analysis of samples LAMN1-FD, LAMN1-350-15m, LAMN1-450-15m and LAMN1-550-15m



The XRD patterns of products LAMN1-350-5m and LAMN1-350-15m are shown in Figure 5.37 and reveal the presence of  $\text{LiNO}_3$  and  $\text{Mg}(\text{NO}_3)_2 \cdot 6\text{H}_2\text{O}$  in all products. The absence of  $\text{Al}(\text{NO}_3)_3 \cdot 9\text{H}_2\text{O}$  in products calcined at 350 °C and above is in agreement with TGA data of this material, with dehydration and denitration occurring below 400 °C (Appendix), to produce a non-crystalline product (Pacewska and Keshr, 2002). This would account for the observed diffuse scattering in the diffraction pattern, implying the presence of an additional non-crystalline phase. The weight loss of product LAMN1-350-15 at 1000 °C was 81 wt%, close to that expected from the weighted contribution of the individual components at this temperature (Figure 5.36). These data suggest that no observable reaction had taken place between the component nitrates during calcination, except for the expected decomposition of  $\text{Al}(\text{NO}_3)_3 \cdot 9\text{H}_2\text{O}$ .



**Figure 5.37 – XRD analysis of samples LAMN1-350-5m and  
b) LAMN1-350-15m using Cu  $K\alpha 1$  radiation ( $\lambda = 1.546 \text{ \AA}$ )**

The XRD pattern of product LAMN1-450-5m (Figure 5.38) shows the retention of  $\text{LiNO}_3$  and  $\text{Mg}(\text{NO}_3)_2 \cdot 6\text{H}_2\text{O}$  after 5 min reaction time at 450 °C; the presence of significant diffuse scattering also implies the presence of an additional non-crystalline phase. No reflections associated with  $\text{Mg}(\text{NO}_3)_2 \cdot 6\text{H}_2\text{O}$  were observed after a reaction time of 15 min at 450 °C, as shown by the XRD pattern of product LAMN1-450-15 (Figure 5.38). Calcination of LAMN1-FD at 450 °C also leads to the formation of an unidentified crystalline phase, as shown in Figure 5.38, associated with unassigned reflections at  $2\theta = 17.12^\circ$ ,  $22.45^\circ$  and  $36.93^\circ$ . These reflections match those associated with the unidentified phase produced by calcination of AMN1 at 450 °C, suggesting the formation of the same phase, which was thought to be an Al bearing compound; these data are consistent with that hypothesis. Product LAMN1-450-15 showed a lower weight loss of 70 wt% at 1000 °C, compared to the product of calcination at 350 °C, consistent with substantial denitration of  $\text{Mg}(\text{NO}_3)_2 \cdot 6\text{H}_2\text{O}$ .

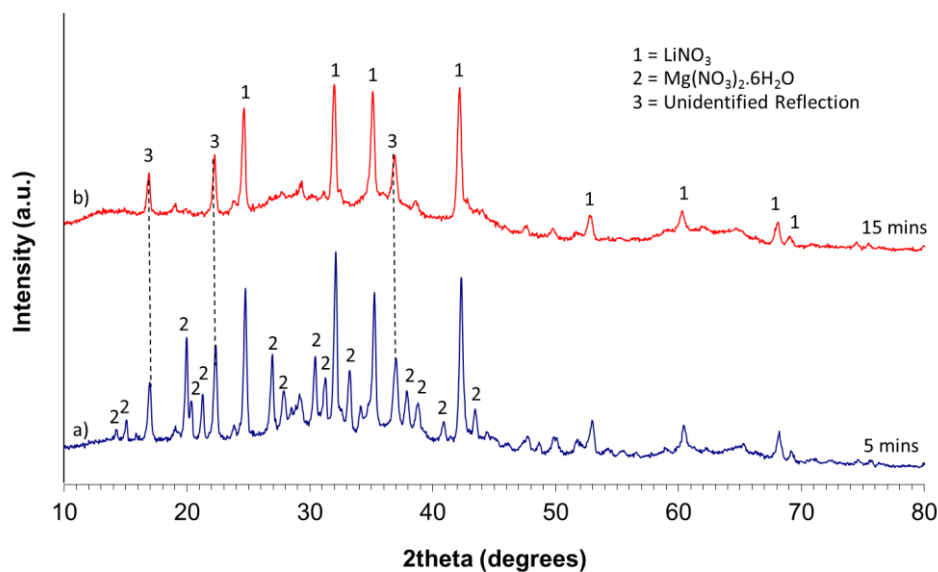
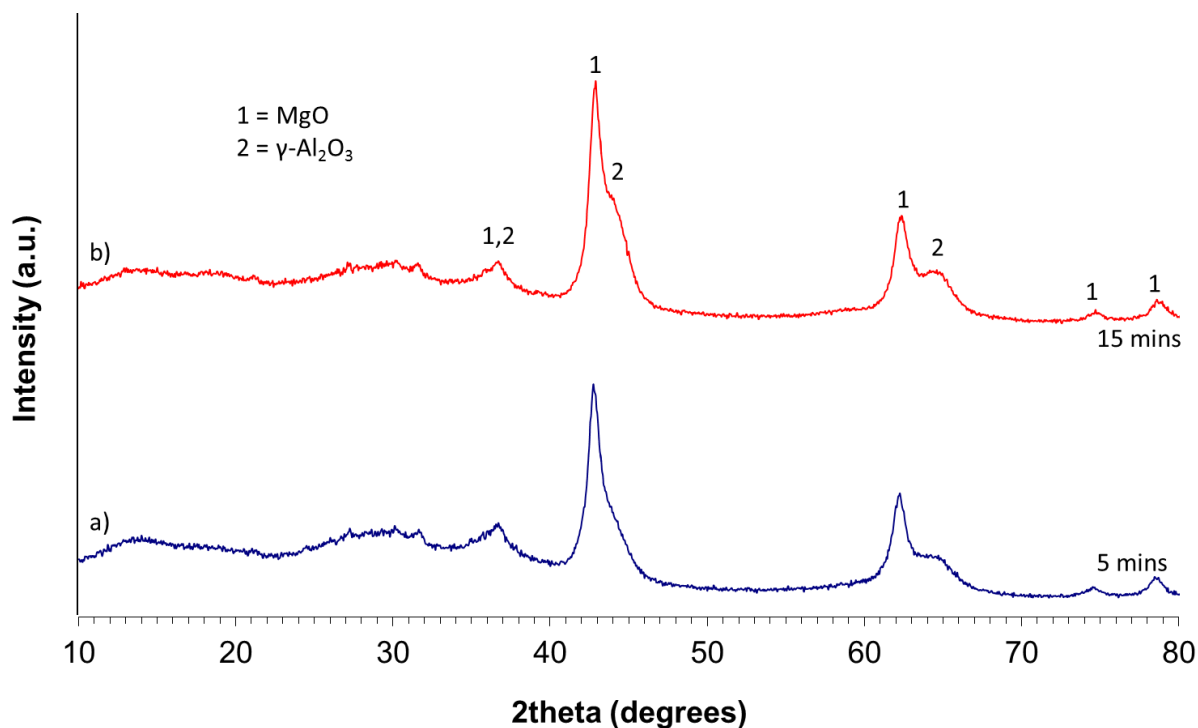


**Figure 5.38 – XRD analysis of samples LAMN1-450-5m and  
b) LAMN1-450-15m using Cu K $\alpha$ 1 radiation ( $\lambda = 1.546 \text{ \AA}$ )**

The XRD patterns of products LAMN1-550-5m and LAMN1-550-15m (Figure 5.39) show that calcination at 550 °C yields MgO plus  $\gamma$ -Al<sub>2</sub>O<sub>3</sub>; reflections attributed to the unidentified phase and LiNO<sub>3</sub> observed at 450 °C were not apparent in these diffraction patterns. The significant diffuse scattering in the diffraction pattern also implies the presence of an additional non-crystalline phase. Product LAMN1-550-15m showed a lower weight loss of 44 wt% at 1000 °C, consistent with further denitration of the freeze dried material. The presence of the weight loss event at 560 °C is consistent with that observed after calcination for 3 h at 550 °C, though after 3 h, the formation of MgAl<sub>2</sub>O<sub>4</sub> appeared to have taken place. This was due to LiNO<sub>3</sub> acting as a molten salt, facilitating the reaction through a template-growth mechanism. This type of reaction takes place through the following pathway (Safaei-Naeini, 2011):

1. Diffusion of dissolved MgO (in the form of Mg<sup>2+</sup>) onto  $\gamma$ -Al<sub>2</sub>O<sub>3</sub> particle surfaces.
2. Diffusion of MgO (probably in the form of Mg<sup>2+</sup>) to the unreacted  $\gamma$ -Al<sub>2</sub>O<sub>3</sub> core through the formed continuous MgAl<sub>2</sub>O<sub>4</sub> spinel layer.
3. Reaction between diffused MgO and unreacted  $\gamma$ -Al<sub>2</sub>O<sub>3</sub>.

The fact that this takes place through a diffusion mechanism suggests the reaction requires a significant time factor to allow it to occur. This is consistent with the observation of both MgO and  $\gamma$ -Al<sub>2</sub>O<sub>3</sub> after 15 mins, with MgAl<sub>2</sub>O<sub>4</sub> being formed after 3 h. These data imply that after calcination at 550 °C, MgO and  $\gamma$ -Al<sub>2</sub>O<sub>3</sub> are formed with Li being incorporated into the non-crystalline phase, same as seen after 3 h. This suggests that MgO and  $\gamma$ -Al<sub>2</sub>O<sub>3</sub> are the kinetic products, relevant to the timescale of the full-scale calcination process, with further reaction yielding MgAl<sub>2</sub>O<sub>4</sub> at longer residence times.



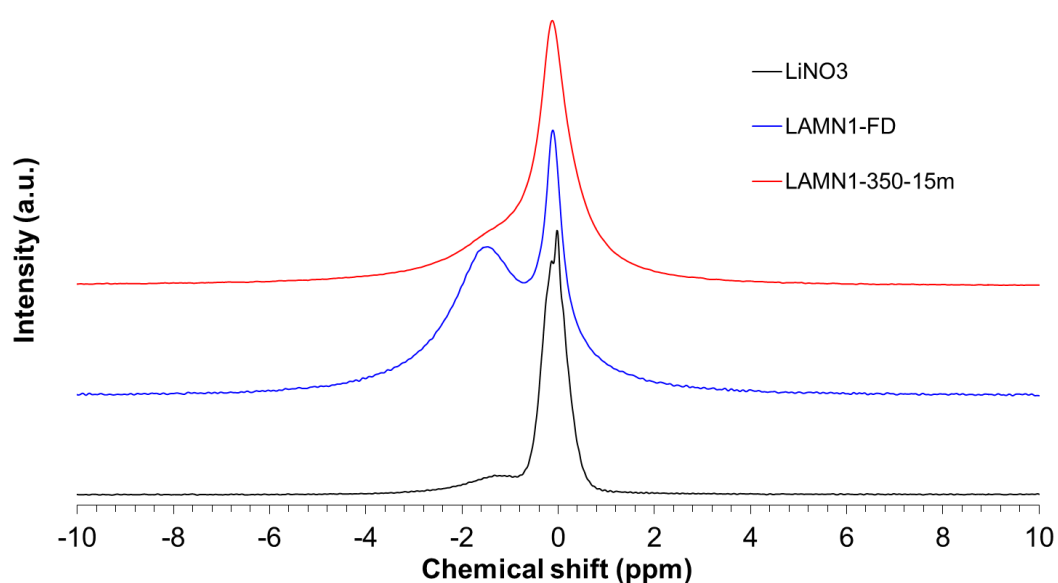
**Figure 5.39 – XRD analysis of samples LAMN1-550-5m and  
b) LAMN1-550-15m using Cu K $\alpha$ 1 radiation ( $\lambda = 1.546 \text{ \AA}$ )**

Figure 5.40 compares  $^7\text{Li}$  MAS NMR data from  $\text{LiNO}_3$ , LAMN1-FD, and LAMN1-350-15m, measured relative to  $\text{LiCl}$  (the estimate accuracy of the derived chemical shifts is  $\pm 0.02$  ppm). The spectrum of  $\text{LiNO}_3$  shows a resonance centered at  $-0.09$  ppm, with a small broad component centered at  $-1.33$  ppm attributed to a small fraction of hydrated non crystalline material. The  $^7\text{Li}$  NMR spectrum of the freeze dried material, LAMN1-FD, exhibits a broad resonance at  $-0.11$  ppm and a very broad resonance  $-1.47$  ppm; the former resonance is therefore attributed to chemical environment  $\text{LiNO}_3$ , whereas the latter is attributed to a distribution of chemical environments present in the amorphous phase(s), consistent with the analysis of XRD data. The  $^7\text{Li}$  NMR spectra of products LAMN1-350-15m and LAMN1-450-15m were dominated by a sharp and intense resonance centred at  $-0.10$  ppm, associated with the Li chemical environment in crystalline  $\text{LiNO}_3$ , consistent with analysis of XRD data. An additional broad signal centered at  $-1.48$  ppm, attributed to the presence of a non-crystalline phase in freeze dried material, was apparent in the spectrum of product LAMN1-350-15m but not LAMN1-450-15m (Figures 5.40 and 5.41). These data therefore suggest that Li is consumed from the non-crystalline component as the reaction proceeds. The  $^7\text{Li}$  NMR spectra of products LAMN1-550-15m and LAMN1-550-3h (Figure 5.41) were dominated by a single, but asymmetric intense resonance centered at  $-0.06$  ppm. The relatively sharp nature and significantly lower chemical shift of this signal suggest that it is associated with a crystalline chemical environment different from  $\text{LiNO}_3$  (consistent with the absence of the latter in XRD data of these products). Since product LAMN1-550-3h was found to comprise highly crystalline  $\gamma\text{-Al}_2\text{O}_3$ , by XRD analysis, the

NMR data may suggest incorporation of Li in this phase (and its metastable precursors) by a solid solution mechanism. This is somewhat contradictory to the XRD data, which suggested a non-crystalline phase, likely to contain Li, was formed. It should be noted, however, that the XRD and  $^7\text{Li}$  MAS NMR were carried out several months apart. It was therefore possible that either, through further diffusion reactions, Li was incorporated into the highly crystalline  $\gamma\text{-Al}_2\text{O}_3$  structure, or the non-crystalline phase becomes crystalline over time. Balsamo et al. (2012) showed that lithium can be incorporated into the  $\text{MgAl}_2\text{O}_4$  structure to form a mixed metal oxide, comprising Li, Mg and Al.

From these data we can infer and conclude the following relevant to the timescale of calciner operation:

- No observable reaction had taken place between the component nitrates during the freeze drying process.
- Below 350 °C: No observable reaction had taken place between the component nitrates during calcination, except for the expected decomposition of  $\text{Al}(\text{NO}_3)_3 \cdot 9\text{H}_2\text{O}$ .
- Between 350-450 °C: An unidentified phase, thought to be an Al bearing compound was formed. At longer reaction times, substantial denitration of  $\text{Mg}(\text{NO}_3)_2 \cdot 6\text{H}_2\text{O}$  occurred.  $\text{LiNO}_3$  remained unreacted in the product.
- Between 450-550 °C:  $\text{MgO}$  and  $\gamma\text{-Al}_2\text{O}_3$  were identified by XRD. The reflections attributed to the unidentified phase observed at 450 °C and those associated with  $\text{LiNO}_3$  were not apparent in these diffraction patterns. The significant diffuse scattering in the diffraction pattern also implies the presence of an additional non-crystalline phase likely containing Li.



**Figure 5.40 –  $^7\text{Li}$  MAS NMR spectra of samples  
LAMN1-FD and LAMN1-350-15m**

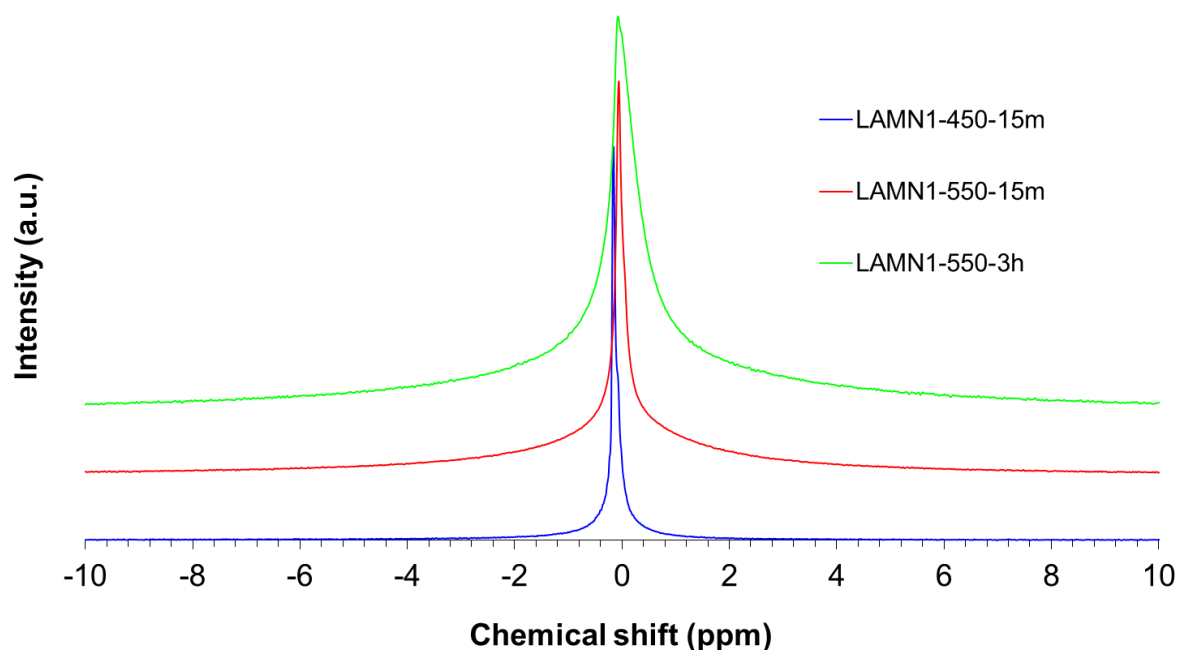


**Figure 5.41 –  $^7\text{Li}$  MAS NMR spectra of samples  
LAMN1-450-15m, LAMN1-550-15m and LAMN1-550-3h**

### 5.3.1.3 Small scale calciner experiments

#### 5.3.1.3.1 LAMN1

In order to determine a best estimate of the temperatures which the calcine experiences in the full scale calcination process, some of the short simulants were run through the small scale calciner. The rotating kiln section (calciner) is approximately a third of the size of the full scale and was the closest representation of the actual process available. By comparing the analysis carried out on the small scale calciner samples with the lab scale and freeze dried samples, the temperatures experienced in the calcination process could be estimated.

The XRD patterns of product LAMN1-SSC-600 (Figure 5.42) showed a set of reflections attributed to poorly crystalline MgO with significant diffuse scattering in the diffraction pattern also implying the presence of an additional non-crystalline phase. No reflections attributable to  $\text{Al}_2\text{O}_3$  or  $\text{LiNO}_3$  were observed. TGA analysis (Figure 5.43) showed a weight loss of 44 wt% at 1000 °C, identical to that of sample LAMN1-550-15m, with the same sharp weight loss event at 560 °C. Identification of MgO by XRD analysis, plus significant diffuse scattering indicating a non-crystalline component, was also in agreement with data from the product calcined at 550 °C for 15 mins.

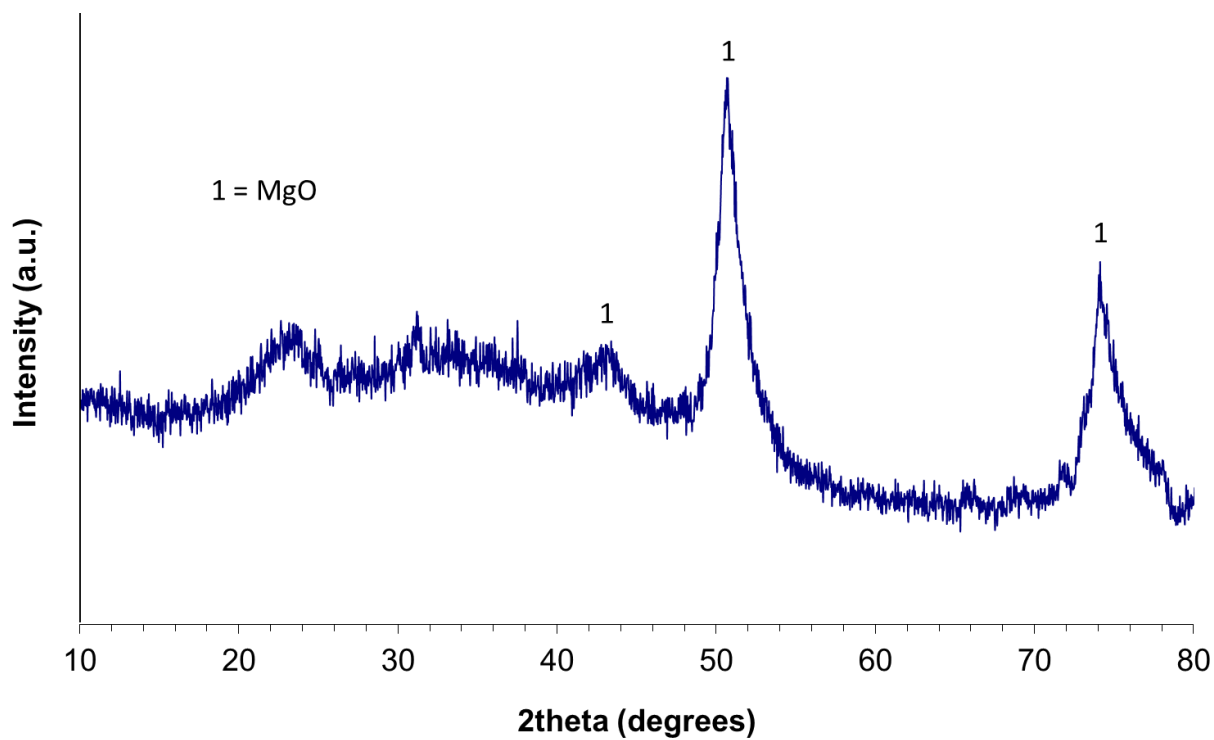


Figure 5.42 – XRD analysis of sample LAMN1-SSC-600 using Co K $\alpha$ 1 radiation ( $\lambda = 1.789 \text{ \AA}$ )

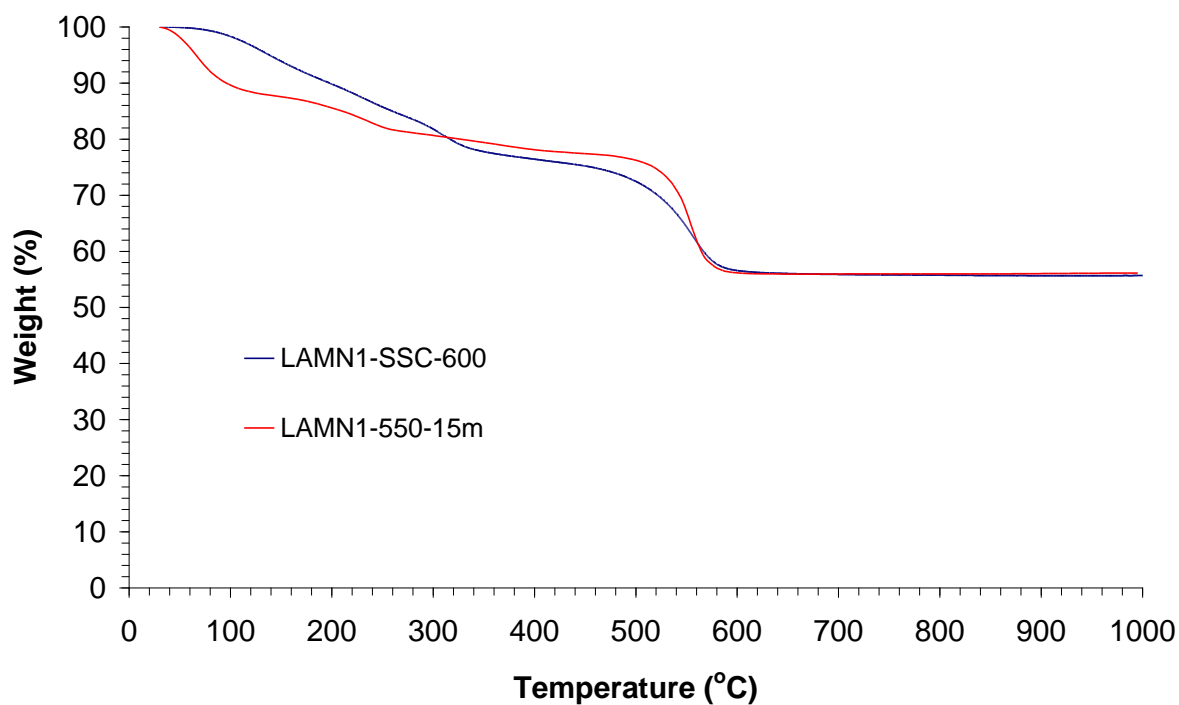
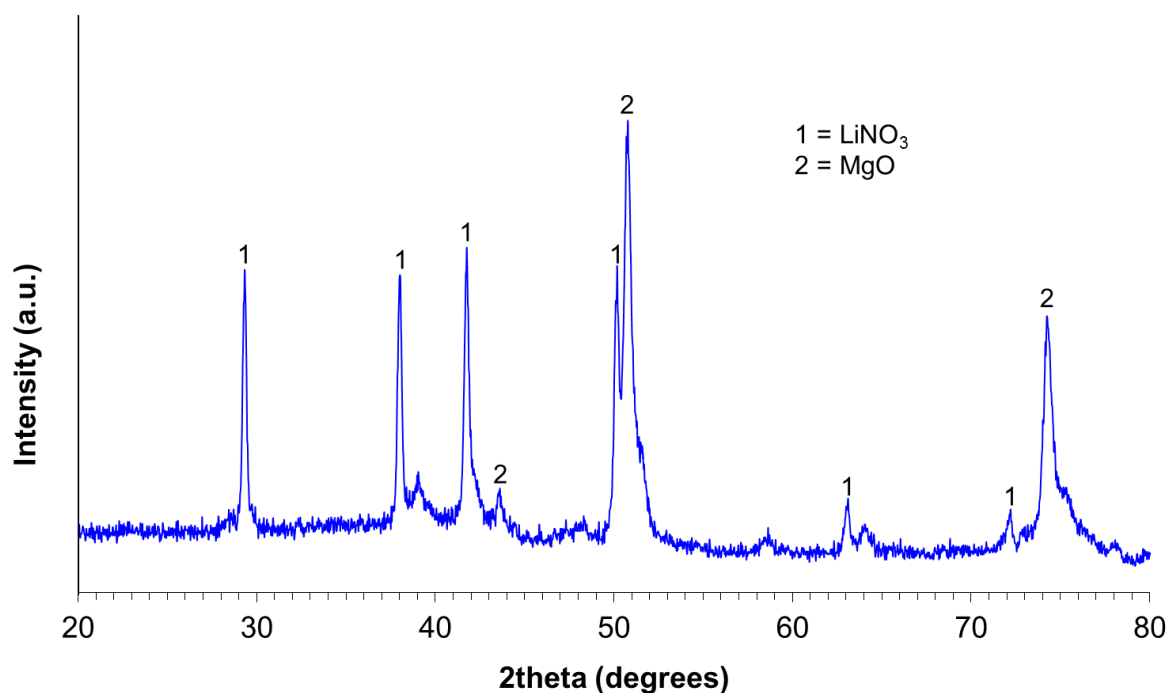


Figure 5.43 – TGA analysis of sample LAMN1-SSC-600

Overall, these data imply that the conditions experienced in the small scale calciner are very similar to those experienced after freeze-drying, followed by calcination in a muffle furnace at 550 °C for 15 mins. It must be noted, however, that the particle size of the calcine product was almost exclusively below 500 µm. The temperatures experienced by the calcine in the calcination process are known to depend on particle size.

### 5.3.1.3.2 LMN1

XRD analysis of sample LMN1-SSC-600 (Figure 5.44) showed the formation of LiNO<sub>3</sub> and MgO, which were identified using the ICDD database (cards [8-466] and [45-946] respectively). TGA analysis (Figure 5.45) showed a weight loss of 45 wt% at 1000 °C, comparable to the 49 wt% weight loss experienced by product LMN1-550-3h. The weight loss profile for product LMN1-SSC-600, however, showed a broad weight loss event between 400-550 °C which was not seen in the product calcined for 3 h at 550 °C. The weight loss above 600 °C, attributable to denitration of LiNO<sub>3</sub> (Appendix; Chun, 1977) was present, consistent with identification by XRD. The only calcination conditions which led to the formation of MgO and LiNO<sub>3</sub> in the LMN1 series of experiments were at 550 °C for 3 hours. It is possible that, due to the fact that lithium nitrate has a melting point of 255 °C, the product was stuck in the calciner tube for the duration of the experiment, until the tube had cooled, which was approximately 3 hours. This would also explain the low yield produced from this experiment.



**Figure 5.44 – XRD analysis of sample LMN1-SSC-600  
using Co K $\alpha$ 1 radiation ( $\lambda = 1.789 \text{ \AA}$ )**

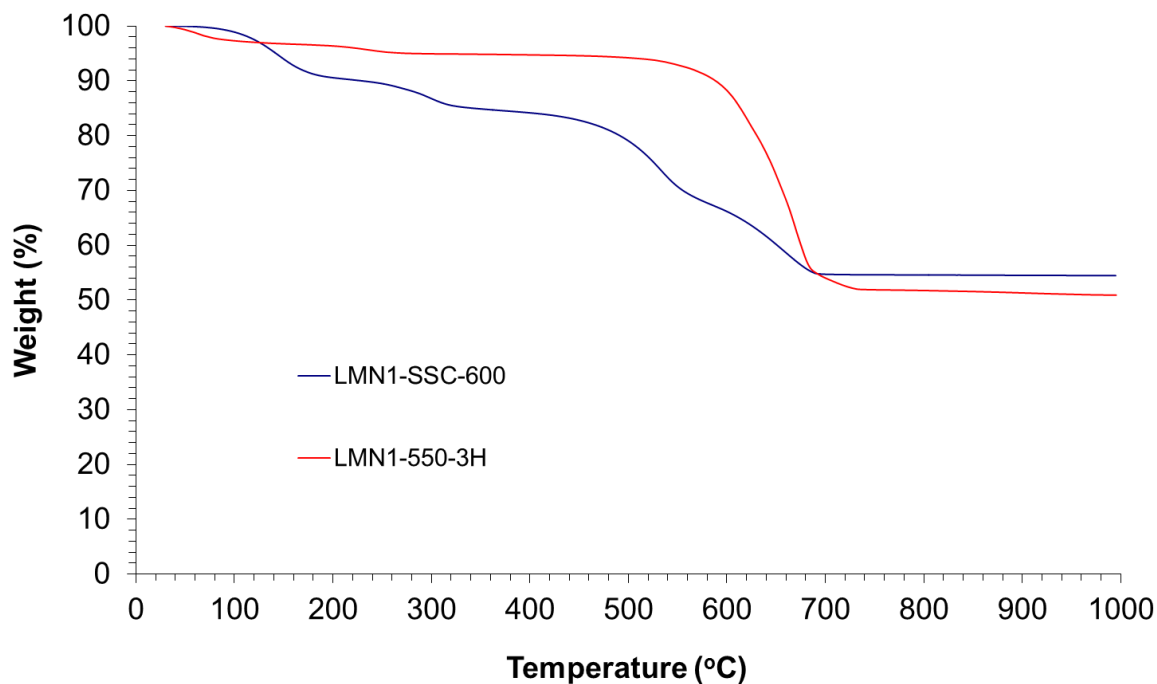


Figure 5.45 – TGA analysis of sample LMN1-SSC-600

#### 5.3.1.4 Discussion

Aluminium and magnesium nitrates are two of the main components present in the Magnox waste stream after nuclear waste reprocessing. It was therefore important to investigate the reactions which occurred between them and any competing reactions, with other major components within the HAL which may occur in the calcination process.

The analysis of sample AMN1 (Table 5.5) showed that the reactions between Al and Mg nitrates were dependant on both time and temperature. When calcined at 350 °C, no reaction between  $\text{Mg}(\text{NO}_3)_2 \cdot 6\text{H}_2\text{O}$  and  $\text{Al}(\text{NO}_3)_3 \cdot 9\text{H}_2\text{O}$  was observed over any timescale, though the partial dehydration and denitration of  $\text{Al}(\text{NO}_3)_3 \cdot 9\text{H}_2\text{O}$  was apparent, resulting in the formation of a non-crystalline product, in agreement with available literature (Pacewska and Keshr, 2002). After calcination at 450 °C for both 5 and 15 minutes, a portion of the  $\text{Mg}(\text{NO}_3)_2 \cdot 6\text{H}_2\text{O}$  starting material remained unreacted in the sample. There was, however, the formation of a crystalline species after 5 mins, which was unidentified, thought to be an Al containing phase, with the reflections increasing in intensity after calcination for 15 mins. When the residence time was increased to 3 hours, a different unidentified product was discovered, alongside the formation of MgO and  $\gamma\text{-Al}_2\text{O}_3$ . This suggested that the unidentified products formed were metastable intermediates which undergo further reaction / decomposition to form MgO and  $\gamma\text{-Al}_2\text{O}_3$ .



When Mg and Al nitrates were reacted together at 550 °C for 5 and 15 minutes, XRD analysis showed the formation of poorly crystalline MgO, with a non-crystalline component being apparent through significant diffuse scattering in the diffraction pattern. It was possible that  $\gamma$ -Al<sub>2</sub>O<sub>3</sub> was formed as it is poorly crystalline so would not appear in the XRD pattern. After 3 hours at 550 °C the products Mg<sub>a</sub>Al(OH)<sub>3+2a-c</sub>(NO<sub>3</sub>)<sub>c</sub>.xH<sub>2</sub>O, MgO and  $\gamma$ -Al<sub>2</sub>O<sub>3</sub> were formed. Available literature (Mascolo and Marino, 1980; Pausch et al., 1986; Roy et al., 1953) showed that the reaction between MgO and  $\gamma$ -Al<sub>2</sub>O<sub>3</sub> yielded the Mg-Al-LDH product. On the addition of more nitric acid to the reaction between Mg(NO<sub>3</sub>)<sub>2</sub>.6H<sub>2</sub>O and Al(NO<sub>3</sub>)<sub>3</sub>.9H<sub>2</sub>O (sample AMN2), MgO and  $\gamma$ -Al<sub>2</sub>O<sub>3</sub> were no longer observed, suggesting the reaction had gone to completion, with Mg<sub>a</sub>Al(OH)<sub>3+2a-c</sub>(NO<sub>3</sub>)<sub>c</sub>.xH<sub>2</sub>O being the only crystalline phase observed in the product. However, in the timescale of calcination, this reaction would not be expected to occur, with the kinetic products of the reaction between Mg(NO<sub>3</sub>)<sub>2</sub>.6H<sub>2</sub>O and Al(NO<sub>3</sub>)<sub>3</sub>.9H<sub>2</sub>O being MgO and a non-crystalline Al containing phase, likely to be  $\gamma$ -Al<sub>2</sub>O<sub>3</sub>.

**Table 5.5 – Summary of the products formed in sample AMN1**

		Temperature (°C)		
		350	450	550
Time (minutes)	180	Mg(NO <sub>3</sub> ) <sub>2</sub> .6H <sub>2</sub> O Non-crystalline Al nitrate hydrate	MgO $\gamma$ -Al <sub>2</sub> O <sub>3</sub> Unidentified Intermediate <sup>9</sup>	MgO $\gamma$ -Al <sub>2</sub> O <sub>3</sub> Mg <sub>a</sub> Al(OH) <sub>3+2a-c</sub> (NO <sub>3</sub> ) <sub>c</sub> .xH <sub>2</sub> O
	15	Mg(NO <sub>3</sub> ) <sub>2</sub> .6H <sub>2</sub> O Non-crystalline Al nitrate hydrate	Mg(NO <sub>3</sub> ) <sub>2</sub> .6H <sub>2</sub> O <b>Unidentified Intermediate</b>	Poorly Crystalline MgO Non-crystalline Al containing phase (possibly $\gamma$ -Al <sub>2</sub> O <sub>3</sub> )
	5	Mg(NO <sub>3</sub> ) <sub>2</sub> .6H <sub>2</sub> O Non-crystalline Al nitrate hydrate	Mg(NO <sub>3</sub> ) <sub>2</sub> .6H <sub>2</sub> O <b>Unidentified Intermediate</b>	Poorly Crystalline MgO Non-crystalline Al containing phase (possibly $\gamma$ -Al <sub>2</sub> O <sub>3</sub> )

<sup>9</sup> The unidentified intermediate formed after 180 minutes was different to those formed after 5 and 15 minutes.

The addition of  $\text{LiNO}_3$  to the reaction between Al and Mg nitrates (Table 5.6) also had a significant impact on the products formed over a range of calcination conditions. After calcination at 350 °C for 5 mins, no reaction had occurred. However, after 15 mins, weak reflections were observed which matched the unidentified intermediate formed in products AMN1 calcined at 450 °C, as well as after calcination at 450 °C for both 5 and 15 minutes in products LAMN1.  $\text{LiNO}_3$  remained un-reacted in these products. The increase in intensity of reflections attributable to the unidentified intermediate combined with the diminishing of  $\text{Mg}(\text{NO}_3)_2 \cdot 6\text{H}_2\text{O}$  reflections at higher temperatures suggested that the intermediate is a metastable nitrate phase containing both Al and Mg. As reflections attributable to  $\text{Mg}(\text{NO}_3)_2 \cdot 6\text{H}_2\text{O}$  were still present in sample AMN1-450-15m, but not LAMN1-450-15m and with the addition of  $\text{LiNO}_3$ , the reaction is observed at 350 °C for 15 mins suggests the  $\text{LiNO}_3$  facilitates this reaction through acting as a molten salt, allowing it to occur more rapidly and at lower temperatures. This metastable intermediate decomposes after calcination at 550 °C, with the formation of  $\text{MgO}$  and  $\gamma\text{-Al}_2\text{O}_3$  being observed, suggesting these are the kinetic products over the timescale of calcination on the full scale process.

After calcination at 350 °C for 3 hours, unidentified crystalline product(s) were formed. This was thought to be complex nitrate hydrate phase(s) containing Li, Al and Mg due to the fact that  $\text{LiNO}_3$  does not react with either  $\text{Mg}(\text{NO}_3)_2 \cdot 6\text{H}_2\text{O}$  or  $\text{Al}(\text{NO}_3)_3 \cdot 9\text{H}_2\text{O}$  under these conditions (sections 5.3.1.1.2 and 5.3.1.1.3). These phase(s) were found to be metastable, as after calcination at 450 and 550 °C for 3 h, dehydration and denitration had occurred resulting in the formation  $\text{MgAl}_2\text{O}_4$  and a non-crystalline phase containing Li and Mg. These are different products than observed without the addition of  $\text{LiNO}_3$ , showing Li had a significant effect on the reactions which occur, especially over longer residence times.

The differences in the reaction products between AMN1 and LAMN1, under all calcination conditions can be attributed to the  $\text{LiNO}_3$  acting as a molten salt in the calcination process. At shorter residence times (5 and 15 mins), the products were essentially the same but the reactions between  $\text{Mg}(\text{NO}_3)_2 \cdot 6\text{H}_2\text{O}$  and  $\text{Al}(\text{NO}_3)_3 \cdot 9\text{H}_2\text{O}$  occurred at lower temperatures and residence times in the presence of  $\text{LiNO}_3$ . After calcination at 550 °C for 5 and 15 mins, poorly crystalline  $\text{MgO}$  was observed in product AMN1, with a non-crystalline Al containing phase (possibly  $\gamma\text{-Al}_2\text{O}_3$ ) observed through diffuse scattering in the diffraction pattern. On addition of  $\text{LiNO}_3$ , crystalline  $\text{MgO}$  and  $\gamma\text{-Al}_2\text{O}_3$  were formed, showing the oxidation reactions had progressed further. This is consistent with the fact that  $\text{LiNO}_3$  acts as a Lux-Flood base (Afanasiev and Geantet, 1998) and is therefore a good  $\text{O}^{2-}$  donor. Over longer residence times (3 h) at temperatures of 450 and 550 °C,  $\text{MgO}$  and  $\gamma\text{-Al}_2\text{O}_3$  appeared to undergo further reaction to form  $\text{MgAl}_2\text{O}_4$  in the presence of  $\text{LiNO}_3$ . This is indicative of a template-growth synthesis in a molten salt media, where  $\text{MgO}$  undergoes diffusive processes into the  $\gamma\text{-Al}_2\text{O}_3$  structure, resulting in the retention of the  $\gamma\text{-Al}_2\text{O}_3$  structure after reaction (Safaei-Naeini et al., 2011; Fazli et al., 2013). The template-growth reaction is not observed without the presence of a

molten salt, and the formation of  $\text{MgAl}_2\text{O}_4$  usually takes place at much higher temperatures in the absence of a molten salt synthesis route (Fazli et al., 2013). The reaction of  $\text{MgO}$  and  $\gamma\text{-Al}_2\text{O}_3$ , without the presence of  $\text{Li}$  (product AMN1-550-3h), therefore resulted in the formation of  $\text{Mg}_a\text{Al}(\text{OH})_{3+2a-c}(\text{NO}_3)_c \cdot x\text{H}_2\text{O}$ , which in turn decomposes to form  $\text{MgO}$  and  $\text{MgAl}_2\text{O}_4$  at higher temperatures (Zhang et al., 2013). Overall, these observations, combined with the available literature, implied that  $\text{LiNO}_3$  acts as a molten salt, helping to facilitate the reactions between  $\text{Mg}(\text{NO}_3)_2 \cdot 6\text{H}_2\text{O}$  and  $\text{Al}(\text{NO}_3)_3 \cdot 9\text{H}_2\text{O}$  (and their decomposition products).

**Table 5.6 – Summary of the products formed in sample LAMN1**

		Temperature (°C)		
		350	450	550
Time (mins)	180	Unidentified Complex Nitrate Hydrate containing Li, Al and Mg	$\text{MgAl}_2\text{O}_4$ Non-crystalline phase containing Li and Mg	$\text{MgAl}_2\text{O}_4$ Non-crystalline phase containing Li and Mg
	15	$\text{Mg}(\text{NO}_3)_2 \cdot 6\text{H}_2\text{O}$ <b>Unidentified</b> <b>Intermediate</b> $\text{LiNO}_3$	<b>Unidentified</b> <b>Intermediate</b> <sup>10</sup> $\text{LiNO}_3$	$\text{MgO}$ $\gamma\text{-Al}_2\text{O}_3$ Non-crystalline phase containing Li and Mg
	5	$\text{Mg}(\text{NO}_3)_2 \cdot 6\text{H}_2\text{O}$ Non-crystalline Al nitrate hydrate $\text{LiNO}_3$	$\text{Mg}(\text{NO}_3)_2 \cdot 6\text{H}_2\text{O}$ <b>Unidentified</b> <b>Intermediate</b> $\text{LiNO}_3$	$\text{MgO}$ $\gamma\text{-Al}_2\text{O}_3$ Non-crystalline phase containing Li and Mg

The reaction of  $\text{Li}$  and  $\text{Mg}$  nitrates (sample LMN1) resulted in the formation of  $\text{Mg}(\text{OH})_2$  after calcination for 5-15 mins at 550 °C, which decomposes to form  $\text{MgO}$  after 3 h. At 450 °C, metastable intermediate(s) were formed, likely to be a mixed nitrate hydrate phase containing  $\text{Mg}$  and  $\text{Li}$ , with no reaction being observed at 350 °C over any timescale.

<sup>10</sup> The unidentified intermediate was the same as that formed in the sample AMN1 under the same calcination conditions.

One of the primary reasons for the addition of  $\text{LiNO}_3$  to the HAL simulant is to reduce the amount of refractory oxides containing Al and Fe (which are difficult to incorporate into the glass matrix) through reactions to form the corresponding Li aluminates and ferrates (Magrabi, 1981; Brace 2004). In these experiments, the reaction between Li and Al nitrates yielded  $\text{LiAl}_2(\text{OH})_6(\text{NO}_3) \cdot x\text{H}_2\text{O}$  as the major product after calcination at 450 and 550 °C for 3 h, in agreement with previous work (Besserguenev et al., 1997).  $\text{LiAl}_2(\text{OH})_6(\text{NO}_3) \cdot x\text{H}_2\text{O}$  undergoes decomposition to form  $\text{LiAlO}_2$  and  $\text{LiAl}_5\text{O}_8$  at 500 °C (Nayak et al., 1997), which suggests the addition of  $\text{LiNO}_3$  will result in a reduction in the formation of  $\text{Al}_2\text{O}_3$  in the calcine, though the experiments were not carried out over the relevant timescales corresponding with full scale calcination. The formation of the Fe analogue of the layered double hydroxide structure, however, is known not to occur, though the  $\text{Fe}^{3+}$  cation can be substituted for  $\text{Al}^{3+}$  in the  $\text{LiAl}_2(\text{OH})_6(\text{NO}_3) \cdot x\text{H}_2\text{O}$  structure (Kustrowski et al., 2005). The calcination of Li and Fe nitrates, for 3 h at 550 °C, showed no reaction occurred between them, except for the expected decomposition of  $\text{Fe}(\text{NO}_3)_3 \cdot 9\text{H}_2\text{O}$  to  $\text{Fe}_2\text{O}_3$  (Melkinov et al., 2014). Available literature, however, showed the formation of  $\text{LiFeO}_2$  and  $\text{LiFe}_5\text{O}_8$  does occur through a variety of pathways (Li et al., 2011) at different residence times and temperatures.

Throughout this series of experiments, it was shown that  $\text{Fe}(\text{NO}_3)_3 \cdot 9\text{H}_2\text{O}$  did not undergo any significant reaction with  $\text{LiNO}_3$ ,  $\text{Mg}(\text{NO}_3)_2 \cdot 6\text{H}_2\text{O}$  or  $\text{Al}(\text{NO}_3)_3 \cdot 9\text{H}_2\text{O}$  under any calcination conditions. However, due to the similar sizes of the atomic radii of  $\text{Al}^{3+}$  and  $\text{Fe}^{3+}$  these can be substituted with each other forming solid solutions (Tsuchida and Sugimoto, 1990).

When samples LMN1 and LAMN1 were run through the small scale calciner, with temperature set points of 400, 400 and 600 °C, in Zones 1, 2 and 3 respectively, they yielded products comparable to those formed after freeze drying, followed by calcination at 550 °C for 15 mins in a muffle furnace. However, the products did not replicate the particle size distributions of full HAL simulants, with the short simulants showing a much smaller particle size. The temperatures experienced in the calciner are known to be dependent on particle size (Chapter 6). Calcines high in Li are known to be sticky due to the low melting point (255 °C) and high decomposition temperature (600 °C), meaning it spends longer in the calciner tube than a simulant without  $\text{LiNO}_3$  added (Brace, 2004), in agreement with observations of the calcine coming out of the tube on cooling and therefore increasing exposure to the rabble bar, breaking down the calcine to fine particles. This would lead to an increase in the temperature experienced by the calcine compared to other simulants, as shown when PZN2 was processed (section 5.3.2.3.1), with particles above 2 mm in diameter experiencing conditions comparable to calcining at 350 °C and particles below 500  $\mu\text{m}$ , 450 °C for 10 mins. This showed that calcines with a high Li content are unsuitable to run on the small scale calciner to give comparable results to full calcine samples and to simulate conditions in the full scale process.

Overall, these data showed that the reactions between Al and Mg nitrates didn't reach completion after 15 mins, which suggested that the reactions in the calcination process do not go to completion. The kinetic products of calcination depend primarily on temperature over the differences in residence time associated with full scale calcination (5-15 mins), though some differences are observed with changing residence time.

### **5.3.2 Reactions between phosphomolybdic acid and zirconyl nitrate**

#### **5.3.2.1 Lab scale experiments**

##### **5.3.2.1.1 PZN1 and PZN2**

XRD and TGA data from the products PZN1 and PZN2 showed almost identical results, therefore results from the former have been omitted for brevity. XRD analysis of sample PZN2-350-3h (Figure 5.46) demonstrated the presence of poorly crystalline phosphomolybdic acid ( $\text{H}_3\text{PMo}_{12}\text{O}_{40}\cdot x\text{H}_2\text{O}$ , PMA), corresponding to ICDD card [43-317]. No reflections attributable to  $\text{ZrO}(\text{NO}_3)_2$  were apparent in the diffraction pattern. Additional weak reflections could not be reliably assigned to additional phases as a result of their broad and weak nature, characteristic of a poorly crystalline material. TGA analysis of PZN2-350-3h confirmed the presence of residual PMA, demonstrating a weight loss event at ca. 100 °C characteristic of dehydration of this material (consistent with TGA analysis of PMA and literature data – Appendix, Tatibouet et al., 1997). TGA data from reaction products derived from PMA and  $\text{ZrO}(\text{NO}_3)_2$  demonstrate significant weight loss occurring at 800 °C (Figure 5.47). This is attributed to volatilisation of  $\text{MoO}_3$  above the melting point of this compound (795 °C, Smolik et al., 2000) the rate of volatilisation is known to increase rapidly above the melting point (Saburi et al., 2001). This hypothesis was confirmed by annealing experiments at 900 °C as discussed below. The overall weight loss of product of PZN-350-3h at 700 °C was 10 wt%, compared to the expected weight loss of 15 wt%, assuming complete denitration and dehydration of the reagents. The TGA data of PZN-350-3h show a distinct weight loss event at 200 °C characteristic of the denitration of  $\text{ZrO}(\text{NO}_3)_2$ , consistent with TGA data of this compound and previous investigation by Hagiwara et al. (1975), which show thermal decomposition proceeds to completion at 450 °C. From these data it is possible to infer dehydration of PMA and dehydration and partial denitration of  $\text{ZrO}(\text{NO}_3)_2$  after 3 h at 350 °C, with the latter yielding poorly crystalline or amorphous  $\text{ZrO}_2$ , consistent with the report of Hagiwara et al. (1975); no evidence of reaction between PMA and  $\text{ZrO}(\text{NO}_3)_2$  was apparent under these conditions.

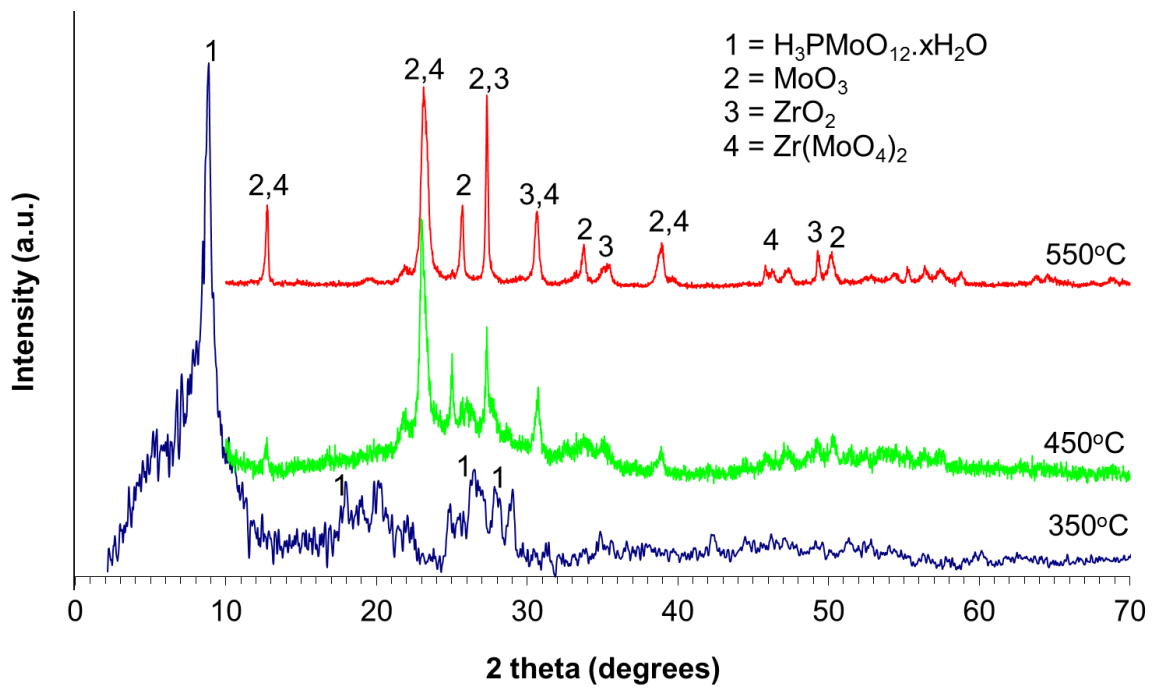


Figure 5.46 - XRD analysis of samples a) PZN2-350-3h, b) PZN2-450-3h and c) PZN2-550-3h using Co K $\alpha$ 1 radiation ( $\lambda = 1.789 \text{ \AA}$ )

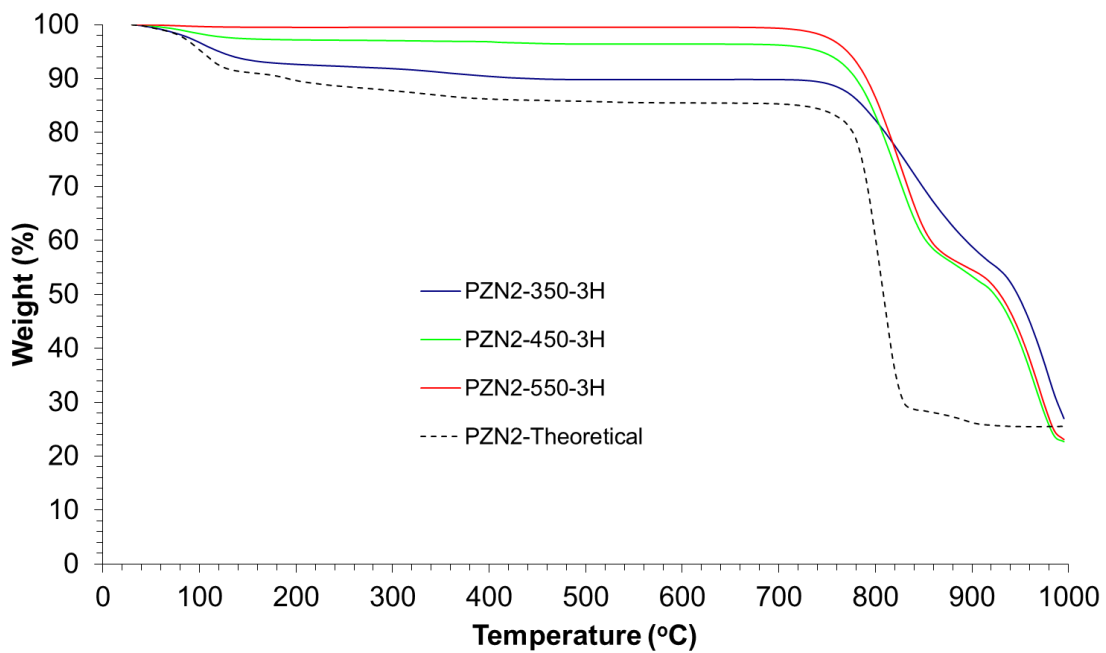


Figure 5.47 - TGA analysis of samples PZN2-350-3h, PZN2-450-3h and PZN2-550-3h

XRD data from product PZN2-450-3h (Figure 5.46) demonstrated the presence of broad reflections characteristic of poorly crystalline  $\text{MoO}_3$  [01-073-6497],  $\text{ZrO}_2$  [01-074-1201], and  $\text{Zr}(\text{MoO}_4)_2$  [01-077-1784]; the presence of significant diffuse scattering implies the co-existence of a non-crystalline material. No reflections attributable to PMA or  $\text{ZrO}(\text{NO}_3)_2$  were apparent in the diffraction pattern. TGA analysis of PZN-450-3h (Figure 5.47) demonstrated an overall weight loss of 4 wt% at 700 °C and no weight loss event at 200 °C was apparent. These data are consistent with near complete thermal decomposition of PMA and  $\text{ZrO}(\text{NO}_3)_2$ , consistent with TGA analysis of these materials and available literature data (Appendix, Tatibouet et al., 1997; Hagiwara et al., 1975). The non-crystalline component is likely to be  $\text{ZrO}_2$ , since it is known that thermal decomposition of  $\text{ZrO}(\text{NO}_3)_2$  produces non-crystalline or poorly crystalline  $\text{ZrO}_2$  in the temperature range 400-450 °C.

XRD data from product PZN2-550-3h (Figure 5.46) demonstrated the presence of sharp reflections attributable to  $\text{MoO}_3$ ,  $\text{ZrO}_2$ , and  $\text{Zr}(\text{MoO}_4)_2$ ; the lack of significant diffuse scattering implies the absence a significant non-crystalline component. TGA analysis of PZN-450-3h (Figure 5.47) demonstrated an overall weight loss of 0.7 wt% at 700 °C, consistent with complete thermal decomposition of PMA and  $\text{ZrO}(\text{NO}_3)_2$ .

Overall, these data imply a sequence of reactions initiated between 350-550 °C:

- Dehydration and denitration of  $\text{ZrO}(\text{NO}_3)_2$  proceeds to completion, yielding  $\text{ZrO}_2$  which is poorly or non-crystalline at 350 °C.
- Above 350 °C, dehydrated PMA reacts with  $\text{ZrO}_2$  to yield  $\text{Zr}(\text{MoO}_4)_2$  and  $\text{MoO}_3$ , presumably with the evolution of  $\text{H}_3\text{PO}_4$ .
- Above 450 °C, crystallisation of the products is assisted by enhanced diffusion at higher temperature.

Significant evaporation of  $\text{MoO}_3$  from the reaction above 800 °C was confirmed by annealing PZN-350-3h at 900 °C for 1 h, XRD data of the product of this reaction (Figure 5.48) revealed only the presence of  $\text{ZrO}_2$  and  $\text{Zr}(\text{MoO}_4)_2$ .

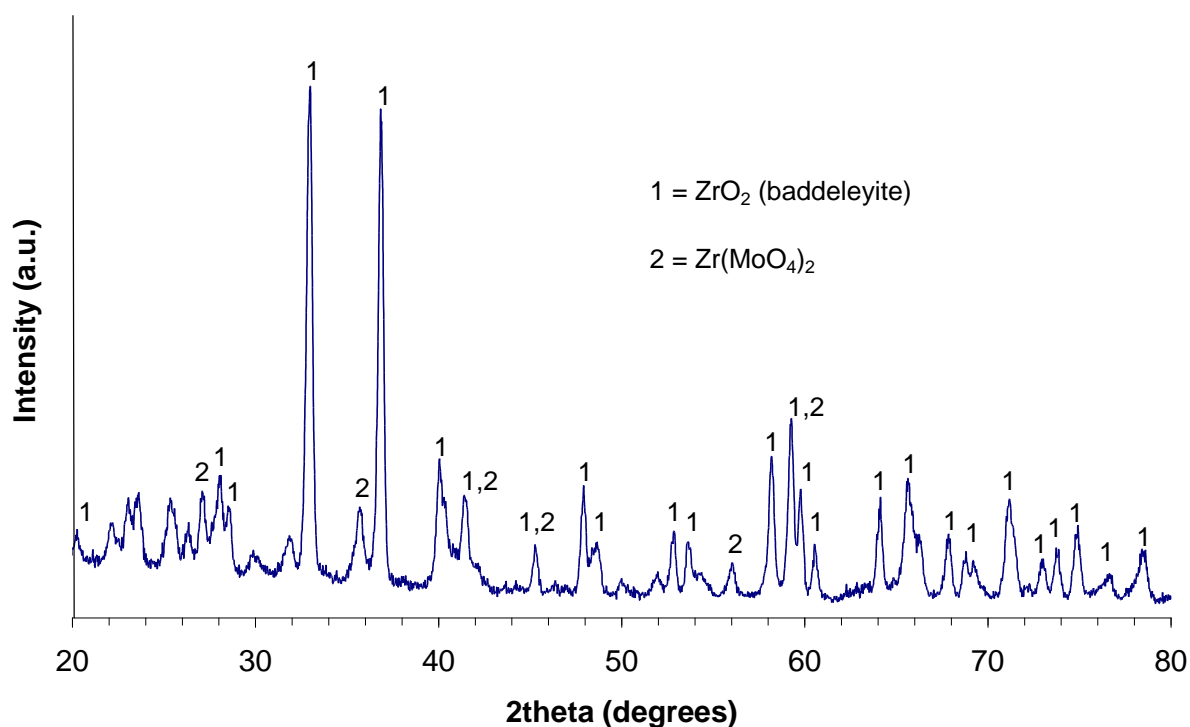


**Figure 5.48 – XRD analysis of sample PZN2-350-3h after calcination at 900 °C for 1 hour using Co K $\alpha$ 1 radiation ( $\lambda = 1.789 \text{ \AA}$ )**

### 5.3.2.1.2 LPN1

XRD analysis of product LPN1-350-3h (Figure 5.49) showed the formation of  $\text{Li}_2\text{MoO}_4$  [12-763],  $\text{MoO}_3$  [01-073-6497] and  $\text{Li}_2\text{Mo}_2\text{O}_7$  [24-461], demonstrating reaction between PMA and  $\text{LiNO}_3$ . The low signal-to-noise ratio of these data suggested the co-existence of a non-crystalline phase. TGA analysis of product LPN1-350-3h (Figure 5.50) showed a total weight loss of 23 wt% at 700 °C, compared to the expected weight loss of 29 wt%, assuming complete denitration and dehydration of the reagents. The TGA data did not exhibit a weight loss event at 600 °C, characteristic of the denitration of  $\text{LiNO}_3$  (Appendix, Chun, 1977). However, a distinct weight loss event at 300 °C was observed, which was attributed to the reaction of PMA and  $\text{LiNO}_3$ , with the liberation of  $\text{NO}_2$  and presumably  $\text{H}_3\text{PO}_4$ . The residual weight loss of the reaction product demonstrates that this reaction had not completed after 3 h at 350 °C, which would also be consistent with the presence of a non-crystalline phase.



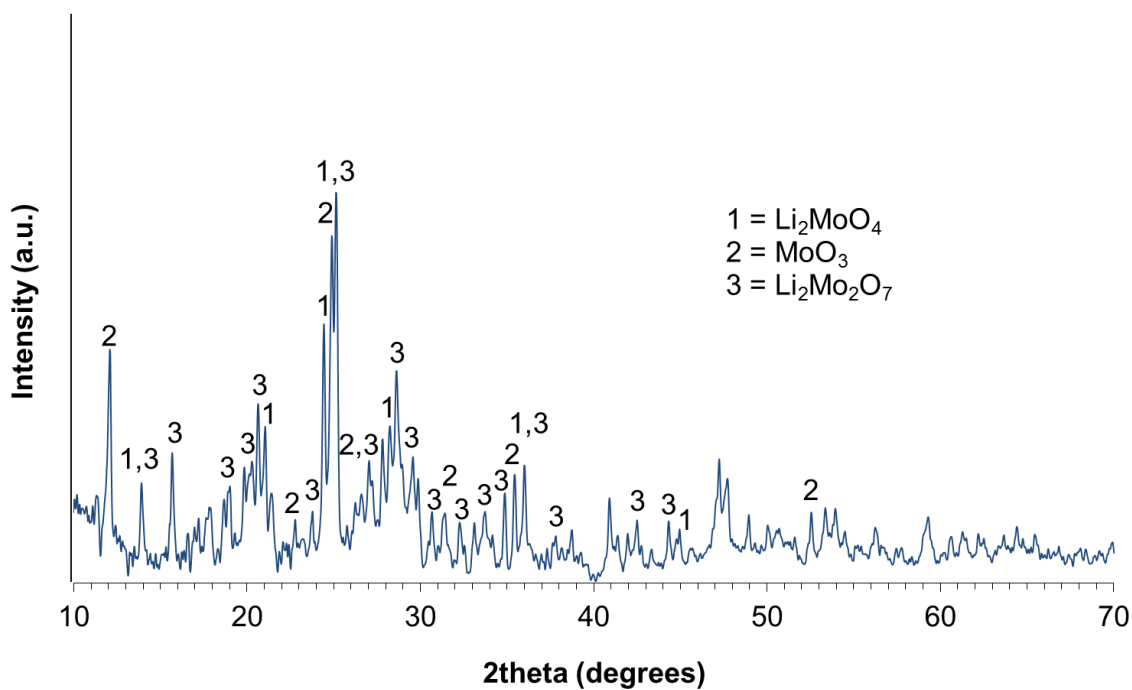


Figure 5.49 – XRD analysis of sample LPN1-350-3h using Co K $\alpha$ 1 radiation ( $\lambda = 1.789 \text{ \AA}$ )

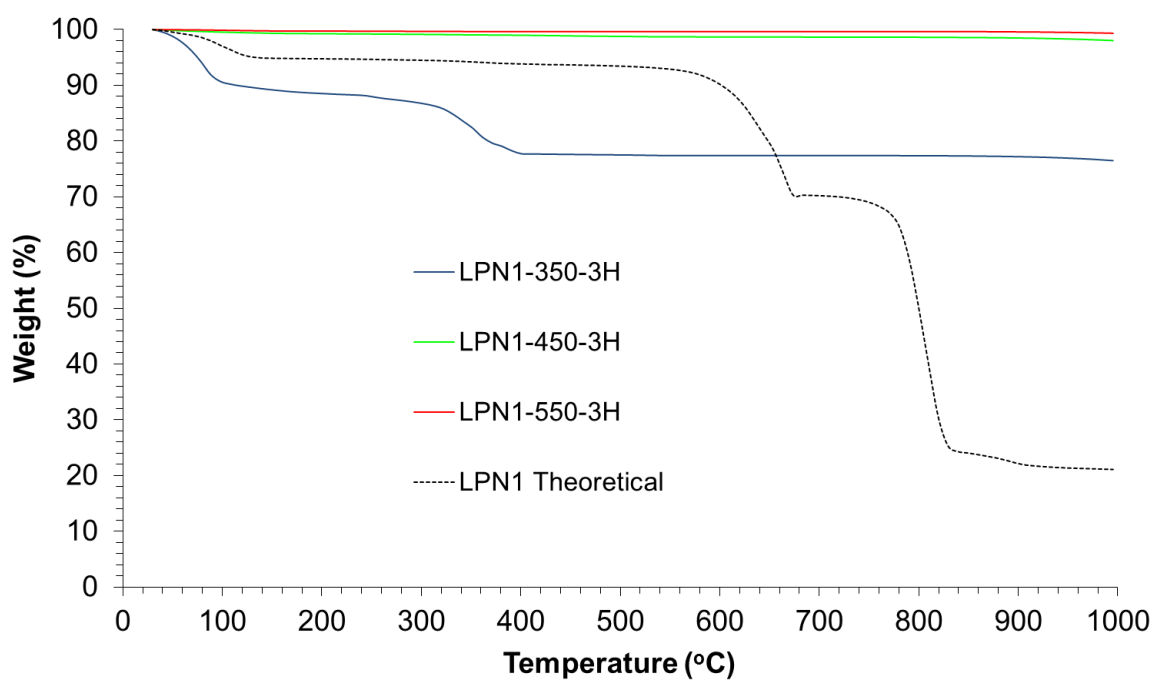
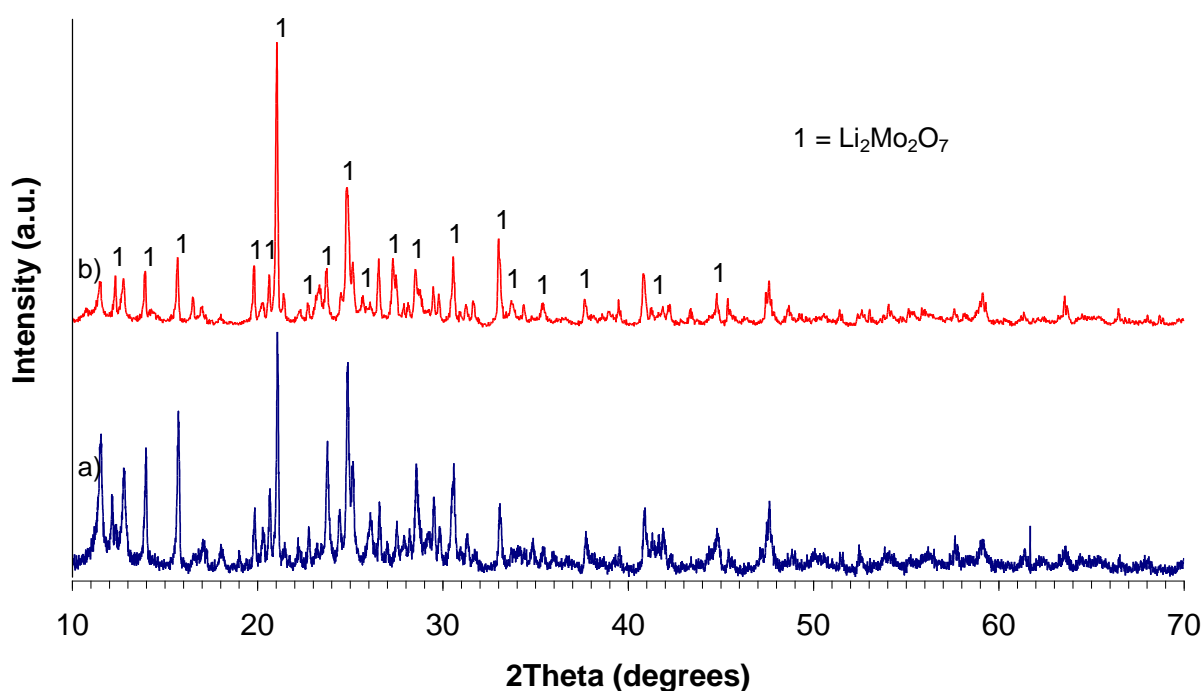


Figure 5.50 – TGA analysis of samples LPN1-350-3h, LPN1-450-3h and LPN1-550-3h

XRD analysis of products LPN1-450-3h and LPN1-550-3h (Figure 5.51) also showed the formation of  $\text{Li}_2\text{Mo}_2\text{O}_7$ , with signal-to-noise ratio improving with increased reaction temperature. Reflections associated with  $\text{Li}_2\text{MoO}_4$  and  $\text{MoO}_3$  were no longer present, suggesting a reaction had occurred to form  $\text{Li}_2\text{Mo}_2\text{O}_7$ . TGA analysis of products LPN1-450-3h and LPN1-550-3h (Figure 5.50) showed a total weight loss of 1.4 wt% and 0.4 wt%, respectively, at 700 °C. The distinct weight loss event at 300 °C observed for product LPN1-350-3h was not apparent, suggesting the reaction between PMA and  $\text{LiNO}_3$  had proceeded to completion. Interestingly, no evidence for significant volatilisation of  $\text{MoO}_3$  from the reaction product was observed above 800 °C, this is somewhat surprising given the reported melting point of  $\text{Li}_2\text{Mo}_2\text{O}_7$  is 530 °C (Cascales et al., 2005).



**Figure 5.51 – XRD analysis of samples a) LPN1-450-3h and b) LPN1-550-3h using Co K $\alpha$ 1 radiation ( $\lambda = 1.789 \text{ \AA}$ )**

Overall, it is possible to infer and conclude:

- PMA and  $\text{LiNO}_3$  react below 350 °C to yield  $\text{Li}_2\text{MoO}_4$ ,  $\text{MoO}_3$  and  $\text{Li}_2\text{Mo}_2\text{O}_7$ , but the reaction is incomplete after 3 h at 350 °C.
- Above 350 °C, the reaction between PMA and  $\text{LiNO}_3$  proceeds to completion, with  $\text{Li}_2\text{MoO}_4$  and  $\text{MoO}_3$  further reacting to yield  $\text{Li}_2\text{Mo}_2\text{O}_7$ .
- $\text{Li}_2\text{Mo}_2\text{O}_7$  does not undergo significant volatilisation below 1000 °C.

### 5.3.2.1.3 LPZN1

Dissolving PMA,  $\text{LiNO}_3$  and  $\text{ZrO}(\text{NO}_3)_2$ , sequentially, in water led to formation of a bright yellow precipitate, which was found to be non-crystalline by XRD (discussed further in section 5.3.2.2.3). XRD analysis of product LPZN1-350-3h (Figure 5.52) demonstrated reaction between  $\text{LiNO}_3$ , PMA and  $\text{ZrO}(\text{NO}_3)_2$  yielding  $\text{Li}_2\text{MoO}_4$ ,  $\text{MoO}_3$  and  $\text{Li}_2\text{Zr}(\text{MoO}_4)_3$ , ICDD cards [12-763], [01-073-6497] and [01-084-0171], respectively. TGA analysis of product LPZN1-350-3h (Figure 5.53) showed a total weight loss of 17 wt% at 700 °C, compared to the expected weight loss of 32 wt%, assuming complete denitration and dehydration of the reagents. The TGA data did not exhibit a weight loss event at 600 °C, characteristic of the denitration of  $\text{LiNO}_3$  (Appendix, Chun, 1977). A distinct weight loss event at 300 °C was observed, similar to that reported for product LPN1-350-3h, this is therefore attributed to the reaction of PMA and  $\text{LiNO}_3$ , with the liberation of  $\text{NO}_2$  and presumably  $\text{H}_3\text{PO}_4$ . The residual weight loss of the reaction product demonstrates that this reaction had not completed after 3 h at 350 °C.

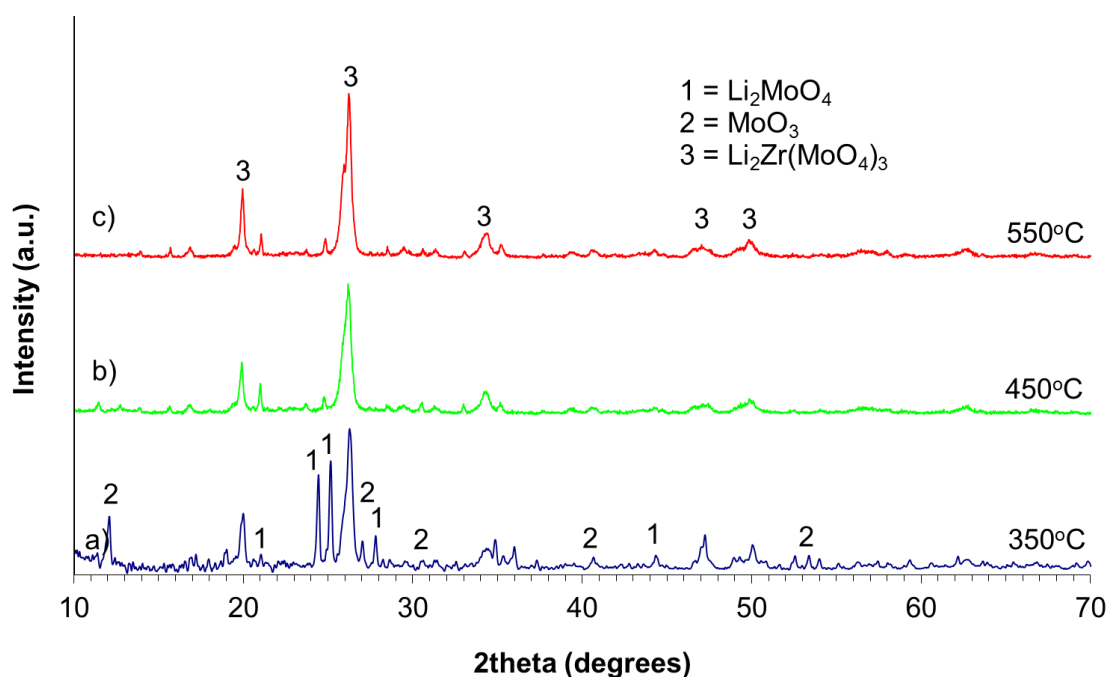


**Figure 5.52 – XRD analysis of the samples a) LPZN1-350-3h, b) LPZN1-450-3h and c) LPZN1-550-3h using Co K $\alpha$ 1 radiation ( $\lambda = 1.789 \text{ \AA}$ )**

XRD analysis of products LPZN1-450-3h and LPZN1-550-3h (Figure 5.52) also showed the formation of  $\text{Li}_2\text{Zr}(\text{MoO}_4)_3$ , with trace  $\text{Li}_2\text{MoO}_4$ . TGA analysis of products LPZN1-450-3h and LPZN1-550-3h (Figure 5.53) showed a total weight loss of 1.2 wt% and 0.2 wt%, respectively, at 700 °C. The distinct weight loss event at 300 °C observed for product LPZN1-350-3h was not apparent, suggesting the reaction had proceeded to completion. Consequently, it is inferred that the reaction mechanism involves:

- At 350 °C and below: formation of  $\text{Li}_2\text{MoO}_4$  by reaction between PMA and  $\text{LiNO}_3$ , and formation of  $\text{Li}_2\text{Zr}(\text{MoO}_4)_3$  by two possible pathways – i) reaction between  $\text{Li}_2\text{MoO}_4$  and  $\text{ZrO}(\text{NO}_3)_2$  or  $\text{ZrO}_2$  (produced by denitration of  $\text{ZrO}(\text{NO}_3)_2$ ); ii) reaction between PMA,  $\text{LiNO}_3$  and  $\text{ZrO}(\text{NO}_3)_2$  or  $\text{ZrO}_2$ . These reactions presumably involve evolution of  $\text{NO}_2$  and  $\text{H}_3\text{PO}_4$ .
- In the temperature window 350-450 °C,  $\text{Li}_2\text{MoO}_4$  reacts with residual non-crystalline  $\text{ZrO}_2$ , to yield  $\text{Li}_2\text{Zr}(\text{MoO}_4)_3$ . The presence of non-crystalline  $\text{ZrO}_2$  is inferred from residual TGA weight loss and XRD data of product PZN2-350-3h, and investigation of the reaction between PMA and  $\text{ZrO}(\text{NO}_3)_2$  (See Section 5.3.2.1.1).

Overall, these experiments reveal a strong influence of the effect of  $\text{LiNO}_3$  on the reaction between PMA and  $\text{ZrO}(\text{NO}_3)_2$ , involving the formation of  $\text{Li}_2\text{MoO}_4$  and  $\text{Li}_2\text{Zr}(\text{MoO}_4)_3$ , in preference to  $\text{Zr}(\text{MoO}_4)_2$ .

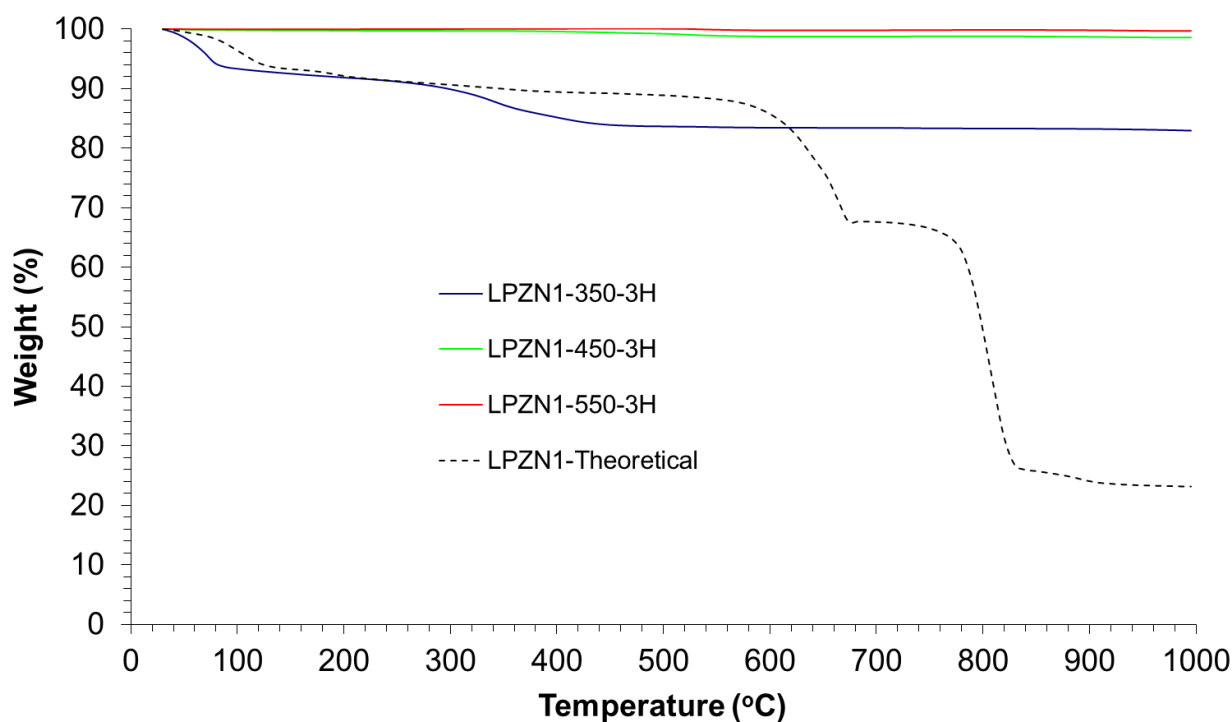


**Figure 5.53 – TGA analysis of samples LPZN1-350-3h, LPZN1-450-3h and LPZN1-550-3h**

### 5.3.2.2 Freeze dryer experiments

#### 5.3.2.2.1 PZN2

XRD data from sample PZN2-FD (Figure 5.54) showed reflections attributable to PMA together with considerable diffuse scattering associated with an additional non-crystalline product. TGA data from PZN2-FD (Figure 5.55) produced a weight loss curve with a very similar profile to that produced from summation of the weighted summed data from of PMA and  $\text{ZrO}(\text{NO}_3)_2$ . The weight loss achieved at 700 °C (prior to significant volatilisation of  $\text{MoO}_3$ ) was 14 wt%, identical to that expected from the weighted contribution of the individual components at this temperature. From these data it is apparent that  $\text{ZrO}(\text{NO}_3)_2$  was retained in the freeze drying step and, consistent with diffuse scattering observed in XRD data, is present in a non-crystalline form. The possibility of reaction between PMA and  $\text{ZrO}(\text{NO}_3)_2$  in the freeze drying step, to yield a non-crystalline product, cannot be excluded; however, this is thought to be unlikely because the evidence is that significant reaction occurs only above 350 °C (see Section 5.3.2.1.1 and below).

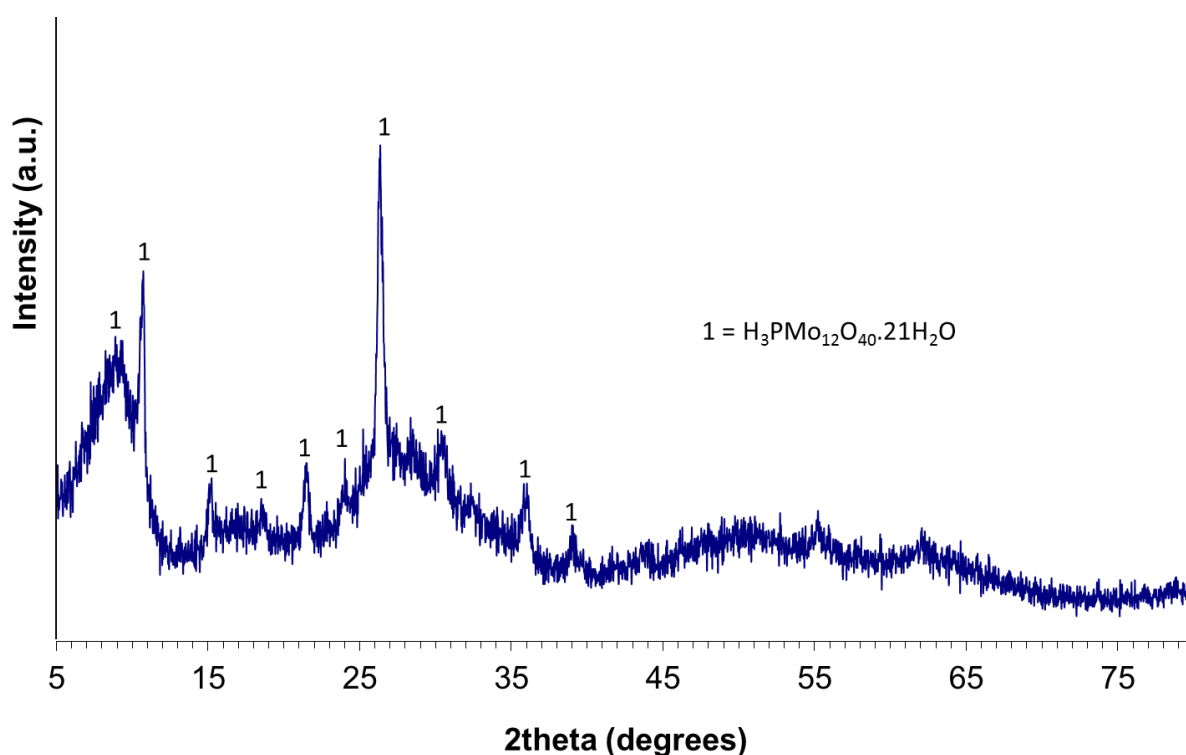


**Figure 5.54 – XRD analysis of sample PZN2-FD  
using Co K $\alpha$ 1 radiation ( $\lambda = 1.789 \text{ \AA}$ )**

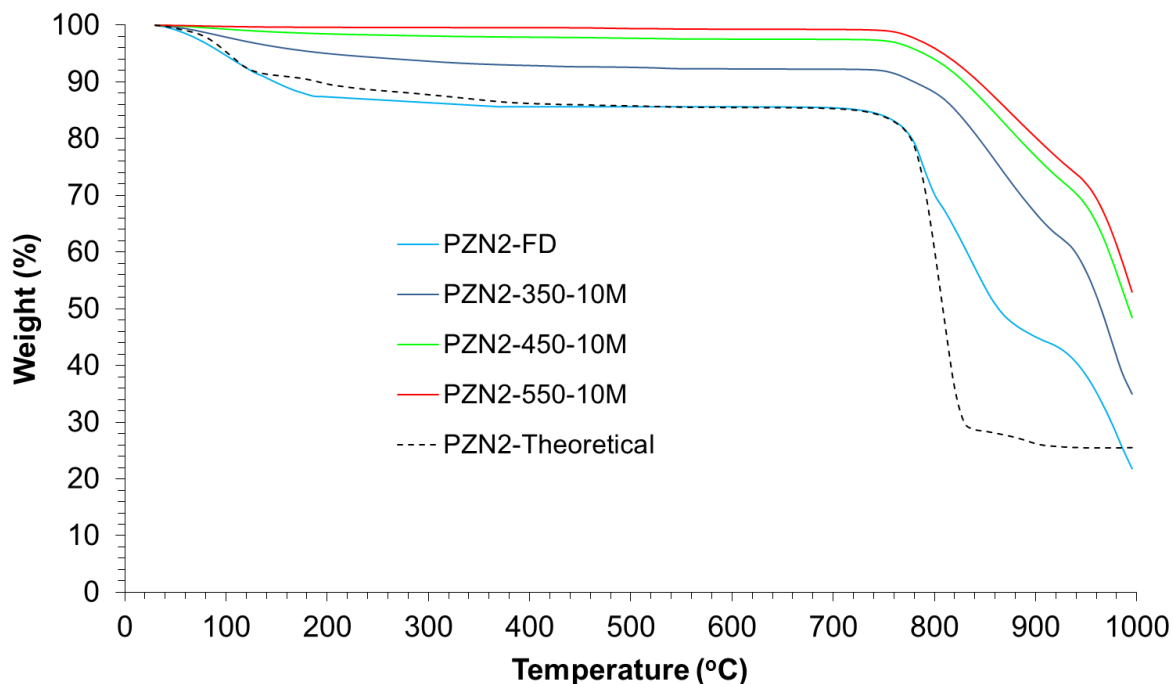


**Figure 5.55 – TGA analysis of samples PZN2-FD, PZN2-350-10m, PZN2-450-10m and PZN2-550-10m**

XRD analysis of products PZN2-350-5m, PZN2-350-10m, and PZN2-350-15m (Figure 5.56), all showed weak and broad reflections characteristic of PMA together with significant diffuse scattering. The TGA analysis of these products produced identical weight loss curves, hence, for clarity, only that for PZN2-350-10m is shown in Figure 5.55. The TGA data from product PZN2-350-10m confirmed the presence of residual PMA, demonstrating a small weight loss event at ca. 100°C characteristic of dehydration of this material (consistent with TGA analysis of PMA and literature data – Appendix, Tatibouet et al., 1997). The overall weight loss of product of PZN2-350-10m at 700 °C was 7.8 wt%, compared to the expected weight loss of 15 wt%, assuming complete denitration and dehydration of the reagents. From these data it is possible to infer dehydration of PMA and dehydration and partial denitration of  $\text{ZrO}(\text{NO}_3)_2$  after 3 h at 350 °C, with the latter yielding poorly crystalline or amorphous  $\text{ZrO}_2$ , consistent with the report of Hagiwara et al. (1975); no evidence of reaction between PMA and  $\text{ZrO}(\text{NO}_3)_2$  was apparent under these conditions. These data are essentially in agreement with reactions carried out on mixed metal nitrate solutions calcined at 350 °C for 3 h.

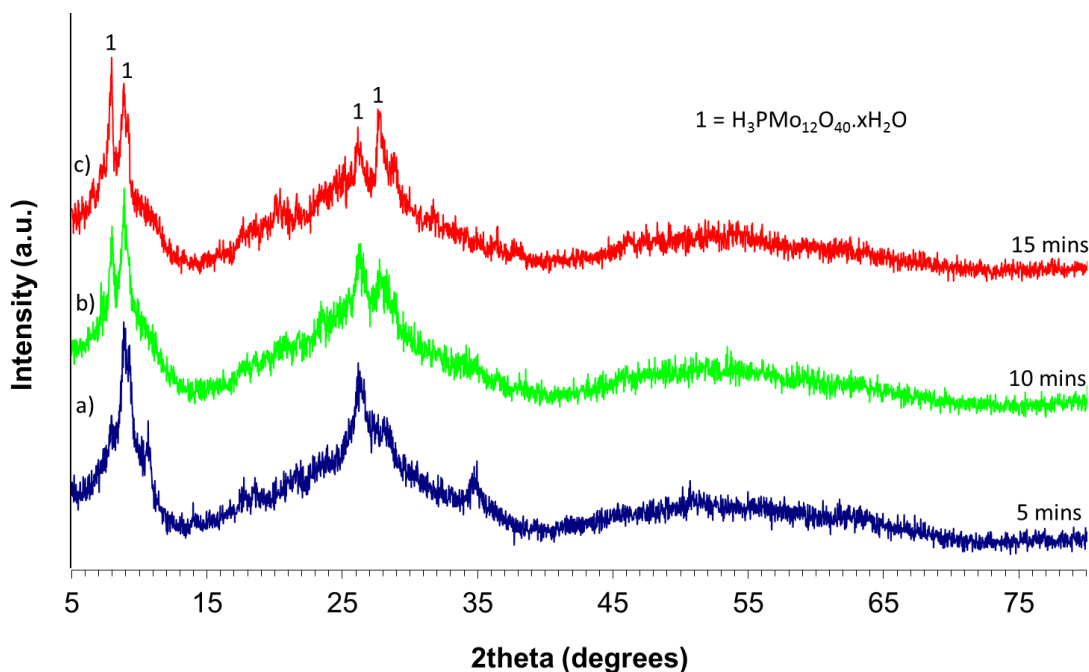


**Figure 5.56 – XRD analysis of samples a) PZN2-350-5m, b) PZN2-350-10m and c) PZN2-350-15m using Cu K $\alpha$ 1 radiation ( $\lambda = 1.546 \text{ \AA}$ )**

XRD analysis of products PZN2-450-5m showed weak and broad reflections characteristic of PMA together with significant diffuse scattering. These reflections were barely discernable in the XRD data of product PZN2-450-10m, which showed reflections attributable to  $\text{ZrO}_2$ ,  $\text{MoO}_3$ , and  $\text{Zr}(\text{MoO}_4)_2$ , in addition to significant diffuse scattering. Increasing the reaction time to 15 mins, product PZN2-450-15m, eliminated all reflections associated with PMA and reduced the contribution of diffuse scattering. The diffuse scattering in these diffraction patterns is attributed to non-crystalline  $\text{ZrO}_2$ , consistent with literature data on the low temperature decomposition of  $\text{ZrO}(\text{NO}_3)_2$ , as described in Section 5.3.2.1.1. The TGA analysis of these products produced similar weight loss curves, hence, for clarity, only that for PZN2-450-10m is shown in Figure 5.55. The TGA data from product PZN2-450-10m demonstrated a weight loss of 3.8 wt% at 700 °C, suggesting near complete thermal decomposition of PMA and  $\text{ZrO}(\text{NO}_3)_2$ , consistent with TGA analysis of these materials and available literature data (Section 5.3.2.1.1, Appendix, Tatibouet et al., 1997; Hagiwara et al., 1975). These data are essentially in agreement with reactions carried out on mixed metal nitrate solutions calcined at 450 °C for 3 h.

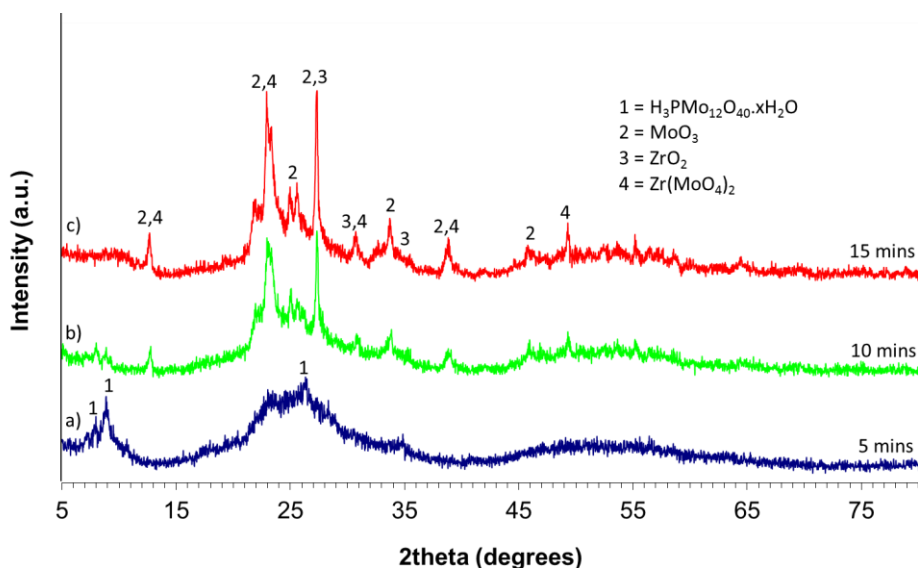


**Figure 5.57 – XRD analysis of samples a) PZN2-450-5m, b) PZN2-450-10m and c) PZN2-450-15m using Cu K $\alpha$ 1 radiation ( $\lambda = 1.546 \text{ \AA}$ )**

XRD analysis of products PZN2-550-5m, PZN2-550-10m and PZN2-550-15m (Figure 5.58) showed reflections attributable to  $\text{ZrO}_2$ ,  $\text{MoO}_3$ , and  $\text{Zr}(\text{MoO}_4)_2$ . The contribution of diffuse scattering in the XRD patterns of products derived from calcination of freeze dried material at  $550 \text{ }^\circ\text{C}$  was much less than that observed in the diffraction patterns acquired from products calcined at lower temperature. In addition, an increase in the relative intensity of reflections associated with  $\text{ZrO}_2$  was discernable, with increasing reaction time, suggesting crystallisation of this phase. The TGA data from product PZN2-550-15m demonstrated a weight loss of 0.8 wt% at  $700 \text{ }^\circ\text{C}$ , suggesting the reaction between PMA and non-crystalline  $\text{ZrO}_2$  had essentially progressed to completion. These data are essentially in agreement with reactions carried out on mixed metal nitrate solutions calcined at  $550 \text{ }^\circ\text{C}$  for 3 h.

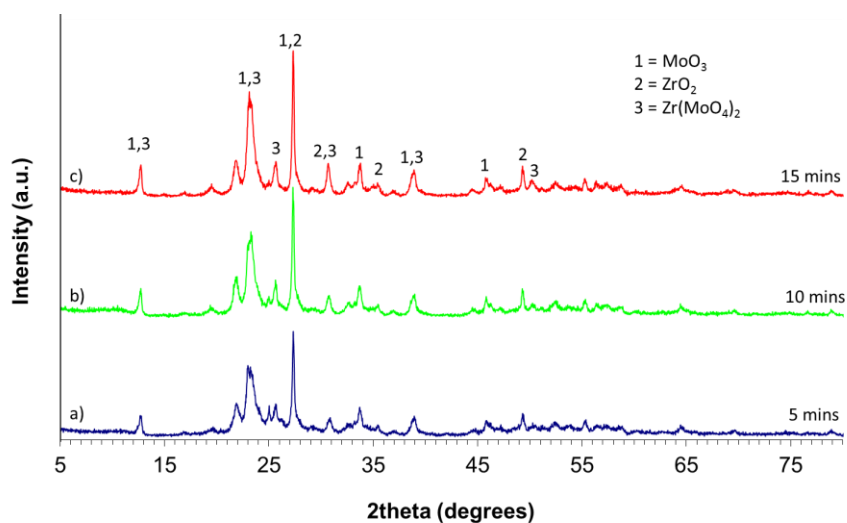


**Figure 5.58 – XRD analysis of samples a) PZN2-550-5m, b) PZN2-550-10m and c) PZN2-550-15m using Cu K $\alpha$ 1 radiation ( $\lambda = 1.546 \text{ \AA}$ )**



In conclusion, these data confirm the sequence of reactions proposed in Section 5.3.2.1.1 and, therefore, further extended discussion is not warranted. The observation of identical products and comparable residual weight loss after reaction for 5 mins and 3 h implies that these reactions are governed by rapid kinetics.

### 5.3.2.2.2 LPN1

XRD data from sample LPN1-FD (Figure 5.59) showed reflections attributable to  $\text{LiNO}_3$  and PMA together with considerable diffuse scattering associated with an additional non-crystalline component. TGA data from LPN1-FD (Figure 5.60) demonstrate a substantial weight loss of 28 wt% up to 150 °C, attributed to dehydration of the freeze dried material. By comparison with the weighted summed TGA weight loss profiles of the reaction components, which show a weight loss of 5.1 wt%, up to 150 °C, it can be inferred that the freeze drying process did not remove the full inventory of water. Loss of this water accounts for the apparent difference between the weight loss achieved at 700 °C for sample LPN1-FD (53 %) and the weighted summed TGA weight loss profiles of the reaction components (29 %). These data suggest that no reaction occurs between PMA and  $\text{LiNO}_3$  in the freeze drying step; this cannot be concluded definitively, due to the presence of a significant non-crystalline component, although this is always observed in the diffraction pattern of PMA.

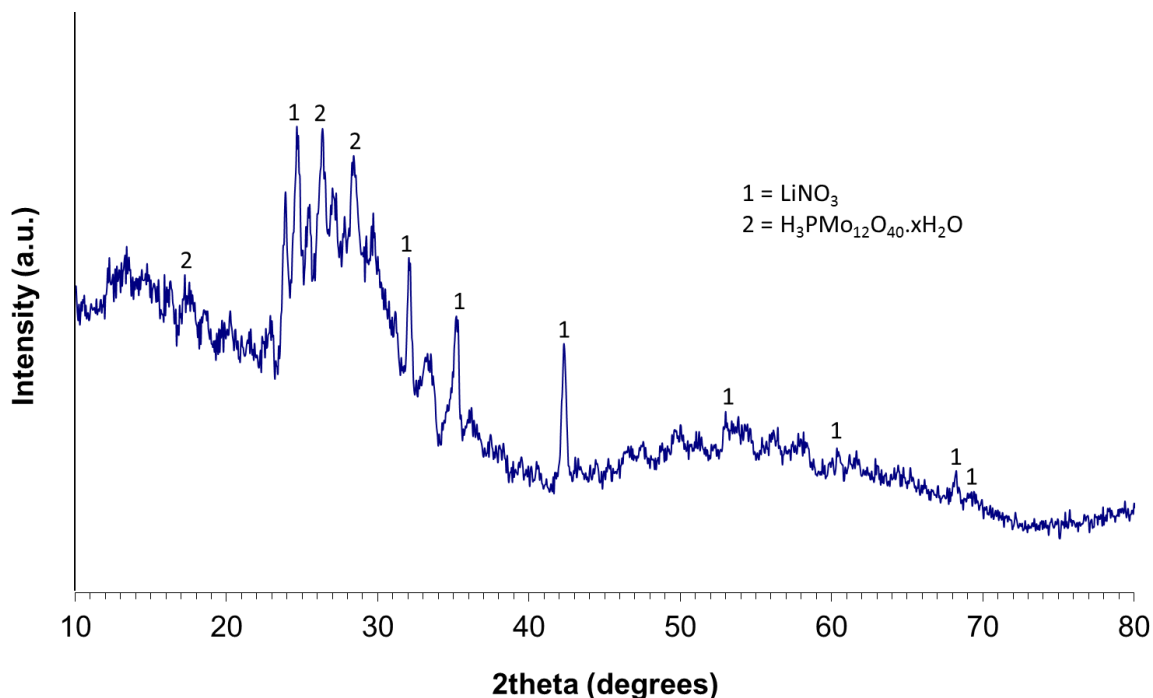
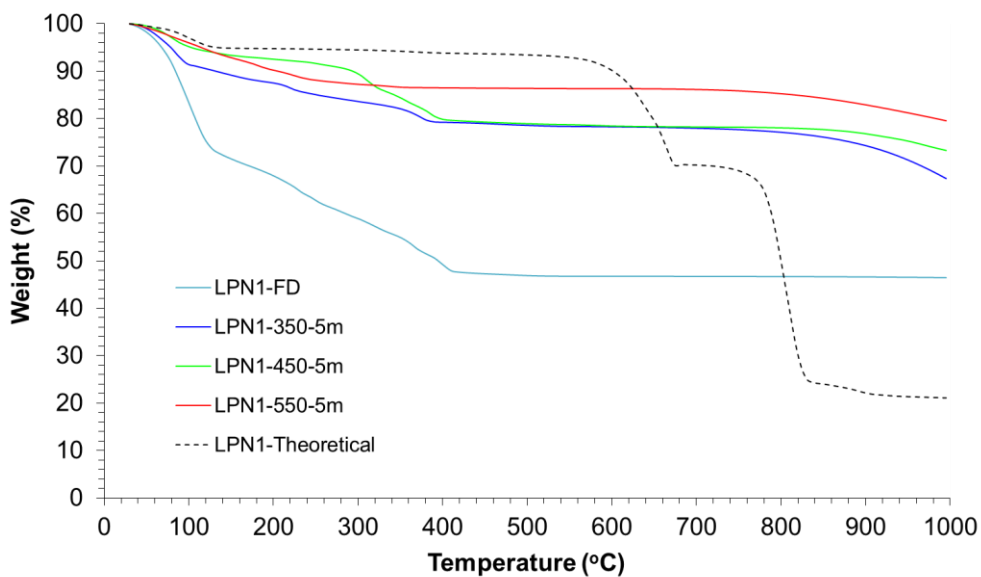


Figure 5.59 – XRD analysis of sample LPN1-FD using Co  $K\alpha 1$  radiation ( $\lambda = 1.789\text{\AA}$ )



**Figure 5.60 – TGA analysis of samples LPN1-FD  
LPN1-350-5m, LPN1-450-5m and LPN1-550-5m**

Figure 5.61 shows the XRD patterns of products LPN1-350-15m, LPN1-450-15m and LPN1-550-15m; the XRD patterns from products from 5 min and 10 min reactions at each temperature appeared identical to those from 15 min reactions and have therefore been omitted for the sake of brevity. The XRD patterns from products LPN1-450-15m and LPN1-550-15m exhibited reflections which matched, almost exclusively, to the reference pattern of  $\text{Li}_2\text{Mo}_2\text{O}_7$  [24-461]. Interestingly, the XRD pattern from product LPN1-350-15m showed reflections attributable to  $\text{Li}_2\text{MoO}_4$  and  $\text{MoO}_3$ , with additional reflections attributed to unidentified phase(s). TGA data of products LPN1-350-15m and LPN1-450-15m (Figure 5.62) showed similar weight loss of 22 wt% at 700 °C, suggesting incomplete reaction and retention of a substantial fraction of the volatile inventory. In comparison, TGA data of product LPN1-550-5m (Figure 5.60) showed a weight loss of 14 wt% at 700 °C, demonstrating an increased extent of, but incomplete, reaction. Overall these data are consistent with the conclusions on the reaction mechanism derived from experiments conducted for 3 h duration at the same temperatures. However, XRD data from product LPN-350-5min suggests that  $\text{Li}_2\text{Mo}_2\text{O}_7$  is formed *via*  $\text{Li}_2\text{MoO}_4$  as an intermediate. Thus, the inferred sequence of reactions is:

- PMA and  $\text{LiNO}_3$  react below 350 °C to yield  $\text{Li}_2\text{MoO}_4$  and  $\text{MoO}_3$  as kinetic products. At extended reaction time  $\text{Li}_2\text{Mo}_2\text{O}_7$  may be formed by reaction between PMA and  $\text{LiNO}_3$  and by reaction between  $\text{Li}_2\text{MoO}_4$  and  $\text{MoO}_3$ ; however, these reactions are incomplete after 3 h at 350 °C.
- Above 350 °C, the reaction between PMA and  $\text{LiNO}_3$  proceeds to completion, yielding  $\text{Li}_2\text{Mo}_2\text{O}_7$ .
- $\text{Li}_2\text{Mo}_2\text{O}_7$  does not undergo significant volatilisation below 1000 °C.

After calcination at 350 °C, the reaction between lithium nitrate and phosphomolybdic acid yielded  $\text{Li}_2\text{MoO}_4$  and  $\text{MoO}_3$  as kinetic products. After calcination at 450 and 550 °C for 15 mins, lithium molybdate, in the form  $\text{Li}_2\text{Mo}_2\text{O}_7$ , was formed (Figure 5.61). These reactions are consistent with the lab scale experiment where the sample was calcined for 3 hours.

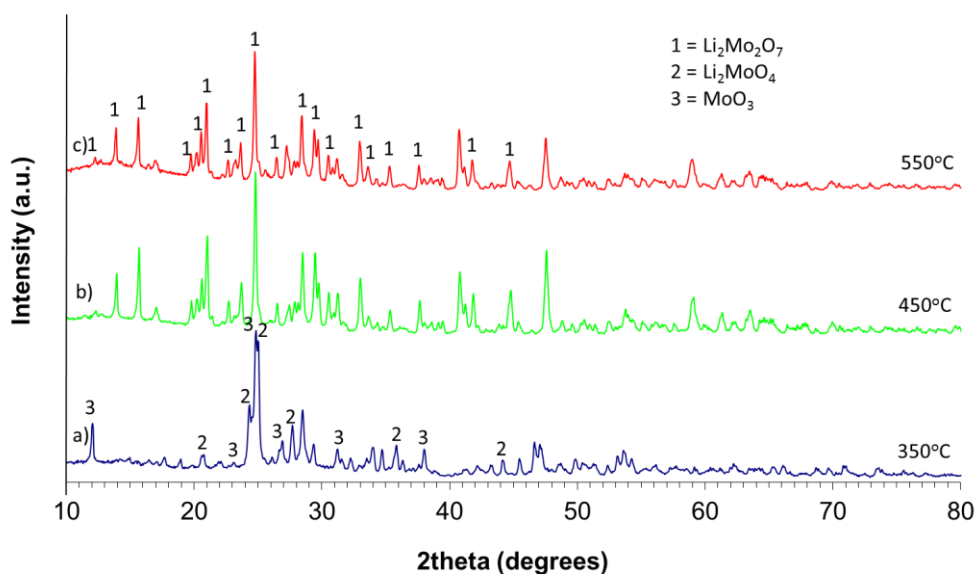


**Figure 5.61 – XRD analysis of samples a) LPN1-350-15m, b) LPN1-450-15m and c) LPN1-550-15m using Cu K $\alpha$ 1 radiation ( $\lambda = 1.546 \text{ \AA}$ )**

### 5.3.2.2.3 LPZN1

Dissolving PMA,  $\text{LiNO}_3$  and  $\text{ZrO}(\text{NO}_3)_2$ , sequentially, in 1.8 M  $\text{HNO}_3$  led to formation of a bright yellow precipitate, which was found to be non-crystalline by XRD (Figure 5.62). The XRD pattern was unchanged after freeze drying. There was a notable absence of reflections associated with  $\text{LiNO}_3$ ,  $\text{ZrO}(\text{NO}_3)_2$  and PMA. The absence of reflections attributable to the starting materials combined with the fact that the formation of this precipitate did not occur between any two of the components, without the presence of the third, suggested that  $\text{LiNO}_3$ ,  $\text{ZrO}(\text{NO}_3)_2$  and PMA all play a role in its formation. It is possible that the precipitate was a non-crystalline form of  $\text{Li}_2\text{Zr}(\text{MoO}_4)_3$ , however, the amorphous nature of the precipitate made it difficult to identify. It is known that caesium phosphomolybdate ( $\text{Cs}_3\text{PMo}_{12}\text{O}_{40} \cdot x\text{H}_2\text{O}$ ) is present in full HAL simulants as a yellow precipitate (Jiang et al., 2004), therefore formation of the lithium analogue ( $\text{Li}_3\text{PMo}_{12}\text{O}_{40} \cdot x\text{H}_2\text{O}$ ) in a non-crystalline form is a possibility.  $\text{ZrHPO}_4$  is also known to be insoluble in  $\text{HNO}_3$  and is found in the insoluble fraction of material present in the HASTs at Sellafield. Another possible explanation, therefore, is that non-crystalline forms of  $\text{Li}_2\text{MoO}_4$  and  $\text{ZrHPO}_4$  were produced in the presence of  $\text{LiNO}_3$ ,  $\text{ZrO}(\text{NO}_3)_2$  and PMA. However, these reactions did not take place in solution without the presence of all three reagents.

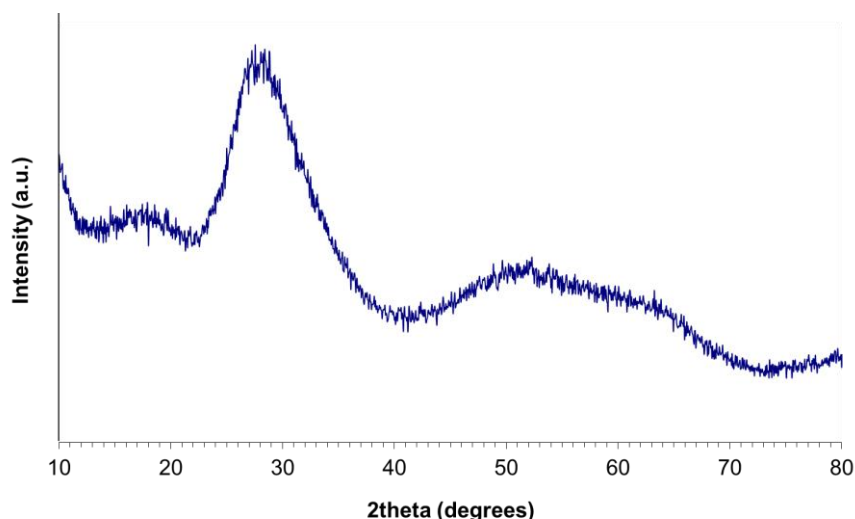


**Figure 5.62 – XRD analysis of sample LPZN1-FD using Cu K $\alpha$ 1 radiation ( $\lambda = 1.546 \text{ \AA}$ )**

Figure 5.63 shows the XRD patterns of products LPZN1-350-5m, LPZN1-350-10m and LPZN1-350-15m. The diffraction patterns of the products from reactions at 5 and 15 mins show only diffuse scattering, similar to the freeze dried product (Figure 5.62). The formation of  $\text{Li}_2\text{MoO}_4$  and  $\text{Li}_2\text{Zr}(\text{MoO}_4)_3$  can be identified in product LPZN1-350-15m, together with at least one other unidentified crystalline associated with unassigned reflections. XRD data from calcination of the freeze dried products at 450 °C and 550 °C appeared identical, irrespective of the calcination time, hence selected data for products LPZN1-450-5m, LPZN1-450-15m and LPZN1-550-15m are shown in Figure 5.66. These diffraction patterns show that the major reaction product formed at these temperatures is  $\text{Li}_2\text{Zr}(\text{MoO}_4)_3$ . Unfortunately, TGA data could not be obtained from the freeze dried products due to prohibitive reaction with the alumina sample pans.

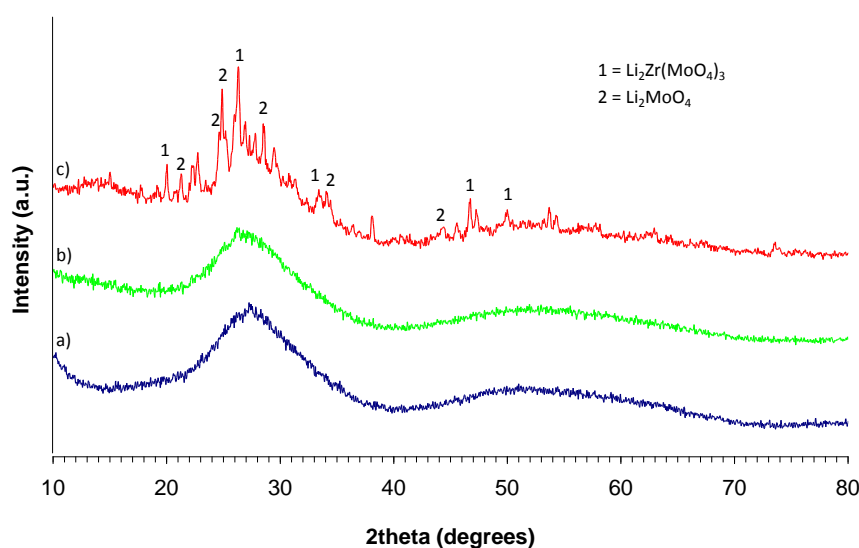


**Figure 5.63 – XRD analysis of samples a) LPZN1-350-5m, b) LPZN1-350-10m and c) LPZN1-350-15m using Cu K $\alpha$ 1 radiation ( $\lambda = 1.546 \text{ \AA}$ )**

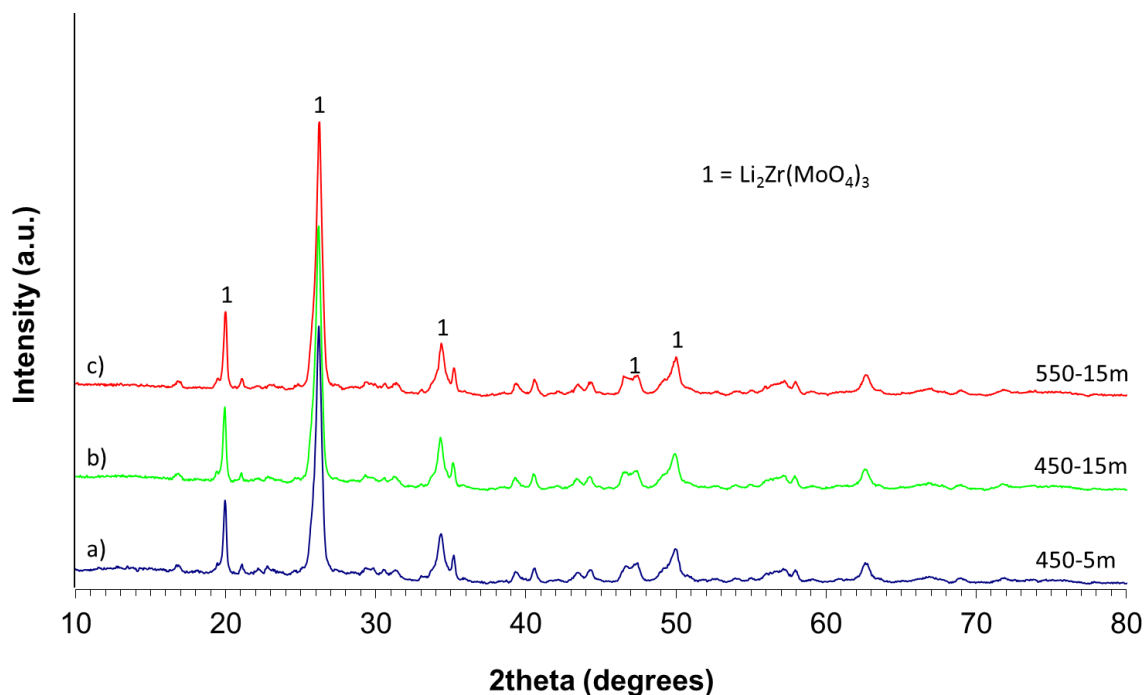


**Figure 5.64 – XRD analysis of samples a) LPZN1-450-5m, b) LPZN1-450-15m and c) LPZN1-550-5m using Co K $\alpha$ 1 radiation ( $\lambda = 1.789 \text{ \AA}$ )**

Figure 5.65 compares  $^7\text{Li}$  MAS NMR data from  $\text{LiNO}_3$ , LPZN1-FD, LPZN1-350-15m, LPZN1-350-3h, and LPZN1-550-15m, measured relative to  $\text{LiCl}$ . The spectrum of  $\text{LiNO}_3$  is dominated by a resonance centered at  $-0.09 \text{ ppm}$ , with a small broad component centered at  $-1.33 \text{ ppm}$  attributed to a small fraction of hydrated non crystalline material. The  $^7\text{Li}$  NMR spectrum of the freeze dried material, LPZN1-FD, exhibits a broad resonance at  $-0.32 \text{ ppm}$  and a very broad resonance  $-1.33 \text{ ppm}$ ; the former resonance is therefore attributed to the Li environment in the amorphous phase observed in XRD data. The  $^7\text{Li}$  NMR spectrum of LPZN1-350-15m was characterised by two resonances, centered at  $-0.38 \text{ ppm}$  and  $0.14 \text{ ppm}$ . The chemical shift of the broad resonance at  $-0.38 \text{ ppm}$  is consistent with that assigned to the non-crystalline phase in the freeze dried material and the observation of a significant non-crystalline phase in XRD data (Figure 5.62). The chemical shift of the relatively sharp resonance at  $0.14 \text{ ppm}$  suggests it is associated with a chemical environment in one of the unidentified crystalline phases observed in XRD data (Figure 5.63), but not  $\text{Li}_2\text{Zr}(\text{MoO}_4)_3$  (see below). The  $^7\text{Li}$  NMR spectrum of LPZN1-550-15m exhibited two resonances, centered at  $-0.14 \text{ ppm}$  and  $-0.40 \text{ ppm}$ . The resonance centred at  $-0.14 \text{ ppm}$  is also the dominant signal in the spectrum of product LPZN1-350-3h. Consistent with XRD data of these products, the signal at  $-0.14 \text{ ppm}$  is assigned to the Li environment in crystalline  $\text{Li}_2\text{Zr}(\text{MoO}_4)_3$ . The resonance centred at  $-0.40 \text{ ppm}$  in the  $^7\text{Li}$  NMR spectrum of LPZN1-550-15m implies the retention of a significant non-crystalline fraction, incorporating Li, which is not detected by XRD.

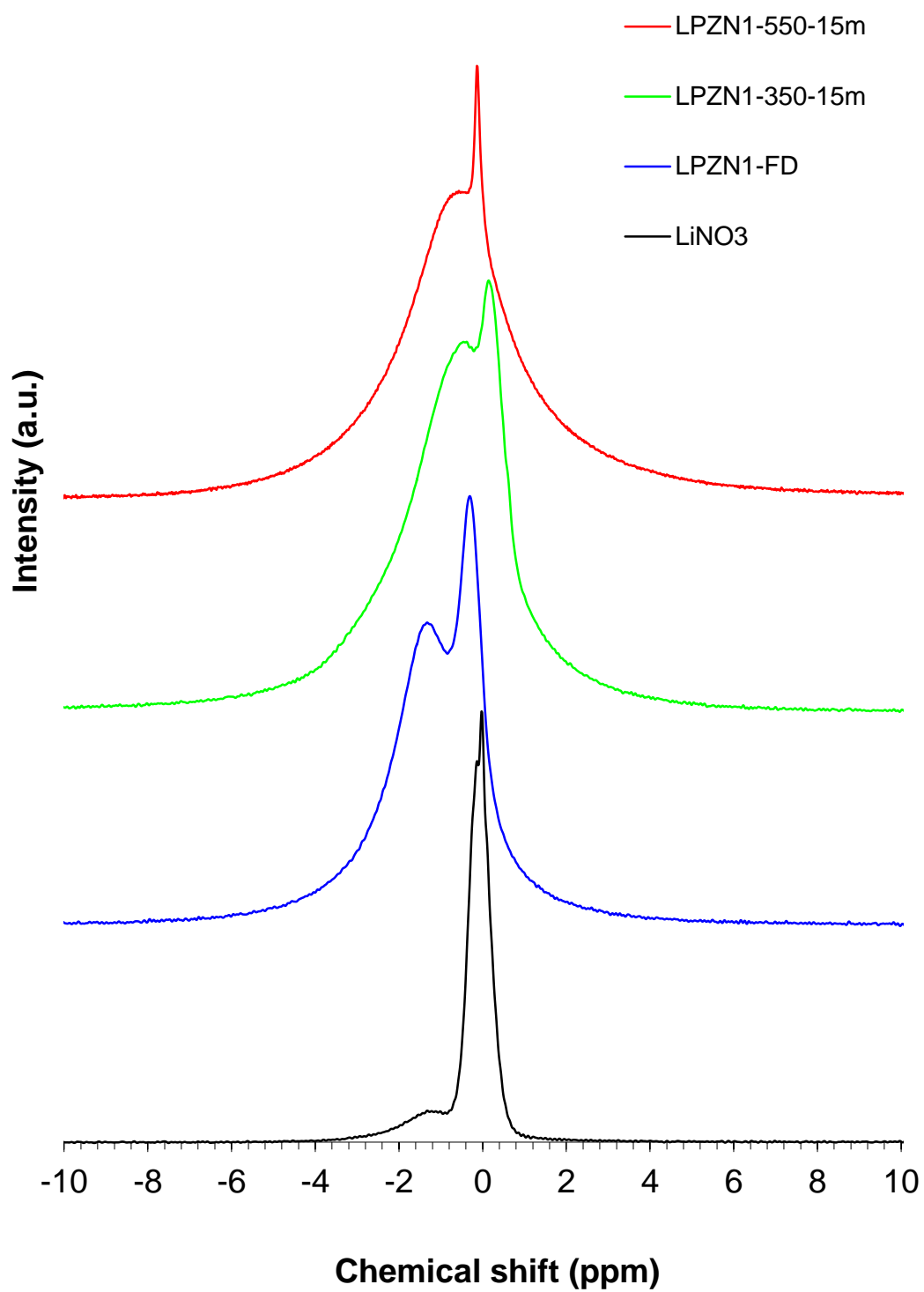
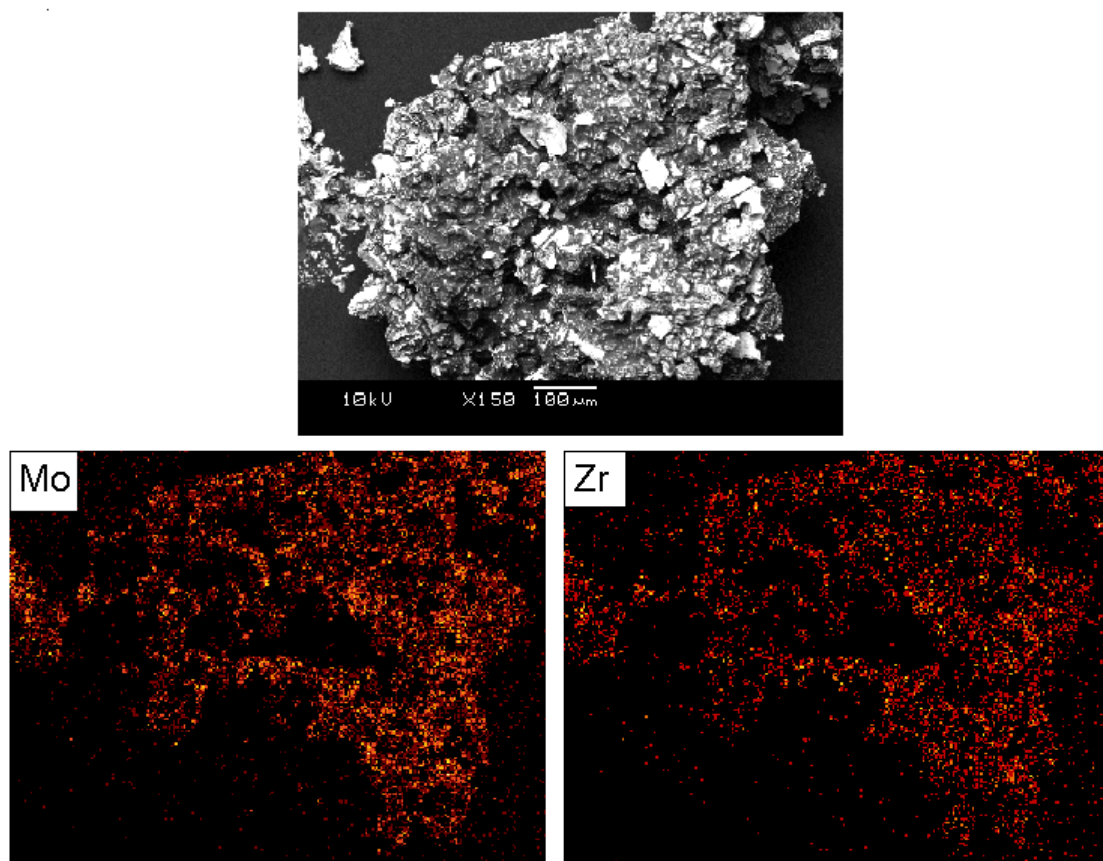


Figure 5.65 –  $^7\text{Li}$  MAS NMR spectra of samples LiNO<sub>3</sub>, LPZN1-FD, LPZN1-350-15m and LPZN1-550-15m

The backscattered electron image of product LPZN1-350-5m (Figure 5.66) showed that the sample was not homogeneous, proving the formation of multiple phases. The X-ray maps revealed a generally intimate association of Zr and Mo (Figure 5.66), however, some small regions were observed to be deficient in one element. This is consistent with the XRD data which showed amorphous phase(s) were formed.



**Figure 5.66 – Backscattered electron image (top) and X-ray maps showing the molybdenum and zirconium distribution (bottom) in sample LPZN1-350-5m**

After calcination at 550 °C for 15 minutes, the backscattered electron image of product LPZN1-550-15m (Figure 5.67) showed homogeneity throughout, with Zr and Mo showing an intimate association in all regions. This supported the XRD and TGA data which showed the formation of  $\text{Li}_2\text{Zr}(\text{MoO}_4)_3$  had occurred.

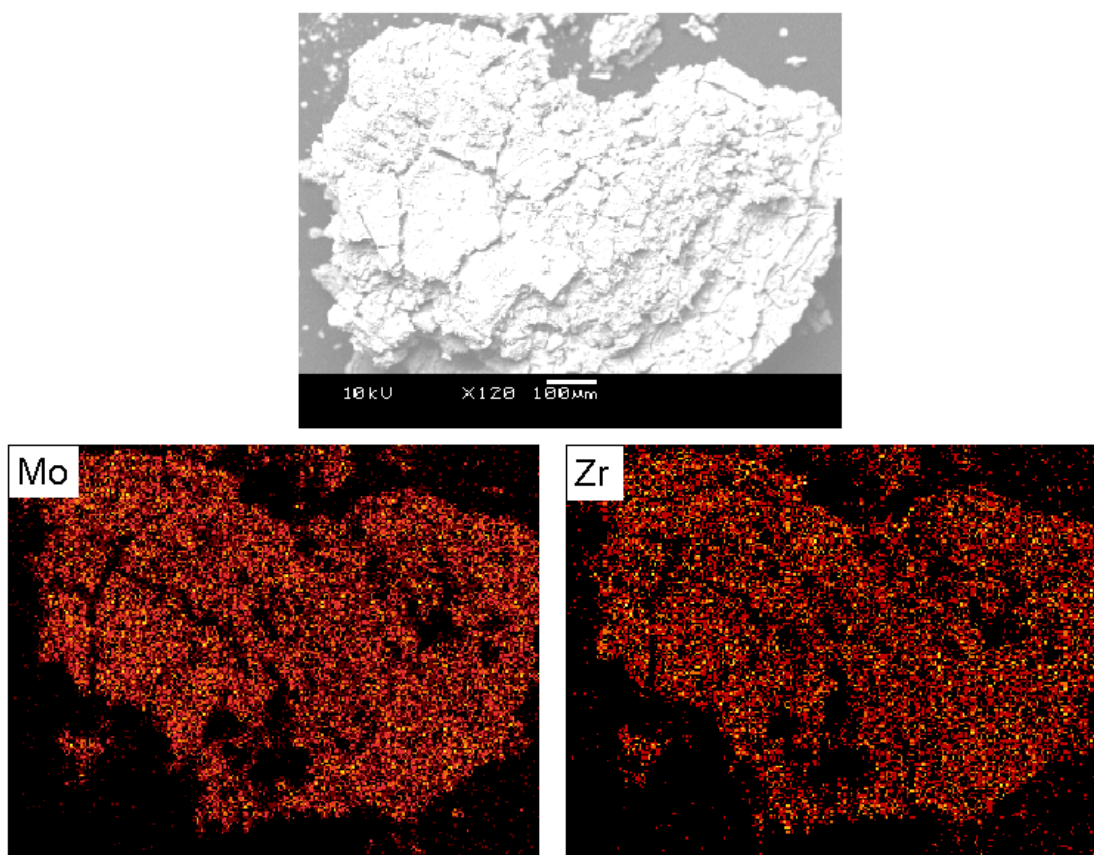


**Figure 5.67 – Backscattered electron image (top) and X-ray maps showing the molybdenum and zirconium distribution (bottom) in sample LPZN1-550-15m**

From these reactions it is possible to infer and conclude the following:

- Dissolving PMA,  $\text{LiNO}_3$  and  $\text{ZrO}(\text{NO}_3)_2$ , sequentially, in water led to formation of a bright yellow precipitate, which was found to be non-crystalline by XRD (figure 5.64). The freeze drying process did not alter the structure of the precipitate.
- Below 350 °C: After reaction times lower than 10 mins, there was no change to the reaction product. After 15 mins, crystallisation of  $\text{Li}_2\text{Zr}(\text{MoO}_4)_3$  and  $\text{Li}_2\text{MoO}_4$  occurred with an unidentified crystalline phase also being observed.
- Between 350-550 °C: The formation of  $\text{Li}_2\text{Zr}(\text{MoO}_4)_3$  occurs, in agreement with the 3 h experiments, showing a kinetically fast reaction under these calcination conditions.

Above 450 °C, the same reaction products are observed after 5 mins and 3h, showing under these conditions the reaction is governed by rapid kinetics.



### 5.3.2.3 Small scale calciner experiments

#### 5.3.2.3.1 PZN2

The product of calcination for sample PZN2-SSC-600 was comprised of a variety of different particle sizes. The portion greater than 2 mm in size was yellow in colour and will be referred to as PZN2-SSC-600-yellow. The calcine with a particle size less than 500  $\mu\text{m}$  was mostly white in colour (with some brown, attributed to residual calcine in the tube from previous experiments) and will be referred to as PZN2-SSC-600-white.

XRD data from sample PZN2-SSC-600-yellow (Figure 5.68) showed reflections attributable to PMA together with considerable diffuse scattering associated with an additional non-crystalline component, consistent with the presence of non-crystalline  $\text{ZrO}_2$  (Hagiwara et al., 1975). TGA analysis of PZN2-SSC-600-yellow (Figure 5.69) produced a weight loss curve with a very similar profile to that produced from product PZN2-350-15m, with the weight loss above 800  $^\circ\text{C}$  attributed to volatilisation of  $\text{MoO}_3$  (discussed in section 5.3.2.1.1). The weight loss achieved at 700  $^\circ\text{C}$  (prior to significant volatilisation of  $\text{MoO}_3$ ) was 13 wt%, almost identical to that shown for sample PZN2 after calcination at 350  $^\circ\text{C}$  for 15 mins. The XRD analysis showed the pattern of product PZN2-SSC-600-yellow was similar to that of the freeze dried sample, rather than when calcined at 350  $^\circ\text{C}$ , suggesting this temperature may not have been reached in the centre of the large particles.

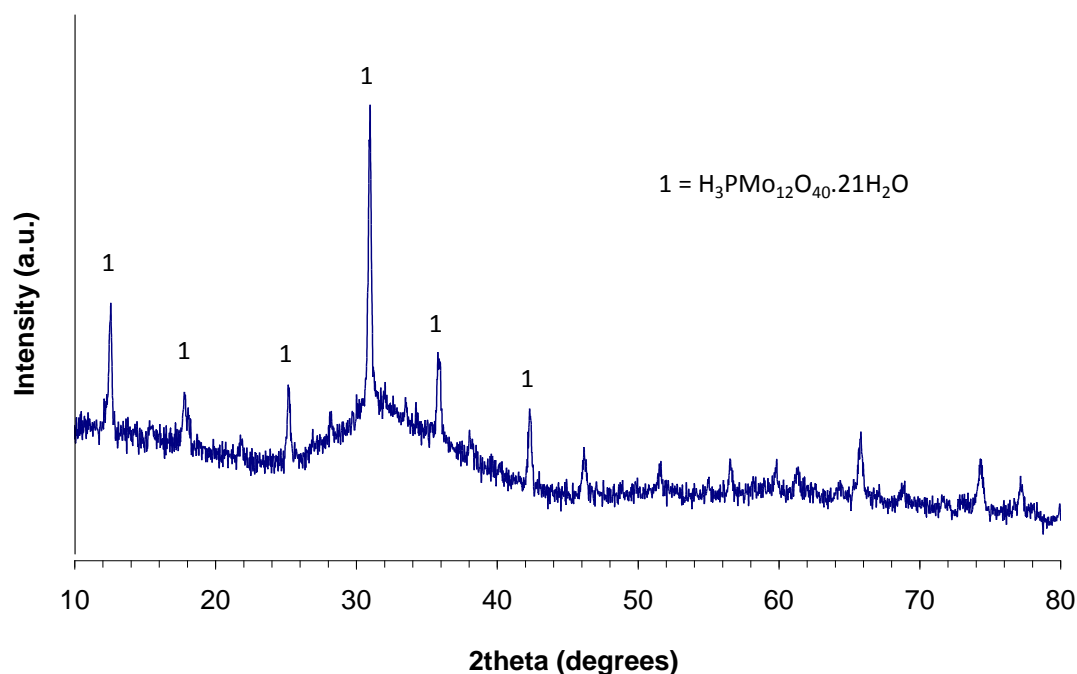


**Figure 5.68 - XRD analysis of sample PZN2-SSC-600-yellow using Co K $\alpha$ 1 radiation ( $\lambda = 1.789 \text{ \AA}$ )**

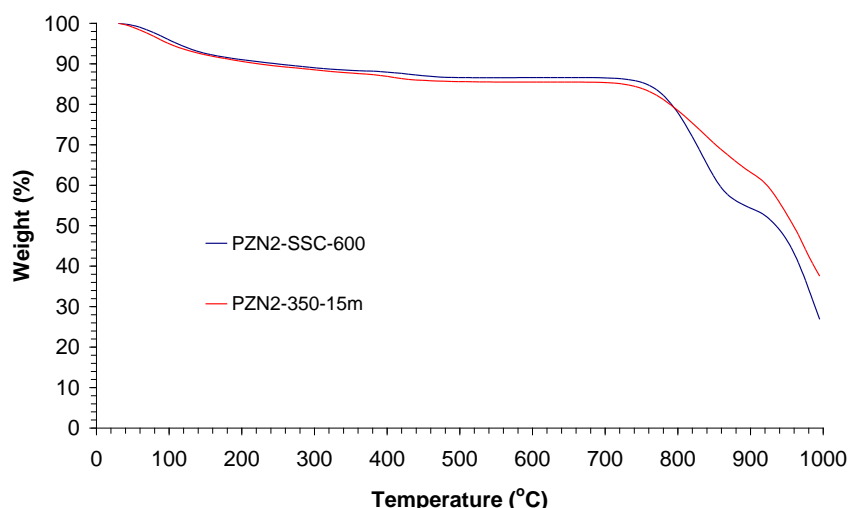


**Figure 5.69 – TGA analysis of sample PZN2-SSC-600-yellow**

Figure 5.70 shows the XRD pattern for sample PZN2-SSC-600-white, with reflections attributable to PMA,  $\text{MoO}_3$ ,  $\text{ZrO}_2$  and  $\text{Zr}(\text{MoO}_4)_2$  being observed. There was also significant diffuse scattering in these diffraction patterns, which is attributed to non-crystalline  $\text{ZrO}_2$ , consistent with literature data on the low temperature decomposition of  $\text{ZrO}(\text{NO}_3)_2$ , as described in Section 5.3.2.1.1. The TGA analysis of product PZN2-SSC-600-white produced similar weight loss curve to that for PZN2-450-10m (Figure 5.71). The TGA data from product PZN2-450-10m demonstrated a weight loss of 3.8 wt% at 700 °C, the same as PZN2-SSC-600-white, suggesting near complete thermal decomposition of PMA and  $\text{ZrO}(\text{NO}_3)_2$ , congruent with TGA analysis of these materials and available literature data (Section 5.3.2.1.1, Appendix, Tatibouet et al., 1997; Hagiwara et al, 1975). This is also consistent with the XRD data for PZN2-450-10m, as the only sample in this series of experiments to have PMA retained in the product, as well as showing the formation of  $\text{MoO}_3$ ,  $\text{ZrO}_2$  and  $\text{Zr}(\text{MoO}_4)_2$ .

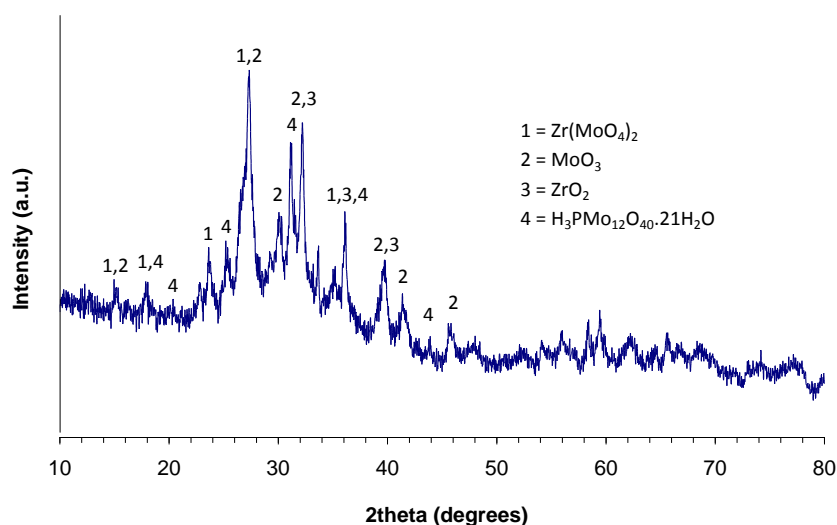


**Figure 5.70 - XRD analysis of sample PZN2-SSC-600-white using Co K $\alpha$ 1 radiation ( $\lambda = 1.789 \text{ \AA}$ )**

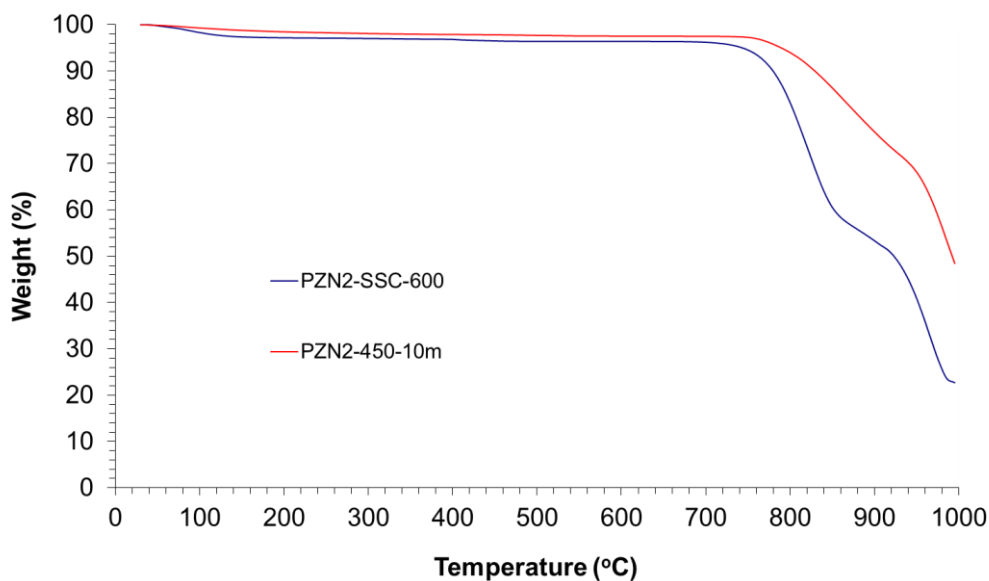


**Figure 5.71 – TGA analysis of sample PZN2-SSC-600-white**

Overall, these data imply that the temperature experienced by the calcine in the calcination process is highly dependent on particle size (shown in Chapter 6). Small particles (<500 µm) of product PZN2 appeared to experience temperatures of approximately 450 °C for 10 mins, with the large particles (>2 mm) not reaching 350 °C, by comparison to freeze dried results, with a zone 3 temperature set point of 600 °C. Previous residence time studies revealed the average time spent in the calciner is between 8-12 mins (Short, 2012) which is in agreement with these experiments. This is in contrast to products LMN1-SSC-600 and LAMN1-SSC-600, which appeared to experience temperatures of 550 °C or above, however, this can be explained by the fact that lithium creates a ‘sticky’ calcine due to its low melting point, increasing the residence time in the calciner.

### 5.3.2.3.2 LPN1

The XRD patterns from product LPN1-SSC-600 (Figure 5.72) exhibited reflections which matched, almost exclusively, the reference pattern of  $\text{Li}_2\text{Mo}_2\text{O}_7$ . TGA data of product LPN1-SSC-600 (Figure 5.73) showed a weight loss of 11 wt% at 700 °C, suggesting incomplete reaction and retention of a portion of the volatile inventory. In comparison, TGA data of product LPN1-550-15m (Figure 5.73) showed a weight loss of 14 wt% at 700 °C, demonstrating that product LPN1-SSC-600 had undergone a more complete reaction than that of the sample calcined at 550 °C for 15 mins. The reaction product is consistent with this series of experiments, identified as  $\text{Li}_2\text{Mo}_2\text{O}_7$  by XRD (Figure 5.72). These data suggest that the product may either have been in the calciner longer than 15 mins, or experienced a higher temperature than 550 °C (possible as the tube temperature was 600 °C in Zone 3). It is known that high lithium content creates a ‘sticky’ calcine as its melting point is 255 °C. This leads to longer residence times in the calciner.

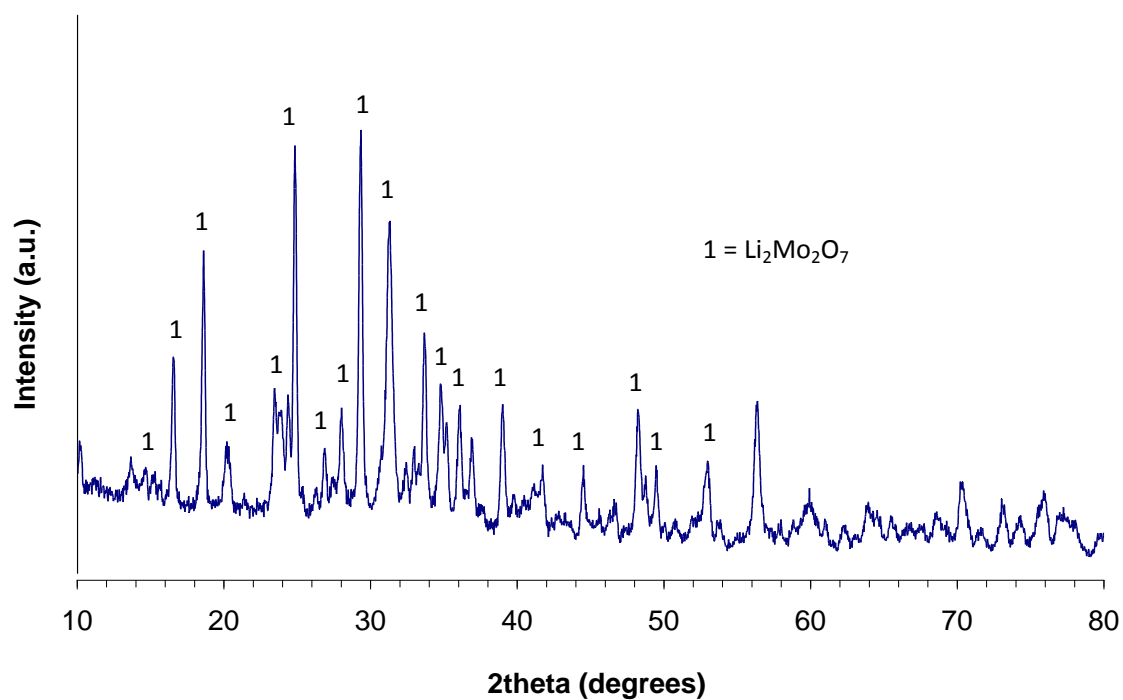


Figure 5.72 – XRD analysis of sample LPN1-SSC-600 using Co K $\alpha$ 1 radiation ( $\lambda = 1.789 \text{ \AA}$ )

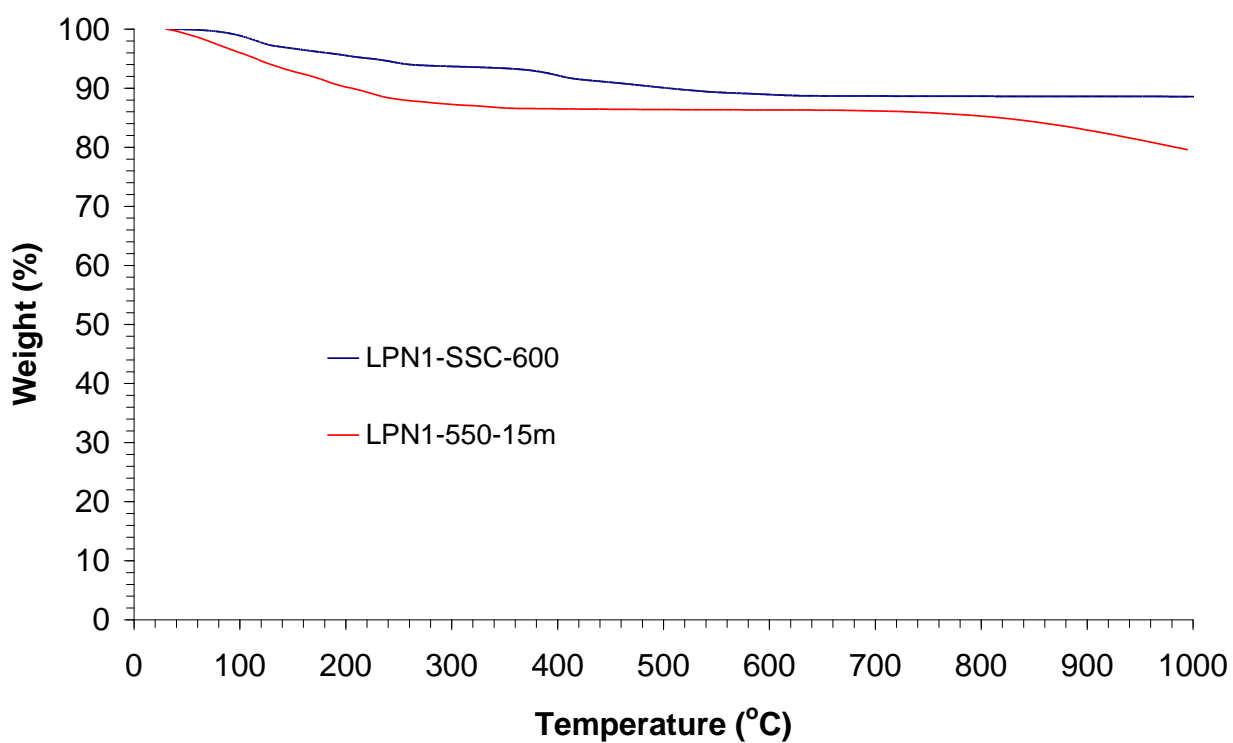
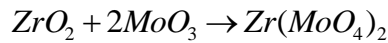
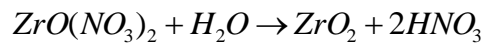
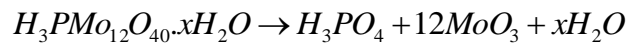


Figure 5.73 – TGA analysis of sample LPN1-SSC-600

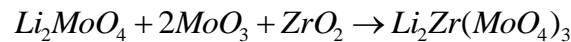
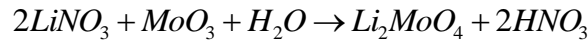
### 5.3.2.4 Discussion

The reaction between PMA and  $ZrO(NO_3)_2$  yielded  $Zr(MoO_4)_2$  as the major reaction product, however, on addition of  $LiNO_3$  there was a preference to the formation of  $Li_2Zr(MoO_4)_3$  via reaction of  $Li_2MoO_4$  with  $ZrO_2$  and  $MoO_3$  under calcination conditions relevant to full scale calcination. The reaction products identified for samples PZN2, LPN1 and LPZN1 after calcination at 350, 450 and 550 °C for 15 mins are summarised in Table 5.7.

The reaction mechanism for the formation of  $Zr(MoO_4)_2$  from PMA and  $ZrO(NO_3)_2$  is thought to be:



This is consistent with  $ZrO_2$ ,  $MoO_3$  and  $Zr(MoO_4)_2$  being the reaction products observed after calcination at 450 °C for 15 mins, with increased crystallisation occurring at 550 °C. The formation of these products on processing through the small scale calciner also show that it is possible to form  $Zr(MoO_4)_2$  under conditions comparable to the full scale process. However, on addition of  $LiNO_3$ , the mechanism changes resulting in the formation  $Li_2MoO_4$  and then  $Li_2Zr(MoO_4)_3$  in preference to  $Zr(MoO_4)_2$ :



Without the addition of  $ZrO(NO_3)_2$ ,  $Li_2Mo_2O_7$  was formed due to the ratio of Mo:Li in the product leaving free  $MoO_3$  to further react, in agreement with available literature (Tangri et al., 1994).

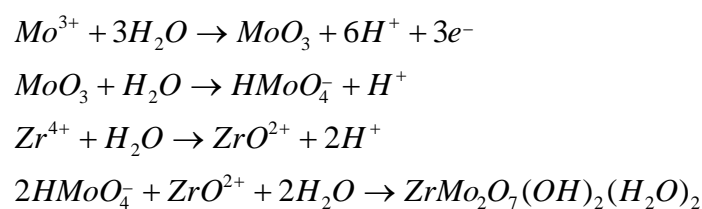


These data suggest that the reaction between PMA and  $ZrO(NO_3)_2$  yields  $Zr(MoO_4)_2$  after calcination above 450 °C. However, the addition of  $LiNO_3$  to a HAL simulant will prevent the formation of  $Zr(MoO_4)_2$  in the calcination process, instead yielding  $Li_2Zr(MoO_4)_3$ .

**Table 5.7 – Summary of the products formed in samples PZN2, LPN1 and LPZN1 after calcination for 15 mins at 350, 450 and 550 °C**

	Temperature (°C)		
	350	450	550
PZN2	H <sub>3</sub> PMo <sub>12</sub> O <sub>40</sub> .xH <sub>2</sub> O Non-crystalline ZrO <sub>2</sub>	MoO <sub>3</sub> ZrO <sub>2</sub> Zr(MoO <sub>4</sub> ) <sub>2</sub>	MoO <sub>3</sub> ZrO <sub>2</sub> Zr(MoO <sub>4</sub> ) <sub>2</sub>
LPN1	MoO <sub>3</sub> Li <sub>2</sub> MoO <sub>4</sub> Li <sub>2</sub> Mo <sub>2</sub> O <sub>7</sub>	Li <sub>2</sub> Mo <sub>2</sub> O <sub>7</sub>	Li <sub>2</sub> Mo <sub>2</sub> O <sub>7</sub>
LPZN1	Non-crystalline phase Li <sub>2</sub> MoO <sub>4</sub> Li <sub>2</sub> Zr(MoO <sub>4</sub> ) <sub>3</sub>	Li <sub>2</sub> Zr(MoO <sub>4</sub> ) <sub>3</sub>	Li <sub>2</sub> Zr(MoO <sub>4</sub> ) <sub>3</sub>

These reaction products were essentially the same after calcination for 3 h as they were after 15 mins, showing the reactions are governed by rapid kinetics and will occur in the timescales relevant to calcination on the full scale process. This is important as one of the major causes of blockages in the off-gas system is the formation of Zr(MoO<sub>4</sub>)<sub>2</sub> (or its hydrated form ZrMo<sub>2</sub>O<sub>7</sub>(OH)<sub>2</sub>(H<sub>2</sub>O)<sub>2</sub>) in the dust scrubber (Short, 2010). In full HAL simulants, caesium phosphomolybdate (CPM) is known to be present as a yellow precipitate (Neepa et al., 2013) and converts to ZrMo<sub>2</sub>O<sub>7</sub>(OH)<sub>2</sub>(H<sub>2</sub>O)<sub>2</sub> over a period of time (Edmondson et al., 2012) in the presence of ZrO(NO<sub>3</sub>)<sub>2</sub> in solution. Recent studies by Taylor et al. (2014) showed that the reaction between LiNO<sub>3</sub> and ZrMo<sub>2</sub>O<sub>7</sub>(OH)<sub>2</sub>(H<sub>2</sub>O)<sub>2</sub> yielded Li<sub>2</sub>MoO<sub>4</sub> and ZrO<sub>2</sub> when run on the small scale calciner. This is consistent with these studies which showed Li<sub>2</sub>MoO<sub>4</sub> was formed along with Li<sub>2</sub>Zr(MoO<sub>4</sub>)<sub>3</sub> in preference to Zr(MoO<sub>4</sub>)<sub>2</sub> on the addition of LiNO<sub>3</sub>. It is also in agreement with the formation of yellow-phase in the glass melt, of which CsLiMoO<sub>4</sub> is a known component (Morgan, 2004). Previous work by Short (2005) showed that the insoluble component of the calcine was high in Zr with a structure in the Fm-3m space group. Structures of this type include Zr<sub>2</sub>Gd<sub>2</sub>O<sub>7</sub> and Sm<sub>0.5</sub>Zr<sub>0.5</sub>O<sub>1.75</sub> (Short, 2005). These data suggest that Zr(MoO<sub>4</sub>)<sub>2</sub>, or its hydrated form, are not produced in the calcination process on full HAL simulants, however, they are known to form in the off-gas system (Short, 2010). An investigation by Izumida and Kawamura (1990) showed the precipitation of zirconium molybdate hydrate, ZrMo<sub>2</sub>O<sub>7</sub>(OH)<sub>2</sub>(H<sub>2</sub>O)<sub>2</sub> occurred from HAL simulant. The following reactions were used to explain this:



This suggests that the formation of  $\text{ZrMo}_2\text{O}_7(\text{OH})_2(\text{H}_2\text{O})_2$  takes place in solution, and is known to occur in the highly active storage tanks (HAST's) under aqueous conditions (Magnaldo et al., 2007; Richardson, 2000; Doucet et al., 2002). This investigation, combined with a review of the available literature, showed that  $\text{Zr}(\text{MoO}_4)_2$  could be formed under the relevant conditions attributed to the calcination process, however, in a full HAL simulant and / or in the presence of  $\text{LiNO}_3$  this would not occur due to competing reactions on heating and in the solid state. This showed that in the full HAL simulant there are many competing reactions due to the wide variety of species present in solution and formed in the calcination process. This highlights the limitations of this study in investigating the reactions which occur in the calcination process.

## 5.4 CONCLUSIONS

### 5.4.1 Reactions between aluminium and magnesium nitrates

- In the timescales relevant to full scale calcination, the kinetic products of the reaction between  $\text{Al}(\text{NO}_3)_3 \cdot 9\text{H}_2\text{O}$  and  $\text{Mg}(\text{NO}_3)_2 \cdot 6\text{H}_2\text{O}$  at 550 °C were poorly crystalline MgO and a non-crystalline phase thought to be  $\gamma\text{-Al}_2\text{O}_3$  via decomposition of an unidentified metastable intermediate formed at 450 °C. No observable reaction occurred after calcination at 350 °C.
- Al and Mg nitrates underwent further reaction after calcination at 550 °C for 3 h to form a Mg-Al-LDH of the form  $\text{Mg}_a\text{Al}(\text{OH})_{3+2a-c}(\text{NO}_3)_c \cdot x\text{H}_2\text{O}$ , through the reaction between MgO and  $\gamma\text{-Al}_2\text{O}_3$ , formed at 450 °C. When excess nitric acid was added, the absence of MgO and  $\gamma\text{-Al}_2\text{O}_3$  suggested the reaction had gone to completion yielding  $\text{Mg}_a\text{Al}(\text{OH})_{3+2a-c}(\text{NO}_3)_c \cdot x\text{H}_2\text{O}$ .
- On addition of  $\text{LiNO}_3$  to the reaction between  $\text{Al}(\text{NO}_3)_3 \cdot 9\text{H}_2\text{O}$  and  $\text{Mg}(\text{NO}_3)_2 \cdot 6\text{H}_2\text{O}$ , crystalline MgO and  $\gamma\text{-Al}_2\text{O}_3$  were formed at 550 °C for between 5-15 mins, with Li being present in a non-crystalline form. The same unidentified metastable intermediate as formed in product AMN1 at 450 °C was observed, though the formation occurred at a lower temperature and faster rate in the presence of  $\text{LiNO}_3$ .
- Further reaction at 450 and 550 °C for 3 h resulted in the formation of  $\text{MgAl}_2\text{O}_4$  through a template-growth reaction, where  $\text{LiNO}_3$  acted as a molten salt facilitating this reaction. However, this would not occur within the timeframe associated with full scale calcination.

- Li and Al nitrates reacted together after calcination between 350 °C and 450 °C for 3 h forming  $\text{LiAl}_2(\text{OH})_6(\text{NO}_3)_x \cdot x\text{H}_2\text{O}$  and an unidentified intermediate thought to be Li rich. This reaction went to completion at 550 °C.
- No observable reactions occurred between Mg or Al nitrates with  $\text{Fe}(\text{NO}_3)_3 \cdot 9\text{H}_2\text{O}$ .
- The reactions between  $\text{Al}(\text{NO}_3)_3 \cdot 9\text{H}_2\text{O}$  and  $\text{Mg}(\text{NO}_3)_2 \cdot 6\text{H}_2\text{O}$  appear to be kinetically slow and therefore would not go to completion within the calcination process.

#### 5.4.2 Reactions between phosphomolybdic acid and zirconyl nitrate

- PMA and  $\text{ZrO}(\text{NO}_3)_2$  appeared to undergo decomposition between 350 and 450 °C to form  $\text{MoO}_3$  and  $\text{ZrO}_2$ , with these resultant products undergoing further reaction to form  $\text{Zr}(\text{MoO}_4)_2$ . On further calcination above 800 °C, any un-reacted  $\text{MoO}_3$  was volatilised.
- When  $\text{LiNO}_3$  was added to the reaction between PMA and  $\text{ZrO}(\text{NO}_3)_2$ ,  $\text{Li}_2\text{Zr}(\text{MoO}_4)_3$  was formed above 350 °C *via* the intermediate  $\text{Li}_2\text{MoO}_4$  formed through the reaction between  $\text{LiNO}_3$  and PMA.
- Without the presence of  $\text{ZrO}(\text{NO}_3)_2$ ,  $\text{LiNO}_3$  and PMA undergo reaction to first form  $\text{Li}_2\text{MoO}_4$  and  $\text{MoO}_3$  at 350 °C for 5-15 mins, with further reaction occurring at longer residence times and higher temperature to form  $\text{Li}_2\text{Mo}_2\text{O}_7$ .
- These reactions are kinetically rapid and therefore would occur in the timescales of full scale calcination.

#### 5.4.3 Small scale calciner experiments

- The short simulants containing high concentrations of  $\text{LiNO}_3$  were held up in the calciner tube due to the low melting point of 255 °C, resulting in higher than normal residence times in the calciner. This made these simulants unsuitable for comparable runs to full HAL simulants.
- Short simulant PZN2 appeared to experience different temperatures at the different particle sizes which were formed during the calcination process. The larger particles were yellow in colour and contained a large portion of the PMA starting material, suggesting they experienced temperatures below 350 °C.
- The smaller particles were white in colour and appeared to have experienced temperatures of approximately 450 °C for a residence time of 10 minutes. This was much more representative of the full HAL simulants than the Li containing simulants.



## 5.5 FUTURE WORK

PMA was used as a starting material during these experiments as this is the compound used in the make-up of the full HAL simulants. However, CPM is known to be present in full HAL simulants as a yellow precipitate. Therefore, carrying out a set of experiments using CPM as the starting material could yield further answers into the reactivity of Mo containing compounds in the calciner. This would be beneficial as  $\text{CsLiMoO}_4$  is known to form during the calcination of full HAL simulants (Morgan, 2004) resulting in the formation of yellow-phase, which causes issues in the final vitrified glass product.  $\text{Zr}(\text{MoO}_4)_2$  (or ZMH in its hydrated form) is also responsible for causing blockages in the off-gas system, highlighting the importance of being able to model the reactivity of Mo throughout the vitrification process.

Work carried out by Short (2005b) suggested that Zr reacts with RE elements at high temperatures in full HAL simulants. Therefore, the reactivity of Zr at higher calcination temperatures with other HAL components should be explored. This would help determine whether ZMH is formed in the calcination process and transported to the off-gas system through the dust, or if Mo and Zr are transported in separate compounds and react together in solution.

The small scale calciner experiments highlighted the need to determine the temperatures experienced in the calcination process, as the addition of  $\text{LiNO}_3$  changed the perceived results as it produced 'sticky' calcine, increasing the residence time. The determination of the temperatures experienced in the calciner was the main focus of the work carried out in chapter 7, however, this only covered the short simulant PZN2. Further exploration of the effects of simulant composition on particle size, and thus temperatures experienced in the calcination process would allow better modelling of the processes which occur in the calcination process.

# 6. Effects of Lithium Nitrate on HAL Simulants in the Calcination Process

## 6.1 INTRODUCTION

The first of the two main focuses from this work was to compare the full HAL simulant samples with the short simulants analysed in chapter 5, to determine whether any comparisons could be drawn. Previous work on lab scale calcination of Magnox and Blend HAL simulants (Owens et al., 1985; Brace, 2005b) have shown that increasing Li concentration and decreasing temperature cause an increase in residual nitrate to be present in the calcine samples. Owens et al. (1985) showed that  $\text{LiNO}_3$  had reacted with a Magnox HAL simulant below 300 °C, however the reaction of lithium nitrate in solution remains unknown. Analysis of a freeze dried HAL simulant, without further heat treatment, has never been carried out. This will help provide an insight of the reactions which occur in solution, before any heat treatment is carried out. Analysis of this material will give a starting point to look at further reactions which take place at higher temperatures. The effects of  $\text{LiNO}_3$  addition, temperature and simulant composition were monitored through a series of systematic experiments.

There is an interest in discovering the composition and particle size of calcine particles which are carried from the calciner to the dust scrubber during VTR and WVP operations. This would allow the determination of the dust composition to see if is the same as the calcine or whether the insoluble components, such as  $\text{ZrMo}_2\text{O}_7(\text{OH})_2(\text{H}_2\text{O})_2$ , are preferentially carried over to the off-gas system. The particle size is also important, as small particles are difficult to remove from the dust scrubber recycle vessel (DSRV) on the VTR. Collecting the dust on the VTR is not possible, as the first sampling point on the VTR in the off-gas system is that of the dust scrubber liquor. As the majority of the dust is dissolved in the nitric acid, it is not possible to measure the size and densities of the soluble calcine particles. The second main focus of this section of work was, therefore, to use the small scale calciner to capture these dust particles<sup>11</sup> under a range of different calcination conditions so further analysis could be carried out. An investigation of the effects of temperature, simulant flow rate and Li addition on dust and calcine compositions and particle sizes was undertaken.

---

<sup>11</sup> The small scale calciner was modified for the purpose of capturing dust particles, as this had not been possible previously. The design, installation and issues with these modifications were discussed in Chapter 4.

## 6.2 EXPERIMENTAL

### 6.2.1 Freeze dryer experiments

As in Chapter 5, freeze drying of the HAL simulants was utilised to simulate the relatively short residence times in the calcination process. This was not possible using liquid samples because introducing the samples at the reaction temperature led to flash boiling and loss of the crucible contents. The samples were therefore first freeze-dried, to remove water, then the resultant solid was placed in the furnace at the desired temperature for 10 mins, shown to be the average residence time in the calciner (Brace, 2004). This approach was thought to give a representative sample, since the freeze-drying simulated the action of calciner Zones 1 and 2 (without heating), and the furnace simulated the conditions in Zones 3 and 4.

As an initial investigation, Blend<sup>12</sup> and Magnox HAL simulants (referred to as WRW16 and WRW17 respectively) with and without the addition of LiNO<sub>3</sub> were freeze dried, giving the products WRW16-RLF<sup>13</sup>, WRW16-RF, WRW17-RLF and WRW17-RF. The resultant products were analysed without further heat treatment and after calcination in a muffle furnace at 350 °C and 550 °C for 10 mins. The simulant compositions are given in Table 6.1.

### 6.2.2 Small scale calciner experiments

A preliminary investigation into the effects of LiNO<sub>3</sub> and calcination temperature on the dust carry-over from the calciner to the off-gas system was carried out using the VTR (Vickers, 2006a; Vickers, 2006c). A significant reduction in dust carry-over was reported on addition of LiNO<sub>3</sub> to the HAL feed, with the reduction increasing with increasing Li concentration. It was also reported that increased reaction temperatures gave rise to higher dust carry-over in the calcination process (Brace, 2006b). The mechanisms by which these observations occurred were unclear and the effects of increased reaction temperature and Li addition on the composition of the dust carried over were not determined. To address this issue, a series of experiments were conducted using the small scale calciner rig, where a Magnox HAL simulant was calcined with and without the addition of LiNO<sub>3</sub> to determine the effects on dust carry-over to the off-gas system. The hypothesis for this work package is:

Composition, particle size and amount of dust carried over to the off-gas system is dependent on calciner operating conditions and feed composition.

---

<sup>12</sup> Blend HAL simulant is a 25%/75% Magnox/UO<sub>2</sub> combined waste-stream.

<sup>13</sup> RLF stands for Ru and Li free. Ru free simulants were used as the VTR was running an experimental campaign using Ru free simulants at the time of experimentation. Ru is a very expensive product, adding significant cost to the simulant, plus there have already been extensive studies on the volatility of Ru in the calcination process. Therefore it was not necessary to use a Ru containing simulant in these experiments.

**Table 6.1 – Elemental composition of WRW16-RLF and WRW17-RLF simulants<sup>14</sup>**

Element	Concentration (g / l)	
	WRW16-RLF	WRW17-RLF
Na	0.21	0.52
Mg	7.00	22.00
Al	7.00	18.21
P	1.38	0.55
S	0.07	0.27
Cr	2.35	3.18
Fe	10.32	16.00
Ni	1.72	2.26
Sr	2.63	1.86
Y	1.70	1.08
Zr	13.44	8.18
Mo	10.81	7.53
Te	1.45	1.04
Cs	10.78	7.84
Ba	6.27	3.36
La	4.30	3.83
Ce	8.30	7.20
Pr	4.10	3.59
Nd	14.32	12.48
Sm	3.02	2.58
Gd	25.80	0

<sup>14</sup> Both simulant types were made up to between 1.5-1.7M HNO<sub>3</sub>. LiNO<sub>3</sub> was added as a 30wt% solution in 1.5M HNO<sub>3</sub> to the above simulants when required in pre-specified quantities as done on the VTR.

To answer this hypothesis, the range of experiments must explore the following:

- Changes in calciner operating temperature
- Changes in HAL simulant feed rate
- Changes in HAL simulant composition

These parameters were chosen as they are the range of variables which can be altered on the VTR and WVP plants. Increasing calcination temperature is known to reduce the residual nitrate content of the calcine (Owens et al., 1985; Brace 2005b) and has been shown to have an effect on the amount of dust generated and transferred to the off-gas system (Brace, 2006c). The rate at which HAL simulant is fed into the calciner is also known to have a significant impact on the residual nitrate of the resultant calcine and dust production (Brace, 2006a). This is due to the fact that reducing the feed rate (if all other parameters are kept constant) effectively reduces the evaporation time (moving the evaporative front closer to the front end of the tube) in the calciner tube, leaving a longer residence time for denitration processes to occur, hence a change in calcine composition is observed. In VTR trials, the temperature set-points of Zones 1 and 2 were increased to keep the evaporative front at the Zone 2/3 interface (half way down the calciner tube) at increased feed rates to keep the calcine composition consistent (Brace, 2006e).

When commissioning the small scale calciner rig, an initial investigation took place to determine the temperature set points and feed rates required to position the evaporative front approximately half way down the calciner tube (Brace, 2005c). These conditions were found to be set points of 400 °C in Zones 1 and 2 and 600 °C in Zone 3, with a feed rate of 3 l / h. This is thought to be as representative as possible in comparison to the VTR,<sup>15</sup> and therefore provided a central point for this series of experiments. Using these settings as a middle point, calcination temperatures of 500, 600 and 700 °C were chosen, with feed rates of 2, 3 and 4 l / h to give the experimental matrix (Table 6.2).

This experimental matrix was used for Magnox HAL simulant both with and without the addition of LiNO<sub>3</sub> (products WRW17-RLF and WRW17-RF). Sample nomenclature is shown in Table 6.1 for a Magnox simulant (WRW17) with Li addition (-RF), where the simulant type is followed by reaction temperature (-600) and finally feed rate (-3 l / h). Therefore, a Magnox simulant containing Li, calcined at 600 °C at a feed rate of 3 l / h would be named WRW17-RF-600-3l/h. Experiments on Blend HAL simulant (WRW16) were also carried out without Li addition at calcination temperatures of 500, 600 and 700 °C. However, due to time constraints and available simulant quantity, the full matrix of experiments could not be carried out using Blend HAL simulant.

---

<sup>15</sup> The calciner tube on the VTR has 4 heating Zones as opposed to the small scale calciners 3 Zones. Zones 1 and 2 are used for evaporation of the HAL simulant on the VTR, with denitration processes occurring in Zones 3 and 4, hence on the small scale calciner the evaporative front should be half way down Zone 2.

**Table 6.2 – Experimental matrix for small scale calciner experiments**

		Zone 3 Temperature (°C) <sup>16</sup>		
		500	600	700
Feed Rate (litres/hour)	2	x	WRW17-RF-600-2l/h	x
	3	WRW17-RF-500-3l/h	WRW17-RF-600-3l/h	WRW17-RF-700-3l/h
	4	x	WRW17-RF-600-4l/h	x

From each of the experiments, the calcine was collected in the pre-weighed calcine collection pot and subsequently weighed to find the mass of calcine produced. This calcine was then sieved through meshes with pore sizes of 0.5 mm and 2 mm and separated into the 3 corresponding fractions (>2 mm, 0.5-2 mm and <0.5 mm). Each fraction was weighed and the mass recorded to give a particle size distribution. Samples from each size fraction were analysed to determine the effects of particle size on the temperature experienced in the calcination process. Dust samples were collected from the dirt trap and the flexible hose connecting the calciner to the off-gas system. The combined mass was taken as the dust carry-over value<sup>17</sup>. Mass balance calculations were then carried out, outlined in section 6.2.2.1.

### 6.2.2.1 Calculating the expected yield from the small scale calciner experiments

Each of the small scale calciner experiments were run for a total of 1 hour with the calciner in feed. The Magnox HAL simulant feed used in these experiments has a total waste oxide concentration of 184.4 g / l<sup>18</sup>. The first step, therefore, was to calculate the total amount of waste oxide processed in the experiment (Equation 6.1).

$$TWO = T \times F \times WO \quad \text{(Equation 6.1)}$$

TWO is the total waste oxide throughput (g)

T is the duration of the experiment (h)

F is the feed rate of HAL simulant in the experiment (l / h)

WO is the waste oxide concentration of the HAL simulant (g / l)

<sup>16</sup> For simplicity, and to allow comparisons to be made between the samples at different temperatures, the decision was made to only alter the Zone 3 setpoint (the main denitration Zone), leaving Zones 1 and 2 set at 400 °C for all experiments carried out on the small scale calciner.

<sup>17</sup> It should be noted that dust is also collected in the upper end fitting of the calciner, which was not possible to collect, and a fraction will have been carried through the trap and dissolved in the dust scrubber.

<sup>18</sup> If all of the metal nitrates were decomposed into their component oxides, then 184.4 g of product would be formed per litre of HAL.

In the calcination process, however, a residual nitrate component is retained in the product and thus must be taken into account when calculating the expected yield. TGA analysis was carried out on each of the size fractions, giving a residual weight loss value for each. As we know the mass of each of the calcine size fractions, the total expected weight can be calculated using Equation 6.2:

$$EW = TWO + (TWO \times CF_{<0.5} \times WL_{<0.5}) + (TWO \times CF_{0.5-2} \times WL_{0.5-2}) + (TWO \times CF_{>2} \times WL_{>2})$$

(Equation 6.2)

EW is the expected weight (g)

CF<sub>x</sub> is the calcine fraction of particle size x (fraction)

WL<sub>x</sub> is the weight loss observed by TGA of particle size x (fraction)

These calculated expected weight values were then used in mass balance calculations to determine if the cumulative mass of the calcine and dust collected correlated with the expected throughput from the calcination experiments.

## 6.3 RESULTS AND DISCUSSION

### 6.3.1 Freeze dryer experiments

#### 6.3.1.1 WRW16-RLF (Blend HAL simulant – Ru and Li Free)

The XRD pattern of the reaction product WRW16-RLF-FD (Figure 6.1) showed a set of intense reflections showing the presence of caesium phosphomolybdate (CPM), a known precipitate in HAL simulants (Neepea et al., 2013; Edmondson et al., 2012). Other lower intensity reflections, attributable to Mg<sub>3</sub>RE<sub>2</sub>(NO<sub>3</sub>)<sub>12</sub>.24H<sub>2</sub>O<sup>19</sup> and Al(NO<sub>3</sub>)<sub>3</sub>.9H<sub>2</sub>O [12-472], were also observed, suggesting they are minor products compared to CPM. Some diffuse scattering was also apparent suggesting the presence of non-crystalline component(s). TGA analysis of product WRW16-RLF-FD (Figure 6.2) showed a total weight loss of 68 wt% at 1000 °C. This value must be the hypothetical weight loss for decomposition of all of the metal nitrates into their component oxides. The weight loss profile demonstrated three events: a sharp weight loss at 200 °C, attributed mainly to dehydration, with partial denitration of some species also occurring in this temperature range, such as Al(NO<sub>3</sub>)<sub>3</sub>.9H<sub>2</sub>O (identified by XRD), by reference to thermal stability data for this compound (Appendix; Pacewska and Keshr, 2002); a sharp weight loss at 250 °C; and a sharp weight loss at 380 °C, consistent with denitration of Mg<sub>3</sub>RE<sub>2</sub>(NO<sub>3</sub>)<sub>12</sub>.24H<sub>2</sub>O, as shown by thermal analysis of a precipitate collected from WRW16-RLF simulant upon evaporation, verified using XRD to be Mg<sub>3</sub>RE<sub>2</sub>(NO<sub>3</sub>)<sub>12</sub>.24H<sub>2</sub>O

---

<sup>19</sup> Mg<sub>3</sub>RE<sub>2</sub>(NO<sub>3</sub>)<sub>12</sub>.24H<sub>2</sub>O, where RE = La, Ce or Eu, are all present in the ICDD database and all have similar diffraction patterns (cards [12-761], [11-684] and [04-011-0137] respectively). Quill et al. (1937) showed Mg RE nitrates, where RE = La, Ce, Pr, Nd, Sm or Gd, could be formed *via* reaction between the corresponding metal nitrates.

(Appendix 2). The observation of  $\text{Mg}_3\text{RE}_2(\text{NO}_3)_{12}\cdot 24\text{H}_2\text{O}$  in the freeze dried material is consistent with studies carried out on the highly active storage tanks (HAST's) at Sellafield which showed precipitation occurs as evaporation of the HAL takes place (Richardson, 2002a). As the freeze drying process removes water from the HAL, essentially concentrating it, this would be expected as a major product due to the high concentration of Mg and rare earth nitrates in solution (Short, 2010c).  $\text{Mg}(\text{NO}_3)_2\cdot 6\text{H}_2\text{O}$  is known to form compounds of the type  $\text{Mg}_3\text{RE}_2(\text{NO}_3)_{12}\cdot 24\text{H}_2\text{O}$  through reaction with rare earth nitrates. These rare earth elements include La, Ce, Pr, Nd, Sm and Gd (Quill et al., 1937). The presence of  $\text{Al}(\text{NO}_3)_3\cdot 9\text{H}_2\text{O}$  in the freeze dried product implies that it undergoes no observable reaction in solution or during the freeze drying process. This is in agreement with the short simulant studies in chapter 5, which showed  $\text{Al}(\text{NO}_3)_3\cdot 9\text{H}_2\text{O}$  did not undergo reactions with  $\text{Mg}(\text{NO}_3)_2\cdot 6\text{H}_2\text{O}$  during the freeze drying process. Overall, these data showed Mg and RE nitrates react together to form  $\text{Mg}_3\text{RE}_2(\text{NO}_3)_{12}\cdot 24\text{H}_2\text{O}$  in solution, with subsequent precipitation during the evaporation process associated with freeze drying.  $\text{Al}(\text{NO}_3)_3\cdot 9\text{H}_2\text{O}$  remains unreacted in the product, which is consistent with TGA data showing a sharp weight loss at 200 °C. CPM was observed as the major crystalline component in the freeze dried product, consistent with the presence of the precipitate in the HAL simulant (Neepea et al., 2013). A co-existing non-crystalline component(s) was also shown to be present through significant diffuse scattering observed in the XRD pattern (Figure 6.1).

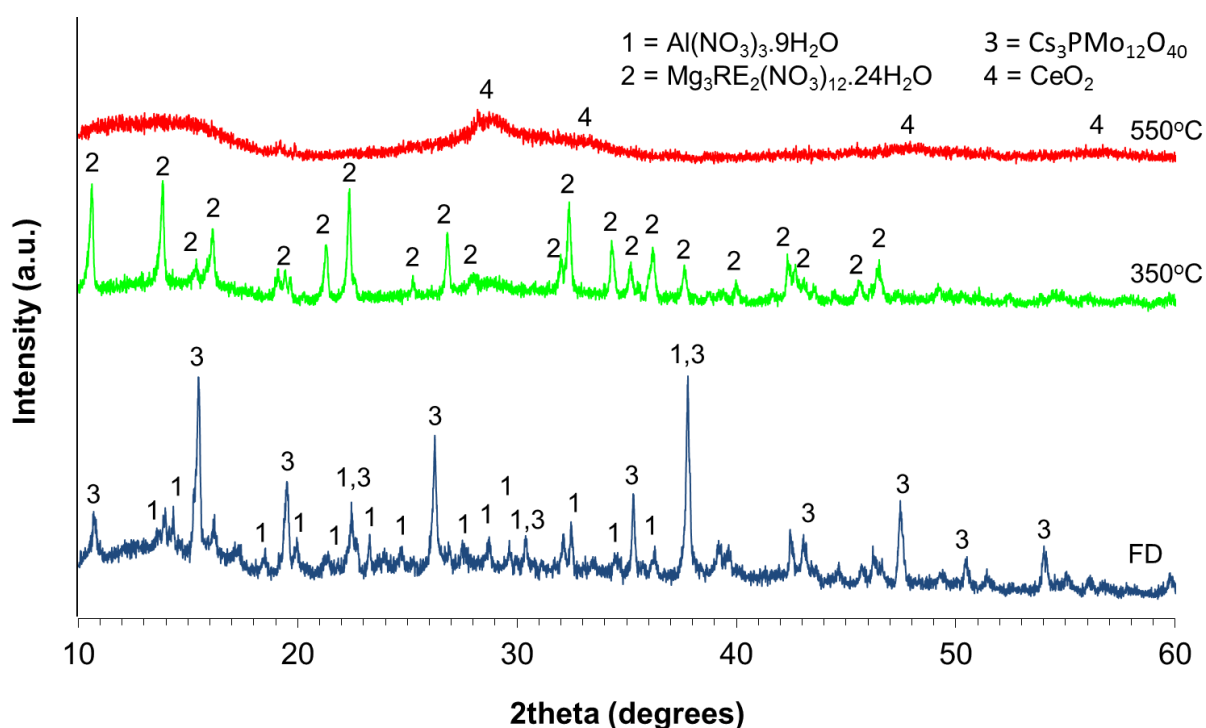


**Figure 6.1 – XRD analysis of products a) WRW16-RLF-FD, b) WRW16-RLF-350 and c) WRW16-RLF-550**



After heating at 350 °C for 10 mins, XRD analysis of product WRW16-RLF showed a set of reflections attributed to  $\text{Mg}_3\text{RE}_2(\text{NO}_3)_{12}\cdot 24\text{H}_2\text{O}$ . This accounted for essentially all of the reflections shown, with no peaks attributable to  $\text{Al}(\text{NO}_3)_3\cdot 9\text{H}_2\text{O}$  or CPM remaining in the product. Absence of the former is consistent with the partial decomposition of  $\text{Al}(\text{NO}_3)_3\cdot 9\text{H}_2\text{O}$ , to form an amorphous nitrate bearing product which is likely also hydrated, reported previously by Pacewska and Keshr (2002). Significant diffuse scattering was also observed, showing the presence of non-crystalline component(s). TGA analysis of product WRW16-RLF-350 (Figure 6.2) showed a total weight loss of 45 wt% at 1000 °C. This showed that significant dehydration and denitration of the freeze dried product had occurred. The weight loss profile demonstrated two events: a sharp weight loss at 200 °C, attributed to dehydration; and a sharp weight loss at 380 °C, consistent with denitration of  $\text{Mg}_3\text{RE}_2(\text{NO}_3)_{12}\cdot 24\text{H}_2\text{O}$  (Appendix 2). The former weight loss event was lower in intensity than for product WRW16-RLF-FD, which is in agreement with the XRD data showing  $\text{Al}(\text{NO}_3)_3\cdot 9\text{H}_2\text{O}$  had undergone partial decomposition to form a non-crystalline phase (consistent with previous work by Pacewska and Keshr, 2002). There was a notable absence of the sharp weight loss at 250 °C in product WRW16-RLF-350. Available literature (Zalewicz and Trzesowska, 2004) suggested this weight loss could be due to partial denitration of rare earth nitrates to form metastable intermediates of the type  $\text{REO}(\text{NO}_3)$ , where RE = La, Nd, Sm, Gd, Tb, Dy, Er or Lu. This is in agreement with the absence of this weight loss event in Magnox simulants (sections 6.3.1.3 and 6.3.1.4), as the increased Mg concentration coupled with reduced amounts of RE elements in solution results in the consumption of the RE elements to form  $\text{Mg}_3\text{RE}_2(\text{NO}_3)_{12}\cdot 24\text{H}_2\text{O}$ . The absence of the intense reflections, attributable to CPM, suggests it must react after calcination at 350 °C for 10 mins, with the resultant product being non-crystalline in nature. CPM is known to undergo transformation to  $\text{Zr}(\text{MoO}_4)_2$  at increased temperatures (Doucet et al., 2002), suggesting a reaction would occur in the calcination process. Overall, these data showed  $\text{Mg}_3\text{RE}_2(\text{NO}_3)_{12}\cdot 24\text{H}_2\text{O}$  was retained in the reaction product, consistent with TGA.  $\text{Al}(\text{NO}_3)_3\cdot 9\text{H}_2\text{O}$  was not observed in the reaction product, in agreement with a reduction in weight loss at 200 °C and in agreement with available literature (Pacewska and Keshr, 2002). The absence of CPM after calcination at 350 °C for 10 mins is consistent with it undergoing a reaction to form an amorphous phase, with significant diffuse scattering, observed in the XRD pattern (Figure 6.1), showing non-crystalline component(s) were present in the product WRW16-RLF-350.

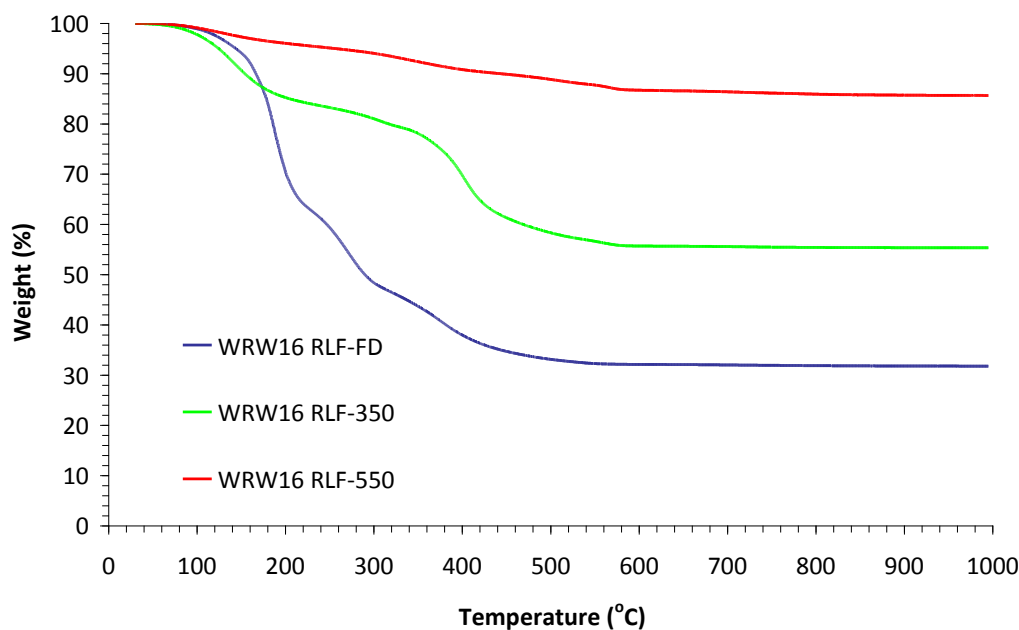


**Figure 6.2 – TGA analysis of products WRW16-RLF-FD, WRW16-RLF-350 and WRW16-RLF-550**

XRD analysis of product WRW16-RLF-550 (Figure 6.1) showed a diffraction pattern with diffuse scattering and very low signal-to noise ratio, indicating the presence of non-crystalline components. A set of very weak, broad reflections associated with the presence of  $\text{CeO}_2$  [04-593] were observed. TGA analysis of product WRW16-RLF-550 (Figure 6.2) exhibited a total weight loss of 14 wt% at 1000 °C, showing retention of the nitrate and hydrate inventory, though a reduction in the residual volatile portion of the product was observed with increasing temperature. The weight loss profile showed no distinct events, with a broad weight loss occurring between 100-600 °C. The sharp weight losses at 200 °C and 380 °C, present in the freeze dried sample and after calcination at 350 °C, were not present in product WRW16-RLF-550 (Figure 6.2). This is in agreement with the absence of reflections attributable to  $\text{Mg}_3\text{RE}_2(\text{NO}_3)_{12} \cdot 24\text{H}_2\text{O}$  in the diffraction pattern (Figure 6.1) and thermal analysis carried out on the precipitate from evaporation of WRW16-RLF simulant (Appendix 2). Denitration of  $\text{Ce}(\text{NO}_3)_3$  is known to occur between 220-240 °C (Strydom and van Vuuren, 1987) to form  $\text{CeO}_2$  in a single irreversible step, suggesting  $\text{CeO}_2$  is also present in product WRW16-RLF-350. However, the presence of  $\text{CeO}_2$  was not observed in the diffraction pattern after calcination at 350 °C, consistent with previous studies (Dunnett et al., 2009) which showed no reflections attributable to  $\text{CeO}_2$  were observed at 400 °C, but were present in a highly crystalline form after calcination at 1050 °C. This implies the crystallisation of  $\text{CeO}_2$  increases as a function of increasing temperature, shown by the presence of poorly crystalline reflections at 550 °C (Figure 6.1). These data showed that none of the crystalline phases, present in the freeze dried product, were present after calcination at 550 °C for 10 mins, in agreement with TGA analysis showing no distinct weight loss. The crystallisation of  $\text{CeO}_2$  was observed as very weak, broad peaks in the diffraction pattern (Figure 6.1).

From these experiments, it is possible to infer and conclude the following sequence of reactions:

- In the freeze dried sample, without further heat treatment, CPM,  $\text{Mg}_3\text{RE}_2(\text{NO}_3)_{12} \cdot 24\text{H}_2\text{O}$  and  $\text{Al}(\text{NO}_3)_3 \cdot 9\text{H}_2\text{O}$  were observed in the diffraction pattern with co-existing amorphous phase(s). These observations implied that Mg reacted with the RE elements in solution which then precipitated during the freeze drying process. The presence of  $\text{Al}(\text{NO}_3)_3 \cdot 9\text{H}_2\text{O}$  in the product suggests that it does not react in solution or in the freeze drying process. CPM is observed as a yellow precipitate in the HAL simulant and therefore undergoes no further reaction during the freeze drying process.
- After calcination at 350 °C,  $\text{Mg}_3\text{RE}_2(\text{NO}_3)_{12} \cdot 24\text{H}_2\text{O}$  appeared to be the only crystalline phase present in product WRW16-RLF-350. Reflections attributable to  $\text{Al}(\text{NO}_3)_3 \cdot 9\text{H}_2\text{O}$  or CPM were not observed, suggesting they undergo decomposition / reaction to form non-crystalline components. Absence of  $\text{Al}(\text{NO}_3)_3 \cdot 9\text{H}_2\text{O}$  is consistent with thermal analysis and available literature (Appendix; Pacewska and Keshr, 2002) which showed the formation of an amorphous product after calcination at 350 °C. A significant amount of non-crystalline material was shown to be present by the strong diffuse scattering in the XRD pattern.
- Between 350-550 °C, there was no significant crystalline contribution to the diffraction pattern, though the crystallisation of  $\text{CeO}_2$  was observed. This showed that  $\text{Mg}_3\text{RE}_2(\text{NO}_3)_{12} \cdot 24\text{H}_2\text{O}$  had decomposed to form a non-crystalline phase, in agreement with thermal analysis carried out on this compound (Appendix 2) and consistent with the absence of distinct weight loss events in the TGA analysis.

### 6.3.1.2 WRW16-RF (Blend HAL Simulant – Ru free)

XRD analysis of the reaction product WRW16-RF-FD (Figure 6.3) showed reflections matching CPM,  $\text{Mg}_3\text{RE}_2(\text{NO}_3)_{12} \cdot 24\text{H}_2\text{O}$  and  $\text{Al}(\text{NO}_3)_3 \cdot 9\text{H}_2\text{O}$  in the diffraction pattern, as observed in the product without the addition of Li (Figure 6.1). Significant diffuse scattering was observed, suggesting the presence of non-crystalline component(s). The only major difference in the diffraction patterns of WRW16 with and without the presence of  $\text{LiNO}_3$ , was the presence of an additional intense crystalline reflection at  $2\theta = 38.57^\circ$  (Figure 6.3). This reflection did not correspond to  $\text{LiNO}_3$  (or any of its hydrated forms) by reference to the ICDD database. TGA analysis of product WRW16-RLF-FD (Figure 6.4) showed a total weight loss of 71 wt% at 1000 °C, slightly higher than the 68 wt% of the Li free product. This is consistent with available literature (Vickers, 2006c) which showed a small increase in weight loss with the addition of  $\text{LiNO}_3$  in Blend HAL simulant. The TGA profile demonstrated the same three events as in sample WRW16-RLF-FD with sharp weight losses being observed at 200, 250 and 380 °C which were attributable to dehydration and partial denitration of  $\text{Al}(\text{NO}_3)_3 \cdot 9\text{H}_2\text{O}$  (identified by XRD), decomposition of RE nitrates and denitration of  $\text{Mg}_3\text{RE}_2(\text{NO}_3)_{12} \cdot 24\text{H}_2\text{O}$  respectively, by reference to thermal stability data for these compounds

(Appendix; Pacewska and Keshr, 2002; Zalewicz and Trzesowska, 2004; Appendix 2). There was a notable absence of a weight loss event above 600 °C, which is typical of the denitration of  $\text{LiNO}_3$  (Appendix; Chun, 1977). This, as well as the absence of reflections attributable to  $\text{LiNO}_3$  in the diffraction pattern, implies that  $\text{LiNO}_3$  undergoes a reaction with components of the HAL simulant in solution, forming a non-crystalline product. This is in agreement with reactions in chapter 5, which showed the formation of a non-crystalline precipitate in solution arising from the reaction of  $\text{LiNO}_3$  with PMA and zirconyl nitrate (chapter 5, section 5.3.2.2.3). The presence of  $\text{Mg}_3\text{RE}_2(\text{NO}_3)_{12}\cdot 24\text{H}_2\text{O}$  and  $\text{Al}(\text{NO}_3)_3\cdot 9\text{H}_2\text{O}$  in the product showed that  $\text{LiNO}_3$  does not react with these components in solution or during the freeze drying process, also in agreement with work carried out in chapter 5. Overall, these data imply that the addition of  $\text{LiNO}_3$  to Magnox HAL simulant does result in extra reactions occurring, though seemingly not with the crystalline phases. An additional reflection does appear at values of  $2\theta = 38.57^\circ$  (Figure 6.3), but was unidentified and was not present in product WRW16-RLF-FD. This was the only major observable change by XRD and TGA analysis. CPM,  $\text{Mg}_3\text{RE}_2(\text{NO}_3)_{12}\cdot 24\text{H}_2\text{O}$  and  $\text{Al}(\text{NO}_3)_3\cdot 9\text{H}_2\text{O}$  were still observed in the diffraction pattern, as formed in Li free product, with co-existing non-crystalline component(s).

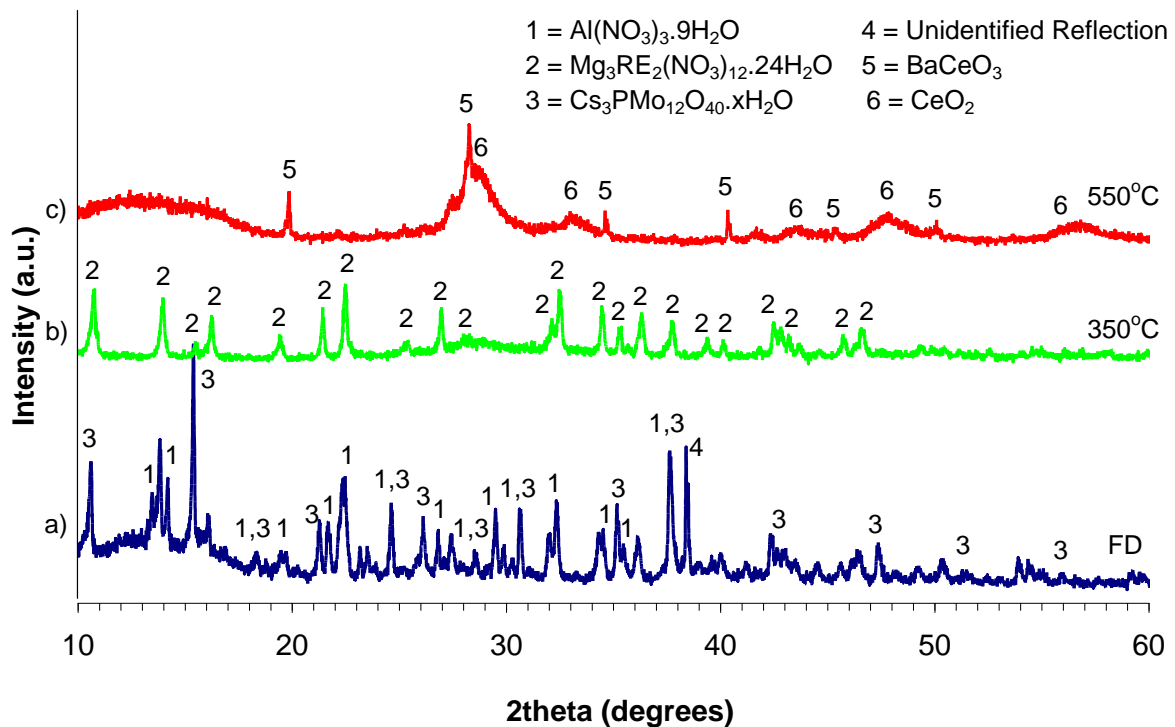


**Figure 6.3 – XRD analysis of products a) WRW16-RF-FD, b) WRW16-RF-350 and c) WRW16-RF-550**

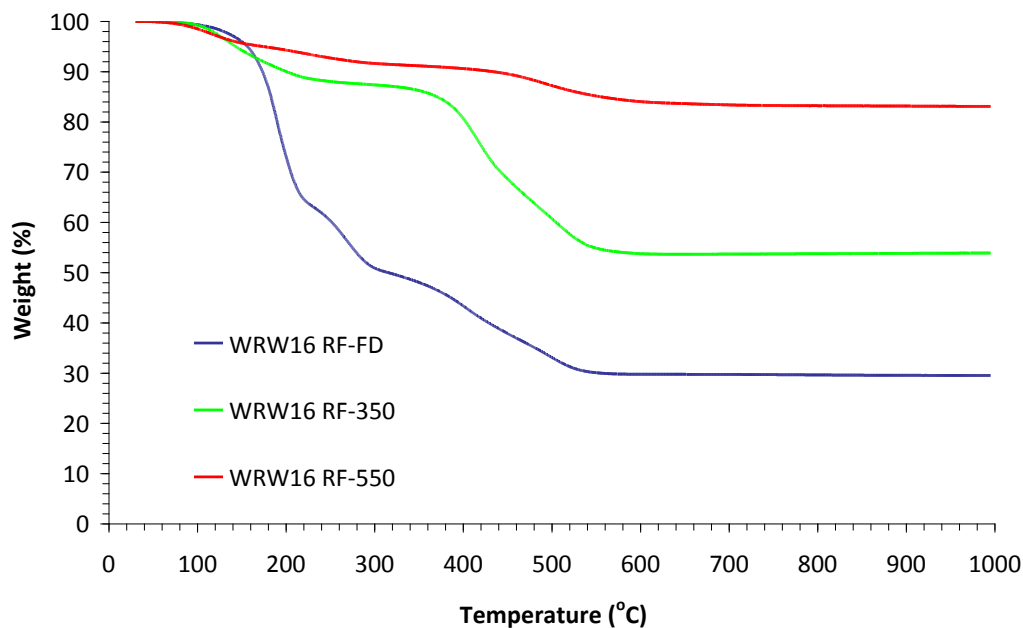


**Figure 6.4 – TGA analysis of products WRW16-RF-FD, WRW16-RF-350 and WRW16-RF-550**

XRD analysis of product WRW16-RF-350 (Figure 6.3) showed a set of reflections attributed to  $\text{Mg}_3\text{RE}_2(\text{NO}_3)_{12} \cdot 24\text{H}_2\text{O}$ . These accounted for essentially all of the reflections shown in the diffraction pattern. No peaks attributable to  $\text{Al}(\text{NO}_3)_3 \cdot 9\text{H}_2\text{O}$  were observed in the product, consistent with findings from the Li free product and in agreement with the partial decomposition of  $\text{Al}(\text{NO}_3)_3 \cdot 9\text{H}_2\text{O}$ , to form an amorphous product, reported previously by Pacewska and Keshr (2002). The intense reflections, associated with CPM, were no longer observed after calcination at 350 °C. Significant diffuse scattering was also observed, showing the presence of non-crystalline component(s). TGA analysis of product WRW16-RF-350 (Figure 6.4) showed a total weight loss of 47 wt% at 1000 °C, slightly higher than the 45wt% observed without the addition of  $\text{LiNO}_3$ , consistent with available literature (Vickers, 2006c). The weight loss profile again demonstrated two sharp weight loss events at 200 °C and 380 °C respectively, with the former attributed to dehydration and the latter denitration of  $\text{Mg}_3\text{RE}_2(\text{NO}_3)_{12} \cdot 24\text{H}_2\text{O}$  (Appendix 2). The sharp weight loss events at 200 °C and 250 °C were not observed after calcination at 350 °C, which is in agreement with the XRD data showing the absence of  $\text{Al}(\text{NO}_3)_3 \cdot 9\text{H}_2\text{O}$  and CPM and consistent with available literature (Pacewska and Keshr, 2002; Neepa et al., 2013). These data showed that  $\text{Mg}_3\text{RE}_2(\text{NO}_3)_{12} \cdot 24\text{H}_2\text{O}$  was the only major crystalline product retained in the reaction product, consistent with TGA analysis (Figure 6.4). Reflections attributable to  $\text{Al}(\text{NO}_3)_3 \cdot 9\text{H}_2\text{O}$  and CPM were no longer present in the reaction product, which is consistent with a reduction in weight loss at 200 °C (compared to the freeze dried product) and in agreement with available literature (Pacewska and Keshr, 2002). Strong diffuse scattering was observed in the XRD pattern (Figure 6.3), which showed non-crystalline component(s) were also present in product WRW16-RF-350.

XRD analysis of product WRW16-RF-550 (Figure 6.3) showed a set of sharp reflections attributable to BaCeO<sub>3</sub> [04-012-0212] and a series of broad, weak reflections associated with poorly crystalline CeO<sub>2</sub> [04-593]. The reflections associated with BaCeO<sub>3</sub> were not observed without the addition of LiNO<sub>3</sub> to the Blend HAL simulant. Significant diffuse scattering showed the presence of amorphous component(s) in product WRW16-RF-550. TGA analysis of product WRW16-RLF-550 (Figure 6.4) showed a total weight loss of 17 wt% was observed at 1000 °C, similar to that of the Li free product. This showed retention of a portion of the volatile inventory, though a reduction in the total weight loss was observed with increasing temperature. The weight loss profile showed a broad weight loss occurring between 450-550 °C. The absence of weight loss events at 200 and 380 °C, present in the freeze dried sample and after calcination at 350 °C, showed that Mg<sub>3</sub>RE<sub>2</sub>(NO<sub>3</sub>)<sub>12</sub>·24H<sub>2</sub>O had decomposed after calcination at 550 °C, in agreement with the absence of reflections in the diffraction pattern (Figure 6.3) and thermal analysis carried out on the precipitate from evaporation of WRW16-RLF simulant (Appendix 2). Crystallisation of CeO<sub>2</sub> at higher calcination temperature was consistent with available literature (Dunnett et al., 2009). Previous studies (Short, 2005) showed that on addition of LiNO<sub>3</sub> to a Blend HAL simulant, there were two additional phases seen using XRD analysis that are not present when the sample was Li free. The first additional phase which arose, belonged to the Pm-3m space group (Short, 2005) consistent with the structure of BaCeO<sub>3</sub>. It should be noted, however, that the Pm-3m structure can incorporate a wide range of elements and therefore other complex oxides are likely to be present. The other additional phase observed by Short (2005) and Morgan et al. (2004) was that of CsLiMoO<sub>4</sub>, which is part of yellow-phase formation in the vitrified product. This phase, however, was not observed in these experiments. The fact that the addition of LiNO<sub>3</sub> gave rise to the formation of complex oxides suggests that it may have acted as a molten salt in the calcine, helping to facilitate reactions which would not otherwise occur in the solid state. LiNO<sub>3</sub> acts as Lux-Flood base, making it a good O<sup>2-</sup> donor, and can therefore lower the temperatures needed for an oxidation reaction to occur (Afanasiev and Geantet, 1998). LiNO<sub>3</sub> is the most powerful O<sup>2-</sup> donor in the alkali metal series, giving it the highest reactivity (Afanasiev, 2007), which in combination with its low melting point makes it a good molten salt to use in the synthesis of metal oxides. This is a likely explanation for the formation of complex oxide phases which are not observed without the presence of LiNO<sub>3</sub>. Overall, these data suggested that the formation of BaCeO<sub>3</sub> (or other complex oxides with the same structure) is a consequence of the addition of LiNO<sub>3</sub> acting as a molten salt, facilitating the formation of these phases, not seen in the Li free product. As LiNO<sub>3</sub> acts as an O<sup>2-</sup> donor, it will no longer be present in its original crystalline form, accounting for the absence in the diffraction pattern.

From these experiments, it is possible to infer and conclude the following sequence of reactions:

- In the freeze dried sample, without further heat treatment, CPM,  $\text{Mg}_3\text{RE}_2(\text{NO}_3)_{12}\cdot 24\text{H}_2\text{O}$  and  $\text{Al}(\text{NO}_3)_3\cdot 9\text{H}_2\text{O}$  were observed in the diffraction pattern with co-existing amorphous phase(s). These observations implied addition of  $\text{LiNO}_3$  did not affect the reaction between Mg and the RE elements in solution. The presence of CPM and  $\text{Al}(\text{NO}_3)_3\cdot 9\text{H}_2\text{O}$  also suggested these products do not react with  $\text{LiNO}_3$ . The absence of reflections attributable to  $\text{LiNO}_3$  in the diffraction pattern and the observation of an additional unidentified reflection showed that a reaction had occurred involving  $\text{LiNO}_3$  in solution.
- After calcination at 350 °C,  $\text{Mg}_3\text{RE}_2(\text{NO}_3)_{12}\cdot 24\text{H}_2\text{O}$  appeared to be the only crystalline phase present in product WRW16-RLF-350. Reflections attributable to CPM,  $\text{Al}(\text{NO}_3)_3\cdot 9\text{H}_2\text{O}$  or the unidentified crystalline phase were not observed, suggesting they undergo (partial) decomposition / reaction to form non-crystalline components. Non-crystalline material was shown to be present by the strong diffuse scattering in the XRD pattern.
- Between 350-550 °C,  $\text{Mg}_3\text{RE}_2(\text{NO}_3)_{12}\cdot 24\text{H}_2\text{O}$  had decomposed to form a non-crystalline phase, in agreement with thermal analysis carried out on this compound (Appendix 2) and consistent with the absence of distinct weight loss events in the TGA analysis.  $\text{BaCeO}_3$  and poorly crystalline  $\text{CeO}_2$  were identified in the XRD pattern, with the former not being observed without the addition of  $\text{LiNO}_3$ . This suggested that  $\text{LiNO}_3$  facilitates the formation of  $\text{BaCeO}_3$  (or other complex oxides), acting as a molten salt in the calcination process.

### 6.3.1.3 WRW17-RLF (Magneox HAL Simulant – Ru and Li free)

XRD analysis of product WRW17-RLF-FD (Figure 6.5) showed reflections attributable to  $\text{Mg}(\text{NO}_3)_2\cdot 6\text{H}_2\text{O}$  [14-101],  $\text{Mg}_3\text{RE}_2(\text{NO}_3)_{12}\cdot 24\text{H}_2\text{O}$  and  $\text{Al}(\text{NO}_3)_3\cdot 9\text{H}_2\text{O}$  [12-472], were present in the diffraction pattern. There appeared to be very strong diffuse scattering in the XRD pattern, compared to the Blend simulant, suggesting the presence of a higher proportion of non-crystalline component(s). There was a notable absence of reflections corresponding to CPM, present in Blend simulants. CPM is observed in Magnox HAL simulants, but is present in a smaller quantity due to the lower concentration of Mo in this simulant type. Added to this, Mg and Al are present in much greater quantities in Magnox simulant than in Blend (Short, 2010b; Short, 2010c). It is possible, therefore, that the peaks attributed to CPM were too weak in intensity to be observed in the diffraction pattern. TGA analysis of product WRW17-RLF-FD (Figure 6.6) showed a total weight loss of 76 wt% at 1000 °C, corresponding to dehydration and denitration of all of the metal nitrates into their component oxides. This is much higher than the 68 wt% weight loss observed in the freeze dried blend simulant. The weight loss profile demonstrated two events: a sharp weight loss at 200 °C, attributed with partial denitration of  $\text{Al}(\text{NO}_3)_3\cdot 9\text{H}_2\text{O}$  (identified by XRD), by reference to thermal stability data for this compound (Appendix) in agreement with previous work by Pacewska and Keshr (2002); and a sharp

weight loss at 380 °C, attributed to the denitration of  $\text{Mg}_3\text{RE}_2(\text{NO}_3)_{12}\cdot 24\text{H}_2\text{O}$ , as shown by thermal analysis of this compound (Appendix 2).  $\text{Mg}(\text{NO}_3)_2\cdot 6\text{H}_2\text{O}$  undergoes denitration at 400 °C (Appendix; Paulik et al., 1988), and would therefore coincide with the weight loss event associated with  $\text{Mg}_3\text{RE}_2(\text{NO}_3)_{12}\cdot 24\text{H}_2\text{O}$ . There was an absence of a weight loss event at 250 °C, as observed in Blend HAL simulants, attributed to the decomposition of RE nitrates (Zalewicz and Trzesowska, 2004). This will be due to the increased Mg and reduced RE element concentrations compared with Blend simulants (Short, 2010b; Short, 2010c) resulting in the consumption of RE elements in the formation of  $\text{Mg}_3\text{RE}_2(\text{NO}_3)_{12}\cdot 24\text{H}_2\text{O}$ . The presence of  $\text{Mg}_3\text{RE}_2(\text{NO}_3)_{12}\cdot 24\text{H}_2\text{O}$  is in agreement with available literature which showed the precipitation of Mg rare earth nitrates occur in the HAST's at Sellafield (Richardson, 2002a), with formation of these components increasing with Mg concentration (Richardson, 2002b).  $\text{Mg}(\text{NO}_3)_2\cdot 6\text{H}_2\text{O}$  is observed in Magnox simulants, but not in Blend. This is due to the reduction in concentration of the RE elements and increase in Mg present in WRW17 (Short, 2010b). The presence of  $\text{Al}(\text{NO}_3)_3\cdot 9\text{H}_2\text{O}$  showed that no reaction took place in solution or during the freeze drying process, consistent with the short simulant studies in chapter 5, which showed  $\text{Al}(\text{NO}_3)_3\cdot 9\text{H}_2\text{O}$  did not undergo reactions with  $\text{Mg}(\text{NO}_3)_2\cdot 6\text{H}_2\text{O}$  during the freeze drying process. Overall, these data showed Mg and RE nitrates react together in solution resulting in the formation of  $\text{Mg}_3\text{RE}_2(\text{NO}_3)_{12}\cdot 24\text{H}_2\text{O}$ .  $\text{Al}(\text{NO}_3)_3\cdot 9\text{H}_2\text{O}$  remains unreacted in the product, which is consistent with TGA data showing a sharp weight loss at 200 °C, with some unreacted  $\text{Mg}(\text{NO}_3)_2\cdot 6\text{H}_2\text{O}$  still present in the reaction product. A co-existing non-crystalline component(s) was also shown to be present through significant diffuse scattering observed in the XRD pattern (Figure 6.5).

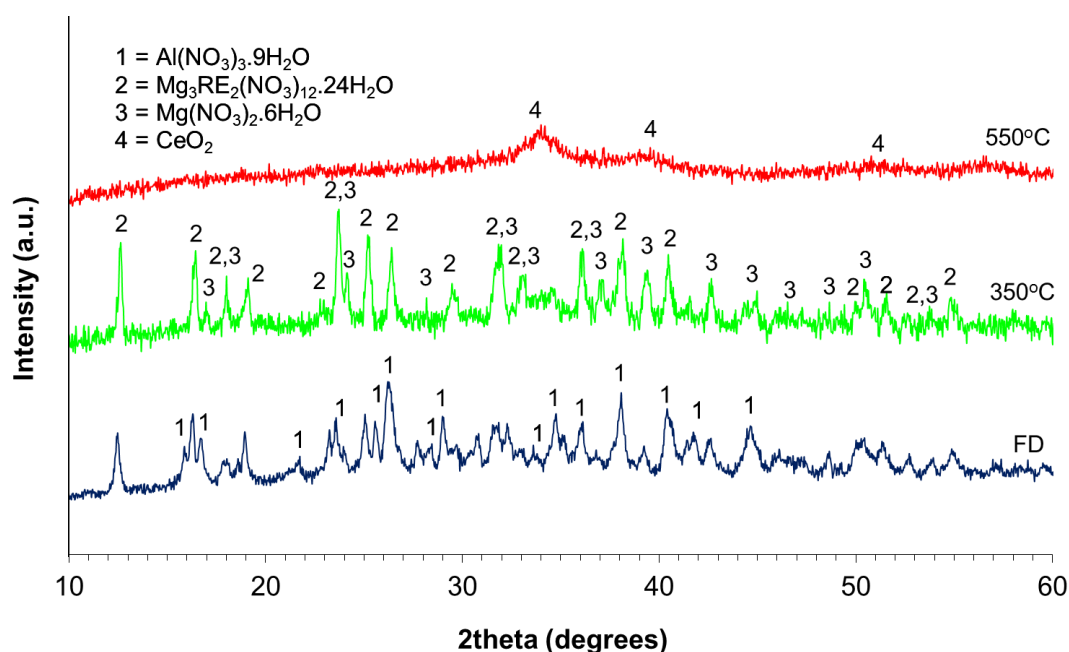


**Figure 6.5 – XRD analysis of products a) WRW17-RLF-FD, b) WRW17-RLF-350 and c) WRW17-RLF-550**



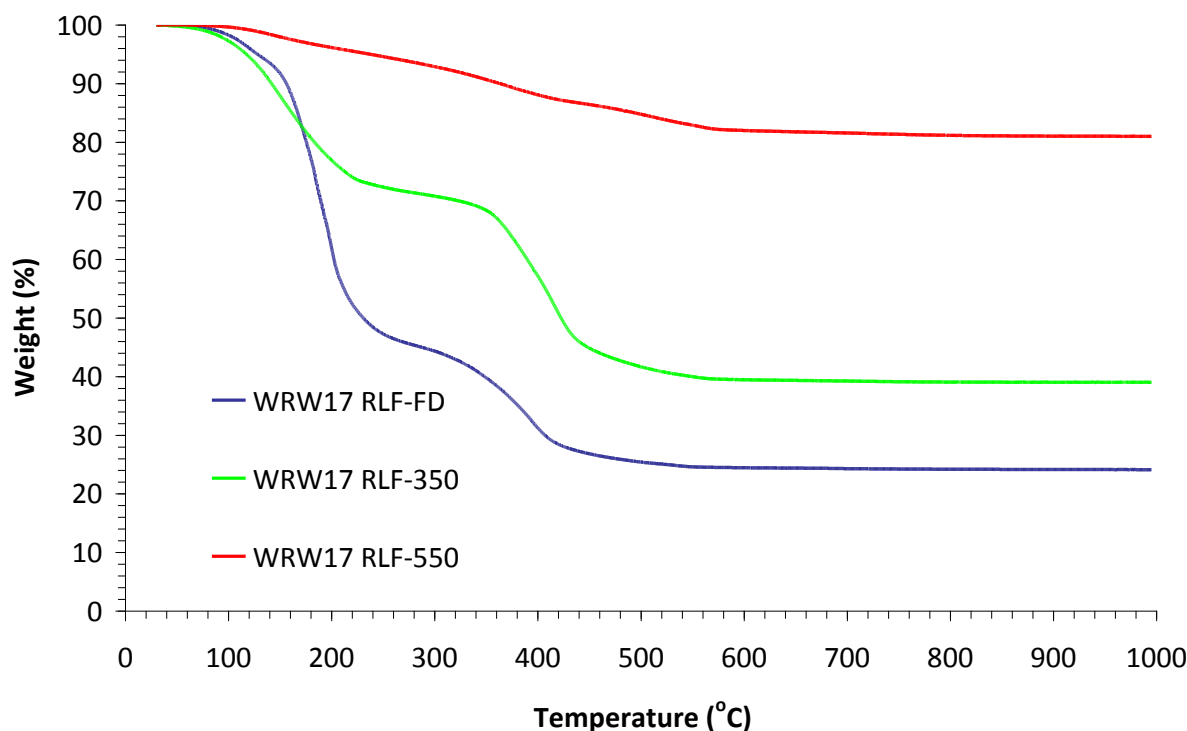


**Figure 6.6 – TGA analysis of products WRW17-RLF-FD, WRW17-RLF-350 and WRW17-RLF-550**

The diffraction pattern of product WRW17-RLF-350 (Figure 6.5) showed a set of reflections attributable to  $\text{Mg}_3\text{RE}_2(\text{NO}_3)_{12} \cdot 24\text{H}_2\text{O}$  and  $\text{Mg}(\text{NO}_3)_2 \cdot 6\text{H}_2\text{O}$ . This accounted for essentially all of the reflections shown, with no peaks attributable to  $\text{Al}(\text{NO}_3)_3 \cdot 9\text{H}_2\text{O}$  remaining in the product, in agreement with Pacewska and Keshr (2002), who showed the partial decomposition of  $\text{Al}(\text{NO}_3)_3 \cdot 9\text{H}_2\text{O}$  forms an amorphous nitrate bearing product. Strong diffuse scattering was apparent, showing a non-crystalline phase(s) was present. TGA analysis of product WRW17-RLF-350 (Figure 6.6) showed a total weight loss of 61 wt% at 1000 °C. This showed Magnox simulants, after calcination at 350 °C, have higher residual nitrate contents than Blend simulants, consistent with historic studies (Vickers, 2006a; Vickers, 2006c). The weight loss profile demonstrated two events: a sharp weight loss at 200 °C, attributed to dehydration; and a sharp weight loss at 380 °C, consistent with denitration of  $\text{Mg}_3\text{RE}_2(\text{NO}_3)_{12} \cdot 24\text{H}_2\text{O}$  (Appendix 2). The weight loss associated with unreacted  $\text{Mg}(\text{NO}_3)_2 \cdot 6\text{H}_2\text{O}$  would be expected to occur at 400 °C (Appendix; Paulik et al., 1988) and would therefore be incorporated into the weight loss event observed at 380 °C. Overall, these data showed  $\text{Mg}_3\text{RE}_2(\text{NO}_3)_{12} \cdot 24\text{H}_2\text{O}$  and the unreacted  $\text{Mg}(\text{NO}_3)_2 \cdot 6\text{H}_2\text{O}$  were retained in the reaction product after calcination of the freeze dried product at 350 °C.  $\text{Al}(\text{NO}_3)_3 \cdot 9\text{H}_2\text{O}$  had undergone partial dehydration and denitration to form a non-crystalline product, with strong diffuse scattering showing the presence of non-crystalline component(s) in the product WRW17-RLF-350.

XRD analysis of product WRW17-RLF-550 (Figure 6.5) showed a diffraction pattern with diffuse scattering and very low signal-to noise ratio, indicating the presence of non-crystalline components. A set of very weak, broad reflections associated with the presence of CeO<sub>2</sub> [02-1306] were observed, as also observed in the Blend simulants (sections 6.3.1.1 and 6.3.1.2). TGA analysis showed a total weight loss of 19 wt% was observed at 1000 °C after calcination at 550 °C (Figure 6.6). The weight loss profile showed no distinct events, with a broad weight loss occurring between 100-600 °C. The sharp weight losses at 200 °C and 380 °C, present in the freeze dried sample and after calcination at 350 °C, were not present in product WRW17-RLF-550. This is in agreement with the absence of reflections attributable to Mg<sub>3</sub>RE<sub>2</sub>(NO<sub>3</sub>)<sub>12</sub>.24H<sub>2</sub>O and Mg(NO<sub>3</sub>)<sub>2</sub>.6H<sub>2</sub>O in the diffraction pattern (Figure 6.5) and thermal analysis carried out on these compounds (Appendix 1; Appendix 2). These data showed that none of the crystalline phases, present in the freeze dried product, were present after calcination at 550 °C for 10 mins, in agreement with TGA analysis showing no distinct weight loss events. The crystallisation of CeO<sub>2</sub> was observed as very weak, broad peaks in the diffraction pattern (Figure 6.5).

The backscattered electron image of product WRW17-RLF-FD showed that this material had a varied composition, with a number of phases being apparent. EDS analysis of the freeze dried product of WRW17-RLF revealed a generally intimate association of Al and Mg, as shown by X-ray maps (Figure 6.7), however, some regions were observed to be deficient in one element. This is consistent with XRD analysis which showed Al(NO<sub>3</sub>)<sub>3</sub>.9H<sub>2</sub>O remained unreacted in the freeze dried product and Mg<sub>3</sub>RE<sub>2</sub>(NO<sub>3</sub>)<sub>12</sub>.24H<sub>2</sub>O was formed. This was also shown by the intimate association of Mg and Nd throughout the product (Figure 6.7). After calcination of the freeze dried product at 550 °C, the backscattered electron image (Figure 6.8) showed a high degree of homogeneity throughout the sample. This was confirmed by EDS analysis which revealed an intimate association of all the selected elements analysed. These data are consistent with the phase assemblage determined from XRD and TGA data.

From these experiments, it is possible to infer and conclude the following sequence of reactions:

- In the freeze dried sample, without further heat treatment, Mg<sub>3</sub>RE<sub>2</sub>(NO<sub>3</sub>)<sub>12</sub>.24H<sub>2</sub>O, Mg(NO<sub>3</sub>)<sub>2</sub>.6H<sub>2</sub>O and Al(NO<sub>3</sub>)<sub>3</sub>.9H<sub>2</sub>O were observed in the diffraction pattern with co-existing amorphous phase(s). These observations showed the reaction of Mg with the RE elements in solution, consistent with observations of precipitation in the HAST's (Richardson, 2002). The presence of unreacted Mg(NO<sub>3</sub>)<sub>2</sub>.6H<sub>2</sub>O is consistent with the chemical composition of the Magnox HAL simulant being high in Mg and lower in RE elements than in Blend (Short, 2010b; Short, 2010c). The presence of Al(NO<sub>3</sub>)<sub>3</sub>.9H<sub>2</sub>O in the product implies that no reaction is undertaken in solution, in agreement with previous findings in chapter 5.

- After calcination at 350 °C,  $\text{Mg}_3\text{RE}_2(\text{NO}_3)_{12}\cdot 24\text{H}_2\text{O}$  and  $\text{Mg}(\text{NO}_3)_2\cdot 6\text{H}_2\text{O}$  were observed in product WRW16-RLF-350. Reflections attributable to  $\text{Al}(\text{NO}_3)_3\cdot 9\text{H}_2\text{O}$  or the unidentified crystalline phase were not observed, suggesting they undergo dehydration and denitration to form non-crystalline components, consistent with thermal analysis and available literature (Appendix; Pacewska and Keshr, 2002). A significant amount of non-crystalline material was shown to be present by the strong diffuse scattering in the XRD pattern.
- Between 350-550 °C, there was no significant crystalline contribution to the diffraction pattern, though the crystallisation of  $\text{CeO}_2$  was observed as very weak, broad reflections. This showed that  $\text{Mg}_3\text{RE}_2(\text{NO}_3)_{12}\cdot 24\text{H}_2\text{O}$  and  $\text{Mg}(\text{NO}_3)_2\cdot 6\text{H}_2\text{O}$  had decomposed to form a non-crystalline phase, in agreement with thermal analysis carried out on these compounds (Appendix 1; Paulik et al., 1988; Appendix 2) and consistent with the absence of distinct weight loss events in the TGA analysis.

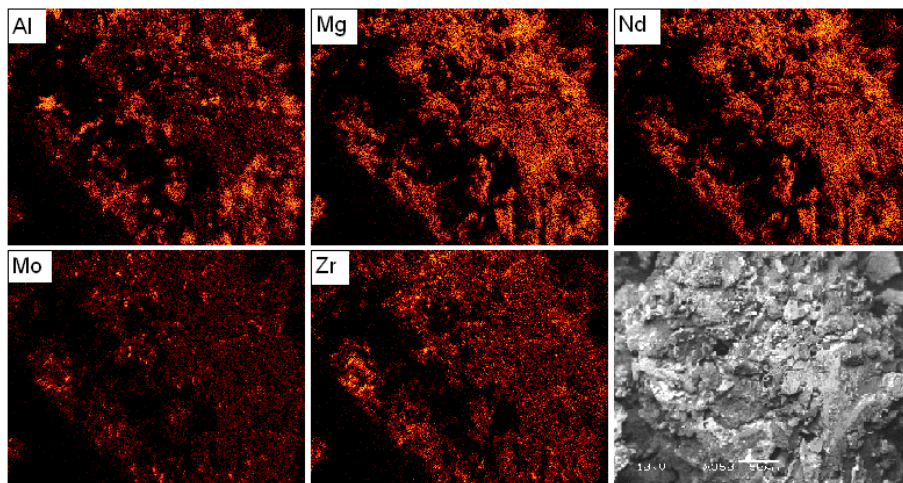


**Figure 6.7 – Backscattered electron image and X-ray maps of product WRW17-RLF-FD**

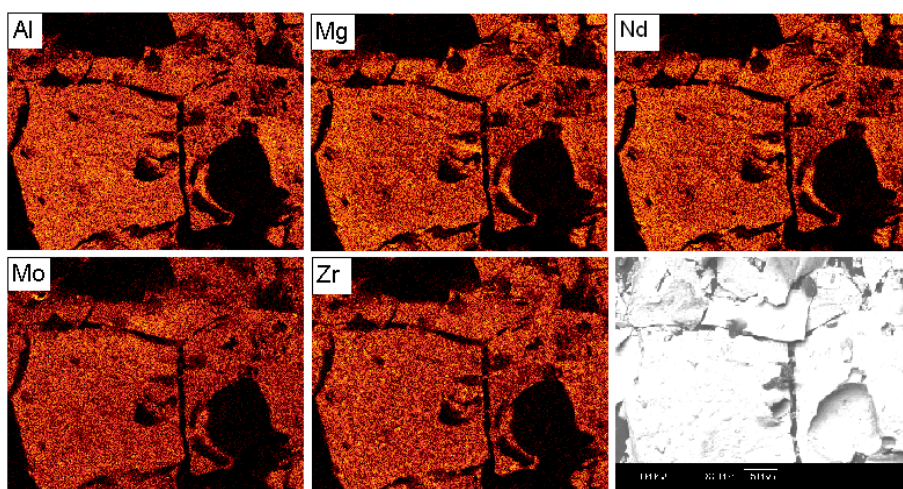


**Figure 6.8 – Backscattered electron image and X-ray maps of product WRW17-RLF-550**

### 6.3.1.4 WRW17-RF (Magnox HAL Simulant – Ru free)

The diffraction pattern of product WRW17-RF-FD (Figure 6.9) was almost identical to that of the Magnox simulant without the addition of  $\text{LiNO}_3$ , with reflections attributable to  $\text{Mg}(\text{NO}_3)_2 \cdot 6\text{H}_2\text{O}$  [14-101],  $\text{Mg}_3\text{RE}_2(\text{NO}_3)_{12} \cdot 24\text{H}_2\text{O}$  and  $\text{Al}(\text{NO}_3)_3 \cdot 9\text{H}_2\text{O}$  [12-472] being observed. Very strong diffuse scattering suggested a significant portion of the product was comprised of non-crystalline component(s). No reflections associated with  $\text{LiNO}_3$  (or any of its hydrated phases) were apparent in the XRD pattern. TGA analysis of product WRW17-RF-FD (Figure 6.10) showed a total weight loss of 76 wt% at 1000 °C, corresponding to dehydration and denitration of all of the metal nitrates into their component oxides. This was identical to the weight loss observed in the freeze dried Magnox simulant without Li addition. The weight loss profile showed the same two events as observed in the Li free simulant with sharp weight losses occurring at 200 and 380 °C, attributed with denitration of  $\text{Al}(\text{NO}_3)_3 \cdot 9\text{H}_2\text{O}$  and  $\text{Mg}_3\text{RE}_2(\text{NO}_3)_{12} \cdot 24\text{H}_2\text{O}$  respectively, in agreement with thermal analyses of these compounds (Appendix; Appendix 2; Pacewska and Keshr, 2002). The absence of a weight loss event above 600 °C, typical of  $\text{LiNO}_3$  (Chun, 1977) suggested that a reaction had taken place in solution, consistent with XRD analysis (Figure 6.9) and the work carried out in chapter 5. Overall, these data showed Mg and RE nitrates react together in solution resulting in the formation of  $\text{Mg}_3\text{RE}_2(\text{NO}_3)_{12} \cdot 24\text{H}_2\text{O}$ , with a portion of  $\text{Mg}(\text{NO}_3)_2 \cdot 6\text{H}_2\text{O}$  remaining unreacted.  $\text{Al}(\text{NO}_3)_3 \cdot 9\text{H}_2\text{O}$  remained in the product, consistent with TGA data showing a sharp weight loss at 200 °C. The absence of reflections attributable to  $\text{LiNO}_3$  in the diffraction pattern, coupled with the absence of a weight loss event at 600 °C, associated with the denitration of  $\text{LiNO}_3$ , imply that a reaction had taken place resulting in the formation of a non-crystalline product(s). A co-existing non-crystalline component(s) was also shown to be present through significant diffuse scattering observed in the XRD pattern (Figure 6.9).

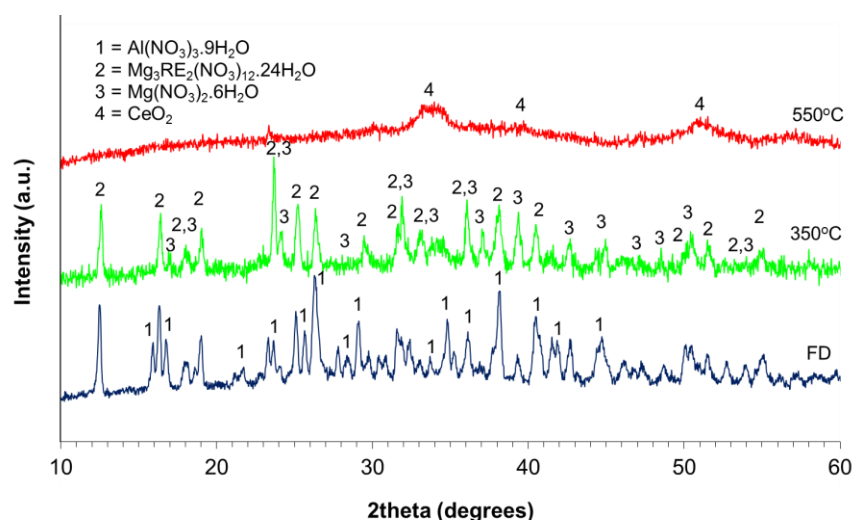


**Figure 6.9 – XRD analysis of products a) WRW17-RF-FD, b) WRW17-RF-350 and c) WRW17-RF-550**

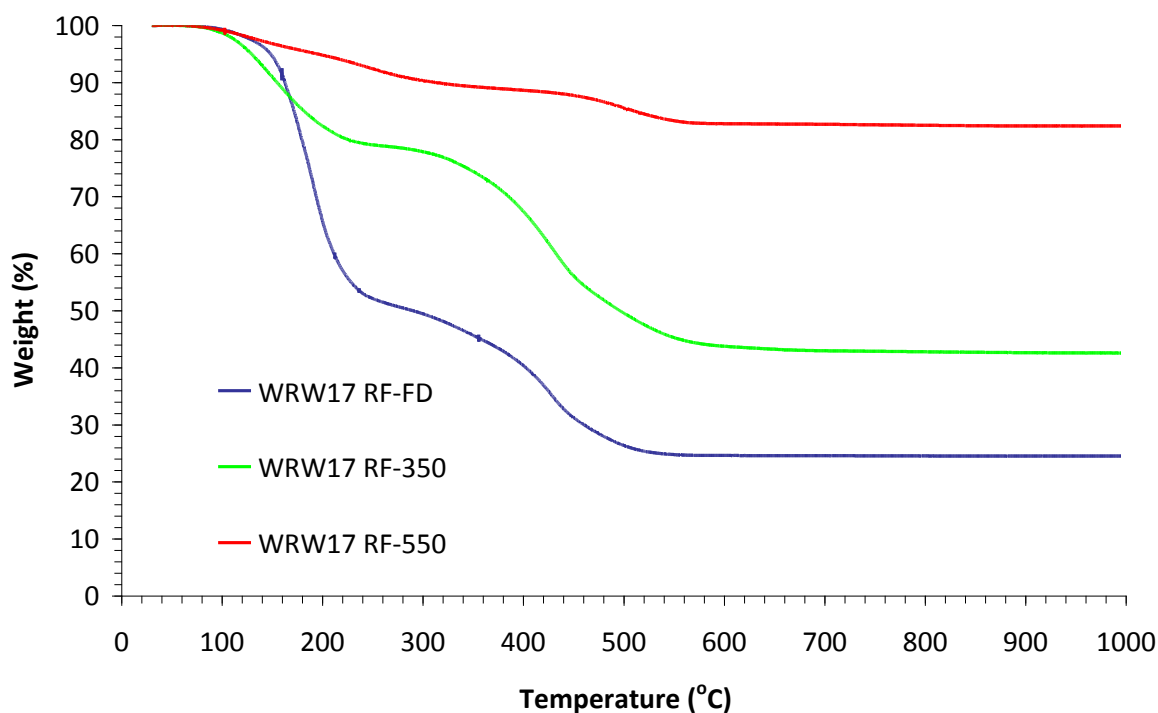


**Figure 6.10 – TGA analysis of products WRW17-RF-FD, WRW17-RF-350 and WRW17-RF-550**

The XRD patterns of products WRW17-RF-350 and WRW-RF-550 (Figure 6.9) were almost identical to the corresponding products without the addition of  $\text{LiNO}_3$ . This suggested that the Li containing phases are all non-crystalline in nature in Magnox simulants. After calcination at 350 °C, reflections attributable to  $\text{Mg}(\text{NO}_3)_2 \cdot 6\text{H}_2\text{O}$  and  $\text{Mg}_3\text{RE}_2(\text{NO}_3)_{12} \cdot 24\text{H}_2\text{O}$  were observed and accounted for essentially all of the reflections. After calcination at 550 °C, the only observed reflections were associated with poorly crystalline  $\text{CeO}_2$ . Strong diffuse scattering was apparent in both products, showing the presence of non-crystalline phase(s). TGA analysis of products WRW17-RF-350 and WRW17-RF-550 (Figure 6.10) showed total weight losses of 61 wt% and 19 wt% respectively at 1000 °C, similar to those observed in the Li free samples. The weight loss profiles were also similar to the corresponding Li free products, demonstrating weight loss events attributed to dehydration and denitration of  $\text{Mg}_3\text{RE}_2(\text{NO}_3)_{12} \cdot 24\text{H}_2\text{O}$  (Appendix 2) at temperatures of 200 °C and 380 °C respectively after calcination at 350 °C, with these weight losses disappearing after calcination at 550 °C, consistent with XRD data. Overall, these data showed  $\text{Mg}(\text{NO}_3)_2 \cdot 6\text{H}_2\text{O}$  and  $\text{Mg}_3\text{RE}_2(\text{NO}_3)_{12} \cdot 24\text{H}_2\text{O}$  were retained in the reaction product at 350 °C, but underwent decomposition between 350-550 °C, with the crystallisation of  $\text{CeO}_2$  occurring in the same temperature range.  $\text{Al}(\text{NO}_3)_3 \cdot 9\text{H}_2\text{O}$  had undergone partial dehydration and denitration to form a non-crystalline product below 350 °C. Significant diffuse scattering showing the presence of non-crystalline component(s) was apparent in both products WRW17-RF-350 and WRW17-RF-550.

The backscattered electron image of WRW17-RF-FD showed that the product had a varied composition, with a number of phases being apparent. EDS analysis of the freeze dried product of WRW17-RLF revealed distinct Al containing phases with little association between Al and Mg shown by X-ray maps (Figure 6.11). This is consistent with XRD analysis which showed  $\text{Al}(\text{NO}_3)_3 \cdot 9\text{H}_2\text{O}$  and  $\text{Mg}_3\text{RE}_2(\text{NO}_3)_{12} \cdot 24\text{H}_2\text{O}$  were present in the product. An intimate association of Mg and Nd was observed throughout the product (Figure 6.11) confirming the presence of  $\text{Mg}_3\text{RE}_2(\text{NO}_3)_{12} \cdot 24\text{H}_2\text{O}$  in the reaction product. A clear association of Zr and Mo could also be seen in the freeze dried product, consistent with work carried out in chapter 5.

After calcination of the freeze dried product at 550 °C, the backscattered electron image (Figure 6.12) showed a high degree of homogeneity throughout the sample, same as observed in the Li free product. This was confirmed by EDS analysis which revealed an intimate association of all the selected elements analysed. This is consistent with XRD and TGA data.

From these experiments, it is possible to infer and conclude the following sequence of reactions:

- In the freeze dried sample, without further heat treatment,  $\text{Mg}(\text{NO}_3)_2 \cdot 6\text{H}_2\text{O}$ ,  $\text{Mg}_3\text{RE}_2(\text{NO}_3)_{12} \cdot 24\text{H}_2\text{O}$  and  $\text{Al}(\text{NO}_3)_3 \cdot 9\text{H}_2\text{O}$  were observed in the diffraction pattern with co-existing amorphous phase(s). These observations implied that Mg reacted with the RE elements in solution which are then precipitated during the freeze drying process. The presence of  $\text{Al}(\text{NO}_3)_3 \cdot 9\text{H}_2\text{O}$  in the product suggests that it does not react in solution or in the freeze drying process. The absence of both reflections in the XRD pattern and a weight loss event above 600 °C, attributable to  $\text{LiNO}_3$ , suggest that it underwent a reaction resulting in the formation of a non-crystalline product. The association of Mo and Zr, observed in EDS analysis, coupled with the work carried out in chapter 5 suggest that  $\text{LiNO}_3$  may react with Mo and Zr forming an amorphous product.
- After calcination at 350 °C,  $\text{Mg}_3\text{RE}_2(\text{NO}_3)_{12} \cdot 24\text{H}_2\text{O}$  and  $\text{Mg}(\text{NO}_3)_2 \cdot 6\text{H}_2\text{O}$  were apparent in the diffraction pattern of product WRW16-RLF-350. Reflections attributable to  $\text{Al}(\text{NO}_3)_3 \cdot 9\text{H}_2\text{O}$  were not observed, suggesting this undergoes dehydration and denitration to form a non-crystalline phase, consistent with thermal analysis and available literature (Appendix; Pacewska and Keshr, 2002). A significant amount of non-crystalline material was shown to be present by the strong diffuse scattering in the XRD pattern.

- Between 350-550 °C, there was no significant crystalline contribution to the diffraction pattern, though the crystallisation of CeO<sub>2</sub> was observed. This showed that Mg<sub>3</sub>RE<sub>2</sub>(NO<sub>3</sub>)<sub>12</sub>·24H<sub>2</sub>O and Mg(NO<sub>3</sub>)<sub>2</sub>·6H<sub>2</sub>O had decomposed to form non-crystalline phases, in agreement with thermal analysis carried out on these compounds (Appendix 1; Paulik et al., 1988; Appendix 2) and consistent with the absence of distinct weight loss events in the TGA analysis and the homogeneous nature of product WRW17-RF-550 observed in the backscattered electron image and X-ray maps of selected elements (Figure 6.12).

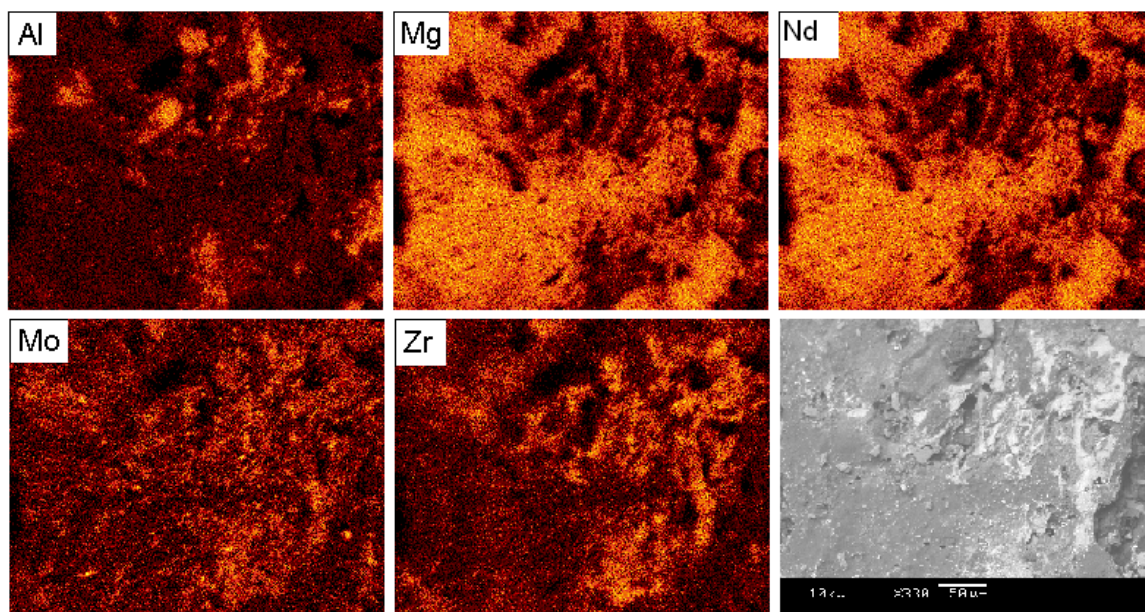


**Figure 6.11 – Backscattered electron image and X-ray maps of product WRW17-RF-FD**

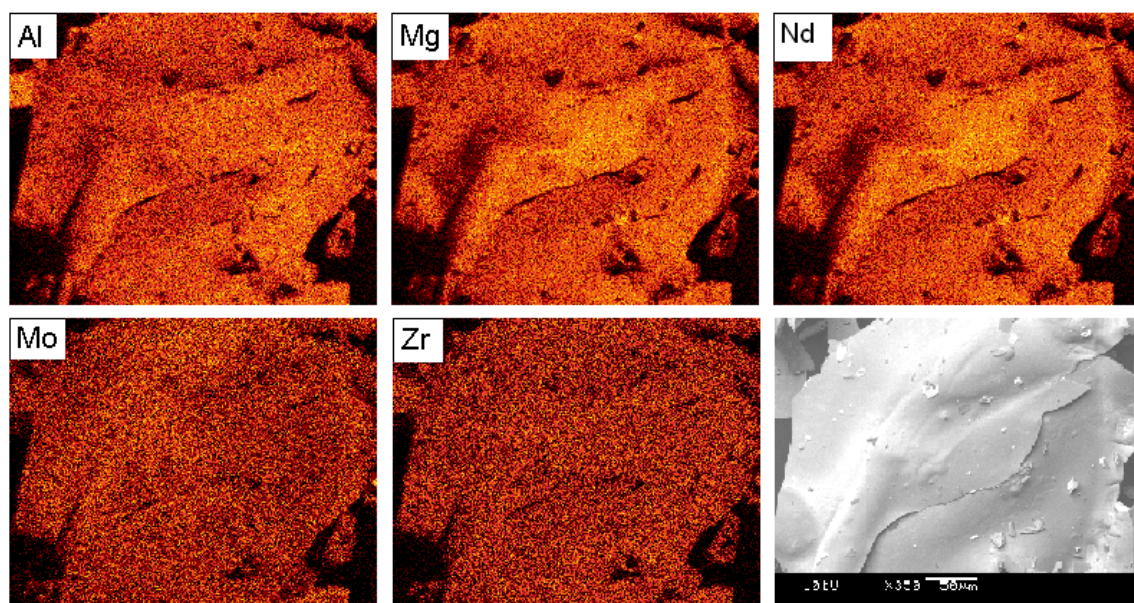


**Figure 6.12 – Backscattered electron image and X-ray maps of product WRW17-RLF-550**

## 6.3.2 Small scale calciner experiments

### 6.3.2.1 WRW17-RLF

Table 6.3 shows the masses of the calcine and dust collected for WRW17-RLF calcined under various conditions using the small scale calciner. The expected weights were calculated by first calculating the total waste oxide throughput during the experiment, then taking into account residual weight loss values (measured by TGA analysis) for each of the calcine size fractions (Table 6.4) and weighting the values accordingly (see section 6.2.2.1). The dust collection was normalised by working out a percentage dust carry-over against the actual weight of calcine collected<sup>20</sup> thus allowing comparisons to be made on the effects of changing temperature and feed rate on the dust carry-over from the calciner to the off-gas system (sections 6.3.2.1.2.1 and 6.3.2.1.2.2 respectively).

**Table 6.3 – Mass of calcine and dust products collected**

<b>Sample</b>	<b>Expected Weight (g)</b>	<b>Actual Weight (g)</b>	<b>Amount of Dust Collected (g)</b>	<b>Dust Collected (wt%)</b>
<b>WRW17-RLF-500-3l/h</b>	820.66	815.41	26.48	3.25
<b>WRW17-RLF-600-3l/h</b>	794.60	751.00	26.29	3.50
<b>WRW17-RLF-700-3l/h</b>	766.78	691.78	32.98	4.77
<b>WRW17-RLF-600-2l/h</b>	494.55	435.26	18.73	4.30
<b>WRW17-RLF-600-4l/h</b>	1050.23	1037.26	36.17	3.49

In the experiments carried out at low temperature (WRW17-RLF-500-3l/h) and high feed rate (WRW17-RLF-600-4l/h), the combined value of the actual weight and dust collected was greater than the expected weight. This could be due to the fact that TGA analysis was carried out on a 50 mg sample of each of the calcine fractions, compared with the much higher yields produced by the calciner. However, trends were observed with increasing temperature and lower feed rates, which resulted in the combined mass of calcine and duct collected being much lower than the expected yield from the experiment. This could be attributed to a higher dust carry-over, as not all of the dust generated during these experiments will have been collected. This is due to the design of the small scale calciner, in which the dust must pass through a chamber and be carried vertically through a pipe 25 mm in diameter before getting to the flexible hose and dirt trap from which the dust samples were collected. Therefore, some dust is not able to be recovered during these experiments. However, a representative yield is thought to be recovered, allowing trends to be recognised (e.g. higher dust levels observed at higher temperatures).

<sup>20</sup> The dust carry-over was worked out against the actual amount of calcine as this was a measured value, rather than calculated, and was therefore thought to give a more representative value.



**Table 6.4 – Size fractions of product WRW17-RLF calcined under varying conditions**

<b>Sample</b>	<b>Fraction above 2 mm</b>	<b>Fraction between 0.5 – 2 mm</b>	<b>Fraction below 0.5 mm</b>
<b>WRW17-RLF-500-3l/h</b>	0.64	0.25	0.11
<b>WRW17-RLF-600-3l/h</b>	0.64	0.23	0.13
<b>WRW17-RLF-700-3l/h</b>	0.78	0.12	0.10
<b>WRW17-RLF-600-2l/h</b>	0.56	0.29	0.15
<b>WRW17-RLF-600-4l/h</b>	0.64	0.26	0.10

Historically, dust has been thought of as the smallest particles of calcine being carried over to the off-gas system, therefore, a higher fraction of small particles (<0.5 mm) would be expected to correlate with higher dust carry-over<sup>21</sup>. However, this is not necessarily the only way in which dust could be generated. In these experiments, a higher normalised dust carry-over is observed at higher calcination temperatures, but there is no clear trend in the fraction produced below 0.5 mm. In fact, a higher fraction of larger particles (>2 mm) were found after calcination at 700 °C, correlating with an increased dust carry-over. It is therefore possible that generation of dust is caused by abrasion of the larger calcine particles, as discussed further in sections 6.3.2.1.1.1 and 6.3.2.1.2.1.

At higher feed rates, a greater mass of dust was collected due to the higher throughput. However, when the data was normalised, a reduction in dust carry-over was realised at higher feed rates. This is due to the fact that at a higher feed rate it takes longer to evaporate off the water, pushing the evaporative front further down the calciner tube (Short, 2012). This effectively shrinks the area of the tube in which denitration processes occur, lowering the residence time in which the calcine experiences increased temperature. In these experiments, a higher fraction of small particles were formed at a feed rate of 2 l / h (Table 6.4), in contrast to the formation of larger particles at higher temperature, correlating with a higher dust carry-over. It is possible that there are competing processes responsible for this discrepancy. The effects of feed rate on dust carry-over are discussed further in sections 6.3.2.1.1.2 and 6.3.2.1.2.2.

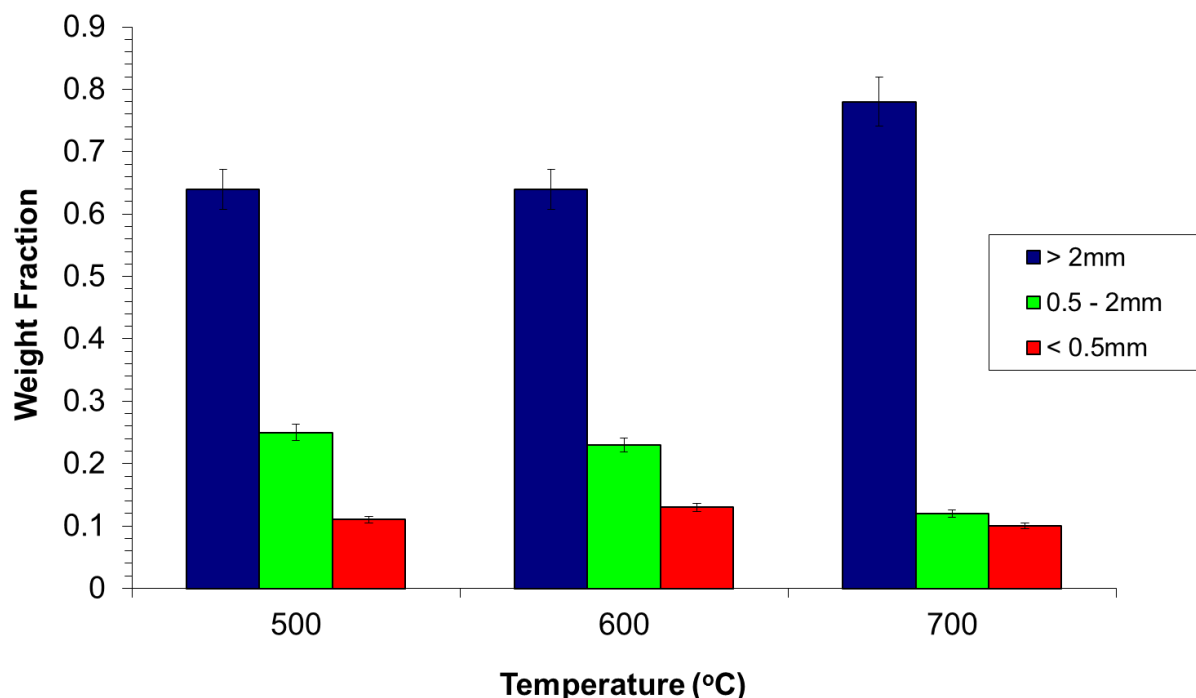
---

<sup>21</sup> To clarify, dust is the term applied to the sample collected from the flexible hose and dirt trap in the off-gas system and small particles (<0.5 mm) refers to the calcine fraction collected in the calcine collection pot.

### 6.3.2.1.1 Calcine Analysis

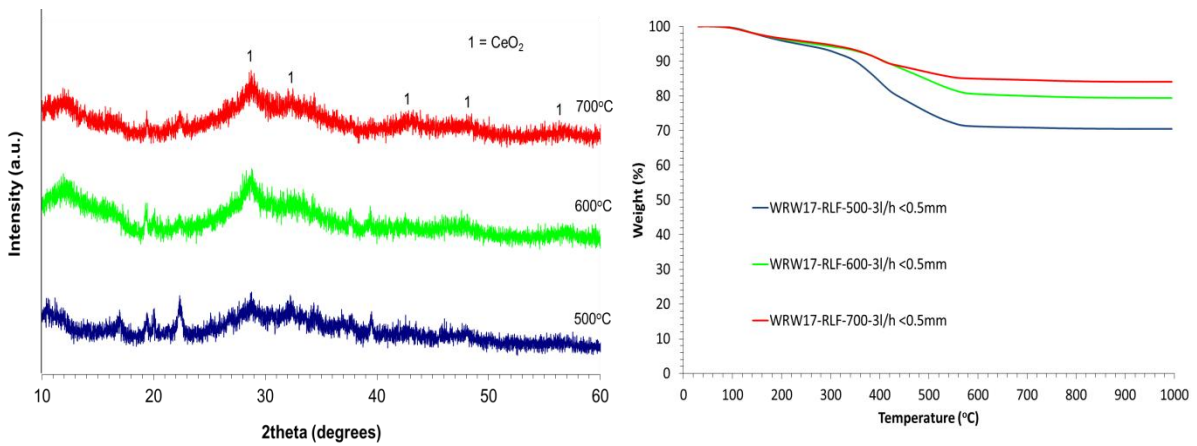
#### 6.3.2.1.1.1 Effects of temperature

Figure 6.13 shows the particle size fractions collected as a function of temperature. This showed that an increase in the mass fraction of particles >2 mm was observed after calcination at 700 °C, with the values at 500 and 600 °C being identical. The particle size range 0.5-2 mm showed a general decrease in the mass fraction at higher calcination temperature, due to the increase in larger particles in the product. There was no specific trend observed of the mass of the <0.5 mm particle size range collected, with the values for 500 and 700 °C being similar. A 5 % error has been assigned to each of the values to account for the residual calcine which will be left in the calciner tube during these experiments. This value was taken from previous small scale calciner trials which showed a 95 % mass recovery was observed (Brace, 2004), although this did not take into account dust carry-over. Therefore, this error is thought to be high, however, it will ensure true trends are observed and are not influenced by the errors associated with the small scale calciner. These errors, associated with residual calcine being left uncollected in the calciner tube, were thought to be more significant than those associated with weighing the samples, since the error associated with the balance used was  $\pm 0.005$  g. As the total mass of the calcine samples were in the order of 800 g, and collection pot was pre-weighed to reduce the error, this was deemed insignificant compared to errors associated with collection from the small scale calciner and were therefore not taken into account.



**Figure 6.13 – Particle size fractions from product WRW17-RLF calcined at 500-700 °C at a feed rate of 3 l / h**

XRD analysis of WRW17-RLF products calcined at 500, 600 and 700 °C with particle sizes <2 mm (Figures 6.14 and 6.15) all showed weak, broad reflections associated with the formation of poorly crystalline CeO<sub>2</sub>, with high levels of diffuse scattering, indicating the presence of non-crystalline component(s) also being observed. After calcination at 500 °C, weak reflections attributable to Mg<sub>3</sub>RE<sub>2</sub>(NO<sub>3</sub>)<sub>12</sub>.24H<sub>2</sub>O were observed in the product, though the low signal-to-noise ratio in the diffraction pattern obscures some of the reflections assigned by reference to the ICDD database (card [12-761]). The intensities of these reflections diminish as a function of increasing temperature and decreasing particle size (Figures 6.14 and 6.15). TGA analysis of products WRW17-RLF-500-3l/h, WRW17-RLF-600-3l/h and WRW17-RLF-700-3l/h showed decreasing weight loss as functions of increasing temperature and a reduction in particle size (Figure 6.17). This is consistent with retention of a higher fraction of the hydrate and nitrate inventory at lower calcination temperatures. The larger particles are thought to experience a lower temperature in the calcination process due to the fact only the surface of the particle comes into contact with the heated calciner tube. The weight loss profiles of products WRW17-RLF calcined between 500-700 °C at a feed rate of 3 l / h, with a particle size <2mm (Figures 6.14 and 6.15) all show three distinct events: a broad weight loss below 300 °C, typical of dehydration; a relatively sharp weight loss at 380 °C, associated with the denitration of Mg<sub>3</sub>RE<sub>2</sub>(NO<sub>3</sub>)<sub>12</sub>.24H<sub>2</sub>O (Appendix 2); and a broad weight loss between 450-600 °C, attributable to further denitration of the more stable nitrate components which make up the HAL simulant, by reference to thermal stability data for individual component nitrates of which the HAL is comprised (Chun, 1977). The weight loss event at 380 °C, attributable to the denitration of Mg<sub>3</sub>RE<sub>2</sub>(NO<sub>3</sub>)<sub>12</sub>.24H<sub>2</sub>O, was more pronounced at lower temperatures and larger particle sizes, as expected, but was still present in all three products. This is in agreement with XRD analysis which showed a reduction in intensity of the peaks associated with Mg<sub>3</sub>RE<sub>2</sub>(NO<sub>3</sub>)<sub>12</sub>.24H<sub>2</sub>O with increasing calcination temperature and a reduction in particle size. The presence of reflections attributable to CeO<sub>2</sub> is consistent with previous studies (Dunnett et al., 2009), which showed that CeO<sub>2</sub> is not observed after calcination of Magnox HAL simulant at 400°C but is highly crystalline at 1050 °C. The freeze dried experiments (section 6.3.1) showed the formation of poorly crystalline CeO<sub>2</sub> after calcination at 550 °C, but not at 350 °C. This observation, in conjunction with the available literature (Dunnett et al., 2009), suggest that the temperatures experienced by a portion of the particles less than 2 mm in diameter is above 400 °C, even at the lowest Zone 3 setpoint of 500 °C. The presence of Mg<sub>3</sub>RE<sub>2</sub>(NO<sub>3</sub>)<sub>12</sub>.24H<sub>2</sub>O, however, shows a portion of the particles experience temperatures lower than 380 °C (in agreement with Appendix 2) in the calcination process. This is consistent with the processes which take place within the calciner, in which each particle of calcine will spend different amounts of time in contact with the heated calciner wall and therefore experience slightly different temperatures. At higher Zone 3 temperatures, Mg<sub>3</sub>RE<sub>2</sub>(NO<sub>3</sub>)<sub>12</sub>.24H<sub>2</sub>O will decompose more quickly, resulting in a reduction in the amount present in the reaction product, as observed in the diffraction patterns (Figures 6.14 and 6.15).



**Figure 6.14 – XRD and TGA analysis of product WRW17-RLF-500-3l/h, WRW17-RLF-600-3l/h and WRW17-RLF-700-3l/h with a particle size of <0.5 mm**

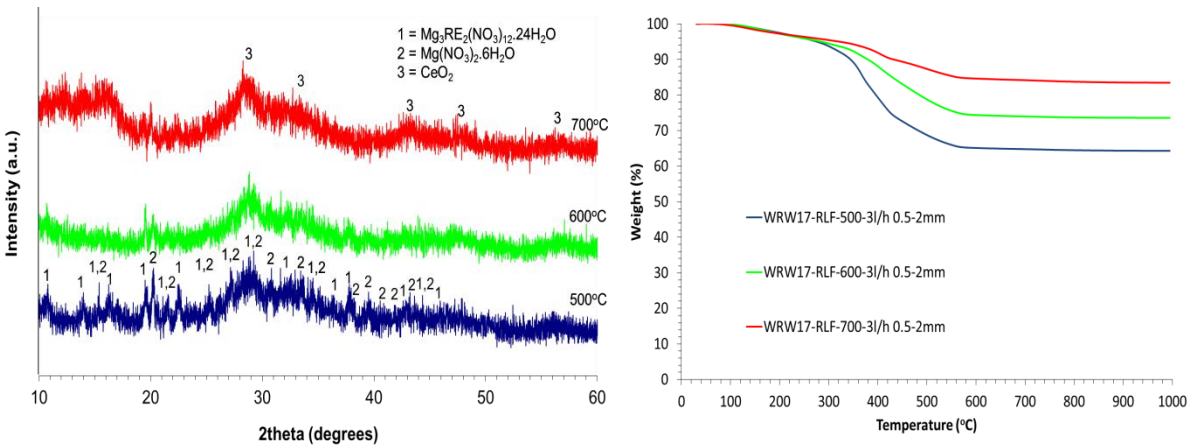


**Figure 6.15 – XRD and TGA analysis of product WRW17-RLF-500-3l/h, WRW17-RLF-600-3l/h and WRW17-RLF-700-3l/h with a particle size of 0.5 – 2 mm**

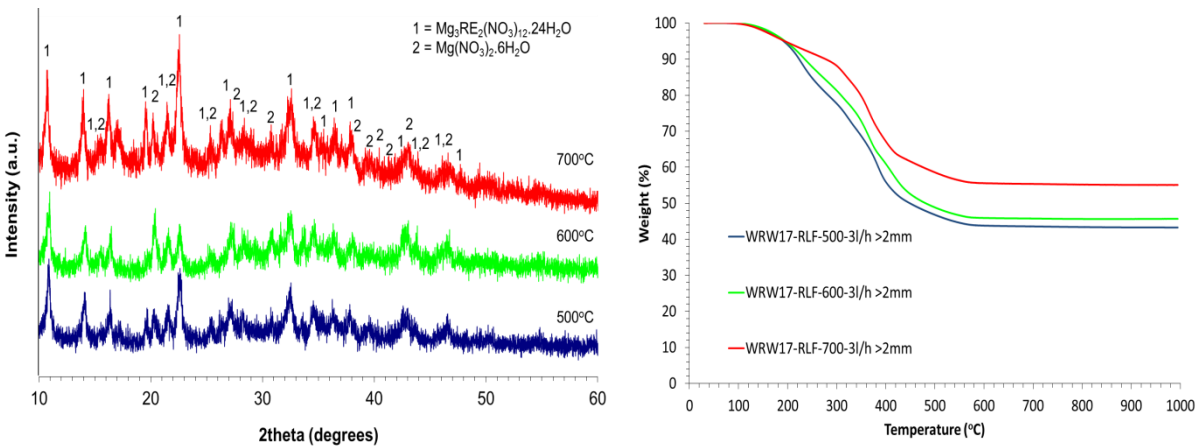


**Figure 6.16 - XRD and TGA analysis of product WRW17-RLF-500-3l/h, WRW17-RLF-600-3l/h and WRW17-RLF-700-3l/h with a particle size of >2 mm**

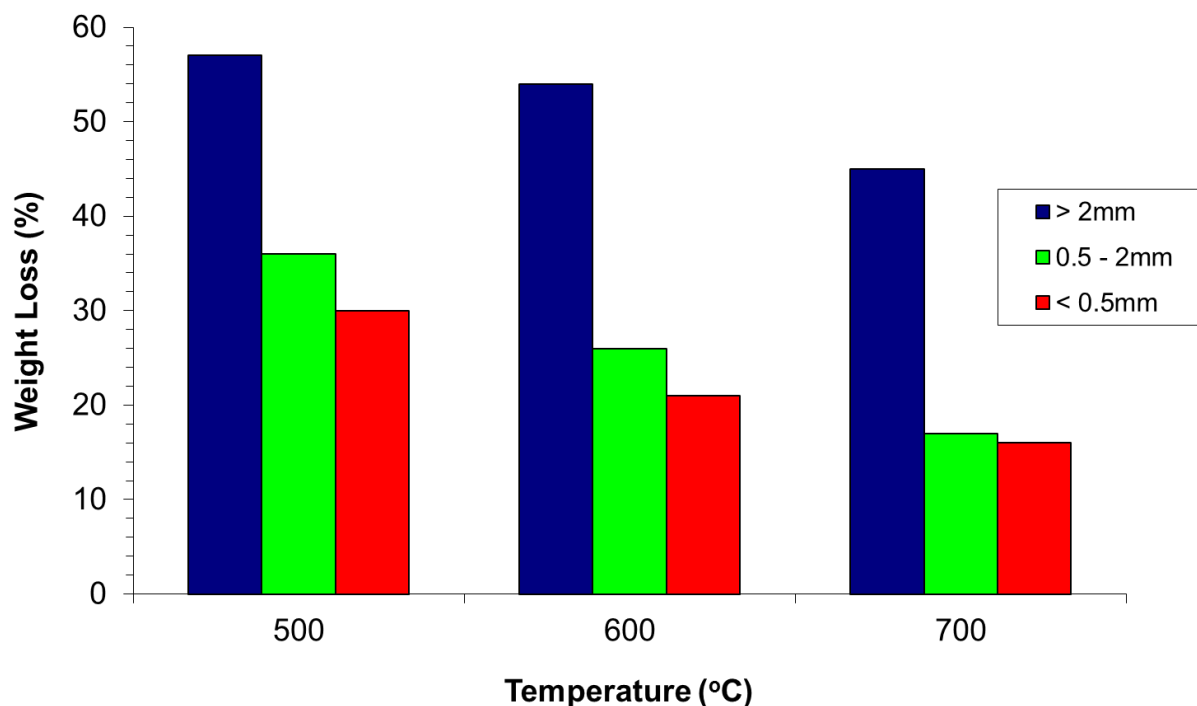


**Figure 6.17 – Weight loss of the different size fractions of products WRW17-RLF-500-3l/h, WRW17-RLF-600-3l/h and WRW17-RLF-700-3l/h**

At particle sizes greater than 2 mm in diameter relatively intense reflections attributable to  $\text{Mg}_3\text{RE}_2(\text{NO}_3)_{12} \cdot 24\text{H}_2\text{O}$  were observed in all XRD patterns of products WRW17-RLF calcined between 500-700 °C at a constant feed rate of 3 l / h (Figure 6.16). These reflections essentially accounted for all of the reflections shown in the diffraction patterns. Strong diffuse scattering was also apparent showing the presence of non-crystalline component(s). TGA analysis of products WRW17-RLF, with a particle size >2 mm (Figure 6.17), showed much greater weight losses than observed in the smaller particle sized samples, with the weight loss decreasing at higher calcination temperatures. This was consistent with previous observations which showed increasing temperature and a reduction in particle size led to lower residual weight losses being recorded. The weight loss profiles for products WRW17-RLF-500-3l/h, WRW17-RLF-600-3l/h and WRW17-RLF-700-3l/h, with a particle size >2 mm, showed the same three distinct events as observed with smaller particle sizes, however, the events below 300 °C (attributable to dehydration), and at 380 °C (associated with denitration of  $\text{Mg}_3\text{RE}_2(\text{NO}_3)_{12} \cdot 24\text{H}_2\text{O}$ ) showed much greater intensities, showing a higher portion of the volatile inventory was retained. This is in agreement with XRD analysis, which showed  $\text{Mg}_3\text{RE}_2(\text{NO}_3)_{12} \cdot 24\text{H}_2\text{O}$  was observed in the reaction products with a particle size >2 mm.

Figure 6.18 shows the effects of particle size on the calcine properties through XRD and TGA analysis for product WRW17-RLF-700-3l/h. These data show a similarity in weight loss and chemical composition in particle size fractions <0.5 mm and 0.5-2 mm, but exhibited significant differences from the size fraction greater than 2 mm. XRD and TGA analysis of the dust sample collected from this experiment showed a close match to the particle size fraction >2 mm but not to the smaller fractions. This implies that the dust is generated from the large particles, which have higher residual nitrate contents. In general, metal nitrates have a much lower density than their component oxides (Phillips, 1995; Perry, 2011). This implies that they will be preferentially carried over to the off-gas system compared to the component oxides of a comparable particle size, consistent with studies of particle movement in a constant air flow, which were found to be dependent on both particle size and density (Dong et al, 2003). Further analysis of the dust carry-over is discussed in section 6.3.2.1.2.1.

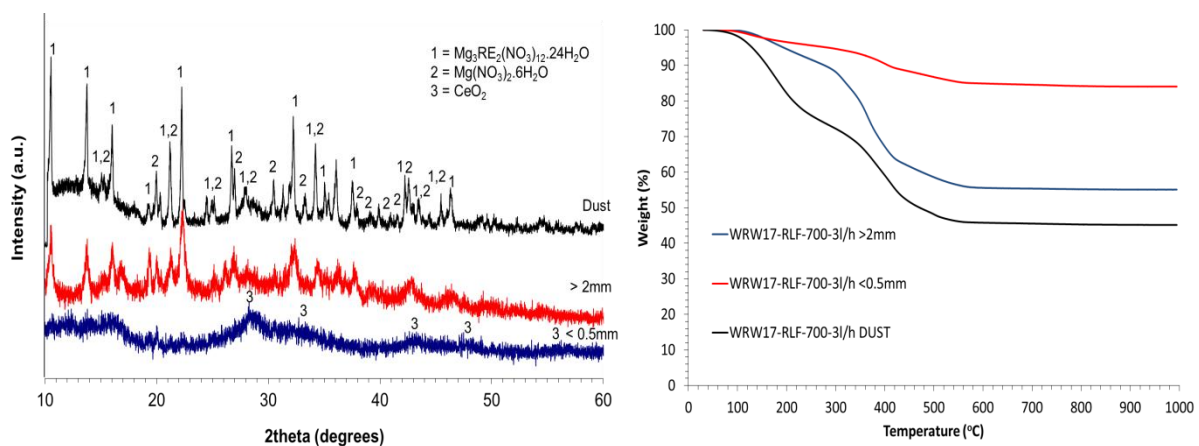


**Figure 6.18 – XRD and TGA analysis of product WRW17-RLF-700-3l/h dust and calcine with particle sizes of <0.5 mm and >2 mm**

### 6.3.2.1.1.2 Effects of feed rate

At higher feed rates, it takes longer to evaporate off the water, pushing the evaporative front further down the calciner tube (Short, 2012). This effectively shrinks the area of the tube in which denitration processes occur. The effect of this is that products formed at high feed rates have a higher residual nitrate content due to the fact that the residence time at high temperature is cut. As a result, there were a higher fraction of small particles formed at lower feed rates (Figure 6.19). These experiments are therefore in agreement with previous work carried out on both the small scale calciner and VTR (Short, 2012; Brace, 2004).

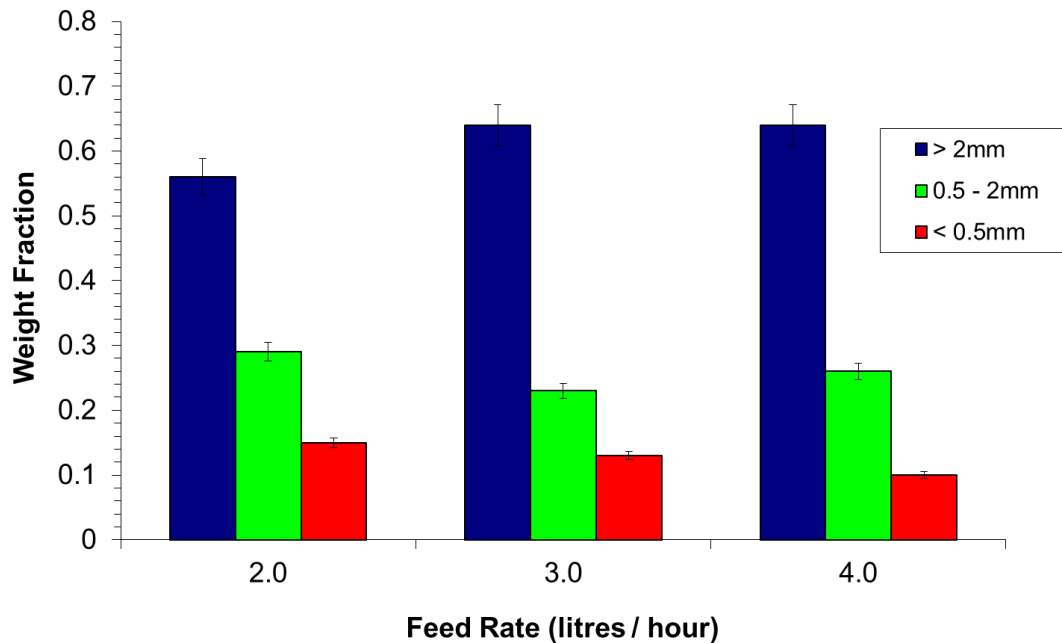


**Figure 6.19 – Particle size fractions from product WRW17-RLF-600 calcined at 2-4 l / h**

XRD analysis of products WRW17-RLF-600 run at feed rates of between 2-4 l / h, with particle sizes <2mm (Figures 6.20 and 6.21) all showed high levels of diffuse scattering, indicating the presence of non-crystalline components. After calcination at 600 °C with a feed rate of 4 l / h, weak reflections attributable to  $\text{Mg}_3\text{RE}_2(\text{NO}_3)_{12}\cdot 24\text{H}_2\text{O}$  were observed in the product. These reflections became less intense as a function of reducing feed rate. These same effects were observed as a function of increasing temperature (section 6.3.2.1.1.1), showing that reducing the feed rate increases the effective temperature through an increase in residence time at higher temperature. The total weight losses at 1000 °C of products WRW17-RLF-600, calcined at feed rates of between 2-4 l / h, as functions of temperature and particle size are shown in Figure 6.23. Higher weight loss values are observed after calcination at higher feed rates due to the retention of a higher portion of the volatile inventory as the residence time is reduced in the heated calciner tube. This shows a higher residual hydrate and nitrate inventory is retained at higher feed rates due to the fact that more liquid has to be evaporated in the calciner tube, therefore the evaporative front is moved down the tube and there is a lower residence time in the area of the tube where denitration occurs. The weight loss profiles of products WRW17-RLF-600 calcined at a feed rates of 2-4 l / h, with a particle size <2 mm (Figures 6.20 and 6.21) all show three distinct events (as observed previously in section 6.3.2.1.1.1) attributed to dehydration, denitration of  $\text{Mg}_3\text{RE}_2(\text{NO}_3)_{12}\cdot 24\text{H}_2\text{O}$  and further denitration of the more stable nitrate components respectively. The weight loss event associated with the denitration of  $\text{Mg}_3\text{RE}_2(\text{NO}_3)_{12}\cdot 24\text{H}_2\text{O}$ , at 380 °C, was more pronounced at higher feed rates and larger particle sizes. This is consistent with XRD analysis, showing the peaks associated with  $\text{Mg}_3\text{RE}_2(\text{NO}_3)_{12}\cdot 24\text{H}_2\text{O}$  diminished with reducing feed rates and particle size.

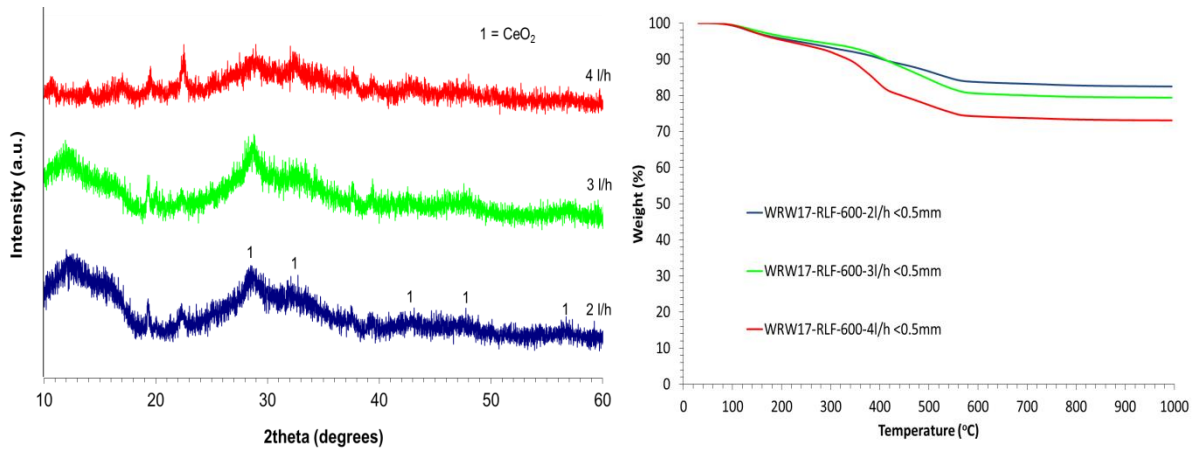


Figure 6.20 – XRD and TGA analysis of product WRW17-RLF-600-2l/h, WRW17-RLF-600-3l/h and WRW17-RLF-600-4l/h with a particle size of <0.5 mm

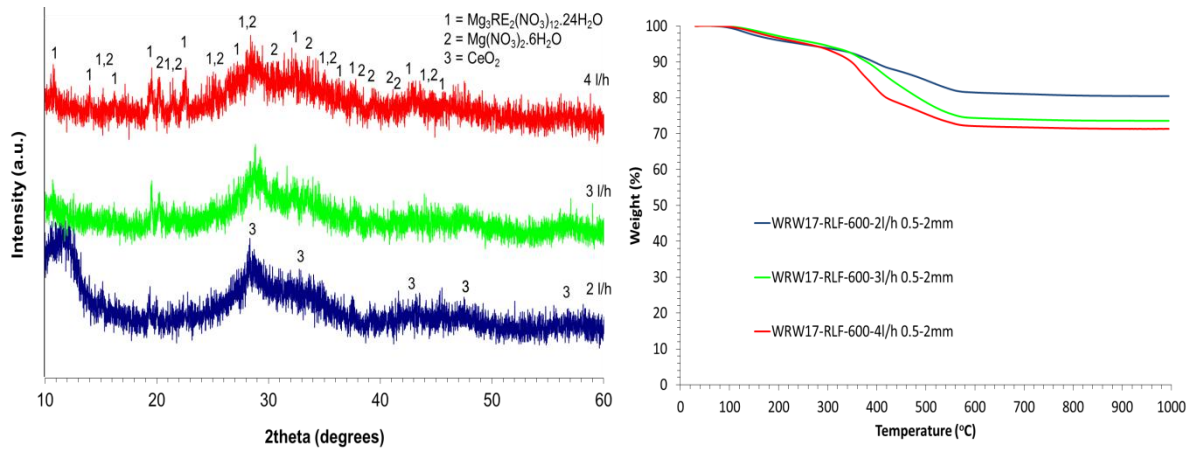


Figure 6.21 – XRD and TGA analysis of product WRW17-RLF-600-2l/h, WRW17-RLF-600-3l/h and WRW17-RLF-600-4l/h with a particle size of 0.5 – 2 mm

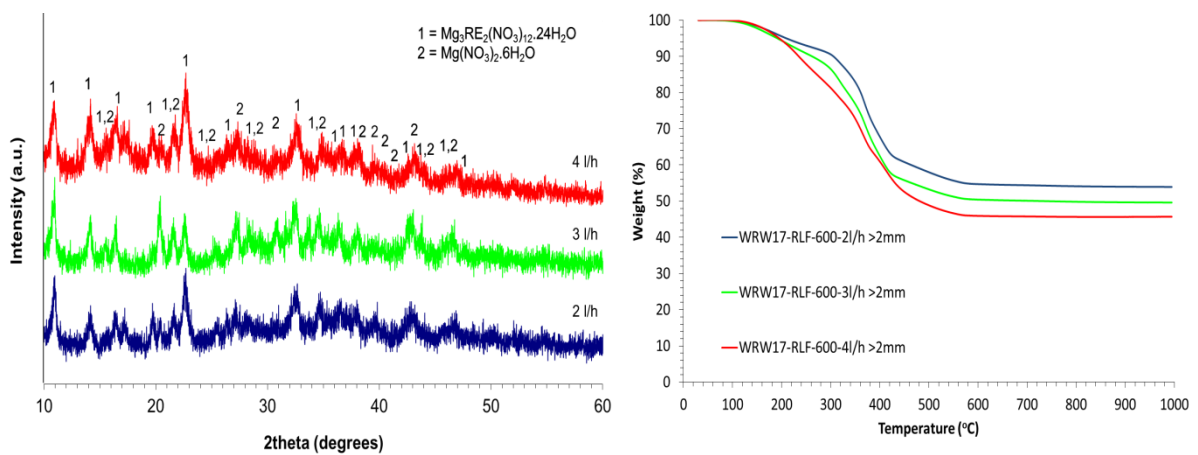
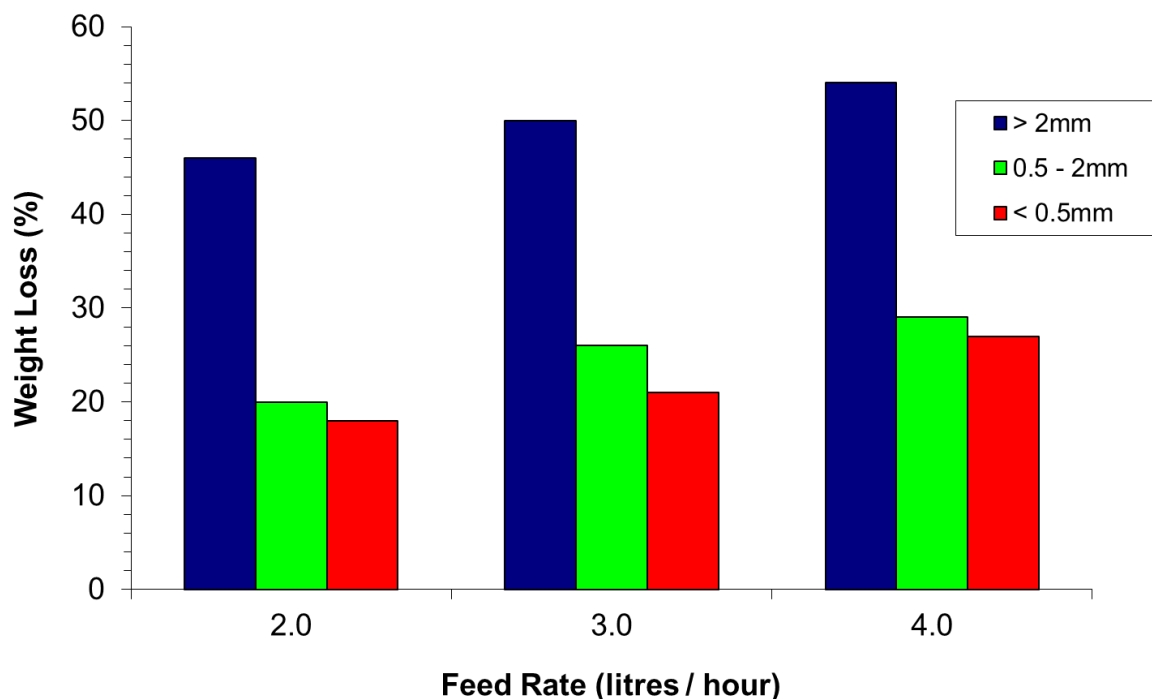


Figure 6.22 – XRD and TGA analysis of product WRW17-RLF-600-2l/h, WRW17-RLF-600-3l/h and WRW17-RLF-600-4l/h with a particle size of >2 mm





**Figure 6.23 – Weight loss of the different size fractions of products  
WRW17-RLF-600-2l/h, WRW17-RLF-600-3l/h and WRW17-RLF-600-4l/h**

XRD analysis of products WRW17-RLF-600, calcined with feed rates of 2-4 l / h and a particle size >2 mm, showed reflections attributable to  $\text{Mg}_3\text{RE}_2(\text{NO}_3)_{12} \cdot 24\text{H}_2\text{O}$  were observed in all the diffraction patterns. These reflections essentially accounted for all of the reflections shown in the XRD patterns, with strong diffuse scattering also present, suggesting the co-existence of an amorphous phase. TGA analysis of products WRW17-RLF-600-2l/h, WRW17-RLF-600-3l/h and WRW17-RLF-600-4l/h, with a particle size >2 mm (Figure 6.22), showed higher weight losses than the smaller particles formed in these experiments, with the weight loss increasing at higher feed rates. The weight loss profiles these products showed the same three distinct events as seen at smaller particle sizes, however, the events below 300 °C (attributable to dehydration), and at 380 °C (associated with denitration of  $\text{Mg}_3\text{RE}_2(\text{NO}_3)_{12} \cdot 24\text{H}_2\text{O}$ ) showed much greater intensities. This was consistent with XRD analysis, which showed  $\text{Mg}_3\text{RE}_2(\text{NO}_3)_{12} \cdot 24\text{H}_2\text{O}$  was observed in all reaction products with a particle size >2 mm.

### 6.3.2.1.2 Dust Analysis

During this project, the small scale calciner was partially re-built and modified to allow the collection of dust particles carried from the calciner tube to the off-gas system in their solid state. This has not previously been possible as there was no sample collection point on the small scale calciner before modifications were put in place, and the first sample point on the VTR is the dust scrubber liquor, in which the dust is mostly dissolved in nitric acid. This allowed analysis to be carried out on the dust to determine particle size, density and composition which has not been possible in historic studies.

#### 6.3.2.1.2.1 Effects of temperature

There was an increase in the mass of dust collected in the off-gas system as the calcination temperature was increased. The mass values were normalised by conversion to a percentage of the actual yield so they could be compared. This gave a range of dust carry-over values of 3.25 wt% after calcination at 500 °C, up to 4.77 wt% at 700 °C, showing an increasing in dust carry-over as a function of increasing temperature (Figure 6.24). As discussed previously (section 6.3.2.1) this is in correlation with an increase in the calcine fraction with a particle size >2 mm. As with the calcine, a 5 % error was associated with the collection of dust from the small scale calciner to take into account the fact that not all of the dust would be recovered in these experiments.

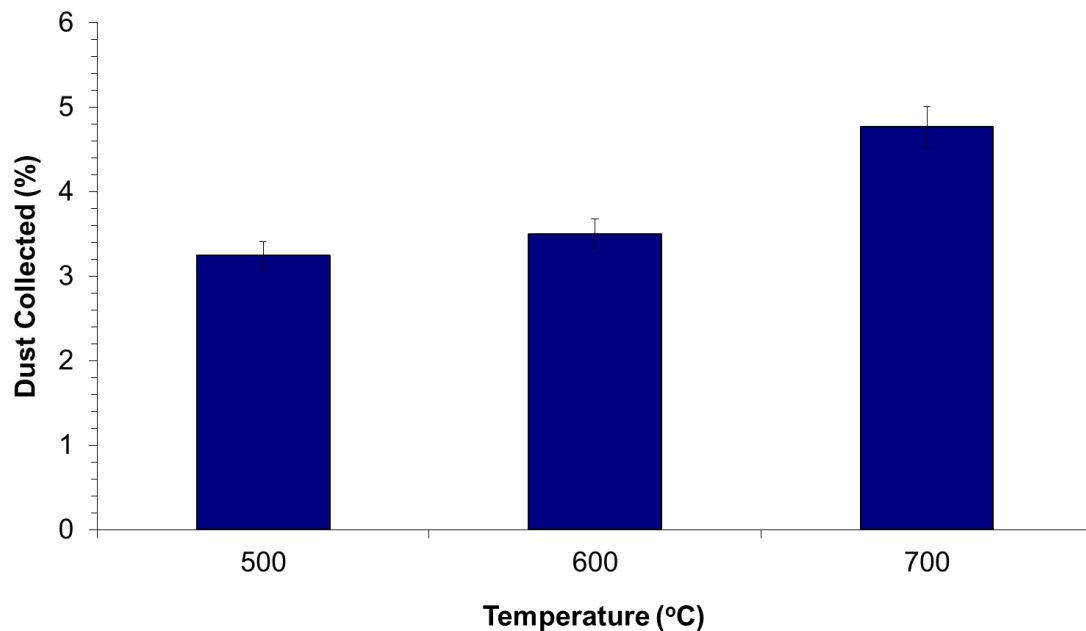


**Figure 6.24 – Dust collected as a percentage of the expected yield from products WRW17-RLF calcined between 500-700 °C at a feed rate of 3 l / h**

XRD analysis of the dust samples produced from WRW17-RLF calcined at 500, 600 and 700 °C (Figure 6.25), at a feed rate of 3 l / h, all showed a set of matching reflections attributable to  $\text{Mg}_3\text{RE}_2(\text{NO}_3)_{12}\cdot 24\text{H}_2\text{O}$  and  $\text{Mg}(\text{NO}_3)_2\cdot 6\text{H}_2\text{O}$  [14-101]. These reflections essentially accounted for all of the reflections shown in the diffraction pattern. As the calcination temperature was increased, the crystallinity of these phases improved. Significant diffuse scattering was observed, showing the presence of a non-crystalline component. TGA analysis showed weight losses of between 45-55 wt% at 1000 °C (Figure 6.26), which were comparable to the values attained from the calcine fraction with a particle size greater than 2 mm. Similar weight loss profiles were also observed for the dust samples as was shown in products WRW17-RLF calcined between 500-700 °C, with a particle size >2 mm. These showed three distinct events: a broad weight loss below 300 °C, typical of dehydration; a relatively sharp weight loss at 380 °C, associated with the denitration of  $\text{Mg}_3\text{RE}_2(\text{NO}_3)_{12}\cdot 24\text{H}_2\text{O}$  (Appendix 2); and a broad weight loss between 450-600 °C, attributable to further denitration of the more stable nitrate components which make up the HAL simulant, by reference to thermal stability data for individual component nitrates of which the HAL is comprised (Chun, 1977). Taken together, the XRD and TGA data, along with the increase in the calcine fraction collected with larger particle size (>2 mm) as the calcination temperature was increased, correlating with an increase in dust carry-over imply that the dust has a similar composition to the calcine fraction with a particle size >2 mm and is far removed from the smaller calcine particles formed in these experiments. This suggests that the mechanism by which dust is created, and subsequently transported to the off-gas system, involves the abrasive breakdown of larger particles.

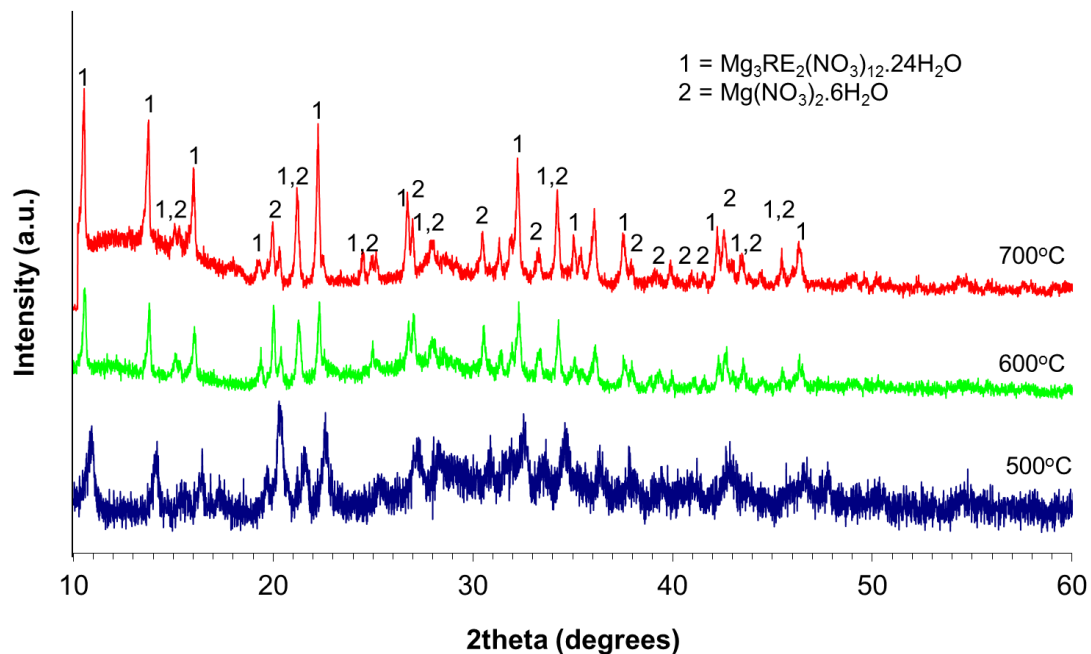


**Figure 6.25 – XRD analysis of products a) WRW17-RLF-500-3l/h, b) WRW17-RLF-600-3l/h and c) WRW17-RLF-700-3l/h dust samples**

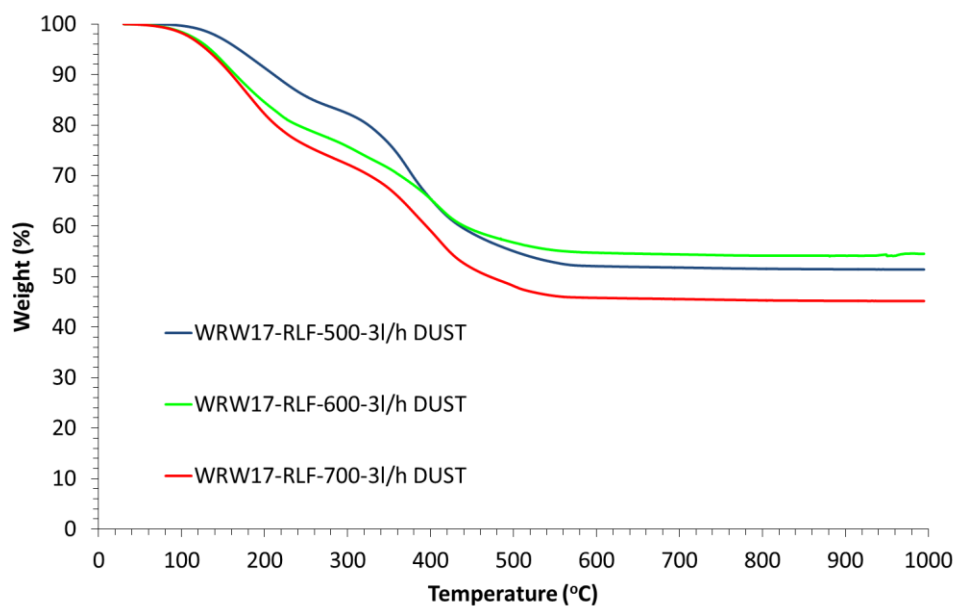


**Figure 6.26 – TGA analysis of products WRW17-RLF-500-3l/h, WRW17-RLF-600-3l/h and WRW17-RLF-700-3l/h dust samples**

Chemical analysis was carried out, using ICP-OES<sup>22</sup>, on products WRW17-RLF-500-3l/h, WRW17-RLF-600-3l/h and WRW17-RLF-700-3l/h with particle sizes of >2 mm and <0.5 mm as well as the dust collected during these experiments. After calcination at 500 °C (Figure 6.27), the ICP analysis showed the composition of the dust was much closer to that of the fraction >2mm than the smaller particle size fractions, in agreement with TGA and XRD analysis. Most of the elements were present in a higher concentration in the calcine fraction >2 mm than in the dust, however, Mo and Zr were both present in a higher concentration in the dust (though Zr matched that of the calcine with particle size >2 mm within error of the experiment), suggesting they were preferentially carried over to the off-gas system (discussed further in section 7.3.2). Mg and the RE elements appeared to be present in a higher concentration in the calcine than in the dust, suggesting that  $Mg_3RE_2(NO_3)_{12} \cdot 24H_2O$  is more difficult to transport to the off-gas system than other elements present in the Magnox HAL simulant under these calcination conditions, consistent with the relatively low intensity XRD reflections attributed to the Mg RE nitrate phase in product WRW17-RLF-500-3l/h dust sample. After calcination at 700 °C, chemical analysis showed that (within error) all elements have the same concentrations in the dust and calcine fraction with a particle size above 2 mm, with the exception of Mo, which showed an increased concentration in the dust (same as after calcination at 500 °C) suggesting preferential carry-over of a Mo containing phase to the off-gas system (Figure 6.28). Zr also had a higher concentration in the dust than the calcine fraction above 2 mm, though was within the error associated with the analysis. All elements showed a higher concentration in the particle size fraction <0.5 mm, due to the lower residual nitrate and hydrate content in the product, consistent with

<sup>22</sup> Cs, H, N and O concentrations could not be analysed using this technique.

TGA analysis. This implied that the dust fraction bared a much closer resemblance to the calcine with a large particle size (>2 mm) rather than the smaller fraction, in agreement with XRD and TGA data which showed  $Mg_3RE_2(NO_3)_{12} \cdot 24H_2O$  was formed in these phases. These data supported the XRD and TGA analysis, along with the density measurements, which suggested that the dust had similar chemical properties to that of the calcine particles with a particle size >2 mm and was different from the small calcine particles (<0.5 mm). This suggested that the dust was formed from the breakdown of the larger particles formed within the calcination process.

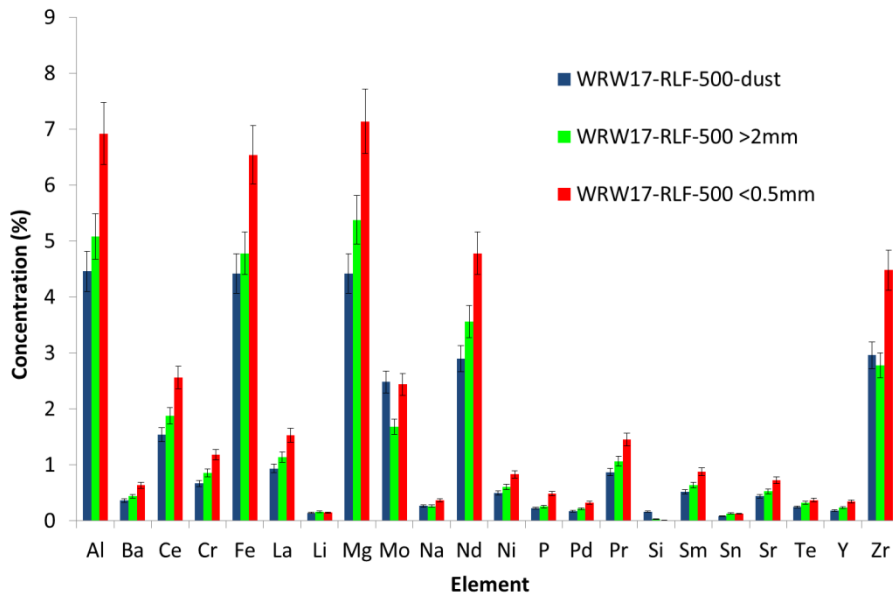


**Figure 6.27 – Chemical Composition of product WRW17-RLF-500-3l/h dust and calcine samples with particle sizes of <0.5 mm and >2 mm determined by ICP-OES**

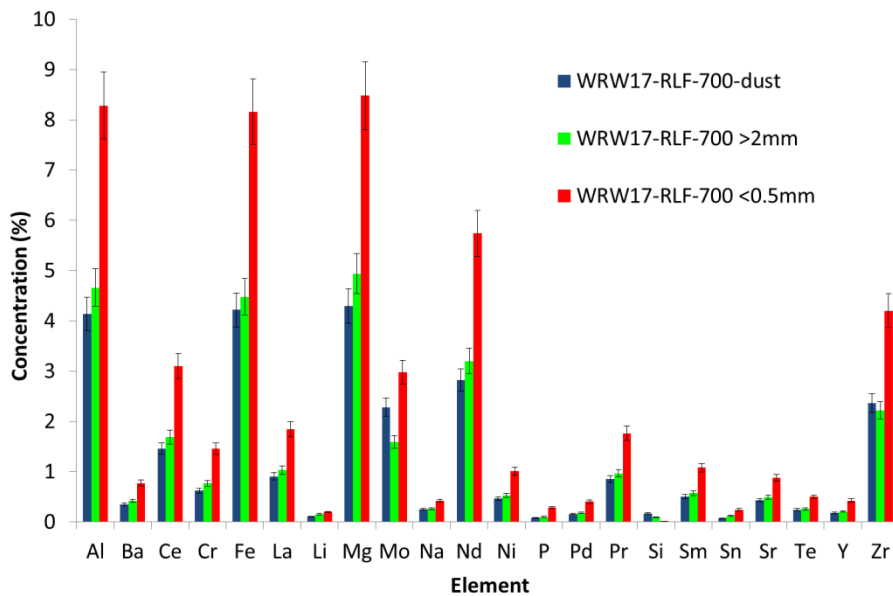


**Figure 6.28 – Chemical Composition of product WRW17-RLF-700-3l/h dust and calcine samples with particle sizes of <0.5 mm and >2 mm determined by ICP-OES**

The backscattered electron image of the dust collected from calcination of product WRW17-RLF-700 at 3 l/h (Figure 6.29) showed a strong co-association of Mg and Nd, consistent with TGA and XRD analysis showing the presence of  $\text{Mg}_3\text{RE}_2(\text{NO}_3)_{12}\cdot 24\text{H}_2\text{O}$ . Al, Mo and Zr all appeared to form phases independent from each other, though some co-habitation of the same areas as the other selected elements was observed due to the intimate mixing in the HAL simulant solution and during the calcination process. The same trends were observed in the dust samples formed after calcination at 500 and 600 °C.

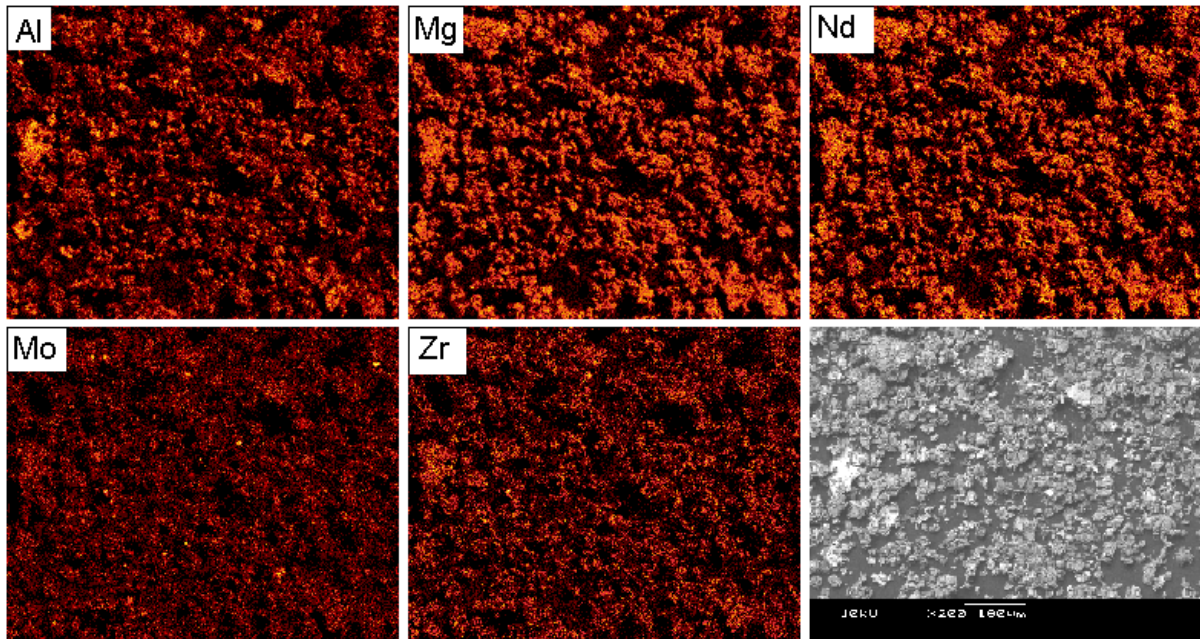


**Figure 6.29 – Backscattered electron image and X-ray maps of product WRW17-RLF-700-3l/h-dust**

From these experiments, it is possible to infer and conclude the following:

- An increase in dust carry-over to the off-gas system was observed at increasing temperature, in correlation with an increase in the formation of larger particles in the calcine.
- XRD and TGA analysis showed the presence of  $\text{Mg}_3\text{RE}_2(\text{NO}_3)_{12}\cdot 24\text{H}_2\text{O}$  in both the dust and larger calcine particles (>2 mm), with this diminishing in the smaller particles and as a function of increasing temperature. This implied that dust is formed from the breakdown of larger calcine particles.
- The ICP-OES and EDS analysis combined with the density measurements also showed similarities between the larger particles and the dust, with the smaller particles being significantly different in chemical composition. The increase in density also suggested that these particles would not be as easily carried over to the off-gas system, supporting the evidence for the dust formation occurring from the abrasive breakdown of larger calcine particles.

### 6.3.2.1.2.2 Effects of feed rate

There was an increase in the mass of dust collected in the off-gas system as the calcination feed rate was increased, due to the increases in throughput in the calciner. However, when the mass values were normalised, by conversion to a percentage of the actual yield, the highest dust carry-over was observed at the lowest feed rate (Figure 6.30). This was expected, as at lower feed rates, the water is evaporated more quickly, effectively increasing the residence time at a higher temperature. At feed rates of 3 l/h and 4 l/h, the dust carry-over was almost identical, which correlated with identical fractions of calcine particles larger than 2 mm in diameter. When the feed rate was 2 l/h, however, the fraction of large particles was lower, even though an increase in dust carry-over was observed. This is in contrast to previous experiments, where increased temperatures gave rise to a higher portion of large particles being formed. It is thought that the effects of feed rate on the position of the evaporative front in the calciner will be affected more greatly by feed rate than Zone 3 temperature, as set-points 1 and 2 were kept the same (400 °C) throughout these experiments. Therefore, at a feed rate of 2 l/h, the longer residence time in a ‘drier’ calciner tube would allow the rabble bar to break up the calcine over a longer portion of the tube, resulting in a decrease in particle size further down the calciner tube. The initial abrasion of larger particles, thought to be responsible for formation of the dust which is subsequently carried over to the off-gas system, could therefore still be occurring initially, with further breakdown of the larger particles taking place due to the longer time in the hotter part of the tube where denitration processes occur. These competing processes could explain the discrepancy in these results.

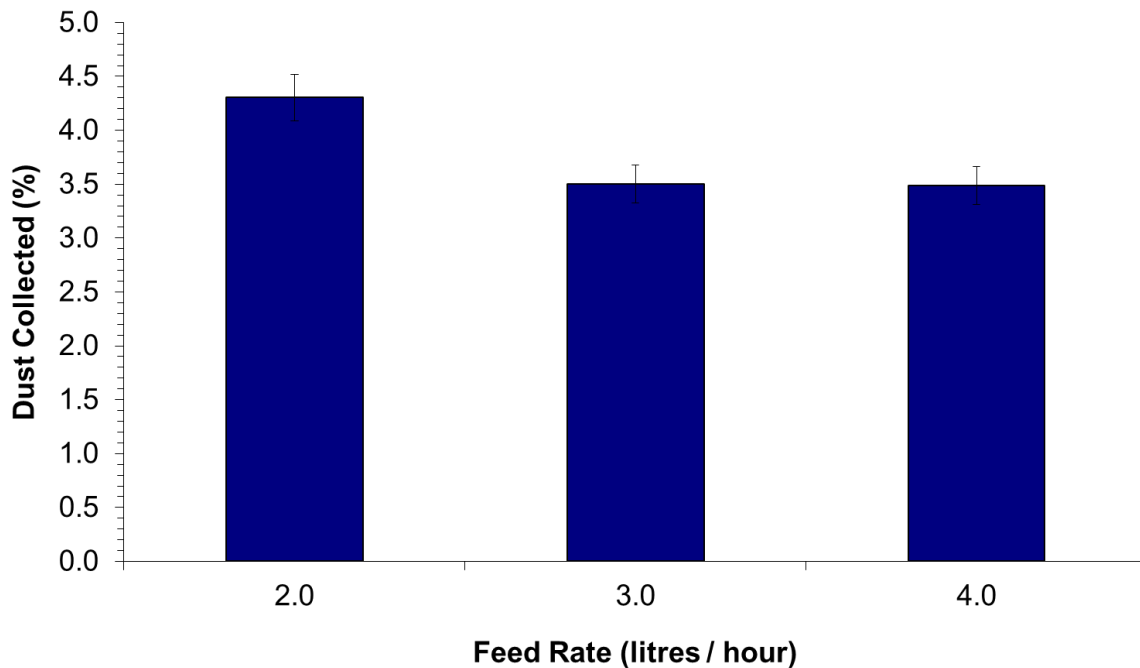


**Figure 6.30 – Dust collected as a percentage of the expected yield from products WRW17-RLF-600 calcined between 2-4 l/h**

XRD analysis of the dust samples produced from WRW17-RLF-600 calcined at feed rates of 2 l/h, 3 l/h and 4 l/h (Figure 6.31) all showed a set of matching reflections attributable to  $\text{Mg}_3\text{RE}_2(\text{NO}_3)_{12}\cdot 24\text{H}_2\text{O}$  and  $\text{Mg}(\text{NO}_3)_2\cdot 6\text{H}_2\text{O}$  [14-101], as observed previously at different calcination temperatures. These reflections essentially accounted for all of the reflections shown in the diffraction pattern, with strong diffuse scattering also observed, showing the presence of non-crystalline component(s). TGA analysis showed weight losses of between 45-49 wt% at 1000 °C, with a slight decrease in weight loss as a function of reducing feed rates (Figure 6.32). These weight loss values and the resultant profiles are comparable to the values attained from the calcine fraction with a particle size greater than 2mm. These showed three distinct events at temperatures of below 300 °C, 380 °C and between 450-600 °C, associated with dehydration, denitration of  $\text{Mg}_3\text{RE}_2(\text{NO}_3)_{12}\cdot 24\text{H}_2\text{O}$  and  $\text{Mg}(\text{NO}_3)_2\cdot 6\text{H}_2\text{O}$ , and further denitration of the more stable nitrate components respectively (Appendix 2; Paulik et al., 1988; Chun, 1977). Taken together, the XRD and TGA data imply that the dust has a similar composition to the calcine fraction with a particle size >2 mm and is far removed from the smaller calcine particles formed in these experiments. This again suggested that the mechanism by which dust was created, and subsequently transported to the off-gas system, was due to the abrasive breakdown of larger particles.

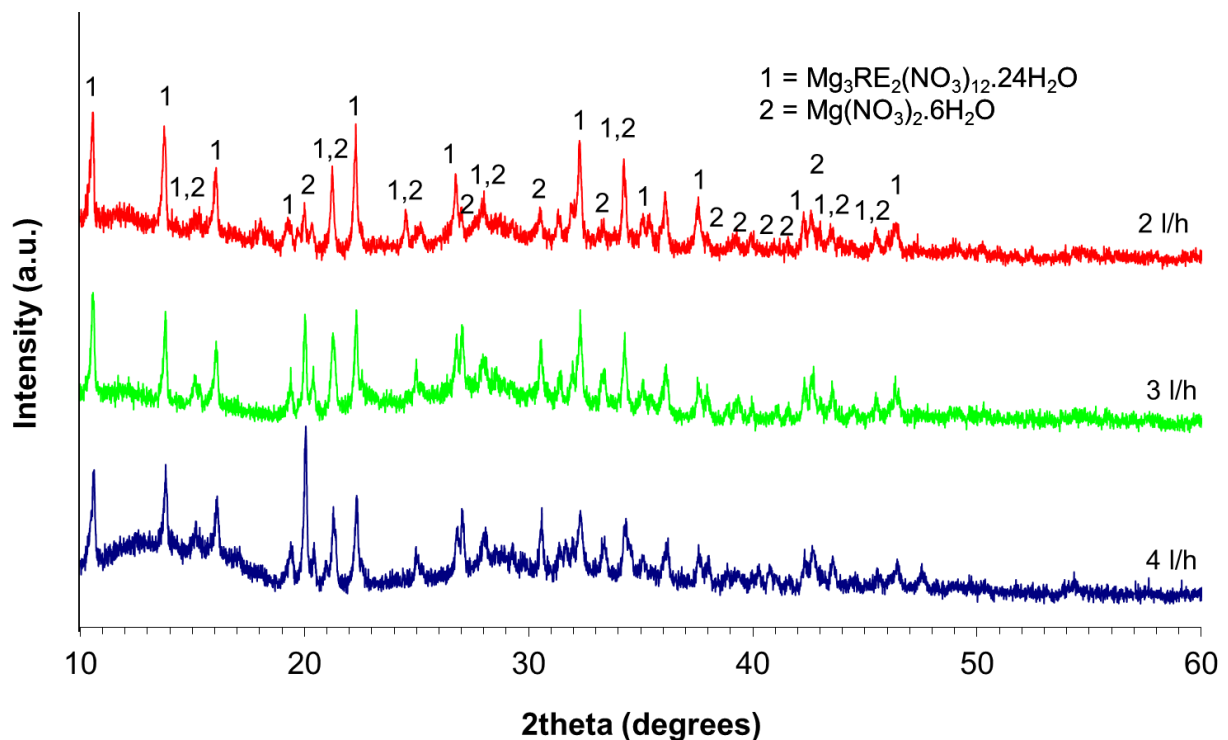


**Figure 6.31 – XRD analysis of products a) WRW17-RLF-600-2l/h, b) WRW17-RLF-600-3l/h and c) WRW17-RLF-600-4l/h dust samples**



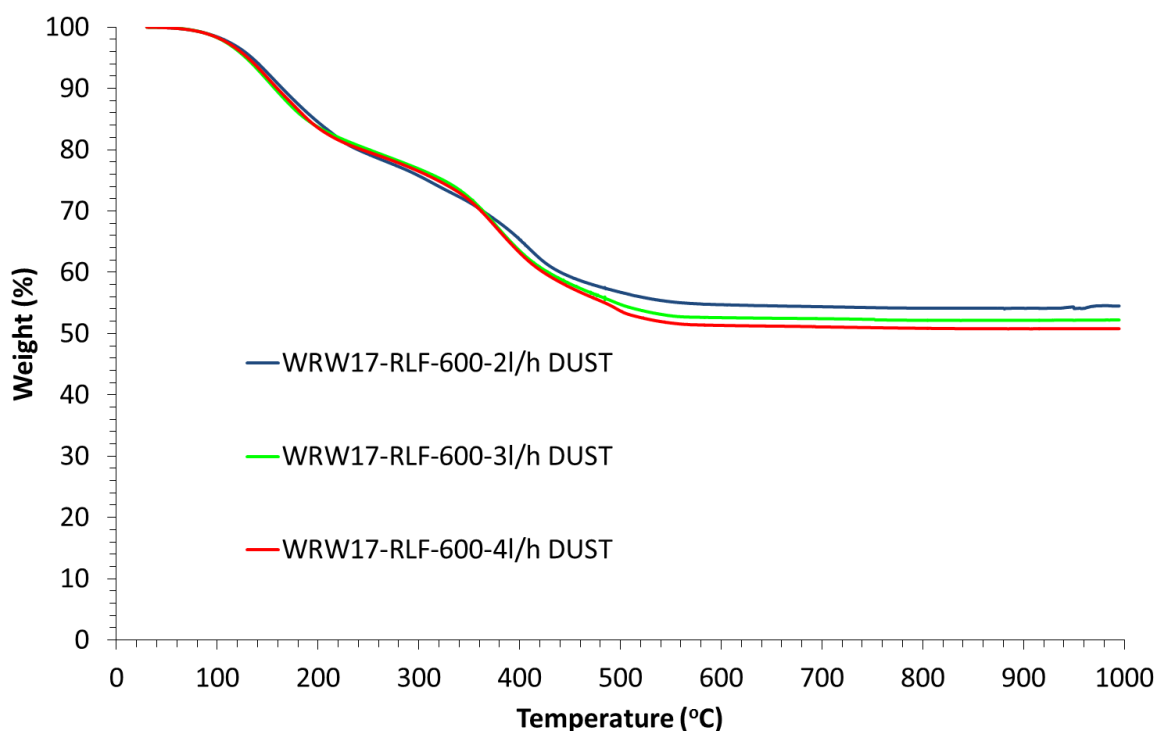


**Figure 6.32 – TGA analysis of products WRW17-RLF-600-2l/h, WRW17-RLF-600-3l/h and WRW17-RLF-600-4l/h dust samples**

From these experiments, it is possible to infer and conclude the following:

- At a low feed rate (2 l / h) there was a decrease in the amount of large particles formed in the calcine, though an increase in dust carry-over was observed, contradictory to the experiments described in section 6.3.2.1.2.1. However, this can be explained by the breakdown of the calcine particles taking place in steps, with initial breakdown forming the dust, while the calcine is still high in residual nitrate and hydrate making the product less dense, and therefore easier to transport to the off-gas system. On further heating, as the calcine travels down the calciner tube, further dehydration and denitration occurs, increasing the density making it harder to be carried over. This would result in an increasing small particle fraction without significantly affecting dust carry-over, as observed in these experiments.
- At feed rates of 3 l / h and 4 l / h, the dust carry-over was identical, correlating with similar fractions of large calcine particle being formed in the small scale calciner. This suggested that only at low feed rates does the breakdown of calcine particles take place in different steps.
- $Mg_3RE_2(NO_3)_{12} \cdot 24H_2O$  and  $Mg(NO_3)_2 \cdot 6H_2O$  were observed as the major crystalline products in the dust, consistent with the formation from the breakdown of larger particles by the rabble bar in the calciner.

### 6.3.2.2 WRW17-RF

The masses of the calcine and dust collected for products formed by calcining Magnox HAL simulants WRW17-RF at various temperatures and feed rates using the small scale calciner are shown in Table 6.5. A combination of the total waste oxide throughput and residual weight loss values for each particle size fraction (measured by TGA analysis) were used to calculate the expected yield (see section 6.2.2.1). The dust collection was converted to a percentage dust carry-over against the actual weight of calcine collected, allowing the effects of changing temperature and feed rate on the dust carry-over from the calciner to the off-gas system to be monitored. The effects of the addition of  $\text{LiNO}_3$  were also taken into account.

**Table 6.5 - Mass of calcine and dust products collected**

Sample	Expected Weight (g)	Actual Weight (g)	Amount of Dust Collected (g)	Dust Collected (wt%)
WRW17-RF-500-3l/h	786.96	777.10	15.61	2.01
WRW17-RF-600-3l/h	767.32	704.78	16.94	2.40
WRW17-RF-700-3l/h	722.13	630.54	18.72	2.97
WRW17-RF-600-2l/h	484.90	430.82	12.73	2.95
WRW17-RF-600-4l/h	1039.06	1027.52	20.11	1.96

As was the case with the Li free HAL simulants, the experiments carried out at low temperature (WRW17-RF-500-3l/h) and high feed rate (WRW17-RF-600-4l/h), yielded a combined mass of dust and calcine greater than that of the expected weight. The trend again showed a reduction in the yield collected, compared to the expected mass, with increasing calcination temperature and a reduction in the feed rate. This discrepancy could therefore be attributed to a combination of the fact that the TGA analysis was carried out on a small sample (~50 mg) of each of the calcine fraction and the fact that not all of the dust would have been collected during these experiments. However, a representative yield was thought to be recovered.

As with the Li free experiments, a higher normalised dust carry-over is observed at higher calcination temperatures, which correlates with a higher fraction of larger particles (>2 mm) being formed (Table 6.6). The fraction produced below 0.5 mm in diameter stayed constant (within error) for the experiments carried out between 500-700 °C, with the increase in larger particles being off-set by a decrease in the particle size fraction between 0.5-2 mm. This suggested the mechanism by which dust is generated is by abrasion of the larger calcine particles, resulting in small low density particles being formed and subsequently carried to the off-gas system.

**Table 6.6 - Size fractions of product WRW17-RF calcined under varying conditions**

Sample	Fraction above 2 mm	Fraction between 0.5 – 2 mm	Fraction below 0.5 mm
WRW17-RF-500-3l/h	0.44	0.38	0.18
WRW17-RF-600-3l/h	0.47	0.35	0.18
WRW17-RF-700-3l/h	0.51	0.30	0.19
WRW17-RF-600-2l/h	0.25	0.45	0.30
WRW17-RF-600-4l/h	0.41	0.41	0.18

When the small scale calciner was run at a low feed rate, a reduced mass of dust was collected due to a decrease in throughput. However, when the data were normalised, an increased dust carry-over was observed, as water is evaporated quickly, allowing a longer residence time to allow denitration processes to occur. In these experiments (as was observed in the Li free products) a higher fraction of small particles were formed at a feed rate of 2 l / h (Table 6.6), in contrast to the formation of larger particles at higher temperature, correlating with a higher dust carry-over.

On addition of LiNO<sub>3</sub> to Magnox HAL simulant (WRW17-RF) a significant reduction in normalised dust carry-over values were apparent, in agreement with previous studies (Vickers, 2006a). This also correlates with a much lower production of large particles (>2 mm) under the same calcination conditions.

### 6.3.2.2.1 Calcine Analysis

#### 6.3.2.2.1.1 Effects of temperature

Figure 6.33 shows the particle size fractions collected as a function of temperature. This showed that an increase in the mass fraction of particles >2 mm was observed as the calcination temperature was increased. The particle size range 0.5-2 mm showed a general decrease in the mass fraction at higher calcination temperature in order to off-set the increase in larger particles, with the mass of the <0.5 mm particle size range staying constant. A 5 % error was again assigned to each of the values, taken from previous trials (Brace, 2004), where a 95 % mass recovery was observed from the calciner (not taking into account dust carry-over). This will ensure the observed trends are not influenced by the errors associated with the small scale calciner. Other errors, associated with weighing the samples, were deemed insignificant and were therefore not taken into account.

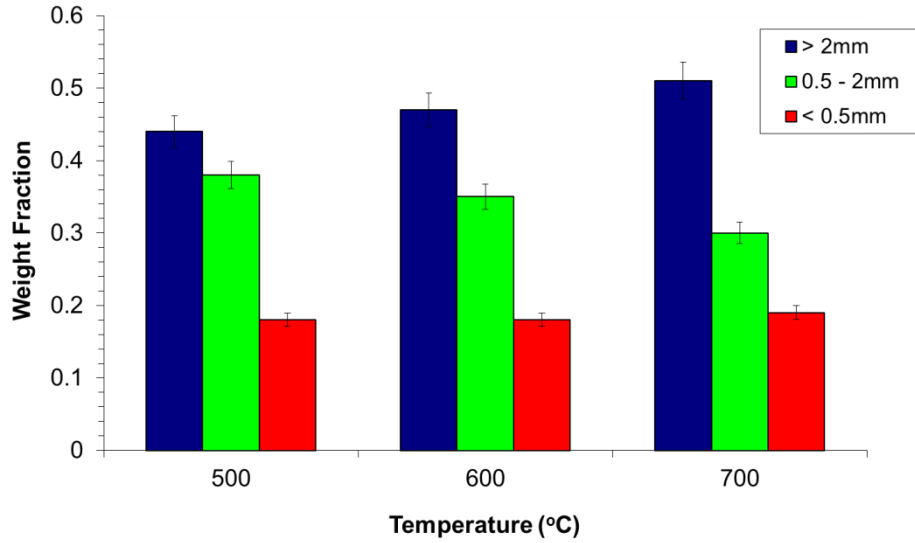


Figure 6.33 – Particle size fractions from product WRW17-RF calcined at 500-700 °C at a feed rate of 3 l/h

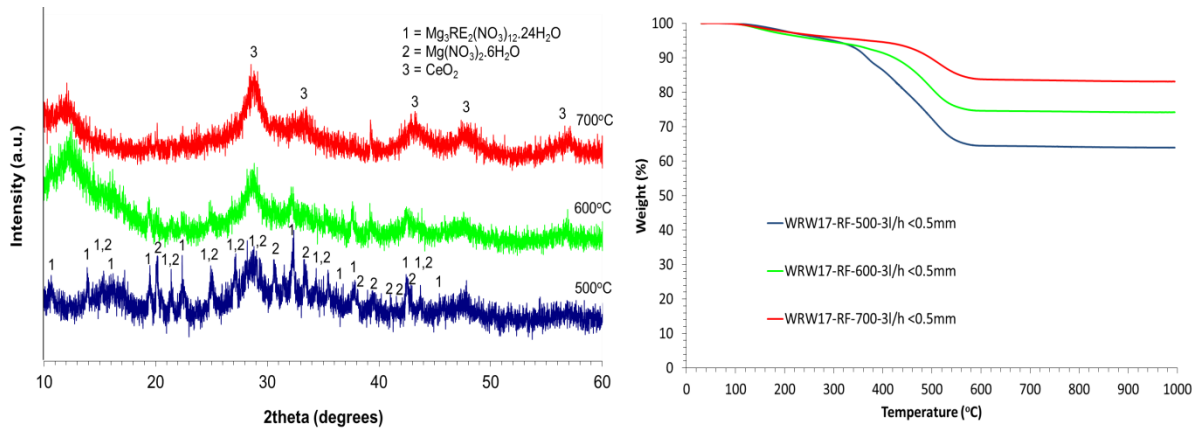


Figure 6.34 – XRD and TGA analysis of products WRW17-RF-500-3l/h, WRW17-RF-600-3l/h and WRW17-RF-700-3l/h with particle size < 0.5mm

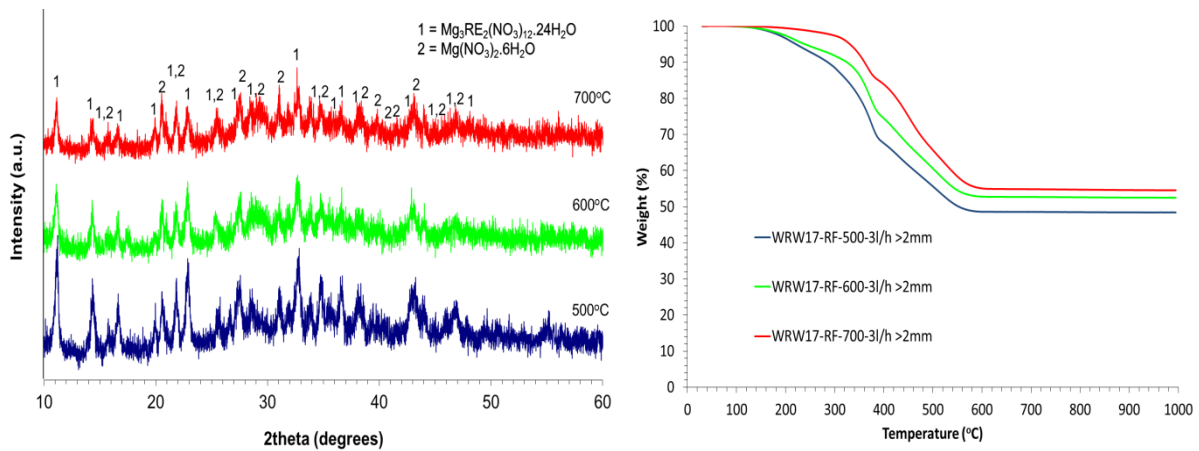


Figure 6.35 – XRD and TGA analysis of products WRW17-RF-500-3l/h, WRW17-RF-600-3l/h and WRW17-RF-700-3l/h with particle size > 2mm

The diffraction patterns of products WRW17-RF-500-3l/h, WRW17-RF-600-3l/h and WRW17-RF-700-3l/h, with particle sizes <0.5 mm (Figure 6.34), all showed high levels of diffuse scattering, indicating the presence of non-crystalline component(s). After calcination at 500 °C, weak reflections associated with  $\text{Mg}_3\text{RE}_2(\text{NO}_3)_{12}\cdot 24\text{H}_2\text{O}$  were observed in the product. These reflections show a reduction in intensity as the calcination temperature was increased. A set of reflections which were broad and weak in nature were also apparent in the XRD patterns for products WRW17-RF after calcination at 500, 600 and 700 °C with a feed rate of 3 l / h and were attributed to  $\text{CeO}_2$ . These reflections show a slight increase in intensity as a function of increasing temperature. The presence of  $\text{CeO}_2$  in Magnox simulants is in agreement with the freeze dryer experiments (sections 6.3.1.3 and 6.3.1.4) which showed the formation of this phase occurred between 350-550 °C. The addition of  $\text{LiNO}_3$  appeared to promote the formation of  $\text{CeO}_2$  in these reaction products. TGA analysis of products WRW17-RF-500-3l/h, WRW17-RF-600-3l/h and WRW17-RF-700-3l/h showed decreasing weight loss as functions of increasing temperature and a reduction in particle size (Figure 6.34), consistent with retention of a higher fraction of the volatile inventory at lower calcination temperatures. Larger particles are thought to experience a lower temperature in the calcination process due to the fact only the surface of the particle comes into contact with the heated calciner tube. The weight loss profiles of products WRW17-RF calcined at 500 °C with a feed rate of 3 l / h and particle size <0.5 mm (Figure 6.34) showed three events: a broad weight loss below 300 °C, typical of dehydration; a relatively sharp weight loss at 380 °C, associated with the denitration of  $\text{Mg}_3\text{RE}_2(\text{NO}_3)_{12}\cdot 24\text{H}_2\text{O}$  (Appendix 2); and a broad weight loss between 450-600 °C, attributable to further denitration of the more stable nitrate components which make up the HAL simulant (Chun, 1977). The weight loss event at 380 °C, attributable to the denitration of  $\text{Mg}_3\text{RE}_2(\text{NO}_3)_{12}\cdot 24\text{H}_2\text{O}$ , was not observed after calcination at 600 and 700 °C. No weight loss was observed above 600 °C, attributable to the denitration of  $\text{LiNO}_3$  (Chun, 1977), suggesting it had undergone a reaction, in agreement with sections 6.3. This is in agreement with XRD analysis which showed a reduction in intensity of the peaks associated with  $\text{Mg}_3\text{RE}_2(\text{NO}_3)_{12}\cdot 24\text{H}_2\text{O}$  with increasing calcination temperature. Overall, these data imply that  $\text{LiNO}_3$  promotes the crystalliation of  $\text{CeO}_2$  in the small particle size fraction (<0.5 mm) of the calcine, shown by an increase in intensity in the reflections compared to those seen in the Li free products. At 500 °C,  $\text{Mg}_3\text{RE}_2(\text{NO}_3)_{12}\cdot 24\text{H}_2\text{O}$  was observed, with the reflections attributable to this phase diminishing at 600 °C, and are not found after calcination at 700 °C, consistent with the absence of a weight loss event at 380 °C in the TGA trace.

The diffraction pattern of products WRW17-RF-500-3l/h, WRW17-RF-600-3l/h and WRW17-RF-700-3l/h with a particle size greater than 2 mm showed relatively intense reflections, attributable to  $\text{Mg}_3\text{RE}_2(\text{NO}_3)_{12}\cdot 24\text{H}_2\text{O}$  (Figure 6.35). Strong diffuse scattering was also observed showing the presence of non-crystalline component(s). No reflections associated with  $\text{LiNO}_3$  or  $\text{CeO}_2$  were apparent in the diffraction patterns. TGA analysis of products WRW17-RF calcined at 500, 600 and 700 °C at a feed rate of 3 l/h, with a particle size >2 mm (Figure 6.35), showed much greater weight losses than observed in the smaller particle size fractions, with an increase in weight loss also being observed at higher calcination temperatures. The weight loss profiles for products WRW17-RF-500-3l/h, WRW17-RF-600-3l/h and WRW17-RF-700-3l/h, with a particle size >2 mm, showed the same three distinct events as seen at smaller particle sizes after calcination at 500 °C. The weight loss event at 380 °C (associated with denitration of  $\text{Mg}_3\text{RE}_2(\text{NO}_3)_{12}\cdot 24\text{H}_2\text{O}$ ), however, showed a greater weight loss than observed in the smaller calcine particles. This was in agreement with XRD analysis which showed the reflections associated with  $\text{Mg}_3\text{RE}_2(\text{NO}_3)_{12}\cdot 24\text{H}_2\text{O}$  were more intense, in relation to the diffuse scattering, suggesting a higher portion remained in the reaction products with a particle size >2 mm. The absence of a weight loss event above 600 °C (typical of denitration of  $\text{LiNO}_3$ , Chun, 1977) and reflections attributable to  $\text{LiNO}_3$  suggest that it had undergone a reaction resulting in the formation of a non-crystalline phase.

Figures 6.36 and 6.37 compare  $^7\text{Li}$  MAS NMR data from WRW17-RF-500-3l/h, WRW17-RF-600-3l/h and WRW17-RF-700-3l/h with a particle size greater than 2 mm (Figure 6.36) and <0.5 mm (Figure 6.37), measured relative to  $\text{LiCl}$ . The spectra are all dominated by a very broad, asymmetric resonance centered at -0.90 ppm, with a series of asymmetric spinning side bands being observed. These spinning side bands grew higher in intensity as a function of increasing temperature and a reduction in particle size (due to the effective increase in temperature which the calcine experiences). Spinning sidebands in  $^7\text{Li}$  MAS NMR can be caused by (Tucker et al., 2002):

- Quadrupolar interactions of the nucleus with a local electric field gradient.
- Nuclear dipolar coupling to  $^7\text{Li}$
- Paramagnetic coupling to localised, unpaired transition metal electrons
- Chemical shift anisotropy
- Bulk magnetic susceptibility effects

Due to the complexity of the calcine products, it was not possible to isolate a single cause for the observation of the spinning sidebands in the  $^7\text{Li}$  MAS NMR spectra of products WRW17-RF-500-3l/h, WRW17-RF-600-3l/h and WRW17-RF-700-3l/h. Paramagnetic coupling to Mo and Zr is a possible explanation, due to the fact that Li is known to react with these elements (Chapter 5). The fact that these sidebands increase in intensity as a function of increasing temperature supported this hypothesis, as increasing reactivity was observed at higher temperatures, which would result in more Mo and Zr being in close proximity to the  $^7\text{Li}$  nuclei. Chemical shift anisotropy is known to cause an asymmetry in the resonances observed in  $^7\text{Li}$  MAS NMR (Tucker et al., 2002), as were seen in Figures 6.36 and 6.37.

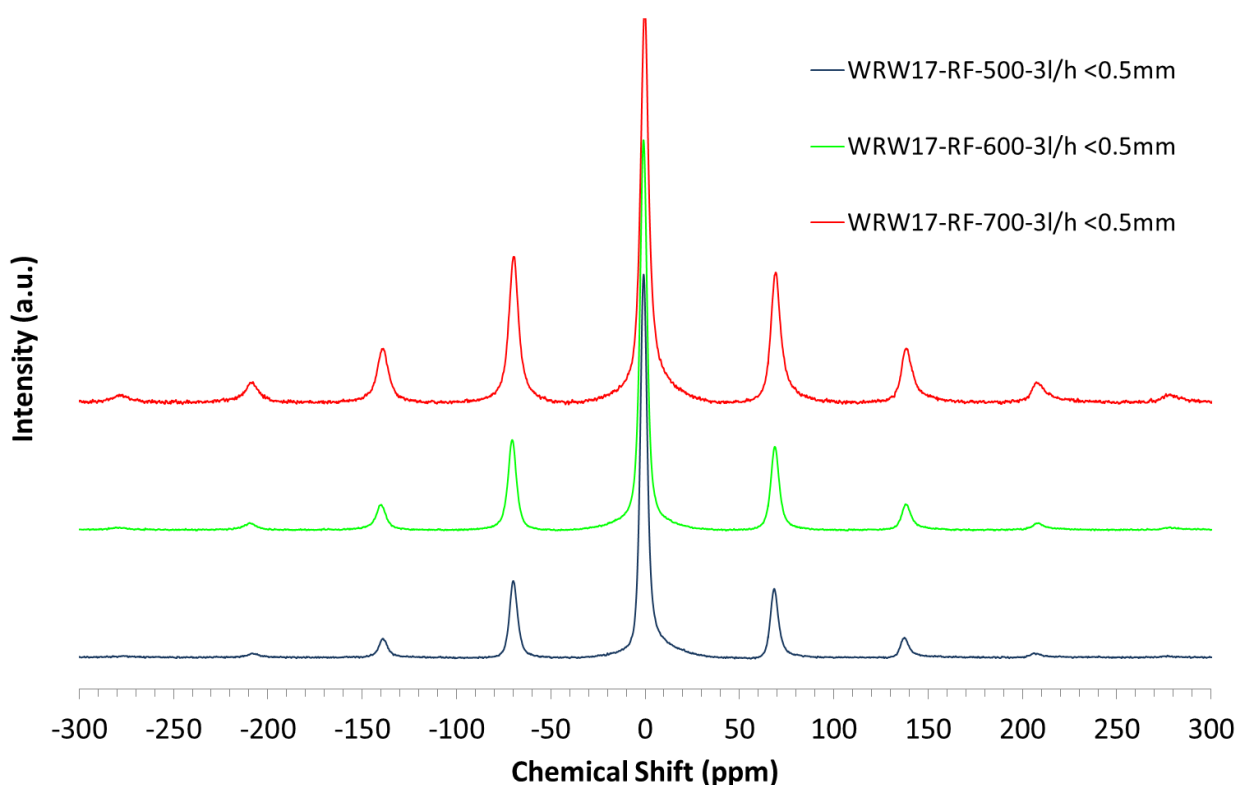


**Figure 6.36 -  $^7\text{Li}$  MAS NMR spectra of samples WRW17-RF-500-3l/h, WRW17-RF-600-3l/h and WRW17-RF-700-3l/h with a particle size  $>2$  mm**

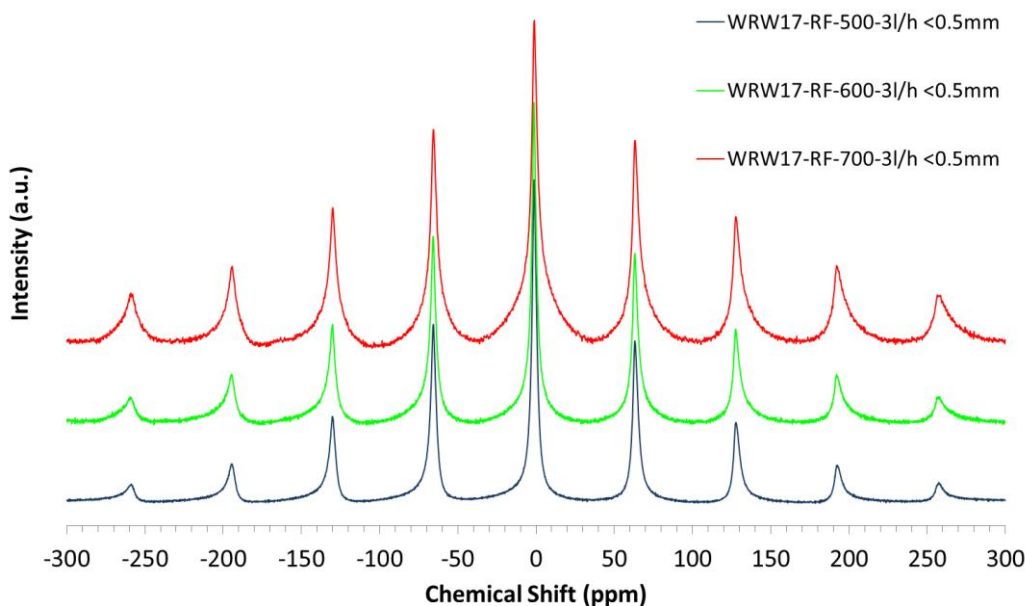


**Figure 6.37 -  $^7\text{Li}$  MAS NMR spectra of samples WRW17-RF-500-3l/h, WRW17-RF-600-3l/h and WRW17-RF-700-3l/h with a particle size <0.5 mm**

From these experiments, it is possible to infer and conclude the following effects of the addition of  $\text{LiNO}_3$  to Magnox HAL simulant:

- A reduction in large particles (>2 mm) was observed compared to the Li free samples, which correlated with a lower dust carry-over being observed.
- As the calcination temperature was increased, there was a corresponding increase in the formation of particles with a diameter greater than 2mm. This was off-set by a reduction in the middle fraction (0.5 – 2 mm) with the amount of small particles being constant. A similar effect was seen without the addition of  $\text{LiNO}_3$ .
- The absence of reflections in the diffraction pattern and a weight loss event attributable to  $\text{LiNO}_3$  imply that a reaction had occurred, resulting in a non-crystalline product being formed.
- $\text{Mg}_3\text{RE}_2(\text{NO}_3)_{12}\cdot 24\text{H}_2\text{O}$  was observed in all particle size fractions after calcination at 500 °C, though reflections reduced in intensity with decreasing particle size.
- At higher calcination temperatures,  $\text{Mg}_3\text{RE}_2(\text{NO}_3)_{12}\cdot 24\text{H}_2\text{O}$  was only retained in the larger particles (>2 mm). Poorly crystalline  $\text{CeO}_2$  was observed in the smaller particle size fractions, same as in the Li free products, although the reflections appeared to be more intense (but still broad in nature) on the addition of  $\text{LiNO}_3$ .

From this, the main effect of the addition of  $\text{LiNO}_3$  to Magnox HAL simulant can be taken to be the effect on particle size distribution of the calcine product, therefore influencing the dust carry-over from the calciner to the off-gas system.



### 6.3.2.2.1.2 Effects of feed rate

Figure 6.38 shows the particle size fractions collected as a function of feed rate, with the calcination temperature remaining constant at 600 °C. A reduction in the mass fraction of particles >2 mm was observed at a feed rate of 2 l/h, same as seen in the Li free experiment. An increase in the mass fraction of large particles was apparent in product WRW17-RF-600-3l/h, with a subsequent drop at a feed rate of 4 l/h. The fraction of small particles produced at 3 l/h and 4 l/h were identical, in agreement with previous experiments. The results for products formed at feed rates of 3 l/h and 4 l/h are consistent with the hypothesis that larger particles are formed as a function of increasing temperature (lower feed rate equates to longer residence time at high temperature), resulting in an increased dust carry-over. At a feed rate of 2 l/h, however, the fraction of large particles was lower, even though an increase in dust carry-over was apparent. This observation was also made in product WRW17-RLF-600-2l/h and could be explained by the position of the evaporative front being closer to the inlet of the tube, as water is evaporated more quickly as a consequence of lower throughput. Therefore, a longer residence time in the hotter part of the calciner tube would allow the rabble bar to break up the calcine over a longer portion of the tube, resulting in a decrease in particle size. The breakdown of larger particles, thought to be responsible for formation of the majority of the dust, could therefore still be occurring initially, with further abrasion giving rise to the formation of smaller calcine particles. The presence of these competing processes could explain the discrepancy in these results.

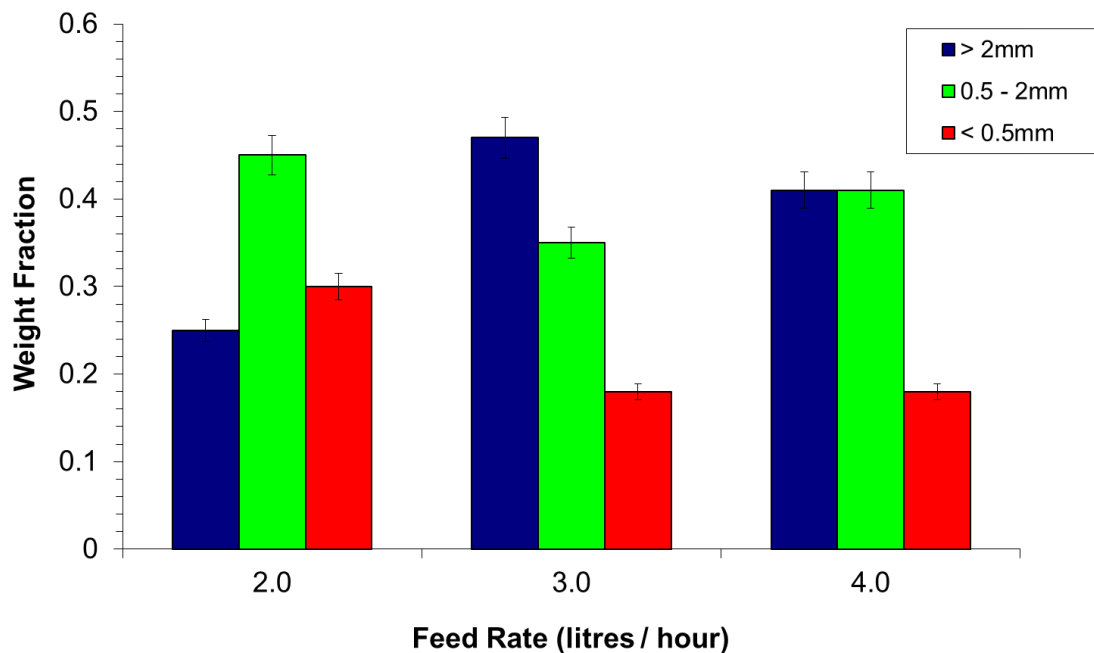
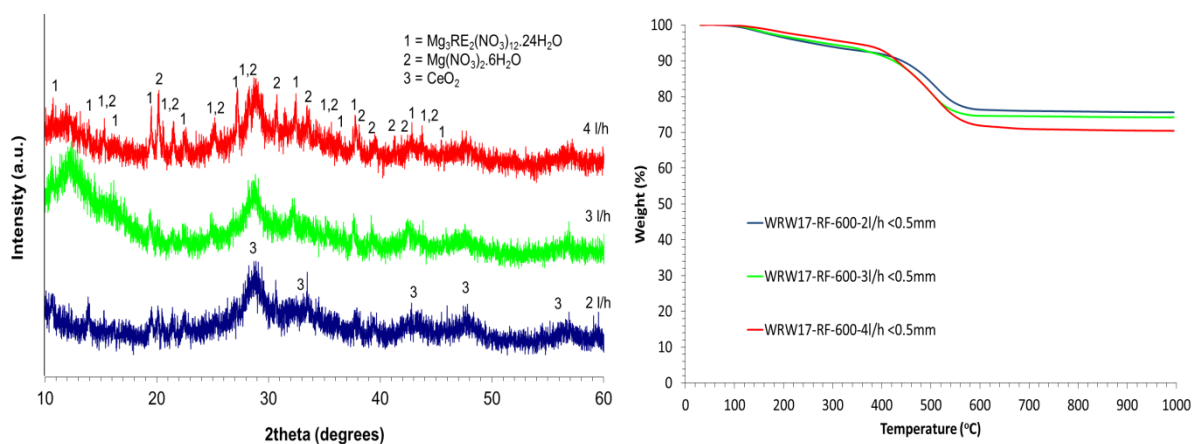
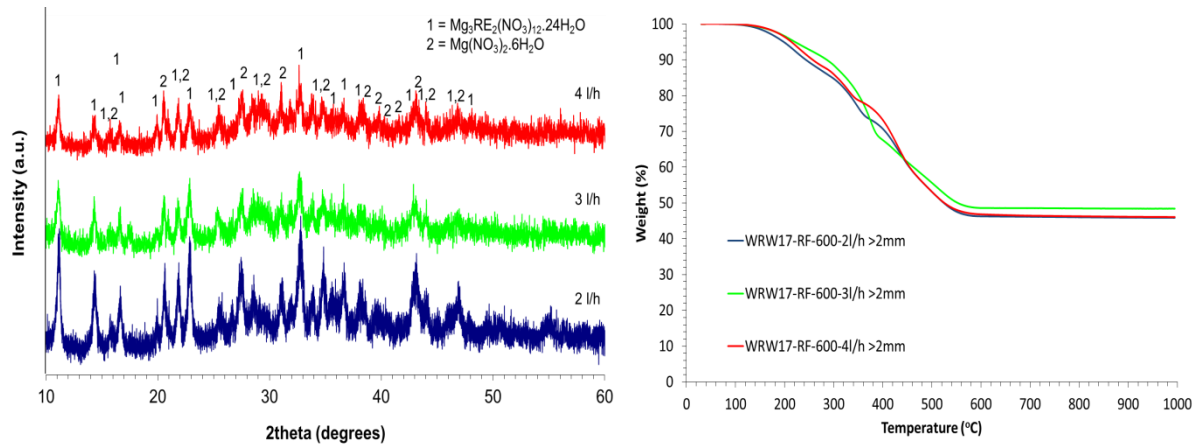


Figure 6.38 – Particle size fractions from product WRW17-RF-600 calcined at 2-4 l/h

XRD analysis of products WRW17-RF-600 run at feed rates of between 2-4 l/h, with particle sizes <0.5 mm (Figure 6.39) all showed a broad, weak set of reflections attributable to poorly crystalline CeO<sub>2</sub>. After calcination at 600 °C with a feed rate of 4 l/h, weak reflections attributable to Mg<sub>3</sub>RE<sub>2</sub>(NO<sub>3</sub>)<sub>12</sub>·24H<sub>2</sub>O were observed in the product, with these reflections becoming less intense as a function of reducing feed rate. These same effects were observed as a function of increasing temperature (section 6.3.2.2.1.1), showing that reducing the feed rate increases the effective temperature through an increase in residence time. The total weight losses at 1000 °C of products WRW17-RF-600, calcined at feed rates of between 2-4 l/h (Figure 6.39), showed higher weight loss values were observed after calcination at higher feed rates. This shows a higher residual hydrate and nitrate inventory is retained at higher feed rates, caused by a move in the evaporative front down the tube, resulting in a shorter residence time in the area of the tube where denitration processes occur. The weight loss profiles of products WRW17-RF-600 calcined at a feed rates of 2-4 l/h, with a particle size <0.5 mm (Figure 6.37) all show three distinct events, as observed previously (section 6.3.2.2.1.1) attributed to dehydration, denitration of Mg<sub>3</sub>RE<sub>2</sub>(NO<sub>3</sub>)<sub>12</sub>·24H<sub>2</sub>O and further denitration of the more stable nitrate components respectively. The weight loss event associated with the denitration of Mg<sub>3</sub>RE<sub>2</sub>(NO<sub>3</sub>)<sub>12</sub>·24H<sub>2</sub>O, at 380 °C, was more pronounced at higher feed rates and larger particle sizes. This is consistent with XRD analysis, showing the peaks associated with Mg<sub>3</sub>RE<sub>2</sub>(NO<sub>3</sub>)<sub>12</sub>·24H<sub>2</sub>O diminished with reducing feed rates and particle size.



**Figure 6.39 – XRD and TGA analysis of products WRW17-RF-600-2l/h, WRW17-RF-600-3l/h and WRW17-RF-600-4l/h with particle size <0.5 mm**



**Figure 6.40 – XRD and TGA analysis of products WRW17-RF-600-2l/h, WRW17-RF-600-3l/h and WRW17-RF-600-4l/h with particle size >2 mm**

XRD analysis of products WRW17-RF-600, calcined with feed rates of 2-4 l/h and a particle size >2 mm, showed reflections attributable to  $\text{Mg}_3\text{RE}_2(\text{NO}_3)_{12} \cdot 24\text{H}_2\text{O}$  were observed in all the diffraction patterns (Figure 6.40). These reflections essentially accounted for all of the reflections shown in the XRD patterns, with strong diffuse scattering also present, suggesting the co-existence of an amorphous phase. Reflections associated with  $\text{CeO}_2$  were not observed in the XRD patterns. TGA analysis of products WRW17-RF-600-2l/h, WRW17-RF-600-3l/h and WRW17-RF-600-4l/h, with a particle size >2 mm (Figure 6.40), showed higher weight losses than the smaller particles formed in these experiments, with the weight loss increasing at higher feed rates. The weight loss profiles of these products showed the same three distinct events as seen at smaller particle sizes, however, the events below 300 °C (attributable to dehydration), and at 380 °C (associated with denitration of  $\text{Mg}_3\text{RE}_2(\text{NO}_3)_{12} \cdot 24\text{H}_2\text{O}$ ) showed much greater intensities. This was consistent with XRD analysis, which showed  $\text{Mg}_3\text{RE}_2(\text{NO}_3)_{12} \cdot 24\text{H}_2\text{O}$  was observed in all reaction products with a particle size >2 mm. These results are consistent with previous experiments without the addition of  $\text{LiNO}_3$ .

The major observations resulting from the addition of  $\text{LiNO}_3$  are the reduction in particle size distribution of the calcine, compared with the Li free experiments. This corresponds to a reduction in the dust carry-over to the off-gas system, in agreement with full scale VTR trials (Vickers, 2006a). The absence of a weight loss event above 600 °C in the TGA analysis and reflections associated with  $\text{LiNO}_3$  in the XRD pattern imply that a reaction is undertaken during the calcination process resulting in the formation of a non-crystalline product. This reactivity must be responsible for a reduction in the particle size of the calcine and subsequent dust formation and carry-over in the calcination process.

### 6.3.2.2.2 Dust Analysis

#### 6.3.2.2.2.1 Effects of temperature

A general increase in the mass of dust collected in the off-gas system was observed as the calcination temperature was increased. These values were normalised by conversion to a percentage of the actual yield so a better comparison could be made. The normalised dust values showed a 2.01 wt% carry-over after calcination at 500 °C, rising to 2.96 wt% at 700 °C in products WRW17-RF (Figure 6.41). This is consistent with previous work (section 6.3.2.1.2.1) which showed increasing temperature resulted in a higher dust carry-over in Li free products. However, when compared to products WRW17-RLF, it was apparent that a much lower dust carry-over took place on addition of  $\text{LiNO}_3$  to the Magnox HAL simulant when calcined between 500-700 °C, in agreement with historic studies (Vickers, 2006a). As discussed previously (section 6.3.2.2) this is in correlation with a decrease in the calcine fraction with a particle size >2 mm.

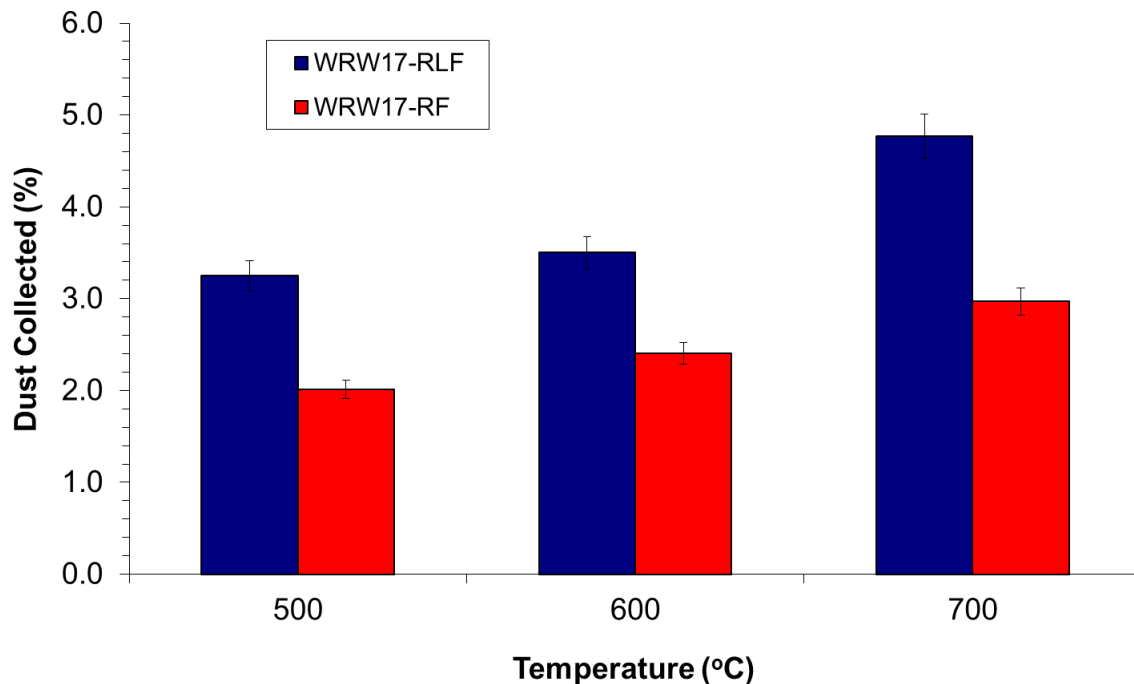


**Figure 6.41 – Dust collected as a percentage of the expected yield from products WRW17-RF and WRW17-RLF calcined between 500-700 °C at a feed rate of 3 l/h**

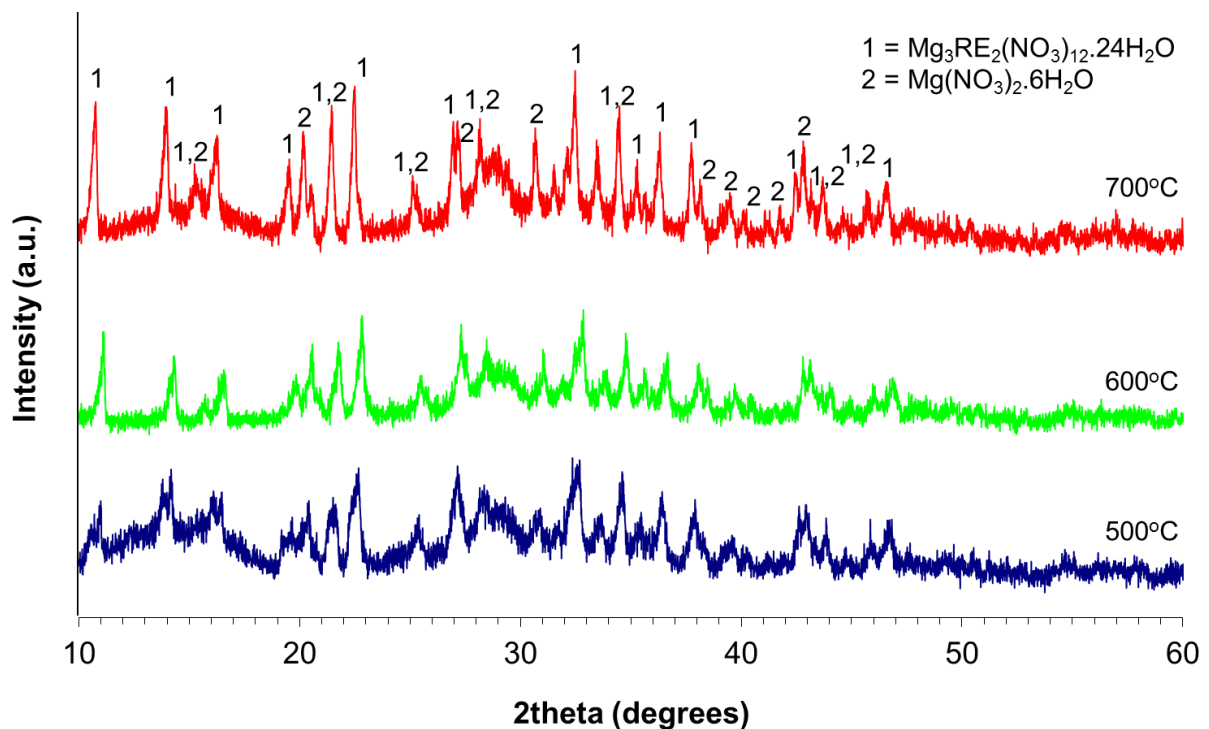
XRD analysis of the dust samples produced from WRW17-RF calcined at 500, 600 and 700 °C, at a feed rate of 3 l / h (Figure 6.42), all showed a set of matching reflections attributable to  $Mg_3RE_2(NO_3)_{12} \cdot 24H_2O$  and  $Mg(NO_3)_2 \cdot 6H_2O$  [14-101]. These reflections essentially accounted for all of the reflections shown in the diffraction pattern. Significant diffuse scattering was also apparent, showing the presence of a non-crystalline component. TGA analysis showed weight losses of between 46-52 wt% at 1000 °C (Figure 6.43), almost identical to the values observed in the calcine fraction with a particle size greater than 2 mm, with the weight loss profiles also showing the same weight loss events. These showed three distinct events: a broad weight loss below 300 °C, typical of dehydration; a relatively sharp weight loss at 380 °C, associated with the denitration of  $Mg_3RE_2(NO_3)_{12} \cdot 24H_2O$  (Appendix 2); and a broad weight loss between 450-600 °C, attributable to further denitration of the more stable nitrate components which make up the HAL simulant, by reference to thermal stability data for individual component nitrates of which the HAL is comprised (Chun, 1977). The XRD and TGA analysis match closely to the results from the corresponding Li free experiments, showing the same mechanism for the formation and carry-over of dust is present on addition of  $LiNO_3$  to the Magnox HAL simulant. However, the observation of a much lower dust carry-over in the presence of  $LiNO_3$  suggested that there was an alteration in the chemical and / or physical properties of the resultant calcine, which manifested as a reduction in the formation of large particles. These data, combined with observation of an increase in the particle size fraction >2 mm with an increase in calcination temperature, resulting in a higher dust carry-over, imply that the dust and calcine fraction with a particle size >2 mm have similar compositions and are significantly different from the smaller calcine particles formed in these experiments. This again suggests dust is created by the abrasive breakdown of larger particles.

**Table 6.7 – Density Measurements of products WRW17-RF and WRW17-RLF dust samples and the calcine fractions with particle sizes >2 mm and <0.5 mm**

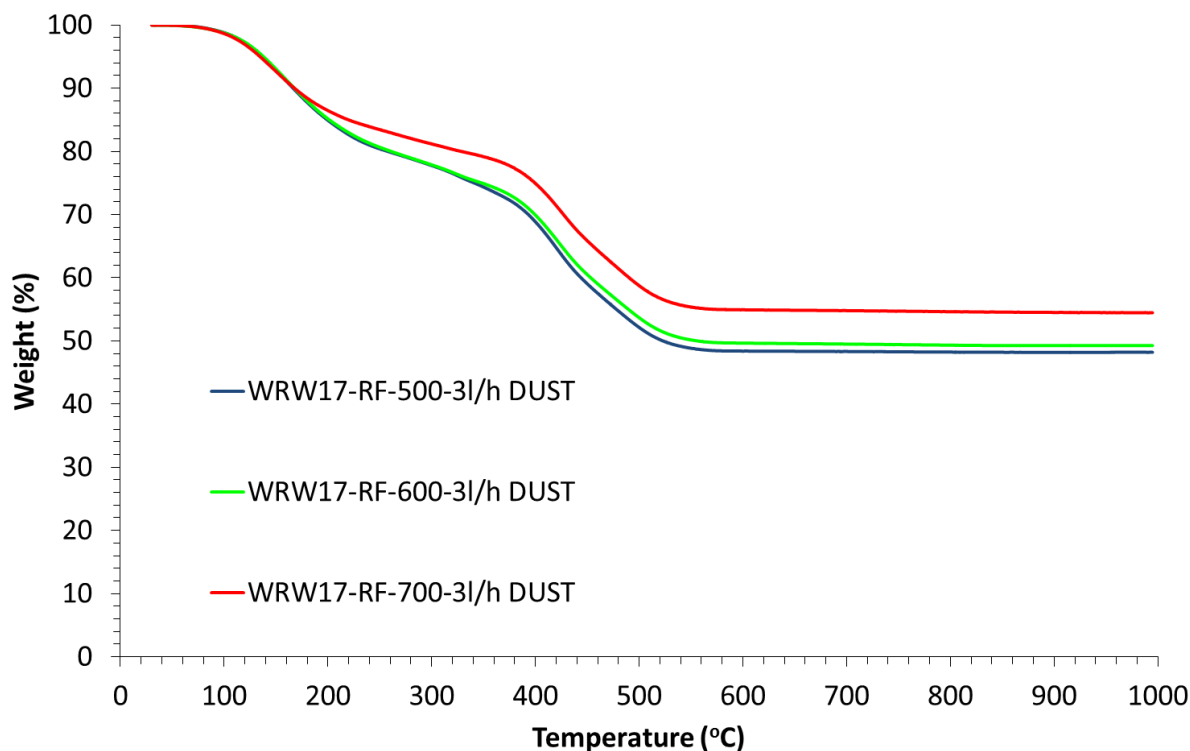
	Particle Size Fraction		
	Dust	>2 mm	<0.5 mm
<b>WRW17-RF-500-3l/h</b>	2.29	2.16	2.84
<b>WRW17-RLF-500-3l/h</b>	2.22	2.10	2.82
<b>WRW17-RF-600-3l/h</b>	2.51	2.34	3.03
<b>WRW17-RLF-600-3l/h</b>	2.38	2.22	2.96
<b>WRW17-RF-700-3l/h</b>	2.55	2.41	3.29
<b>WRW17-RLF-700-3l/h</b>	2.42	2.30	3.07

Table 6.6 shows the density measurements of the different size calcine fractions and dust of products WRW17-RLF and WRW17-RF calcined at 500, 600 and 700 °C at a feed rate of 3 l / h. This showed that the dust has a slightly higher density than that of the larger calcine fraction (particle diameter >2 mm) and much lower than the fraction with a particle size <0.5 mm. The relatively high density of the small particles, compared to the larger particles, is due to the fact that a higher fraction of the calcine had undergone dehydration and denitration, forming metal oxides. In general, metal oxides are known to be higher in density than their nitrate forms (Perry, 2011; Phillips, 1995). The fact that the density of the dust lies between these calcine fractions could be due to the fact that a portion of the dust could be generated from the smaller calcine fraction, with the major portion being formed from the abrasive breakdown of the larger particles (as suggested by the TGA and XRD analysis).

There was a minor increase in the density of the calcine products observed on the addition of LiNO<sub>3</sub> to WRW17 HAL simulant (Table 6.7). This could have been due to the fact that LiNO<sub>3</sub> appeared to facilitate the decomposition reactions of metal nitrates to form their component oxides, despite LiNO<sub>3</sub> being relatively low in density at 2.38 g / cm<sup>3</sup> (Perry, 2011; Phillips, 1995). The higher oxide content would lead to an increased density being measured.

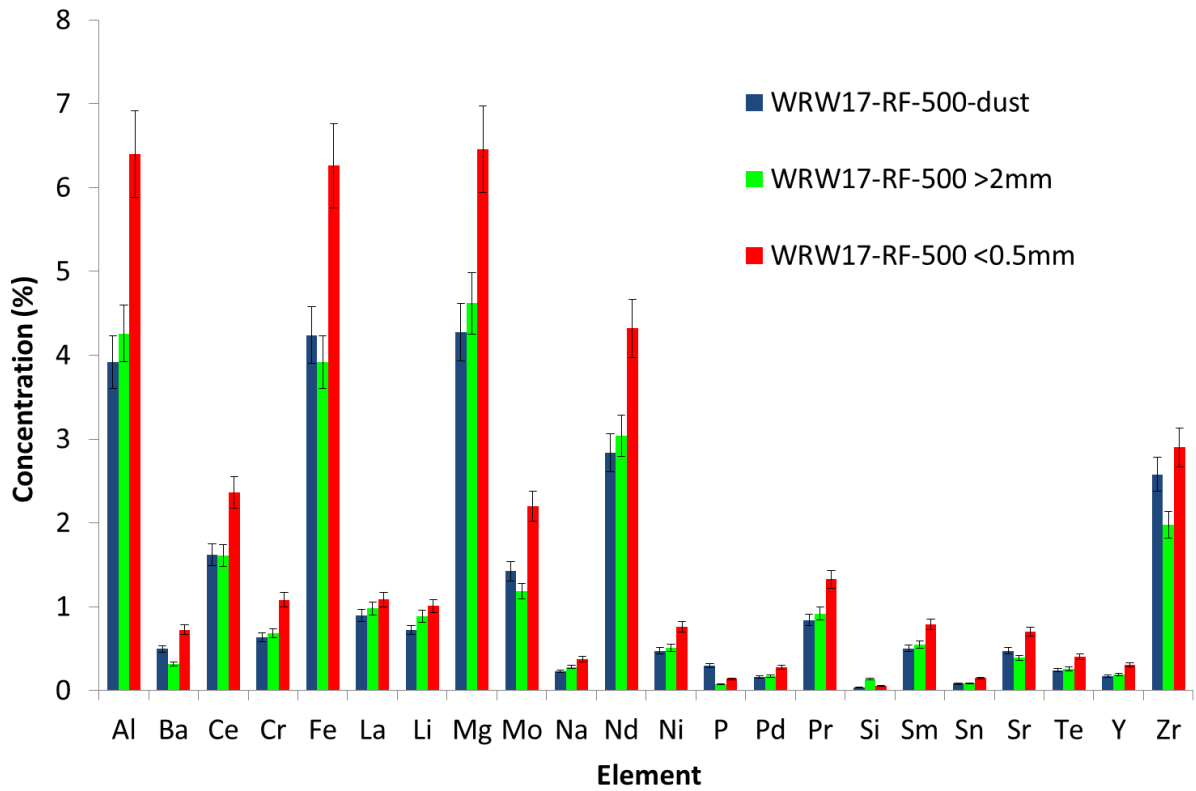


**Figure 6.42 – XRD analysis of products a) WRW17-RF-500-3l/h, b) WRW17-RF-600-3l/h and c) WRW17-RF-700-3l/h dust samples**

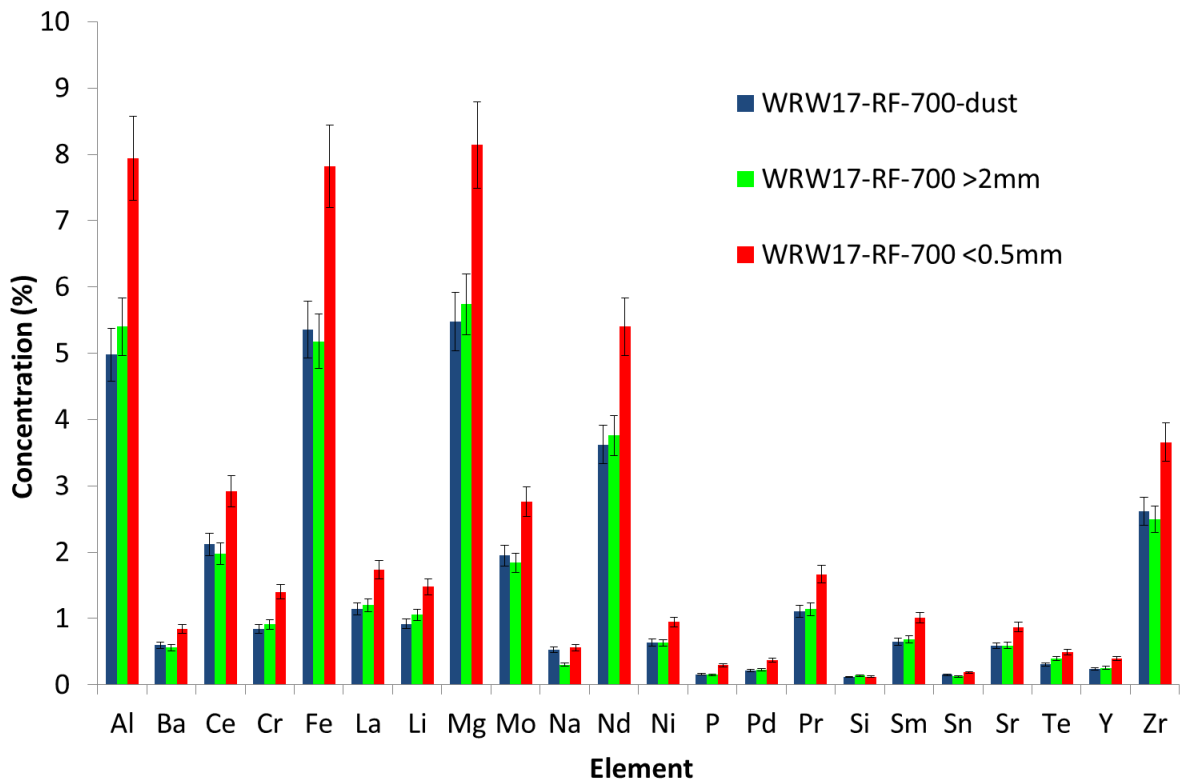


**Figure 6.43 – TGA analysis of products WRW17-RF-500-3l/h, WRW17-RF-600-3l/h and WRW17-RF-700-3l/h dust samples**

Chemical analysis was carried out, using ICP-OES, on products WRW17-RF-500-3l/h, WRW17-RF-600-3l/h and WRW17-RF-700-3l/h with particle sizes of >2 mm and <0.5 mm as well as the dust collected during these experiments. After calcination at 500 °C (Figure 6.44), chemical analysis showed the composition of the dust and calcine fraction >2 mm were similar in composition, in agreement with TGA and XRD analysis. The majority of the elements in these fractions were present at the same concentrations (within error), however, Ba, Sr, Mo and Zr were all present in a higher concentration in the dust, suggesting they were preferentially carried over to the off-gas system. After calcination at 700 °C, chemical analysis showed that (within error) all elements have the same concentrations in the dust and calcine fraction with a particle size above 2 mm, with the exception of Na (Figure 6.45). All elements showed a higher concentration in the particle size fraction <0.5 mm, due to the lower residual nitrate and hydrate content in the product, after calcination at both 500 and 700 °C, consistent with TGA analysis. This implied that the dust fraction was closer in composition to the calcine with a large particle size (>2 mm) rather than the smaller fraction. This was in agreement with XRD and TGA data which showed  $Mg_3RE_2(NO_3)_{12} \cdot 24H_2O$  was formed in these phases. These data supported the XRD and TGA analysis, along with the density measurements, which suggested that the dust had similar chemical properties to that of the calcine particles with a particle size >2 mm and was different from the small calcine particles (<0.5 mm). This again implied that dust is created from the breakdown of the larger particles formed within the calcination process.



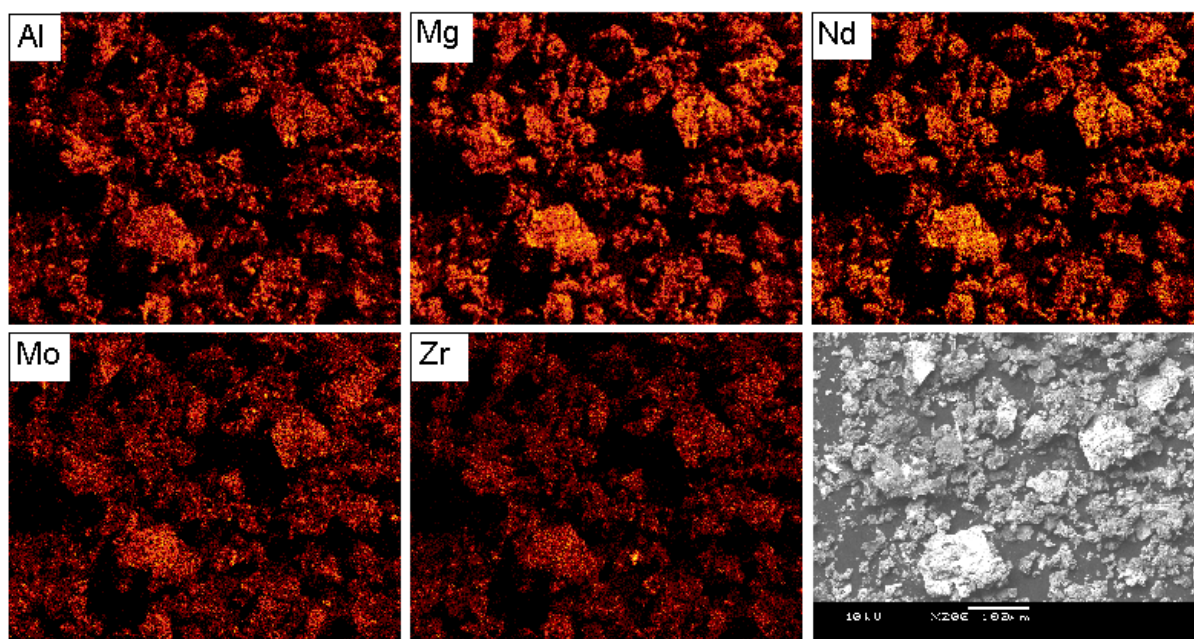
**Figure 6.44 – Chemical Composition of product WRW17-RF-500-3l/h dust and calcine samples with particle sizes of <0.5 mm and >2 mm determined by ICP-OES**



**Figure 6.45 – Chemical Composition of product WRW17-RF-700-3l/h dust and calcine samples with particle sizes of <0.5 mm and >2 mm determined by ICP-OES**



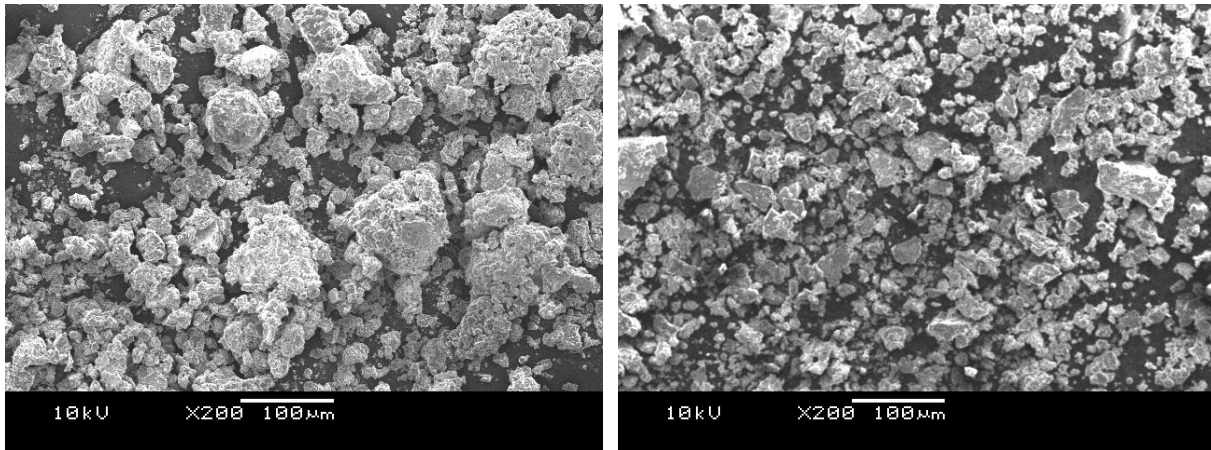
EDS analysis showed a strong association of Mg and Nd within the dust sample formed from the calcination of product WRW17-RF-700-3l/h (Figure 6.46), in agreement with XRD and TGA analysis which showed the presence of  $Mg_3RE_2(NO_3)_{12} \cdot 24H_2O$ . Co-association of Mo and Zr was also apparent in the dust samples, consistent with available literature which showed the formation of  $Zr(MoO_4)_2$  (or the hydrated phase  $ZrMo_2O_7(OH)_2 \cdot 2H_2O$ ) occurs in the dust scrubber on the VTR (Short, 2010; Morris and Haig, 2010). However, the presence of  $Zr(MoO_4)_2$  was not observed in XRD analysis, therefore if it was formed during these experiments, it was either present in a small quantity, or the phase was non-crystalline in nature. The same observations were made for the dust formed from the calcination of WRW17-RF at 500 and 600 °C at 3 l / h.



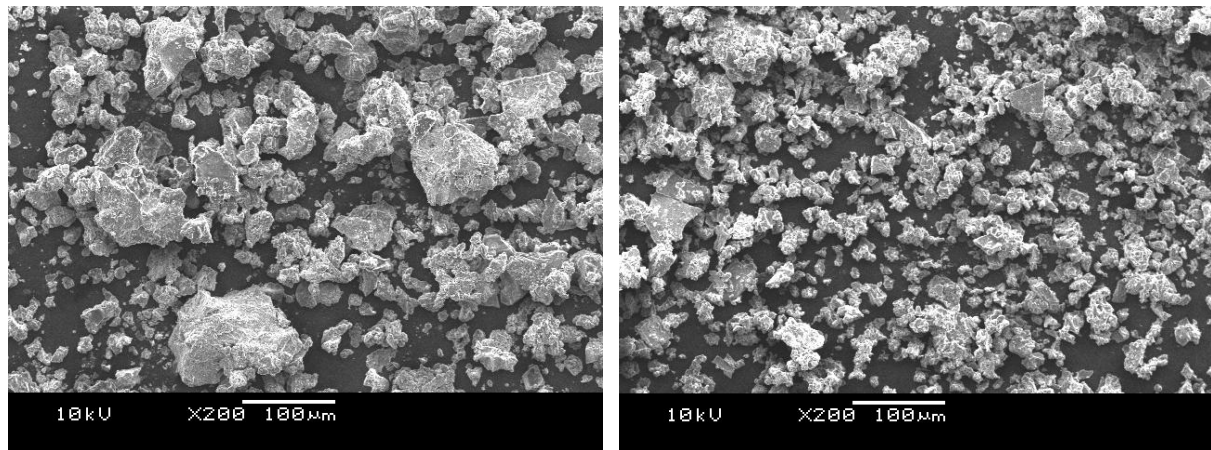
**Figure 6.46 – Backscattered electron image and X-ray maps of product WRW17-RF-700-dust**

Due to the solubility of the calcine in aqueous media, particle size analysis was not possible. However, the secondary electron images (Figures 6.47 and 6.48) showed a clear increase in the primary particle size of the dust from ~20-30 μm in products WRW17-RLF-500-3l/h and WRW17-RLF-700-3l/h up to ~50-100 μm on the addition of  $LiNO_3$  to Magnox HAL simulant. As this analysis was carried out on a small portion of the product (~50 mg compared to the 20-30 g collected during these experiments), however, the results are not conclusive. As the addition of  $LiNO_3$  caused a slight increase in the density of the calcine and dust samples, it would be expected that the particle sizes would have been similar, or slightly smaller in the Li containing samples. A possible explanation for this discrepancy, other than the small amount of product tested possibly not being a representative sample, is that  $LiNO_3$  acts as molten salt, binding the calcine together more strongly. When the dust was removed from the flexible hose, the non Li containing sample could then have been more brittle, breaking up into smaller particles upon collection.

Another possible explanation for the increase in particle size observed in the Li containing samples was that  $\text{LiNO}_3$  was present as a liquid in the calcination process, resulting in the formation of a ‘sticky’ calcine. Upon collision, the dust particles could have agglomerated, causing an increase in particle size of the dust. This could also have contributed to the lower dust carry-over observed in the Li containing samples, with larger, agglomerated particles being kept in the calcine fraction. The evidence for this, however, is inconclusive.

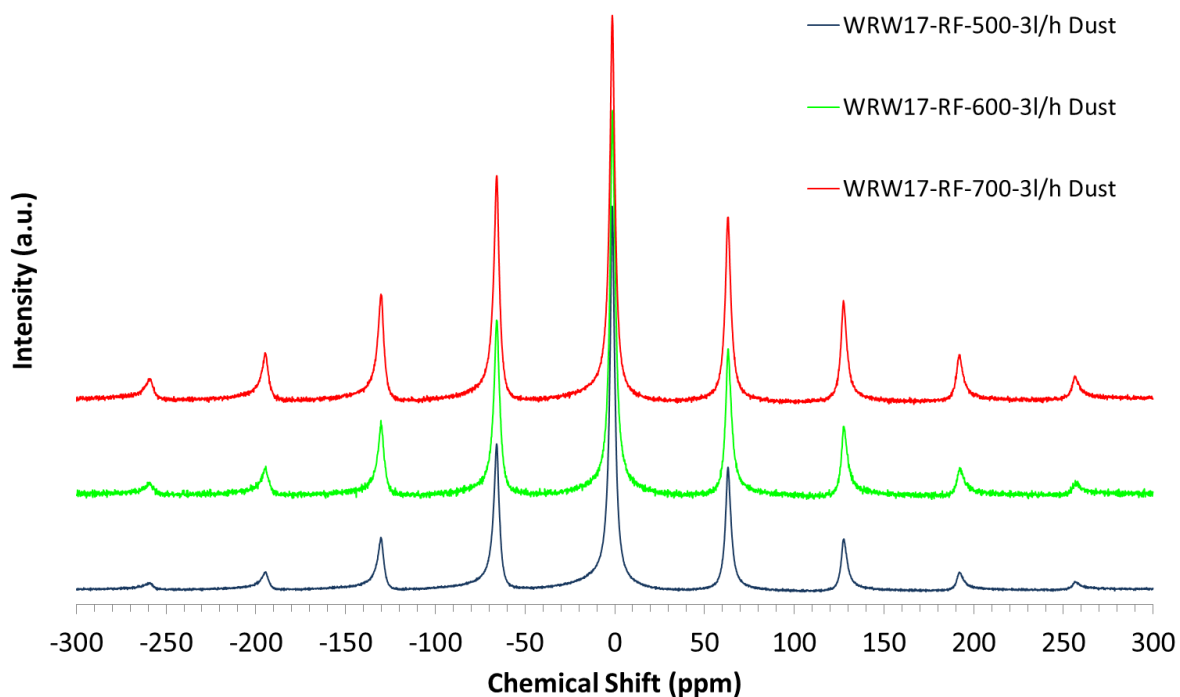


**Figure 6.47 – Secondary electron images of WRW17-RF-500-3l/h-dust (left) and WRW17-RLF-500-3l/h-dust (right)**



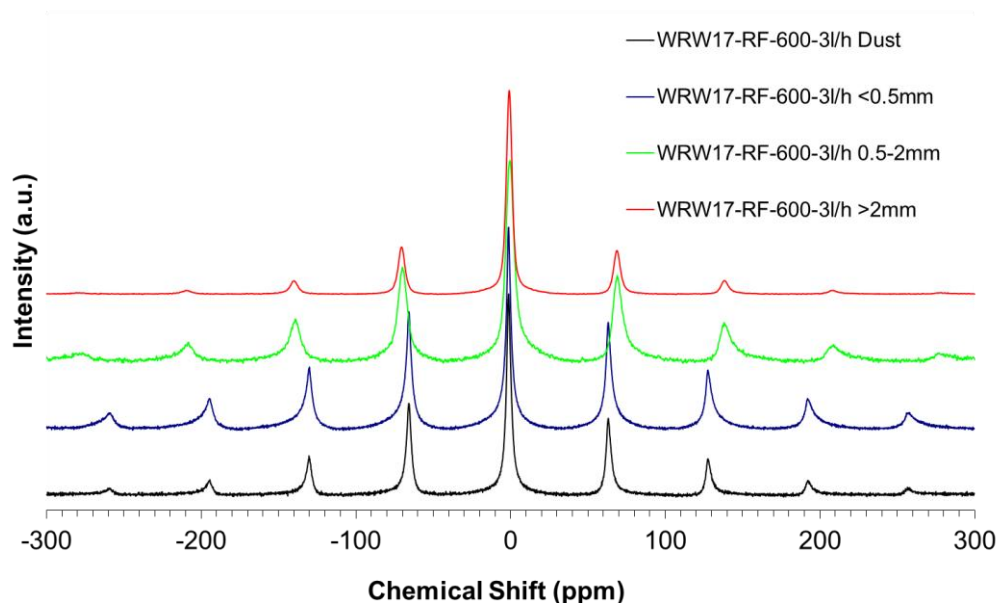
**Figure 6.48 – Secondary electron images of WRW17-RF-700-3l/h-dust (left) and WRW17-RLF-700-3l/h-dust (right)**

Figure 6.49 compares  $^7\text{Li}$  MAS NMR data from WRW17-RF-500-3l/h, WRW17-RF-600-3l/h and WRW17-RF-700-3l/h dust samples, measured relative to LiCl. The spectra are all dominated by a very broad, asymmetric resonance centered at -0.90 ppm, with a series of asymmetric spinning side bands being observed, as seen in the calcine fractions (Figures 6.36 and 6.37). The relative intensities of these spinning side bands also increase at higher calcination temperature, which was also consistent with the trends observed in the corresponding calcined products.



**Figure 6.49 -  $^7\text{Li}$  MAS NMR spectra of dust collected from samples WRW17-RF-500-3l/h, WRW17-RF-600-3l/h and WRW17-RF-700-3l/h**

The relative intensities of the spinning sidebands of the dust sample in the  $^7\text{Li}$  NMR spectra of product WRW17-RF-500-3l/h lay in between those of the calcine fractions with particle sizes of <0.5 mm and >2 mm (Figure 6.50). This could suggest that the dust carried over to the off-gas system is generated from both the larger particles (>2 mm), consistent with XRD data, as well as a portion arising from the carry-over of the smallest calcine fraction (<0.5 mm). This is in agreement with the density measurements, which showed the density of the dust also lies between that of the calcine fractions <0.5 mm and >2 mm, implying both contributed to the formation of dust in the small scale calcination process. It should be noted that the differences in the chemical shifts of the spinning sidebands was due to the different rates at which the samples were spun, not the differences in the samples. Figure 6.50 does, however, highlight the differences in relative intensity of the varying particle size fractions.



**Figure 6.50 -  $^7\text{Li}$  MAS NMR spectra of sample WRW17-RF-500-3l/h calcine fractions with particle sizes of >2 mm, 0.5-2 mm, <0.5 mm and dust sample**

From these experiments, it is possible to infer and conclude the following:

- On addition of  $\text{LiNO}_3$  to the Magnox HAL simulant, before calcination, the resultant dust carry-over was reduced with a strong correlation to the reduction in large particles collected in the calcine.
- An increase in dust carry-over to the off-gas system was observed at increasing temperature, also in correlation with an increase in the formation of larger particles in the calcine.
- XRD and TGA analysis showed the presence of  $\text{Mg}_3\text{RE}_2(\text{NO}_3)_{12} \cdot 24\text{H}_2\text{O}$  in both the dust and larger calcine particles (>2 mm), with this diminishing in the smaller particles and as a function of increasing temperature. This implied that dust is formed from the breakdown of larger calcine particles, as observed in the Li free experiments. The ICP-OES and EDS analysis showed similarities between the larger particles and the dust, in agreement with the hypothesis that dust was created from the breakdown of calcine particles above 2 mm in diameter. The  $^7\text{Li}$  MAS NMR data combined with the density measurements suggested a portion of the dust is generated from the smaller particle size calcine fraction.
- It is implied that the mechanism by which  $\text{LiNO}_3$  reduces the dust carry-over to the off-gas system involves the facilitation of oxidation reactions, increasing the density of the resultant calcine therefore making it more difficult to be carried to the off-gas system. This is consistent with  $\text{LiNO}_3$  being a known  $\text{O}^{2-}$  donor (Afanisiev, 2007) and the fact that it will be molten under the conditions of calcination used in these experiments, so will act as a molten salt, further facilitating reactions.

### 6.3.2.2.2 Effects of feed rate

An increased mass of dust collected in the off-gas system was observed as a function of increased calcination feed rate due to a higher throughput in the calciner. However, when the mass values were normalised, by conversion to a percentage of the actual yield, the highest dust carry-over was observed at the lowest feed rate (Figure 6.51). This same trend was observed in the Li free experiments, which was expected, as at a reduced feed rate, evaporation takes place more rapidly, leaving a longer section of the tube for denitration to occur, increasing the residence time. An increase in the mass fraction of large particles was apparent in product WRW17-RF-600-3l/h (compared to product WRW17-RF-600-2l/h), with a subsequent drop at a feed rate of 4 l / h. The results for products formed at feed rates of 3 l / h and 4 l / h are consistent with the hypothesis that larger particles are formed as a function of increasing temperature (lower feed rate equates to longer residence time at high temperature), resulting in an increased dust carry-over. At a feed rate of 2 l / h, however, the fraction of particles >2 mm was lower, even though higher dust carry-over was observed. This is in agreement with the Li free experiments, as it is thought that the effects of feed rate on the position of the evaporative front in the calciner will be affected more greatly by feed rate than Zone 3 temperature, as set-points 1 and 2 were kept the same (400 °C) throughout these experiments. This is thought to lead to competing process occurring in which initial abrasion of larger particles, thought to be responsible for formation of the dust takes place, with further breakdown of the larger particles taking place due to the longer time in the hotter part of the tube where denitration processes occur. This is a possible explanation for the decreasing particle sizes formed at low feed rates.

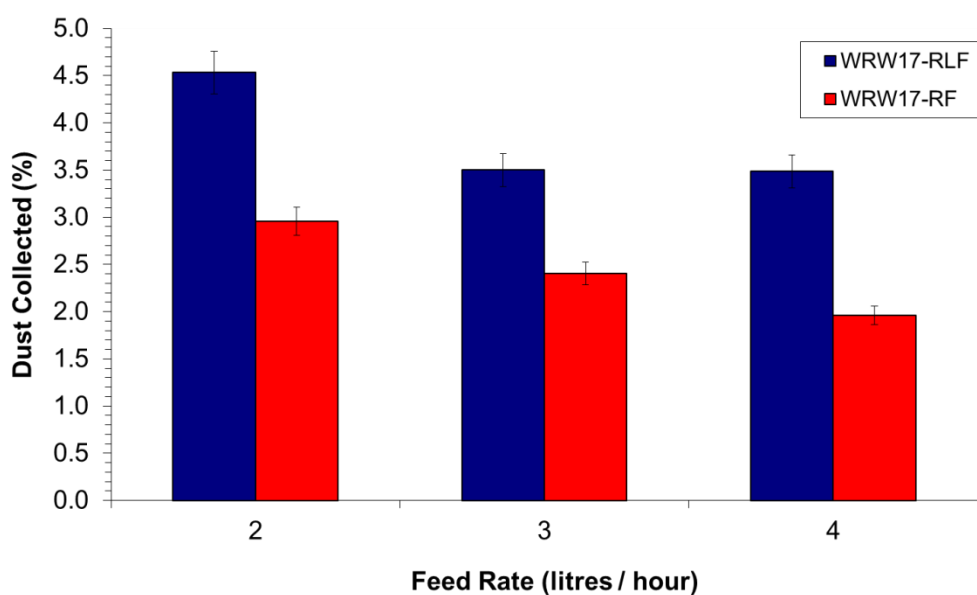


**Figure 6.51 – Dust collected as a percentage of the expected yield from products WRW17-RF-600 and WRW17-RLF-600 calcined between 2-4 l / h**

The XRD patterns of the dust samples produced from WRW17-RF-600 calcined at feed rates of 2 l/h, 3 l/h and 4 l/h (Figure 6.52) all showed a set of matching reflections attributable to  $\text{Mg}_3\text{RE}_2(\text{NO}_3)_{12}\cdot 24\text{H}_2\text{O}$  and  $\text{Mg}(\text{NO}_3)_2\cdot 6\text{H}_2\text{O}$  [14-101], as observed previously at different calcination temperatures and in the Li free experiments. The presence of significant diffuse scattering suggested the presence of non-crystalline component(s). TGA analysis showed weight losses of between 45-51 wt% at 1000 °C (Figure 6.53). These weight loss values and the resultant profiles are comparable to the values attained from the calcine fractions with a particle size greater than 2 mm and to the corresponding Li free experiments. These showed three distinct events at temperatures of below 300 °C, 380 °C and between 450-600 °C, associated with dehydration, denitration of  $\text{Mg}_3\text{RE}_2(\text{NO}_3)_{12}\cdot 24\text{H}_2\text{O}$  and  $\text{Mg}(\text{NO}_3)_2\cdot 6\text{H}_2\text{O}$ , and further denitration of the more stable nitrate components respectively (Appendix 2; Paulik et al., 1988; Chun, 1977). Taken together, the XRD and TGA data imply that the dust has a similar composition to the calcine fraction with a particle size >2 mm and is far removed from the smaller calcine particles formed in these experiments. The data is also very similar to that observed in the experiments without the addition of  $\text{LiNO}_3$ . This again suggested that the mechanism by which dust was created, and subsequently transported to the off-gas system, was due to the abrasive breakdown of larger particles. The formation of a lower fraction of large particles (>2 mm) at a lower feed rate is contradictory to this hypothesis, although this can be explained by the effective increase in residence time allowing further breakdown of the large particles further down the calciner tube.

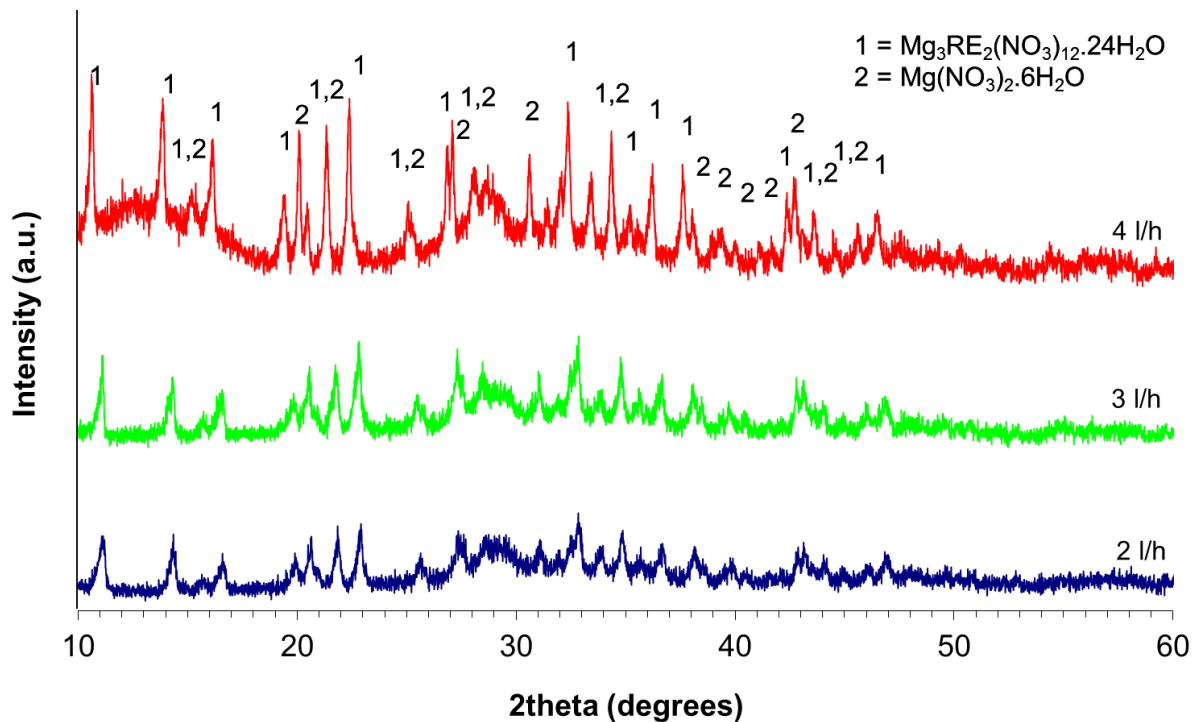


**Figure 6.52 – XRD analysis of products a) WRW17-RF-600-2l/h, b) WRW17-RF-600-3l/h and c) WRW17-RF-600-4l/h dust samples**

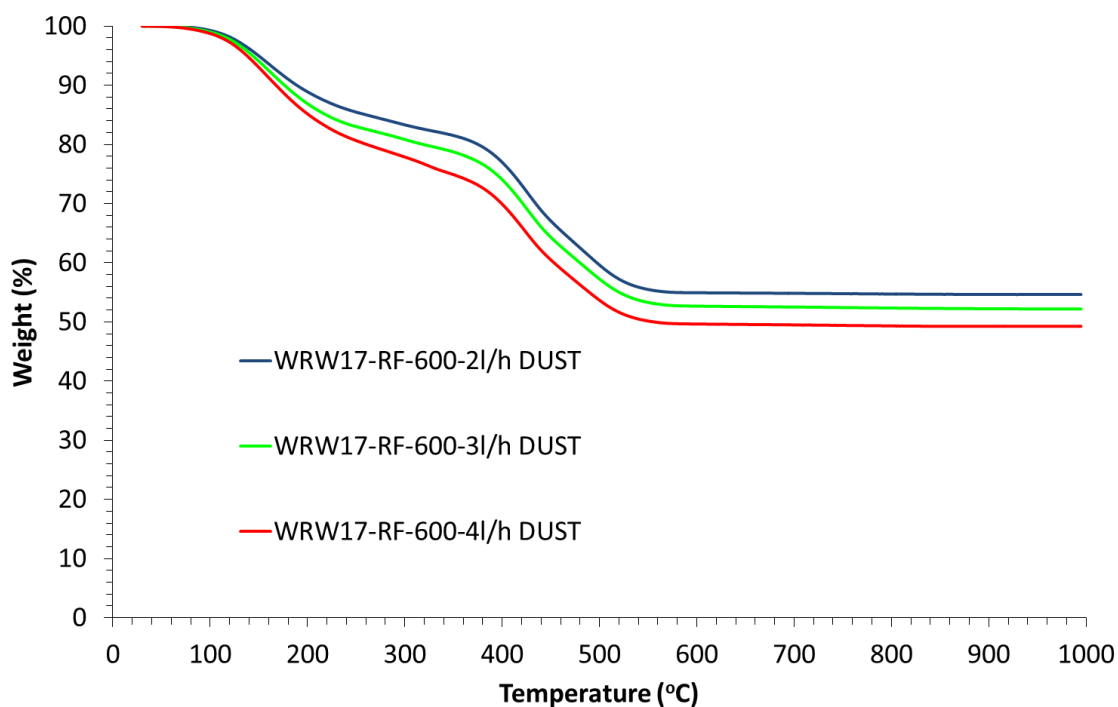


**Figure 6.53 – TGA analysis of products WRW17-RF-600-2l/h, WRW17-RF-600-3l/h and WRW17-RF-600-4l/h dust samples**

From these experiments, it is possible to infer and conclude the following:

- At a low feed rate (2 l / h) there was a decrease in the amount of large particles formed in the calcine, though an increase in dust carry-over was observed, the same as seen in the Li free experiment calcined under the same conditions. However, this can be explained by the breakdown of the calcine particles taking place in stages, with initial breakdown forming the dust, with further breakdown forming the smaller particles with higher density and therefore are retained in the calcine.
- At feed rates of 3 l / h and 4 l / h, the normalised dust carry-over decreased at higher feed rates, correlating with higher formation of large calcine particles being formed in the calcination process. Higher feed rates caused the evaporative front to be pushed down the calciner tube, effectively reducing the residence time at high temperature where denitration occurs. Therefore, calcines formed at higher feed rates are thought to correlate with a reduction in calcination temperature, causing the reduction in dust carry-over. This again suggested that only at low feed rates does the breakdown of calcine particles take place in different steps.
- $Mg_3RE_2(NO_3)_{12} \cdot 24H_2O$  and  $Mg(NO_3)_2 \cdot 6H_2O$  were observed as the major crystalline products in the dust, consistent with the formation from the breakdown of larger particles by the rabble bar in the calciner.

### 6.3.2.3 WRW16-RLF

Blend HAL simulant is a 75 % / 25 % mix of UO<sub>2</sub> and Magnox waste streams. It has higher concentrations of Mo, Zr and RE elements with a reduction in Al and Mg compared to Magnox (WRW17) simulants (Short, 2010b; Short, 2010c). With this change in simulant composition, the masses of the calcine and dust collected for WRW16-RLF showed a significant increase compared to the corresponding experiments carried out on Magnox HAL simulant (Table 6.8). The increased calcine fraction was expected due to the higher amounts of heavier elements present in the Blend simulant, meaning the weight losses observed due to dehydration and denitration processes (measured by TGA) were lower. This resulted in a higher yield being collected. An increase in the dust carry-over from the processing of Blend simulants in comparison with Magnox is in agreement with previous studies by (Ramshaw et al., 1992). As with the Magnox experiments, the expected weights were worked out by first calculating the total waste oxide throughput during the experiment, then taking into account residual weight loss values (measured by TGA analysis) for each of the calcine size fractions (Table 6.9) and weighting the values accordingly (see section 6.2.2.1). The dust collection was normalised by working out a percentage dust carry-over against the actual weight of calcine collected thus allowing comparisons to be made on the effects of changing temperature and feed rate on the dust carry-over from the calciner to the off-gas system.

**Table 6.8 – Mass of calcine and dust products collected**

<b>Sample</b>	<b>Expected Weight (g)</b>	<b>Actual Weight (g)</b>	<b>Amount of Dust Collected (g)</b>	<b>Dust Collected (wt%)</b>
<b>WRW16-RLF-500-3l/h</b>	1227.87	1025.56	58.75	5.73
<b>WRW16-RLF-600-3l/h</b>	1198.63	949.74	59.98	6.32
<b>WRW16-RLF-700-3l/h</b>	1163.49	891.77	63.03	7.07

The combined mass of calcine and dust collected in these experiments are lower than the expected yield, with the discrepancy becoming greater at increased temperature. This could be partially attributed to a higher dust carry-over, as not all of the dust generated during these experiments will have been collected, in agreement with previous work in this chapter (section 6.3.2.1). This is due to the design of the small scale calciner, meaning a portion of the dust was not able to be recovered during these experiments, however, a representative yield is thought to be recovered.



**Table 6.9 – Size fractions of product WRW17-RLF calcined under varying conditions**

<b>Sample</b>	<b>Fraction above 2 mm</b>	<b>Fraction between 0.5 – 2 mm</b>	<b>Fraction below 0.5 mm</b>
<b>WRW16-RF-500-3l/h</b>	<b>0.28</b>	<b>0.44</b>	<b>0.28</b>
<b>WRW16-RF-600-3l/h</b>	<b>0.23</b>	<b>0.48</b>	<b>0.29</b>
<b>WRW16-RF-700-3l/h</b>	<b>0.20</b>	<b>0.51</b>	<b>0.29</b>

A lower mass fraction of particles >2 mm in diameter was observed as the calcination temperature was increased, in contrast to experiments carried out on Magnox HAL simulants. An increased normalised dust carry-over was observed at higher temperature, in agreement with the Magnox experiments, however, this correlated with a reduction in the fraction of large particles, contradictory to Magnox experiments and the hypothesis that dust is created by the breakdown of large particles. The smallest particle size fraction (<0.5 mm) stayed constant with increasing temperature, which suggests that dust is not formed from this fraction of the calcine. As with the issue of increasing feed rate, there appears to be competing processes resulting in dust creation and then further breakdown of the large particles which remain in the calcine collected from these experiments (discussed in section 6.3.2.3.2.1).

### **6.3.2.3.1 Calcine Analysis**

#### **6.3.2.3.1.1 Effects of temperature**

Figure 6.54 shows the particle size fractions collected as a function of temperature. This showed that a decrease in the mass fraction of particles >2 mm was observed as the calcination temperature was increased. The particle size range 0.5-2 mm showed a general increase in the mass fraction at higher calcination temperature, due to the decrease in larger particles in the product, with the small particle fraction, <0.5 mm, remaining constant. The trends in the larger particles were contradictory to those observed in Magnox simulants calcined under identical conditions, with a larger fraction of small particles being observed in Blend simulants. This suggested that the Blend simulant was easier for the rabble bar to breakdown. A 5 % error was again assigned to each of the values to account for the residual calcine and dust which will be left in the calciner tube during these experiments, taken from previous small scale calciner trials (Brace, 2004). The error associated with weighing the products were deemed insignificant compared to errors associated with collection from the small scale calciner and were therefore not taken into account.

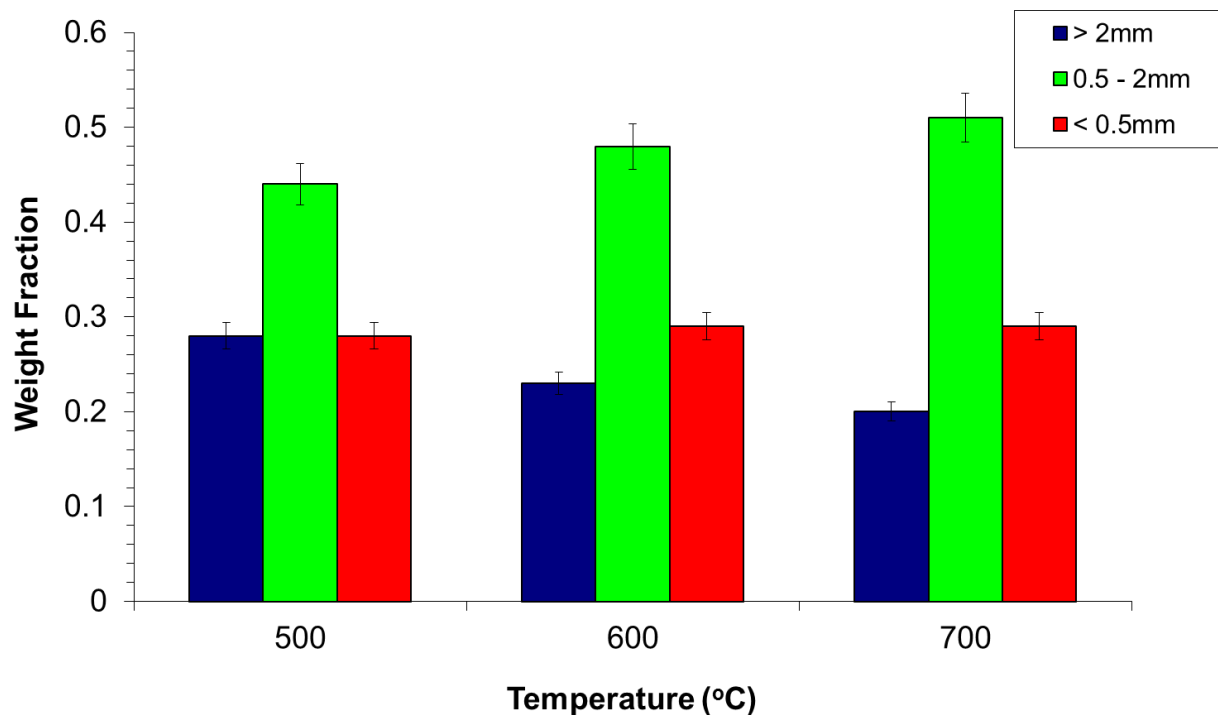


**Figure 6.54 – Particle size fractions from product WRW16-RLF calcined at 500-700 °C at a feed rate of 3 l / h**

XRD analysis of products WRW16-RLF calcined at 500, 600 and 700 °C with particle sizes <0.5 mm (Figure 6.55) all showed weak, broad reflections associated with the formation of poorly crystalline  $\text{CeO}_2$ , with high levels of diffuse scattering being apparent, indicating the presence of non-crystalline component(s). After calcination at 500 °C, weak reflections attributable to  $\text{Mg}_3\text{RE}_2(\text{NO}_3)_{12}\cdot 24\text{H}_2\text{O}$  were observed in the product, though the low signal-to-noise ratio in the diffraction pattern obscures some of the reflections assigned by reference to the ICDD database (card [12-761]). The intensities of these reflections diminish as a function of increasing temperature (Figure 6.56). This was observed previously in Magnox simulants, although the reflections attributable to  $\text{Mg}_3\text{RE}_2(\text{NO}_3)_{12}\cdot 24\text{H}_2\text{O}$  had a lower signal to noise ratio, consistent with the lower amount of Mg present in the simulant. TGA analysis of products WRW16-RLF-500-3l/h, WRW16-RLF-600-3l/h and WRW16-RLF-700-3l/h all showed decreasing weight losses as a function of increasing temperature (Figure 6.55). This is consistent with retention of a higher fraction of the hydrate and nitrate inventory at lower calcination temperatures. The weight loss values, however, were much lower than those observed after the calcination of Magnox simulants under the same conditions, consistent with the higher fraction of heavy elements present in Blend simulants. The weight loss profiles of products WRW16-RLF calcined at 500 and 600 °C at a feed rate of 3 l / h, with a particle size <0.5 mm (Figure 6.56) both show two distinct events: a relatively sharp weight loss at 380 °C, associated with the denitration of  $\text{Mg}_3\text{RE}_2(\text{NO}_3)_{12}\cdot 24\text{H}_2\text{O}$  (Appendix 2); and a broad weight loss between 450-600 °C, attributable to further denitration of the more stable nitrate components which make up the HAL simulant, by

reference to thermal stability data for individual component nitrates of which the HAL is comprised (Chun, 1977). After calcination at 700 °C, the weight loss event at 380 °C was no longer observed, suggesting the denitration of  $Mg_3RE_2(NO_3)_{12} \cdot 24H_2O$  had gone to completion. This is in agreement with XRD analysis which showed the absence of reflections associated with  $Mg_3RE_2(NO_3)_{12} \cdot 24H_2O$  after calcination at 700 °C in the particle size fraction below 0.5 mm. The presence of reflections attributable to  $CeO_2$  is consistent with the corresponding Magnox experiments, freeze dryer work and previous studies (Dunnett et al., 2009), which showed that  $CeO_2$  is not observed after calcination at 400 °C but is highly crystalline at 1050 °C. These data suggest that in the small particle size fraction (<0.5 mm) the temperatures experienced in the calciner were above 400°C at all Zone 3 set-points. The temperatures experienced by the calcine also increases at higher Zone 3 temperatures, as expected, shown by the lack of reflections associated with  $Mg_3RE_2(NO_3)_{12} \cdot 24H_2O$  when calcined at 700 °C.

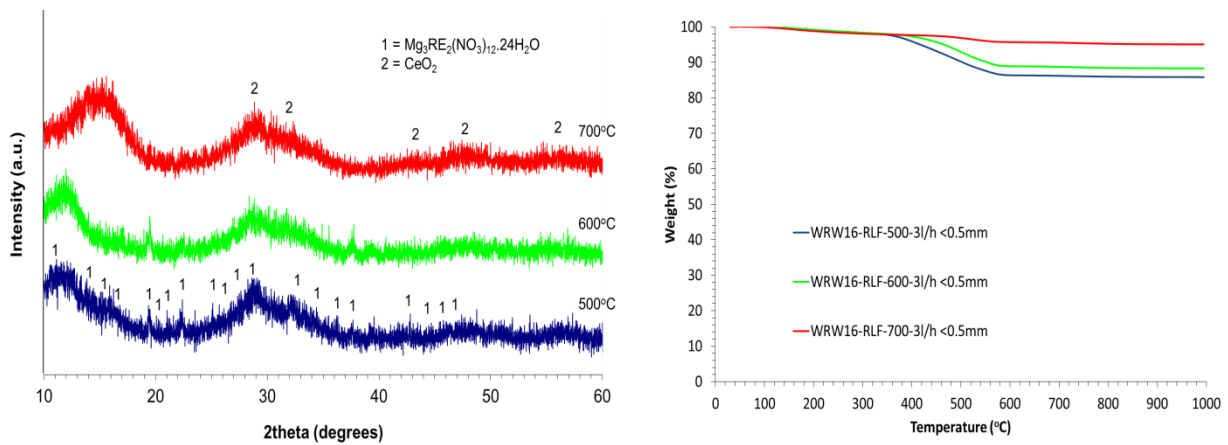


**Figure 6.55 – XRD and TGA analysis of product WRW16-RLF-500-3l/h, WRW17-RLF-600-3l/h and WRW17-RLF-700-3l/h with a particle size of <0.5 mm**

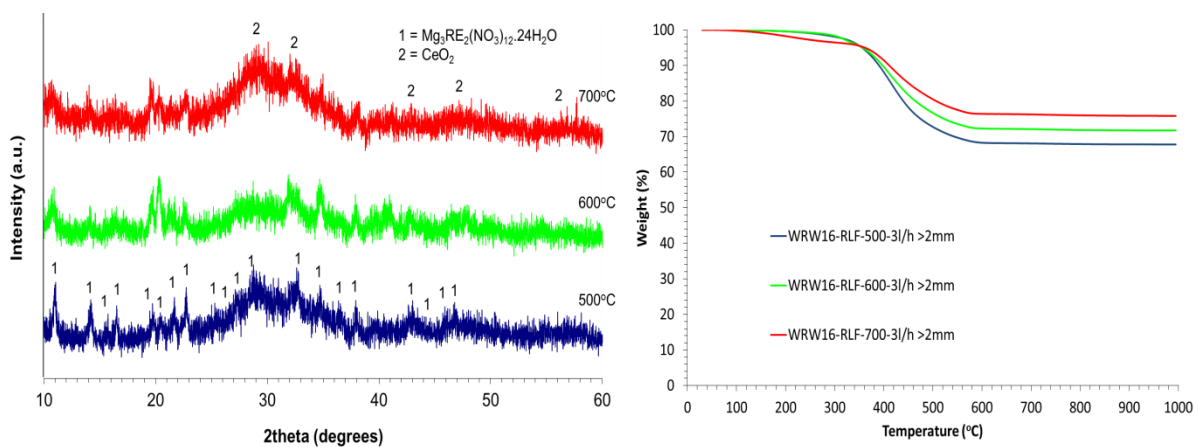


**Figure 6.56 - XRD and TGA analysis of product WRW16-RLF-500-3l/h, WRW17-RLF-600-3l/h and WRW17-RLF-700-3l/h with a particle size of >2 mm**

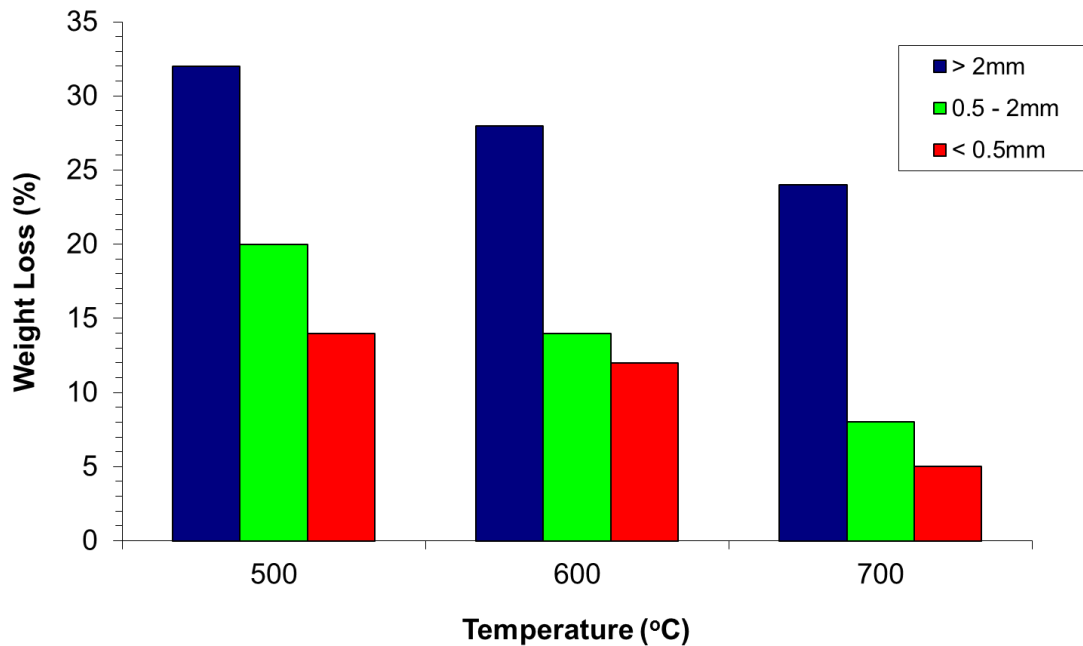


**Figure 6.57 – Weight loss of the different size fractions of products WRW16-RLF-500-3l/h, WRW16-RLF-600-3l/h and WRW16-RLF-700-3l/h**

In the calcine fraction >2 mm in diameter, relatively intense reflections, attributable to  $\text{Mg}_3\text{RE}_2(\text{NO}_3)_{12} \cdot 24\text{H}_2\text{O}$ , were observed in the XRD pattern of product WRW16-RLF500-3l/h, with these peaks reducing in intensity as the calcination temperature was increased. Broad, weak reflections, associated with the formation of poorly crystalline  $\text{CeO}_2$ , were also observed. Strong diffuse scattering was also apparent showing the presence of non-crystalline component(s). Weight loss values of between 24-32 wt% were observed in the TGA analysis of products WRW16-RLF, with a particle size >2 mm (Figure 6.56) compared to the 45-55 wt% seen from the calcination of a Magnox HAL simulant under the same conditions. This was consistent with previous observations which showed Blend simulants have a lower residual nitrate content than Magnox due the heavier elements being present in a greater concentration. The weight loss profiles for products WRW16-RLF-500-3l/h, WRW16-RLF-600-3l/h and WRW16-RLF-700-3l/h, with a particle size >2 mm, showed the same two distinct events as seen at smaller particle sizes, however, the event at 380 °C (associated with denitration of  $\text{Mg}_3\text{RE}_2(\text{NO}_3)_{12} \cdot 24\text{H}_2\text{O}$ ) showed a much greater intensity, in agreement with XRD analysis, which showed  $\text{Mg}_3\text{RE}_2(\text{NO}_3)_{12} \cdot 24\text{H}_2\text{O}$  was observed in the reaction products with a particle size >2 mm.

### 6.3.2.3.2 Dust Analysis

#### 6.3.2.3.2.1 Effects of Temperature

There was an increase in the mass of dust collected in the off-gas system as the calcination temperature was increased, consistent with the experiments carried out on Magnox simulants and with previous studies using the small scale calciner (Brace, 2006b). The mass values were normalised by conversion to a percentage of the actual yield to give a range of dust carry-over values for comparison (Figure 6.58). The normalised dust values range from 5.73 wt% after calcination at 500 °C up to 7.07 wt% at 700 °C, higher than the values associated with the corresponding Magnox experiments, which showed dust carry-over values of 3.25 wt% and 4.77 wt% respectively. In contrast to the Magnox experiments, however, this is in correlation with a decrease in the calcine fraction with a particle size >2 mm. This suggested that competing processes occur in the calciner for both dust formation and the further breakdown of larger particles which are retained in the calcine. As with the calcine, a 5 % error was associated with the collection of dust from the small scale calciner to take into account the fact that not all of the dust would be recovered in these experiments.

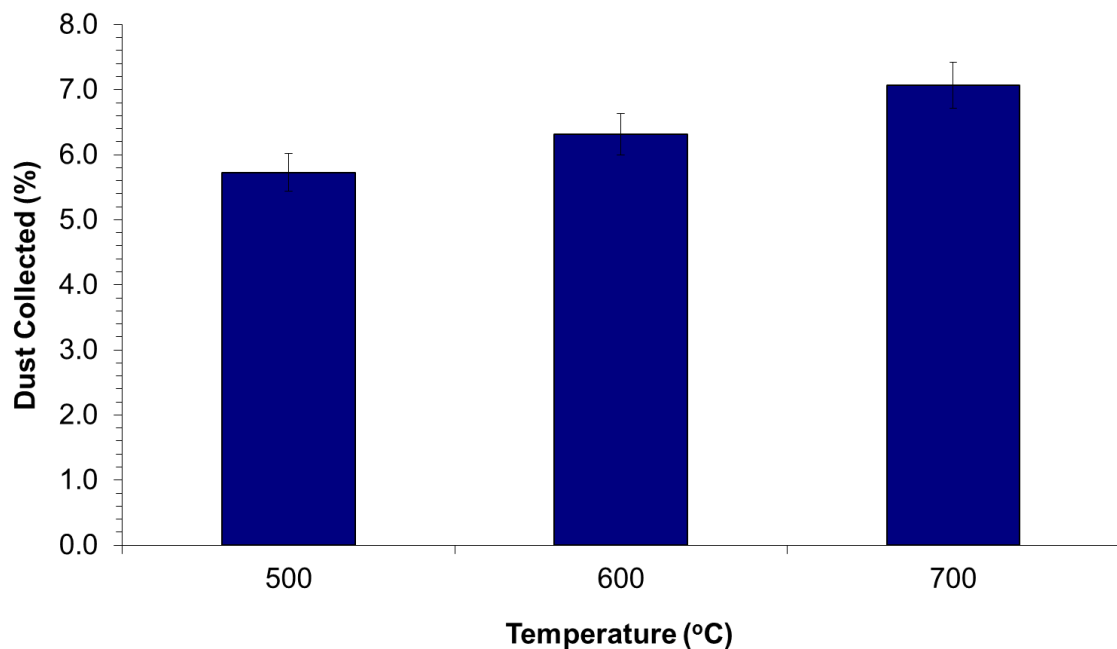


**Figure 6.58 – Dust collected as a percentage of the expected yield from products WRW16-RLF calcined between 500-700 °C at a feed rate of 3 l / h**

XRD analysis of the dust samples produced from WRW16-RLF calcined at 500, 600 and 700 °C, at a feed rate of 3 l / h (Figure 6.59), all showed a set of matching reflections attributable to  $\text{Mg}_3\text{RE}_2(\text{NO}_3)_{12}\cdot 24\text{H}_2\text{O}$ . Significant diffuse scattering was also apparent, showing the presence of a non-crystalline component. These observations are the same as those observed in Magnox experiments, although  $\text{Mg}(\text{NO}_3)_2\cdot 6\text{H}_2\text{O}$  was not observed due to the reduction in Mg concentration in Blend simulants. TGA analysis showed weight losses of between 31-34 wt% at 1000 °C (Figure 6.60), higher than the values attained from the calcine fraction with a particle size greater than 2 mm and much greater than those seen in particles smaller than 0.5 mm. The weight loss profiles of products WRW16-RLF calcined between 500-700 °C, with a particle size >2 mm were also similar to that observed in the dust samples, except there appeared to be a greater weight loss below 300 °C, associated with dehydration, in the dust samples. It is possible that the large particles are broken down and carried over to the off-gas system (where the dust particles are trapped but have a constant stream of steam and nitric acid vapour passing over it) where they are rehydrated / adsorb water, resulting in a greater weight loss being observed. The weight loss profiles showed three distinct events: a broad weight loss below 300 °C, typical of dehydration; a relatively sharp weight loss at 380 °C, associated with the denitration of  $\text{Mg}_3\text{RE}_2(\text{NO}_3)_{12}\cdot 24\text{H}_2\text{O}$  (Appendix 2); and a broad weight loss between 450-600 °C, attributable to further denitration of the more stable nitrate components which make up the HAL simulant, by reference to thermal stability data for individual component nitrates of which the HAL is comprised (Chun, 1977). Taken together, the XRD and TGA data show that the dust has a similar composition to the calcine fraction with a particle size >2 mm and is different from the smaller calcine particles formed in these experiments. This suggests that the mechanism by which dust is created, and subsequently transported to the off-gas system, involves the abrasive breakdown of larger particles. However, the decrease in the fraction of large particles formed at higher calcination temperatures suggest that the process for the breakdown of large particles for the formation of dust and further breakdown of the calcine are contrasting. It is possible that the formation of dust takes place at the start of the denitration process, towards the front of the calciner tube, where the higher residual nitrate will result in the particles being less dense<sup>23</sup> and therefore particles of comparable size will be transferred to the off-gas system more easily, as the movement of particles in a consistent airflow is known to depend on both particle size and density (Dong et al., 2003). As the particles are subjected to a higher temperature, further denitration occurs causing an increase in density of the small particles. The increase in density could result in a lower fraction of this material being carried over to the off-gas system, therefore manifesting as a reduction in the particle size distribution in the calcine without significantly affecting dust carry-over. This is in agreement with XRD and TGA data, which show the dust has similar properties to the larger calcine particles, suggesting it is created from the breakdown of these particles with a diameter >2 mm.

---

<sup>23</sup> In general, the metal nitrates present in the HAL have a lower density than their corresponding oxides (Perry, 2011; Phillips, 1995)

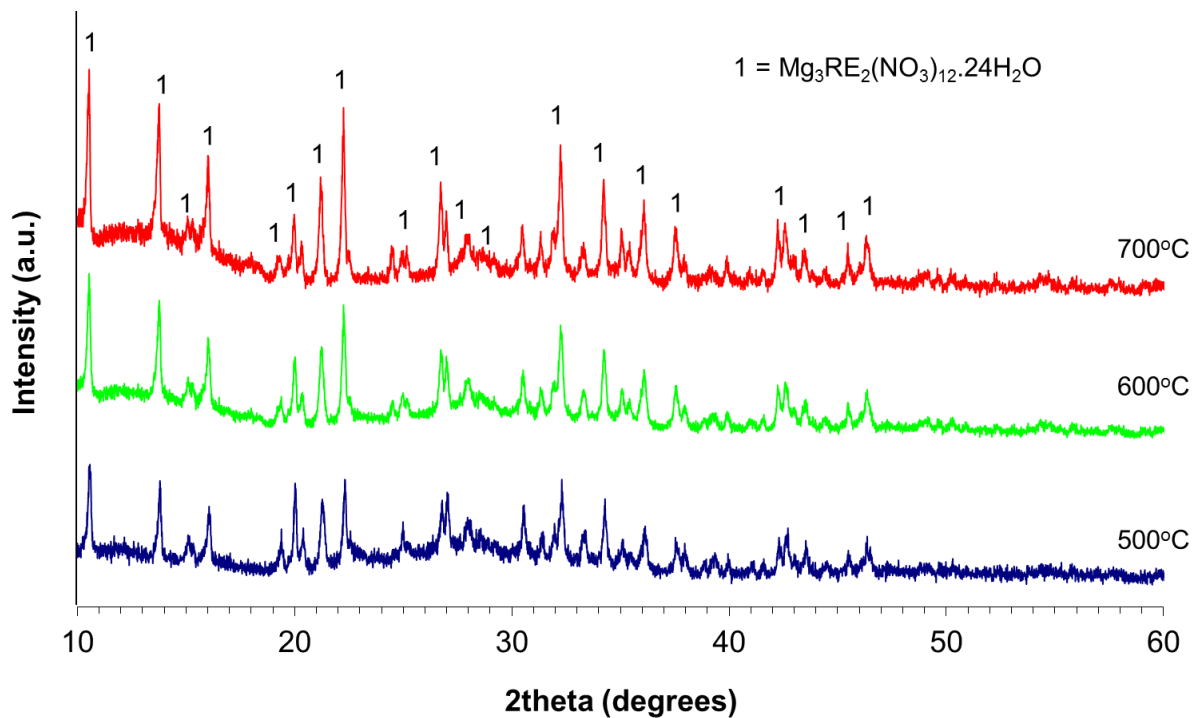


**Figure 6.59 – XRD analysis of products a) WRW17-RLF-500-3l/h, b) WRW17-RLF-600-3l/h and c) WRW17-RLF-700-3l/h dust samples**

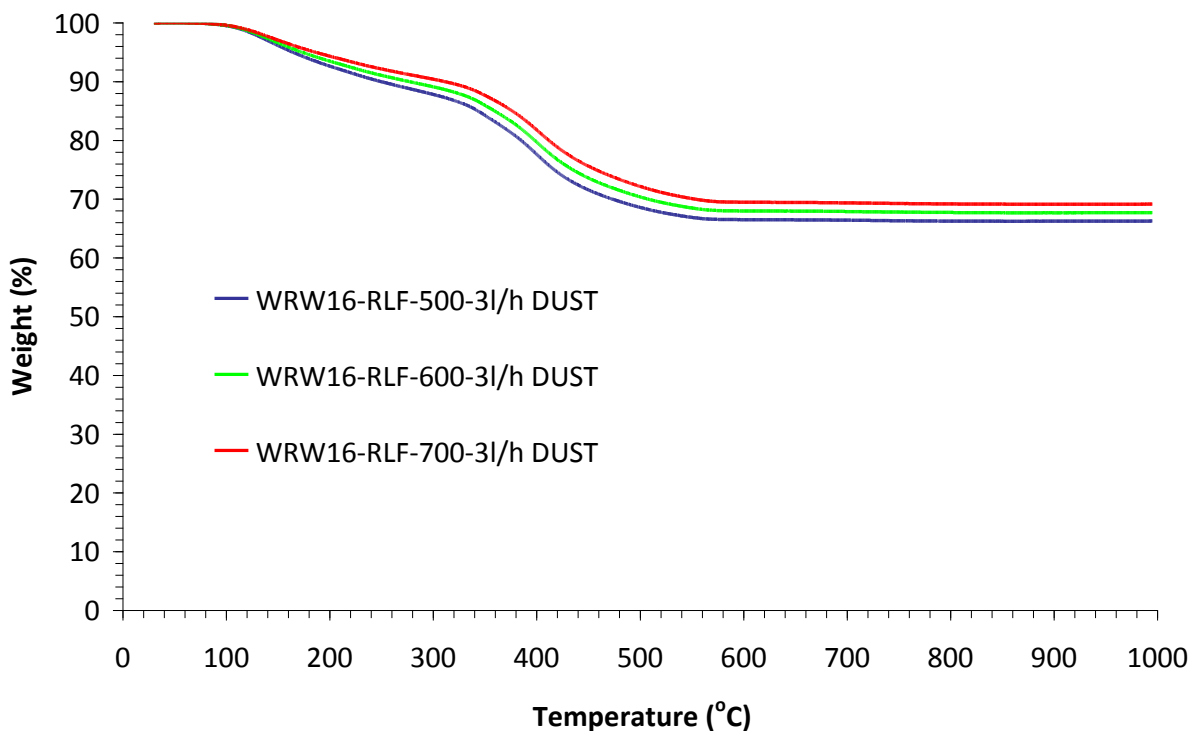


**Figure 6.60 – TGA analysis of products WRW17-RLF-500-3l/h, WRW17-RLF-600-3l/h and WRW17-RLF-700-3l/h dust samples**

From these experiments, it is possible to infer and conclude the following:

- A greater dust carry-over is observed as a function of increasing temperature, consistent with the Magnox experiments. However, this, correlated with a reduction in the formation of larger particles, is contradictory to observations made in the Magnox experiments. This suggested that calcine composition has a significant effect on dust carry-over.
- The major crystalline product in the dust was  $\text{Mg}_3\text{RE}_2(\text{NO}_3)_{12}\cdot 24\text{H}_2\text{O}$ , as observed in the Magnox simulant experiments. The presence of  $\text{Mg}_3\text{RE}_2(\text{NO}_3)_{12}\cdot 24\text{H}_2\text{O}$  was again seen in both the dust and larger calcine particles (>2 mm), with this diminishing in the smaller particles and as a function of increasing temperature. This implied that dust is formed from the breakdown of larger calcine particles.
- There was a notable decrease in the residual nitrate in Blend simulants compared with Magnox, calcined under the same conditions. This is associated with the increase in heavier elements present in the Blend simulant. The presence of a lower volume of metal nitrates in the calcine suggest that there will be less molten material binding the calcine together, allowing the rabble bar to breakdown the calcine more efficiently. This would result in the lower mass fraction of large particles being formed in calcine resulting from the calcination of Blend simulant, compared to Magnox, as seen in these experiments.

### 6.3.3 Discussion

#### 6.3.3.1 Freeze dryer experiments

The freeze drying of both Magnox and Blend simulants (WRW16 and WRW17) showed that  $\text{Mg}_3\text{RE}_2(\text{NO}_3)_{12}\cdot 24\text{H}_2\text{O}$  was formed in the freeze dried product, in agreement with previous studies on crystallisation in the HAST tanks at Sellafield (Richardson, 2002a). This suggested that Mg and RE nitrates react together in solution, where RE = La, Ce, Pr, Nd, Sm or Gd, to form  $\text{Mg}_3\text{RE}_2(\text{NO}_3)_{12}\cdot 24\text{H}_2\text{O}$  *via* reaction between the corresponding metal nitrates (Quill et al., 1937). All of the  $\text{Mg}(\text{NO}_3)_2\cdot 6\text{H}_2\text{O}$  appeared to be consumed in the Blend simulant due to the high levels of RE elements compared to Mg, whereas in the Magnox simulant,  $\text{Mg}(\text{NO}_3)_2\cdot 6\text{H}_2\text{O}$  was partially unreacted due to the reduction in concentration of RE elements and a higher Mg content within the simulant (Short, 2010b; Short, 2010c). These data suggest this reaction goes to completion in the HAL simulant with no competing reactions involving  $\text{Mg}(\text{NO}_3)_2\cdot 6\text{H}_2\text{O}$  taking place in solution. After calcination at 350 °C for 10 mins, the presence of  $\text{Mg}_3\text{RE}_2(\text{NO}_3)_{12}\cdot 24\text{H}_2\text{O}$  was still observed in the calcine product of both Blend and Magnox HAL simulants, but had decomposed at 550 °C, consistent with thermal analysis of this compound (Appendix 2). The addition of  $\text{LiNO}_3$  had no observed effect on the formation or decomposition properties of  $\text{Mg}_3\text{RE}_2(\text{NO}_3)_{12}\cdot 24\text{H}_2\text{O}$ .



$\text{Al}(\text{NO}_3)_3 \cdot 9\text{H}_2\text{O}$  was present in both Blend and Magnox simulants after freeze drying (with no further heat treatment), which implied no reaction took place in solution. This is consistent with findings in Chapter 5, which showed  $\text{Al}(\text{NO}_3)_3 \cdot 9\text{H}_2\text{O}$  was present in all the freeze-dried products. After calcination at 350 °C, no reflections attributable to  $\text{Al}(\text{NO}_3)_3 \cdot 9\text{H}_2\text{O}$  were observed in the XRD patterns of WRW16 or WRW17, in agreement with available literature (Pacowska and Keshr, 2002) which showed formation of an amorphous product on the (partial) dehydration and denitration between 200-550 °C.

In Blend simulant, CPM was observed as the major crystalline component in the freeze dried product, due to the high levels of Mo (Short, 2010c) and is consistent with the observation of a yellow precipitate in the simulant (Neepe et al., 2013). This precipitate is observed in Magnox simulants, though in a reduced amount. XRD analysis, however, did not show the presence of CPM in the diffraction pattern of product WRW17-RLF-FD, which suggested it was not present in a large enough proportion to overcome the increased diffuse scattering observed. On calcination at 350 °C, CPM was not observed in any of the products suggesting it had undergone a reaction, resulting in the formation of a non-crystalline product.

The observation of an additional reflection in the diffraction pattern of WRW16-RF-FD, compared to the Li free product, and the absence of reflections attributable to  $\text{LiNO}_3$  (or any of its hydrated forms) suggested that a reaction had occurred in solution. However, due to the fact that only one additional reflection was observed and the complexity of the HAL simulant, the reaction product(s) remained unidentified.

After calcination at 550 °C,  $\text{CeO}_2$  was formed in both Magnox and Blend simulants. This is in agreement with previous studies (Dunnett et al., 2009) which showed no reflections attributable to  $\text{CeO}_2$  were observed at 400 °C, but were highly crystalline at 1050 °C. The addition of  $\text{LiNO}_3$  resulted in the reflections attributable to  $\text{CeO}_2$  becoming more intense, suggesting that  $\text{LiNO}_3$  acted as a molten salt, increasing the rate at which the oxidation reaction occurred.

The formation of  $\text{BaCeO}_3$  (or complex oxide(s) with the same structure) was observed in Blend simulant with the addition of  $\text{LiNO}_3$ , in agreement with previous studies (Short, 2005), which showed that on addition of  $\text{LiNO}_3$  to a Blend HAL simulant, there were 2 additional phases observed. The first additional phase which arose, belonged to the Pm-3m space group (Short, 2005) consistent with the structure of  $\text{BaCeO}_3$ . The other additional phase observed was  $\text{CsLiMoO}_4$ , which was not observed in these experiments.  $\text{LiNO}_3$  is used in molten salt synthesis of metal oxides (Xu et al., 2009; Li et al., 2008) as it has a low melting point and acts as Lux-Flood base, making it a good  $\text{O}^{2-}$  donor, and can therefore lower the temperatures needed for an oxidation reaction to occur (Afanasiev and Geantet, 1998). The fact that the addition of  $\text{LiNO}_3$  gave rise to the formation of complex oxides suggests that it may act as a molten salt in the calcine, helping to facilitate reactions which would not otherwise occur in aqueous media or in the solid state after evaporation had occurred. This is a likely explanation for the formation of complex oxide phases which are not observed without the presence of  $\text{LiNO}_3$ .

Throughout these experiments, XRD was used as the main method of identifying species found within the HAL simulants. However, this showed that a significant portion of the species were non-crystalline in nature, thus highlighting a major limitation of this study. EDX analysis was utilised to show the distribution of the major elements throughout the samples, but this did not provide information about the chemical environment in which elements such as Zr reside. These elements were not identified as being part of the crystalline portion of the calcination products, therefore the form they take, both in the HAL simulant and after calcination, is unknown. Further characterisation, through techniques such as solid state NMR, could be utilised to provide an insight into the chemical environment(s) of the elements not identified as being present in the crystalline phases of the calcination products.

Previous work by Sutrisno et al. (2012) has shown that  $^{91}\text{Zr}$  SSNMR carried out on poorly crystalline zirconium phosphate materials led to characterisation of the metal centre environments, where XRD patterns did not provide conclusive information about the crystal structure. This is due to advancements in SSNMR techniques. Another possible use of SSNMR would be to show the decomposition of CPM by monitoring the chemical environment(s) of both  $^{31}\text{P}$  and  $^{94}\text{Mo}$  in samples calcined at various temperatures. As a wide range of nuclei can be analysed using this technique, providing information about the chemical environment(s) of these elements, it could be utilised in future experiments to provide more information about the species which exist in both Magnox and Blend HAL simulants.

### 6.3.3.2 Small scale calciner experiments

The small scale calciner was modified to allow the capture of dust carried from the calciner to the off-gas system, which had not been possible previously. On the VTR, dust carry-over is calculated from the solids present in the dust scrubber, as this is the first sample point in the off-gas system. However, the majority of the dust is soluble in the nitric acid and therefore analysis such as XRD, TGA and density measurements could not be carried out. By collecting the dust as a solid, before reaching the dust scrubber, this analysis could be carried out, giving new information on the mechanism of dust formation and the chemical composition, density and particle size of the dust particles.

XRD and TGA analysis of the collected dust samples, for all experiments, showed the presence of  $\text{Mg}_3\text{RE}_2(\text{NO}_3)_{12}\cdot 24\text{H}_2\text{O}$ , known to decompose at  $\sim 380^\circ\text{C}$ , thus showing the dust does not experience temperatures above this during calcination. This phase was also present in the larger calcine particles ( $>2\text{ mm}$ ), with reducing quantities being present in smaller particles. This showed the dust had a similar composition to the larger particles ( $>2\text{ mm}$ ) formed in the calcination process and were different from the smaller particles ( $<0.5\text{ mm}$ ) collected in the calcine, backed up by chemical analysis (ICP-OES). Historically, dust was thought to be formed from the smallest calcine fraction, however, these experiments showed a correlation was observed between the dust and larger calcine particles. The abrasive breakdown of larger particles is therefore thought to be responsible for the creation of dust in the small scale calciner, which is subsequently transported to the off-gas system. The following processes are thought to contribute to this:

- Metal nitrates are generally lower in density than their corresponding oxides (Table 6.10; Perry, 2011; Phillips, 1995), allowing them to be transported more easily, as particle size and density are both known to influence the movement of particles in a constant airflow (Dong et al., 2003).
- The larger, lower density particles will be broken down more easily by the rabble bar than the smaller, denser calcine fraction.
- As only the surface of the larger particles come into contact with the heated calciner tube walls, small particles will be broken off as the remainder, in the centre of the large particle, will be held together by the molten metal nitrates.

These findings showed that the formation of dust is likely to occur through the abrasive breakdown of larger calcine particles by the rabble bar inside the calciner tube. The calcination conditions and the addition of  $\text{LiNO}_3$  are known to affect the dust carry-over (discussed in sections 6.3.3.2.1 to 6.3.3.2.3), however, all the small scale calciner experiments showed that the similarities in chemical composition and density between the dust and large particles of calcine, combined with the differences in the small calcine fraction, is strong evidence that the dust fraction is created through the breakdown of particles  $>2$  mm in diameter during the calcination process.

**Table 6.10 – Densities of metal nitrates and oxides contained in HAL simulants and calcine (Perry, 2011; Phillips, 1995)**

Element	Nitrate	Oxide
Al	1.72 g / cm <sup>3</sup>	3.97 g / cm <sup>3</sup>
Fe	1.68 g / cm <sup>3</sup>	5.24 g / cm <sup>3</sup>
Gd	2.33 g / cm <sup>3</sup>	7.41 g / cm <sup>3</sup>
Li	2.38 g / cm <sup>3</sup>	2.01 g / cm <sup>3</sup>
Mg	1.64 g / cm <sup>3</sup>	3.58 g / cm <sup>3</sup>
Mo	-	4.69 g / cm <sup>3</sup>
Zr	-	5.60 g / cm <sup>3</sup>

#### 6.3.3.2.1 The effects of lithium nitrate

On addition of  $\text{LiNO}_3$  to a Magnox HAL simulant, processed on the small scale calciner, a significant reduction in the dust carry-over was observed at calcination temperatures between 500-700 °C. This was in conjunction with a reduced mass fraction of calcine produced with a particle size  $>2$  mm. Together with XRD and TGA analysis, showing the similarities in the properties of the dust and large calcine particles ( $>2$  mm) at all calcination temperatures and feed rates, this suggested that the breakdown of large particles was responsible for the creation of dust. As a lower fraction of large particles were formed on addition of  $\text{LiNO}_3$ , there was a lower dust carry-over observed.

LiNO<sub>3</sub> appeared to react with the Magnox HAL simulant in solution, as shown in the freeze dryer experiments (section 6.3.1). The products of these reactions, after calcination between 350-550 °C for 10 minutes in a muffle furnace, or after calcination in the small scale calciner with a Zone 3 temperature between 500-700 °C, appeared to be non-crystalline in nature so were not identifiable by XRD analysis.

Metal nitrates, of which the HAL simulants are comprised, have low melting points and will therefore be molten in the calcination process until decomposition to the corresponding metal oxide occurs. If the metal nitrates are molten, they will not be available to be broken down by the rabble bar and will agglomerate to form large particles. TGA analysis of products WRW17-RLF-500-31/h and WW17-RF-500-31/h (Figure 6.61) showed a significant decrease in weight loss after the addition of LiNO<sub>3</sub> in the calcine fraction >2 mm, but an increased weight loss at smaller particle sizes. This implies denitration is occurring faster in the early stages of calcination, when the particles are larger, but due to the extra nitrate from the stable LiNO<sub>3</sub>, this decreases as the reaction progresses in the smaller particles. This suggests the LiNO<sub>3</sub> could be acting as a molten salt, helping to facilitate reactions. If the addition of LiNO<sub>3</sub> facilitates reactions within the calciner, causing the oxidation to occur more quickly, the rabble bar will have longer to break up the calcine, resulting in a reduction in the large particles formed. However, this would be expected to correlate with a higher dust carry-over, whereas the opposite was true in these experiments. A possible explanation for this is that the increase in density of the metal oxides, compared to the nitrates, means that the increased smaller fraction are not as easily carried to the off-gas system. This is in agreement with XRD analysis which suggests low temperature nitrate and hydrate containing phases, such as Mg<sub>3</sub>RE<sub>2</sub>(NO<sub>3</sub>)<sub>12</sub>.24H<sub>2</sub>O, are present in both the large particles and dust, but are decomposed at higher temperatures and smaller particle sizes. The absence of weak reflections attributable to CeO<sub>2</sub> in the large particles and dust (which are present in particle smaller than 0.5 mm in diameter) also imply that the smaller, denser fraction of the calcine (<0.5 mm) are not preferentially carried over to the off-gas system.

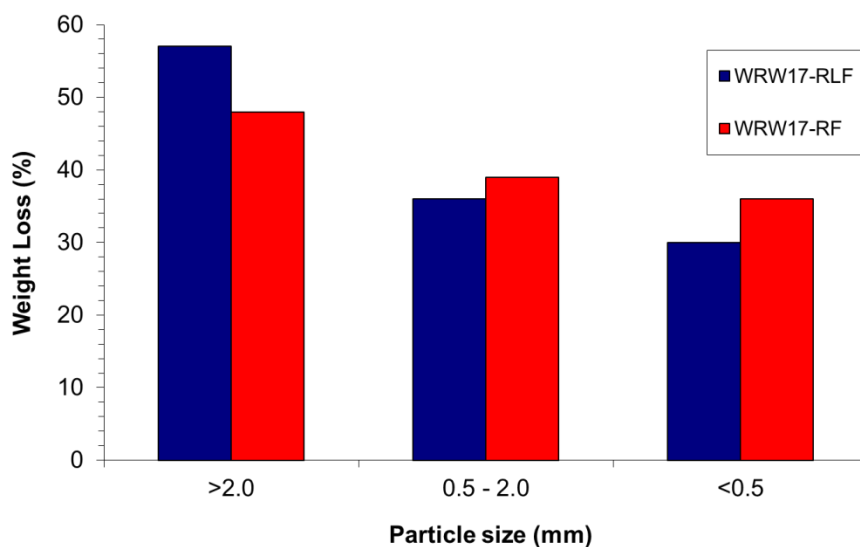


**Figure 6.61 – Weight loss values for products WRW17-RF-500-3l/h and WRW17-RLF-500-3l/h with differing particle sizes**

#### **6.3.3.2.2 The effects of temperature**

An increase in calcination temperature results in the transfer of a greater mass of dust to the off-gas system in all cases where the other parameters were kept constant. In Magnox HAL simulants, both with and without Li addition processed on the small scale calciner, this correlated with an increasing fraction of calcine being formed with a larger particle size. As there was an increased fraction of larger particles, there will have been more particles available to be broken up, resulting in a greater volume of dust created and therefore transported to the off-gas system. As the set-points for Zones 1 and 2 were kept constant at 400 °C throughout these experiments, with only the Zone 3 temperature changing, this was thought to have no significant effect on the position of the evaporative front, leaving the same portion of the tube available for denitration processes to occur. The formation of a higher fraction of larger particles at higher temperature, therefore, is likely to be caused by an increase in the amount of molten material formed, which will agglomerate to form the larger particles. This is consistent with the fact that at higher temperature there is the potential for more of the material to be above its melting point. However, at a higher temperature, denitration would also be expected to occur at a faster rate, causing the particles to become denser and therefore more difficult to transport to the off-gas system. It is therefore possible for Magnox simulants, that at a feed rate of 3 l / h, the residence time in the calciner tube was too short to allow the denitration to occur so the smaller particles are not formed efficiently from the breakdown of larger particles, as molten nitrates bind the calcine together. This is consistent with the observation that there was no significant difference observed in the fraction of small particles formed as a function of temperature throughout these experiments.

In Blend simulants, there was a decrease in the fraction of larger particles formed as a function of temperature. This implies that the breakdown of the larger particles had begun to occur at a feed rate of 3 l/h. This is in agreement with the observation of a lower residual nitrate in the calcine formed from Blend simulants, compared to Magnox, suggesting there will be a lower fraction of molten metal nitrates binding the calcine together. As a result, the agglomeration of larger particles will occur more quickly, with an initial increase in the fraction of large particles formed at higher temperature due to more molten material being formed at high temperature (i.e. the temperature will be above the melting point of a higher fraction of the material in the calciner as it is increased), resulting in the increased dust carry-over observed. However, due to the higher temperatures, denitration will also occur more rapidly causing the breakdown of these large particles to form the smaller, denser fraction of the calcine product. This accounted for the differences observed in the behaviours of Magnox and Blend HAL simulants in the calcination process.


#### **6.3.3.2.3 The effects of feed rate**

At a feed rate of 2 l/h, the calcination of Magnox HAL simulant both with and without Li addition, there was a significant reduction in the amount of large particles formed than at feed rates of 3 l/h and 4 l/h, though an increase in dust carry-over was observed. An increase in the amount of small particles formed was also observed (Table 6.11). It is known that at a lower feed rate, the residence time at higher temperature effectively increases as the position of the evaporative front in the calciner moves further up the calciner tube. This will be affected more greatly by feed rate than Zone 3 temperature, as set-points 1 and 2 were kept the same (400 °C) throughout these experiments. As the evaporative front is further up the tube, the large particles will also be formed higher up the tube. The initial abrasion of larger particles, thought to be responsible for formation of the majority of the dust which is subsequently carried over to the off-gas system, would therefore occur initially, with further breakdown of the larger particles taking place due to the longer time in the hotter part of the tube where denitration processes occur. The increase in dust carry-over will therefore be due to the longer residence time (as opposed to a larger amount of large particles forming due to higher temperature), allowing the rabble bar to break up a larger portion of the large particles, causing the formation of more dust.

**Table 6.11 – Table showing the patterns of dust carry-over and the relationship with the different particle size calcine fractions for WRW17-RF when processed at 3 l/h through the small scale calciner**

		Zone 3 Temperature (°C)		
		500	600	700
Feed Rate (l/h)	4		1.96% Dust Carry-Over 41% Particles >2mm 18% Particles <0.5mm	
	3	2.01% Dust Carry-Over 44% Particles >2mm 18% Particles <0.5mm	2.40% Dust Carry-Over 47% Particles >2mm 18% Particles <0.5mm	2.97% Dust Carry-Over 51% Particles >2mm 19% Particles <0.5mm
	2		2.95% Dust Carry-Over 25% Particles >2mm 30% Particles <0.5mm	

 Increasing % dust carry-over

 Increasing % Particles >2 mm

 Increasing % Particles <0.5 mm



### 6.3.3.3 The mechanism of dust creation and breakdown of calcine

Taking together all of the analysis carried out on this series of small scale calciner experiments, the following observations can be made:

- The dust appeared to have been mostly formed from the abrasive breakdown of larger calcine particles as the properties of large particles and dust were similar. The density and  $^7\text{Li}$  NMR measurements suggested that a portion of the dust may also have been generated from carry-over of the smaller calcine fraction with a particle size  $<0.5$  mm.
- As the increase in temperature causes an increase in large particles formed in the calcine (at feed rates of 3 l/h and above), the formation of large particles appeared to occur from the agglomeration of molten nitrates. A higher fraction of the calcine will be molten at higher temperature, increasing the mass of large particles formed.
- At low feed rates, a decrease in the large fraction of calcine collected was apparent, as well as an increase in small particles formed. This implied a further breakdown of the larger particles was occurring as the effective residence time was increased. This was thought to occur in a later process than that of dust formation.
- The significant differences in both chemical and physical properties of the dust and smaller calcine particles suggested the majority of the dust was not formed in the same manner as these smaller, denser particles.

With this information, it was possible to postulate a mechanism for the formation of larger particles and subsequent breakdown to initially form dust, which is carried to the off-gas system, followed by further reduction in particle size, increasing the portion of fines within the calcined product. This involved four main processes (Figure 6.62):

- Evaporation of the HAL simulant, resulting in a stage where molten nitrate hydrates are formed.
- Molten nitrates are agglomerated to form large calcine particles.
- The large particles undergo initial breakdown to form the dust which is transported to the off-gas system.
- As the large particles get smaller and increase in density due to further denitration, they breakdown further to form the smaller calcine fractions, the smallest of which will be carried to the off-gas system as dust.

Figure 6.62 shows a simplistic overview of these processes occurring within the calcine tube. Each of these processes would not occur in its own distinct section of the calciner tube, but overlap due to the different conditions each individual particle experiences. This is due to the process giving rise to different amounts of time spent against the heated calciner tube walls, resulting in the range of particle sizes and residual nitrates observed in the calcine product. The section of the tube in which these processes take place will be highly dependent on the calcination conditions, such as temperature, feed rate and chemical composition of the HAL simulant.

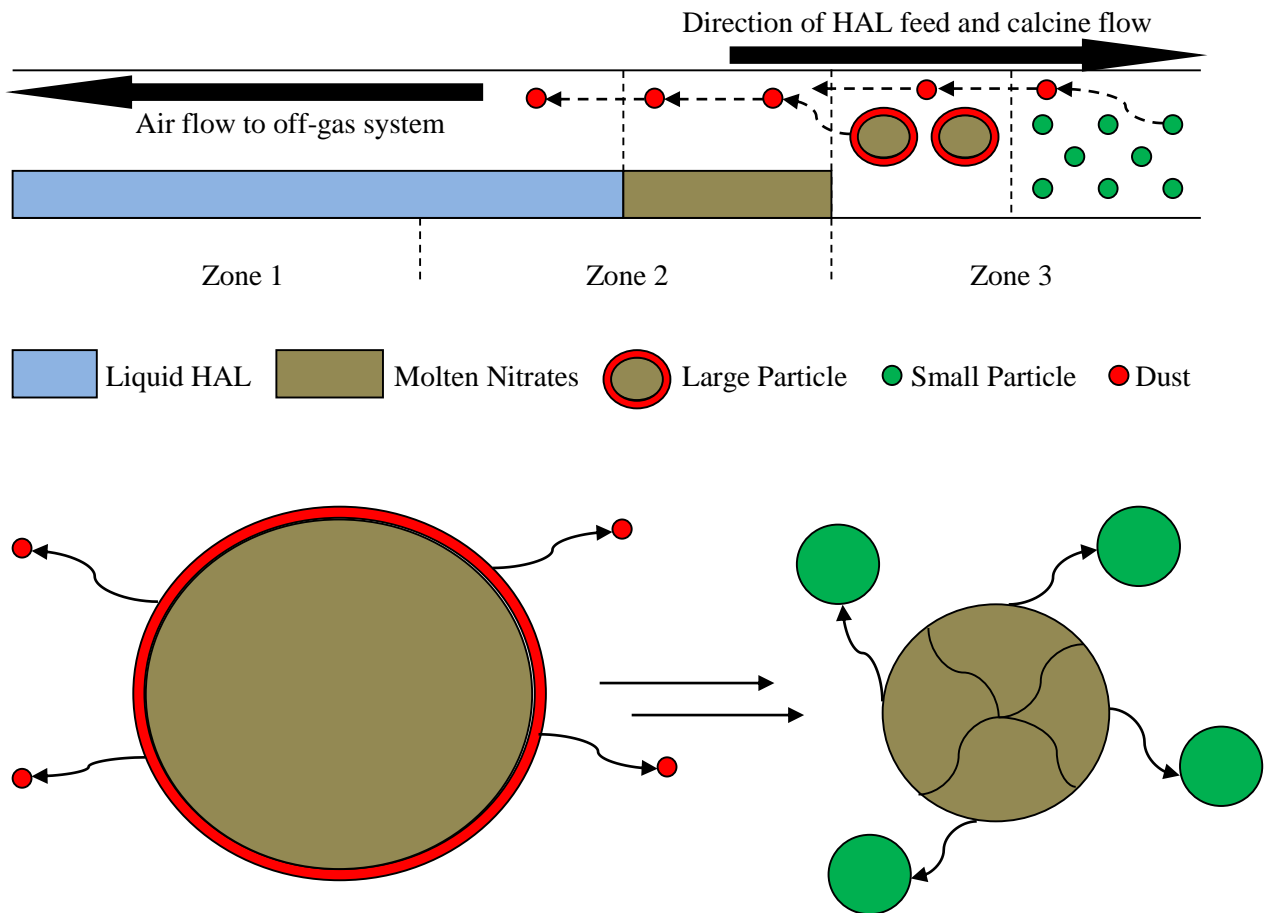


**Figure 6.62 – Schematic diagram of the postulated mechanisms from which dust and calcine particles could be formed within the small scale calciner tube**

As feed rates and calcination temperatures can be changed in the vitrification process, and the composition of the HAL simulants stored in the HAST's at Sellafield are well researched, the parts of the tube in which these processes occur can be controlled. Further experiments, utilising the small scale calciner and VTR, could lead to a quantifiable model being produced showing how different feed rates and calcination temperatures impact on the calcination process and thus affect the amount of dust generated. This is important in reducing the amount of downtime on WVP caused by blockages in the off-gas system.

## 6.4 CONCLUSIONS

### 6.4.1 Freeze dryer experiments

#### 6.4.1.1 Blended HAL Simulant (WRW16)

- On freeze drying of WRW16-RLF,  $\text{Mg}_3\text{RE}_2(\text{NO}_3)_{12} \cdot 24\text{H}_2\text{O}$ ,  $\text{Al}(\text{NO}_3)_3 \cdot 9\text{H}_2\text{O}$  and CPM were identified as the three crystalline components. This suggested that Mg and RE nitrates react together in solution, with  $\text{Al}(\text{NO}_3)_3 \cdot 9\text{H}_2\text{O}$  not undergoing any reaction without heating.
- After calcination at 350 °C for 10 minutes,  $\text{Mg}_3\text{RE}_2(\text{NO}_3)_{12} \cdot 24\text{H}_2\text{O}$  was the only crystalline component remaining in the calcine.
- At 550 °C,  $\text{Mg}_3\text{RE}_2(\text{NO}_3)_{12} \cdot 24\text{H}_2\text{O}$  appeared to have decomposed, with the formation of poorly crystalline  $\text{CeO}_2$  being observed.
- On addition of  $\text{LiNO}_3$ , an unidentified product was formed, implying that  $\text{LiNO}_3$  reacts in solution with component(s) of the WRW16 HAL simulant.
- After calcination at 550 °C, with the addition of  $\text{LiNO}_3$ , the formation of  $\text{BaCeO}_3$  (or compound(s) with the same crystal structure) was observed. This was thought to arise through the facilitation of oxidation reactions by  $\text{LiNO}_3$  acting as a molten salt.

#### 6.4.1.2 Magnox HAL Simulant (WRW17)

- $\text{Mg}_3\text{RE}_2(\text{NO}_3)_{12} \cdot 24\text{H}_2\text{O}$ ,  $\text{Mg}(\text{NO}_3)_2 \cdot 6\text{H}_2\text{O}$  and  $\text{Al}(\text{NO}_3)_3 \cdot 9\text{H}_2\text{O}$  were identified as the crystalline products present in the freeze dried product WRW17-RLF. Although observed in the solution as a yellow precipitate, CPM was not observed in the XRD pattern, implying it was a minor component.
- After calcination at 350 °C,  $\text{Mg}_3\text{RE}_2(\text{NO}_3)_{12} \cdot 24\text{H}_2\text{O}$  and  $\text{Mg}(\text{NO}_3)_2 \cdot 6\text{H}_2\text{O}$  remained in the calcined product WRW17-RLF.
- At 550 °C,  $\text{Mg}_3\text{RE}_2(\text{NO}_3)_{12} \cdot 24\text{H}_2\text{O}$  and  $\text{Mg}(\text{NO}_3)_2 \cdot 6\text{H}_2\text{O}$  underwent decomposition, with the formation of  $\text{CeO}_2$  being observed.
- $\text{LiNO}_3$  appeared to undergo a reaction in solution resulting in the formation of a non-crystalline phase.
- The addition of  $\text{LiNO}_3$  appeared to promote the formation of  $\text{CeO}_2$  through the facilitation of oxidation reactions by  $\text{LiNO}_3$  acting as a molten salt.

## 6.4.2 Small scale calciner experiments

### 6.4.2.1 Calcine analysis

#### 6.4.2.1.1 Effects of temperature

- Increasing the Zone 3 set-point on the small scale calciner led to the formation of a higher fraction of the calcine being >2 mm in diameter in Magnox HAL simulant. The calcine fraction <0.5 mm remained relatively unchanged as a function of temperature.
- There was a reduction in the quantity of  $\text{Mg}_3\text{RE}_2(\text{NO}_3)_{12}\cdot 24\text{H}_2\text{O}$  and  $\text{Mg}(\text{NO}_3)_2\cdot 6\text{H}_2\text{O}$  in the calcine fraction <0.5 mm, indicating the temperature acting on the calcine was increased.
- The calcine fraction >2 mm contained significant quantities of  $\text{Mg}_3\text{RE}_2(\text{NO}_3)_{12}\cdot 24\text{H}_2\text{O}$  and  $\text{Mg}(\text{NO}_3)_2\cdot 6\text{H}_2\text{O}$  at all Zone 3 temperatures (500, 600 and 700 °C) suggesting the core of the larger particles are subjected to much lower temperatures than those of the smaller particles.

#### 6.4.2.1.2 Effects of feed rate

- Decreasing the feed rate increased the temperature experienced by the calcine.
- At a feed rate of 2 l / h, there was a significant reduction in the quantity of large particles (>2 mm) formed in the calcine and a subsequent increase in the fraction <0.5 mm in diameter.

#### 6.4.2.1.3 Effects of $\text{LiNO}_3$ addition

- The addition of  $\text{LiNO}_3$  to Magnox HAL simulant resulted in a reduction in the amount of larger particles formed in the calcined product.
- The smaller particles appeared to have undergone further reaction to form a larger quantity of  $\text{CeO}_2$ , suggesting that  $\text{LiNO}_3$  acts as a molten salt, helping to facilitate oxidation reactions in the calcination process.

#### 6.3.2.1.4 Effects of simulant composition

Blended HAL simulant (WRW16) behaved in the same manner as Magnox HAL simulant (WRW17) except for the following observations:

- A much higher fraction of the particles were <0.5mm in diameter in the Blended HAL simulant than in Magnox, with a subsequent decrease in the larger fraction (>2mm).

- As the temperature was increased, there was a slight reduction in the amount of larger particles formed, suggesting the rabble bar breaks down Blended HAL simulant easier than Magnox.

## **6.4.2.2 Dust analysis**

### **6.4.2.2.1 Effects of temperature**

- The amount of dust generated from small scale calcine experiments increases at higher Zone 3 temperatures. This correlated with an increase in the fraction of larger particles formed at higher temperatures.

### **6.4.2.2.2 Effects of feed rate**

- An increase in the normalised dust carry-over was observed at lower feed rates, due to the increase in effective temperature experienced. The actual dust carry-over values, however, were higher at increased feed rate due to the higher throughput of material through the calciner.

### **6.4.2.2.3 Effects of LiNO<sub>3</sub> addition**

- The addition of LiNO<sub>3</sub> to Magnox HAL simulant significantly reduced the dust carry-over to the off-gas system on the small scale calciner.

### **6.3.2.2.4 Effects of simulant composition**

- The processing of Blended HAL simulant (WRW16) produced a much higher dust carry-over than was observed from Magnox.

### **6.4.2.3 Mechanism of dust carry-over**

- The normalised amount of dust generated in small scale calciner experiments increases as a function of increasing temperature and a reduction in feed rate.
- The physical and chemical properties of the dust are similar in nature to that of the calcine fraction with a particle size >2 mm for Magnox HAL simulants.
- The mechanism by which the dust is formed in the small scale calciner appeared to occur first by the abrasive breakdown of larger calcine particles, which creates the majority of the dust, followed by carry-over of the smallest calcine particles, making up a minor fraction of the dust.

## 6.5 FUTURE WORK

Due to the issues with the small scale calciner (see Chapter 4), the effects of  $\text{LiNO}_3$  addition and feed rate on Blended HAL simulants (WRW16) were not investigated. WRW16 appeared to behave differently in the calcination process than WRW17 (Magnox simulant), in that the particle size distribution of the calcine showed a preference for the formation of smaller particles, with an increase in dust carry-over also being observed. This was the opposite of the behaviour exhibited by WRW17, which showed an increasing particle size as dust carry-over increased. It would therefore be of interest to determine whether the addition of  $\text{LiNO}_3$  and changing feed rate has similar effects on the calcination properties of Blended HAL simulant as was observed for Magnox.

A parameter which was not investigated in these experiments was the effects of residence time on calcine properties and dust formation. This could be altered by changing the calciner tube angle, speeding up the flow by increasing the slope down the tube or increasing the time in the calciner by flattening the angle. By changing the residence time in the tube, the amount of time spent undergoing each of the four main processes which could take place in the calciner (Figure 6.62) will also change. The effects of this on the calcine properties and dust carry-over could then be monitored.

It was discovered that  $\text{Mg}_3\text{RE}_2(\text{NO}_3)_{12}\cdot 24\text{H}_2\text{O}$  was one of the major products formed in full HAL simulants, with  $\text{Al}(\text{NO}_3)_3\cdot 9\text{H}_2\text{O}$  remaining unreacted. Therefore, further studies on the reactivity of  $\text{Mg}_3\text{RE}_2(\text{NO}_3)_{12}\cdot 24\text{H}_2\text{O}$  with other components of the HAL would be beneficial to understanding the processes which occur in the calciner. At higher temperatures (above  $550\text{ }^\circ\text{C}$ ) RE oxides and complexes were identified in full HAL simulants (especially in Blend) aided in their formation by  $\text{LiNO}_3$  acting as a molten salt. Hence, a series of systematic experiments, similar to those undertaken during this project, should be conducted using  $\text{Mg}_3\text{RE}_2(\text{NO}_3)_{12}\cdot 24\text{H}_2\text{O}$  as a starting material and reacting this with other HAL components over a range of temperatures and acidities.

$\text{Mg}_3\text{RE}_2(\text{NO}_3)_{12}\cdot 24\text{H}_2\text{O}$  was found to be the major crystalline component found in the dust samples for both Blend and Magnox HAL simulants. The available evidence suggested that this phase was carried over in the dust, formed from the abrasive breakdown of the larger calcine particles. However, another possible way  $\text{Mg}_3\text{RE}_2(\text{NO}_3)_{12}\cdot 24\text{H}_2\text{O}$  could be formed in the dust, other than direct carry-over, is through dissolution and re-nitration of the calcine, as steam and nitric acid vapour are constantly passed over the dust during the experiments.  $\text{Mg}_3\text{RE}_2(\text{NO}_3)_{12}\cdot 24\text{H}_2\text{O}$  could then precipitate out, accounting for its presence in the dust. To determine the possibility of this occurring, the calcine fraction with a particle size  $<0.5\text{ mm}$  could be placed in a tube, with a combination of steam and nitric acid vapours passing over it for a period of 1 hour. Subsequent analysis of this calcine would determine whether  $\text{Mg}_3\text{RE}_2(\text{NO}_3)_{12}\cdot 24\text{H}_2\text{O}$  can be formed in this manner.

Previous work has suggested that Ru is preferentially carried over to the off-gas system through the volatilisation of RuO<sub>4</sub>. Though a substantial amount of research has been undertaken in this area, it has not been previously possible to collect and analyse dust samples. Therefore the measurement of Ru carry-over had been carried out by analysis of the dust scrubber and condenser liquors. If Ru is volatile, there should be very little present in the dust, as it will be carried over separately in a gaseous phase. A series of experiments on the small scale calciner, using full Ru containing HAL simulants, could provide conclusive evidence of the mechanism by which Ru is transferred from the calciner to the off-gas system.

Looking towards future feed stocks, there is an increasing interest in the behaviour of POCO waste-streams in the vitrification process. In these experiments, Mo and Zr appeared to be preferentially carried to the off-gas system whilst processing Magnox simulants. The calcination of Blend HAL simulant (higher in Zr and Mo) resulted in a higher dust carry-over being observed, suggesting that for POCO waste-streams, the dust carry-over could be very high. This could result in blockages forming in the WVP plant off-gas system. There would therefore be an interest in running a POCO simulant on the small scale calciner, under a range of varying conditions, to determine the severity of the dust carry-over, and how different temperatures and feed rates affect this. The effects of the addition of LiNO<sub>3</sub>, or other additives/dilutants, on the dust carry-over would also be beneficial at a lab scale, so any potential issues on the full scale processing of POCO waste streams can be identified.

The ultimate aim for this area of research is to be able to model the processes which occur in the WVP's at Sellafield. By building up the knowledge base surrounding calcination chemistry, and the effects this has on dust carry-over, it gives a good base for understanding how different parameters affect the vitrification of HAL.

# 7. Determination of Temperatures Experienced in the Calcination Process

## 7.1 INTRODUCTION

Previous work carried out in this study (Chapters 5 and 6) have shown that the temperatures experienced in the calcination process are dependent on feed rate, calcine particle size and temperature set points. However, the range of temperatures experienced by the calcine in the calcination process on the small scale calciner, VTR and WVP plants under different conditions is currently unknown. This work, therefore, focusses on using lab scale results over a range of temperatures and comparing them to small scale calciner experiments to try to determine the temperatures experienced in the calciner. An experimental programme was also drawn up for a series of full scale experiments using the VTR.

## 7.2 EXPERIMENTAL

Work carried out on the short simulant PZN2 in Chapter 5 showed that at short reaction times (5-15 mins), the kinetic products changed as a function of temperature. The small scale calciner experiment showed that the temperature experienced by product PZN2 was also dependent on particle size. However, this short simulant would not be suitable to run pure on the VTR due to the corrosive nature of the PMA on the calciner tube. Therefore, a number of dilutants were tried, with  $\text{Al}(\text{NO}_3)_3 \cdot 9\text{H}_2\text{O}$  proving the best due to its unreactive nature with both PMA and  $\text{ZrO}(\text{NO}_3)_2$  and the fact that it is non-crystalline after calcination between 200-550 °C (Pacewska and Keshr, 2002). The simulant used in this series of experiments was therefore a mix of PZN2 and  $\text{Al}(\text{NO}_3)_3 \cdot 9\text{H}_2\text{O}$  solutions (subsequently known as APZN1) made by combining the following reagents sequentially:

**Table 7.1 – Simulant make-up for both freeze dryer and small scale calciner experiments**

	<b>Reagent</b>	<b>Freeze dryer</b>	<b>Small scale calciner</b>
1	$\text{Al}(\text{NO}_3)_3 \cdot 9\text{H}_2\text{O}$	9.22 g	737.6 g
2	PMA	8.04 g	643.2 g
3	$\text{ZrO}(\text{NO}_3)_2$ solution (161 g/l)	7.31 g	584.8 g
4	Distilled Water	62.92 g	5,033.6 g
5	16M Nitric Acid	9.18 g	734.4 g
6	Sugar Solution (200 g/l)	3.33 g	266.4 g

These simulants were mixed thoroughly then left overnight before being calcined under the appropriate calcination conditions.



### **7.2.1 Freeze dryer experiments**

As in Chapters 5 and 6, freeze drying of the HAL simulants was utilised to simulate the relatively short residence times in the calcination process. This was not possible using liquid samples because introducing the samples at the reaction temperature led to flash boiling and loss of the crucible contents. The samples were therefore first freeze-dried, to remove water, then the resultant solid was placed in the furnace at temperatures of 400, 450 and 500 °C for 10 mins, shown to be the average residence time in the calciner (Brace, 2004). This approach was thought to give a representative sample, since the freeze-drying simulated the action of calciner Zones 1 and 2 (without heating), and the furnace simulated the conditions in Zones 3 and 4.

### **7.2.2 Small scale calciner experiments**

To bridge the gap between lab scale and VTR experiments, the small scale calciner was used to carry out a preliminary investigation on the effects of the temperature set-points in Zone 3 on the temperature experienced by the calcine. The short simulant APZN1 was therefore calcined at a feed rate of 3 l/h with Zone 3 temperatures of 500, 600 and 700 °C through the small scale calciner. The resultant calcine product was passed through sieves with pore sizes of 0.5 and 2 mm to divide it into three size fractions (<0.5 mm, 0.5-2 mm and >2 mm). These products, as well as the dust captured during these experiments, were analysed and compared to the lab scale results to determine the temperatures experienced at the different Zone 3 set-points and by the calcine samples with differing particle sizes.

## **7.3 RESULTS AND DISCUSSION**

### **7.3.1 Freeze dryer experiments**

XRD data from sample APZN1-400-10m (Figure 7.1) showed reflections attributable to PMA together with considerable diffuse scattering associated with additional non-crystalline phase(s). From previous experiments and available literature (Hagiwara et al., 1975; Pacewska and Keshr, 2002), it is known that the decomposition products of  $ZrO(NO_3)_2$  and  $Al(NO_3)_3 \cdot 9H_2O$  are amorphous after calcination at this temperature. The weight loss achieved at 800 °C (prior to significant volatilisation of  $MoO_3$ ) was 16 wt%. The weight loss profile showed a broad weight loss below 300 °C, consistent with retention of a portion of the volatile inventory, associated with Al nitrate (Pacewska and Keshr, 2002), with very little weight loss occurring between 300-900 °C. The weight loss above 900 °C can be attributed to the volatilisation of  $MoO_3$ , in agreement with previous work (section 5.3.2.1.1) and available literature (Smolik et al., 2000). These data are consistent with previous work carried out on short simulant PZN2 (section 5.3.2.2.1) which showed reflections

attributable to PMA were observed in the product after calcination at both 350 and 450 °C. The reaction to form  $Zr(MoO_4)_2$  did not occur after calcination for 10 minutes at 400 °C.

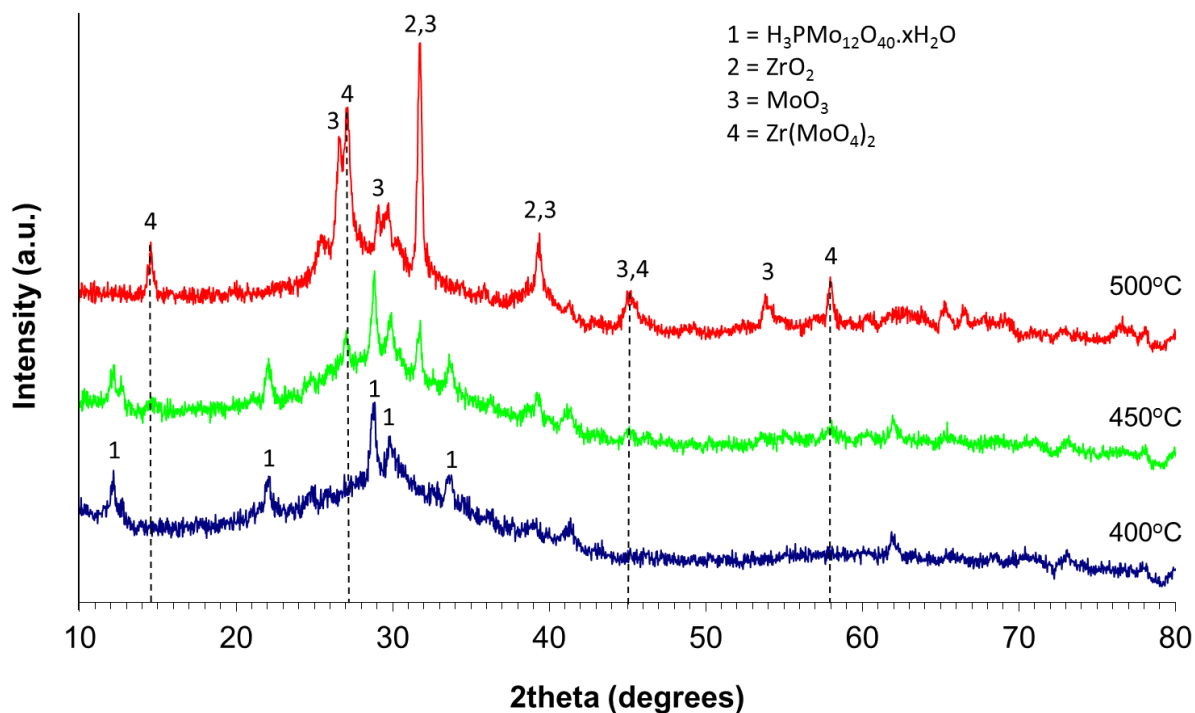


Figure 7.1 – XRD analysis of samples APZN1-400-10m, APZN1-450-10m and APZN1-500-10m

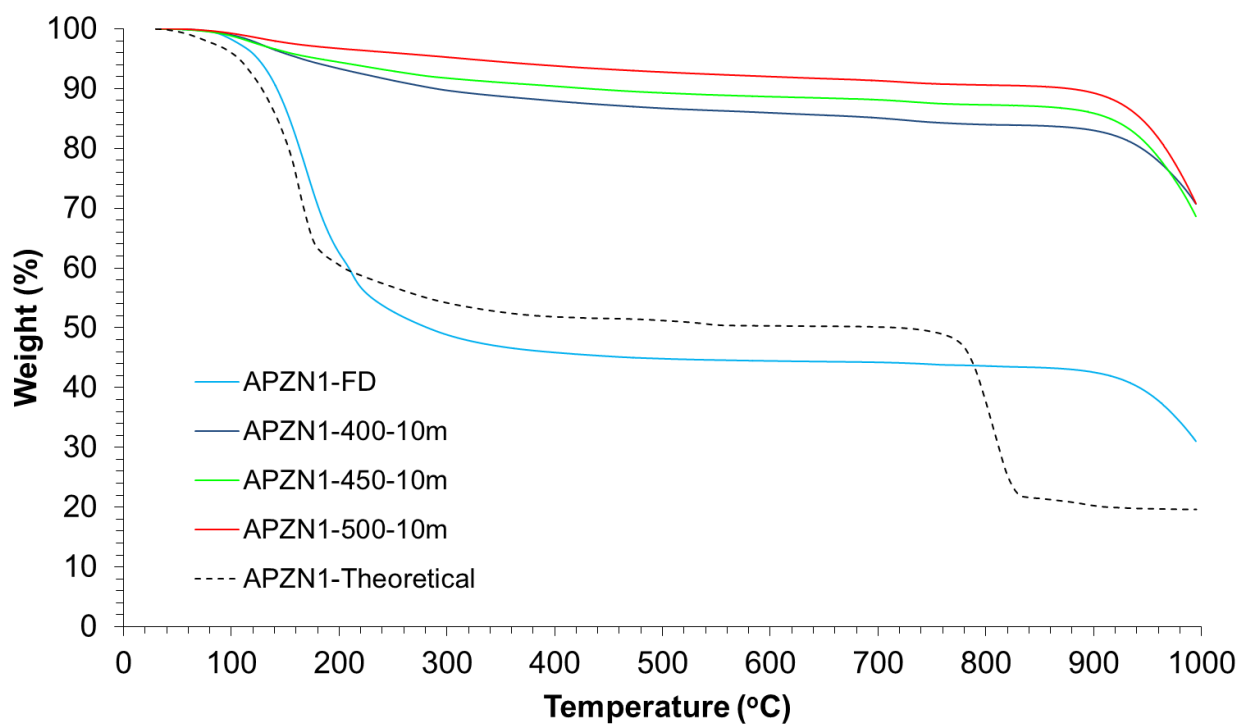


Figure 7.2 – TGA analysis of samples APZN1-400-10m, APZN1-450-10m and APZN1-500-10m

XRD analysis of product APZN1-450-10m (Figure 7.1), showed reflections characteristic of PMA were still present as well as extra reflections attributable to  $ZrO_2$ ,  $MoO_3$  and  $Zr(MoO_4)_2$ . Significant diffuse scattering was also present in the diffraction pattern. The overall weight loss of product APZN1-450-10m at 800 °C was 13 wt% (Figure 7.2), with the weight loss profile being similar in nature to product APZN1-400-10m. From these data it is possible to infer, for a residence time of 10 minutes, that the partial decomposition of PMA to form  $MoO_3$  occurs between 400-450 °C, with further reaction between  $MoO_3$  and  $ZrO_2$  resulting in the formation of  $Zr(MoO_4)_2$ .

The diffraction pattern of product APZN1-500-10m (Figure 7.1) showed reflections attributable to  $ZrO_2$ ,  $MoO_3$ , and  $Zr(MoO_4)_2$ , in addition to significant diffuse scattering. The reflections associated with  $ZrO_2$ ,  $MoO_3$ , and  $Zr(MoO_4)_2$  were much higher in intensity than after calcination at 450 °C for 10 minutes. There was a noticeable absence of reflections associated with PMA, suggesting complete decomposition had occurred. TGA analysis of APZN1-500-10m is shown in Figure 7.2. The TGA data demonstrated a weight loss of 9.3 wt% at 700 °C, with the weight loss profile again showing a broad weight loss below 300 °C. This was in agreement with findings by Pacewska and Keshr (2002) showing some retention of the volatile inventory associated with dehydration and denitration of  $Al(NO_3)_3 \cdot 9H_2O$  under these calcination conditions. Overall, these data showed PMA underwent complete decomposition to form  $MoO_3$  after calcination at 500 °C for 10 minutes.  $ZrO_2$  and  $MoO_3$  reacted together to form  $Zr(MoO_4)_2$ , although this reaction did not go to completion.

From this series of experiments, it is possible to infer and conclude the following series of reactions:

- Below 400 °C: PMA was the only crystalline species observed in the diffraction pattern, consistent with available literature (Hagiwara et al., 1975; Pacewska and Keshr, 2002) which showed the decomposition products of  $ZrO(NO_3)_2$  and  $Al(NO_3)_3 \cdot 9H_2O$  are amorphous after calcination at this temperature. This suggests no reaction occurred between PMA,  $ZrO(NO_3)_2$  and  $Al(NO_3)_3 \cdot 9H_2O$  under these calcination conditions.
- Between 400-450 °C: Reflections associated with  $ZrO_2$ ,  $MoO_3$  and  $Zr(MoO_4)_2$  are all observed in the diffraction pattern as well as some retention of the PMA starting material. This suggested that PMA underwent partial decomposition to form  $MoO_3$ , which reacted further with  $ZrO_2$  to form  $Zr(MoO_4)_2$ . The decomposition product of  $Al(NO_3)_3 \cdot 9H_2O$  remained non-crystalline in nature.
- Between 450-500 °C: Reflections attributable to  $ZrO_2$ ,  $MoO_3$  and  $Zr(MoO_4)_2$  showed increased intensity. PMA was not observed in the XRD pattern, showing complete decomposition had occurred. Further reaction between  $MoO_3$  and  $ZrO_2$  has occurred, though the reaction had not gone to completion after calcination at 500 °C for 10 minutes.

Using these data, we can estimate the temperature ranges experienced in the small scale calciner and full scale VTR and WVP processes under variable conditions can be determined.

### 7.3.2 Small scale calciner experiments

Table 7.2 shows the masses of the calcine and dust collected for short simulants APZN1 calcined under various conditions using the small scale calciner. The expected weights were calculated by first calculating the total waste oxide throughput during the experiment, then taking into account residual weight loss values (measured by TGA analysis) for each of the calcine size fractions (Table 7.3) and weighting the values accordingly (see section 6.2.2.1). The dust collection was normalised by working out a percentage dust carry-over against the actual weight of calcine collected thus allowing comparisons to be made on the effects of changing temperature and feed rate on the dust carry-over from the calciner to the off-gas system.

**Table 7.2 – Mass of calcine and dust products collected**

<b>Sample</b>	<b>Expected Weight (g)</b>	<b>Actual Weight (g)</b>	<b>Amount of Dust Collected (g)</b>	<b>Dust Collected (wt%)</b>
<b>APZN1-SSC-500</b>	355.05	314.73	18.74	5.95
<b>APZN1-SSC-600</b>	329.83	275.52	20.16	7.32
<b>APZN1-SSC-700</b>	326.20	252.38	27.11	10.33

There is a notable discrepancy between the combined mass of calcine and dust collected to the expected yield for these experiments. This could be attributed to a higher dust carry-over, as not all of the dust generated during these experiments will have been collected. This is due to the design of the small scale calciner, in which the dust must pass through the upper end fitting before getting to the flexible hose and dirt trap from which the dust samples were collected. Therefore, some dust could not be recovered during these experiments. However, a representative yield was thought to be recovered, allowing trends to be recognised (e.g. higher dust levels observed at higher temperatures).

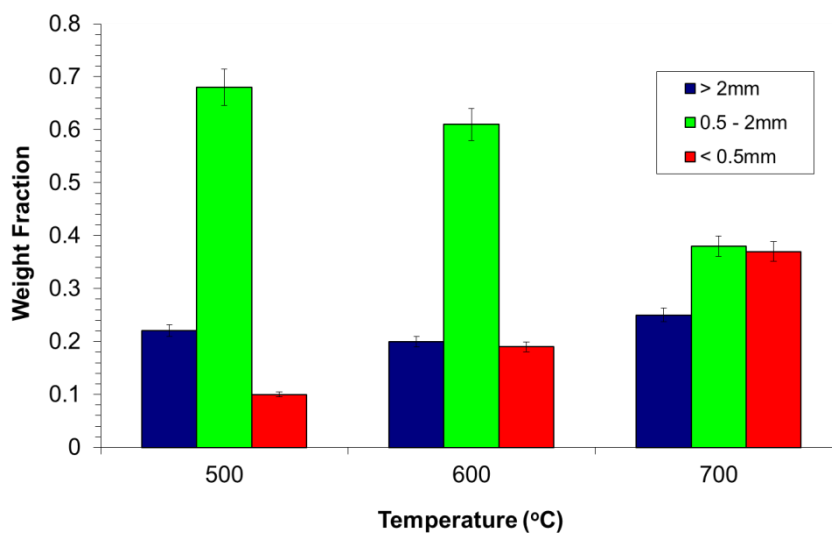
**Table 7.3 – Size fractions of product APZN1 calcined under varying conditions**

<b>Sample</b>	<b>Fraction above 2 mm</b>	<b>Fraction between 0.5 – 2 mm</b>	<b>Fraction below 0.5 mm</b>
<b>APZN1-SSC-500</b>	0.22	0.68	0.10
<b>APZN1-SSC-600</b>	0.20	0.61	0.19
<b>APZN1-SSC-700</b>	0.25	0.38	0.37

Table 7.2 showed that there was an increase in the dust carry-over as a function of increasing temperature whilst processing simulant APZN1 on the small scale calciner. This correlated with an increase in the fraction of particles <0.5 mm in diameter (Table 7.3), suggesting the formation of small particles played a significant role in the creation of dust carried to the off-gas system. There was a subsequent fall in the fraction of calcine produced with a particle size between 0.5-2 mm due to the increase in small particles formed, with the fraction >2mm showing no significant differences. This differed from the trends observed from the calcination of Magnox simulants (WRW17) but did show some similarities to Blended simulants (WRW16) which are higher in Mo and Zr. This implies that  $ZrO_2$ ,  $MoO_3$  and  $Zr(MoO_4)_2$  were more easily broken down to form smaller particles than the full HAL simulants and therefore significantly contribute to the dust generated through this process. This is also a possible explanation for the elevated levels of Mo and Zr in the dust formed in the full HAL simulant experiments.

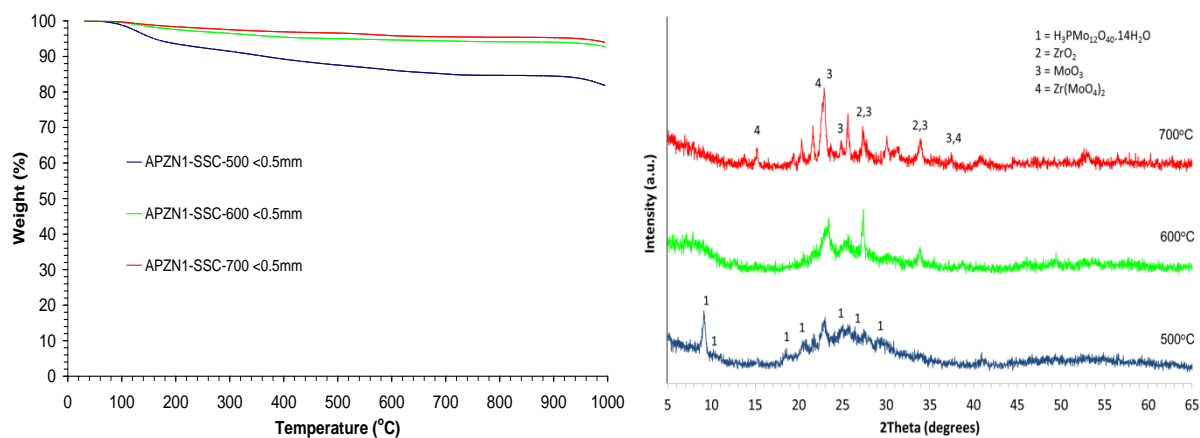
### 7.3.2.1 Calcine Analysis

Figure 7.3 shows the particle size fractions collected as a function of temperature. This showed that an increase in the mass fraction of particles <0.5 mm was observed as the Zone 3 temperature was increased. The particle size range 0.5-2 mm showed a general decrease in the mass fraction at higher calcination temperature, due to the increase in smaller particles in the product. There was no specific trend observed of the mass of the >2 mm particle size range collected, with the values for 500 and 700 °C being similar. A 5 % error has been assigned to each of the values to account for the residual calcine which will be left in the calciner tube during these experiments. This value was taken from previous small scale calciner trials which showed a 95 % mass recovery was observed (Brace, 2004), and is the same as used in the small scale calciner experiments in Chapter 6.



**Figure 7.3 – Particle size fractions from product APZN1 calcined at 500-700 °C at a feed rate of 3 l / h**

XRD analysis of APZN1 calcined at 500 °C with particle sizes <0.5 mm (Figure 7.4) showed reflections associated with PMA, with significant diffuse scattering, indicating the presence of non-crystalline component(s) also being observed. This is consistent with previous experiments and available literature (Hagiwara et al., 1975; Pacewska and Keshr, 2002), which showed the decomposition products of  $ZrO(NO_3)_2$  and  $Al(NO_3)_3 \cdot 9H_2O$  are amorphous after calcination at this temperature. TGA analysis of APZN1-SSC-500 (Figure 7.4) showed a total weight loss of 16 wt% at 800 °C. The weight loss profile of product APZN1-SSC-500 showed a distinct weight loss at 100 °C, associated with dehydration of PMA (Tatibouet et al., 1997) with a further gradual weight loss taking place between 200-700 °C, attributable to the partial dehydration and denitration of  $Al(NO_3)_3 \cdot 9H_2O$  to form  $Al_2O_3$  (Pacewska and Keshr, 2002). Further weight loss above 900 °C, associated with the volatilisation of  $MoO_3$  (Smolik et al., 2000), was also observed. These data suggested that product APZN1 calcined with a Zone 3 temperature of 500 °C using the small scale calciner and with a particle size <0.5 mm experiences a temperature of approximately 400 °C, assuming a residence time of 10 minutes (Brace, 2005a). This is consistent with the freeze dryer experimental results, which showed PMA was the only identifiable crystalline component in product APZN1-400-10m with an observed weight loss of 16 wt%. This was identical to product APZN1-SSC-500 with a particle size <0.5 mm.



**Figure 7.4 – XRD and TGA analysis of product APZN1-SSC-500, APZN1-SSC-600 and APZN1-SSC-700 with a particle size of <0.5 mm**

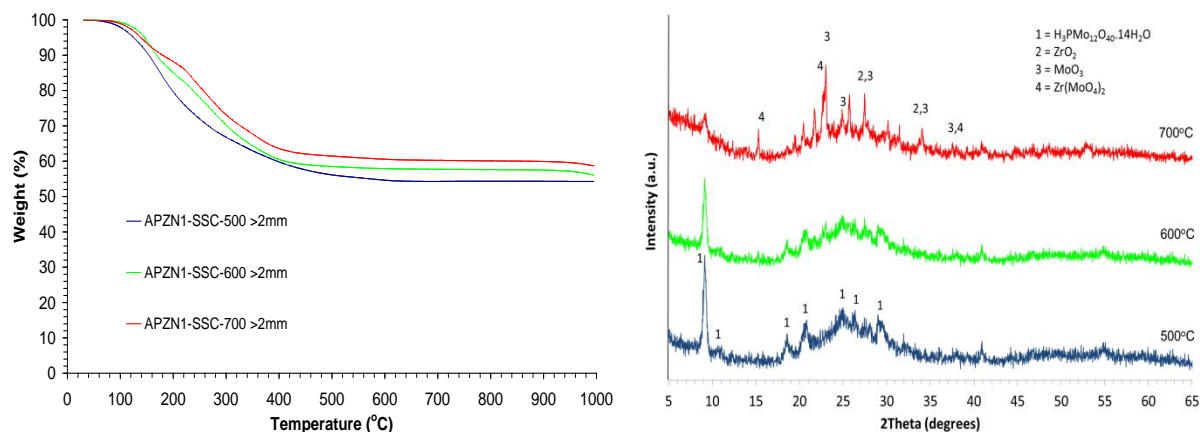


**Figure 7.5 - XRD and TGA analysis of product APZN1-SSC-500, APZN1-SSC-600 and APZN1-SSC-700 with a particle size of >2 mm**

XRD analysis of APZN1 products calcined at 600 and 700 °C with particle sizes <0.5 mm (Figure 7.4) showed reflections attributable to  $ZrO_2$ ,  $MoO_3$  and  $Zr(MoO_4)_2$ , with some diffuse scattering observed, indicating the presence of non-crystalline component(s). These reflections showed increased intensity at higher temperature. There was a notable absence of reflections associated with PMA in the diffraction pattern. TGA analysis of APZN1-SSC-600 and APZN1-SSC-700 (Figure 7.4) showed total weight losses of 5.9 wt% and 4.6 wt% respectively at 800 °C. The weight loss profiles showed a gradual weight loss taking place between 100-700 °C attributable to the partial dehydration and denitration of  $Al(NO_3)_3 \cdot 9H_2O$  to form  $Al_2O_3$  (Pacowska and Keshr, 2002) with further weight loss above 900 °C, associated with the volatilisation of  $MoO_3$  (Smolik et al., 2000), also being observed. There was an absence of the distinct weight loss at 100 °C, associated with dehydration of PMA, consistent with the absence of reflections attributable to PMA in the XRD pattern. These data suggested that product APZN1-SSC-600 with a particle size <0.5 mm experiences a temperature of between 450-500 °C, again assuming the residence time in the small scale calciner was approximately 10 minutes (Brace, 2005a). The freeze dryer experimental results for product APZN1-500-10m showed an absence of reflections associated with PMA and a total weight loss of 9.3 wt% at 800 °C. However, the XRD pattern for sample APZN1-SSC-600 showed lower intensity reflections attributable to  $ZrO_2$ ,  $MoO_3$  and  $Zr(MoO_4)_2$  than for product APZN1-500-10m, suggesting the temperature experienced was lower than 500 °C, despite the total weight loss being lower. This could have been due to adsorption of atmospheric water, after calcination, in the freeze dryer experiments and would explain the discrepancy between the XRD and TGA results for product APZN1-SSC-600 compared to APZN1-500-10m. Product APZN1-SSC-700 with a particle size <0.5 mm appeared to experience temperatures above 500 °C, shown by the high intensity reflections in the diffraction pattern and the low weight loss of 4.6 wt% in the TGA analysis.

At particle sizes >2 mm in diameter, relatively intense reflections attributable to PMA were observed in the XRD patterns of products APZN1 calcined with Zone 3 temperatures 500, 600 and 700 °C at a constant feed rate of 3 l / h using the small scale calciner (Figure 7.5). These reflections essentially accounted for all of the reflections shown in the diffraction pattern of product APZN1-SSC-500, but products APZN1-SSC-600 and APZN1-SSC-700 also showed reflections associated with  $\text{ZrO}_2$ ,  $\text{MoO}_3$  and  $\text{Zr}(\text{MoO}_4)_2$ , with these becoming more intense at increasing temperature. Strong diffuse scattering was also apparent showing the presence of non-crystalline component(s), consistent with previous experiments and available literature (Hagiwara et al., 1975; Pacewska and Keshr, 2002), which showed the amorphous nature of the decomposition products of  $\text{ZrO}(\text{NO}_3)_2$  and  $\text{Al}(\text{NO}_3)_3 \cdot 9\text{H}_2\text{O}$  after calcination at this temperature. TGA analysis of products APZN1-SSC-500, APZN1-SSC-600 and APZN1-SSC-700, with particle sizes >2 mm, showed weight losses of 45 wt%, 42 wt% and 40 wt% respectively at 800 °C. The weight loss profiles all demonstrated three weight loss events: a small weight loss at 100 °C, associated with dehydration of PMA (Tatibouet et al., 1997); an event between 200-500 °C, typical of partial dehydration and denitration of  $\text{Al}(\text{NO}_3)_3 \cdot 9\text{H}_2\text{O}$  (Pacewska and Keshr, 2002); and a third weight loss above 900 °C, attributable to the volatilisation of  $\text{MoO}_3$  (Smolik et al., 2000). TGA results are consistent with the presence of PMA being observed in the diffraction patterns of APZN1-SSC-500 and APZN1-SSC-600, with a significant portion of the volatile inventory, attributable to the decomposition products of  $\text{ZrO}(\text{NO}_3)_2$  and  $\text{Al}(\text{NO}_3)_3 \cdot 9\text{H}_2\text{O}$ , remaining in the products with a particle size >2 mm. These data suggest that a portion of the calcine with a particle size >2 mm experiences temperatures well below 400 °C, shown by the large weight loss of the calcine. However, in products APZN1-SSC-600 and APZN1-SSC-700, the XRD pattern showed weak reflections attributable to  $\text{ZrO}_2$ ,  $\text{MoO}_3$  and  $\text{Zr}(\text{MoO}_4)_2$ , showing the outer surface of the calcine experienced temperatures of at least 400 °C, possibly up to 500 °C. This was to be expected, as only the outer surface of the calcine particles will come into contact with the heated calciner tube walls, which would result in the core of the calcine particles (especially the larger particles) experiencing a much lower temperature than the surface.



From these experiments, it is possible to infer and conclude the following:

- With Zone 3 temperature set at 500 °C, the small calcine particles (<0.5 mm) experience temperatures of approximately 400 °C in the small scale calciner. The bulk of the material within the larger particles (>2 mm) appeared to experience temperatures much lower than 400 °C, due to the fact that only the surface of the particle comes into contact with the heated calciner walls.
- At a Zone 3 temperature of 600 °C, the calcine fraction <0.5 mm experiences a temperature of between 450-500 °C, shown by the absence of PMA in the diffraction pattern but the low intensity of reflections attributed to other components. Larger particles showed weak reflections associated with ZrO<sub>2</sub>, MoO<sub>3</sub> and Zr(MoO<sub>4</sub>)<sub>2</sub>, indicating the surface of the particles experience temperatures in the region of 450 °C, though the core will experience much lower temperatures, shown by the high portion of the volatile inventory remaining in the product.
- At a Zone 3 temperature of 700 °C, the smaller particles appear to experience temperatures above 500 °C. The larger particles also showed signs of being partially subjected to temperatures in the region of 500 °C, suggesting the surface of the calcine fraction >2 mm experiences similar temperatures to the smaller particles, but the core appears to remain relatively cold, holding on to a significant portion of the hydrate and nitrate inventory.

#### **7.3.2.2 Dust Analysis**

There was an increase in the mass of dust collected in the off-gas system as the calcination temperature was increased whilst processing APZN1 through the small scale calciner. The mass values were normalised by conversion to a percentage of the actual yield so they could be compared. This gave a range of dust carry-over values of 5.95 wt%, 7.32 wt% and 10.33 wt% after calcination at 500, 600 and 700 °C respectively (Figure 7.6). This showed an increase in dust carry-over as a function of increasing temperature. This was in correlation with an increase in the calcine fraction with a particle size <0.5 mm, suggesting dust is formed, at least partially, from this size fraction. As with the calcine, a 5 % error was associated with the collection of dust from the small scale calciner to take into account the fact that not all of the dust would be recovered in these experiments.

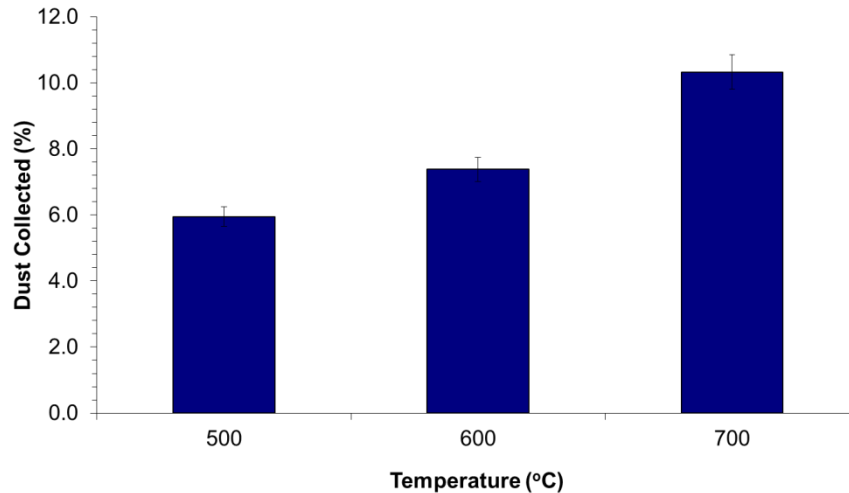


**Figure 7.6 – Dust collected as a percentage of the expected yield from products APZN1 calcined between 500-700 °C at a feed rate of 3 l / h**

XRD analysis of the dust sample produced from APZN1 calcined at 500 °C (Figure 7.7), at a feed rate of 3 l / h, showed reflections attributable to PMA, with strong diffuse scattering showing the presence of non-crystalline component(s). This is consistent with the decomposition products of  $\text{Al}(\text{NO}_3)_3 \cdot 9\text{H}_2\text{O}$  and  $\text{ZrO}(\text{NO}_3)_2$  being amorphous (Hagiwara et al., 1975; Pacewska and Keshr, 2002). After calcination at 600 and 700 °C, reflections attributable to PMA remained, with reflections associated with  $\text{ZrO}_2$ ,  $\text{MoO}_3$  and  $\text{Zr}(\text{MoO}_4)_2$  becoming more intense at higher calcination temperature. TGA analysis of the dust samples created from products APZN1-SSC-500, APZN1-SSC-600 and APZN1-SSC-700 showed weight losses of 28 wt%, 27 wt% and 22 wt% respectively at 800 °C. These values were lower than those observed in the calcine particles with a diameter >2 mm but higher than seen in the smaller particles (<0.5 mm). The weight loss profiles all demonstrated three weight loss events: a small weight loss at 100 °C, associated with dehydration of PMA (Tatibouet et al, 1997); an event between 200-500 °C, typical of partial dehydration and denitration of  $\text{Al}(\text{NO}_3)_3 \cdot 9\text{H}_2\text{O}$  (Pacewska and Keshr, 2002); and a third weight loss above 900 °C, attributable to the volatilisation of  $\text{MoO}_3$  (Smolik et al., 2000). These data suggest that the composition of the dust produced from the calcination of product APZN1 between 500-700 °C was made up from component material from both small and large calcine particles. The XRD pattern for product APZN1-SSC-600 showed both PMA and the other components which make up the smaller particles ( $\text{ZrO}_2$ ,  $\text{MoO}_3$  and  $\text{Zr}(\text{MoO}_4)_2$ ) and the TGA values are between the values observed for the particles >2 mm and <0.5 mm, which imply the dust as formed from a combination of these fractions. This is consistent with the mechanism for dust formation postulated in chapter 6 for full HAL simulants, in which firstly the larger particles (>2 mm in diameter) are broken down followed by further breakdown to smaller calciner particles, of which the smallest (less than 0.1 mm in diameter) are carried over to the off-gas system.

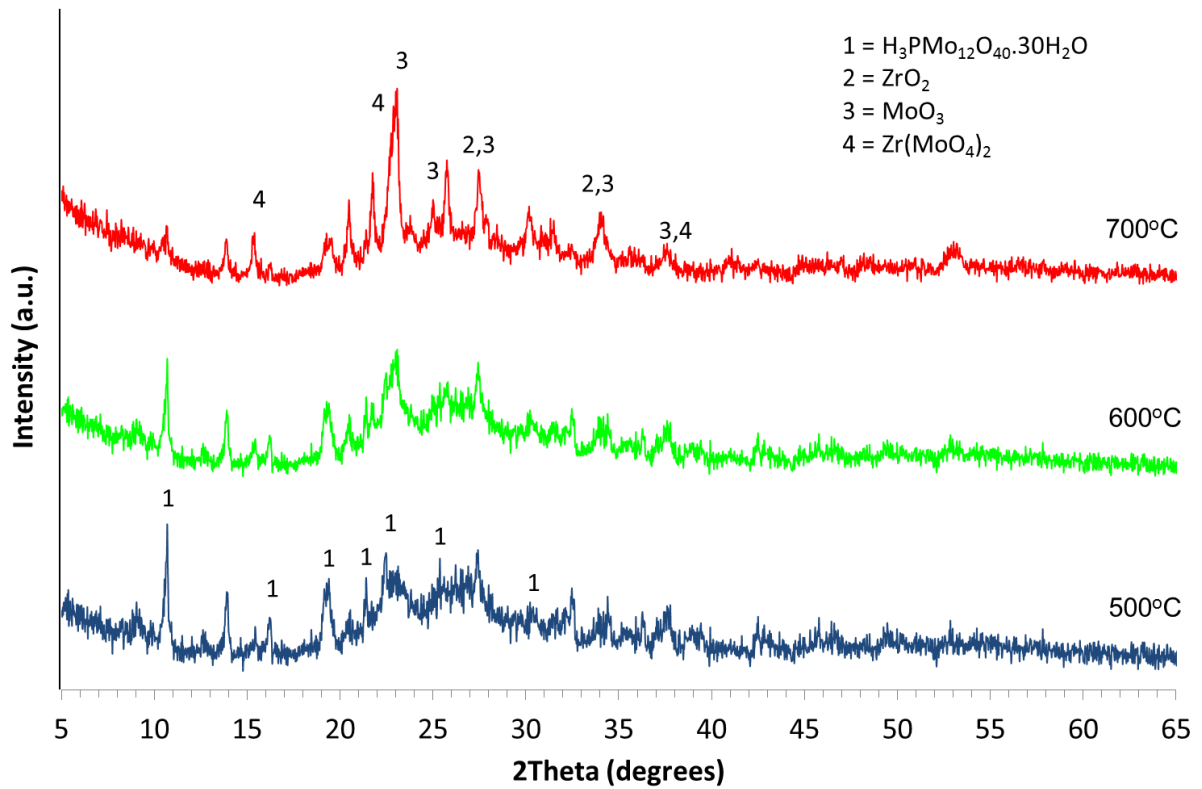


Figure 7.7 – XRD analysis of products APZN1-SSC-500, APZN1-SSC-600 and APZN1-SSC-700 dust samples

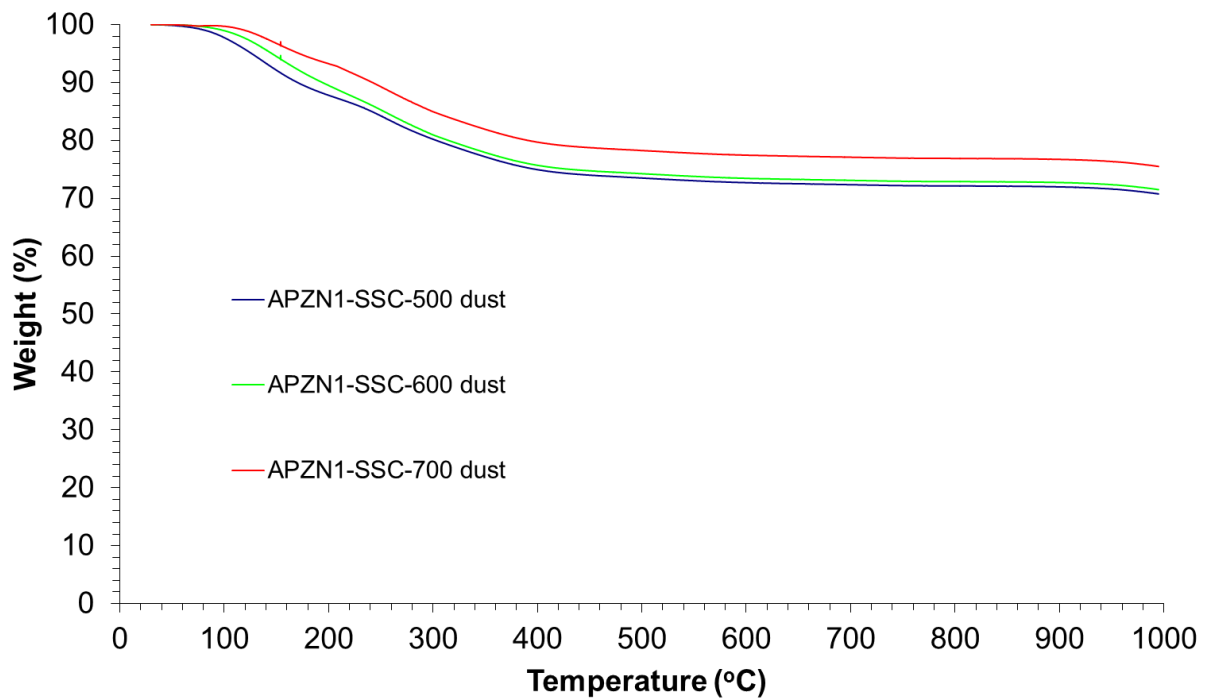
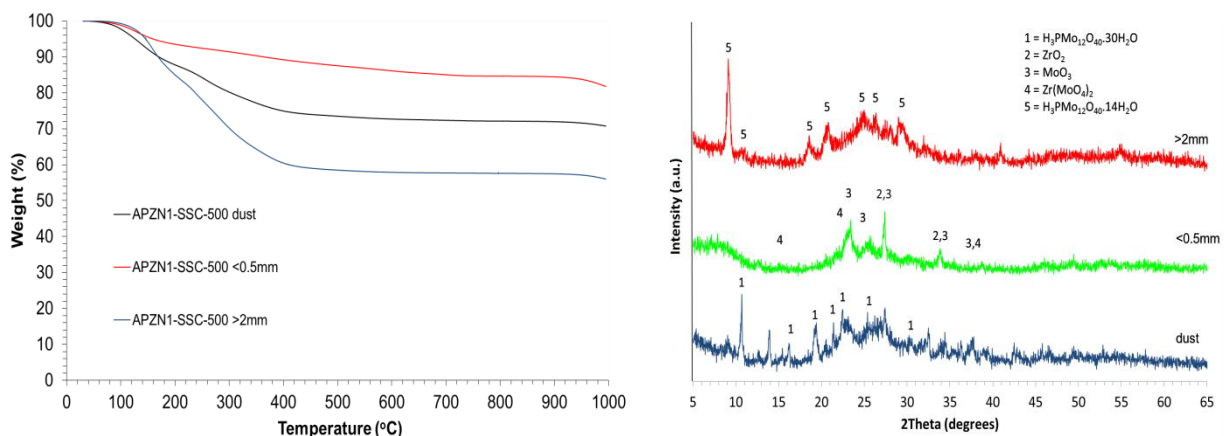


Figure 7.8 – TGA analysis of products APZN1-SSC-500, APZN1-SSC-600 and APZN1-SSC-700 dust samples

Figure 7.9 shows the TGA and XRD results for product APZN1-SSC-600 for the calcine fractions <0.5 mm and >2 mm, comparing them to the dust sample. The XRD pattern for the dust sample showed reflections attributable to PMA, ZrO<sub>2</sub>, MoO<sub>3</sub> and Zr(MoO<sub>4</sub>)<sub>2</sub>, whereas the calcine sample with a particle size >2 mm only showed reflections attributable to PMA and the fraction <0.5 mm showed reflections associated with ZrO<sub>2</sub>, MoO<sub>3</sub> and Zr(MoO<sub>4</sub>)<sub>2</sub>, with no PMA being observed. This suggested the dust comprised a mix of these calcine fractions being carried over to the off-gas system. It should be noted, that a different form of PMA was observed in the calcine than was found in the dust. The PMA in the dust sample appeared to contain 30 water molecules compared to the 14 in the calcine sample, shown by the differences in the diffraction patterns. The fact that the PMA in the dust is more hydrated than in the calcine can be explained by the fact that steam is constantly passed over the dust sample as it is being collected, allowing adsorption to take place. The TGA results (Figure 7.9) also supported the hypothesis that the mechanism for dust formation comes from both the larger and smaller particles, with the total weight loss of the dust sample being approximately half way between the two calcine fractions, despite the PMA containing more water. The weight loss profile of the dust showed a more rapid weight loss below 200 °C, associated with the dehydration of the PMA, consistent with the XRD findings. These data suggest that dust is formed initially from the abrasive breakdown of larger particles (>2 mm) followed by further breakdown to form smaller particles, which have experienced higher temperatures and therefore undergone further reaction, the smallest of which are transported to the off-gas system. This is in agreement with the mechanism postulated in Chapter 6 for full HAL simulants.



**Figure 7.9 - XRD and TGA analysis of product APZN1-SSC-600 dust sample and calcine with particle sizes <0.5 mm and >2 mm**

From these experiments, it is possible to infer and conclude the following:

- An increase in dust carry-over to the off-gas system was observed at increasing temperature, in correlation with an increase in the formation of smaller particles (<0.5 mm) in the calcine.
- XRD and TGA analysis showed the presence of PMA, ZrO<sub>2</sub>, MoO<sub>3</sub> and Zr(MoO<sub>4</sub>)<sub>2</sub> in the dust samples taken for product APZN1 calcined at 500, 600 and 700 °C. PMA is not present in the small particles after calcination through the small scale calciner with a Zone 3 temperature of 600 and 700 °C, thus implying that dust is partially formed from the abrasive breakdown of larger calcine particles. However, the fact that the increasing dust correlates with an increase in smaller particles and the XRD pattern showing higher levels of ZrO<sub>2</sub>, MoO<sub>3</sub> and Zr(MoO<sub>4</sub>)<sub>2</sub> in the dust than in the larger particles suggest the smaller, further reacted particles also play a role in the formation of dust carried over to the off-gas system.
- The mechanism for dust formation is in agreement with that postulated for dust generation for the full HAL simulants (Chapter 6).

### 7.3.3 Discussion

When short simulant APZN1 was freeze dried, followed by calcination at 400, 450 and 500 °C for 10 minutes, the reaction between PMA and ZrO(NO<sub>3</sub>)<sub>2</sub> yielded different products at these various temperatures. Using these results, knowing that the approximate residence time in the small scale calciner is 10 minutes (Brace, 2005a), the temperatures experienced in the calciner at different Zone 3 set-points were determined (Table 7.4). This showed that as the temperature was increased, the higher the temperature experienced by the calcine became for particles of all sizes. However, in the calcine fraction >2 mm, the core of the particle appeared to experience temperatures much lower than the calciner set-points, shown by the high total weight loss values in the TGA analysis, due to the fact that only the surface of the particle would have come into contact with the heated calciner wall. Due to this fact, the surface of all of the particles appear to experience similar temperatures, though the random nature of the path of the calcine particles through the heated tube will mean each individual particle spends varying amounts of time in contact with the heated calciner walls.

**Table 7.4 – Temperatures experienced in the small scale calciner**

Particle Size	Zone 3 Temperatures (°C)		
	500	600	700
<0.5 mm	~400	450-500	>500
>2 mm (surface)	~400	450-500	>500
>2 mm (core)	<400	<400	<400

The mechanism by which the dust was formed during the calcination of short simulat APZN1 in the small scale calciner appeared to be the same as for the full HAL simulants processed in Chapter 6. This was shown by the fact that reflections associated with PMA,  $ZrO_2$ ,  $MoO_3$  and  $Zr(MoO_4)_2$  were all present in the XRD patterns for the dust samples whereas the calcine sample with a particle size  $>2$  mm only showed reflections attributable to PMA and the fraction  $<0.5$  mm showed reflections associated with  $ZrO_2$ ,  $MoO_3$  and  $Zr(MoO_4)_2$ , with no PMA being observed. The TGA results (Figure 7.9) also supported the hypothesis that the mechanism for dust formation comes from both the larger and smaller particles, with the total weight loss of the dust sample being in the middle of the calcine fractions  $>2$  mm and  $<0.5$  mm. The evidence therefore suggested that dust was formed initially from the abrasive breakdown of larger particles ( $>2$  mm) followed by further breakdown to form smaller particles, which are transported to the off-gas system. This supported the mechanism postulated in Chapter 6 for the generation and transportation of dust to the off-gas system in the small scale calcination process.

The determination of the temperatures experienced in the calcination process is important to allow a conceptual model to be proposed of the processes which occur in the calciner. As the extent of reactions in the calcination process is highly dependent on temperature, controlling the temperature experienced by the calcine is an important parameter of the vitrification process. As the small scale calciner is different to the full scale VTR, there are limitations to this work. However, future experiments on the VTR (outlined in section 7.5.3) could provide a comparison between these two processes, possibly allowing SSC experiments to be run in the place of VTR experiments, resulting in a large cost saving.

## 7.4 CONCLUSIONS

### 7.4.1 Temperature experienced in the calcination process

- When running the small scale calciner with Zone 1 and 2 temperatures of  $400\text{ }^{\circ}\text{C}$  and a Zone 3 temperature of  $500\text{ }^{\circ}\text{C}$ , at a feed rate of  $3\text{ l/h}$ , the temperature experienced by the calcine fraction  $<0.5$  mm was approximately  $400\text{ }^{\circ}\text{C}$ .
- When the Zone 3 temperature was increased to  $600\text{ }^{\circ}\text{C}$ , the temperature experienced by the calcine rose to between  $450\text{-}500\text{ }^{\circ}\text{C}$ .
- At a Zone 3 temperature of  $700\text{ }^{\circ}\text{C}$ , the calcine experienced a temperature above  $500\text{ }^{\circ}\text{C}$ .
- The larger calcine fraction ( $>2$  mm) appeared to experience temperatures similar to the smaller particles at the surface but much lower than  $400\text{ }^{\circ}\text{C}$  in the core of the particle at all Zone 3 temperatures between  $500\text{ - }700\text{ }^{\circ}\text{C}$ .

## **7.4.2 Dust generation in the small scale calciner**

- The formation of dust increased as a function of increasing temperature, which correlated with an increase in the formation of small calcine particles.
- The mechanism by which dust was generated was firstly by abrasive breakdown of the larger particles, followed by further breakdown and reaction to form smaller particles, the smallest of which were carried to the off-gas system. This was in agreement with the mechanism postulated in Chapter 6.

## **7.5 FUTURE WORK**

### **7.5.1 Further freeze dryer experiments**

In order to more accurately determine the temperature experienced by the calcine in the small scale calciner (and ultimately the VTR), the freeze dried product APZN1 could be calcined in steps of 10 °C (410, 420, 430 °C etc) to narrow the temperature range in which the small scale calciner products are being compared to. This would allow the temperatures at which  $ZrO_2$ ,  $MoO_3$  and  $Zr(MoO_4)_2$  crystallise to be more accurately observed by XRD analysis.

### **7.5.2 Further small scale calciner experiments**

As this work was an initial investigation, only the effects of Zone 3 set-points on the effect of the temperature experienced took place. Further experiments could therefore be carried out varying the feed rate, tube angle (residence time) and simulant composition, to determine whether these factors have any effect on the temperature experienced by the calcine. It is possible that differing simulant composition will affect the temperature experienced in the core of the larger particles, either by being easier to break down to smaller particles or allowing better thermal conductivity through the calcined product.

### **7.5.3 VTR experimental proposal**

To allow the temperatures experienced by the calcine on the VTR to be monitored, the APZN1 short simulant could be processed at a range of Zone 3 and 4 temperatures on the full scale facility and compared to results obtained from freeze drying and small scale calciner experiments.

The primary aims of this short simulant trial would be to:

- Monitor the effects of Zone 3 and 4 set-points on the temperature experienced by the calcine in the calcination process.
- Allow better understanding of the effects of temperature to be carried forward for future VTR and WVP campaigns.

Completion of this experiment would allow a better understanding of the temperature experienced by the calcine in the tube at a range of calciner set-points. It could also help with setting up zone 3 and 4 set-points in future VTR and WVP campaigns to allow better control of the reactions occurring in the calcination process. Lab scale trials have shown that both the residence time and temperature of the calciner will have an effect on the reactions which occur, greatly changing the chemical structure of the calcine product. As monitoring the temperature within the calciner tube on the VTR calciner is very difficult, running the short simulant on the VTR will give valuable insight into the temperatures which are experienced by the calcine in the full scale process. This will be done by analysing the calcine produced and comparing the results with those obtained in the lab scale trials. By comparing VTR, small scale calciner and bench top prepared calcines, a link could be made to the differences in the samples due to scale-up issues.

The short simulant APZN1 has been chosen due to the change in chemical composition which takes place after calcination over a range of different temperatures. These changes can be seen in the XRD analysis (Figure 7.10) with the diffraction patterns changing as a function of temperature. This would allow the approximate temperature experienced by the calcine in the calciner to be measured.

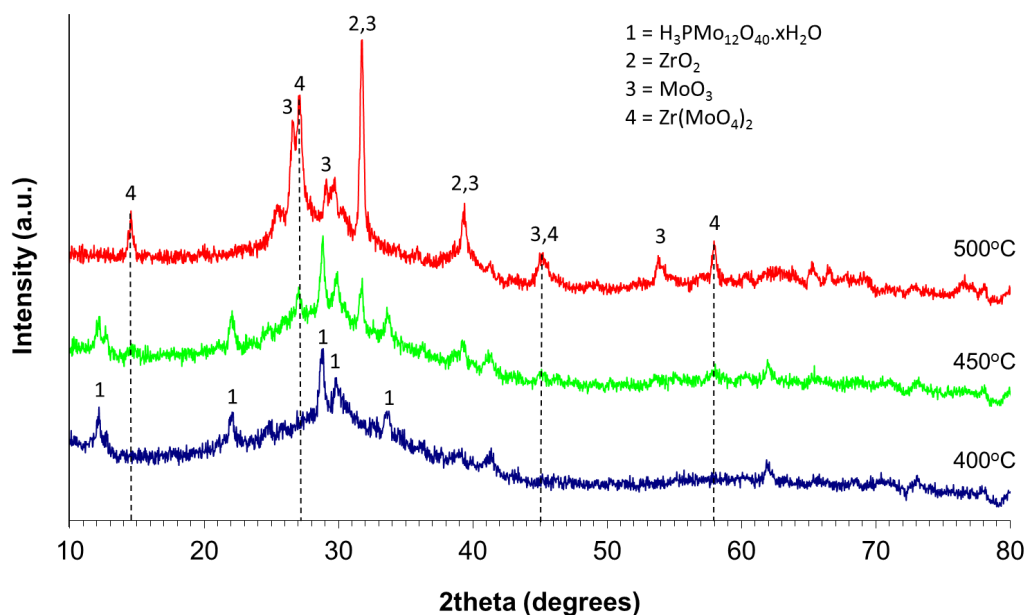


Figure 7.10 – XRD analysis of APZN1 at a range of temperatures



A range of Zone 3 and 4 temperatures have been chosen, at the high and low end of the workable range of calciner settings, to monitor the effects of temperature on the reactions which occur in the calciner. At the start of the experiment, zones 3 and 4 will be set to 550 °C as this is as low a temperature as the calciner is likely to be run at on WVP without the risk of causing blockages in the calciner. Once the calciner has settled, the short stimulant LAMN1 (Table 1) will be fed at 40 litres per hour to give a waste oxide throughput of 3600 g per hour. This will be run for 1.5 hours (1 hour for the calciner to reach equilibrium and 0.5 hours to take a sample) before the calciner is switched to water feed and the Zone 3 and 4 setpoints turned up to 600 °C. The cycle will then be repeated at Zone 3 and 4 setpoints of 650 °C, 700 °C and 750 °C. To run this experiment on the VTR it will take approx 15 hours, 1.5 hours of HAL feed for each of the 5 different Zone 3 and 4 setpoints and 1.5 hours for the calciner to settle in water feed at each of the temperatures. Feeding at 40 litres per hour for 7.5 hours of HAL feed will require 300 litres of simulant. An extra 80 litres is also required to allow the feed to be taken from the feed tank, giving a minimum simulant requirement of 380 litres to run this experiment.

**Table 7.5 – Composition of short simulant APZN1 (400 litres)**

<b>Chemical</b>	<b>Concentration (g / l)</b>	<b>Total Required (kg)</b>
Phosphomolybdic Acid	80.40	32.16
Aluminium Nitrate Nonahydrate	92.20	36.88
Zirconyl Nitrate	11.77	4.707

To make up this simulant the following solutions should be ordered from Johnson Matthey:

- 68.875 litres of PMA (466.9342 g / l) solution in nitric acid<sup>24</sup>.
- 331.125 litres of aluminium nitrate (111.3779 g / l) and zirconyl nitrate (14.2152 g / l) combined solution in nitric acid.
- When the solutions are combined they should be at an acidity of 1.8 M.

<sup>24</sup> This is the same PMA solution concentration as is currently ordered from Johnson Matthey for WRW16 HAL simulant for use on the VTR.

# 8. Project Impact

## 8.1 INTRODUCTION

This chapter brings together all of the research detailed in this thesis and discusses the industrial relevance of the findings, a key differentiator between EngD and PhD projects. The initial scope of this project was aimed at reducing the amount of blockages which would occur on WVP. Reducing the amount of downtime on WVP would assist Sellafield Ltd in meeting the targets of lowering the HLLW stocks set by the NII (Bradshaw et al., 2007). The approach taken throughout this thesis was to attempt to understand the chemical processes which take place in the calciner, resulting in the formation of dust from which these blockages arise. Accordingly, two areas are discussed: the effects this work could have on future running of the VTR and WVP; and the benefits to NNL and Sellafield Ltd of the small scale calciner rebuild.

## 8.2 PROJECT SUMMARY AND BENEFITS TO WVP

### 8.2.1 Simulant composition

The work carried out in Chapter 6 showed that the major crystalline components present in Blend HAL simulant solution, without heat treatment, were  $\text{Mg}_3\text{RE}_2(\text{NO}_3)_{12}\cdot 24\text{H}_2\text{O}$ ,  $\text{Al}(\text{NO}_3)_3\cdot 9\text{H}_2\text{O}$  and CPM. The same components were identified in Magnox HAL simulant with the addition of  $\text{Mg}(\text{NO}_3)_2\cdot 6\text{H}_2\text{O}$  due to the high concentration of Mg present in the simulant. This accounts for most of the elements present in high concentrations, except for Zr, which must have been present in a non-crystalline form, consistent with freeze-drying work carried out in Chapter 5.

On addition of  $\text{LiNO}_3$  to Blend HAL simulant an additional reflection was present in the diffraction pattern and there was a notable absence of reflections attributable to  $\text{LiNO}_3$ , suggesting a reaction had occurred in solution. However, this was unidentifiable due to the complexity of the XRD pattern. In Magnox HAL simulants, the addition of  $\text{LiNO}_3$  showed no change to the diffraction pattern, suggesting it had reacted (due to the fact that no reflections associated with  $\text{LiNO}_3$  were observed by XRD) but the product was either non-crystalline in nature or present in a quantity such that it was obscured by the more intense reflections in the XRD pattern. This was backed up by work carried out in Chapter 5, which showed  $\text{LiNO}_3$  had reacted with PMA and  $\text{ZrO}(\text{NO}_3)_2$  in solution.

The reactivity of  $\text{LiNO}_3$  in solution was previously unknown as analysis of freeze dried material had not been carried out. This gives an idea of which species are present in both Blend and Magnox HAL simulants before calcination. This adds to the knowledge base surrounding the calcination process, allowing for more accurate models to be postulated by WVP in the future.

### 8.2.2 The effects of lithium nitrate addition

Historically, it had been noted that  $\text{LiNO}_3$  acts as a binding agent in the calciner, thus aiding the reduction of dust carry-over to the off-gas system (Magrabi, 1981). However, these studies suggested that  $\text{LiNO}_3$  both acts as a molten salt, facilitating oxidation reactions and (at least partially) reacts in solution and during the calcination process. This was shown to be the case in both sort simulants (Chapter 5) and in the full HAL simulants (Chapter 6).

The addition of  $\text{LiNO}_3$  had a significant effect on the amount of dust carried over during the processing of Magnox HAL simulant on the small scale calciner rig (Chapter 6). This showed a reduction in dust carry-over of from 3.50 wt% (without Li addition), down to 2.40 wt% on the addition of  $\text{LiNO}_3$ . This could be due to the fact that  $\text{LiNO}_3$  facilitates oxidation reactions, thus increasing the density of the calcine. As the movement of dust in a constant air-flow is known to depend on both particle size and density (Dong et al., 2003), this increase in density would be expected to cause a reduction in dust carry-over. It is likely that this is combined with the fact that  $\text{LiNO}_3$  has a melting point of 255 °C and therefore is molten in the calcination process, helping binding the calcine together (Magrabi, 1981), thus reducing dust carry-over to the off-gas system.

Work carried out in Chapter 5 showed that the addition of  $\text{LiNO}_3$  stopped the formation of  $\text{Zr}(\text{MoO}_4)_2$  in the calcination process, preferably forming  $\text{Li}_2\text{Zr}(\text{MoO}_4)_3$  in the short simulant LPZN1. A separate study, carried out in parallel by Taylor et al. (2014), showed the the addition of  $\text{LiNO}_3$  to ZMH resulted in the formation of  $\text{Li}_2\text{MoO}_4$  and  $\text{ZrO}_2$ , again showing that the formation of  $\text{Zr}(\text{MoO}_4)_2$  (or its hydrated form, ZMH) would not occur in the presence of  $\text{LiNO}_3$ . This is evidence that ZMH, the major cause of blockages in the off-gas system, is formed in the dust scrubber and is not directly carried over from the calciner.

These observations show that the addition of  $\text{LiNO}_3$  has a significant impact on dust carry-over, in agreement with previous studies (Magrabi, 1981; Brace, 2005b; Vickers, 2006a). However, there is a better understanding of the different ways in which  $\text{LiNO}_3$  aids the reduction of dust generation in the calciner. This will again aid in the postulation of an overall model of the processes and the variety of species which are formed during calcination.

### 8.2.3 Temperatures experienced in the calciner

The determination of temperatures experienced in the calcination process was carried out on the small scale calciner using short simulant APZN1, shown in Chapter 7. This work showed that the temperature experienced is highly dependant on particle size as only the surface comes into contact with the heated calciner tube wall (Table 8.1).

**Table 8.1 – Temperatures experienced in the small scale calciner**

Particle Size	Zone 3 Temperatures (°C)		
	500	600	700
<0.5 mm	~400	450-500	>500
>2 mm (surface)	~400	450-500	>500
>2 mm (core)	<400	<400	<400

The small calcine particles (<0.5 mm in diameter) effectively appeared to experience a uniform temperature throughout the calcine particle due to their small size, with this temperature being dependant on the Zone 3 set-point (Table 8.1). The larger calcine particles (>2 mm in diameter), however, appeared to experience much lower temperatures within the core of each particle (Table 9.1), caused by the fact that only the surface of the particle contacts the calciner tube.

As this work was carried out on the small scale calciner, scale-up issues must be taken into account when applying this to WVP. Therefore, it is suggested that a similar series of experiments should be carried out on the VTR, as outlined in section 7.5.3. Using this information, a more accurate model of the processes which occur during calcination could be proposed. This had not been possible in previous studies as there is no current method of measuring temperatures within the calciner tube on both the small scale calciner, VTR or WVP, and no studies of this type had been considered.

#### **8.2.4 Conceptual model of dust generation**

From the work carried out in Chapter 6, a conceptual model for the processes which occur in the calciner tube was proposed (section 6.3.3.3). This postulated that there are four main processes which occur during calcination:

- Evaporation of the HAL simulant, resulting in a stage where molten nitrate hydrates are formed.
- Molten nitrates are agglomerated to form large calcine particles.
- The large particles undergo initial breakdown to form the majority of the dust which is transported to the off-gas system.
- As the large particles get smaller and increase in density due to further denitration, they breakdown further to form the smaller calcine fractions, the smallest of which will be carried to the off-gas system as dust.

Each of these processes does not occur in its own distinct section of the calciner tube as each particle experiences different amounts of time in contact with the calciner tube wall and differing interaction with the rabble bar which breaks up the calcine. The calcination conditions, such as temperature, feed rate and chemical composition of the simulant used, will also affect where these processes occur within the calciner tube.

Historically, the generation of dust was thought to arise from the carry-over of the smallest particles of calcine to the off-gas system. However, these studies have shown that the abrasive breakdown of large calcine particles (>2 mm in diameter) appears to be responsible for the production of the majority of the dust formed during calcination. Higher dust formation appeared to correlate with the formation of a greater fraction of calcine particles with a diameter >2 mm in Magnox HAL simulant when processed at feed rates of 3 l / h or higher.

A competing process to the abrasive breakdown of the larger calcine particles was also apparent and was prominent at a low feed rate of 2 l / h. This resulted in an increased fraction of smaller particles being produced due to the increased residence time at high temperature, with the evaporative front moving up the tube as there was less water to evaporate. The increased fraction of smaller particles correlated with a higher dust carry-over in these cases, showing a portion of the smaller particles were carried to the off-gas system. This was also observed in simulants containing high levels of Mo and Zr, suggesting these components are more easily broken down by the rabble bar and thus more small particles are generated, resulting in a higher contribution to the overall dust carry-over value.

As dust can not be collected on the full scale facilities, it would not be possible to determine the effects of each of these dust generation process on WVP. However, the particle size of the calcine can be monitored on the VTR, which may give an indication of the effects of calcination conditions on the major method of dust generation. These processes are thought to be competing and will therefore both contribute to the formation of dust in the calcination process.

With Sellafield Ltd becoming more interested in POCO waste-streams, high in Zr and Mo, the findings from Chapter 6 suggest that these will result in a higher dust carry-over, increasing the risk of blockages occurring, and a calcine with a higher fraction of small particles. To minimise dust carry-over, the following operating conditions should be employed:

- Low Zone 3 and 4 temperatures
- High feed rate
- Addition of  $\text{LiNO}_3$
- Minimise the levels of Zr and Mo in the feed-stock

VTR trials should be carried out to determine the correct balance between dust carry-over and the generation of a suitable calcine which would not cause blockages in the calciner tube.

## 8.3 BENEFITS OF THE SMALL SCALE CALCINER RIG REBUILD TO SELLAFIELD LTD

The National Nuclear Laboratory maintains the capacity to create calcine on both lab scale and full scale facilities, using the small scale calciner and VTR respectively. The small scale calciner is a vital tool in assessing the calcination characteristics of new simulant formulations. The main benefits of running a preliminary experimental campaign using the small scale calciner, as opposed to the VTR include:

- The small scale calciner is much cheaper to run than the VTR as:
  - Only 5-10 litres of simulant are required for a small scale calciner experiment as opposed to the 300 litres for the shortest of VTR experiments.
  - Only one operator is required to run the small scale calciner compared to the minimum shift team of four required to run the VTR.
  - From cold, the small scale calciner tube takes approximately an hour to reach temperature and stabilise at a constant tube expansion compared to four hours on the VTR.
- An operational envelope for the VTR can be pre-determined, reducing the amount of experiments required at full-scale.
- The small scale calciner is more versatile than the VTR, allowing quicker changes to tube angle, flowrates etc to be utilised, changing the residence time.
- Much lower consequences using the small scale calciner when trying out the extremes of simulant processing
  - Blocking calciner tube on VTR might take three days to clear costing large amounts in shift time, whereas small scale calciner can be cleared in a day by one operator.
  - Spare parts are much cheaper to replace on the small scale calciner.
  - NO<sub>x</sub> releases are contained in the designated fumehood on the small scale calciner, but VTR releases go out into the open rig hall.
- Dust can be collected and analysed using the small scale calciner rig, where as the first analysis point in the VTR off-gas system is the DSL.

By running a small scale calciner campaign, therefore, new experimental simulants can be calcined under different conditions with minimal risk. Determination of the operational envelope for the VTR reduces the amount of experiments which are required, again minimising risk and results in a large cost saving for Sellafield Ltd, as the lab scale facility is much cheaper to run than the VTR.

### 8.3.1 Future plans for the small scale calciner rig

As a direct consequence of the issues with the small scale calciner during this project, there was a review into maintaining and developing the rig. The major findings from this review were (Wilson, 2013):

- To design and install a simplified off-gas system.
- To improve the seals on the upper and lower end fittings of the calciner tube.
- To establish a maintenance regime for the small scale calciner.
- To create a critical spares inventory to avoid significant periods of down-time.
- To design and install a method of monitoring calciner tube temperature.
- To design and implement a method of particle size reduction of the calcine produced on the small scale calciner rig.

The most common causes of delay during this project stemmed from failures within the off-gas system, with the primary issue being with the off-gas fan. Due to high in-leakage within the calciner, the off-gas fan had to be run at high speed in order to maintain the required depression throughout the system. This resulted in the entrainment of condensate through the off-gas system, coming to rest in the off-gas fan casing. This caused corrosion to occur within fan casing, resulting in the fan seizing on a regular basis. This issue was improved (but not resolved) by replacing the seals in the upper and lower end fittings on the calciner, reducing the in-leakage and therefore lowering the fan speed required to maintain depression. It was decided, however, that a new, simplified off-gas system would result in fewer issues being encountered. This, combined with the implementation of a maintenance regime and a critical spares inventory, will lead to an improvement in the reliability of the rig for future experimental programmes.

The main aim of conducting experiments on the small scale calciner and the VTR are to allow modelling of the processes which occur during vitrification. Therefore, the collection of as much information as possible is beneficial. As a consequence, there is a push to allow the tube temperature to be measured during an experiment on the small scale calciner, as is possible on the VTR. Also, the calcine produced on the small scale calciner has some large agglomerates exiting the tube which are not seen on the VTR, due to the fact the VTR has a set of 4 mm slots which the calcine must pass through before being collected. Previous attempts to achieve these objectives were unsuccessful, but new ideas are due to be tested in the future. The proposed future uses of the small scale calciner rig include:

- Carrying out preliminary testing of new simulants to determine an operating envelope for future VTR trials.
- Producing calcine for use in a lab scale melter.

As the HALES facility enters its post operational clean out (POCO) phase, there is a greater demand for research investigating simulants which more closely represent these waste streams. It will therefore be beneficial to run these previously untested simulants through the small scale calciner to assess their behaviour and develop an operational envelope before being run on the VTR. This will result in significant cost savings compared to running all experiments on the VTR.

The current methods for producing glass samples are either in a crucible, which is filled with glass frit and calcine and placed in a muffle furnace, or on the full-scale VTR. However, there are plans to develop a new method using a lab scale melter. In order to produce the required amount and variety of calcine samples, the small scale calciner rig will be utilised. Therefore, the calciner rig must run efficiently to ensure there is sufficient feedstock to supply the melter. The proposed improvements to the small scale calciner are therefore essential to the future plans for the rig, which has been brought about by the issues encountered during this project.

In summary, by modifying and rebuilding the small scale calciner rig, the NNL maintain the capacity to produce calcine on a lab scale through a process which replicates, though is not identical to, full scale calcination. The addition of the smooth bore flexible hose and the dirt trap loop allow dust samples to be collected and analysed, which was not possible previously and is not possible on the VTR or WVP. This tool allows Sellafield Ltd to propose lab scale experiments on new simulant types and experiment with new operating conditions with a much lower risk and at much lower cost. This has allowed a future plan to be drawn up for the calciner rig, whereas before this project it had sat idle for a number of years. This will lead to a large cost saving for Sellafield Ltd, as the small scale calciner rig costs approximately £400-600 per day to run compared to ~£20,000 per day on the VTR.



## 9. References

- Afanasiev, P., 2007, Molten Salt Synthesis of Barium Molybdate and Tungstate Microcrystals, *Materials Letters*, Vol. 61, pp. 4622-4626.
- Afanasiev, P. And Geantet, C., 1998, Synthesis of Solid Materials in Molten Nitrates, *Coordination Chemistry Reviews*, Vol. 178-180, pp. 1725-1752.
- Aligizaki, K. K., 2006, *Pore Structure of Cement-Based Materials: Testing, Interpretation and Requirements*, Taylor and Francis, Abingdon, Oxon.
- Amphlett, C. B., 1961, *Treatment and Disposal of Radioactive Wastes*, Pergamon Press, New York, USA.
- Balsamo, N., Mendieta, S., Oliva, M., Eimer, G. And Crivello, M., 2012, Synthesis and Characterisation of Mixed Metal Oxides from Layered Double Hydroxides, *Procedia Materials Science*, Vol. 1, pp. 506-513.
- Benbow, R., 1997, The Efficient Transport and Storage of Nuclear Waste, *Nuclear Engineering and Design*, Vol. 176, pp. 187-189.
- Berg, J., Monteith, J. E., 1998, Literature Survey of Ruthenium Volatilisation Applicable to HLW Plant Operations, HLWTC/98/154.
- Besserguenev, A. V., Fogg, A. M., Francis, R. J., Price, J. And O'Hare, D., 1997, Synthesis and Structure of the Gibbsite Intercalation Compounds  $[\text{LiAl}_2(\text{OH})_6]\text{X}$  {X = Cl, Br,  $\text{NO}_3$ } and  $[\text{LiAl}_2(\text{OH})_6]\text{Cl}\cdot\text{H}_2\text{O}$  Using Synchrotron X-ray and Neutron Powder Diffraction, *Chemistry of Materials*, Vol. 9, pp. 241-247.
- BERR (Department of Business, Enterprise and Regulatory Reform), 2008, Meeting the Energy Challenge: A White Paper on Nuclear Power. Available: [http://www.decc.gov.uk/en/content/cms/what\\_we\\_do/uk\\_supply/energy\\_mix/nuclear/white\\_paper\\_08/white\\_paper\\_08.aspx](http://www.decc.gov.uk/en/content/cms/what_we_do/uk_supply/energy_mix/nuclear/white_paper_08/white_paper_08.aspx) (Accessed: 27<sup>th</sup> September 2009).
- Bonnetier, A., 2007, Nuclear Waste Immobilisation by Vitrification in a Cold Crucible Melter: 3D magnetic model of a melter, *Scientific Basis for Nuclear Waste Management XXXI*, edited by Lee, W. E., Roberts, J. W., Hyatt, N. C. And Grimes, R.W., (Materials Research Society Symposium Proceedings 1107, Warrendale, PA, 2008), pp. 191-198

- Bowersox, P., 2012, Lise Meitner's fantastic explanation: Nuclear Fission. Available: <http://ansnuclearcafe.org/2012/02/14/lise-meitners-fantastic-explanation-nuclear-fission/> (Accessed: 15<sup>th</sup> July 2012).
- Brace, J., 2003, Calcination Programme in Support of WVP, RAT 4282, BNFL.
- Brace, J., 2004, Residence Time Trials using the Small Scale Calciner Rig, NSTS 5498.
- Brace, J., 2005a, Calcine Solubility Trials in Support of the WVP Dust Scrubber Operating Envelope, Nexia Solutions 6357.
- Brace, J., 2005b, The Effect of Lithium in a 75%/25% Oxide/Magnox Waste, Nexia Solutions 6433.
- Brace, J., 2005c, The Effect of HAL acidity, Waste Oxide Concentration and Sugar Concentration on the Calcine Properties, Nexia Solutions 6281.
- Brace, J., 2006a, VTR 2479 – The Effect of HAL Acidity and Waste Oxide Feed Rate and Concentration on the Sugar Requirement for Calcination, Nexia Solutions 7285.
- Brace, J., 2006b, VTR 2480 – An Investigation into the Effect of Calciner Temperatures and Sugar on the Calcination of a 75%/25% Oxide/Magnox HA Waste, Nexia Solutions 7286.
- Brace, J., 2006c, DSRV Solids Carryover, VTR Calculation 38, Nexia Solutions.
- Brace, J., 2006d, An Investigation into the Effect of Sugar on the Calcination of a 75%/25% Oxide/Magnox HA Waste, Nexia solutions 7130.
- Brace, J., 2006e, VTR 2477 – An Investigation into the Calciner Evaporative Load Limit (VTR Campaign 4A), Nexia Solutions 7110.
- Bradley, D., 2010, OP2136 – Calciner Normal Operations Presentation, Vitrification Assistance Training Package, British Nuclear Group.
- Bradley, D. F., Qualyle, M. J., Ross, E., Ward, T. R. And Watson, N., 2004, Promoting the Conversion of Caesium Phosphomolybdate to Zirconium Molybdate, Proceedings of the International Conference ATALANTE, P1-45.
- Bradshaw, K., Gribble, N. R., Hughes, D. O. And Riley, A. D., 2007, UK Full-scale Non-active Vitrification Development and Implementation of Research Findings onto the Waste Vitrification Plant, Waste Management Conference 2007, Tuscon, Arizona, USA.

British Nuclear Fuels Ltd (BNFL), 2007, Glass Making and Pouring – Presentation to the VTR Team Members.

Brown, P. G. M., Fletcher, J. M., Hardy, C. J., Kennedy, J., Scargill, D., Wain, A. G., Woodhead, J. L., 1961, The Significance of Certain Complexes of Ruthenium, Niobium, Zirconium and Uranium in Plant Processes.

Cains, P. W., 1980, Volatilisation of Ruthenium in Vitrification; Evaporation of Ruthenium Solutions in Nitric Acid, AERE-M3141.

Cascales, C., Mendez Blas, A., Rico, M., Volkov, V. And Zaldo, C., 2005, The Optical Spectroscopy of Lanthinides R<sup>3+</sup> in A<sub>2</sub>Bi(XO<sub>4</sub>)<sub>2</sub> (A = Li, Na; X = Mo, W) and LiYb(MoO<sub>4</sub>)<sub>2</sub> Multifunctional Single Crystals: Relationship with the Structural Local Disorder, Optical Materials, Vol. 27, pp. 1672-1680.

Chun, K. S., 1977, Studies on the Thermal Decomposition of Nitrates found in Highly Active Waste and of Chemicals used to Convert the Waste to Glass, UKAEA Harwell, Oxfordshire, AERE – R 8735.

Cullity, B. D. And Stock, S. R., 2001, Elements of X-ray Diffraction, 3<sup>rd</sup> Edition, Pearson Education Limited, Harlow, UK.

Dawson, M., 2010, OP2135 – Melter Normal Operations Presentation, Vitrification Assistance Training Package, British Nuclear Group.

DEFRA – Department for Environment, Food and Rural Affairs, 2001, Managing Radioactive Waste Safely – Proposals for Developing a Policy for Managing Solid Radioactive Waste in the UK, pp. 14-15.

DeVolpi, A., Minkov, V. E., Stanford, G. S. And Simonenko, V. A., 2005, Nuclear Shadowboxing: Legacies and Challenges, Kalamazoo, Michigan, USA.

Donald, I. W., Metcalfe, B. L. And Taylor, R. N. J., 1997, The Immobilization of High Level Radioactive Wastes using Ceramics and Glasses, Journal of Materials Science, Vol. 32, pp. 5851-5887.

Dong, Z., Liu, X., Wong, H. And Wong, X., 2003, Aeolian Sand Transport: A Wind Tunnel Model, Sedimentary Geology, Vol. 161, pp. 71-83.

Doucet, F. J., Goddard, D. T., Taylor, C. M., Denniss, I. S., Hutchison, S. M. And Bryan, N. D., 2002, The Formation of Hydrated Zirconium Molybdate in Simulated Spent Nuclear Fuel Reprocessing Solutions, Physical Chemistry Chemical Physics, Vol. 4, pp. 3491-3499.

- Duer, M. J., 2008, Solid State NMR Spectroscopy, Blackwell Science Ltd, Oxford, UK.
- Duer, M. J., 2004, Introduction to Solid-State NMR Spectroscopy, Blackwell Publishing Ltd, Malden, USA.
- Dunnett, B. F., McIntyre, L., May, S. And Hodge, N., 2009, Investigation into the Formation of Uranates during Calcination of HASTs 1 and 2 Liquor using XRD, NNL (09) 10489.
- Edmondson, M. J., Maxwell, L. J. And Ward, T. R., 2012, A Methodology for Post Operational Clean Out of a Highly Active Facility Including Solids Behaviour – 12386, WM2012 Conference, Phoenix, Arizona, USA.
- Edmondson, M. J., 2010, HALES PhD Year End Report – Morphological Studies of Zirconium Molybdate, NNL (10) 10860.
- Edmondson, M. J., 2009, HALES PhD Year End Report – Morphological Studies of Zirconium Molybdate, NNL (09) 10179.
- Egerton, R. F., 2005, Physical principles of electron microscopy: An Introduction to TEM, SEM and AEM, Springer Science and Business Media inc, New York, USA.
- Fazli, R., Fazli, M., Safaei-Naeini, Y. And Golestani-Fard, F., 2013, The Effects of Processing Parameters on Formation of Nano-Spinel ( $MgAl_2O_4$ ) From LiCl Moltensalt, Ceramics International, Vol. 39, pp. 6265-6270.
- Freundlich, A. And Hedley, D., 1988, The World Nuclear Handbook, Euromonitor Publications Limited, London, UK.
- Gabbott, P., 2007, Principles and Applications of Thermal Analysis, Blackwell Publishing, Oxford, UK.
- Goodhew, P. J., Humphreys, J. And Beanland, R., 2001, Electron Microscopy and Analysis, 3<sup>rd</sup> Edition, Taylor and Francis, New York, USA.
- Greenwood, N. N. And Earnshaw, A., 2002, Chemistry of the Elements, Second Edition, Butterworth-Heinemann, Oxford.
- Hagiwara, Z., Inoue, S. And Hideo, O., 1975, The Nature of the Thermal Decomposition Products of Zirconium Salts, Journal of Inorganic Nuclear Chemistry, Vol. 37, pp. 929-936.
- Harrison, M. T., Humphreys, S., Price, T., 2010, The Effect of Waste Incorporation on Vitrified HLW, NNL (10) 10840.

Hollebecque, J. F., 2008, POG – The Key Factors: VAP/Cascade Training, Commissariat à l'Énergie Atomique (CEA), Marcoule, France.

Hollebecque, J. F., 2008, The Dust Scrubber: VAP/Cascade Training, Commissariat à l'Énergie Atomique (CEA), Marcoule, France.

IAEA (International Atomic Energy Authority), 2006, Storage and Disposal of Spent Fuel and High Level Radioactive Waste. Available: [http://www.iaea.org/About/Policy/GC/GC50/GC50InfDocuments/English/gc50inf-3-att5\\_en.pdf](http://www.iaea.org/About/Policy/GC/GC50/GC50InfDocuments/English/gc50inf-3-att5_en.pdf) (Accessed: 29<sup>th</sup> September 2009).

Inoue, S., Oki, H. And Hagiwara, Z., 1975, The Nature of the Thermal Decomposition Products of Zirconium Salts, *Journal of Inorganic Nuclear Chemistry*, Vol. 37, pp 929-936.

Izumida, T. And Kawamura, F., 1990, Precipitates Formation Behaviour in Simulated High-Level Liquid Waste of Fuel Reprocessing, *Journal of Nuclear Science and Technology*, Volume 27, Issue 3, pp. 267-274.

Jervis, M., 1985, Operational Experience of the Denitration of Simulated Highly Active Wastes during Vitrification, *Vit Note 86/4*, Sellafield R&DD.

Klein, M., Weyers, C., Goosens, W. R. A., 1985, Behaviour of Ruthenium, Cesium and Antimony in High Temperature Processes for Waste Conditioning, *Radioactive Waste Management and the Nuclear Waste Cycle*, pp. 255-276.

Kolodziejczyk, A. H., 2013, Towards a Standard Methodology for Determining Hydrogen Storage in Nanoporous Materials, University of Bath, UK.

Kubota, M. And Fukase, T., 1980, Formation of Precipitate in High-Level Liquid Waste from Nuclear Fuel Reprocessing, *Journal of Nuclear Science and Technology*, Vol. 17, pp. 783-790.

Kustrowski, P., Wegrzyn, A., Rafalska-Lasocha, A., Pattek-Janczyk, A. And Dziembaj, R., 2005, Substitution of Fe<sup>3+</sup> for Al<sup>3+</sup> Cations in Layered Double Hydroxide [LiAl<sub>2</sub>(OH)<sub>6</sub>]<sub>2</sub>CO<sub>3</sub>.nH<sub>2</sub>O, *Clays and Clay Minerals*, Vol. 53, pp. 18-27.

Larkin, M. J., 1986, Development of Highly Active Waste Conditioning at Sellafield, *Nuclear Energy*, Vol. 25, pp. 343-354.

Li, F. B., Li, X. Z., Liu, C. S. And Liu, T. X., 2007, Effect of Alumina on Photocatalytic Activity of Iron Oxides for Bisphenol A Degradation, *Journal of Hazardous Materials*, Vol. 149, pp. 199-207.

- Li, J., Li, J., Luo, J., Wang, L. And He, X., 2011, Recent Advances in the LiFeO<sub>2</sub>-based Materials for Li-ion Batteries, International Journal of Electrochemical Science, Vol. 6, pp. 1550-1561.
- Li, L., Shi, L., Cao, S., Zhang, Y. And Wang, Y., 2008, LiNO<sub>3</sub> Molten Salt Assisted Synthesis of Spherical Nano-sized YSZ Powders in a Reverse Microemulsion System, Materials Letters, Vol. 62, pp. 1909-1912.
- Lutze, W. And Ewing, R. C., 1988, Radioactive Waste Forms for the Future, North-Holland, Amsterdam, The Netherlands.
- Madarasz, J., Varga, P. P. And Pokol, G., 2007, Evolved Gas Analyses (TG/DTA-MS and TG-FTIR) on Dehydration and Pyrolysis of Magnesium Nitrate Hexahydrate in Air and Nitrogen, Journal of Analytical and Applied Pyrolysis, Vol. 79, pp 475-478.
- Magnaldo, A., Masson, M. And Champion, R., 2007, Nucleation and Crystal Growth of Zirconium Molybdate Hydrate in Nitric Acid, Chemical Engineering Science, Vol. 62, pp. 766-774.
- Magrabi, C., 1981, The Role of Lithium in the Continuous Vitrification Process, R&DD - Vitrification Note 81/P78, Sellafield.
- Marples, J. A. C., 1988, The Preparation, Properties and Disposal of Vitrified High Level Waste form Nuclear Fuel Reprocessing, Glass Technology, Vol. 29, pp. 230-247.
- Mascalò, G. And Marino, O., 1980, A New Synthesis and Characterisation of Magnesium-Aluminium Hydroxides, Mineralogical Magazine, Vol. 43, pp. 619-621.
- Mattinson, M., 2013, OCM / SO for NNL Inspection Report No 461, Sellafield Ltd.
- Melkinov, P., Nascimento, V. A. And Arkhangelsky, I. V., 2014, Thermal Decomposition Mechanism of Iron (III) Nitrate and Characterization of Intermediate Products by the Technique of Computerized Modeling, Journal of Thermal Analysis and Calorimetry, Vol. 115, pp. 145-151.
- Morgan, S., Rose, P. B., Hand, R. J., Hyatt, N. C., Lee, W. E. And Scales, C. R., 2004, The Characterisation and Dissolution of High Level Waste Calcine in Alkali Borosilicate Glass, Ceramic Transactions, Volume 155, pp. 101-110.
- Morris, Y., 2010, Review of the Species Present in VTR Dust Scrubber Liquors and Calcines, NNL (10) 10750.

- Morris, Y. And Haig, A., 2010, Dust Scrubber Liquor and Dissolved Calcine Ru Volatility Studies 2009 – 2010, NNL (10) 10758.
- Moss, A. H., Haile, A. J., 2004, Investigation of Ruthenium Volatilisation from Dust Scrubber Recycle Vessel Liquor in Support of the Waste Vitrification Plant Fully Developed Safety Case (fdSC), RAT 594, BNFL.
- Motojima, K., 1989, Removal of Ruthenium from the PUREX process. Extraction of Ruthenium Tetroxide with Parafin Oil and Filtration of Ruthenium Dioxide, Journal of Nuclear Science and Technology, Volume 25, Issue 3, pp. 358-364.
- Nayak, M., Kutty, T. R. N., Jayaraman, V. And Periaswamy, G., 1997, Preparation of the Layered Double Hydroxide (LDH)  $\text{LiAl}_2(\text{OH})_7 \cdot 2\text{H}_2\text{O}$ , by Gel to Crystallite Conversion and a Hydrothermal Method, and its Conversion to Lithium Aluminates, Journal of Materials Chemistry, Vol. 7, pp. 2131-2137.
- Neepa, P., Biggs, S., Edmondson, M., Hunter, T. N. And Hammond, R. B., 2013, Characterising Highly Active Nuclear Waste Simulants, Chemical Engineering Research and Design, Vol. 91, pp. 742-751.
- Newby, B. J., Rhodes, D. W., 1978, Ruthenium Behaviour During Calcination, ICP-1164.
- Oldham, C., 2004, Underway on nuclear power: 50<sup>th</sup> anniversary of USS Nautilus, Faircount LLC, Michigan, USA.
- Owens, I. F., Leung, T. K. And Magrabi, C., 1985, The Reaction Chemistry of HAL Simulates, Lithium Nitrate and Sucrose under Calcination Conditions, BNFL Memorandum 754(w).
- Pacewska, B. And Keshr, M., 2004, Thermal Transformations of the Products of Partial Hydrolysis of Hydrous Aluminium Nitrate, Journal of Thermal Analysis and Calorimetry, Vol. 75, pp. 113-123.
- Pacewska, B. And Keshr, M., 2002, Thermal Transformations of Aluminium Nitrate Hydrate, Thermochimica Acta, Vol. 385, pp 73-80.
- Paulik, F., Paulik, J., Arnold, M. And Naumann, R., 1988, Investigation on the Thermal Behaviour of  $\text{Mg}(\text{NO}_3)_2 \cdot 6\text{H}_2\text{O}$ : I. The Decomposition Behaviour, Journal of Thermal Analysis, Vol. 34, pp 627-635.
- Pausch, I., Lohse, H.-H., Schürmann, K. And Allmann, R., 1986, Syntheses of Disordered and Al-rich Hydrotalcite-Like Compounds, Clays and Clay Minerals, Vol. 34, pp. 507-510.

- Perry, D. L., 2011, Handbook of Inorganic Compounds, 2<sup>nd</sup> Edition, Taylor and Francis Group, Florida, USA.
- Phillips, J. G. E., 1995, Table of Physical and Chemical Constants, 16<sup>th</sup> Edition, 3.2 Properties of Inorganic Compounds, Kaye & Laby Online Version 1.0 (2005), [www.kayelaby.npl.co.uk](http://www.kayelaby.npl.co.uk).
- Quill, L. L., Robey, R. F. And Seifter, S., 1937, The Rare Earth Metals and their Compounds: Thermal Analysis of Rare Earth Nitrate Mixtures, Industrial and Engineering Chemistry, Vol. 9, pp. 389-395.
- Ramshaw, C., Gribble, N. And Owens, I., 1992, An Assessment of the Performance of the Primary Off-Gas System During FSIF Trials C28, V29, C31 and V32, TDM 317, HLWPTC/92/P107.
- Rempe, N. T., 2008, Deep Geological Repositories, The Geological Society of America, Colorado, USA.
- Richardson, S., 2002a, Deconvolution of the 1978 – 1988 Magnox HAST Crystallisation Data, RAT (02) 2251, BNFL.
- Richardson, S., 2002b, Crystallisation as Determined by SEM3 for Magnox and Blended HASTs Including Acidity, Mg Levels and SFMAC Additions, RAT (02) 2471, BNFL.
- Richardson, S., Long, S. And Hall, R., 2000, Experimental Evidence for the Conversion of Caesium 1:12 Phosphomolybdate Solids to Zirconium Molybdate in Simulated Highly Active Raffinate Systems, BNFL R&T – RAT 469, Sellafield.
- Roe, J. I., 2003, Factor Influencing Operation of the WVP Dust Scrubber System, BNFL R&T, Sellafield.
- Roy, D. M., Roy, R. And Osborn, E. F., 1953, The System MgO-Al<sub>2</sub>O<sub>3</sub>-H<sub>2</sub>O and the Influence of Carbonate and Nitrate Ions on the Phase Equilibria, American Journal of Science, Vol. 251, pp. 337-361.
- Ruiz, M. L., Lick, I. D., Ponzi, M. L., Castellon, E. R., Jimenez-Lopez, A. And Ponzi E. N., 2010, Thermal Decomposition of Supported Lithium Nitrate Catalysts, Thermochemica Acta, Vol. 499, pp 21-26.
- Saburi, T., Murata, H., Suzuki, T., Fujii, Y. And Kiuchi, K., 2002, Oxygen Plasma Interactions with Molybdenum: Formation of Volatile Molybdenum Oxides, Journal of Plasma and Fusion Research, Vol. 78, pp. 3-4.



Safaei-Naeini, Y., Golestani-Fard, F., Khorasanizodeh, F., Aminzare, M. And Zhang, S., 2011, Low Temperature Molten Salt Synthesis of Nano Crystalline MgAl<sub>2</sub>O<sub>4</sub> Powder, Iranian Journal of Materials Science and Engineering, Vol. 8, pp. 23-28.

Sarsfield, M., 2004, Zirconium Chemistry of Acidic Systems – Part 1, NSTS (04) 5402.

Sarsfield, M. J., Crowley, D., Maxwell, K. P., 2008, Ruthenium Volatility Tests on Boiling VTR Dust Scrubber Liquor and Dissolved Calcine, Nexia Solutions (08) 9205.

Sarsfield, M. J., Jones, C. J., Brown, G. C., McKendrick, D., 2004, Ageing of HA Liquor Simulants – Phase 2; The Effects of Time on HA Liquor Simulants, NSTS (04) 5470, BNFL.

Sellafield Ltd, 2008, POG Normal Operations Presentation, Vitrification Assistance Training Package, Sellafield.

Shaheen, W. M. And Hong, K. S., 2002, Thermal Characterisation and Physicochemical Properties of Fe<sub>2</sub>O<sub>3</sub>-Mn<sub>2</sub>O<sub>3</sub>/Al<sub>2</sub>O<sub>3</sub> System, Thermochemica Acta, Vol. 381, pp. 153-164.

Short, R. J., 2012, VTR 4607 – Calciner Residence Time, NNL (12) 12179.

Short, R. J., 2010, Operational Envelope for 32% Magnox, NNL (09) 9744.

Short, R. J., 2010b, VTR 2924 – Simulant Specification for WRW17 – LF for Contract with Johnson Matthey, Technical Memorandum WV04771/06/09/04.

Short, R. J., 2010c, Updated Material Master VTR 1882 – Specification for WRW16 Material Master, Technical Memorandum WV04771/06/09/01.

Short, R. J., 2006, Dust Scrubber – Calcine Dissolution in Nitric Acid.

Short, R. J., 2006b, VTR 2984 - Laboratory scale trials of full Li base glass with Li-free Magnox HAL, Nexia Solutions (06) 7844.

Short, R. J., 2005, Report on Calcination Work Performed at PNNL, WA.

Short, R. J., 2005b, Calciner Setpoints for High Evaporative Loads, Nexia Solutions (05) 8177.

Singh, V., Chakradhar, R. P. S., Rao, J. L. And Kim, D-K., 2008, EPR and Luminescence Properties of Combustion Synthesized LiAl<sub>5</sub>O<sub>8</sub>:Mn Phosphors, Materials Chemistry and Physics, Vol. 110, pp. 43-51.

- Smolik, G. R., Petti, D. A. And Schuetz, S. T., 2000, Oxidation, Volatilization, and Redistribution of Molybdenum from TZM Alloy in Air, INEEL/EXT-99-01353, U.S Department of Energy, Idaho, USA.
- Spano, J. D., 2011, Solid-State NMR Studies of Polymeric and Biomembranes, Virginia Polytechnic Institute and State University, Blacksburg, Virginia, USA.
- Strydom, C. A. And van Vuuren, C. P. J., 1987, The Thermal Decomposition of Cerium (III) Nitrate, *Journal of Thermal Analysis*, Vol. 32, pp. 157-160.
- Sutrisno, A., Lei, L., Jinxiang, D., And Yining, H., 2012, Solid-State  $^{91}\text{Zr}$  NMR Characterization of Layered and Three-Dimensional Framework Zirconium Phosphates, *Journal of Physical Chemistry C*, Vol 116, pp. 17070–17081.
- Svensk Karnbranslehantering AB, 2006, Our Method of Final Disposal. Available: [http://www.skb.se/Templates/Standard\\_\\_\\_\\_24109.aspx](http://www.skb.se/Templates/Standard____24109.aspx) (Accessed: 3<sup>rd</sup> February 2010).
- Tadros, N. And Metwally, E., 2006, Adsorption of some Radionuclides from their Aqueous Solutions using Zirconium Molybdate Ion Exchanger, *Radiochemistry*, Vol. 48, pp 387-391.
- Talford, M., 2003, Managing and Developing the WVP Dust Scrubber, BNFL HLWP Technical Report, HLWTC321.
- Tangri, R. P., Venugopal, V. And Bose, D. K., 1994, Standard Molar Enthalpy of Formation of Lithium Molybdates ( $\text{Li}_2\text{Mo}_n\text{O}_{3n+1}$  with  $n = 1, 2, 3$  and 4) at 298.15 K, *Journal of Alloys and Compounds*, Vol. 205, pp. 129-133.
- Tatibouet, J-M., Montalescot, C., Bruckman, K., Haber, J. And Che, M., 1997, A Two-Step Transformation of the Magnesium Salt of Phosphomolybdic Acid  $\text{HMgPMo}_{12}\text{O}_{40}$  Supported on Silica, *Journal of Catalysis*, Vol. 169, pp. 22-32.
- Taylor, T. A., Crowley, D. M. And Brown, G. C., 2014, VTR 5004 – Calcination of Zirconium Molybdate, NNL (14) 12864.
- The Generation IV International Forum, 2008, Annual Report 2008. Available: <http://www.gen-4.org/Technology/evolution.htm> (Accessed: 4<sup>th</sup> November 2009).
- Tsuchida, T. And Sugimoto, K., 1990, Effect of Grinding of Mixtures of Goethite and Hydrated Alumina on the Formation of  $\text{Fe}_2\text{O}_3\text{-Al}_2\text{O}_3$  Solid Solutions, *Thermochimica Acta*, Vol. 170, pp. 41-50.

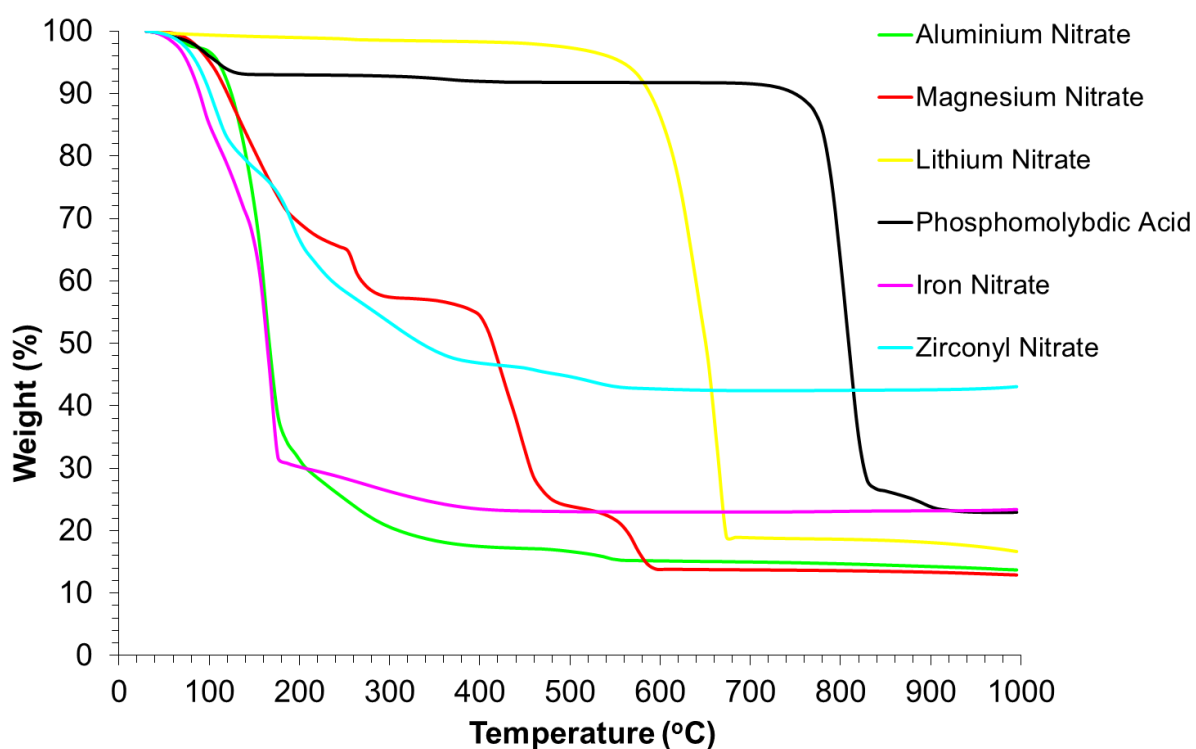
- Turner, E., 2007, VTR 3391 – Results of Full Scale Trials Using a Pressure Washer for Cleaning Instrument Lines, Nexia Solutions (07) 8573.
- Undre, I., 1985, FSIF Run C17:- Calcination Run for Optimising Sucrose Concentration for use on FSIF and WVP Flowsheets, RM 213283, Calcination No. 227.
- United States Nuclear Regulatory Commission, 2009, PWR Schematic. Available: <http://www.nrc.gov/.../teachers/pwr-schematic.html> (Accessed: 16<sup>th</sup> April 2010).
- Veyer, C., 1995, Technical Note – Calciner Tube Knowledge File: Revision A, COGEMA.
- Vickers, J., 2006a, Calcination of Magnox HAL Simulants With and Without Lithium in the VTR, Nexia Solutions (06) 7499.
- Vickers, J., 2006b, Calcination of Old Side HAL Simulants With and Without Lithium in the VTR, Nexia Solutions (06) 7659.
- Vickers, J., 2006c, Calcination of Blended HAL Simulants With and Without Lithium in the VTR, Nexia Solutions (06) 7660.
- Waring, J., 1999, A Literature Review on the Behaviour of Ruthenium During Vitrification of High Level Waste and Implications for Discharges from the Sellafield WVP Plant, RDR 1658, BNFL.
- Watson, B., 1997, Enquiry number 97/32 – Final Report – Group Board of Enquiry into the Ruthenium Stack Release, BNFL.
- Webb, K. J., 2014, Central Laboratory Facilities Work Request Form, Issue 22, IMS\_GN\_SEL\_101A, NNL.
- Webb, K. J., 2012, Laboratory Good Practice Guide, IMS\_GN\_SEL\_061, NNL.
- Weisenburger, S., Weiss, K., 1980, Ruthenium Volatility Behaviour During HLLW-Vitrification in a Liquid-Fed Ceramic Waste Melter, Processing of Nuclear Wastes, pp. 901-910.
- Wills, R., 2002, Assessment of the Lithium Nitrate and Sugar Additions to the Vitrification Process, HLWTC/226, BNFL.
- Wilson, M., 2013, Review into Maintaining and Developing the Small Scale Calciner, WV08082/06/10/05, NNL.

- Wilson, P. D., 1996, *The Nuclear Fuel Cycle: From Ore to Waste*, Oxford Science Publications, Oxford, UK.
- Wong, A., 2001, *Solid-State Nuclear Magnetic Resonance of Alkali Metals in Antibiotic Ionophore Complexes*, Queens University, Kingston, Ontario, Canada.
- World Nuclear Association, 2008a, *Fast Neutron Reactors*. Available: <http://www.world-nuclear.org/info/inf98.html> (Accessed: 27<sup>th</sup> September 2009).
- World Nuclear Association, 2008b, *Waste Management: Overview*. Available: <http://www.world-nuclear.org/education/wast.htm> (Accessed: 27<sup>th</sup> September 2009).
- World Nuclear Association, 2009, *Processing of Used Nuclear Fuel*. Available: <http://www.world-nuclear.org/info/Nuclear-Fuel-Cycle/Fuel-Recycling/Processing-of-Used-Nuclear-Fuel> (Accessed: 27<sup>th</sup> September 2009).
- World Nuclear Association, 2010, *Outline History of Nuclear Energy*. Available: <http://www.world-nuclear.org/info/Current-and-Future-Generation/Outline-History-of-Nuclear-Energy/> (Accessed: 10<sup>th</sup> March 2010).
- Wright, J. D., Brace, J. W., 2004, *Ruthenium Volatilisation Experiments in Support of the Waste Vitrification Plant (WVP) Safety Case, HLWTC 394 P(04)/NSTS 4394*, Nexia Solutions.
- Wright, J. D., Brown, G. C., 2003, *Ruthenium Volatilisation Experiments in Support of the Waste Vitrification Plant (WVP) Safety Case, HLWTC 315 P(03)/RAT 3874*, BNFL.
- Xu, T., Zhou, X., Jiang, Z., Kuang, Q., Xie, Z. And Zheng, L., 2009, *Syntheses of Nano/Submicrostructured Metal Oxides with all Polar Surfaces Exposed via a Molten Salt Route*, *Crystal Growth and Design*, Vol. 9, pp. 192-196.
- Yuvaraj, S., Fan-Yuan, L., Tsong-Huei, C. And Chuin-Tih, Y., 2003, *Thermal Decomposition of Metal Nitrates in Air and Hydrogen Environments*, *Journal of Physical Chemistry B*, Vol. 107, pp 1044-1047.
- Zalewicz, M. And Trzesowska A., 2004, *The Coupled TG-MS Investigations of Lanthanide (III) Nitrate Complexes with Hexamethylenetetramine*, *Journal of Thermal Analysis and Calorimetry*, Vol. 78, pp. 525–534.
- Zhang, F., Du, N., Song, S., Liu, J. And Hou, W., 2013, *Mechano-hydrothermal Synthesis of Mg<sub>2</sub>Al-NO<sub>3</sub> Layered Double Hydroxides*, *Journal of Solid State Chemistry*, Vol. 206, pp 45-50.

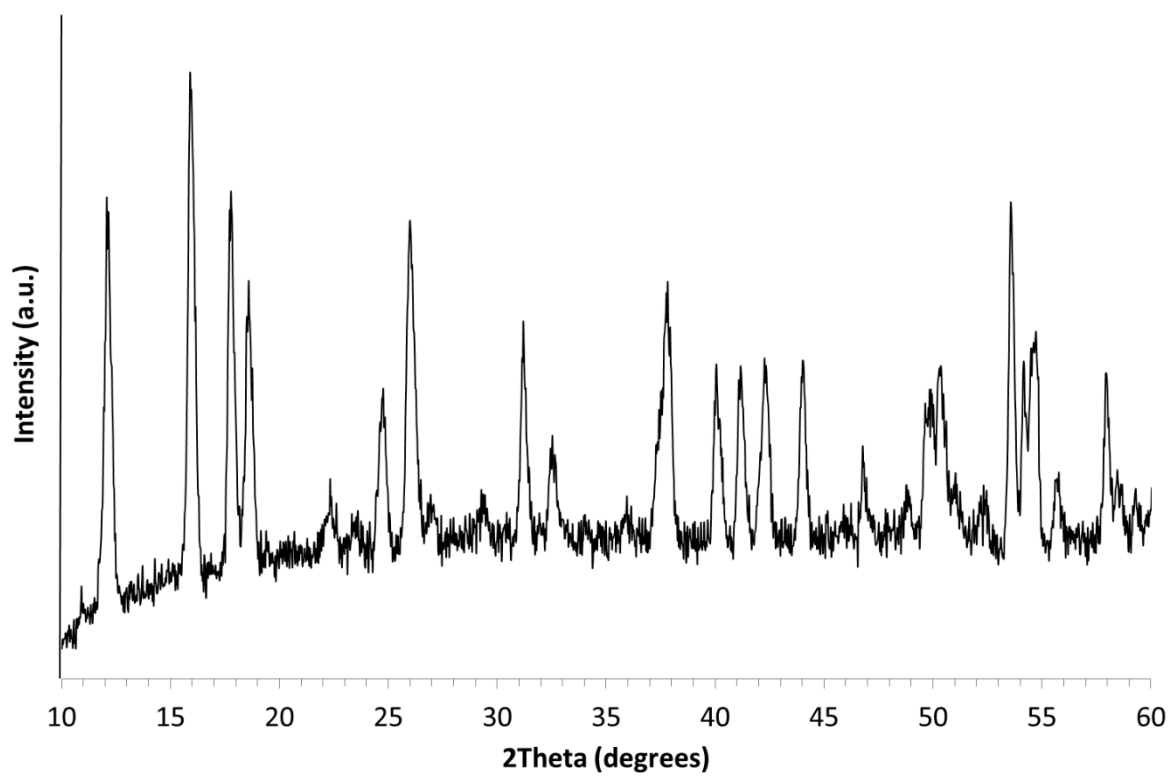
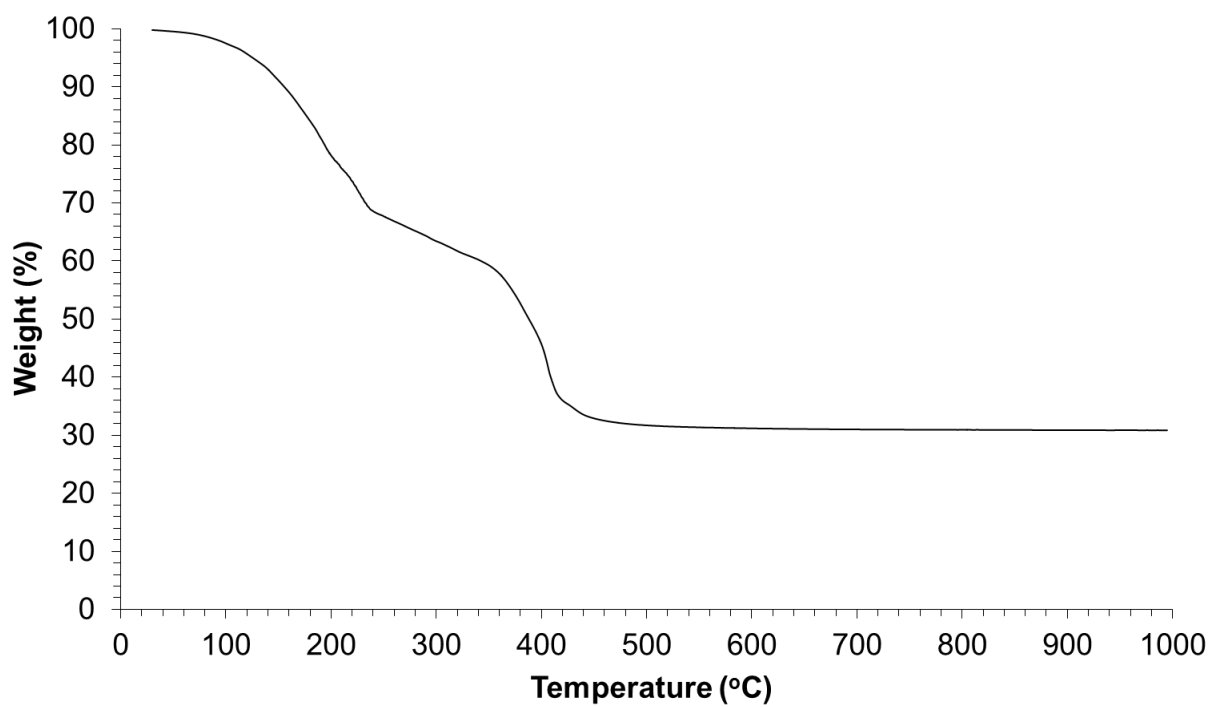
Zhang, S., 2007, Low Temperature Synthesis of Complex Refractory Oxide Powders from Molten Salts, J Pak Mat Soc, Vol. 1, pp. 49-53.

Zhang, X. And Li, S., 2013, Mechanochemical Approach for Synthesis of Layered Double Hydroxides, Applied Surface Science, Vol. 274, pp. 158-163.

## 10. Appendix



Appendix 1 – TGA analysis of the starting materials



Appendix 2 – TGA and XRD analysis of  $\text{Mg}_3\text{RE}_2(\text{NO}_3)_{12} \cdot 24\text{H}_2\text{O}$

### Appendix 3 - Sample Preparation Table

Sample Name	Anhydrous Lithium Nitrate	Aluminium Nitrate Nonahydrate	Magnesium Nitrate Hexahydrate	Iron Nitrate Nonahydrate	Chromium Nitrate Nonahydrate	Phospho-molybdic Acid	Zirconyl Nitrate (161 g / l)	Nitric Acid (16 M)	Sugar Solution (200 g / l)	Water
LAN1	1.739 g	7.481 g	-	-	-	-	-	4.588 g	3.349 g	36.192 g
LMN1	1.885 g	-	7.335 g	-	-	-	-	4.588 g	3.339 g	36.192 g
LIN1	3.171 g	-	-	6.049 g	-	-	-	4.588 g	3.494 g	36.192 g
LPN1	2.711 g	-	-	-	-	6.509 g	-	4.588 g	2.230 g	36.192 g
LZN1	6.824 g	-	-	-	-	-	14.875 g	4.588 g	4.199 g	23.713 g
AMN1	-	4.841 g	4.379 g	-	-	-	-	4.588 g	3.053 g	36.192 g
AIN1	-	6.387 g	-	2.833 g	-	-	-	4.588 g	3.033 g	36.192 g
MIN1	-	-	6.187 g	3.033 g	-	-	-	4.588 g	3.001 g	36.192 g
PZN1	-	-	-	-	-	8.044 g	7.307 g	4.588 g	1.517 g	30.061 g
LAMN1	1.003 g	4.315 g	3.903 g	-	-	-	-	4.588 g	3.214 g	36.192 g
LAIN1	1.279 g	5.502 g	-	2.440 g	-	-	-	4.588 g	3.244 g	36.192 g
LMIN1	1.356 g	-	5.726 g	2.587 g	-	-	-	4.588 g	3.312 g	36.192 g
LPZN1	2.457 g	-	-	-	-	5.899 g	5.357 g	4.588 g	2.323 g	31.697 g
AMN2	-	4.315 g	3.903 g	-	-	-	-	5.936 g	3.214 g	36.192 g
AIN2	-	5.502 g	-	2.440 g	-	-	-	6.307 g	3.244 g	36.192 g
MIN2	-	-	5.726 g	2.587 g	-	-	-	6.411 g	3.312 g	36.192 g
PZN2	-	-	-	-	-	5.899 g	5.357 g	7.891 g	2.323 g	31.697 g
LAMCN1	0.959 g	4.126 g	3.731 g	-	0.401 g	-	-	4.588 g	3.202 g	36.192 g
AMCN2	-	4.126 g	3.731 g	-	0.401 g	-	-	5.877 g	3.202 g	36.192 g
AMCN1	-	4.607 g	4.167 g	-	0.448 g	-	-	4.588 g	3.048 g	36.192 g

#### Appendix 4 - Molar ratios of elements

Sample Name	Molar Ratios of Elements Present in the Sample								
	Li	Al	Mg	Fe	Cr	P	Mo	Zr	C
LAN1	1.3	1.0	-	-	-	-	-	-	0.5
LMN1	1.0	-	1.0	-	-	-	-	-	0.4
LIN1	3.1	-	-	1.0	-	-	-	-	0.7
LPN1	1.0	-	-	-	-	0.1	1.1	-	0.2
LZN1	1.5	-	-	-	-	-	-	1.0	0.2
AMN1	-	1.0	1.3	-	-	-	-	-	0.7
AIN1	-	2.4	-	1.0	-	-	-	-	1.3
MIN1	-	-	3.2	1.0	-	-	-	-	1.2
PZN1	-	-	-	-	-	0.1	1.7	1.0	0.1
LAMN1	1.3	1.0	1.3	-	-	-	-	-	0.8
LAIN1	1.3	1.0	-	0.4	-	-	-	-	0.6
LMIN1	3.1	-	3.2	1.0	-	-	-	-	1.5
LPZN1	1.5	-	-	-	-	0.1	1.7	1.0	0.3
AMN2	-	1.0	1.3	-	-	-	-	-	0.8
AIN2	-	2.4	-	1.0	-	-	-	-	1.6
MIN2	-	-	3.2	1.0	-	-	-	-	1.5
PZN2	-	-	-	-	-	0.1	1.7	1.0	0.3
LAMCN1	1.3	1.0	1.3	-	0.1	-	-	-	0.9
AMCN2	-	1.0	1.3	-	0.1	-	-	-	0.9
AMCN1	-	1.0	1.3	-	0.1	-	-	-	0.7